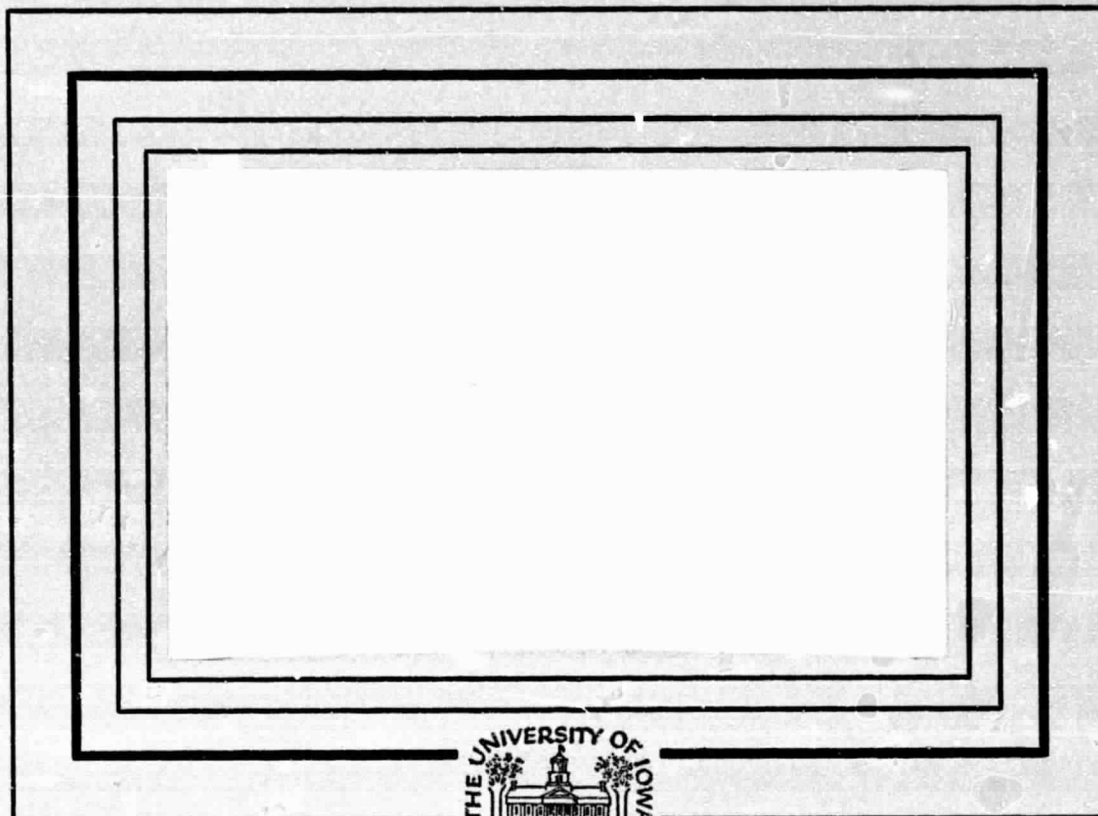


N O T I C E

THIS DOCUMENT HAS BEEN REPRODUCED FROM
MICROFICHE. ALTHOUGH IT IS RECOGNIZED THAT
CERTAIN PORTIONS ARE ILLEGIBLE, IT IS BEING RELEASED
IN THE INTEREST OF MAKING AVAILABLE AS MUCH
INFORMATION AS POSSIBLE

NASA CR-160024



{NASA-CR-160024} IMP-8. VOLUME 2:
SCIENTIFIC SECTION Final Report (Iowa
Univ.) 335 p HC A15/MF A01 CSCL 22A

N80-33451

Unclas
G3/15 28856



Department of Physics and Astronomy
THE UNIVERSITY OF IOWA

Iowa City, Iowa 52242

IMP-8 FINAL REPORT

Volume Two

Scientific Section

NASA Contract NAS5-11431

May, 1980

The scientific section of this report presents results of the analysis of the IMP-8 data, which was collected during the first six and one-half years after launch of the IMP-8 spacecraft. Essentially, all of the plasma wave experiment data has been processed and is available in an easily accessible summary form. These data continue to provide a valuable source for comparative studies with plasma wave experiments on other spacecraft operating in the solar wind and within the Earth's magnetosphere (S³-A, IMP-6, Helios-A and -B, ISEE-1 and -2, Hawkeye). In addition, reduced data has been submitted to the National Space Science Data Center, and this data is presently being used for additional research beyond that performed by the plasma wave group at the University of Iowa.

The scientific results of research carried out by the University of Iowa group are presented in this section. As in the past, the IMP-8 spacecraft continues to provide a strong base for independent and correlative study of the Earth's magnetosphere and the solar wind. Under the IMP-8 contract detailed studies have been made of such phenomenon as Type-III radio bursts and electromagnetic emissions and boundary layers in the Earth's magnetosphere. The following abstracts are from the published papers and reports that present the results of this study, which is continuing as a part of current data analysis efforts with experiments on other spacecraft. Copies of the entire papers are also included as Appendix A of this section of the final report.

1. Donald A. Gurnett
 "The Earth as a Radio Source: Terrestrial Kilometric Radiation"
J. Geophys. Res., 79, 4227, 1974

Radio wave experiments on the IMP 6 and 8 satellites have shown that the Earth emits very intense electromagnetic radiation in the frequency range of about 50-500 kHz. At peak intensity the total power emitted in this frequency range is about 10^9 W. The Earth is therefore a very intense planetary radio source, with a total power output comparable to the decametric radio emission from Jupiter. We refer to this radio emission from the Earth as terrestrial kilometric radiation. Terrestrial kilometric radiation appears to originate from low altitudes (less than $3.0 R_E$) in the auroral region. The intensity of the noise has a pronounced dependence on both the local time and the magnetic latitude of the observing point. At large radial distances the radiation is primarily observed on the poleward side of two cone-shaped surfaces that are centered on the Earth and symmetrically located with respect to the northern and southern auroral zones. The magnetic latitude of the cone-shaped boundaries varies from greater than 50° in the local morning to near the magnetic equator in the local evening. Poleward of these boundaries the noise occurs in sporadic 'storms' lasting from 1/2 hour to several hours. Comparisons with auroral photographs obtained from the low-altitude polar-orbiting Dapp satellite show that the terrestrial kilometric radiation is closely correlated with the occurrence of discrete auroral arcs, which occur in the local evening region of the auroral zone. This association indicates that the kilometric radiation is probably generated by intense 'inverted V' electron precipitation bands, which cause the discrete auroral arcs. Possible mechanisms that can explain the generation and propagation of the terrestrial kilometric radiation are discussed.

2. Paul Rodriguez and Donald A. Gurnett
 "Electrostatic and Electromagnetic Turbulence Associated With the Earth's Bow Shock"
J. Geophys. Res., 80, 19, 1975

The electric and magnetic field spectral densities of plasma waves in the Earth's bow shock have been measured in the frequency range 20 Hz to 200 kHz by using two 16-channel spectrum analyzers on the IMP 6 spacecraft. The electric field spectrum in the bow shock consists of two distinct components: one component has a broad peak typically centered between 200 and 800 Hz with an average (5.12-s time constant) spectral density at the peak of about $10^{-9} \text{ V}^2 \text{ m}^{-2} \text{ Hz}^{-1}$, and the other component increases monotonically with decreasing frequency approximately as $f^{-(2.0 \pm 0.5)}$ and has an average spectral density of about $3.0 \times 10^{-9} \text{ V}^2 \text{ m}^{-2} \text{ Hz}^{-1}$ at 36.0 Hz. The magnetic field spectrum in the shock has only one component that increases monotonically with decreasing frequency approximately as $f^{-(4.0 \pm 0.5)}$ and has an upper cutoff frequency near the local electron gyrofrequency. This magnetic field spectrum appears to be associated with the monotonic component of the electric field spectrum. The electric to magnetic energy density ratio ϵ_E/ϵ_B of

this noise is about 10^{-3} to 10^{-4} , which is consistent with the energy density ratio expected for electromagnetic whistler mode waves in the bow shock. The broad peak in the electric field spectrum between 200 and 800 Hz has a large electric to magnetic energy density ratio, $\sim 10^2$ to 10^3 , indicating that this component consists of almost purely electrostatic waves. Electrostatic noise with a spectrum similar to the turbulence in the shock but with lower intensities is observed throughout the magnetosheath region downstream of the shock. This magnetosheath electric field turbulence often includes many bursts with a distinct "parabolic" frequency-time variation on a time scale of a few seconds. Spin modulation measurements of the electric field direction show that the electric field vectors in both the shock transition region and the magnetosheath region are preferentially oriented parallel to the static magnetic field direction. The electric field of upstream electron plasma oscillations also is oriented parallel to the static magnetic field.

3. William S. Kurth, Mark M. Raumbach, and Donald A. Gurnett
 "Direction-Finding Measurements of Auroral Kilometric Radiation"
J. Geophys. Res., 80, 2764, 1975

Direction-finding measurements with plasma wave experiments on the Hawkeye 1 and IMP 8 satellites are used to locate the source region of auroral kilometric radiation. This radiation has peak intensities between about 100 and 300 kHz and is emitted in intense sporadic bursts lasting for from half an hour to several hours. At peak intensity the total power emitted in this frequency range exceeds 10^9 W. The occurrence of this radiation is known to be closely associated with bright auroral arcs which occur in the local evening auroral regions. Hawkeye 1 provides direction-finding measurements of kilometric radiation from observations at high latitudes ($5-20R_E$) over the northern polar regions, and IMP 8 provides similar observations at large radial distances ($23-46 R_E$) near the equatorial plane. Results from both satellites place the source of the intense auroral kilometric radiation in the late local evening at about 22.0 hours LT and at a distance of about $0.75 R_E$ from the polar axis of the Earth. These direction-finding measurements, together with earlier results from the IMP 6 satellite, strongly indicate that the intense auroral kilometric radiation generated by energetic auroral electrons at low altitudes in the evening auroral zone. The observed source location is in good quantitative agreement with the source position expected from simple propagation and ray path consideration.

4. Donald A. Gurnett
 "The Earth as a Radio Source: The Nonthermal Continuum"
J. Geophys. Res., 80, 2751, 1975

In addition to the intense and highly variable auroral kilometric radiation the Earth also radiates a weak nonthermal continuum from energetic electrons in the outer radiation zone. The intensity of this continuum radiation decreases with increasing frequency and is usually below the cosmic noise level at frequencies above 100 kHz. In this

paper we show that the frequency spectrum of the continuum radiation consists of two components, a trapped component, which is permanently trapped within the magnetosphere at frequencies below the solar wind plasma frequency, and an escaping component, which propagates freely away from the Earth at frequencies above the solar wind plasma frequency. The low-frequency cutoff of the continuum radiation spectrum is at the local electron plasma frequency, which can be as low as 500 Hz in the low-density regions of the distant magnetotail. Direction-finding measurements and measurements of the spatial distribution of intensity for both the trapped and the freely escaping components are used to determine the region in which the continuum radiation is generated. These measurements all indicate that the continuum radiation is generated in a broad region which extends through the morning and early afternoon from about 4.0 to 14.0 hours local time immediately beyond the plasmopause boundary. In contrast to the auroral kilometric radiation, which is generated in the high-latitude auroral zone regions, the continuum radiation appears to be generated over a broad range of latitudes, including the magnetic equator. In some cases the continuum radiation appears to be closely associated with intense bands of electrostatic noise which are observed near the electron plasma frequency at the plasmopause. Possible mechanisms by which this radiation could be generated, including gyrosynchrotron radiation from energetic electrons in the outer radiation zone, are discussed.

5. D. A. Gurnett and L. A. Frank
 "Continuum Radiation Associated With Low-Energy Electrons in the Outer Radiation Zone"
J. Geophys. Res., 81, 3875, 1976

A weak nonthermal continuum radiation is generated by the Earth's magnetosphere in the frequency range from about 500 Hz to greater than 100 kHz. During magnetically disturbed periods the intensity of this continuum radiation increases significantly, by as much as 20 dB during large disturbances. In this paper we present a series of observations obtained by the Hawkeye 1 and IMP 8 spacecraft during a period of greatly enhanced continuum radiation intensity which occurred from October 14-21, 1974. The enhanced continuum radiation intensities observed during this event are found to be closely correlated with the injection of very intense fluxes of energetic, ~ 1 -30 keV, electrons into the outer radiation zone. Direction-finding measurements of the continuum radiation observed during this event show that the radiation is primarily coming from the dawn side of the magnetosphere, in agreement with the observed dawn-dusk asymmetry in the 1-to 30-keV electron distribution. These results suggest that the continuum radiation may be generated by a coherent plasma instability involving relatively low-energy, ~ 1 to 30 keV, electrons rather than by gyrosynchrotron radiation from very energetic, 200 keV to 1 MeV, electrons as has been previously suggested.

6. Mark M. Baumbach, William S. Kurth, and Donald A. Gurnett
"Direction-Finding Measurements of Type III Radio Bursts Out of the
Ecliptic Plane"
Solar Physics, 48, 361, 1976

Direction-finding measurements with the plasma wave experiments on the HAWKEYE 1 and IMP 8 satellites are used to find the source locations of type III solar radio bursts in heliocentric latitude and longitude in a frequency range from 31.1 kHz to 500 kHz. IMP 8 has its spin axis perpendicular to the ecliptic plane; hence, by analyzing the spin modulation of the received signals the location of the type III burst projected into the ecliptic plane can be found. Hawkeye 1 has its spin axis nearly parallel to the ecliptic plane; hence, the location of the source out of the ecliptic plane may also be determined. Using an empirical model for the emission frequency as a function of radial distance from the sun the three-dimensional trajectory of the type III radio source can be determined from direction-finding measurements at different frequencies. Since the electrons which produce these radio emissions follow the magnetic field lines from the Sun these measurements provide information on the three-dimensional structure of the magnetic field in the solar wind. The source locations projected into the ecliptic plane follow an Archimedean spiral. Perpendicular to the ecliptic plane the source locations usually follow a constant heliocentric latitude. When the best fit magnetic field line through the source locations is extrapolated back to the Sun this field line usually originates within a few degrees from the solar flare which produced the radio burst. With direction-finding measurements of this type it is also possible to determine the source size from the modulation factor of the received signals. For a type III event on June 8, 1974, the half angle source size was measured to be $\sim 60^\circ$ and 500 kHz and $\sim 40^\circ$ at 56.2 kHz as viewed from the Sun.

7. Donald A. Gurnett
"The Earth as a Radio Source"
Magnetospheric Particles and Fields, B. M. McCormac, Ed.,
Reidel Publishing Co., Dordrecht, Holland, 1976.

Satellite low frequency radio measurements have revealed that the Earth is a very intense and interesting radio source with characteristics similar to other astronomical radio sources such as Jupiter, Saturn and the Sun. In this paper we summarize the primary characteristics of radio emissions from the Earth's magnetosphere, consider the origin of these emissions, and discuss the similarities to other astronomical radio sources.

8. D. A. Gurnett, L. A. Frank, and R. P. Lepping
"Plasma Waves in the Distant Magnetotail"
J. Geophys. Res., 81, 6059, 1976

In this study we identify the principal types of plasma waves which occur in the distant magnetotail, and we investigate the relationship of these waves to simultaneous plasma and magnetic field measurements made

on the same spacecraft. The observations used in this study are from the IMP 8 spacecraft, which passes through the magnetotail at radial distances ranging from about 23.1 to 46.3 R_E . Three principal types of plasma waves are detected by IMP 8 in the distant magnetotail: broad band electrostatic noise, whistler mode magnetic noise bursts, and electrostatic electron cyclotron waves. The electrostatic noise is a broad band emission which occurs in the frequency range from about 10 Hz to a few kilohertz and is the most intense and frequently occurring type of plasma wave detected in the distant magnetotail. This noise is found in regions with large gradients in the magnetic field near the outer boundaries of the plasma sheet and in region with large plasma flow speeds, 10^3 km s^{-1} , directed either toward or away from the Earth. The whistler mode magnetic bursts observed by IMP 8 consist of nearly monochromatic tones which last from a few seconds to a few tens of seconds. These noise bursts occur in the same region as the broad band electrostatic noise, although much less frequently, and are thought to be associated with regions carrying substantial field-aligned currents. Electrostatic electron cyclotron waves are seldom detected by IMP 8 in the distant magnetotail. Although these waves occur very infrequently, they may be of considerable importance, since they have been observed in regions near the neutral sheet when the plasma is extremely hot.

9. D. A. Gurnett and L. A. Frank
"A Region of Intense Plasma Wave Turbulence on Auroral Field Lines"
J. Geophys. Res., 82, 1031, 1977

Plasma wave measurements from the Hawkeye 1 and IMP 6 satellites show that a broad region of intense plasma wave turbulence occurs on the high-latitude auroral field lines at altitudes ranging from a few thousand kilometers in the ionosphere to many earth radii in the distant magnetosphere. This turbulence occurs in an essentially continuous band on the auroral L shells at all local times around the Earth and its most intense during periods of auroral activity. The electric field intensity of this turbulence is often quite large, with maximum field strengths of about 10 mVm^{-1} and peak intensities in the frequency range 10-50 Hz. Magnetic field perturbations indicative of field-aligned currents and weak bursts of whistler mode magnetic noise are also observed in the same region as the electric field turbulence. In the local afternoon and evening the electric field turbulence is closely associated with V-shaped auroral hiss emissions. In some cases the electric field turbulence appears as a lowering and intensification of the low-frequency portion of the auroral hiss spectrum. Comparisons with plasma measurements and with similar measurements from other satellites strongly suggest that this plasma wave turbulence occurs on magnetic field lines which connect with regions of intense inverted V electron precipitation at low altitudes and with regions of intense earthward plasma flow in the distant magnetotail. The plasma instabilities which could produce this turbulence and the possible role which this turbulence may play in the heating and acceleration of the auroral particles are considered.

10. Donald A. Gurnett
"Electrostatic Turbulence in the Magnetosphere"
Physics of Solar Planetary Environments, Vol. II, ed. by D. J.
Williams, American Geophysical Union, Washington, DC 760, 1976

Plasma wave measurements from the IMP 6, IMP 8 and Hawkeye 1 satellites show that a broad region of intense low-frequency electric field turbulence occurs on the high latitude auroral field lines at altitudes ranging from a few thousand kilometers in the ionosphere to many earth radii in the distant magnetosphere. A qualitatively similar, but less intense, type of electric field turbulence is also observed at the plasmopause during magnetic storms. In the auroral regions the turbulence occurs in an essentially continuous band on the auroral L-shells at all local times around the Earth and is most intense during periods of auroral activity. In this paper we summarize the basic characteristics of this electric field turbulence and consider the possible role this turbulence may play in the heating and acceleration of plasma in the magnetosphere.

11. James Lauer Green, Donald A. Gurnett, and Stanley D. Shawhan
"The Angular Distribution of Auroral Kilometric Radiation"
J. Geophys. Res., 82, 1825, 1977

Measurements of the angular distribution of auroral kilometric radiation (AKR) are presented by using observations from the Hawkeye 1, IMP 6, and IMP 8 satellites. The University of Iowa plasma wave experiments on Hawkeye 1 and IMP 6 provide electric field measurements of AKR in narrow frequency bands centered at 178, 100, and 56.2 kHz, and the IMP 8 experiment provides measurements at 500 kHz. From a frequency of occurrence survey, at radial distances greater than $7 R_E$ (earth radii) it is shown that AKR is preferentially and instantaneously beamed into solid angles of approximately 3.5 sr at 178 kHz, 1.8 sr at 100 kHz, and 1.1 sr at 56.2 kHz, directed upward from the nighttime auroral zones. Simultaneous multiple satellite observations of AKR in the northern hemisphere show that the radiation occurs simultaneously throughout these solid angles and that the plasmopause acts as an abrupt propagation cutoff on the nightside of the Earth. No comparable cutoff is observed at the plasmopause on the dayside of the Earth.

The results of computer ray tracing calculations for both the right-hand (R-X) and left-hand (L-O) polarized modes are also presented in an attempt to understand the propagation characteristics of the magnetic field line at 70° invariant latitude near local midnight. The approximate altitude of the source can be determined for each of the two modes of propagation by adjusting the source altitude to give the best fit to the observed angular distribution. The R-X mode is found to give the best agreement with the observed angular distributions.

12. G. R. Voots and D. A. Gurnett
"Auroral Kilometric Radiation as an Indicator of Auroral Magnetic Disturbances"
J. Geophys. Res., 82, 2259, 1977

Satellite low-frequency radio measurements have shown that an intense radio emission from the Earth's auroral regions called auroral kilometric radiation is closely associated with auroral and magnetic disturbances. In this paper we present a detailed investigation of this relationship, using the auroral electrojet (AE) index as an indicator of auroral magnetic disturbances and radio measurements from the IMP 6 spacecraft. This study indicates that the mean power flux of the 178-kHz radiation tends to be proportional to $(AE)^{1,2}$ for $AE > 100 \gamma$. The correlation coefficient between $\log AE$ and the logarithm of the power flux is 0.514. Occasionally, a kilometric radiation event is detected which is not detected by the ground magnetometer stations, even though an auroral substorm is in progress. This study shows that the remote detection of kilometric radio emissions from the Earth can be used as a reasonably reliable indicator of auroral substorm activity.

13. D. A. Gurnett, M. M. Baumbach, and H. Rosenbauer
"Stereoscopic Direction Finding Analysis of a Type III Solar Radio Burst: Evidence for Emission at $2f_p^-$ "
J. Geophys. Res., 83, 616, 1978

Stereoscopic direction finding measurements from the IMP 8, Hawkeye 1, and Helios 2 spacecraft over base line distances of a substantial fraction of an astronomical unit are used to directly determine the three-dimensional trajectory of a type III solar radio burst. By comparing the observed source positions with the direct in situ solar wind plasma density measurements obtained by Helios 1 and 2 near the sun relationship of the emission frequency to the local plasma frequency can be determined directly without any modeling assumptions. These comparisons show that the type III radio emission occurs near the second harmonic, $2f_p^-$, of the local electron plasma frequency. Other characteristics of the type III radio emission, such as the source size, which can be obtained from this type of analysis are also discussed.

14. D. A. Gurnett and L. A. Frank
"Ion Acoustic Waves in the Solar Wind"
J. Geophys. Res., 83, 58, 1978

Plasma wave measurements on the Helios 1 and 2 spacecraft have revealed the occurrence of electric field turbulence in the solar wind at frequencies between the electron and ion plasma frequencies. Wavelength measurements with the IMP 6 spacecraft now provide strong evidence that these waves are short wavelength ion acoustic waves which are Doppler-shifted upward in frequency by the motion of the solar wind. Comparison of the Helios results with measurements from the Earth-orbiting IMP 6 and 8 spacecraft shows that the ion acoustic wave turbulence detected in interplanetary space has characteristics essentially

identical to those of bursts of electrostatic turbulence generated by protons streaming into the solar wind from the Earth's bow shock. In a few cases, enhanced ion acoustic wave intensities have been observed in direct association with abrupt increases in the anisotropy of the solar wind electron distribution. This relationship strongly suggests that the ion acoustic waves detected by Helios far from the Earth are produced by an electron heat flux instability, as was suggested by Forslund. Possible related mechanisms which could explain the generation of ion acoustic waves by protons streaming into the solar wind from the Earth's bow shock are also considered.

15. Donald A. Gurnett

"Electromagnetic Plasma Wave Emissions From the Auroral Field Lines"

J. Geomag. Geoelectr., 30, 257, 1978

Several types of electromagnetic waves are known to be emitted by charged particles on the auroral field lines. In this paper we review the most important types of auroral radio emissions, both from a historical perspective as well as considering the latest results. Particular emphasis is placed on four types of electromagnetic emissions which are directly associated with the plasma on the auroral field lines. These emissions are (1) auroral hiss, (2) saucers, (3) ELF noise bands, and (4) auroral kilometric radiation. Ray tracing and radio direction finding measurements indicate that both the auroral hiss and auroral kilometric radiation are generated along the auroral field lines relatively close to the Earth, at radial distances from about 2.5 to 5 R_E , probably in direct association with the acceleration of auroral particles by parallel electric fields. The exact mechanism by which these radio emissions are generated has not been firmly established. For the auroral hiss the favored mechanism appears to be amplified Cerenkov radiation. For the auroral kilometric radiation several mechanisms have been proposed, usually involving the intermediate generation of electrostatic waves by the precipitating electrons.

16. D. A. Gurnett, R. R. Anderson, F. L. Scarf, and W. S. Kurth

The Heliocentric Radial Variation of Plasma Oscillations Associated With Type III Radio Bursts

J. of Geophys. Res., 83, 4147, 1978

A survey is presented of all the electron plasma oscillation events found to date in association with low-frequency type III solar radio bursts using approximately 9 years of observations from the IMP 6 and 8, Helios 1 and 2, and Voyager 1 and 2 spacecraft. Plasma oscillation events associated with type III radio bursts show a pronounced increase in both the intensity and the frequency of occurrence with decreasing heliocentric radial distance. This radial dependence explains why intense electron plasma oscillations are seldom observed in association with type III radio bursts at the orbit of the Earth. Possible interpretations of the observed radial variation in the plasma oscillation intensity are considered.

17. Lewis L. Callagher and Donald A. Gurnett
 "Auroral Kilometric Radiation: Time-Averaged Source Location"
J. Geophys. Res., 84, 6501, 1979

The location of the average generation region of auroral kilometric radiation is found by studying average electric field strengths as a function of spacecraft position in narrow frequency bands centered at 178, 100, and 56.2 kHz. A combined 5 years of data from the University of Iowa plasma wave experiments on satellites Hawkeye 1 and IMP 6 provide the basis for determining the average electric field strengths. Hawkeye 1 was in a highly elliptical, polar orbit with an apogee near 21 R_E over the northern polar region, and IMP 6 was in a highly elliptical, near-equatorial orbit with an apogee of 33 R_E . Together these satellites provide extensive coverage from 3 to 21 R_E in the northern hemisphere and inside of 3 R_E in the southern hemisphere. Intense sources of auroral kilometric radiation are found in the northern and southern hemispheres. Their locations are near 65° invariant latitude in their respective hemispheres, between 22 and 24 hours magnetic local time, and near 2.5 R_E . The total time-averaged power generation is found to be about 10^7 W, assuming a spectral bandwidth of 200 kHz. Propagation effects limit the emission cone of auroral kilometric radiation in a given hemisphere to roughly 4.1 sr at 178 kHz, 2.2 sr at 100 kHz, and 1.5 sr at 56.2 kHz. Evidence that the polar cusp region is illuminated at distances as close as 4 R_E suggests the possibility that previously observed polar cusp sources are the result of scattering from field-aligned density irregularities.

18. Robert R. Shaw and Donald A. Gurnett
 "A Test of Two Theories for the Low Frequency Cutoffs of Nonthermal Continuum Radiation"
J. Geophys. Res., (accepted for publication), 1980

Two theories have been proposed that differently identify the frequencies of the low frequency cutoffs of nonthermal continuum radiation. The first of these theories states that the two low frequency cutoffs occur at the local plasma frequency and $R = 0$ cutoff frequency, with the continuum radiation propagating in the ordinary mode between the cutoffs and a mixture of ordinary and extraordinary mode above the upper cutoff. The second theory suggests that the two low frequency cutoffs occur at the local $L = 0$ cutoff frequency and plasma frequency, with the continuum radiation being generated by Cerenkov emission in the Z-mode between the local plasma frequency and upper hybrid resonance frequency. Mode coupling at the local plasma frequency is suggested to generate continuum radiation in the ordinary mode which freely propagates to remote regions of the magnetosphere. In this paper, several examples of continuum radiation observed in the outer magnetosphere by IMP 6 and ISEE 1 are analyzed in detail, and it is shown that these cutoff frequencies occur at the local plasma frequency and $R = 0$ cutoff frequency. In addition, no substantive evidence is found in the outer magnetosphere for a component of continuum radiation propagating in the Z-mode.

19. D. A. Gurnett, R. R. Anderson, and R. L. Tokar
"Plasma Oscillations and the Emissivity of Type III Radio Bursts"
Radio Physics of the Sun, ed. by M. Kundu, Reidel Publishing Co.,
Dordrecht, Netherlands, 1979

Plasma wave electric field measurements with the solar orbiting Helios spacecraft have shown that intense electron plasma oscillations occur in association with type III solar radio bursts, thereby confirming a well known mechanism for generating solar radio emissions first proposed by Ginzburg and Zheleznyakov in 1958. In this paper we review the principal characteristics of these plasma oscillations and compare the observed plasma oscillation intensities with recent measurements of the emissivity of type III radio bursts. The observed emissivities are shown to be in good agreement with two current models for the conversion of electrostatic plasma oscillations to electromagnetic radiation.

20. L. Burlaga, R. Lepping, R. Weber, T. Armstrong, C. Goodrich, J. Sullivan, D. Gurnett, P. Kellogg, E. Keppler, F. Mariani, F. Neubauer, H. Rosenbauer, R. Schwenn
"Interplanetary Particles and Fields, November 22 - December 6, 1977: Helios, Voyager, and IMP Observations Between 0.6 AU and 1.6 AU"

In the period November 22 -December 6, 1977, three types of interplanetary flows are observed--a corotating stream, a flare-associated shock wave, and a shock wave driven by ejecta. Helios 2, IMP 7, 8, and Voyager 1, 2 were nearly radially aligned at ≈ 0.6 AU, 1 AU and 1.6 AU, (respectively, while Helios 1 was at ≈ 0.6 AU and 35° of Helios 2. The instruments on these spacecraft provided an exceptionally complete description of the particles and fields associated with the three flows and corresponding solar events. Analysis of these data revealed the following results. 1) A coronal hole associated corotating stream, observed at 0.6 AU and 1 AU, which was not seen at 1.6 AU. The stream interface corotated and persisted with little change in structure even though the stream disappeared. A forward shock was observed ahead of the interface, and moved from Helios 2 at 0.6 AU to Voyager 1, 2 at 1.6 AU; although the shock was ahead of a corotating stream and interface, the shock was not corotating, because it was not seen at Helios 1, probably because the corotating stream was not stationary. 2) An exceptionally intense type III burst was observed in association with a 2B flare of November 22. The exciter of this burst--(a beam of energetic electrons)--and plasma oscillations (presumably caused by the electron beam) were observed by Helios 2. 3) A non-spherical shock was observed in association with the November 22 flare. This shock interacted with another shock between 0.6 AU and 1 AU, and they coalesced to form a single shock that was identified at 1 AU and at 1.6 AU. 4) A shock driven by ejecta was studied. In the ejecta the density and temperature were unusually low and the magnetic field intensity was relatively high. This region was preceded by a directional discontinuity at which the magnetic field dropped appreciably. The shock appeared to move globally

at a uniform speed, but locally there were fluctuations in speed and direction of up to 100 km/s and 40° , respectively. 5) Three types of electrostatic waves were observed at the shocks, in different combinations. The detailed wave profiles differed greatly among the shocks, even for spacecraft separations ≤ 0.2 AU, indicating a strong dependence on local conditions. However, the same types of fluctuations were observed at 0.6 AU and at 1.6 AU. 6) Energetic (50-200 keV) protons were accelerated by the shocks. The intensities and durations of the fluxes varied by a factor of 12 over longitudinal distances of 0.2 AU. The intensities were higher and the durations were lower at 1.6 AU than at 0.6 AU, suggesting a cumulative effect. 7) Energetic (≈ 50 keV) protons from the November 22, flare were observed by all the spacecraft. During the decay, Helios 1 observed no change in intensity when the interface moved past the spacecraft, indicating that particles were injected and moved uniformly on both sides of the interface. Helios 2 observed an increase in flux not seen by Helios 1, reaching maximum at the time that a shock arrived at Helios 2. The intensity dropped abruptly when the interface moved past Helios 2, indicating that the "extra" particles seen by Helios 2 did not penetrate the interface.

21. R. L. Tokar and D. A. Gurnett
 "The Volume Emissivity of Type III Radio Bursts"
J. Geophys. Res., (accepted for publication), 1980

The volume emissivity has been calculated for thirty-six type III solar radio bursts obtained from approximately 6.5 years of IMP 8 and ISEE 1 satellite data. Although the emissivities for these events vary over a large range, all the emissivities decrease rapidly with increasing heliocentric radial distance. The best fit power law for the emissivity, using the average power law index for all events analyzed, is $J = J_0 R^{-6.0}$, with $J_0 = 1.5 \times 10^{-24}$ watts m^{-3} ster $^{-1}$. This best fit emissivity is used to estimate the expected radial variation of the plasma oscillations responsible for the type III radio emission.

APPENDIX A

Papers and Reports Resulting from the
University of Iowa Plasma Wave Experiment
on the IMP-8 Spacecraft

The Earth as a Radio Source: Terrestrial Kilometric Radiation

DONALD A. GURNETT

Department of Physics and Astronomy, University of Iowa, Iowa City, Iowa 52242

Radio wave experiments on the Imp 6 and 8 satellites have shown that the earth emits very intense electromagnetic radiation in the frequency range of about 50–500 kHz. At peak intensity the total power emitted in this frequency range is about 10^9 W. The earth is therefore a very intense planetary radio source, with a total power output comparable to the decametric radio emission from Jupiter. We refer to this radio emission from the earth as terrestrial kilometric radiation. Terrestrial kilometric radiation appears to originate from low altitudes (less than $3.0 R_E$) in the auroral region. The intensity of the noise has a pronounced dependence on both the local time and the magnetic latitude of the observing point. At large radial distances the radiation is primarily observed on the poleward side of two cone-shaped surfaces that are centered on the earth and symmetrically located with respect to the northern and southern auroral zones. The magnetic latitude of the cone-shaped boundaries varies from greater than 50° in the local morning to near the magnetic equator in the local evening. Poleward of these boundaries the noise occurs in sporadic 'storms' lasting from $\frac{1}{2}$ hour to several hours. Comparisons with auroral photographs obtained from the low-altitude polar-orbiting Dapp satellite show that the terrestrial kilometric radiation is closely correlated with the occurrence of discrete auroral arcs, which occur in the local evening region of the auroral zone. This association indicates that the kilometric radiation is probably generated by intense 'inverted V' electron precipitation bands, which cause the discrete auroral arcs. Possible mechanisms that can explain the generation and propagation of the terrestrial kilometric radiation are discussed.

Intense electromagnetic radiation is commonly observed propagating outward from the earth in the frequency range of about 50–500 kHz with the University of Iowa plasma wave experiments on the Imp 6 and 8 satellites. Since the wavelength of this radiation is usually in the kilometric range, we shall refer to this radiation as terrestrial kilometric radiation. Terrestrial kilometric radiation was first discovered by *Durckel et al.* [1970] from very low frequency (VLF) radio measurements with the Ogo 1 satellite. *Durckel et al.* refer to this radiation as 'high-pass' noise because the upper frequency of the Ogo VLF receiver (100 kHz) was too low to reach the peak in the emission spectrum. As we shall show, the spectrum of the terrestrial kilometric radiation extends with significant intensities up to about 500 kHz and typically reaches maximum intensity at about 200 kHz. *Brown* [1973] has also commented on observations of earth-related radio emissions at 150–300 kHz with the Goddard Space Flight Center (GSFC) radio astronomy experiment on Imp 6 and refers to this noise as 'midfrequency' radiation.

At peak intensity we will show that the total power of the terrestrial kilometric radiation is about 10^9 W. The earth is therefore a very intense planetary radio source, with a total power output comparable to the decametric (3.0–30.9 MHz) radio emission from Jupiter. For comparison, the total power of the Jovian decametric radiation is estimated by *Warwick* [1963] to be about 2×10^7 W. As we shall also show, the terrestrial kilometric radiation appears to originate from relatively low altitudes (less than $3 R_E$) in the auroral regions and is closely correlated with the occurrence of discrete auroral arcs detected optically by the low-altitude polar-orbiting Dapp reconnaissance satellite. Since the maximum energy dissipated by the auroral charged-particle precipitation is about 10^{11} W, the mechanism for generating this radiation must be very efficient ($\sim 1\%$). Because the terrestrial kilometric radiation has many features in common with Jovian, solar, and other astrophysical radio sources, the understanding of this radiation is of considerable general interest, particularly since in this case direct in situ measurements can be made in

the source region. The purpose of this paper is to present a comprehensive study of terrestrial kilometric radiation as observed by the Imp 6 and 8 satellites.

INSTRUMENTATION

The Imp 6 spacecraft was launched on March 13, 1971, into a highly eccentric earth orbit with initial perigee and apogee geocentric radial distances of 6613 and 212,630 km, respectively, orbit inclination of 28.7° , and period of ~ 18 days. The Imp 8 spacecraft was launched on October 26, 1973, into a slightly eccentric earth orbit with initial perigee and apogee geocentric radial distances of 147,434 and 295,054 km, respectively, orbit inclination of 28.6° , and period of 11.98 days. Both spacecraft are spin-stabilized, their spin axes being oriented very nearly perpendicular to the ecliptic plane.

The University of Iowa plasma wave experiment on Imp 6 is designed to study plasma wave phenomena in the frequency range 20 Hz to 200 kHz. The antennas for this experiment consist of three mutually orthogonal 'long' dipole antennas for electric field measurements and three mutually orthogonal loop antennas for magnetic field measurements. Two of the electric dipole antennas are perpendicular to the spacecraft spin axis. These antennas, E_x and E_y , have tip-to-tip lengths of 53.5 and 92.5 m, respectively. The third electric antenna, E_z , lies along the spin axis and has a tip-to-tip length of 7.7 m. The signals from these antennas are analyzed by two 16-channel spectrum analyzers with center frequencies from 36 Hz to 178 kHz. The filter for each channel has a bandwidth of approximately 15% of the center frequency, and there are four filters per decade of frequency. Each frequency channel has two detectors: a peak detector and an average detector. The peak detector has a response time constant of 0.1 s and measures the largest signal occurring in a given sample interval (5.11 s), and the average detector measures the average noise intensity during the same sample interval. The output of each detector is a voltage proportional to the logarithm of the signal amplitude. The dynamic range of each spectrum analyzer channel is 100 dB. Further details of the Imp 6 plasma wave experiment are given by *Gurnett and Shaw* [1973].

The University of Iowa plasma wave experiment on Imp 8 is similar to the Imp 6 experiment. The antennas for the Imp 8 experiment consist of two orthogonal fine-wire (0.020 inch in diameter) dipole antennas for electric field measurements and three mutually orthogonal search coil magnetometers for magnetic field measurements. The electric dipole antennas are extended outward, perpendicular to the spacecraft spin axis, by centrifugal force. The nominal tip-to-tip length of the electric dipole antennas is 121.8 m. Because of a mechanical failure in one of the antenna extension mechanisms, only the E_y antenna is extended to the full length. All data presented in this report are obtained with the E_y antenna. The spectrum analyzer used in the Imp 8 experiment is very similar to the Imp 6 spectrum analyzer. Fifteen channels are used for electric field measurements covering the frequency range 40 Hz to 178 kHz, there being approximately four channels per decade of frequency. Each channel is sampled once every 10.24 s. In addition to the 15 channel spectrum analyzers the Imp 8 experiment also has a wide-band receiver that can provide wave form measurements over the frequency range 10 Hz to 1 kHz from any selected antenna. The wide-band receiver can also be tuned to frequencies of 2.0 MHz, 500 kHz, 125 kHz, and 31.25 kHz, so that wave form measurements can be obtained at these frequencies. An amplitude output is also available from the wide-band receiver, so that frequency spectrum measurements can be obtained at frequencies up to 2.0 MHz by stepping the center frequency of the wide-band receiver.

OBSERVATIONS

Survey of basic characteristics. An example of terrestrial kilometric radiation observed by Imp 6 is illustrated in Figure 1, which shows the electric field strength in the 178-, 100-, 56.2-, and 31.1-kHz channels for a 24-hour period while the spacecraft is near apogee in the geomagnetic tail region. The ordinate for each frequency channel in this figure is proportional to the logarithm of the electric field strength. The interval from the base line of one channel to the base line of the next higher channel corresponds to a dynamic range of 75 dB. The vertical bars indicate the average field strength over the time interval between samples, and the dot above each bar indicates the peak field strength over this same interval. The distinct enhancements in the 100- and 178-kHz channels of Figure 1, extending as much as 60 dB above the receiver noise level, are typical of the terrestrial kilometric radiation observed by Imp 6. The intensity of this noise often varies con-

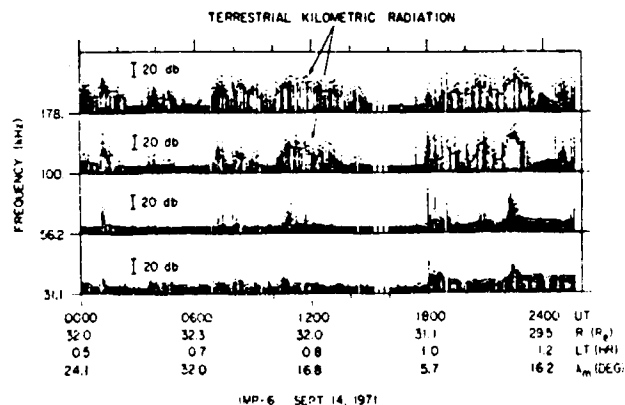


Fig. 1. A 24-hour period of Imp 6 electric field data near apogee in the geomagnetic tail region, which shows several periods of intense terrestrial kilometric radiation in the 100- and 178-kHz channels.

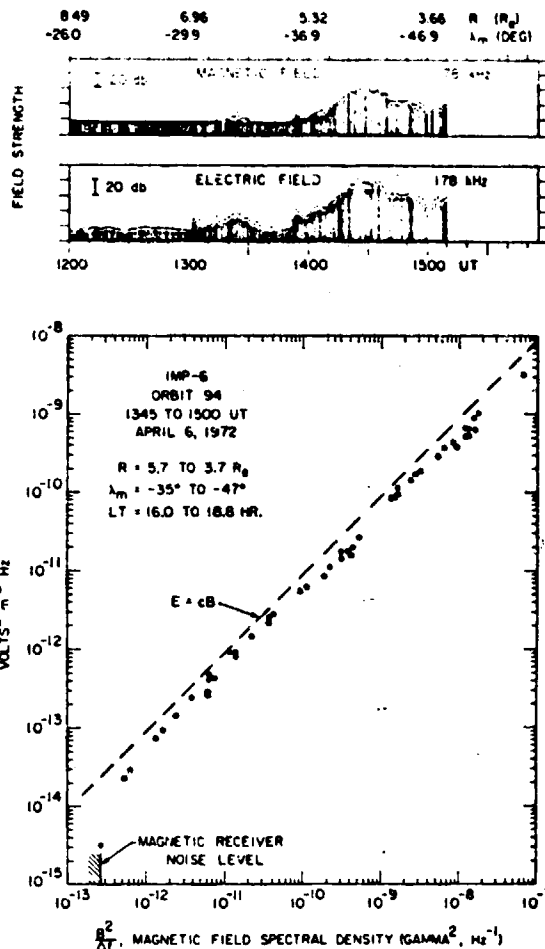


Fig. 2. Simultaneous electric and magnetic field intensities from an inbound Imp 6 pass in the local evening, which show that the terrestrial kilometric radiation consists of electromagnetic waves. The dashed line $E = cB$ gives the electric to magnetic ratio of an electromagnetic wave in free space.

siderably (by as much as 20 dB) on a time scale of a few minutes or less. The kilometric radiation occurs in distinct 'storms' lasting for periods from 1/2 hour to several hours (Figure 1). Between the storms the noise may be completely undetectable, sometimes for periods lasting as long as 24 hours. On a time scale of a minute or less the peak and average field strengths tend to vary together, the typical difference being about 3 dB. As will be shown later, this difference between the peak and the average field strengths is primarily caused by the antenna rotation and indicates that the source has a small angular size as viewed by Imp 6 at large radial distances from the earth.

It is easily shown that the kilometric noise detected by the electric antenna on Imp 6 is electromagnetic radiation, since the same noise is also detected with the magnetic loop antenna on Imp 6. Figure 2 illustrates the electric and magnetic field amplitudes for an intense kilometric noise storm observed during an inbound Imp 6 pass from about 6.0- to 3.7- R_E radial distance. The close correspondence between the electric and the magnetic field amplitudes is clearly evident in the top panel of Figure 2. The bottom panel of Figure 2 shows the corresponding electric and magnetic field spectral densities computed at several points from about 1345 to 1500 UT during this pass. The electric field strength is determined by dividing the measured ac voltage at the antenna terminals by one half

of the
na imp
electric
the bot
that the
tromag
tric fie
waves i
the inp
solute
mined
antenn
field m
The
shown
a radi
power
tric fi
propag
polariz
shows
kilome
reach
the
below
and
quency
com
E₀

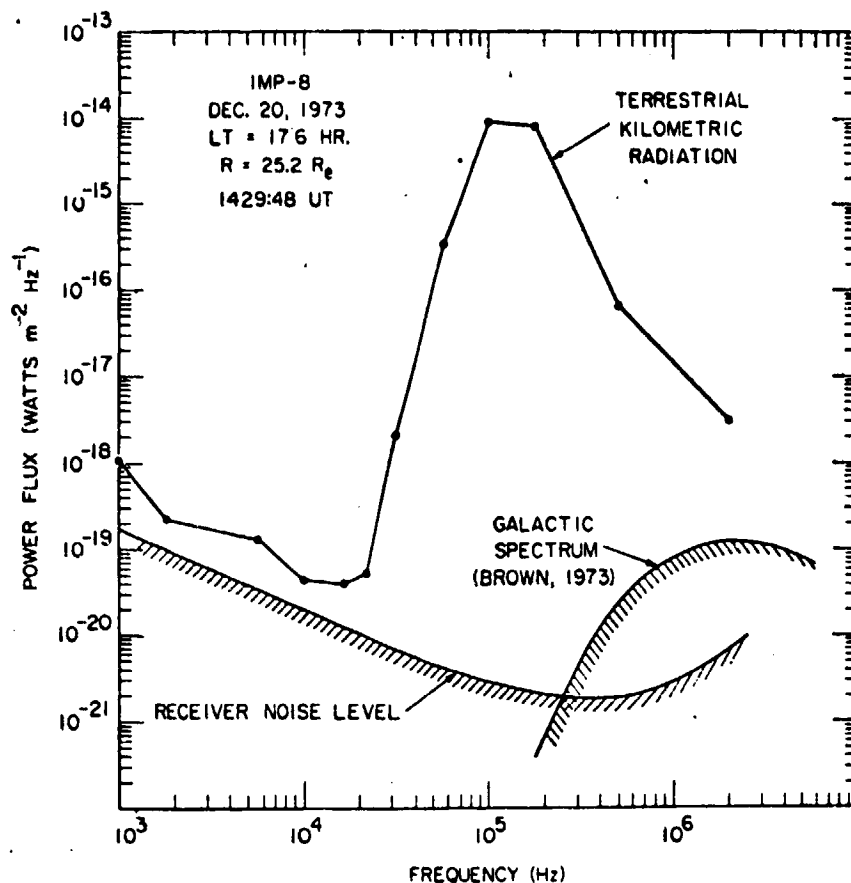


Fig. 3. Power spectrum of terrestrial kilometric radiation as observed by Imp 8 at a radial distance of $25.2 R_E$ in the local evening.

of the tip-to-tip length of the antenna and ignoring any antenna impedance corrections. The linear relation between the electric and the magnetic field spectral densities illustrated in the bottom panel of Figure 2 provides convincing evidence that the terrestrial kilometric noise detected by Imp 6 is electromagnetic radiation. The small deviation ($\sim 20\%$) of the electric field amplitude from the $E = cB$ line for electromagnetic waves in free space is believed to be due to the loading effect of the input capacity at the base of the electric antenna. The absolute sensitivity of the electric antenna can be directly determined by comparison with the loop antenna response, since no antenna impedance corrections are necessary for the magnetic field measurements.

The frequency spectrum of a typical kilometric noise event is shown in Figure 3. This spectrum was obtained from Imp 8 at a radial distance of about $25.2 R_E$ in the local evening. The power flux in Figure 3 was computed from the measured electric field spectrum by assuming that the radiation is propagating radially outward from the earth and that both polarizations have equal power. The spectrum in Figure 3 shows the main spectral characteristics of the terrestrial kilometric radiation observed by Imp 6 and 8: (1) the spectrum reaches peak intensity in the range of about 100–300 kHz, (2) the spectrum decreases rapidly with decreasing frequency below about 100 kHz and is seldom detectable at 31.1 kHz, and (3) the spectrum decreases rapidly with increasing frequency above about 300 kHz and is usually down to near the cosmic noise level at 2.0 MHz.

Evidence of near-earth origin. Several characteristics of the

terrestrial kilometric radiation indicate that the noise is generated very close to the earth, probably at a radial distance of less than $3 R_E$. As was mentioned earlier, the measured intensity of the kilometric noise has a very distinct modulation due to the rotation of the antenna. Figure 4 shows an example

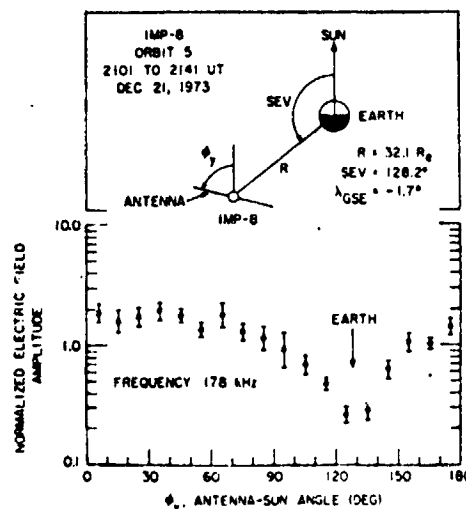


Fig. 4. Angular distribution of the electric field component parallel to the electric antenna axis as a function of the antenna orientation. The deep null when the antenna is pointed at the earth shows that the kilometric radiation appears to be coming from the earth and that the source has a small angular size ($< 6^\circ$ half angle) as viewed from Imp 8 at $32.1 R_E$.

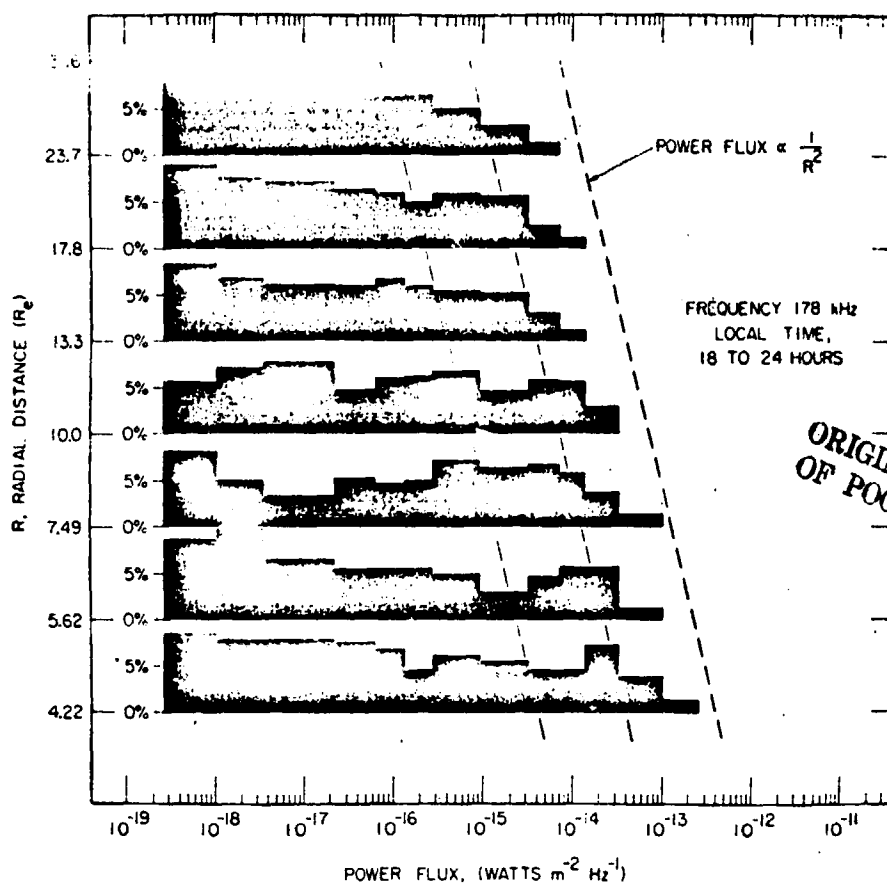


Fig. 5. Power flux distribution of terrestrial kilometric radiation at 178 kHz as a function of radial distance. The radial distance intervals are logarithmically spaced so that a $(1/R)^2$ variation is indicated by a straight dashed line in this diagram.

of spin modulation from the Imp 8 spacecraft. As is indicated in Figure 4, the spacecraft is at a radial distance of about $32.1 R_E$ in the local evening, and the sun-earth-vehicle (SEV) angle, projected onto the ecliptic plane, is about 128.2° . The geocentric solar ecliptic latitude, $\lambda_{GSE} = -1.7^\circ$, is such that the earth is located very close to the plane of rotation of the antenna, thereby assuring a sharp null for radiation coming directly from the earth.

The antenna orientation angle ϕ_y in Figure 4 is the angle between the electric antenna axis and the spacecraft-sun line. Because of the rapid intensity fluctuations and the slow sampling rate (one sample every 10.24 s) it is necessary to average a large number of measurements to obtain a suitable angular distribution. The amplitudes plotted in Figure 4 are an average of 40 min of data from the 178-kHz channel during a period when intense kilometric noise was being detected. To reduce the error caused by intensity variations, the measured field strengths are blocked into 3.6-min intervals and are normalized by dividing by the average field strength. The normalized electric field amplitudes shown in Figure 4 are the average of the normalized field strengths obtained in each 10° interval from 0° to 180° . Because of the symmetry of the dipole antenna pattern, angles in the range $180^\circ < \phi_y \leq 360^\circ$ are shifted by 180° into the range $0^\circ < \phi_y \leq 180^\circ$.

A null is clearly evident in Figure 4 at an antenna orientation angle of about 130° . This null position corresponds almost exactly to the angular position of the earth (SEV angle of 128.2°). The null is also very deep, the null amplitude being almost a factor of 10 below the peak amplitude. The deep null

indicates that the source must have a small angular size, less than about 6° half width, as viewed from Imp 8 at $32.1 R_E$. This angular size shows that the source does not extend more than about $3.0 R_E$ from the center of the earth.

If the source of the kilometric radiation is located close to the earth, then the power flux should vary inversely with the square of the radial distance from the earth. This radial dependence can be verified directly with the Imp 6 data. Figure 5 shows the power flux distribution as a function of radial distance from the earth in the 178-kHz electric field channel. The bar graph within each radial distance interval gives the percentage occurrence of the kilometric noise as a function of the power flux within that range of radial distances. These percentage occurrences are computed by using all data points (327.6-s averages) obtained during 1 year of in-flight operation totaling 22,802 measurements. To reduce the effect of local time variations, only local times in the range 18–24 hours are considered. All points are included without regard to the type of noise being detected. From the 24-hour survey plots, such as that shown in Figure 1, we have established that virtually all of the noise detected in the 178-kHz channel consists of terrestrial kilometric radiation. The radial distance ranges in Figure 5 are logarithmically spaced so that a $(1/R)^2$ dependence of the power flux is a straight line in this diagram. The peak power flux is seen to follow closely the $(1/R)^2$ dependence indicated by the dashed lines in Figure 5, thereby providing further evidence of the near-earth origin of the kilometric radiation. The data in Figure 5 also provide quantitative information on the intensity of the kilometric radiation at any given radial dis-

tance. At
about

$(1/R)^2$ is
pronounced
the observed
Figure 6
indicates
channel

threshold

The $(1/R)$
correct for
radial dis-
 8.16×10^4
than the
essential
Figure 6
thereby
provide
points in
samples
Figure
frequent
4.0 hour
seldom
Figure 6
at a radi

tance. At a radial distance of $30 R_E$ the maximum intensity is about $10^{-14} \text{ W m}^{-2} \text{ Hz}^{-1}$ at 178 kHz.

Spatial distribution of the radiation. In addition to the $(1/R)^2$ radial variation the kilometric radiation also has a pronounced dependence on the local time and the latitude of the observing point. The local time dependence is illustrated in Figure 6, which shows the local time and radial distance coordinates of Imp 6 for times when the power flux in the 178-kHz channel exceeds a threshold power flux of

$$\text{threshold} = \left(\frac{R_E}{R}\right)^2 \times (7.35 \times 10^{-16}) \text{ W m}^{-2} \text{ Hz}^{-1}$$

The $(1/R)^2$ factor in the threshold for counting an event is to correct for the expected $(1/R)^2$ variation of the power flux with radial distance. This threshold corresponds to a power flux of $8.16 \times 10^{-19} \text{ W m}^{-2} \text{ Hz}^{-1}$ at $R = 30 R_E$, which is much less than the average power flux of the kilometric radiation, so that essentially all events that occur should be detected. The data in Figure 6 represent 1 complete year of in-flight operation, thereby assuring coverage of all local times. In order to provide an unbiased representation the time interval between points in Figure 6 is adjusted to give a constant number of samples per unit length along the trajectory.

Figure 6 shows that the kilometric radiation is much more frequently observed in the local evening (from about 16.0 to 4.0 hours local time) than in the local morning. The noise is seldom observed from about 6.0 to 12.0 hours local time. Figure 6 also shows a sharp cutoff in the kilometric radiation at a radial distance of about $3.0 R_E$ at all local times. The loca-

tion of this cutoff (near the expected location of the plasmapause boundary) suggests that the plasmasphere is affecting the propagation of the kilometric radiation in this region.

To investigate this plasmapause effect further, the frequency of occurrence has been determined as a function of the magnetic latitude and radial distance in the local time range 18.0–24.0 hours, where the noise is most frequently observed. Magnetic latitude λ_m is used as a parameter because the plasmasphere is known to be controlled strongly by the geomagnetic field. To correct for the expected $(1/R)^2$ variation of the power flux, the threshold for counting an event is again varied as

$$\text{threshold} = \left(\frac{R_E}{R}\right)^2 \times (7.35 \times 10^{-16}) \text{ W m}^{-2} \text{ Hz}^{-1}$$

Data from 2 years of in-flight operation are used to determine the frequency of occurrence. Because of the limitations imposed by the Imp 6 orbit it is necessary to combine the northern hemisphere and southern hemisphere data, the sign of the magnetic latitude being ignored, in order to obtain an adequate number of samples in each λ_m, R block. The percentage occurrences computed from these data are shown in Figure 7. All latitudes below the upper border marked 'limit of latitudinal coverage' have at least 20 samples in each λ_m, R block. A well-defined low-latitude cutoff in the occurrence of kilometric radiation is evident in Figure 7, varying from about 40° magnetic latitude at $3.0 R_E$ to about 10° magnetic latitude at $10.0 R_E$. At radial distances of less than about $4.0 R_E$ this

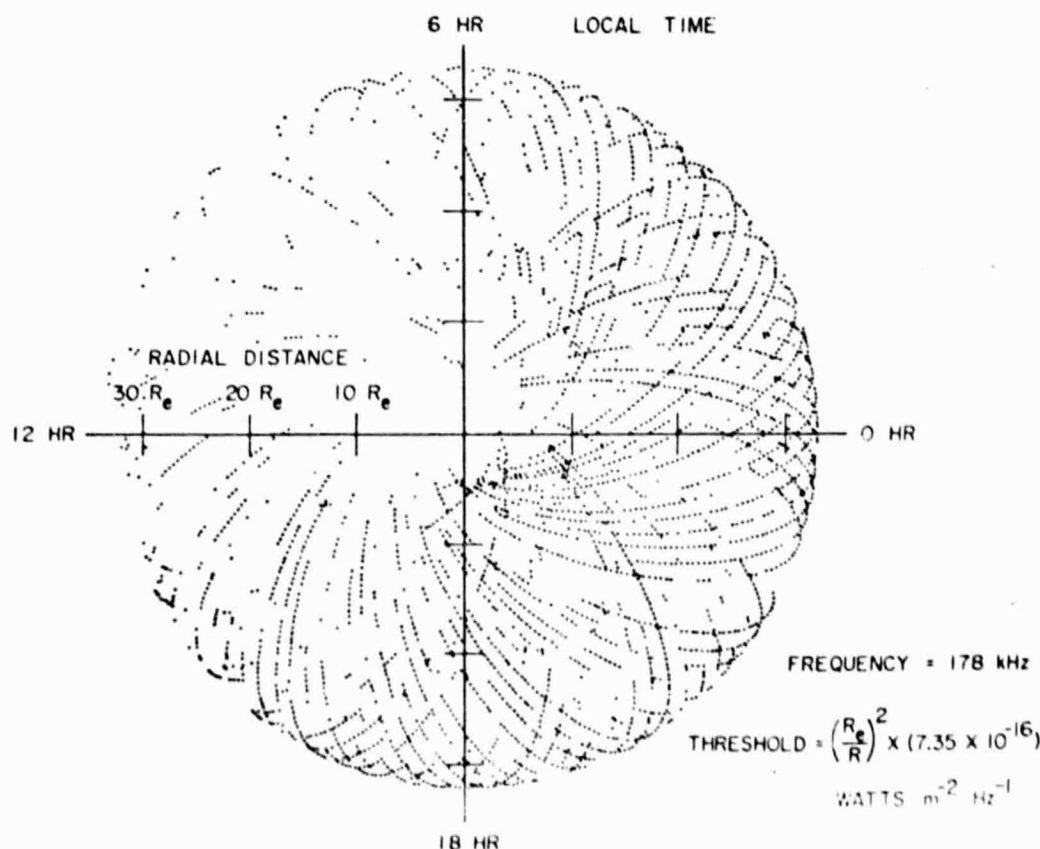


Fig. 6. Spatial survey of points along the Imp 6 orbit at which the power flux in the 178 kHz channel exceeds the specified threshold. The threshold is varied as $(1/R)^2$ to correct for the expected radial variation in the power flux. The coordinates are geocentric radial distance and local time.

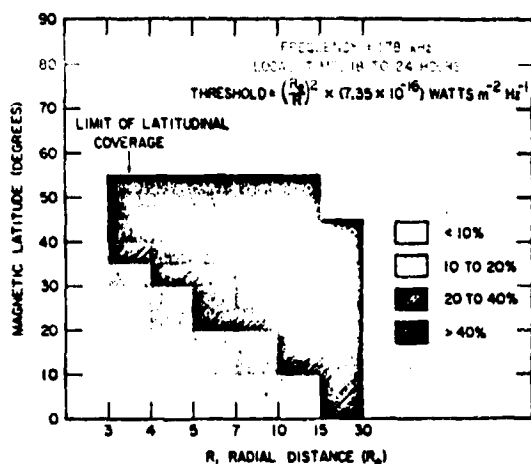


Fig. 7. Percentage occurrence of terrestrial kilometric radiation as a function of magnetic latitude and radial distance. Again the threshold is varied as $(1/R)^2$ to correct for the expected radial variation in the power flux. Note the shadow zone extending from about 40° magnetic latitude at 3.0 R_E to about 10° magnetic latitude at 10.0 R_E .

cutoff coincides closely with the rapid increase in the plasma density that occurs at the plasmapause. Figure 8 shows a low-altitude Imp 6 pass selected to illustrate this cutoff at the plasmapause. The plasmapause in this case was identified from the abrupt change in the low-frequency (<300 Hz) electric field interference generated by the spacecraft solar array (see the discussion by Gurnett and Shaw [1973]). Figure 8 shows that the kilometric radiation detected during this pass disappears abruptly as the spacecraft crosses the plasmapause at 1913 UT. This abrupt termination is believed to be due to a propagation cutoff that occurs when the plasma frequency f_p exceeds the wave frequency as the spacecraft enters the plasmasphere. Note in Figure 8 that the cutoff in the 100-kHz channel (at 1913 UT) occurs before the cutoff in the 178-kHz channel (at 1918 UT). This sequence of cutoffs is consistent with the expected rapid increase in the plasma density and plasma frequency as the spacecraft passes into the plasmasphere.

The systematic difference between the peak (dots) and average (bars) intensities of the kilometric radiation observed during the inbound low-altitude pass in Figure 8 indicates that a significant amount of spin modulation (30% null-to-peak ratio) still exists even at radial distances as close as 2.8 R_E , thereby implying that the source of the radiation still subtends a small angular size even at this low altitude. These results indicate that the kilometric radiation must originate from the high-latitude low-altitude regions of the magnetosphere. The Imp 6 spacecraft probably does not pass through the source region, since as is evident in Figure 8, the orbit does not provide high-latitude ($\lambda_m > 50^\circ$) measurements at radial distances of less than about 3.0 R_E .

At higher altitudes (greater than about 4.0 R_E) the low-latitude cutoff of the kilometric radiation is not as abrupt as the example shown in Figure 8, and the cutoff does not correspond with the local plasmapause location. As is shown by Figure 7, there appears to be a 'shadow zone' near the magnetic equator extending out to radial distances of about 10–15 R_E . The existence of this shadow zone is further confirmed by the fact that terrestrial kilometric radiation is almost never detected by the University of Iowa plasma wave experiment on the S³-A satellite, which has an orbit near the

magnetic equator even though the spacecraft often crosses into the region beyond the plasmapause to radial distances of 5.24 R_E .

To determine the angular distribution of the kilometric radiation, as would be observed far from the earth, the frequency of occurrence has also been determined as a function of magnetic local time (MLT) and magnetic latitude. Magnetic coordinates are used because of the expected geomagnetic control of the source. To avoid effects due to the propagation cutoff at the plasmapause, we have used only measurements obtained at radial distances greater than 5 R_E . The threshold for counting events is again varied according to the relation

$$\text{threshold} = \left(\frac{R_E}{R}\right)^2 \times (7.35 \times 10^{-16}) \text{ W}^2 \text{ m}^{-2} \text{ Hz}^{-1}$$

to correct for the expected variation in the power flux with radial distance. The results of this investigation, using 2 years of Imp 6 data from the 178-kHz channel, are shown in Figure 9. The limits of the latitudinal coverage provided by Imp 6 are indicated by the solid lines at the outer boundaries of the shaded region in this diagram.

The frequency-of-occurrence contours in Figure 9 show that in the northern hemisphere the kilometric radiation is confined to a single region with a distinct cone-shaped equatorward boundary. A similar region with a cone-shaped equatorward boundary is also evident in the southern hemisphere. Near local midnight the two cone-shaped boundaries appear to merge, and the radiation is detected at all magnetic latitudes sampled by Imp 6, although there is a reduced frequency of occurrence near the magnetic equator. On the day side of the earth (from about 6.0 to 12.0 hours MLT) the radiation is observed only at very high magnetic latitudes: $\lambda_m > 45^\circ$ in the northern hemisphere and $\lambda_m < -45^\circ$ in the southern

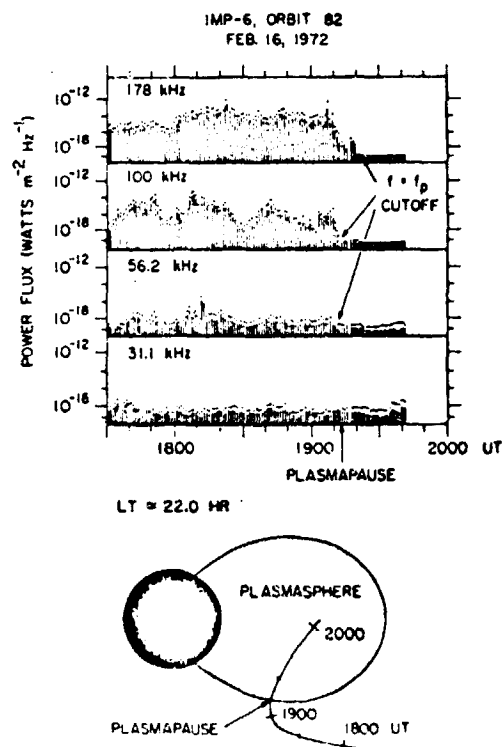


Fig. 8. Low-altitude Imp 6 pass illustrating the propagation cutoff of kilometric radiation near the plasmapause.

hemisphere. In the local midnight region the frequency of occurrence does not show any tendency to decrease at high latitudes. From about 12 to 20 hours MLT, however, a distinct latitudinal maximum exists in the frequency of occurrence, varying in location from about $\lambda_m = 30^\circ$ at 20 hours MLT to about $\lambda_m = 45^\circ$ at 12 hours MLT. This latitudinal maximum suggests that a poleward minimum probably exists in the frequency of occurrence over the polar cap regions.

CORRELATION WITH AURORA

Because the terrestrial kilometric radiation appears to be coming from low altitudes in the auroral zone, we have investigated the relationship of this radio noise to the occurrence of aurora by using auroral photographs from the U.S. Air Force Dapp satellite. The Dapp spacecraft is in a sun-synchronous dawn-dusk polar orbit at an altitude of 830 km. An optical scanner on the spacecraft provides a synoptic view of almost the entire nighttime auroral oval on each polar pass. It is found that the occurrence of intense kilometric radiation is closely associated with the occurrence of aurora. This conclusion is based on a study of about 150 Dapp auroral photographs (one photograph per orbit) obtained during January 1973. Because of the difficulty in providing a quantitative auroral index from the Dapp photographs the results of this study are qualitative. Whenever a bright extensive auroral display occurs in the Dapp photographs, intense kilometric radiation is always detected by Imp 6 if the spacecraft is located in a favorable region for receiving this radiation. When no auroral light is evident, the kilometric radiation is usually weak or undetectable.

To illustrate the observed relationship between the aurora and the kilometric radiation, a particular day, January 25, 1973, has been selected for discussion. This day was selected both because this day is representative of the relationships observed during other periods and because the Dapp auroral photographs for this day have previously been published by Snyder *et al.* [1974] and are available for comparison. Figure 10 shows the envelope of the ground magnetogram records (H component) for this day and the power flux in the 178-kHz channel of Imp 6. The difference between the upper and the lower magnetogram envelopes in Figure 10 is the auroral elec-

trojet index AE , frequently used as a measure of auroral substorm activity.

The only significant activity evident in the Dapp photographs from 0000 to 1000 UT occurs on orbit 1089 (see the paper by Snyder *et al.* [1974] for the Dapp photograph from this orbit). The aurora observed during orbit 1089 is associated with the weak magnetic activity from about 0200 to 0400 UT, and a corresponding small enhancement in the 178-kHz power flux is evident in Figure 10.

The first major auroral substorm activity on January 25, 1973, starts at about 1000 UT. The Dapp auroral photographs obtained during this substorm are shown in Figure 11. The magnetic pole in each of these photographs is located near the top center of the photograph, dusk being on the left and dawn on the right (see the paper by Snyder *et al.* [1974] for further details). The photograph for orbit 1093, which was taken at about 0940 UT (before the onset of the substorm), shows essentially no auroral activity. No kilometric radiation is detected in the 178-kHz channel at this time. The next photograph, that for orbit 1094, which was taken at about 1125 UT (near the time of maximum magnetic disturbance), shows an extensive region of bright auroral light emission extending along the entire auroral oval from dawn to dusk. Several bright arcs, called discrete auroras, are evident on the poleward boundary of the auroral oval extending from local early evening, in the upper left-hand corner, around to local midnight in an almost continuous band. In the local midnight region, equatorward of the discrete arcs, a broad band of diffuse aurora is also evident extending beyond the lower edge of the photograph. The bottom panel of Figure 10 shows that very intense kilometric radiation ($\sim 5 \times 10^{-12} \text{ W m}^{-2} \text{ Hz}^{-1}$) is observed by Imp 6 simultaneous with the auroral light emissions observed by Dapp on orbit 1094. On the following Dapp photograph, taken on orbit 1095, the discrete arcs have completely disappeared, and the 178-kHz kilometric radiation has correspondingly disappeared. A small band of diffuse aurora, however, is still seen near the lower edge of the photograph.

The second major substorm activity on January 25, 1973, starts at about 1330 UT. The next Dapp photograph, that for orbit 1096, which was taken at about 1440 UT, again occurs near the time of maximum magnetic activity, and an extensive region of bright auroral light emission is evident. Figure 10 shows that again, in association with the aurora, very intense kilometric radiation ($\sim 3 \times 10^{-12} \text{ W m}^{-2} \text{ Hz}^{-1}$) is observed by Imp 6. On the next Dapp orbit, 1097, the kilometric radiation has decreased to near the receiver noise level, and the auroral photograph for this orbit shows that the aurora has correspondingly disappeared.

The third major auroral substorm activity on January 25, 1973, starts at about 1950 UT. The Dapp photographs obtained during this substorm are shown in Figure 12. The photograph for Dapp orbit 1099, which was taken at about 1805 UT (before the onset of the substorm), shows no significant auroral activity, and no kilometric radiation is detectable by Imp 6 at this time. The next photograph, that for Dapp orbit 1099, which was taken at about 1955 UT (during the period of increasing magnetic activity associated with the expansive phase of the substorm), shows a small bright discrete arc in the local evening. This initial brightening of the discrete arc occurs at the onset of a period of intense kilometric radiation. On the following Dapp photograph, that for orbit 1100, which was taken at about 2135 UT, a moderately bright discrete arc is

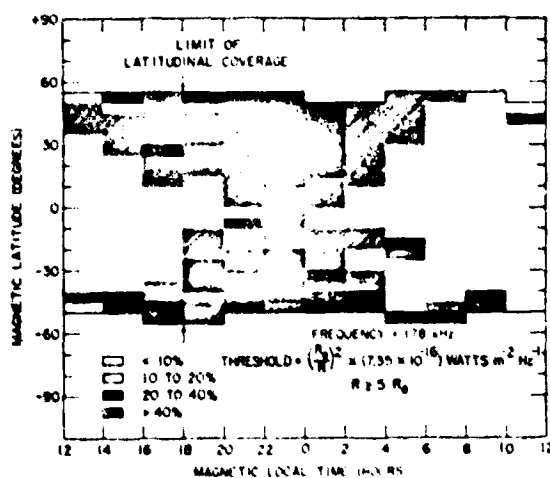


Fig. 9. Percentage occurrence of terrestrial kilometric radiation as a function of magnetic latitude and magnetic local time. Again the threshold is varied as $(1/R)^2$ to correct for the expected radial variation in the power flux. Note the cone shaped equatorward boundary of the emission regions in the northern and southern hemispheres.

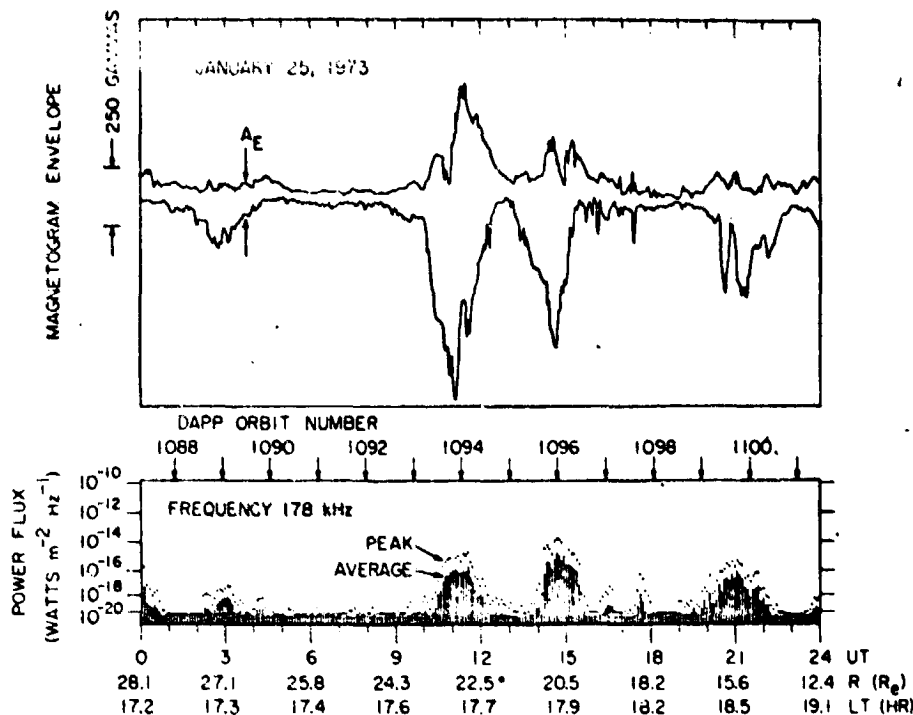


Fig. 10. The 178-kHz power flux observed by Imp 6 and the corresponding ground magnetogram envelopes for January 25, 1973. Three main periods of magnetic substorm activity occurred during this day (1000–1230 UT, 1330–1530 UT, and 1950–2300 UT), and each of these substorms is associated with a period of intense kilometric radiation.

seen, and a broad region of diffuse aurora is evident in the local midnight region. Moderately intense kilometric radiation ($\sim 10^{-16} \text{ W m}^{-2} \text{ Hz}^{-1}$) is also detected by Imp 6 at this time. Both the magnetic activity and the 178-kHz power flux are decreasing, probably indicating that this photograph was obtained during the recovery phase of the substorm. On the next Dapp orbit, 1101, both the discrete aurora and the kilometric radiation have disappeared. The band of diffuse aurora is still evident, though with reduced intensity, near the bottom of the photograph for this orbit.

These data show that the kilometric radiation detected by Imp 6 is closely associated with the occurrence of aurora in the Dapp photographs. The association with aurora is in fact to be expected, since *Dunckel et al.* [1970] showed that the occurrence of kilometric radiation (referred to in their study as high-pass noise) is closely correlated with the *AE* index. However, the Imp 6/Dapp comparisons now show that the kilometric radiation is mainly associated with the discrete arcs found at high latitudes in the local evening. The kilometric radiation does not appear to be as closely associated with the diffuse aurora observed at lower latitudes near local midnight, since the diffuse aurora is sometimes evident in the Dapp photographs after the kilometric radiation has disappeared (as is true in orbits 1095 and 1101).

DISCUSSION

Substantial evidence has been presented showing that the terrestrial kilometric radiation detected by Imp 6 and 8 is generated at low altitudes ($R < 3.0 R_E$) near the earth in association with discrete auroral arcs. Since this radio emission occurs at frequencies much greater than either the plasma frequency or the electron gyrofrequency in the outer magnetosphere, it is not surprising that the radiation is generated at relatively low altitudes, because only in this

region are the characteristic frequencies of the plasma comparable to the frequency of the radiation. At low altitudes the propagation and the generation of the kilometric radiation are strongly influenced by the propagation cutoffs produced by the ionospheric plasma. Figure 13 shows a model of the expected variation of the plasma frequency f_p (proportional to the square root of the electron density) and the electron gyrofrequency f_g as a function of the geocentric radial distance for a representative auroral field line ($L = 8$). The polar ionospheric model used to compute the plasma frequency is that of *Banks and Holzer* [1969]. The electron density is given by Banks and Holzer only for $R < 2.0 R_E$. The electron density used for $R > 2.0 R_E$ is a qualitative extrapolation of Banks and Holzer's model to an asymptotic density of about 1 el cm^{-3} at large radial distances.

Two propagation cutoffs occur for the free-space electromagnetic modes propagating in a plasma [*Stix*, 1962]. The left-hand-polarized ordinary (*L*, *O*) mode has a cutoff at the plasma frequency f_p , and the right-hand-polarized extraordinary (*R*, *X*) mode has a cutoff at a frequency f_{R-O} , given by

$$f_{R-O} = (f_g/2) + [(f_g/2)^2 + f_p^2]^{1/2}$$

These propagation cutoffs are indicated by the crosshatched lines labeled (*R*, *X*) cutoff and (*L*, *O*) cutoff in Figure 13. These cutoffs represent the low-frequency limit of the electromagnetic modes that can propagate freely away from the earth and therefore are the altitude limits above which the kilometric radiation must be generated. Figure 13 shows, for example, that at a frequency of 178 kHz the minimum radial distances at which the right- and left-hand-polarized modes can propagate are about 2.5 and $1.8 R_E$, respectively. At present, the polarization of the terrestrial kilometric radiation has not been determined, although such measurements are possible with the University of Minnesota plasma wave experiment

on Imp 6 (1) the mode is almost certainly magnetic field likely that it is polarized. Regarding distribution from the illustrates generated. The surface tension is the of fixed frequency modes of in Figure cutoff sur

on Imp 6 (P. Kellogg, personal communication, 1973), and so the mode of propagation is not known. Since the radiation is almost certainly emitted by electrons, which rotate around the magnetic field in the right-hand sense, it is considered highly likely that the kilometric radiation is emitted in the right-hand-polarized (R, X) mode.

Regardless of the mode of propagation the observed spatial distribution of the kilometric radiation can be understood from the ray paths of the emitted radiation. Figure 14 illustrates the expected ray paths for electromagnetic waves generated at relatively low altitudes on an auroral field line. The surface labeled 'propagation cutoff surface' in this illustration is the three-dimensional surface defined by the radial distance of the propagation cutoff for a particular mode and a fixed frequency. This surface has a similar shape for both modes of propagation, and so only one cutoff surface is shown in Figure 14. At magnetic latitudes of less than about 45° the cutoff surface tends to follow the contour of the plasmasphere

boundary because of the rapid increase in the plasma density (hence an increase in f_p and f_{R-X}) at the plasmapause. At higher latitudes (outside the plasmasphere) the cutoff surface is located at lower altitudes and is determined by the parameters of the polar ionosphere (Figure 13).

Since the index of refraction goes to zero at a propagation cutoff [Stix, 1962], there is a strong tendency for the ray paths to be refracted away from the cutoff surface (Figure 14). This tendency is strongest for waves generated close to the cutoff and decreases as the generation region moves to higher altitudes above the cutoff point. The general effect of this refraction, when a distribution of emitted wave normal directions is considered, is to direct the radiation into the interior of a conical region whose axis is aligned roughly normal to the propagation cutoff surface. The half angle of this cone depends strongly on the altitude of generation above the cutoff surface (Figure 14).

The observed angular distribution of the kilometric radiation

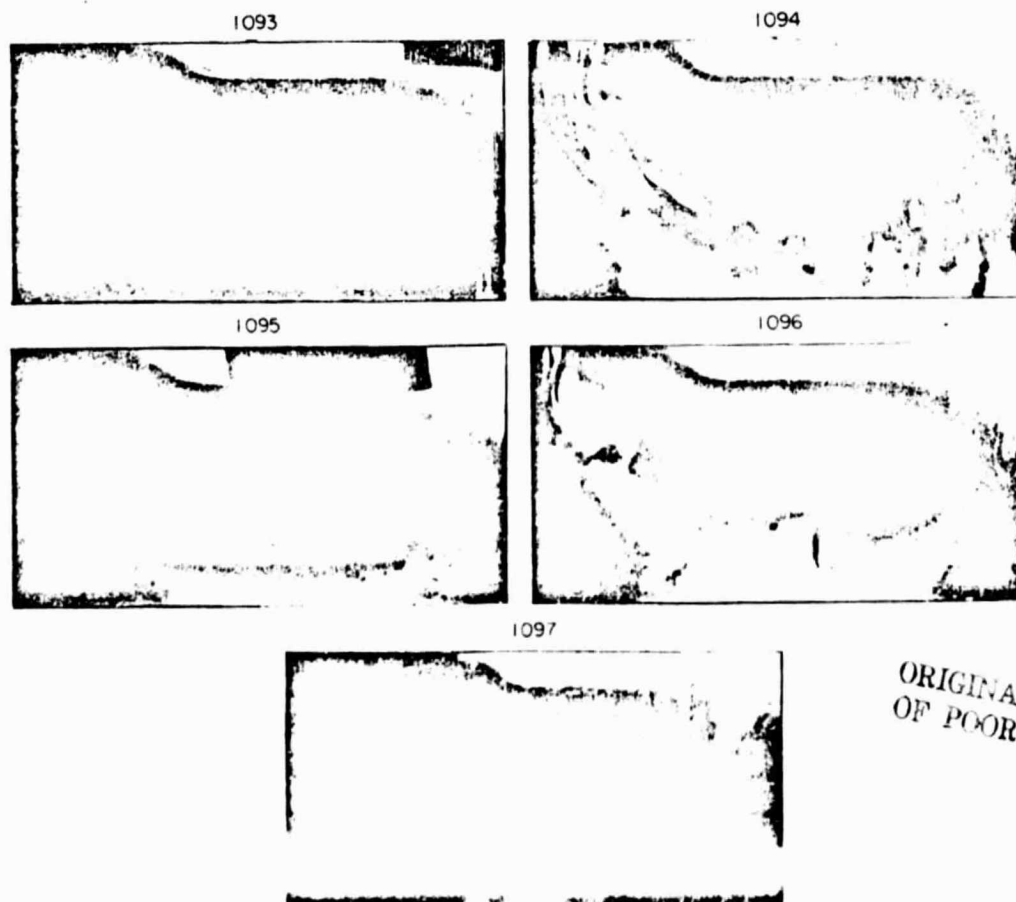
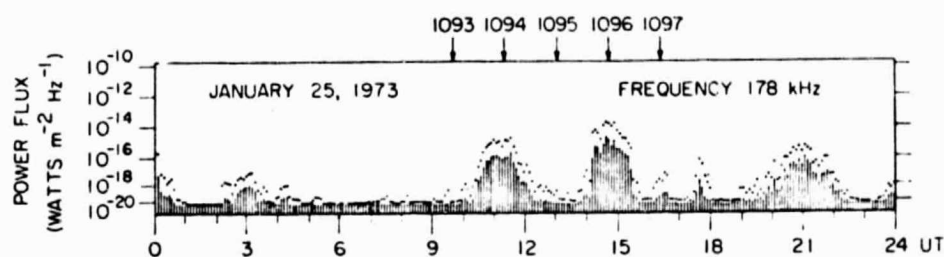


Fig. 11. The Dapp auroral photographs obtained during the first two periods of major substorm activity in Figure 10. Note that the kilometric radiation appears to be more closely related to discrete auroral arcs than to the diffuse aurora, as is true in orbit 1095, for which a diffuse aurora is present near local midnight but no kilometric radiation is evident.

ORIGINAL PAGE IS
OF POOR QUALITY

tion (Figure 9) can largely be explained from the conical distribution of ray paths illustrated in Figure 14 and the spatial location of the source. It is well known that very bright discrete auroral arcs are most pronounced in the local evening [Akasofu, 1968; Snyder *et al.*, 1974]. If the kilometric radiation is generated by electron precipitation associated with discrete arcs in the local evening region, it is evident from the ray paths in Figure 14 that the radiation can be observed only at very high magnetic latitudes in the local morning, in agreement with the Imp 6 observations in Figure 9. In the local evening the radiation should be observed at essentially all latitudes, provided that the observing point is beyond the shadow zone produced by the plasmasphere boundary, again in agreement with the Imp 6 observations.

At a radial distance of $30 R_E$ the terrestrial kilometric radiation is found to have a maximum average power flux (1% occurrence) of about $10^{-14} \text{ W m}^{-2} \text{ Hz}^{-1}$ at 178 kHz. By means of this power flux and on the assumption that the effective bandwidth of the emission is 300 kHz and that the radiation is emitted uniformly over a solid angle of about 6.5 sr (estimated from Figure 9), the total power radiated is about $7.0 \times 10^8 \text{ W}$. Since the solid angle used to calculate the total radiated power is based on the average solid angle at a relatively low power flux, it is possible that the instantaneous solid angle of the

emitted radiation may be substantially smaller when high intensities are observed. The solid angle can be determined accurately by comparing the power flux simultaneously at two or more points. The preliminary result of comparing simultaneous Imp 6 and 8 data is that comparable peak power fluxes are observed at widely different locations, provided that both spacecraft are within the region where the radiation has a high probability of occurrence (Figure 9). These comparisons indicate that the radiation is emitted over a large solid angle event at high intensities and that the peak total power radiation is of the order of 10^9 W . Further analysis of simultaneous Imp 6 and 8 data should provide a firm determination of the total radiated power.

The maximum power dissipated by charged particles in the aurora during an auroral substorm is about 10^{11} W [Akasofu, 1968]. If the corresponding maximum power of the kilometric radiation is 10^9 W , then the efficiency with which this radiation is generated must be about 1%. From all present knowledge of magnetospheric radio emissions the generation of terrestrial kilometric radiation represents a very efficient conversion of charged-particle energy into radio emission.

Since electromagnetic radiation occurs above the plasma frequency in a wide variety of physical situations—for example, in type 3 solar radio noise bursts [Wild, 1950] and in Jovian decametric radiation [Warwick, 1967], it is of considerable

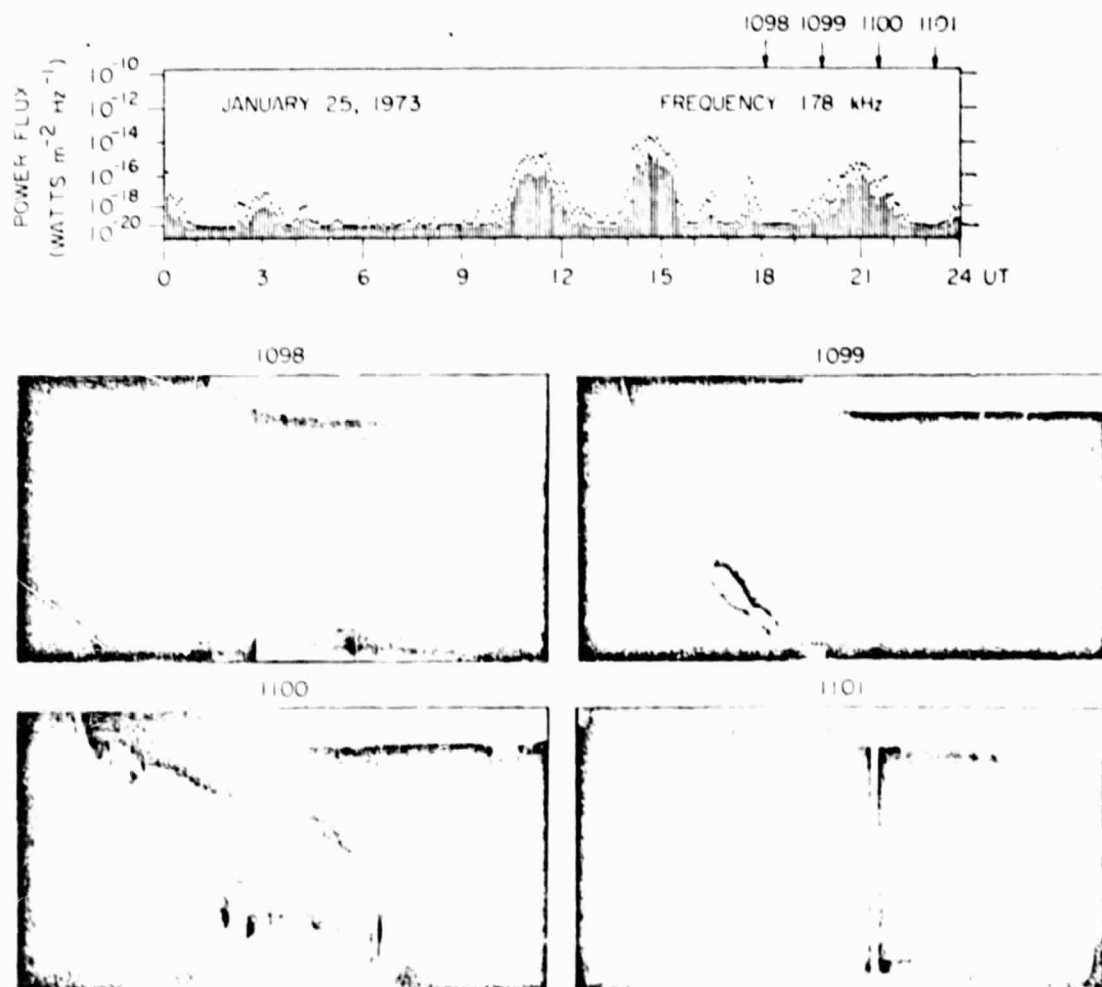


Fig. 12. The Dapp auroral photographs obtained during the third period of major substorm activity in Figure 10. Note orbit 1099, which shows the onset of a discrete auroral arc at the time when the kilometric radiation is just beginning.

Fig. 13. Variation of hand-pole lower-frequency from energy.

general kilometric consider involved distributed about the Discrete tense in low-altitude 1971-4 associated discrete trons in kilometric events of energetic events.

Two general may be trons, an unstable kilometric that through cycle of small time and appear tensile.

When is a steady radiated a fact moving radiated kilometric electron about

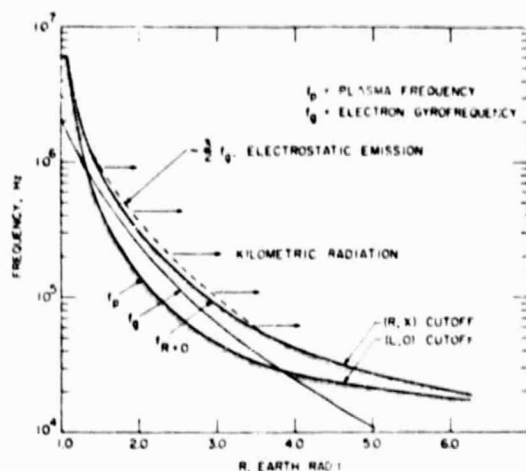


Fig. 13. Polar ionospheric model showing the expected radial variation of the cutoff frequencies f_p and $f_{R=0}$ for the left- and right-hand-polarized free-space electromagnetic modes. The upper- and lower-frequency limits of the terrestrial kilometric radiation can be explained if the radiation is generated by coherent cyclotron radiation from energetic auroral electrons.

general interest to establish the origin of the terrestrial kilometric radiation. In this case it should be possible to make considerable progress toward identifying the basic mechanism involved, since a great deal is known about the electron energy distribution and intensities associated with auroral arcs and about the basic plasma parameters in the generation region. Discrete auroral arcs have been directly associated with intense 'inverted V' electron precipitation bands observed by low-altitude polar-orbiting satellites [Frank and Ackerson, 1971; Ackerson and Frank, 1972]. Because of the observed association between the terrestrial kilometric radiation and discrete auroral arcs it is almost certain that the energetic electrons in these inverted V events are directly responsible for the kilometric radiation. The inverted V electron precipitation events have fluxes of up to 10^9 el $\text{cm}^{-2} \text{ s}^{-1} \text{ sr}^{-1}$ and maximum energies of about 10 keV. Detailed energy spectra for these events are given by Frank and Ackerson [1971].

Two general mechanisms can be considered to explain the generation of the terrestrial kilometric radiation: (1) the noise may be generated by incoherent radiation from energetic electrons, or (2) the noise may be generated by a coherent plasma instability. Because of the very high efficiency with which the kilometric radiation is generated it is considered very unlikely that this noise is produced by an incoherent mechanism. A rough calculation shows that the power radiated by incoherent cyclotron radiation from energetic auroral electrons is too small by a factor of about 10^6 . Similarly, the power radiated by incoherent Cerenkov radiation [Taylor and Shawhan, 1974] and by incoherent gyrosynchrotron radiation [Frankel, 1973] appears to be much too small to account for the observed intensities of the kilometric radiation.

What is needed to explain the terrestrial kilometric radiation is a suitable mechanism for providing coherence between the radiating electrons in order to increase the radiated power (by a factor of N^2 , where N is the number of electrons that are moving in phase). Recently, to explain the low-altitude decametric radiation, which may in fact be very similar to the terrestrial kilometric radiation, Scarf [1973] has suggested that a purely electrostatic plasma instability that occurs at a frequency of about $3f_{R=0}/2$ may organize the phase of the energetic electrons

in the Jovian magnetosphere, thereby greatly increasing the power radiated by these electrons. This same mechanism had also been proposed by Gurnett and Shaw [1973] to explain the generation of electromagnetic waves trapped in the magnetosphere above the local plasma frequency. It is not known whether electrostatic emissions at $3f_{R=0}/2$ actually occur in the region where the kilometric radiation is generated, because Imp 6 does not go through this region (see the trajectory in Figure 8, for example). However, these electrostatic emissions do occur over large regions of the magnetosphere [Kennel et al., 1970] and are expected in regions of field-aligned currents associated with discrete auroral arcs. If the kilometric radiation is generated at $3f_{R=0}/2$ by this mechanism, then a simple explanation arises for the observed bandwidth of the radiation. Figure 13 shows that the right-hand-polarized free-space mode cannot propagate at a frequency less than the (R, X) cutoff at $f_{R=0}$. If the radiation is emitted as right-hand-polarized electromagnetic waves at $3f_{R=0}/2$, then this radiation can only propagate away from the generation region in a limited frequency range, from about 50 kHz to 1.2 MHz for the model in Figure 13.

To explain the intense decametric radio emissions associated with Jupiter's moon Io, Goldreich and Lynden-Bell [1969] have proposed a coherent cyclotron mechanism for directly generating intense electromagnetic radiation from a beam of weakly relativistic electrons. This mechanism may also be able to account for the main characteristics of the terrestrial kilometric radiation, since many similarities exist between the terrestrial kilometric radiation and the Jovian decametric radiation. These similarities include the following:

1. In both cases the radiation appears to be associated with magnetic field-aligned beams of electrons with energies of the order of tens of keV.
2. In both cases the frequency of the radiation appears to be closely associated with the electron gyrofrequency (hence the magnetic field strength) in the emitting region.

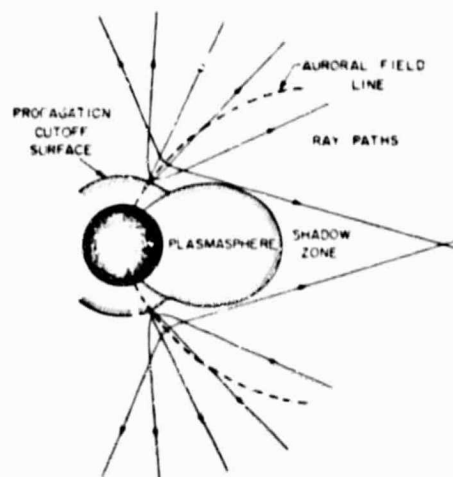


Fig. 14. Qualitative sketch of the ray paths of electromagnetic radiation emitted at low altitudes and fixed frequency along an auroral field line. Because the refractive index goes to zero at the propagation cutoff, there is a strong tendency for the ray paths to be refracted upward, away from the propagation cutoff surface. The propagation cutoff surface is shown as a solid line, and the shadow zone is shown as a dashed line. The refractive index goes to zero at the propagation cutoff surface, which accounts for the low-latitude cutoff evident in Figure 7. Also, note that radiation from the local evening can reach the local morning only at very high magnetic latitudes, in agreement with the observed angular distribution in Figure 9.

3. In both cases the angular distribution of the emitted radiation is associated with a distinct cone-shaped boundary that is at a large angle to the magnetic field direction in the emitting region.

4. In both cases the total emitted power (10^6 W and 2×10^7 W) and field-aligned currents (10^6 A in both cases) are quantitatively similar.

It is interesting to note that the coherent cyclotron mechanism could also account for the primary frequency range of the kilometric radiation, since the resonance energy at which the emission occurs decreases rapidly as the ratio of the electron plasma frequency to electron gyrofrequency, f_p/f_e , decreases (S. Shawhan, personal communication, 1974). On the assumption that the number of electrons in the auroral electron beam increases with decreasing energy, the maximum growth rate, and hence the intensity, occurs where the ratio f_p/f_e is a minimum; this is at a frequency of about 150 kHz for the ionospheric model used in Figure 13.

Acknowledgments I wish to extend my special thanks to S.-I. Akasofu, who provided the magnetogram records used in this study and to W. S. Kurth and R. R. Anderson, who assisted in the data analysis. The Dapp photographs were provided by the NOAA World Data Center. This work was supported in part by NASA under contracts NASS-11074 and NASS-11431 and grant NGL-16-001-043 and by the Office of Naval Research under grant N00014-68-A-0196-0009.

The Editor thanks R. E. Barrington and N. Dunckel for their assistance in evaluating this paper.

REFERENCES

- Ackerson, K. L., and L. A. Frank, Correlated satellite measurements of low-energy electron precipitation and ground-based observations of a visible auroral arc, *J. Geophys. Res.*, **77**, 1128, 1972.
- Akasofu, S.-I., *Polar and Magnetospheric Substorms*, p. 223, D. Reidel, Dordrecht, Netherlands, 1968.
- Banks, P. M., and T. E. Holzer, High-latitude plasma transport: The polar wind, *J. Geophys. Res.*, **74**, 6317, 1969.
- Brown, I. W., The galactic radio spectrum between 130 kHz and 2600 kHz, *Astrophys. J.*, **180**, 359, 1973.
- Dunckel, N., B. Ficklin, L. Rorden, and R. A. Helliwell, Low-frequency noise observed in the distant magnetosphere with Ogo 1, *J. Geophys. Res.*, **75**, 1854, 1970.
- Frank, L. A., and K. L. Ackerson, Observations of charged-particle precipitation into the auroral zone, *J. Geophys. Res.*, **76**, 3612, 1971.
- Frankel, M. S., LF radio noise from the earth's magnetosphere, *Radio Sci.*, **8**, 991, 1973.
- Goldreich, P., and D. Lynden-Bell, Io, A Jovian unipolar inductor, *Astrophys. J.*, **156**, 59, 1969.
- Gurnett, D. A., and R. R. Shaw, Electromagnetic radiation trapped in the magnetosphere above the plasma frequency, *J. Geophys. Res.*, **78**, 8136, 1973.
- Kennel, C. F., F. L. Scarf, R. W. Fredricks, J. H. McGehee, and F. V. Coroniti, VLF electric field observations in the magnetosphere, *J. Geophys. Res.*, **75**, 6136, 1970.
- Scarf, F. L., A new model for the high-frequency decametric radiation from Jupiter, *Rep. 24876-6001-RU-00*, 8 pp., TRW Syst. Group, Redondo Beach, Calif., 1973.
- Snyder, A. L., S.-I. Akasofu, and T. N. Davis, Auroral substorms observed from above the north polar region by a satellite, *J. Geophys. Res.*, **79**, 1393, 1974.
- Stix, T. H., *The Theory of Plasma Waves*, p. 27, McGraw-Hill, New York, 1962.
- Taylor, W. W. L., and S. D. Shawhan, A test of incoherent Cerenkov radiation for VLF hiss and other magnetospheric emissions, *J. Geophys. Res.*, **79**, 105, 1974.
- Warwick, J., Dynamic spectra of Jupiter's decametric emission, 1961, *Astrophys. J.*, **137**, 41, 1963.
- Warwick, J. W., Radiophysics of Jupiter, *Space Sci. Rev.*, **6**, 841, 1967.
- Wild, J. P., Observations of the spectrum of high-intensity solar radiation at meter wavelengths, 3. Isolated bursts, *Aust. J. Sci. Res., Ser. A*, **3**, 541, 1950.

(Received February 14, 1974;
accepted June 21, 1974)

Electrostatic and Electromagnetic Turbulence Associated With the Earth's Bow Shock

PAUL RODRIGUEZ AND DONALD A. GURNETT

Department of Physics and Astronomy, University of Iowa, Iowa City, Iowa 52242

The electric and magnetic field spectral densities of plasma waves in the earth's bow shock have been measured in the frequency range 20 Hz to 200 kHz by using two 16-channel spectrum analyzers on the Imp 6 spacecraft. The electric field spectrum in the bow shock consists of two distinct components: one component has a broad peak typically centered between 200 and 800 Hz with an average (5.12-s time constant) spectral density at the peak of about $10^{-9} \text{ V}^2 \text{ m}^{-2} \text{ Hz}^{-1}$, and the other component increases monotonically with decreasing frequency approximately as $f^{-1.5}$ and has an average spectral density of about $3.0 \times 10^{-9} \text{ V}^2 \text{ m}^{-2} \text{ Hz}^{-1}$ at 36.0 Hz. The magnetic field spectrum in the shock has only one component that increases monotonically with decreasing frequency approximately as $f^{-1.5}$ and has an upper cutoff frequency near the local electron gyrofrequency. This magnetic field spectrum appears to be associated with the monotonic component of the electric field spectrum. The electric to magnetic energy density ratio ϵ_E/ϵ_B of this noise is about 10^{-2} to 10^{-4} , which is consistent with the energy density ratio expected for electromagnetic whistler mode waves in the bow shock. The broad peak in the electric field spectrum between 200 and 800 Hz has a large electric to magnetic energy density ratio, $\sim 10^2$ to 10^4 , indicating that this component consists of almost purely electrostatic waves. Electrostatic noise with a spectrum similar to the turbulence in the shock but with lower intensities is observed throughout the magnetosheath region downstream of the shock. This magnetosheath electric field turbulence often includes many bursts with a distinct 'parabolic' frequency-time variation on a time scale of a few seconds. Spin modulation measurements of the electric field direction show that the electric field vectors in both the shock transition region and the magnetosheath region are preferentially oriented parallel to the static magnetic field direction. The electric field of upstream electron plasma oscillations also is oriented parallel to the static magnetic field.

A basic problem of shocks in collisionless plasmas is to identify and understand the dissipation mechanism that occurs in the transition region connecting the upstream and downstream states. In the absence of binary collisions, dissipation must occur through collective coulomb interactions of the charged particles. This results in the self-consistent generation of a turbulent spectrum of electrostatic waves that stochastically accelerates the charged particles. Experimentally, this is often described in terms of an 'anomalous' or effective resistivity for Ohm's law, $\mathbf{E} = \eta^* \mathbf{J}$, through which turbulent electric fields heat the plasma. The earth's bow shock provides a very convenient steady state laboratory for the study of high Mach number collisionless shocks. Electron and proton velocity distributions measured in the solar wind and magnetosheath near the bow shock indicate that strong thermalization occurs in relatively thin regions within the shock structure [Montgomery *et al.*, 1970; Formisano and Hedgecock, 1973a, b]. Magnetometer measurements of the magnetic field in the bow shock up to 10 Hz show a broad turbulent spectrum 2-3 orders of magnitude above the interplanetary spectrum [Olson *et al.*, 1969; Holzer *et al.*, 1966, 1972]. Electric field spectra in the range 560 Hz to 70 kHz [Fredricks *et al.*, 1968, 1970a, b] show electrostatic turbulence in the shock strongly correlated with magnetic field gradients, indicating the presence of some form of current-driven instability [Wu and Fredricks, 1972].

In this report we present some simultaneous measurements of electric and magnetic field spectral densities in the bow shock as obtained with the University of Iowa plasma wave experiment on the Imp 6 spacecraft. The frequency range of the plasma wave detector, 20 Hz to 200 kHz, covers most of the characteristic plasma frequencies for electrons and protons in average solar wind conditions. Electric fields are measured with long dipole antennas (~ 100 m tip to tip) with high sen-

sitivity, of the order of $1 \mu\text{V/m}$. Magnetic fields are measured with single-turn loop antennas.

The electric field measurements of Fredricks *et al.* [1968] were obtained with short dipole antennas (effective length of 0.5 m) on the Ogo 5 spacecraft, which are less sensitive than the long Imp 6 antennas (the ratio of effective lengths is ~ 100). To provide a basis for comparison between the Imp 6 and the Ogo 5 measurements, Imp 6 also has a short dipole antenna (effective length of 0.38 m).

The Imp 6 spacecraft was launched on March 13, 1971, with initial orbit parameters as follows: period, 4.18 days; perigee, 6614 km; apogee, 212,269 km ($\sim 34 R_E$); inclination, 28.7° . The satellite is spin stabilized with its spin vector perpendicular to the ecliptic plane and pointing toward the south celestial pole and with a nominal spin period of 11.1 s.

The measurements of the present study were obtained during the first 30 orbits, covering the noon to dawn quadrant of local time. During this time, from March 17, 1971, to July 15, 1971, the solar wind conditions were usually relatively quiet with intermittent noisy periods as indicated by daily average values of K_p . The overall average K_p was about 2.0. In 30 orbits the spacecraft would have to cross the shock at least 60 times, but multiple crossings (due to the oscillatory motion of the bow shock structure past the spacecraft) have increased this number to over 150.

EXPERIMENT DESCRIPTION

Electric antennas. The spacecraft has three mutually perpendicular long dipole antennas identified in the spacecraft frame as $\pm X$, $\pm Y$, and $\pm Z$. The spacecraft spin vector is in the $+Z$ direction, and the X - Y plane is parallel to the ecliptic plane. The antennas are formed from prestressed conducting ribbons that assume a tubular shape as they are extended outward from the spacecraft. An insulating material covers all but the outer 16.8 m of the antennas. Extensions of the antennas

were made in seven steps over the time interval of the first nine orbits. The final tip-to-tip lengths are as follows: $E_X = 54.0$ m, $E_Y = 93.2$ m, and $E_Z = 7.7$ m. The effective lengths for the long antennas are taken as one-half the tip-to-tip lengths. The short dipole antenna is attached to the magnetometer boom and oriented in the Z direction. Two spherical wire cages at the ends of insulating rods form the elements of the short dipole antenna, its effective length thus being 0.38 m. This antenna was designed to serve as a backup to the long antennas and to provide the measurements at a different effective length.

Magnetic antennas. A system of three orthogonal loops at the end of a boom forms the magnetic antennas (M_X , M_Y , M_Z). They are oriented to conform to the coordinate system defined by the long electric antennas. Each loop is made of a single turn of aluminum tubing and has an area of 0.81 m².

Spectrum analyzers. Two 16-channel spectrum analyzers (A and B) are used to provide spectrum measurements. Each spectrum analyzer covers the frequency range from 20 Hz to 200 kHz with four filters per decade of frequency. The filter bandwidths range from about 20% of the center frequency at low frequencies to about 10% at high frequencies. Each filter is connected to a logarithmic receiver with 100-dB dynamic range and 10- μ V sensitivity. The receiver output is proportional to the logarithm of the input voltage. By using the long electric antenna, electric fields as low as 0.2 μ V/m can be detected. The magnetic field sensitivities depend on the wave frequency and range from 2.0 mV at 36 Hz to about 10.0 μ V at 16.5 kHz.

In the usual mode of operation, analyzer A is connected to the E_Y antenna, and analyzer B is connected to the M_X antenna. However, on command, each analyzer can be switched to any of the seven available antennas. In the high-rate data sampling mode the 32 analyzer channels are sampled in rapid sequence once every 5.12 s for average and peak outputs. The peak measurement gives the maximum receiver output over the 5.12-s interval between samples. The time constants are 5.12 s for the average measurement and 0.10 s for the peak measurement. A complete set of average and peak spectrum measurements is obtained for all channels once every 5.12 s and is called a snapshot. A snapshot is the basic data unit for the spectral density calculations presented in this paper. In addition to the spectrum measurements, there is a rapid-sample mode in which a given channel is sampled every 0.32 s. The rapid-sample measurements cycle through eight spectrum analyzer channels in a fixed sequence, 128 consecutive samples thus resulting from a given channel.

Shortly after launch it was determined that intense low-frequency (below 1 kHz) electric field interference was being produced by the spacecraft solar array. The main component of this noise is strongly spin modulated and is due to voltage transients caused by the shadow of the magnetic antenna boom and loops moving across the solar cell panels. The near 2:1 relationship between the spacecraft spin period (11.1 s) and the sampling interval (5.12 s) means that noise contamination in the peak measurements occurs in alternate snapshots and is easily identified.

Wide band receivers. Two wide band receivers provide broadband coverage over the ranges 10 Hz to 1 kHz and 650 Hz to 30 kHz. These analog signals are used to reconstruct analog frequency-time spectra for studying cutoffs, resonances, and other wave characteristics that require good frequency-time resolution.

PLASMA WAVE SPECTRA IN THE BOW SHOCK

General characteristics. Figure 1 illustrates the electric and magnetic field intensities typically observed in a bow shock crossing with the Imp 6 plasma wave experiment. Average and peak electric and magnetic field amplitudes are shown as a function of universal time for seven channels of both spectrum analyzers. The average field amplitudes are indicated by vertical lines, and the peak field amplitudes, by dots. The constant level for the peak measurements in the 36-Hz and 120-Hz electric field channels is caused by the previously mentioned interference from the solar array. The spacecraft crosses the bow shock, passing from the magnetosheath into the solar wind, at about 1048 UT, as is indicated by the sharp enhancement in the electric field strength above the average levels of both the magnetosheath and the solar wind at all frequencies below about 10.0 kHz. The electric field noise in the bow shock typically extends over a very broad frequency range, usually from 36.0 Hz, which is the lowest frequency measured, to greater than 10.0 kHz. In some cases, electric field noise associated with the bow shock has been detected up to 56.2 kHz.

The regions upstream and downstream of the bow shock are distinguished by their correspondingly low and high levels of electric field noise. In the magnetosheath the peak electric field spectral density in the 1.00-kHz and 3.11-kHz channels is typically about 3 orders of magnitude above the solar wind levels. In the solar wind the peak, and to a lesser extent the average, field strengths are strongly modulated at the lower frequencies by the solar array noise.

Immediately upstream of the bow shock a distinct enhancement is evident in the 31.1-kHz electric field strength from about 1048 UT to 1055 UT. This noise is primarily electrostatic, since no comparable enhancement is evident in the 31.1-kHz magnetic field data, and is caused by electron plasma oscillations at the local electron plasma frequency. Several accounts of electron plasma oscillations of this type, generated by electrons streaming into the solar wind from the bow shock, have been reported previously [Fredricks *et al.*, 1968; Scarf *et al.*, 1971; Fredricks *et al.*, 1971, 1972]. Electron plasma oscillations upstream of the bow shock are observed on almost all shock crossings with Imp 6.

Figure 1 shows only a slight increase in the magnetic field intensities at the bow shock. In the solar wind upstream of the bow shock the magnetic field intensities are below the sensitivity threshold of the receiver in all except the lowest-frequency channel. In the magnetosheath downstream of the bow shock, magnetic field fluctuations are evident in all frequency channels below about 1.00 kHz. These fluctuations are usually most evident in the peak measurements, indicating that the fluctuations occur on a time scale much less than the 5.12-s time constant for the average field strength measurements. Often the magnetic field measurements in the magnetosheath indicate turbulence at only two or three intermediate frequencies (such as 120 Hz and 200 Hz). The magnetosheath noise starts abruptly at the bow shock. The magnetic field fluctuations at the shock are usually only slightly larger than those in the magnetosheath.

Figure 2 shows a double crossing of the bow shock, the first at about 1251 UT and the second at about 1252 UT, caused by the oscillatory motion of the shock structure. A clean separation of the upstream and downstream regions by the shock transition occurs in this example, the upstream solar wind

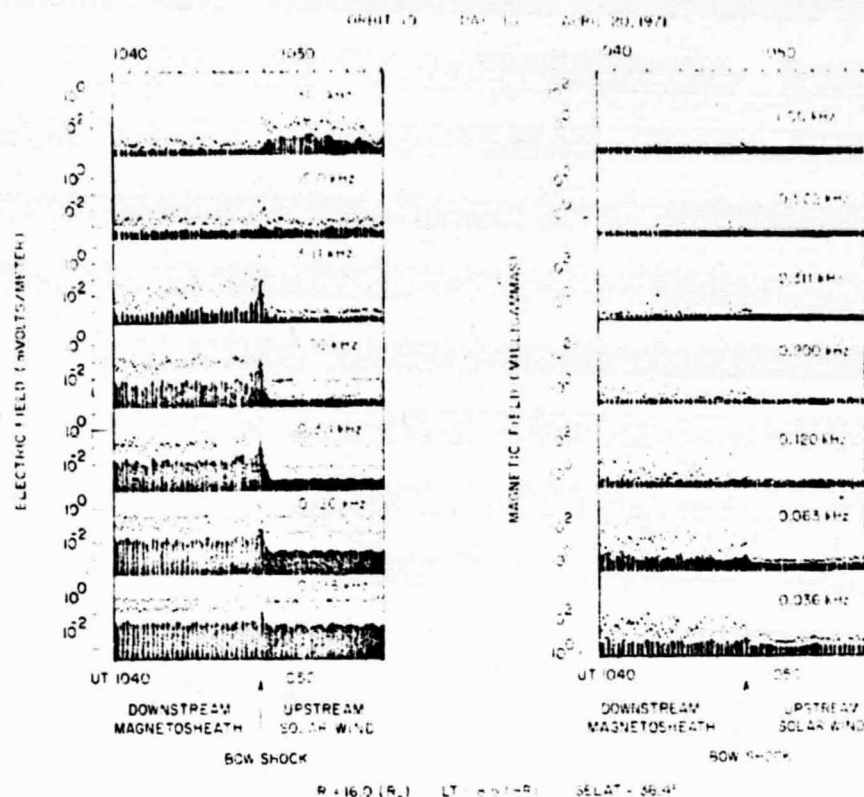


Fig. 1. A typical bow shock crossing as detected by the Imp 6 plasma wave experiment. Average measurements (5.12-s time constant) are plotted as vertical lines; peak measurements (0.1-s time constant) are plotted as dots. The shock transition occurs at about 1048 UT. The electric field measurements (left) show upstream plasma oscillations at 31.1 kHz after 1048 UT.

region being between 1251 and 1252 UT. The magnetic field measurements from the Goddard Space Flight Center (GSFC) magnetometer on Imp 6 show a clear jump in the magnetic field at each crossing from a steady upstream value, $B_1 \approx 5 \gamma$, to a downstream value, $B_2 \approx 20 \gamma$. The angle between the upstream field and the shock normal calculated from the model of Fairfield [1971] is $\psi(\mathbf{B}, \hat{n}) \approx 92^\circ$ for both crossings (D. Fairfield, personal communication, 1974). The bow shock in this case is therefore a perpendicular shock.

Electric and magnetic field spectral densities, $E^2(\omega)$ and $B^2(\omega)$, have been computed for 16 snapshots obtained for the second crossing of the shock shown in Figure 2. Each snapshot of data provides a complete electric and magnetic field spectrum for both average and peak measurements. The electric field strength is determined by dividing the measured ac voltage at the antenna terminals by one half of the tip-to-tip length, any antenna impedance corrections being ignored. The computed electric field spectral densities for the average field strength measurements are shown in the three-dimensional plot in Figure 3. The time axis is at an oblique angle in this plot, and successive spectra are 5.12 s apart. The time indicated at the bottom of the figure is the universal time of the first snapshot. For ease of reference, each spectrum is labeled by a snapshot number. Figure 4 shows the corresponding magnetic field spectra for the same time interval.

Beginning with snapshot 1 in Figure 3, strong electric field noise is present in the 16.5-kHz channel, which steadily decreases in magnitude as the shock is approached. This noise is the previously mentioned electrostatic electron plasma

oscillations associated with electrons streaming into the solar wind from the bow shock. Low-frequency noise associated with the shock begins in snapshot 3 and steadily increases in intensity to a maximum in snapshot 7, by which time the electron plasma oscillations have disappeared. For the crossing at 1252 UT, the maximum rms electric field E_{rms} integrated across the entire frequency range, from 20 Hz to 200 kHz, occurs in snapshot 7 and has a value of $8.73 \times 10^{-4} \text{ V m}^{-1}$. Up to 98% of the contribution to E_{rms} comes from below 1 kHz, and the spectrum has a broad maximum in the frequency range from about 200 Hz to 800 Hz. After the seventh snapshot the low-frequency noise decreases in magnitude, but the characteristic shape of the spectrum at the shock is maintained through the last snapshot in the figure. Examination of spectra taken when the spacecraft is well into the downstream magnetosheath region on this and other crossings reveals that the shape of the magnetosheath spectrum is the same as that of the shock except for variations in the low-frequency part of the spectrum. Thus the electric field spectrum in the shock appears to be carried into the downstream region. The downstream spectra also have a roughly periodic modulation of low-frequency intensities with a period of about four snapshots, or about 20 s. This modulation appears to be a general feature of the downstream electric field spectra near the bow shock. Periods range up to 60–70 s.

The magnetic field spectra in Figure 4 reveal the shock transition as merely an enhancement of low-frequency noise. Above about 3 kHz the spectral densities are close to or at the receiver noise level. The maximum rms magnetic field intensity

ORIGINAL PAGE IS
OF POOR QUALITY

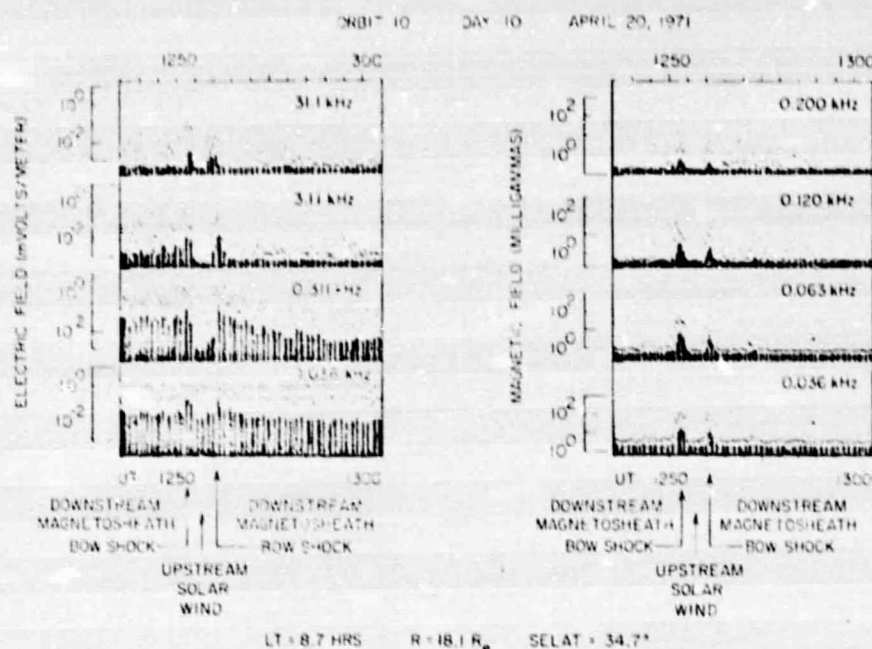


Fig. 2. A double crossing of the earth's bow shock as detected by the Imp 6 plasma wave experiment. The bow shock was very nearly a perpendicular shock during these crossings.

integrated across the entire frequency range, 20 Hz to 200 kHz, occurs in snapshot 6 and has a value of $5.49 \times 10^{-2} \gamma$. Most of the contribution to B_{rms} comes from below 100 Hz.

Electric and magnetic field spectra in the bow shock. For purposes of surveying the electric and magnetic field spectra for a large number of shock crossings, one spectrum that is representative of each shock crossing must be selected. The snapshot that gives the maximum rms field amplitude, found by using the average spectral density measurements integrated from 20 Hz to 200 kHz, is selected as the shock spectrum. The electric and magnetic field spectra thus selected are denoted by $E^2(\omega)_s$ and $B^2(\omega)_s$ and are referred to as the shock spectra.

A typical shock transition as resolved by the spectral measurements takes place over four or five snapshots, sometimes as many as 10. In the series of values of E_{rms} calculated for a given shock crossing there is usually only one maximum in E_{rms} , and thus $E^2(\omega)_s$ is clearly defined. However, the series of values of B_{rms} calculated through the same shock crossing may have several maximums, none of which occur at the same time as the maximum in E_{rms} . For these cases we choose as the shock magnetic field spectrum the one that gives the largest value of B_{rms} within three snapshots of the shock electric field spectrum.

From the discussion above, it can be seen that our determination of the characteristic electric and magnetic field shock spectra is based on the snapshot in which the most intense low-frequency electric field noise occurs. We consider this to be appropriate, since the shock transition would be characterized by the spectrum $E^2(\omega)_s$ that represents the greatest dissipation, i.e., the one with the greatest turbulent electric field energy density.

Figure 5 shows the shock electric field spectrum selected for the shock crossing at 1252 UT. This spectrum corresponds to snapshot 7 in Figure 3. Both the peak and the average electric field strengths obtained during this snapshot are shown. The noise level indicated in Figure 5 is the ambient noise level (both interference and natural noise) that existed in the solar wind just ahead of the shock. The shape of both the average and the

peak electric field spectrum is characteristic of all the shock spectra examined in this study. However, as will be shown, the intensities at a given frequency vary over 2 orders of magnitude. The inflection in the spectrum, at about 200 Hz in Figure 5, sometimes becomes very pronounced, so that a broad peak develops in the spectrum between 200 and 800 Hz. The existence of a distinct peak in the spectrum suggests that this component of the electric field noise (indicated by the dashed curve in Figure 5) may result from a discrete noise source in the wave spectrum that is broadened by Doppler shifts and nonlinear interactions. The tendency for the electric field spectral density to continue to increase with decreasing frequency below about 100 Hz suggests that a second component also exists in the electric field spectrum varying approximately as f^{-2} (straight dashed line in Figure 5).

The electric field spectrum from the peak measurements in Figure 5 is from the same 5.12-s averaging period as the average measurements. The peak spectrum has approximately the same shape as the average spectrum but is shifted upward in intensity by about an order of magnitude. The large ratio between the peak and the average measurements indicates that the field strength has large (order of magnitude) fluctuations on a time scale less than the averaging time (5.12 s). The peak measurements give the upper bound on these fluctuations. For many shocks the peak spectrum does not have a smooth shape like that of the average spectrum but has a more irregular appearance with several sharp maximums. Most of these sharp maximums are grouped around two frequencies: one near the local electron plasma frequency in the upstream solar wind and the other near the broad peak in the average shock electric field spectrum.

Figure 6 shows the shock magnetic field spectrum selected for the shock crossing at 1252 UT in Figure 2. This spectrum corresponds to snapshot 6 in Figure 4; however, in accordance with our selection criterion, this shock spectrum does not correspond in time with the shock electric field spectrum, since in this case the maximum rms magnetic field intensity occurred slightly before (upstream of) the maximum rms electric field

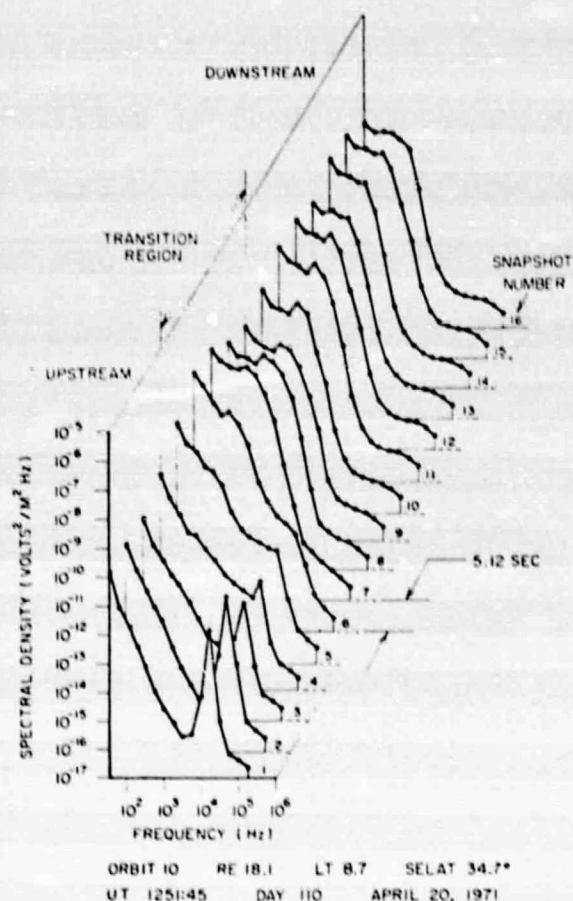


Fig. 3. The electric field spectra, based on average measurements, for the crossing at 1252 UT in Figure 2. The time indicated is for the first spectrum, and the averaging time of 5.12 s occurs between succeeding spectra thereafter. Snapshot 7 is the shock electric field spectrum.

intensity. Both average and peak magnetic field spectra exhibit a generally smooth monotonic decrease with increasing frequency, varying approximately as f^{-4} in the range from 20 Hz to 200 Hz, with no evidence of a peak in the spectrum comparable to the peak in the electric field spectrum. A distinct steepening of the spectrum is also evident at a frequency of about 200 Hz. This steepening of the spectrum occurs at a frequency slightly below the local electron gyrofrequency, which in this case is about 350 Hz. The peak magnetic field spectral density is about an order of magnitude greater than the average magnetic field spectral density, indicating the presence of large fluctuations on a time scale less than 5.12 s.

In Figure 7 we have overlaid the peak and average electric field spectra $E^2(\omega)_n$ for 36 shock crossings selected at random from the Imp 6 data to illustrate the range and variability of the electric field spectrum in the shock. In the majority of cases these spectra exhibit the spectral shape illustrated in Figure 5. Two distinct components are evident in the average electric field spectra and to a lesser extent in the peak spectra: at low frequencies one component decreases monotonically with increasing frequency approximately as $f^{-2.0 \pm 0.5}$, and the other component has a broad peak centered between 200 Hz and 800 Hz. The greatest variation in the spectral shape appears to occur in the spectra with the lowest intensities, ranging from spectra that decrease monotonically with no evidence of a peak to spectra that have a distinct peak that is displaced toward higher frequencies (~ 3 kHz). The largest intensity

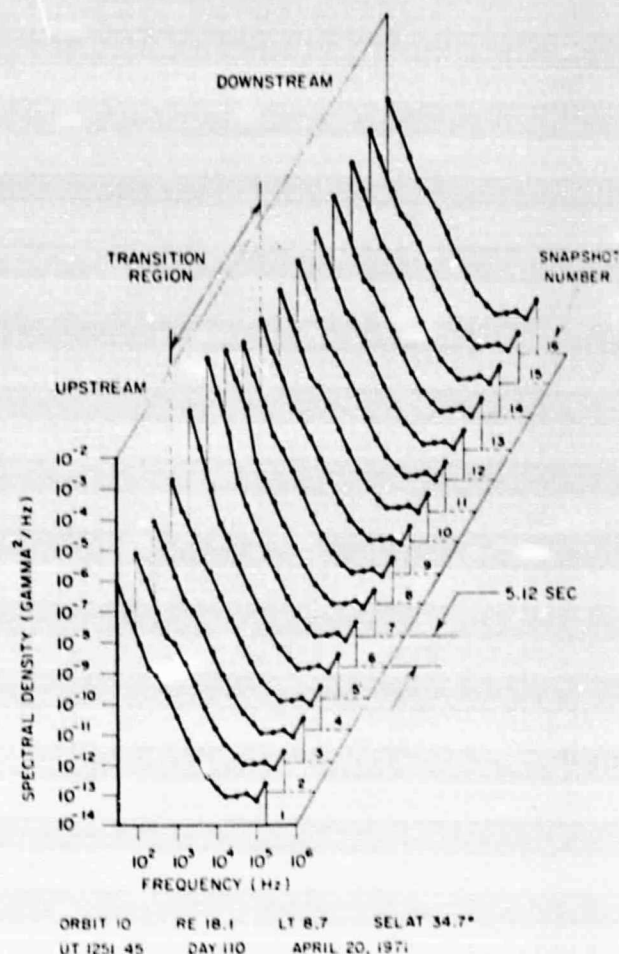


Fig. 4. The magnetic field spectra, based on average measurements, for the crossing at 1252 UT in Figure 2 and corresponding to the electric field spectra in Figure 3. Snapshot 6 is the shock magnetic field spectrum.

variation, which occurs in the range from about 200 Hz to 3 kHz, is associated with the broad peak in the spectrum. As the electric field intensity increases, starting from the lowest level, the peak initially becomes more pronounced until at an intermediate level the intensity of the monotonic component starts to increase and gradually merges with the broad peak. Except for the lowest intensities the main contribution to the rms electric field strength comes from the peak. As will be shown, the broad peak in the spectrum is caused by electrostatic waves, and the monotonic component is caused by electromagnetic whistler mode turbulence. In this study the largest rms electric field strength encountered from the peak measurements is 2.3×10^{-2} V m⁻¹. The largest rms electric field strength from the average measurements is 6.6×10^{-3} V m⁻¹.

Figure 8 shows the overlaid peak and average magnetic field spectra for the 36 shock crossings used in Figure 7. These spectra tend to show a monotonic decrease with increasing frequency, varying approximately as $f^{-4.0 \pm 0.5}$ in the range from about 30 Hz to 100 Hz with clear evidence of a steepening in the spectrum at about 100–200 Hz. This steepening in the magnetic field spectrum usually occurs slightly below the local electron gyrofrequency.

Electric to magnetic energy density ratio. To aid in identifying the plasma wave modes involved in the bow shock turbulence, we have investigated the electric to magnetic field

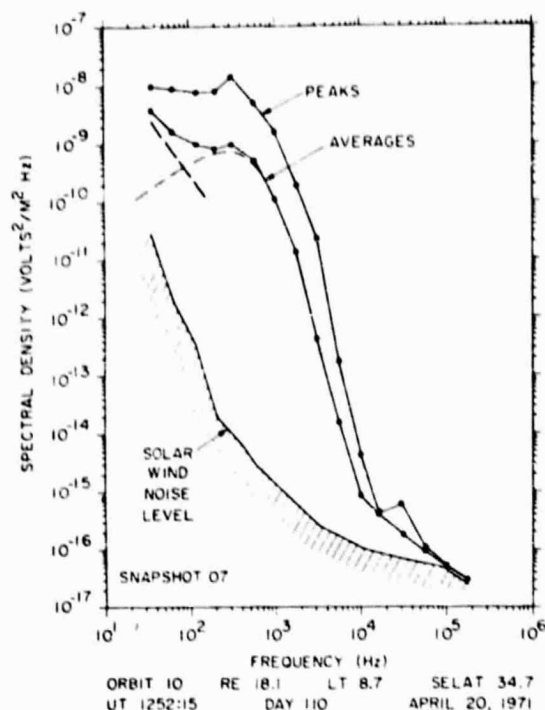


Fig. 5. The shock electric field spectrum $E^2(\omega)_s$ selected on the basis of the rms electric field amplitude. The peak spectrum obtained during the averaging time of the average measurements is also shown. The two distinct components in the shock electric field spectrum are shown by dashed lines.

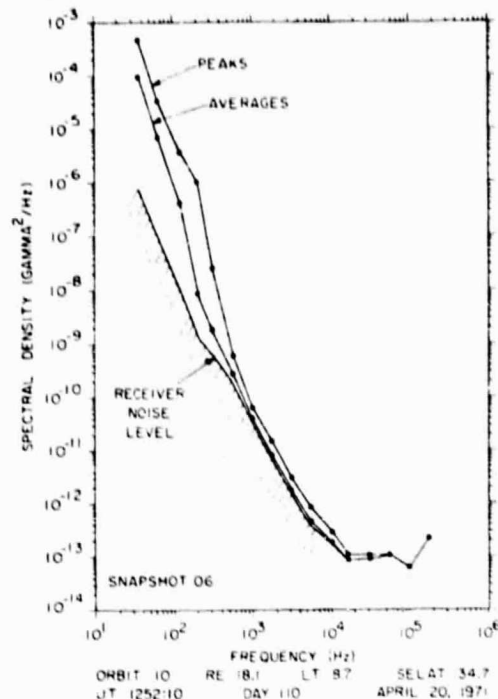


Fig. 6. The shock magnetic field spectrum $B^2(\omega)_s$ for the shock crossing of 1252 UT. The characteristic frequency dependence f^{-1} is present in both the peak and the average spectrum. The spectrum steepens at about 200 Hz, below the local electron gyrofrequency at about 350 Hz.

energy density ratio as the spacecraft passes through a shock. Figure 9 shows the ratio of simultaneously measured energy densities ϵ_E/ϵ_B (where the energy densities are $\epsilon_E = E^2/8\pi$ and $\epsilon_B = B^2/8\pi$) at a sequence of snapshots for the shock crossing at 1252 UT in Figure 2. The snapshot numbers refer to the

spectra of Figures 3 and 4. Because the magnetic field intensities at high frequencies (>3 kHz) are often comparable to or less than the receiver noise level, the magnetic energy densities must be corrected for the receiver noise level. Only magnetic field measurements that exceed the receiver noise level by at

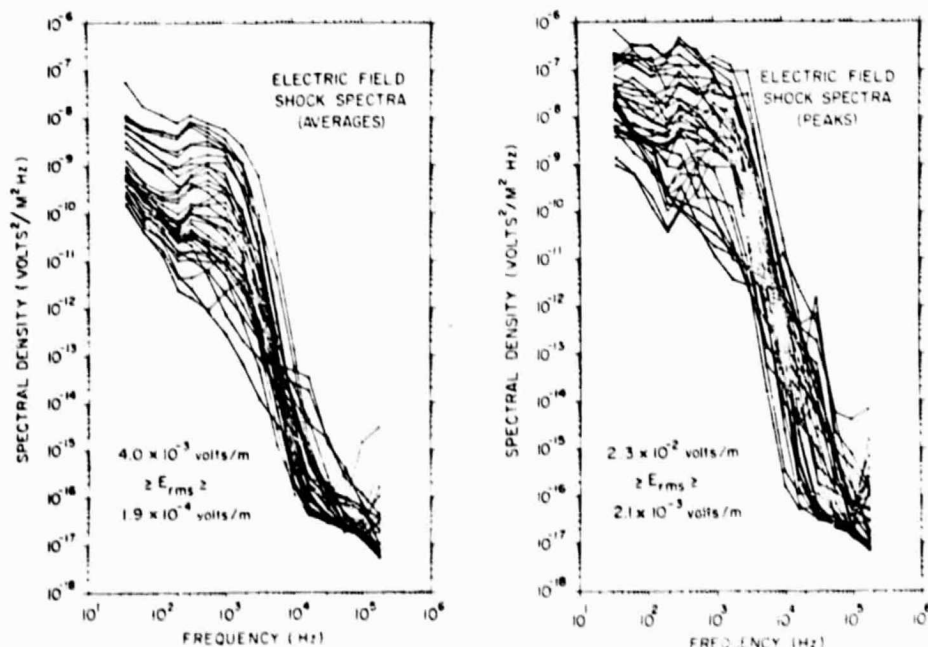


Fig. 7. A representative distribution of electric field shock spectra including average and peak measurements. The average spectra show that the broad peak in the electric field spectra becomes more distinct as the overall intensity of the spectra increases up to some intermediate range and then becomes less distinct as the very low frequency electric field spectral density saturates. The peak spectra are generally similar to the average spectra in shape but range up to an order of magnitude more in intensity.

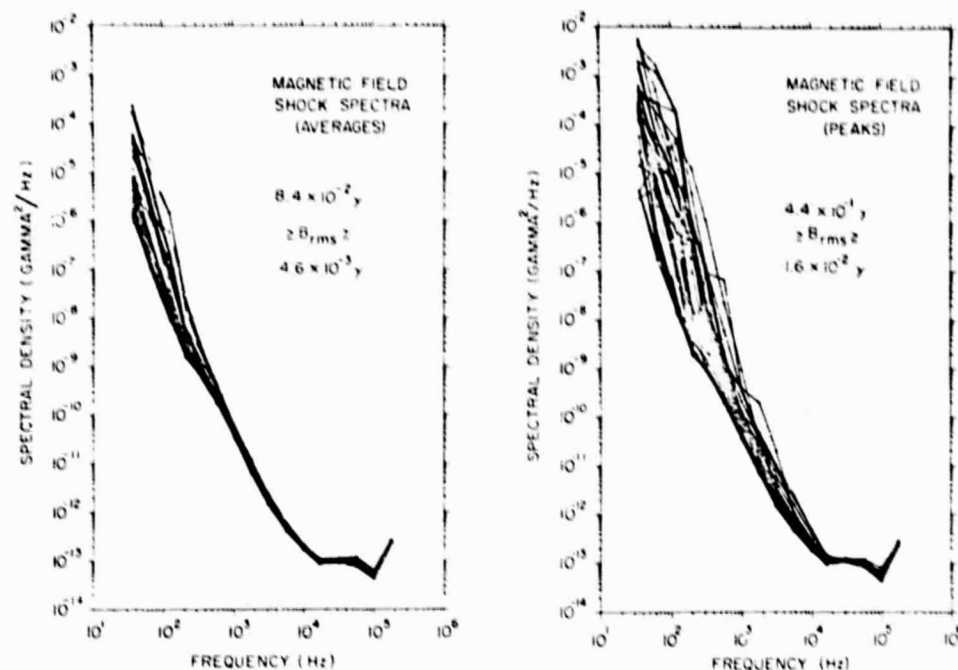


Fig. 8. Representative distribution of magnetic field shock spectra including average and peak measurements corresponding to the electric field spectra of Figure 7. Some of the peak spectra indicate the presence of distinct wave modes.

least two quantizing steps (0.8 dB) are used. At frequencies greater than about 10 kHz the magnetic field intensity is usually too small to be measured accurately, and so the energy density ratio cannot be determined at these high frequencies. As the spacecraft passes through the shock, a prominent peak develops in the energy density ratio at about 1 kHz. At snapshot 7, which is the time at which the most intense rms electric field occurs (Figure 3), the maximum energy density ratio is $\epsilon_E/\epsilon_B \approx 5 \times 10^2$. This large ratio coincides in frequency with the broad peak in the electric field spectrum and indicates

that this component of the spectrum consists of almost purely electrostatic waves.

If we consider the lower-frequency limit of the electrostatic turbulence to be given by the frequency for which $\epsilon_E/\epsilon_B = 1$ (indicated by the horizontal broken line in Figure 9), it is seen that the electrostatic noise broadens toward lower frequencies as the electric field intensity increases. There is thus an indication that as the shock is traversed from the upstream side to the downstream side, the electrostatic turbulence first begins at high frequencies and is then transferred toward lower frequencies further into the transition region, where the main shock dissipation occurs. Only the increase to maximum intensity is shown in Figure 9, the decrease to the downstream state having approximately the same curves. At frequencies below about 120 Hz the energy density ratio remains approximately constant through the transition region, as it does in snapshots 5, 6, and 7, indicating that at these frequencies the shock turbulence involves a distinct electromagnetic mode.

To indicate the range and distribution of electric and magnetic energy density ratios in the bow shock, Figure 10 shows an overlay of the energy density ratio for 10 shock crossings selected at random. The simultaneous electric and magnetic field energy spectra used to calculate these ratios were selected on the basis of the maximum rms electric field intensity obtained from the average measurements. The energy density ratios for the shocks selected in Figure 10 show the same basic features evident for the single shock crossing in Figure 9. In the frequency range above about 200 Hz the electric field energy density exceeds the magnetic field energy density, sometimes by a factor of as much as 10^4 , this feature confirming that the broad peak in the electric field spectrum consists of almost purely electrostatic waves. At frequencies below about 200 Hz the spectra with the lowest energy density ratio, in the range from 10^{-3} to 10^{-4} , show a distinct change in the slope, similar to that in snapshots 5, 6, and 7 in Figure 9. These energy density ratios correspond to the low frequency

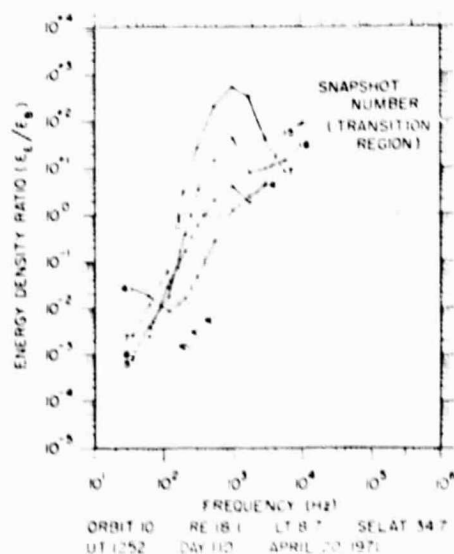


Fig. 9. The ratio of electric energy density to magnetic energy density for the shock crossing of 1252 UT in Figure 2. The low-frequency portion of snapshots 5, 6, and 7 is consistent with whistler waves. At higher frequencies, electrostatic noise is the dominant wave mode. The region of electrostatic noise is observed to broaden toward lower frequencies further into the transition region.

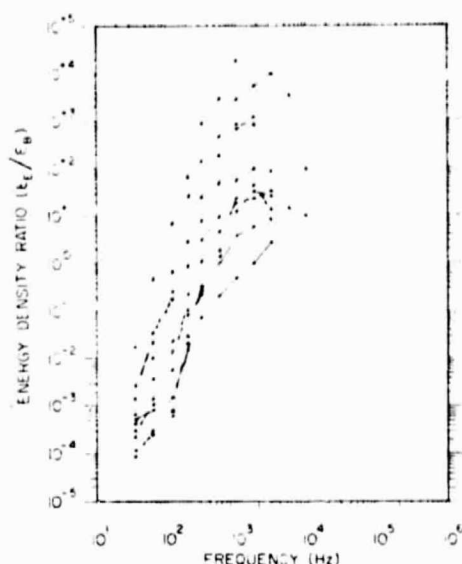


Fig. 10. A representative distribution of energy density ratios for 10 shock crossings selected at random from the shock electric and magnetic field spectra.

monotonic components of the electric and magnetic field spectra. In this frequency range the only electromagnetic wave that can propagate is in the whistler mode. The observed energy density ratios, 10^{-3} to 10^{-4} , are consistent with the electric to magnetic field ratio expected for whistler mode waves. The tendency for the energy density ratio to increase with increasing frequency, approximately proportional to $f^{1.5 \pm 0.5}$, is also consistent with the expected variation of the whistler mode refractive index, hence the electric to the magnetic field ratio, in this frequency range. The steepening of the magnetic field spectrum at $f \approx 200$ Hz, evident in Figures 6 and 8, can be attributed to the whistler mode propagation cutoff at the local electron gyrofrequency. On the basis of this evidence we conclude that the low-frequency monotonic components of the electric and magnetic field spectra are caused by whistler mode turbulence generated in the bow shock.

High-resolution spectra. Wide band analog spectra of the shock crossings at 1251 and 1252 UT in Figure 2 are shown in Figure 11 for the range 0–500 Hz. The quiet upstream and tur-

bulent downstream regions are clearly evident in the electric field spectrum. The shock transition region is most evident in the magnetic spectrum. Both the electric field spectrum and the magnetic field spectrum show a relatively unstructured noise enhancement in the shock transition. In the downstream region the electric field spectrum shows many 2- to 3-s bursts that have a distinct 'parabolic' frequency-time structure, sweeping rapidly downward in frequency from about 800 Hz, reaching a minimum of about 50 Hz, and then rapidly sweeping back upward in frequency. These parabola-shaped bursts are almost purely electrostatic, since no associated magnetic field is detected. They occur randomly in time and are characteristic of the downstream magnetosheath electric field spectrum. The distinctive frequency-time structure of these noise bursts has never previously been reported, and this electrostatic noise appears to represent a basic new turbulence dissipation mechanism operative in the magnetosheath. The time scale of these bursts is not resolved by the 5.12-s average measurements in the digital data of Figure 2; however, the peak measurements are indicative of the peak amplitude of the bursts.

An expanded time scale spectrogram of the shock crossing at 1252 UT is shown in Figure 12 for frequencies up to 1 kHz. The low-frequency electric field turbulence in the shock can be seen between 1252:10 and 1252:15 UT, corresponding to the time interval of snapshot 7 in Figure 5. The intense broad band electric field noise in the shock is clearly distinguished from the downstream region (after 1252:15 UT), in which a few parabola-shaped bursts are intermingled with the background noise. The most intense portion of the low-frequency magnetic noise occurs between 1252:00 and 1252:10 UT (corresponding to snapshot 6 of Figure 4) slightly upstream of the point where the most intense electric field noise occurs.

ELECTRIC FIELD POLARIZATION

Since plasma waves are usually strongly influenced by the static magnetic field, it is important to establish the orientation of the wave electric field relative to the static magnetic field. The wave electric field direction, projected onto the plane of rotation of the electric antenna, can be determined from the modulation of the measured electric field amplitude due to the antenna rotation. A null in the measured electric field amplitude occurs when the antenna axis is perpendicular to the

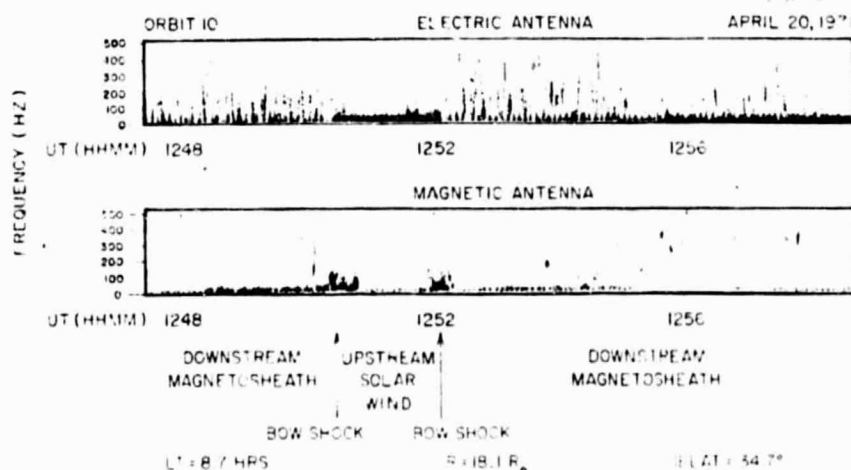


Fig. 11. Wide band spectra for the shock crossings of Figure 2 for frequencies 0–500 Hz. The turbulence of the shock transition appears more homogeneous than downstream turbulence for both the electric and the magnetic field. Discrete noise structure characterizes the downstream regions.

ORIGINAL PAGE IS
OF POOR QUALITY

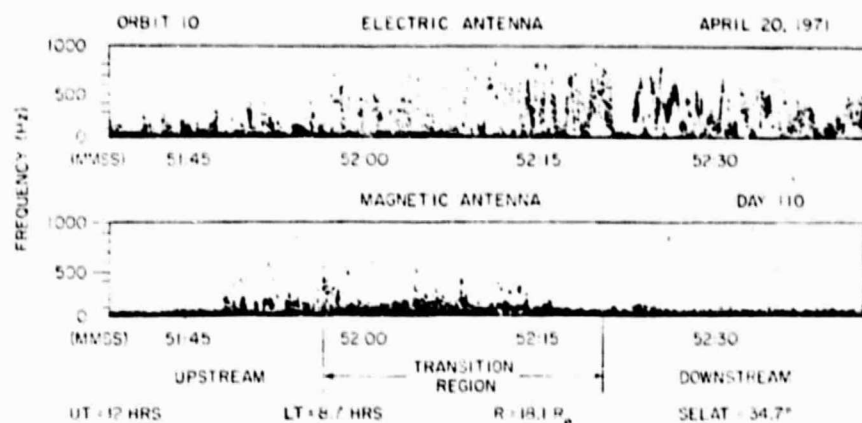


Fig. 12. Expanded time scale wide band spectra for the second shock crossing of Figures 2 and 11. The shock turbulence retains a homogeneous appearance, and the downstream noise shows a few parabola-shaped bursts in the electric field.

electric field direction, and a maximum occurs when the antenna axis is parallel to the electric field direction. Since high time resolution measurements are required, rapid-sample data must be used for this type of analysis.

This method of determining the electric field direction assumes that the noise intensity will remain nearly constant during at least one rotation (~ 11.1 s). For the upstream and downstream waves, which often have an approximately constant amplitude for many rotations, the electric field direction can be determined reliably by using this technique. Because the time required to traverse a shock is often comparable to the rotation period, it is more difficult to apply this technique to the noise that occurs in the shock. Only shock crossings that have an approximately constant amplitude for at least 10 s or more can be analyzed. The number of cases that can be analyzed is further restricted by the requirement that rapid-sample measurements must be available in the correct frequency channel for the event of interest.

Upstream electron plasma oscillations. Figure 13 shows an example of upstream electron plasma oscillations for which suitable rapid-sample measurements are available to determine the electric field direction. The electron plasma frequency in this case is estimated to be about 20 kHz. The spectrum of the plasma oscillations is sufficiently broad that moderate electric field intensities are evident in the 31.1-kHz channel throughout the entire region prior to the shock crossing at 1548:30 UT. The electrostatic noise labeled precursor at 3.11 kHz appears to be a component of the electron plasma oscillation spectrum that has broadened to frequencies well below the local electron plasma frequency about 5 min before the shock is encountered. Precursor effects of this type are frequently observed in association with the bow shock, usually starting a few minutes before the shock is encountered.

Two periods, labeled A and B, during which rapid-sample measurements were obtained are shown in Figure 13. The spin modulation of the electron plasma oscillations in the 31.1-kHz channel, starting at 1541:29 UT, is shown in the polar plot labeled A in Figure 13. The points shown in this polar plot are the electric field strengths obtained during the rapid-sample interval and plotted radially outward from the origin according to the logarithmic scale shown below the plot. The polar angle is the angle between the electric antenna axis and the satellite-

sun line, measured counterclockwise as it is viewed from the north ecliptic pole (the spacecraft spin axis is perpendicular to the ecliptic plane). The static magnetic field direction, projected onto the ecliptic plane, is at an angle $\phi_B = 94^\circ$, as is indicated by the dashed line in the polar plot. The magnetic field vector lies at an angle of 16° above the ecliptic plane.

The points shown in the polar plot include four complete rotations of the spacecraft. The electric field intensities have a pronounced maximum when the antenna axis is parallel to the projected magnetic field direction and a minimum when the antenna axis is perpendicular to the magnetic field. Since the magnetic field direction in this case is very close to the plane of rotation of the electric antenna (the ecliptic plane), it is evident that the electric field direction of the upstream electron plasma oscillations is parallel to the static magnetic field, as would be expected if these waves are excited by electrons streaming along the static magnetic field. Polar plot B in Figure 13 shows that the electric field direction of the precursor waves is also aligned parallel to the static magnetic field. Similar observations for other shock crossings with widely varying magnetic field directions show that the electric field direction of these upstream electron plasma oscillations is always parallel to the static magnetic field.

Electrostatic waves in the bow shock. In Figure 14 we show an example of the spin modulation observed for the electrostatic noise in the bow shock. The shock crossing in this case occurred near the ecliptic plane at 10.3 hours LT with very quiet upstream conditions. The GSFC magnetometer shows that the upstream magnetic field direction is very nearly perpendicular to the shock normal, $\psi(B, \hat{n}) \approx 87^\circ$, so that the bow shock is a perpendicular shock. The electrostatic noise associated with the shock is near maximum intensity for one complete rotation, so that a definite spin modulation pattern can be obtained.

The detailed electric field amplitude obtained from the rapid-sample data in the 3.11-kHz electric field channel is shown as a function of time in the upper panel of Figure 14, and the polar plot corresponding to the interval between points a and b is shown in the lower panel. The electrostatic turbulence associated with the shock transition occurs between about 1440:37 and 1440:49 UT. In this same time interval the GSFC magnetometer data show the magnetic field increasing

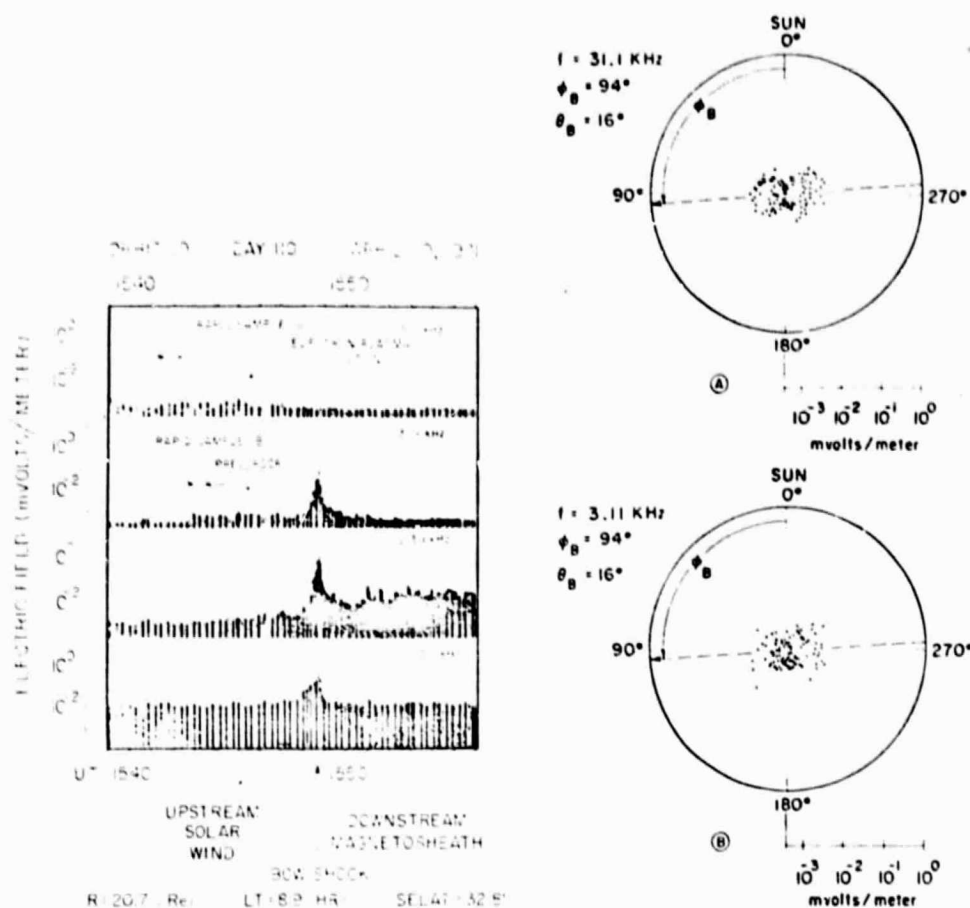


Fig. 13. Upstream electrostatic plasma oscillations and precursor encountered a few minutes before the shock crossing at about 1548.30 UT. The rapid-sample measurements A and B give the spin-modulated electric field amplitudes shown in the two polar plots. The electric field vector of these waves is predominantly aligned parallel to the static magnetic field.

monotonically from about 12 γ to about 50 γ . The solar ecliptic longitude and latitude of the magnetic field direction remain constant at approximately $\phi_B = 255^\circ$ and $\theta_B = 43^\circ$, respectively, through the transition. The magnetic field direction, projected onto the plane of rotation of the electric antenna, is indicated by the dashed line in the polar plot of Figure 14.

The angular distribution of electric field strengths is seen to be symmetrically distributed with respect to the magnetic field direction with two distinct maximums when the antenna axis is parallel to the projected magnetic field direction and a minimum when the antenna axis is perpendicular to the static magnetic field. Since only one rotation occurs in the region where the intense electrostatic noise occurs, it is possible that this apparent spin modulation may be due to a coincidental variation of the noise intensity rather than a spin modulation effect. However, the magnetic field gradient, which is expected to be correlated with the electrostatic noise intensity, appears to increase smoothly up to a single maximum and does not indicate a variation associated with the two maximums (at about 1440.40 UT and 1440.46 UT), which occur when the antenna axis is parallel to the magnetic field. Thus it is felt that the angular distribution in the polar plot of Figure 14 is representative of the actual distribution of electric field directions in the shock. Since the magnetic field in this case has an appreciable component perpendicular to the plane of rotation of the electric antenna ($\theta_B = 43^\circ$), we cannot definitely establish that the electric field is aligned parallel to the magnetic field vector,

although this is certainly the simplest and most obvious interpretation of the observed modulation. Other similar cases that have been examined usually show definite evidence of spin modulation; however, it is never as pronounced as it is for the upstream plasma oscillations. The modulation factor is usually less than 2 to 1 for maximum and minimum amplitudes, this ratio indicating that wave vector directions of the electrostatic waves in the bow shock are distributed over a relatively broad range of angles. When a definite spin modulation is evident, as it is in Figure 14, the maximum electric field amplitude in the shock usually tends to occur in a direction parallel to the static magnetic field.

Electrostatic turbulence in the magnetosheath. As was previously discussed, a moderate level of electrostatic turbulence is always present in the magnetosheath downstream of the shock. Since the intensity of the magnetosheath electric field noise is usually relatively steady for several rotations of the spacecraft, the electric field direction can be determined with a high degree of confidence in this region. Figure 15 shows the polar plot of a series of rapid-sample measurements obtained in the magnetosheath about 1 min after the shock crossing at 1612.20 UT. These rapid-sample measurements are from the 3.11-kHz electric field channel and include four complete rotations of the spacecraft. The maximum electric field amplitude again occurs when the electric antenna axis is oriented parallel to the static magnetic field direction (projected onto the ecliptic plane). The magnetic field vector in this

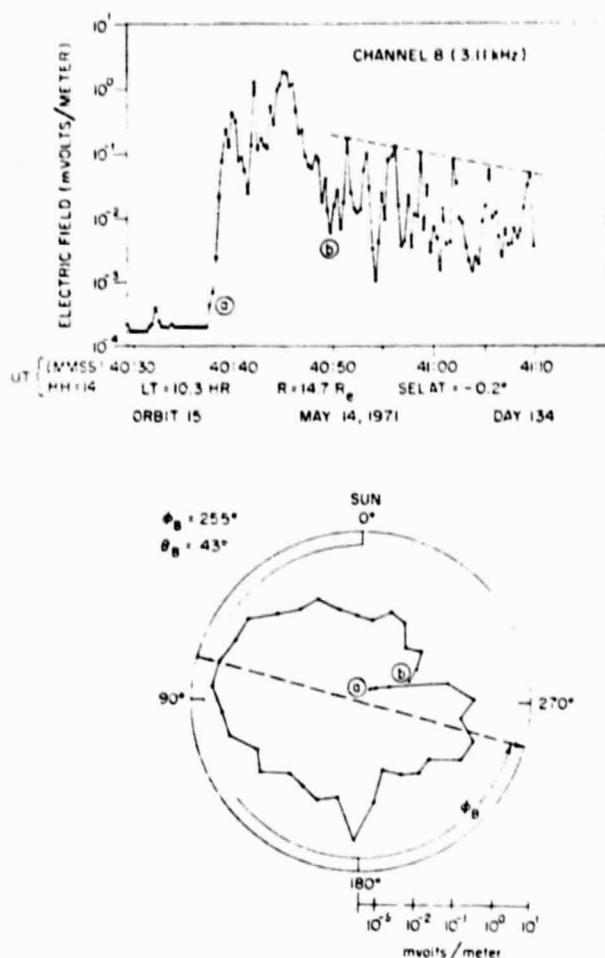


Fig. 14. Rapid-sample measurement of electric field at 3.11 kHz for the bow shock transition and downstream regions. The electric field fluctuations are correlated with magnetic field gradients in both the transition and the downstream region. The polar plot shows the spin modulation of electric field amplitude for the transition region for interval *a* to *b*; ϕ_B is the solar ecliptic longitude of the magnetic field upstream of the shock.

case lies at an angle of $\theta_B = 35^\circ$ above the ecliptic plane. Other similar cases that have been analyzed show that the electric field direction of the magnetosheath turbulence is always oriented nearly parallel to the magnetic field direction. Usually the electric field amplitude perpendicular to the magnetic field is a factor of 3–5 below the amplitude parallel to the magnetic field, indicating that the distribution of electric field directions is rather closely aligned along the static magnetic field direction (within 20° or less).

SUMMARY OF RESULTS AND DISCUSSION

Upstream of the bow shock, intense narrow band electrostatic plasma oscillations are frequently observed by the Imp 6 plasma wave experiment at frequencies of 10–30 kHz. The spectrum and intensity of these electron plasma oscillations agree with the previous observations of *Fredricks et al.* [1968] and confirm the main features already known about these waves. The Imp 6 spin modulation measurements show that the electric field vector of these plasma oscillations is oriented parallel to the local static magnetic field direction. This electric field direction is consistent with the direction expected if the plasma oscillations are produced by a two-stream instability from electrons that are streaming into the solar

wind along magnetic field lines that intersect the shock transition. Broad band electrostatic noise, referred to as a precursor, is also frequently observed by Imp 6 immediately upstream of the shock. This broad band electrostatic noise typically extends from the local electron plasma frequency (which is usually at about 20–30 kHz) down to frequencies of about 1 kHz. The electric field direction of these precursor waves is also oriented parallel to the static magnetic field. Since these precursor waves appear to be closely associated with the long-wavelength narrow band electron plasma oscillations (they have the same electric field polarization, and the upper-frequency limit of the precursor spectrum is the local plasma frequency), it seems most likely that these waves are simply shorter-wavelength electron plasma oscillations that are strongly Doppler shifted downward in frequency from the local plasma frequency. A downward shift in frequency would be expected for waves propagating upstream into the solar wind.

In the shock transition region, two distinct components are evident in the electric field spectrum: one component has a broad peak centered between 200 and 800 Hz, and the other component increases monotonically with decreasing frequency approximately as $f^{-2.0 \pm 0.5}$. The magnetic field spectrum has only a single component, which increases monotonically with decreasing frequency approximately as $f^{-4.0 \pm 0.5}$. The magnetic field spectrum shows a distinct steepening of the spectrum, indicative of an upper cutoff frequency, at about 100–200 Hz. Since the whistler mode is the only electromagnetic mode that can propagate in this frequency range (above the proton gyrofrequency but below the electron gyrofrequency), this magnetic field turbulence must be caused by whistler mode waves. The steepening of the magnetic field spectrum is thought to be associated with the whistler mode propagation cutoff at the local electron gyrofrequency, which is typically at about 350 Hz in the shock transition region. The monotonic component of the electric field spectrum is thought to be the electric field spectrum of these whistler mode waves. The electric to magnetic field energy density ratio $\epsilon_E/\epsilon_B \approx 10^{-2}$ to 10^{-4} of the monotonic component is consistent with the electric to magnetic field ratio expected for whistler mode waves. Also the steeper magnetic field spectrum compared with the electric field spectrum is expected because of the increase in the index of refraction, hence in the magnetic to the electric field ratio, with decreasing frequency for the whistler mode in this frequency range.

The broad peak in the electric field spectrum within the shock, centered between 200 and 800 Hz, consists of almost purely electrostatic waves with $\epsilon_E/\epsilon_B \approx 10^2$ to 10^4 . These waves almost certainly correspond to the electrostatic waves discussed by *Fredricks et al.* [1968, 1970a, b] and *Scarf et al.* [1971], using electric field measurements from Ogo 5. The electrostatic character of these waves, the general frequency range, and their occurrence in association with the magnetic field gradient at the shock transition are in good agreement with the Ogo 5 results. Detailed comparisons of the shape of the frequency spectrum are not possible, since the Ogo 5 data only provide measurements at a single frequency on a given shock crossing. The only area of disagreement concerns the electric field amplitude. Whereas *Scarf et al.* [1970] quote peak electric field strengths for the bow shock of about 30 mV m^{-1} for an equivalent 5-kHz sine wave, the largest peak electric field strength encountered by Imp 6 in this frequency range is about 10 mV m^{-1} . This difference in measured shock electric fields has not been resolved. Electric field spectral densities of 1–3

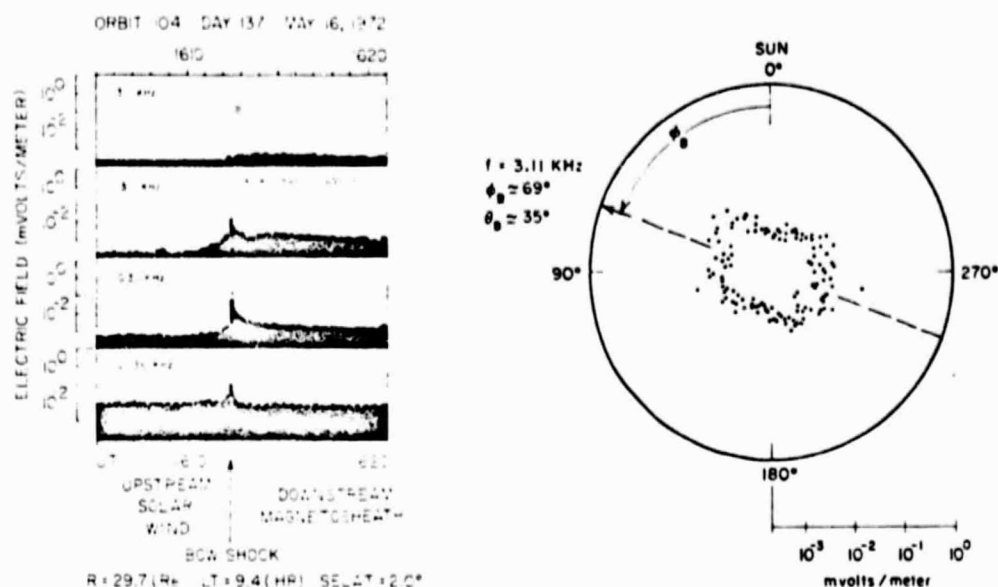


Fig. 15. A series of rapid-sample measurements of the magnetosheath electric field turbulence that shows that the electric field vector of this noise is aligned parallel to the static magnetic field.

kHz reported by *Fredricks et al.* [1970b] in the discussion of their Figure 4, p. 3757, that result in electric field strengths an order of magnitude greater than Imp 6 measurements are a typographical error (F. L. Scarf, personal communication, 1974). One possible explanation for the different electric fields measured is that the wavelength of the electrostatic waves may be much shorter than the length of the long electric antennas on Imp 6. However, sufficiently short wavelengths (~ 10 m) to account for such a large error would have a Doppler shift (~ 10 kHz) too large to account for the low frequency (200–800 Hz) at which the peak in the spectrum occurs. Also comparisons between the two long antennas on Imp 6, which have different lengths, give consistent results, and cross calibrations with the magnetic antennas, using electromagnetic waves with a known electric to magnetic field ratio, give consistent results [Gurnett and Shaw, 1973]. Further studies are being conducted, using the short electric antenna on Imp 6, which is similar to the short electric antenna on Ogo 5, to determine the reason for this apparent disagreement in the peak electric field amplitudes.

The Imp 6 spin modulation measurements show that the electric field directions of the electrostatic waves in the bow shock tend to be oriented parallel to the static magnetic field. Since only one rotation is normally available in the shock transition region, this result is not as reliable for the upstream electron plasma oscillations, where many rotations are usually available. However, sufficient cases have been examined that one can be reasonably confident of the electric field orientation in the transition region. This electric field orientation is consistent with the electric field directions expected for ion sound waves propagating along the magnetic field direction [Tidman and Krall, 1971] and is inconsistent with the electric field directions expected for the Bernstein mode turbulence suggested by Gary and Sanderson [1970], Wu and Fredricks [1972], and others.

In the magnetosheath downstream of the shock a moderate level of electrostatic turbulence is always present. This electrostatic turbulence has a spectrum that is similar to that of the electrostatic turbulence in the shock transition region but has an electric field strength about 1–2 orders of magnitude

smaller than that of the spectrum in the transition region. The spin modulation measurements show that the electric field direction of this turbulence is also oriented parallel to the static magnetic field. The similarity of the spectrum and the electric field direction of electrostatic turbulence in the bow shock and in the magnetosheath suggests that the same instability mechanism may be operative in both these regions, the intensity of the turbulence being roughly proportional to the diamagnetic currents and magnetic field gradients that occur in these two regions.

Acknowledgments. We wish to extend our thanks to N. Ness and D. Fairfield for providing the Imp 6 magnetic field data used in this study and to E. Scow, G. Voots, R. West, and W. Kurth for their assistance in the data analysis. This work was supported in part by the National Aeronautics and Space Administration under contracts NAS5-11074 and NAS5-11431 and grant NGL-16-001-043 and by the Office of Naval Research under grant N00014-68-A-0196-0009.

The Editor thanks R. W. Fredricks and R. E. Holzer for their assistance in evaluating this paper.

REFERENCES

- Fairfield, D. H., Average and unusual locations of the earth's magnetopause and bow shock, *J. Geophys. Res.*, **76**, 6700, 1971.
- Formisano, V., and P. C. Hedgecock, Solar wind interaction with the earth's magnetic field, 3, On the earth's bow shock structure, *J. Geophys. Res.*, **78**, 3745, 1973a.
- Formisano, V., and P. C. Hedgecock, On the structure of the turbulent bow shock, *J. Geophys. Res.*, **78**, 6522, 1973b.
- Fredricks, R. W., C. F. Kennel, F. L. Scarf, G. M. Crook, and I. M. Green, Detection of electric-field turbulence in the earth's bow shock, *Phys. Rev. Lett.*, **21**, 1761, 1968.
- Fredricks, R. W., F. V. Coroniti, C. F. Kennel, and F. L. Scarf, Fast time-resolved spectra of electrostatic turbulence in the earth's bow shock, *Phys. Rev. Lett.*, **24**, 994, 1970a.
- Fredricks, R. W., G. M. Crook, C. F. Kennel, I. M. Green, and F. L. Scarf, Ogo 5 observations of electrostatic turbulence in bow shock magnetic structures, *J. Geophys. Res.*, **75**, 3751, 1970b.
- Fredricks, R. W., F. L. Scarf, and L. A. Frank, Nonthermal electrons and high-frequency waves in the upstream solar wind, 2, Analysis and interpretation, *J. Geophys. Res.*, **76**, 6691, 1971.
- Fredricks, R. W., F. L. Scarf, and I. M. Green, Distributions of electron plasma oscillations upstream from the earth's bow shock, *J. Geophys. Res.*, **77**, 1300, 1972.

- Gary, S. P., and J. J. Sanderson, Longitudinal waves in a perpendicular collisionless plasma shock, I. Cold ions, *J. Plasma Phys.*, **4**, 739, 1970.
- Gurnett, D. A., and R. R. Shaw, Electromagnetic radiation trapped in the magnetosphere above the plasma frequency, *J. Geophys. Res.*, **78**, 8136, 1973.
- Holzer, R. E., M. G. McLeod, and E. J. Smith, Preliminary results from the Ogo 1 search coil magnetometer. Boundary positions and magnetic noise spectra, *J. Geophys. Res.*, **71**, 1481, 1966.
- Holzer, R. E., T. G. Northrup, J. V. Olson, and C. T. Russell, Study of waves in the earth's bow shock, *J. Geophys. Res.*, **77**, 2264, 1972.
- Montgomery, M. D., J. R. Asbridge, and S. J. Bame, Vela 4 plasma observations near the earth's bow shock, *J. Geophys. Res.*, **75**, 1217, 1970.
- Olson, J. V., R. E. Holzer, and E. J. Smith, High-frequency magnetic fluctuations associated with the earth's bow shock, *J. Geophys. Res.*, **74**, 4601, 1969.
- Searf, F. L., R. W. Fredricks, and C. F. Kennel, AC electric and magnetic fields and collisionless shock structures, in *Particles and Fields in the Magnetosphere*, edited by B. M. McCormac, p. 102, D. Reidel, Dordrecht, Netherlands, 1970.
- Searf, F. L., R. W. Fredricks, L. A. Frank, and M. Neugebauer, Nonthermal electrons and high-frequency waves in the upstream solar wind. I. Observations, *J. Geophys. Res.*, **76**, 5162, 1971.
- Tidman, D. A., and N. A. Krall, *Shock Waves in Collisionless Plasmas*, p. 118, Interscience, New York, 1971.
- Wu, C. S., and R. W. Fredricks, Cyclotron drift instability in the bow shock, *J. Geophys. Res.*, **77**, 5585, 1972.

(Received April 15, 1974;
accepted September 25, 1974.)

Direction-Finding Measurements of Auroral Kilometric Radiation

WILLIAM S. KURTIL, MARK M. BAUMBACH, AND DONALD A. GURNETT

Department of Physics and Astronomy, University of Iowa, Iowa City, Iowa 52242

Direction-finding measurements with plasma wave experiments on the Hawkeye 1 and Imp 8 satellites are used to locate the source region of auroral kilometric radiation. This radiation has peak intensities between about 100 and 300 kHz and is emitted in intense sporadic bursts lasting for from half an hour to several hours. At peak intensity the total power emitted in this frequency range exceeds 10^9 W. The occurrence of this radiation is known to be closely associated with bright auroral arcs which occur in the local evening auroral regions. Hawkeye 1 provides direction-finding measurements of kilometric radiation from observations at high latitudes ($5-20 R_E$) over the northern polar regions, and Imp 8 provides similar observations at large radial distances ($23-46 R_E$) near the equatorial plane. Results from both satellites place the source of the intense auroral kilometric radiation in the late local evening at about 22.0 hours LT and at a distance of about $0.75 R_E$ from the polar axis of the earth. These direction-finding measurements, together with earlier results from the Imp 6 satellite, strongly indicate that the intense auroral kilometric radiation is generated by energetic auroral electrons at low altitudes in the evening auroral zone. The observed source location is in good quantitative agreement with the source position expected from simple propagation and ray path considerations.

INTRODUCTION

Satellite measurements of low-frequency radio emissions have shown that the earth is a very intense emitter of electromagnetic radiation with peak intensities in the frequency range from about 100 to 300 kHz [Dunckel *et al.*, 1970; Brown, 1973; Gurnett, 1974]. This radiation is generated at frequencies above the local plasma frequency in the ionosphere and can propagate freely away from the earth. Since the wavelength of this radiation at peak intensity is in the kilometric range, it is called kilometric radiation. The early satellite measurements by Benediktov *et al.* [1965, 1968] of radio emissions at 0.725–2.3 MHz correlated with geomagnetic activity probably represent the first observations of auroral kilometric radiation, since this radiation often has measurable intensities extending to frequencies as high as 2.0 MHz. Kilometric radio emissions are observed to occur in sporadic 'storms' lasting for periods from half an hour to several hours with power fluxes at $30 R_E$ ranging from about 10^{-10} to 10^{-14} W m $^{-2}$ Hz $^{-1}$. At peak intensity the total power emitted by the earth in this frequency range is very large, of the order of 10^9 W. The occurrence of these sporadic bursts of kilometric radiation is closely correlated with the occurrence of discrete auroral arcs detected optically by the low-altitude polar-orbiting DAPP reconnaissance satellite. Figure 1 shows an example of the close association observed between kilometric radio emissions and auroral arcs. The photographs in this illustration are from the DAPP satellite and show the distribution and occurrence of aurora over the northern polar region for two dawn-dusk (left to right) passes through the local midnight region. The north magnetic pole is located near the top center of each photograph. The top panel shows the intensity of kilometric radiation at 178 kHz detected by the Imp 6 satellite far from the earth during this same period. The occurrence of an intense kilometric noise burst during orbit 831 is clearly related to the occurrence of the bright auroral arcs in the corresponding DAPP photograph. More examples of this correlation can be found in Gurnett [1974]. This correlation strongly implies that the radiation is generated by the electrons which produce these auroral arcs. Measurements of the angular distribution of the kilometric

radiation [Gurnett, 1974] also indicate that the noise is generated at low altitudes of $1.0-1.5 R_E$ along auroral field lines in the local evening region. To distinguish the intense aurora-related kilometric radio emissions from other weaker radiation from the earth at kilometer wavelengths, such as the continuum emission discussed by Brown [1973], Frankel [1973], and Gurnett [1975], we will refer to this noise as auroral kilometric radiation.

Although both the angular distribution of the intense auroral kilometric radiation and the correlation of this radiation with auroral arcs indicate that the noise is generated in the local evening auroral region, no direct measurements have been made confirming that the radiation comes from this region. In fact, some evidence to the contrary has been presented using direction-finding measurements with the Imp 6 spacecraft. Stone [1973] comments that a sporadic component at 250 kHz appears to be coming from the tail region of the magnetosphere and that this radiation may be caused by particle precipitation into the auroral region. Later Stone *et al.* [1974], using measurements from the Imp 6 and RAE 2 satellites, identified a spatially compact source on the day side of the earth with a sporadic time structure which seems to correspond in all basic respects to the intense auroral kilometric radiation. The day side location of this source is not, however, consistent with the local time and angular variation of intensity reported by Gurnett [1974]. The purpose of this paper is to establish the region of generation of the auroral kilometric radiation.

DIRECTION-FINDING MEASUREMENTS WITH HAWKEYE 1

Instrumentation description. The Hawkeye 1 spacecraft was launched on June 3, 1974, into a highly eccentric polar orbit with initial perigee and apogee geocentric radial distances of 6,847 and 130,856 km, respectively, orbit inclination of 89.79° , and period of 49.94 hours. The initial argument of perigee is 274.6° so that the apogee is located almost directly over the north pole as shown in Figure 2. The spacecraft is spin stabilized and has a rotation period of about 11.00 s. As indicated in Figure 2, the spin axis is oriented parallel to the orbital plane and approximately perpendicular to the spacecraft-earth line when the spacecraft is at apogee.

The plasma wave experiment on Hawkeye 1 uses an electric

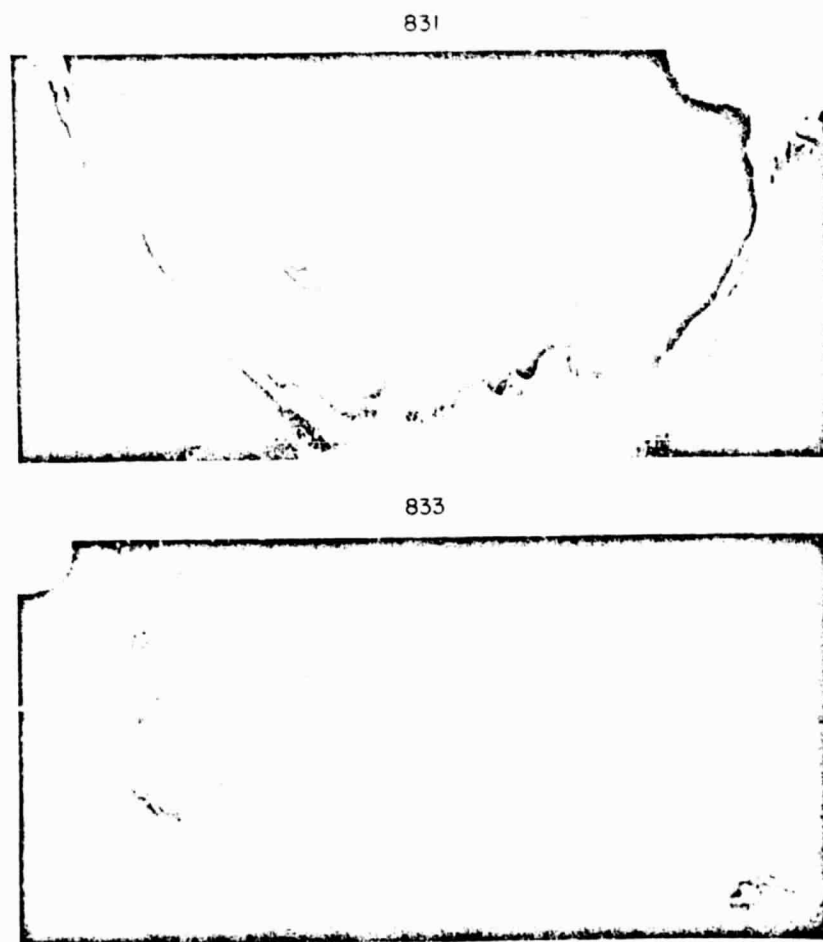
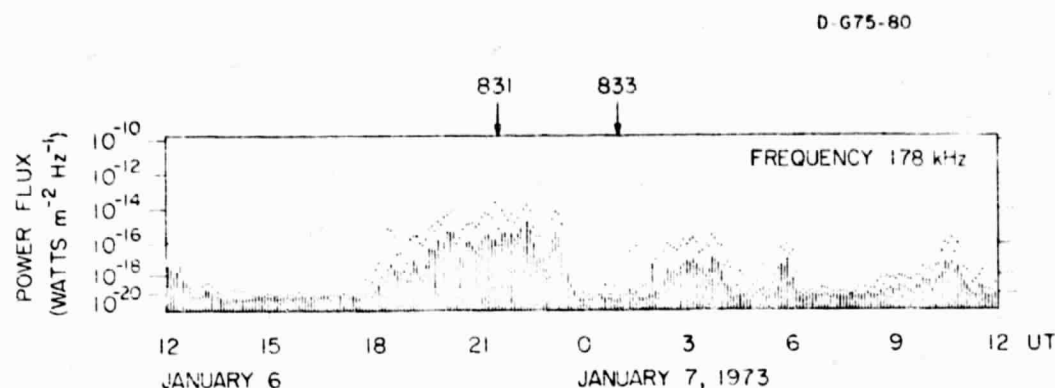


Fig. 1. Simultaneous observations of auroral kilometric radiation far from the earth by Imp 6 and low-altitude auroral photographs obtained on two polar passes with the DAPP satellite. The intense burst of 178-kHz noise during orbit 831 is seen to be closely associated with discrete auroral arcs in the local evening and midnight regions of the auroral zone.

dipole antenna with a tip-to-tip length of 42.45 m for electric field measurements. The electric antenna is extended perpendicular to the spin axis as shown in Figure 2. Electric field spectrum measurements are made in 16 frequency channels extending from 1.78 Hz to 178 kHz, and magnetic field spectrum measurements are made in 8 frequency channels extending from 1.78 Hz to 5.62 kHz. Wide band measurements can also be obtained from either the electric or magnetic antennas. The wide band receiver can have a bandwidth of either 10 or 45 kHz, depending on the mode of operation.

Method of analysis. The intensity of the auroral kilometric radiation detected by Hawkeye 1 shows a pronounced modulation caused by the rotation of the electric antenna. The angular position of the null in the spin modulation can be used to determine the direction of propagation projected into the plane of rotation of the antenna. Since the electric field of an electromagnetic wave in free space is always perpendicular to the direction of propagation, the null in the spin modulation occurs when the antenna axis is parallel to the direction of propagation. The deepest nulls, and the best accuracy for

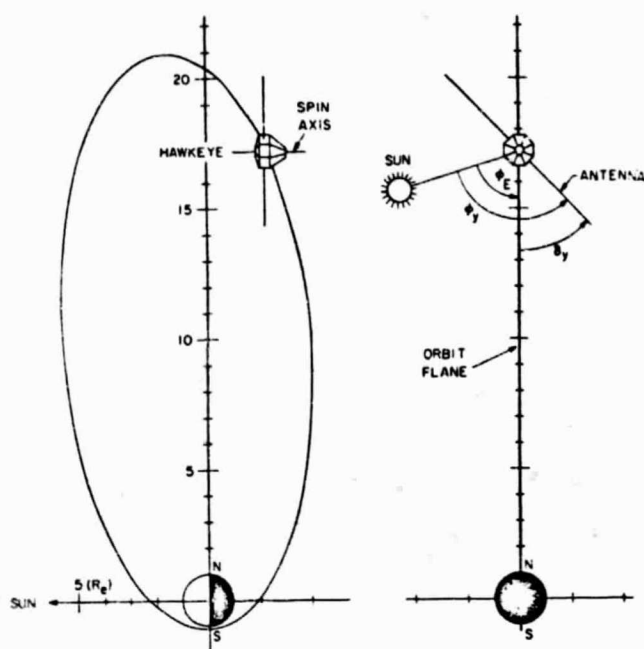


Fig. 2. The Hawkeye 1 orbit and spin axis orientation relative to the orbit plane. The angle δ_y is the angle between the antenna axis and the projection of the satellite-earth direction into the spin plane of the antenna. The angle δ , at which a null occurs determines a meridian plane through the spin axis on which the source must be located.

direction finding, occur when the propagation vector lies exactly in the spin plane of the antenna. When the propagation vector lies out of the spin plane, the null depth decreases, and the directional determination becomes increasingly subject to errors caused by polarization effects as the angle between the propagation vector and the spin plane increases. For the Hawkeye 1 orbit the angular position of the earth is relatively close to the spin plane of the antenna over the entire high-altitude portions of the orbit, so that deep nulls and good accuracy ($\sim \pm 1^\circ$) for direction-finding measurements of kilometric radiation are possible over most of the orbit.

The antenna orientation angle used in the Hawkeye 1 direction-finding analysis is the angle δ_y between the projection of the spacecraft-earth line into the spin plane and the antenna (y) axis, measured in the right-hand sense with respect to the spin vector as shown in Figure 2. This angle is determined by measuring the angle ϕ_y between the projection of the spacecraft-sun line in the spin plane and the y axis of the spacecraft using the spacecraft optical aspect system and by computing the angle ϕ_E between the spacecraft-sun and spacecraft-earth vectors projected into the spin plane. In addition to the strictly geometric determination of the antenna orientation, the angle δ_y must also be corrected for the phase shift caused by the nonzero time constant of the receiver. For the Hawkeye 1 experiment the phase shift due to the receiver time constant is quite small, about $1.3^\circ \pm 0.2^\circ$ for the nominal spin period.

Because the sampling rate for each frequency channel is comparable to the spin rate (one sample every 11.52 s), many rotations are required to determine the null direction. Since the noise intensity often fluctuates considerably on a time scale comparable to the spin period, the null direction can be strongly affected by these fluctuations unless some signal averaging technique is used. The signal averaging technique employed is to sort the intensity measurements according to

the antenna orientation angle and then average the intensities within each angle interval. Since the modulation pattern remains the same on successive spins, the error introduced by the intensity fluctuations decreases as more and more measurements are averaged. Usually averaging intervals of 1 hour or more are required to reduce the error in the null direction introduced by these fluctuations to an acceptable level. During the averaging process the field strengths are periodically normalized by dividing by a short-term average over a time interval corresponding to one complete cycle of the angle sampled through 360° .

Figure 3 shows the normalized electric field strengths obtained for a 1-hour averaging interval during a period for which intense auroral kilometric radiation was being detected by Hawkeye 1 at a radial distance of about $18.9 R_E$. The normalized field strengths in this example are sorted into eighteen 10° intervals in the angle δ_y , from -90° to $+90^\circ$. Because of the symmetry of the dipole antenna pattern, angles in the range $90^\circ < \delta_y \leq 270^\circ$ are shifted into the range $-90^\circ < \delta_y \leq 90^\circ$ by subtracting 180° . The 1.3° phase shift correction due to the receiver time constant has already been taken into account in computing δ_y .

A clearly defined null is evident in the normalized field strengths when the antenna axis is pointed toward the earth. A precise determination of the null direction δ is obtained by finding the best fit of the measured normalized field strengths E/E_0 to a theoretical expression for the modulation envelope given by

$$\left(\frac{E}{E_0}\right)^2 = \left(1 - \frac{m}{2}\right) - \frac{m}{2} \cos [2(\delta_y - \delta)] \quad (1)$$

The modulation factor m provides a quantitative measure of the null depth: m is zero for no spin modulation, and m is one for the maximum possible modulation. Standard techniques of Fourier analysis are used to obtain the best fit values for m and δ . For the case shown in Figure 3 the best fit is obtained when

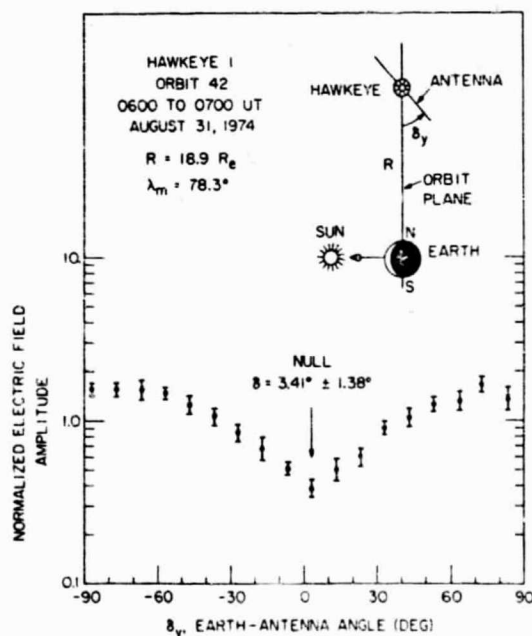


Fig. 3. The average normalized electric field amplitude parallel to the antenna axis of auroral kilometric radiation at 178 kHz detected by Hawkeye 1 as a function of the antenna orientation. A distinct null is evident when the antenna is pointed near the earth. The precise angle at which the null occurs is determined by Fourier analysis.

the null angle is $\delta = 3.4^\circ \pm 1.4^\circ$. The statistical uncertainty of $\pm 1.4^\circ$ is evaluated from the mean square error in the best fit.

Other sources of systematic error may be present which could add to the uncertainty in the null angle. Four sources of systematic error have been considered: (1) errors in the receiver phase shift correction, (2) errors in the optical aspect determination of ϕ_s , (3) errors in the earth-sun angle ϕ_E due to either orbital errors and/or errors in the spin axis determination, and (4) errors caused by misalignment of the electric antenna axis with respect to the y axis of the spacecraft. Of these errors the uncertainty of the alignment of electric antenna axis is considered to be the dominant error for the Hawkeye direction-finding measurements. Investigations of the misalignment of the flight spare electric antenna and calculations by the antenna manufacturer indicate that the misalignment of the electric antenna axis relative to the y axis of the spacecraft should not exceed 2° .

Results. To reduce the statistical uncertainty in the null-earth angle to of the order of $\pm 1.0^\circ$ or less, only auroral kilometric radiation events lasting for 1 hour or more are used in this analysis. Normally, several such events occur in each orbit. Since auroral kilometric radiation usually has the maximum intensity in the 178-kHz frequency channel of Hawkeye 1, this channel is used for all measurements presented in this paper. To insure that the low-level continuum radiation discussed by Frankel [1973] is not included in this study, only events which have a power flux continuously exceeding $10^{-16} \text{ W m}^{-2} \text{ Hz}^{-1}$ at 178 kHz are used. Since the direction-finding technique only provides a one-dimensional determination of the source position, many orbits with spin axis orientations at various local times must be used to obtain a two-dimensional determination of the average source position. Figure 4 summarizes a series of direction-finding measurements of kilometric radiation at 178 kHz obtained from two orbits which have their orbit planes, hence spin axis directions, approximately at right angles (using sun-referenced coordinates). The null directions measured for the various events observed on these two orbits are shown as straight lines drawn outward

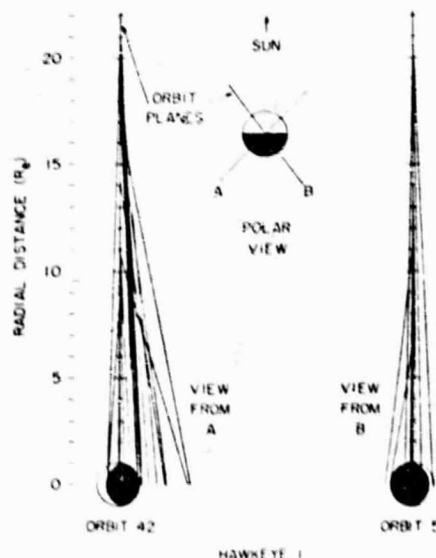


Fig. 4. Two representative orbits showing the null directions for auroral kilometric radiation at 178 kHz observed at various points along the orbit. Orbit 42 shows a clear tendency for the radiation to originate from the night side of the earth.

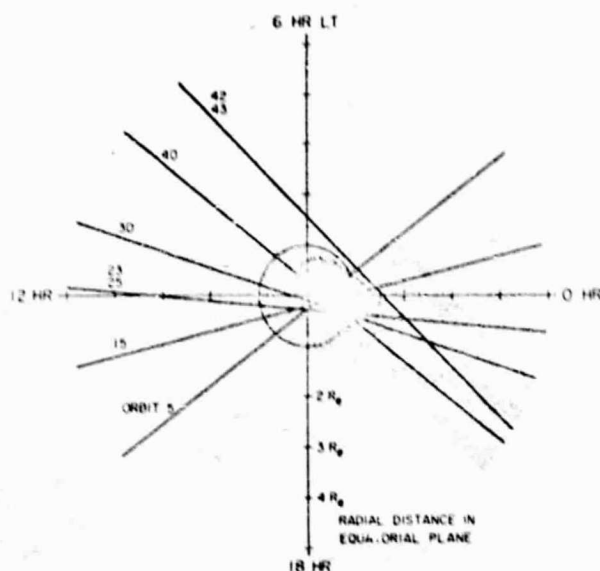


Fig. 5. An equatorial plane projection of the average null directions of auroral kilometric radiation at 178 kHz for a series of Hawkeye 1 orbits at various local times. The shaded region for each orbit gives the rms spread (plus or minus the standard deviation) in the distribution of null positions for all events analyzed during that orbit. The average source position is located in the late local evening at a local time (i.e.) of 22.7 hours and at a distance of $0.65 R_E$ from the polar axis.

from the spacecraft at the point along the orbit where the measurement was obtained. These lines are shown as viewed from a direction parallel to the spin axis (edgewise to the orbital plane).

Considerable variability is evident in the null directions determined during these two orbits. This variability is due to actual fluctuations in the position of the centroid of the source, since the statistical errors in determining the null direction are typically much less than the scatter in the observed null directions. Since the averaging interval for the direction finding is typically 1 hour or more, the fluctuations actually observed are necessarily at time scales greater than 1 hour. It seems quite likely that the fluctuations in the source position extend to even smaller time scales which cannot be resolved by Hawkeye. For orbit 5 the average source position is very close to the orbital plane, with a slight tendency for the average position to lie to the left of the orbital plane, toward local evening, as viewed from point B. For orbit 42 the average source position is shifted very distinctly to the right of the orbital plane, again toward local night, as viewed from point A. Projecting the average source positions obtained from these two orbits into the equatorial plane, the average source position would be located on the night side of the earth at about 2 hours LT and about $1.2 R_E$ from the polar axis.

To provide a better determination of the average source location, direction-finding measurements of auroral kilometric radiation at 178 kHz have been made for the series of orbits spaced at approximately even intervals in local time. The results of this analysis are illustrated in Figure 5, which shows the projection of the average null position into the geographic equatorial plane for each orbit (or pair of orbits) analyzed. Pairs of orbits are used in some cases because too few events sometimes occurred on a single orbit to provide a meaningful analysis. The average null position consists of a straight line in this diagram because the null determination is one dimen-

sional, and the source could in principle lie anywhere along this line and still be consistent with the null angle observed at the spacecraft. The width of the shaded region shown for each orbit gives the rms spread (plus and minus the standard deviation) in the distribution of the null positions observed during that orbit.

The average location of the auroral kilometric radiation source projected into the equatorial plane can be qualitatively estimated from the intersections of the average null lines for each orbit, taking into account the fact that lines which intersect at nearly right angles provide a better position determination than lines which intersect at a shallow angle. Almost all of the intersections occur on the night side of the earth. The average position of all intersections, without regard to the angle at which the intersection occurs, is in the late local evening at a local time of 22.7 hours and at a distance of $0.65 R_E$ from the polar axis. The approximate range of variation in the source position from this average position can be seen from the shaded regions in Figure 5. Evidently, considerable variability, of the order of $1.0 R_E$, exists in the source position averaged over 1 hour relative to the source position averaged over a complete orbit.

DIRECTION-FINDING MEASUREMENTS WITH IMP 8

Instrumentation description. The Imp 8 spacecraft was launched on October 26, 1973, into a low-eccentricity orbit with initial perigee and apogee geocentric radial distances of 147,434 and 295,054 km, respectively, orbit inclination of 28.6° , and period of 11.98 days. The spacecraft is spin stabilized with a nominal rotation period of 2.59 s. The spin axis is oriented perpendicular to the ecliptic plane.

The University of Iowa plasma wave experiment on Imp 8 uses an electric dipole antenna with a tip-to-tip length of 121.8 m for electric field measurements and a triaxial search coil magnetometer for magnetic field measurements. The electric dipole is extended outward, perpendicular to the spacecraft spin axis, by centrifugal force. Electric field spectrum measurements are made in 15 frequency channels extending from 40 Hz to 178 kHz, and magnetic field spectrum measurements are made in 7 frequency channels extending from 40 Hz to 1.78 kHz.

Method of analysis. The method of analyzing the Imp 8 data to provide direction-finding measurements is essentially identical to the method used for Hawkeye 1, except that the null angle measured is in the ecliptic plane. Long averaging periods, of an hour or more, must also be used on the Imp 8 data to reduce statistical fluctuations to an acceptable level. Since Imp 8 is at larger distances from the earth than Hawkeye, greater accuracy is needed in the directional determination. However, much more data is currently available from Imp 8, and since the orbital period of Imp 8 is much longer than Hawkeye, it is possible to use very long averaging periods (of the order of 12 hours or more) to provide smaller statistical errors in the null direction.

The largest sources of systematic error in the Imp 8 direction-finding measurements are thought to be the uncertainty in the phase shift correction caused by the receiver time constant and the antenna misalignment. Because of the higher spin rate of Imp 8 the phase shift due to the receiver time constant is relatively large, approximately 7.16° . The uncertainty in this phase shift is estimated to be about $\pm 2.0^\circ$. Since comparable errors may also exist in the antenna alignment and overall accuracies of $\pm 1^\circ$ are needed, it is absolutely essential that some method be used in flight to calibrate the overall

systematic error in the direction determination. The method used is to require that the average null-earth angle for measurements obtained on opposite sides of the earth (correcting for radial distance variations) be zero. This averaging condition has been applied to a large number of direction-finding measurements of auroral kilometric radiation, and the best estimate of the phase shift correction is 11.96° . This phase shift correction includes the phase shift due to the receiver time constant and is used for all Imp 8 direction-finding measurements presented in this paper. As will be pointed out, however, the position of the source can be determined independent of this phase shift correction.

Results. Figures 6 and 7 show two Imp 8 direction-finding measurements of auroral kilometric radiation at 178 kHz obtained from positions near the equatorial plane on approximately opposite sides of the earth (local times of 2.76 and 16.85 hours, respectively). In both cases the measurements were made during an exceptionally long and steady auroral kilometric radiation event lasting for over 12 hours and at times when the angular position of the earth was very close to the spin plane of the antenna, thereby assuring a deep null in the spin modulation and a very small statistical error in the null direction. The null directions at 2.76 and 16.85 hours LT are $\delta = 1.0^\circ \pm 0.4^\circ$ and $\delta = -1.1^\circ \pm 0.4^\circ$, respectively. The positive direction for measuring the earth-antenna angle δ , for Imp 8 is shown in the sketches in Figures 6 and 7 as viewed looking down from the north ecliptic pole. The measured null directions are seen to be consistent with a source located in the local evening region.

Other similar measurements, all using averaging intervals of several hours and restricted to events with large modulation factors ($m > 0.766$), to assure small statistical errors, and intensities greater than $10^{-16} \text{ W m}^{-2} \text{ Hz}^{-1}$, have been made at a

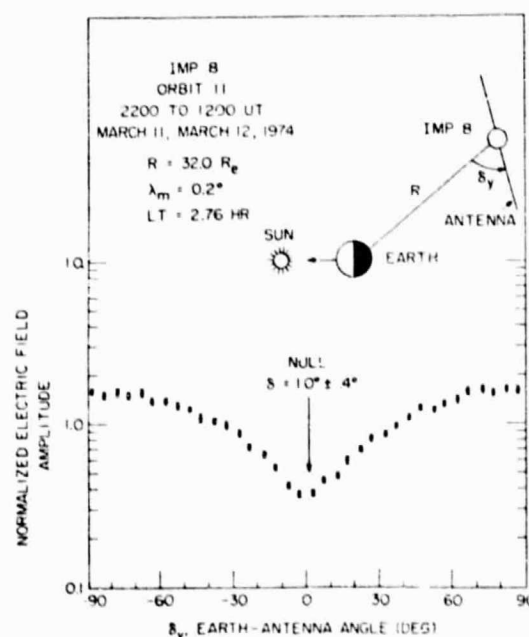


Fig. 6. The average normalized electric field strength as a function of the antenna orientation for a period during which intense auroral kilometric radiation at 178 kHz was being detected by Imp 8 at a local time of about 2.76 hours. The averaging period in this case is made very long, 14 hours, to reduce the statistical error in the null determination to only $\pm 0.4^\circ$. The null position in this case is slightly to the left of the earth's polar axis and on the night side of the earth as viewed from the spacecraft.

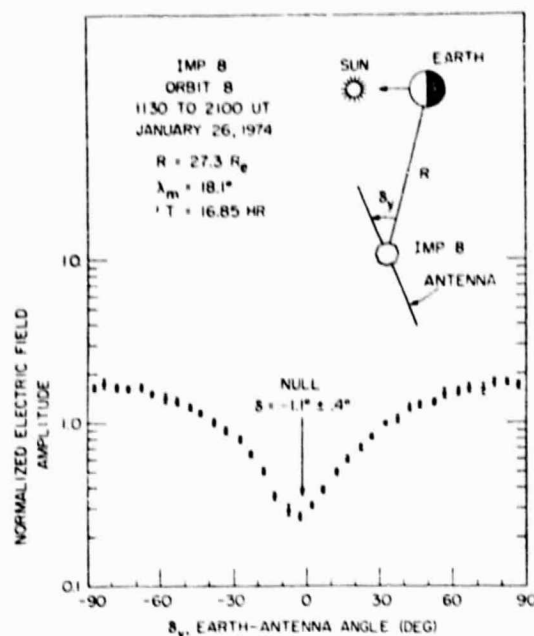


Fig. 7. Another null determination using Imp 8 similar to the case in Figure 6, except at a local time of about 16.85 hours. The null position in this case is slightly to the right of the earth's polar axis, again on the night side of the earth, as viewed from the spacecraft.

variety of local times. Figure 8 shows the null directions obtained from these events as a function of local time. A very clear trend is evident in these data with the null-earth angles negative in the local afternoon and positive in the local morning, consistent with a source located on the night side of the earth. The local time position of the source and the approximate offset from the polar axis can be determined completely independent of the constant phase shift correction to δ . Since δ is always small for the Imp 8 orbit, the local time and distance of the source from the polar axis are completely determined by the phase and amplitude of the best sine wave fit to δ as a function of local time, appropriately correcting δ for radial distance effects. This sine wave analysis technique has been applied to the data in Figure 8 and gives an average source position, projected into the equatorial plane, of 21.25 ± 0.41 hours LT at a distance of $0.84 \pm 0.09 R_E$ from the polar axis.

The null directions shown in Figure 8 are plotted as seen from above the northern polar region in Figure 9 to provide

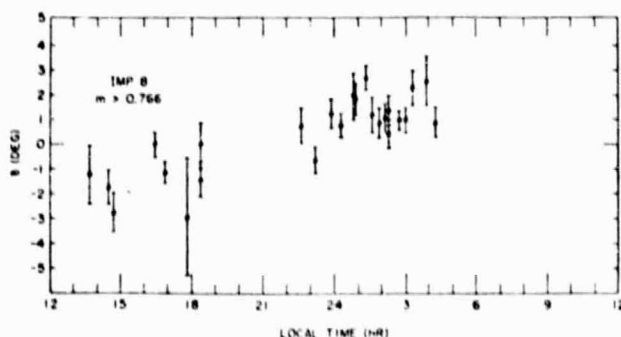


Fig. 8. A series of null directions for auroral kilometric radiation at 178 kHz obtained by Imp 8 as a function of local time. The null angle in all cases is larger in the local morning than in the local evening. This dependence places the source on the night side of the earth independent of any systematic errors which may be present in determining the null direction.

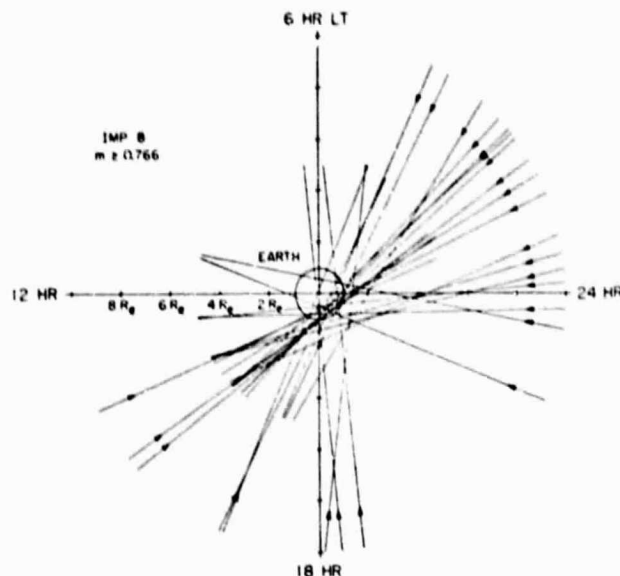


Fig. 9. A view from above the northern polar region of the null directions given in Figure 8. The arrows indicate the direction from the spacecraft to the source. These null direction measurements place the average source position in the late local evening at a local time of 21.25 hours and at a distance of $0.835 R_E$ from the polar axis.

a qualitative indication of the scatter and distribution of null directions observed by Imp 8. The arrows on each line indicate the direction from the spacecraft to the source. Considerable variability from the average source position is also evident in the Imp 8 direction-finding measurements. Both qualitatively and quantitatively, the Imp 8 direction-finding measurements of auroral kilometric radiation are seen to be in close agreement with the Hawkeye 1 results.

DISCUSSION

Evidence has been presented showing that the intense bursts of auroral kilometric radiation ($> 10^{-10} \text{ W m}^{-2} \text{ Hz}^{-1}$) detected by Hawkeye 1 and Imp 8 originate from the local evening side of the earth. At a frequency of 178 kHz the average position of the source, projected into the equatorial plane, is at a local time of about 22.0 hours and at a distance of about $0.75 R_E$ from the polar axis. These results strongly support the previous evidence presented by Gurnett [1974] indicating that the auroral kilometric radiation is produced at relatively low altitudes ($1.0\text{--}1.5 R_E$ for 178 kHz) in the local evening auroral zone.

Simple geometric considerations and reasonable estimates of the altitude at which the auroral kilometric radiation is generated appear to be in good agreement with the observed offset of the average source position from the polar axis. As discussed by Gurnett [1974], the radiation must be generated at an altitude above the propagation cutoff surface for the mode of propagation in which the radiation is generated. Since wave-particle interactions cannot occur at frequencies substantially above the local plasma frequency or gyrofrequency and since these frequencies are relatively close together in the region of the ionosphere where this noise is generated, the radiation must be generated rather close to the propagation cutoff surface. For a frequency of 178 kHz the propagation cutoff surface, and hence the generation region, is located at an altitude of about $1.0 R_E$ [Gurnett, 1974]. If we follow a

representative auroral field line at 70° invariant latitude up to an altitude of $1.0 R_E$ and assume that the source is located at this point, the source position projected into the equatorial plane would be $0.96 R_E$ from the polar axis. These estimates of the source location are in good quantitative agreement with the observed distance of the source from the polar axis and with previous models of the source location [Gurnett, 1974, Figure 14].

The observed time- and space-averaged local time position of the centroid of the emitting region in the late local evening is consistent with the location expected from the known association between auroral kilometric radiation and auroral arcs. It is well known that the most intense auroral electron precipitation and the brightest auroral arcs occur in the local evening [Akasofu, 1968; Snyder *et al.*, 1974]. The observed source position is also consistent with the angular distribution of the kilometric radiation, which shows a broad maximum centered on about 22.0 hours LT [Gurnett, 1974]. More recent studies by Kaiser and Stone [1975] now indicate that the day side source discussed by Stone *et al.* [1974], although in the same frequency range and qualitatively similar to the auroral kilometric radiation, is actually at much lower intensities ($<10^{-16} \text{ W m}^{-2} \text{ Hz}^{-1}$) and probably represents a distinctly different source. Because of the close association of the auroral kilometric radiation with geomagnetic activity the observed temporal variations in the source position are thought to be associated with the westward traveling surge and other spatial evolutions which occur during auroral substorms. Since the time scale of substorm variations is usually much less than the averaging periods used, the detailed temporal variations in the source position probably cannot be resolved with either the Hawkeye or Imp 8 experiments.

Acknowledgments. This work was supported in part by the National Aeronautics and Space Administration under contracts NAS1-11257, NAS1-13129, and NAS5-11431 and grant NGL-16-001-

043 and by the Office of Naval Research under grant N00014-68-A-0196-0009.

The Editor thanks T. R. Hartz and R. G. Stone for their assistance in evaluating this paper.

REFERENCES

- Akasofu, S.-I., *Polar and Magnetospheric Substorms*, p. 223, D. Reidel, Dordrecht, Netherlands, 1968.
- Benediktov, E. A., G. G. Getmantsev, Yu. A. Sazonov, and A. F. Tarasov, Preliminary results of measurement of the intensity of distributed extraterrestrial radio-frequency emission at 725- and 1525-kHz frequencies by the satellite electron-2, *Kosm. Issled.*, **3**, 614, 1965.
- Benediktov, E. A., G. G. Getmantsev, N. A. Mityakov, V. O. Rapoport, and A. F. Tarasov, Relation between geomagnetic activity and the sporadic radio emission recorded by the electron satellites, *Kosm. Issled.*, **6**, 946, 1968.
- Brown, L. W., The galactic radio spectrum between 130 kHz and 2600 kHz, *Astrophys. J.*, **180**, 359, 1973.
- Dunckel, N., B. Ficklin, L. Rorden, and R. A. Helliwell, Low-frequency noise observed in the distant magnetosphere with Ogo 1, *J. Geophys. Res.*, **75**, 1854, 1970.
- Frankel, M. S., LF radio noise from the earth's magnetosphere, *Radio Sci.*, **8**, 991, 1973.
- Gurnett, D. A., The earth as a radio source: Terrestrial kilometric radiation, *J. Geophys. Res.*, **79**, 4227, 1974.
- Gurnett, D. A., The earth as a radio source: The nonthermal continuum, *J. Geophys. Res.*, **80**, this issue, 1975.
- Kaiser, M. L., and R. G. Stone, Earth as an intense planetary radio source: Similarities to Jupiter and Saturn, *Science*, in press, 1975.
- Snyder, A. L., S.-I. Akasofu, T. N. Davis, Auroral substorms observed from above the north polar region by a satellite, *J. Geophys. Res.*, **79**, 1393, 1974.
- Stone, R. G., Radio physics of the outer solar system, *Space Sci. Rev.*, **14**, 534, 1973.
- Stone, R. G., M. L. Kaiser, and R. Johnson, Radio emission from the magnetosphere (abstract), *Eos Trans. AGU*, **55**, 398, 1974.

(Received October 21, 1974,
revised January 24, 1975;
accepted February 24, 1975.)

The Earth as a Radio Source: The Nonthermal Continuum

DONALD A. GURNETT

Department of Physics and Astronomy, University of Iowa, Iowa City, Iowa 52242

In addition to the intense and highly variable auroral kilometric radiation the earth also radiates a weak nonthermal continuum from energetic electrons in the outer radiation zone. The intensity of this continuum radiation decreases with increasing frequency and is usually below the cosmic noise level at frequencies above 100 kHz. In this paper we show that the frequency spectrum of the continuum radiation consists of two components, a trapped component, which is permanently trapped within the magnetosphere at frequencies below the solar wind plasma frequency, and an escaping component, which propagates freely away from the earth at frequencies above the solar wind plasma frequency. The low-frequency cutoff of the continuum radiation spectrum is at the local electron plasma frequency, which can be as low as 300 Hz in the low-density regions of the distant magnetotail. Direction-finding measurements and measurements of the spatial distribution of intensity for both the trapped and the freely escaping components are used to determine the region in which the continuum radiation is generated. These measurements all indicate that the continuum radiation is generated in a broad region which extends through the morning and early afternoon from about 4.0 to 14.0 hours local time immediately beyond the plasmopause boundary. In contrast to the auroral kilometric radiation which is generated in the high-latitude auroral zone regions, the continuum radiation appears to be generated over a broad range of latitudes, including the magnetic equator. In some cases the continuum radiation appears to be closely associated with intense bands of electrostatic noise which are observed near the electron plasma frequency at the plasmopause. Possible mechanisms by which this radiation could be generated, including gyrosynchrotron radiation from energetic electrons in the outer radiation zone, are discussed.

INTRODUCTION

Brown [1973], using radio measurements from the Imp 6 satellite, has identified a weak continuum component to the radiation coming from the earth's magnetosphere in the frequency range from about 30 to 110 kHz. The intensity of this continuum radiation decreases rapidly with increasing frequency, varying approximately as $f^{-2.8}$ (f is frequency), and is usually below the cosmic noise level at frequencies above about 100 kHz. The low-frequency limit at about 30 kHz is apparently caused by the propagation cutoff at the local plasma frequency in the solar wind. Frankel [1973] has also studied this radiation and concludes that the noise is produced by gyrosynchrotron radiation from energetic electrons in the outer radiation zone.

Gurnett and Shaw [1973] have identified another somewhat more intense continuum component at even lower frequencies, from about 5 to 20 kHz. This continuum radiation occurs at frequencies below the solar wind plasma frequency and is permanently trapped within the low-density regions of the magnetospheric cavity. The purpose of this paper is to investigate the basic features of the nonthermal continuum radiation from the earth's magnetosphere by using radio and plasma wave measurements from the Imp 6 and Imp 8 satellites. We show that the continuum radiation reported by Brown [1973] and the trapped radiation reported by Gurnett and Shaw [1973] are simply different portions of a single nonthermal continuum spectrum which extends from frequencies as low as 500 Hz to greater than 100 kHz. Direction-finding measurements and spatial surveys of the intensity of this radiation are used to determine the region of the magnetosphere in which the noise is generated.

The data analyzed in this study are obtained from the University of Iowa plasma wave experiments on the Imp 6 and Imp 8 satellites. The Imp 6 spacecraft is in a highly eccentric orbit with initial perigee and apogee geocentric radial dis-

tances of 1.04 and 33.0 R_E , respectively, an orbit inclination of 28.7°, and a period of 4.18 days. The Imp 8 spacecraft is in a low eccentric orbit with initial perigee and apogee geocentric radial distances of 23.1 and 46.3 R_E , respectively, an orbit inclination of 28.6°, and a period of 11.98 days. The Imp 6 measurements are particularly useful for studying the radial dependence of terrestrial radio emissions over a very wide range of radial distances, whereas the Imp 8 measurements are particularly useful for obtaining a rapid survey of all local times at a roughly constant radial distance.

The plasma wave experiments on both spacecraft are designed to make measurements over a very broad frequency range, 20 Hz to 200 kHz for Imp 6 and 40 Hz to 2.0 MHz for Imp 8. Both experiments use 'long' electric dipole antennas, 92.5 m tip to tip for Imp 6 and 121.5 m tip to tip for Imp 8, which are extended outward perpendicular to the spacecraft spin axis. The spin axes of both spacecraft are oriented very nearly perpendicular to the ecliptic plane. Further technical details of these experiments are given by Gurnett and Shaw [1973] and Gurnett [1974].

CHARACTERISTICS OF THE NONTHERMAL CONTINUUM

The term continuum, as used in this paper, refers to radiation which has a smooth monotonic frequency spectrum extending over a frequency range of several octaves with an essentially constant intensity on a time scale of a few hours or more. Nonthermal continuum radiation from the earth's magnetosphere is difficult to detect because the radiation is very weak, only slightly above the noise level of the Imp 6 and Imp 8 plasma wave experiments, and is often masked by other intense radio and plasma wave emissions which occur in the same frequency range. Auroral kilometric radiation [Gurnett, 1974], which occurs in the frequency range from about 50 to 500 kHz, often has intensities of 60–80 dB above the level of the quiescent continuum. Electrostatic plasma wave turbulence in the magnetosheath and bow shock, electron plasma

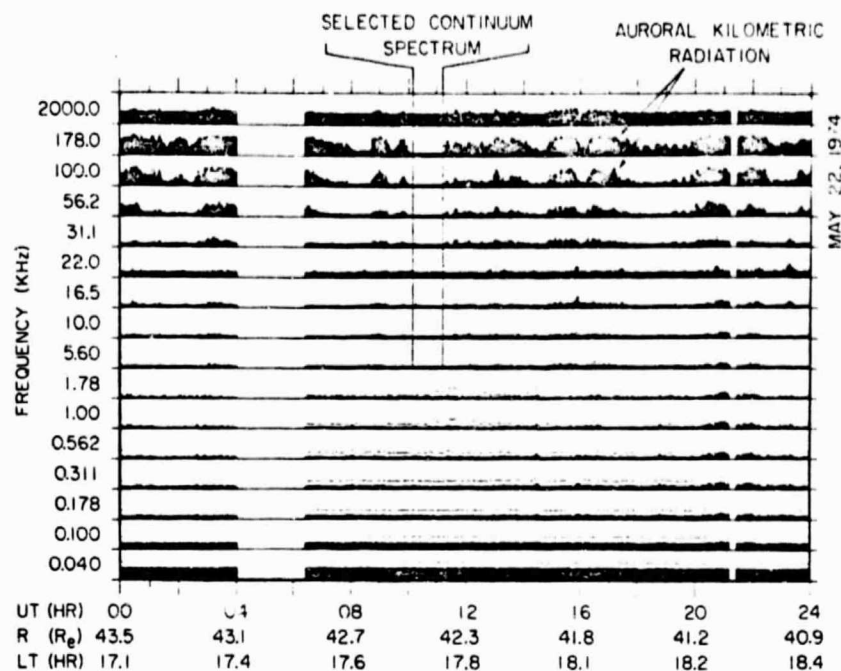


Fig. 1. The electric field intensities observed at 16 frequencies for a 24-hour period of Imp 8 data in the solar wind. The amplitude range for each frequency represents a dynamic range of 100 dB. During this day only one interval, from about 1005 to 1115 UT, occurs in which the intensity of the auroral kilometric radiation drops to a level sufficiently low to determine the complete spectrum of the nonthermal continuum.

oscillations in the solar wind, and type 3 radio noise bursts also frequently interfere with measurements of the continuum radiation. Measurements of the nonthermal continuum radiation from the earth's magnetosphere must therefore be carefully selected to avoid contamination from other sources. The continuum radiation events used in this study were selected by

requiring that the noise level in a given frequency range be constant within about 3 dB for a period of at least 1 hour and that the noise not correspond to any other known type of radio emission.

A typical Imp 8 measurement of the continuum radiation is illustrated in Figure 1. The outputs from 16 channels of the

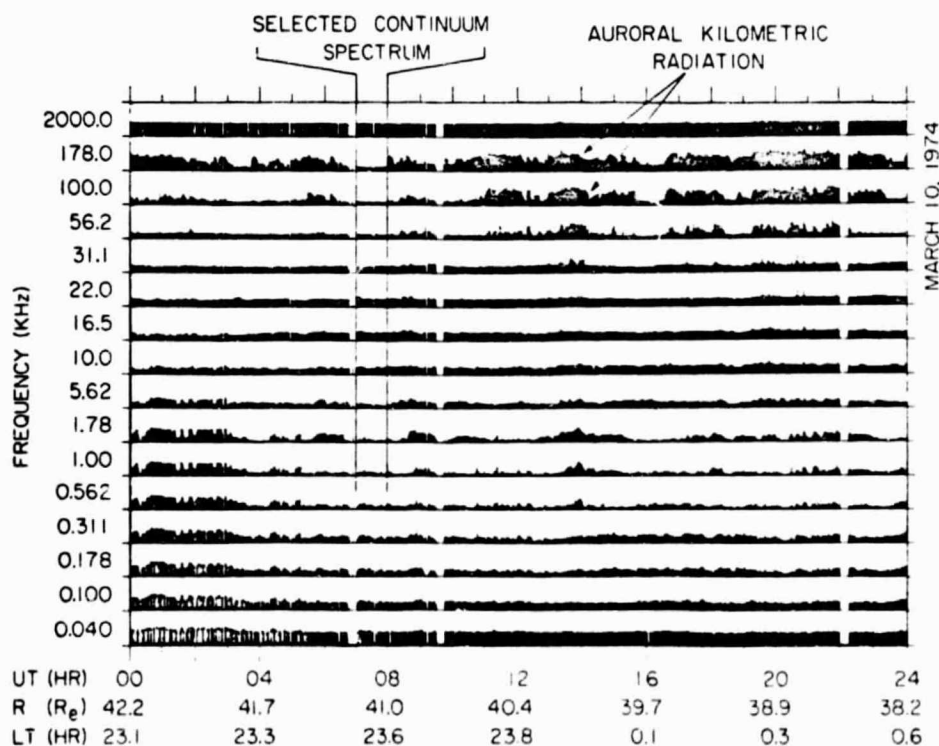


Fig. 2. A selected continuum spectrum in the distant magnetotail. Note that the spectrum of the continuum radiation extends to considerably lower frequencies in the magnetotail than in the solar wind.

ORIGINAL PAGE
IS OF POOR QUALITY

electric field spectrum analyzer are shown for a 24-hour period for which the spacecraft is located in the solar wind at a geocentric radial distance of about $42.0 R_E$ and a local time of about 17.5 hours. The ordinate for each frequency channel is proportional to the logarithm of the electric field amplitude in that frequency channel. The interval from the base line of one channel to the base line of the next higher channel represents a dynamic range of 100 dB. The vertical bars, which make up the black portion of each plot, indicate the amplitude averaged over a time interval of 163.48 s, and the dots indicate the maximum amplitude over the same time interval. Throughout this 24-hour period, many intense bursts of auroral kilometric radiation are evident in the higher-frequency channels. Only one brief period, from about 1005 to 1115 UT, occurs during which the intensity of the auroral kilometric radiation is sufficiently low to permit an accurate measurement of the spectrum of the quiescent continuum radiation. During this period the

average noise level in all channels is essentially constant. The noise levels in the 22.0- to 178.0-kHz channels are, however, slightly above the receiver noise level. Spin modulation measurements during this period show that the radiation detected in these channels is coming from the vicinity of the earth. The frequency spectrum of this radiation has a distinct peak in the 22.0-kHz channel and decreases in intensity at higher frequencies. No radiation is detected from the direction of the earth above 178.0 kHz or below 22.0 kHz. The relatively high constant noise level evident in the 2.0-MHz channel is the galactic background.

Another example in which the spectrum of the nonthermal continuum is clearly evident in the Imp 8 data is illustrated in Figure 2. In this case the spacecraft is in the distant magnetotail at a geocentric radial distance of about $41.0 R_E$ and a local time of about 23.5 hours. At high frequencies the spectrum of the continuum radiation is qualitatively similar to

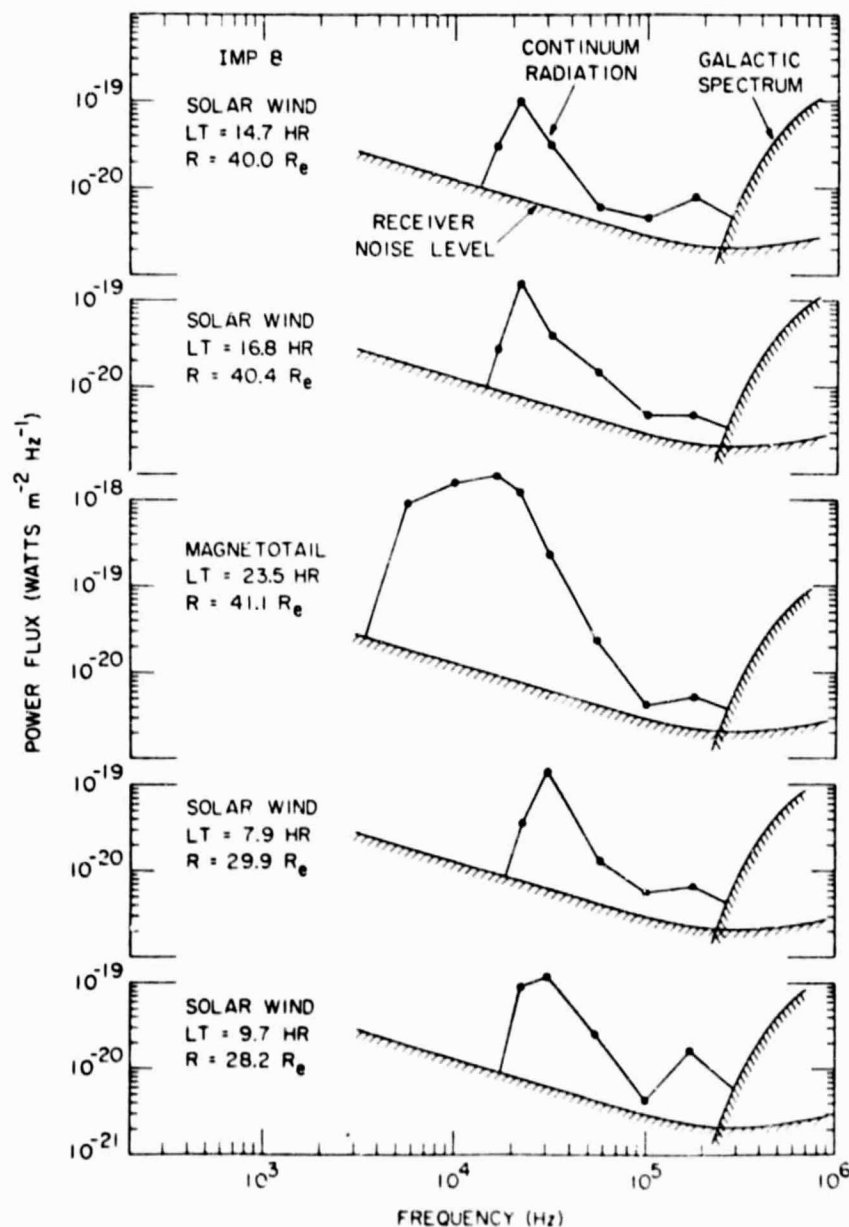


Fig. 3. Selected spectra of the nonthermal continuum at various local times. The abrupt cutoff in the solar wind spectra at about 20 kHz occurs at the local solar wind plasma frequency. Note that the spectrum in the magnetotail extends to frequencies well below the cutoff observed in the solar wind.

the spectrum observed in the solar wind; however, in this case the radiation extends down to a frequency of about 5.60 kHz, which is considerably below the cutoff frequency observed in the solar wind. At the lower frequencies, where no auroral kilometric radiation is present, it is evident that the continuum radiation exists with an essentially constant amplitude throughout the magnetotail. In some cases, such as the case at about 1400 UT, the spectrum of the continuum radiation extends down to frequencies as low as 562 Hz. It is sometimes difficult to identify the low-frequency limit of the continuum radiation clearly because of the occurrence of intense electrostatic plasma wave turbulence at frequencies below about 1 kHz. The ratio of the peak to average field strength, which is always close to one for the continuum radiation, often provides a useful identifying characteristic to distinguish the continuum radiation from the low-frequency plasma wave turbulence.

To illustrate the general character of the continuum spectrum at different points around the earth, Figure 3 shows five spectra selected at various representative local times. Four of these spectra were obtained in the solar wind, and one (the center panel) was obtained in the distant magnetotail. The spectra in the solar wind all show the same basic characteristics, consisting of a monotonic decrease in intensity with increasing frequency and a sharp cutoff near the solar wind plasma frequency at about 20–30 kHz. These spectra are in good qualitative and quantitative agreement with the continuum radiation spectra reported by Brown [1973] and Frankel [1973]. The spectrum in the magnetotail shows the same basic characteristics as the trapped electromagnetic radiation described by Gurnett and Shaw [1973]: a flat peak extending from about 5 to 20 kHz, a sharp low-frequency cutoff at the local electron plasma frequency, and a rapidly decreasing intensity above 20 kHz. When the continuum radiation spectra obtained in the solar wind and in the magnetotail are compared, it is evident that the spectra are nearly identical at all frequencies above the propagation cutoff at the solar wind plasma frequency. This similarity strongly suggests that the noise in both regions comes from the same source and that the spectrum observed in the solar wind represents that

portion of the continuum radiation which can escape into the solar wind above the solar wind plasma frequency.

The relationship between these various spectra is summarized in Figure 4, which shows representative spectra for the galactic continuum, the very intense and highly variable auroral kilometric radiation, and the relatively steady nonthermal continuum radiation. As will be discussed, direction-finding measurements clearly show that the continuum radiation and the auroral kilometric radiation come from different regions of the magnetosphere and therefore constitute two distinctly different sources. The spectrum of the continuum radiation can be divided into two components, a trapped component, which is permanently trapped within the magnetospheric cavity at frequencies below the solar wind plasma frequency, and an escaping component, which can propagate freely away from the earth at frequencies above the solar wind plasma frequency. This categorization of the various radio emission spectra of the earth should not be regarded as being final, since it is virtually certain that other weak but possibly significant components may also exist. For example, a small but distinct peak is evident at about 178 kHz in all the spectra shown in Figure 3. It is not known whether this peak is associated with a distinctly different source, as suggested by Kaiser and Stone [1974], or simply represents a quiescent level of the auroral kilometric radiation.

TRAPPED COMPONENT

Direction-Finding Measurements

The distinction between the trapped and free escape components of the nonthermal continuum is particularly evident in the direction-finding measurements of this radiation. Since the spin axes of both Imp 6 and Imp 8 are perpendicular to the ecliptic plane and the electric dipole antenna axis is perpendicular to the spin axis, the position of a radio source in the ecliptic plane can be determined from the spin modulation of the observed signal strength. The null direction δ and modulation factor m are determined by fitting the equation

$$\left(\frac{E}{E_0}\right)^2 = \left(1 - \frac{m}{2}\right) - \frac{m}{2} \cos [2(\delta_s - \delta)] \quad (1)$$

to the normalized field strength, E/E_0 . The angle δ_s is the azimuthal orientation of the antenna with respect to the satellite-earth line. The detailed procedures used to compute the best fit values for δ and m are discussed by Kurth *et al.* [1975].

Typical sets of direction-finding measurements obtained by Imp 8 in the distant magnetotail are shown in Figures 5 and 6. In each case the trapped continuum radiation is evident at low frequencies, less than about 50 kHz, and auroral kilometric radiation is evident at high frequencies, greater than 50 kHz. The null direction δ measured positive eastward with respect to the spacecraft-earth line is shown as a function of frequency in the bottom panel of each figure. At high frequencies, above about 30 kHz, the null directions of both the continuum radiation and the auroral kilometric radiation are within a few degrees of the direction to the earth. At frequencies below about 30 kHz a distinct shift in the null direction away from the earth is evident. In both cases, one in the late evening (LT = 22.5 hours) and the other in the early morning (LT = 1.8 hours), the null direction shifts toward the sun at frequencies below about 30 kHz. A corresponding decrease in the modulation factor also occurs at this frequency, from $m \approx 0.8$ at frequencies above 30 kHz to $m \approx 0.2$ at frequencies below 30 kHz. The

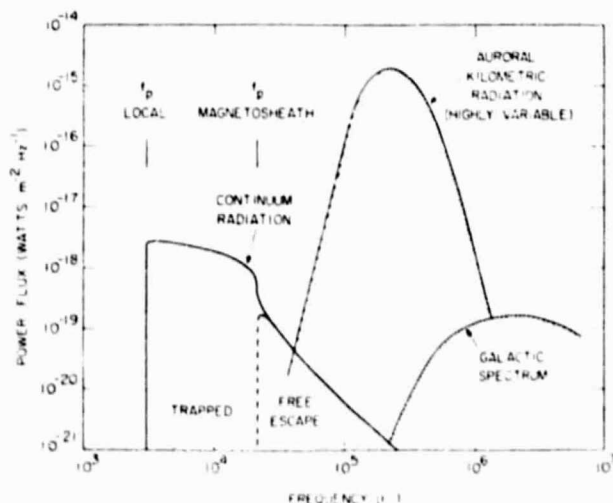


Fig. 4. The spectra of the galactic background, the auroral kilometric radiation, and the nonthermal continuum radiation as would be observed by a satellite about 30 R_E from the earth. The trapped continuum radiation can only be detected within the magnetospheric cavity.

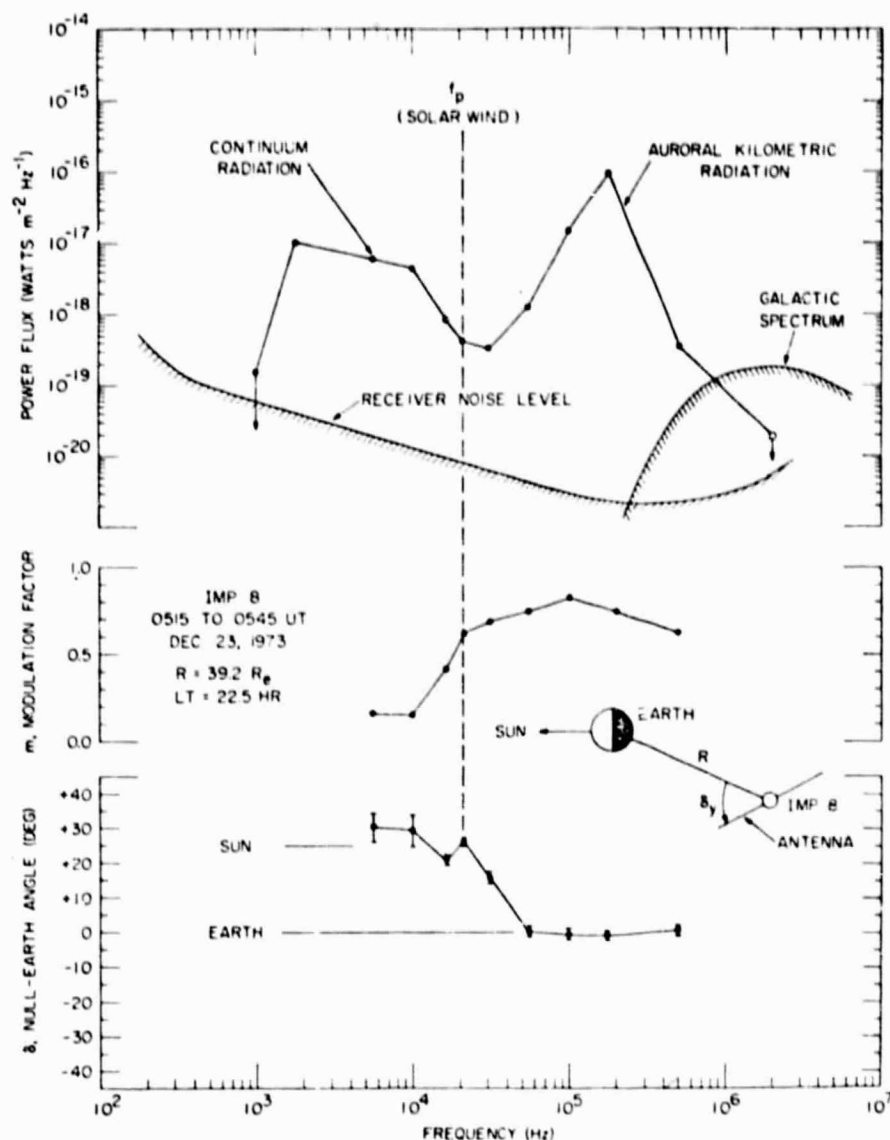


Fig. 5. Direction-finding measurements showing the shift in the null direction δ and the modulation factor m of the continuum radiation at the solar wind plasma frequency. These measurements were made in the magnetotail at a local time of 22.5 hours.

frequency at which this transition occurs corresponds closely with the solar wind plasma frequency as indicated by the vertical dashed line labeled ' f_p solar wind' in Figures 5 and 6. The solar wind plasma frequency measurements were obtained from the Los Alamos solar wind plasma experiment on the Imp 7 spacecraft (M. Montgomery, personal communication, 1974). Imp 7 was located in the solar wind upstream from the earth at the time that the measurements in Figures 5 and 6 were made. The shifts in the null direction and modulation factor at approximately the solar wind plasma frequency evidently correspond to the transition from the free escape to the trapped regimes illustrated in Figure 4. The tendency for the null direction to lie along the earth-sun line is a general characteristic of all the Imp 3 direction-finding measurements of the trapped continuum radiation in the distant magnetotail. This dependence is illustrated in Figure 7, which shows a series of null direction measurements made at 16.5 kHz during three Imp 8 passes through the distant magnetotail. The null direction is seen to follow the sun direction closely, except for a slight deviation toward the earth near

the magnetopause boundaries, which occur at about $\phi_{GSE} = 140^\circ$ and 220° during these passes.

The shift in the null direction near the solar wind plasma frequency and the tendency for the null direction of the trapped continuum radiation to be aligned along the earth-sun line can be explained from simple propagation considerations. Since radiation at frequencies below the magnetosheath plasma frequency is reflected at the magnetopause, the surface of the magnetopause apparently acts as a large parabolic reflector, directing radiation from near the earth into the magnetotail as illustrated in Figure 8. Because the direction-finding measurement responds to the average source position, the null direction tends to be aligned along the earth-sun line in the distant magnetotail. It is of interest to consider to what extent the magnetospheric cavity acts as a perfectly lossless cavity. If the cavity has an extremely high ' Q ,' then the radiation would be expected to be isotropic, since multiple reflections would rapidly randomize the radiation, and no spin modulation would be evident. Since a significant and easily detectable level of spin modulation ($m > 0.2$) does exist, it is concluded that a

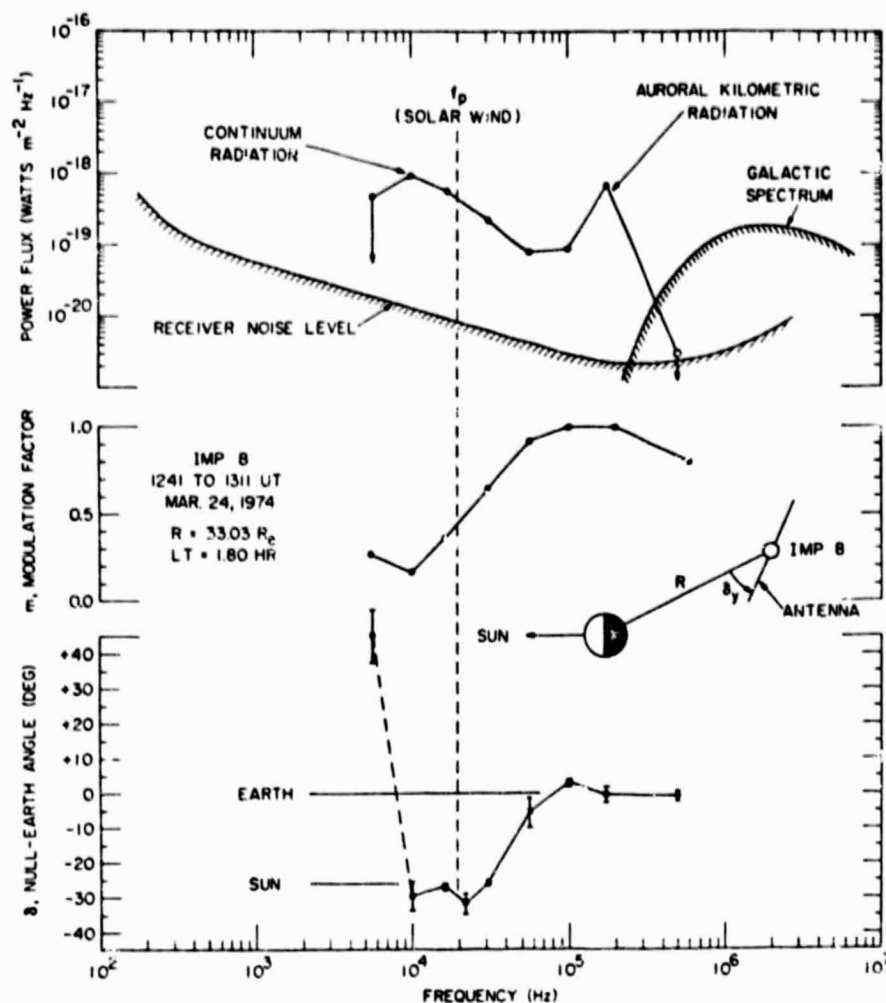


Fig. 6. Direction-finding measurements in the magnetotail similar to those in Figure 5 except at a local time of 1.8 hours. In both cases the null direction of the trapped continuum radiation shifts toward the sun at frequencies below the solar wind plasma frequency.

sizable flux of radiation is lost into the downstream tail region, resulting in a relatively low Q for the cavity. Further evidence that the Q of the cavity is quite small is given by the fact that the intensity of the continuum radiation increases only slightly (by a factor of about 2-5) as the frequency changes from the free escape to the trapped regime. Thus there is relatively little build up of the radiation intensity within the cavity due to multiple reflections. Note that the transition from the trapped to free escape regime is actually not an abrupt transition, since the magnetosheath plasma frequency varies from approximately the solar wind value in the downstream region to approximately twice this value at the stagnation point. Also some reflection or scattering of the incident radiation may occur in the magnetosheath, even at frequencies above the local plasma frequency.

Spatial Distribution of Intensity

To understand the origin of continuum radiation, we must first establish the region in which the noise is generated. Unfortunately, for the trapped component, direction-finding measurements do not provide much useful information on the source location because of the complicated reflections which occur at the magnetopause. We have therefore investigated the spatial distribution of the intensity of the trapped continuum

to try to determine the source region. Because the intensity of the trapped continuum radiation undergoes long-term temporal fluctuations of the order of 10 dB [Gurnett and Shaw, 1973], a large number of measurements must be used to obtain a reliable spatial distribution. Three years of Imp 6 data, totaling about 600,000 intensity measurements (163.48-s averages), are used in this study. Since it is impossible to manually identify the continuum radiation for such a large number of measurements, a criterion was devised to provide computer identification of the trapped continuum radiation. The criterion requires that the ratio of the peak to average field strength in each 163.48-s period not exceed 1.2 and that the average difference between adjacent peak field strengths not exceed 1 dB. This criterion eliminates impulsive noise bursts such as whistlers, chorus, and magnetosheath electrostatic turbulence. The criterion was tested manually on several orbits and has been verified to provide correct identification of the trapped continuum radiation with a very high degree of confidence. The 16.5-kHz channel was chosen as being representative of the trapped continuum radiation. This frequency was chosen because it is almost always below the solar wind plasma frequency and yet above the local plasma frequency inside the magnetospheric cavity. The measured intensities in this channel were averaged in blocks defined by 16 radial distance inter-

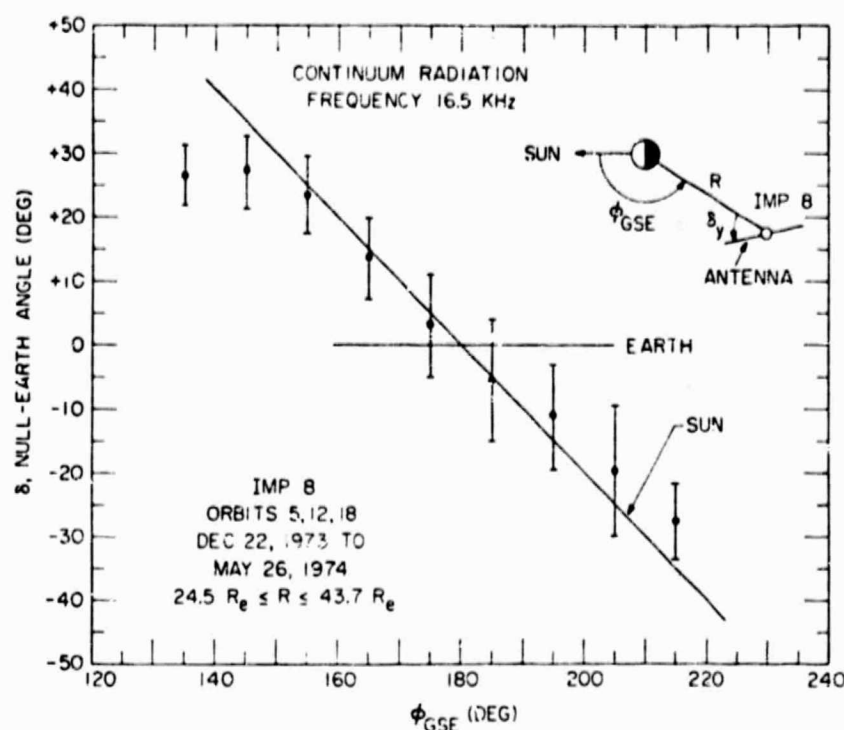


Fig. 7. A series of measurements in the magnetotail showing that the null direction of the trapped continuum radiation is consistently aligned along the satellite sun line.

vals from 1.0 to $39.8 R_E$ and 12 local time intervals from 0.0 to 24.0 hours. The results of this averaging procedure are shown in Figure 9.

The intensity of the continuum radiation at 16.5 kHz is seen to be remarkably constant at a level of about $0.5\text{--}1.0 \times 10^{-18} \text{ W m}^{-2} \text{ Hz}^{-1}$. As is expected, a sharp cutoff is evident at radial distances corresponding to the magnetopause and plasmapause boundaries. Although the intensity is constant over a large region of the magnetosphere, a distinct maximum, considerably above the statistical uncertainty in the average computation and approximately a factor of 2 above the overall average, occurs in the local time range from 4.0 to 14.0 hours and in the radial distance range from 5.01 to $7.94 R_E$. The existence of this maximum can also be verified by direct comparison of individual passes through this region with passes through other regions of the magnetosphere. Although the interpretation of this intensity distribution is greatly complicated by the many reflections and complicated ray paths which can occur within the magnetospheric cavity (thereby accounting for the nearly uniform intensity distribution), the existence of a distinct region of maximum intensity strongly suggests that a major fraction of the trapped continuum radiation is generated within this region.

ESCAPING COMPONENT

Direction-Finding Measurements

Direction-finding measurements of the escaping continuum radiation provide a much better method of determining the source region of the continuum radiation, since this radiation propagates directly to the spacecraft without reflection at the magnetopause. The 56.2-kHz frequency channel has been chosen to perform direction-finding measurements of the escaping continuum radiation. This frequency is chosen because it is usually below the frequency range of the intense auroral

kilometric radiation, which often masks the weak continuum radiation, and yet well above the plasma frequency normally encountered in the magnetosheath and solar wind.

A total of 184 intervals, each from 1 to 4 hours in duration, have been selected from the first 18 orbits of Imp 8 to study the direction of propagation of the escaping continuum radiation at 56.2 kHz. These intervals are all selected such that no radiation other than the continuum is detectable. For each interval the best fit null direction δ and modulation factor m are computed, and the rms error in the fit of (1) to the measured field strengths is determined. From these quantities the distance of closest approach of the ray path to the earth, ρ_1 , projected into the ecliptic plane and the rms uncertainty, σ_{ρ_1} , in ρ_1 are computed. Because the power flux is sometimes too small to provide reliable direction-finding measurements, only those cases for which the uncertainty in ρ_1 is less than $2 R_E$ ($\sigma_{\rho_1} \leq 2 R_E$) are used in this study. Of the 184 cases selected, 82 satisfied this error criterion. The threshold power flux for providing

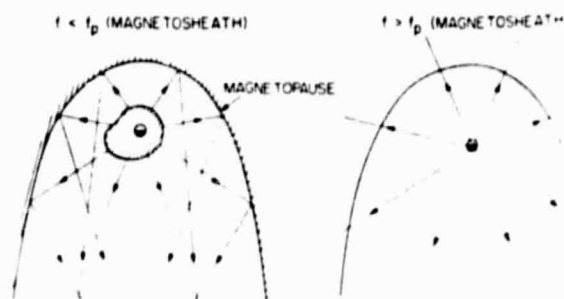


Fig. 8. A qualitative indication of the ray paths from a source region of the earth at frequencies above and below the plasma frequency in the magnetosheath. When $f < f_p$ (magnetosheath), the escaping rays are reflected back into the magnetosphere. When $f > f_p$, the escaping rays tend to align the average ray path direction with the sun line in the magnetotail along the earth-sun line.

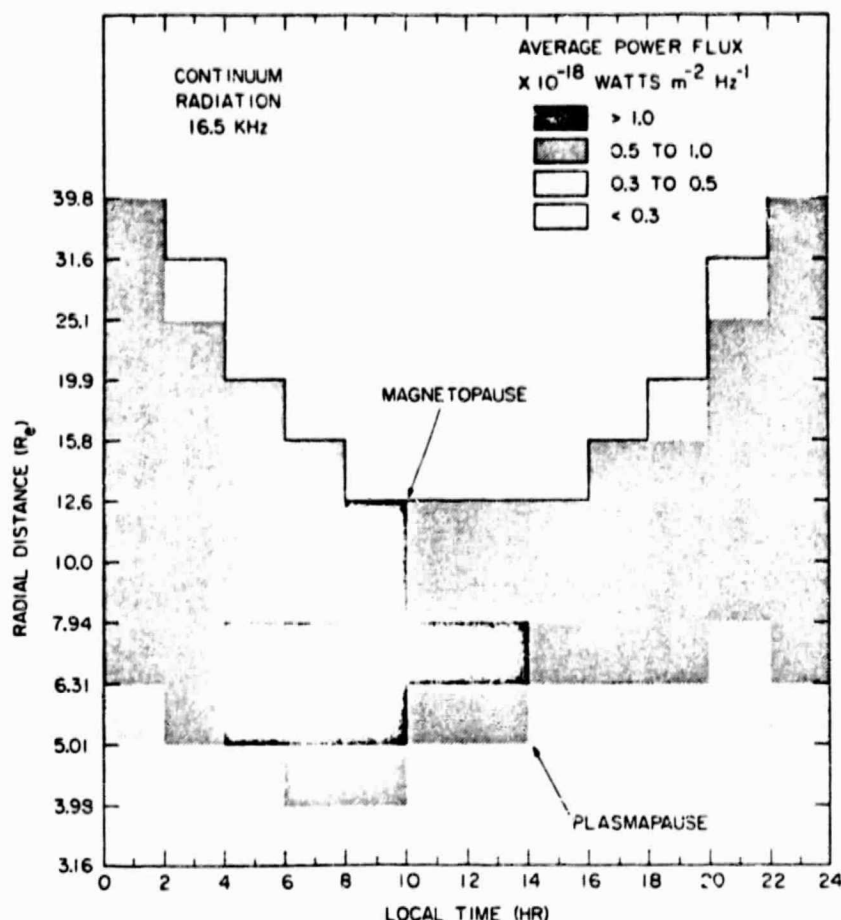


Fig. 9. The intensity distribution of the trapped continuum radiation at 16.5 kHz. A distinct maximum in the radiation intensity occurs in the local time range from 4.0 to 14.0 hours at radial distances from about 5.01 to 7.94 R_E .

reliable direction-finding measurements ($\sigma_{\rho_{\perp}} \leq 2 R_E$) at 56.2 kHz is about $5 \times 10^{-21} \text{ W m}^{-2} \text{ Hz}^{-1}$. The median power flux of the 82 cases selected for this study is about $1.0 \times 10^{-20} \text{ W m}^{-2} \text{ Hz}^{-1}$, and the maximum power flux observed is $2 \times 10^{-19} \text{ W m}^{-2} \text{ Hz}^{-1}$.

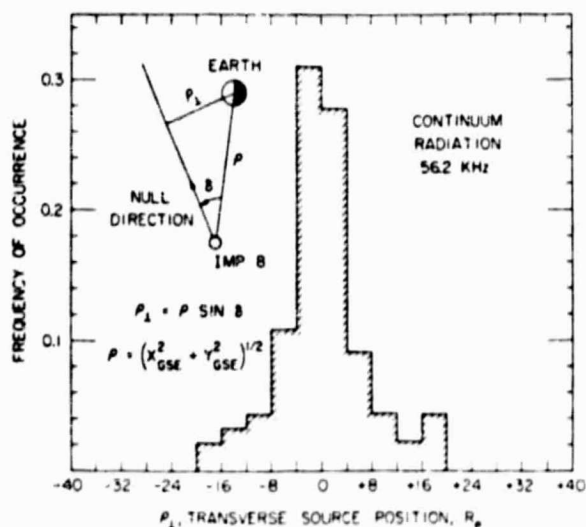


Fig. 10. The distribution of transverse source positions obtained for 82 direction-finding measurements of the escaping continuum radiation at various local times around the earth.

The distribution of transverse source positions determined for these 82 cases is shown in Figure 10. Most of the direction-finding measurements show an apparent source position well inside the magnetosphere, with transverse source positions typically less than $8 R_E$. However, a few cases are observed with source positions as much as $20 R_E$ from the earth. For the present we consider only those cases for which the source appears to be definitely within the magnetosphere, specifically, those with $|\rho_{\perp}| \leq 8 R_E$. The anomalous cases with $|\rho_{\perp}| > 8 R_E$ are discussed later.

The ray paths for the cases with $|\rho_{\perp}| \leq 8 R_E$ are shown in Figure 11, projected into the ecliptic plane. The spacecraft position for each ray path is shown as a dot, and the arrow indicates the direction of the null. The apparent center of the source region can be estimated from the intersection of ray paths observed at various local times. It is evident that most of the ray paths tend to intersect on the local morning side of the earth at a radial distance, projected into the ecliptic plane, of about 2 to 3 R_E from the center of the earth. It is also evident that a great deal of scatter exists in the apparent source position, indicative of a broad and somewhat variable source region.

A quantitative estimate of the angular size of the source can be obtained from the modulation factor m . If the source is located in the plane of rotation of the antenna, a very small (point) source produces a very deep null ($m \approx 1$), whereas a very broad source produces very little modulation ($m \approx 0$). In practice, quantitative estimates of the source size are com-

kilometric radiation, which typically has a modulation factor of 0.95–0.98.

Spatial Distribution of Intensity

Further information on the source region of the escaping continuum radiation can be obtained from the spatial distribution of intensity. Since the escaping continuum radiation is not reflected by the magnetopause, the region of maximum intensity should provide a good indication of the source region. Data from the Imp 6 spacecraft, which has a highly eccentric orbit, must be used to provide measurements in the source region. Unfortunately, the Imp 6 experiment is about a factor of 5 less sensitive than the Imp 8 experiment, so the continuum radiation generally cannot be detected by Imp 6 at large radial distances or when the radiation is very weak. The noise level of the Imp 6 experiment is about $2.5 \times 10^{-20} \text{ W m}^{-2} \text{ Hz}^{-1}$ at 56.2 kHz. Since the intensity of continuum radiation does vary considerably, many periods do, however, exist when the continuum radiation is sufficiently intense to provide good measurements of the spatial distribution with the Imp 6 experiment.

Three cases in which the continuum radiation at 56.2 kHz is sufficiently intense to clearly show the radial variation of the intensity are shown in Figure 13. In each case the spacecraft is moving outward to larger radial distances, from about 3.0 to $8.0 R_E$, in the local morning region of the magnetosphere. The plasmapause location is identified on each plot as the point where the local plasma frequency f_p is approximately equal to 56.2 kHz. The plasma frequency is obtained from the upper

hybrid resonance noise band, which occurs immediately following the arrow marked $f \approx f_p$ in each plot (see Shaw and Gurnett [1975] for a discussion of the upper hybrid resonance noise). No continuum radiation whatever is detectable inside the plasmapause. Outside the plasmapause, where $f > f_p$, moderately intense continuum radiation is evident in each case. In the top two examples the maximum intensity of the continuum radiation occurs at the point where the intense upper hybrid noise band occurs. In the bottom example, the maximum intensity occurs well beyond the plasmapause, at a radial distance of about $5.0 R_E$.

To provide a quantitative determination of the region of maximum intensity for the escaping continuum radiation, the average power flux has also been computed as a function of local time and radial distance at 56.2 kHz by using 3 years of Imp 6 data. To assure that only continuum radiation is included in this average, only measurements which fluctuate by less than 1 dB in any 163.48-s interval and which have a ratio of peak to average field strength less than 1.4 are used. The average field strengths obtained with this selection criterion for the 56.2-kHz channel are shown in Figure 14. Although considerable scatter is evident in the radial distribution at low intensities, a very distinct maximum is evident in the average power flux at radial distances from about 3.98 to $7.94 R_E$ and in the local time range from about 4.0 to 14.0 hours local time. The average power flux in this region, $>5.0 \times 10^{-20} \text{ W m}^{-2} \text{ Hz}^{-1}$, is well above the receiver noise level.

The region of maximum intensity for the escaping continuum radiation shown in Figure 14 agrees well with the

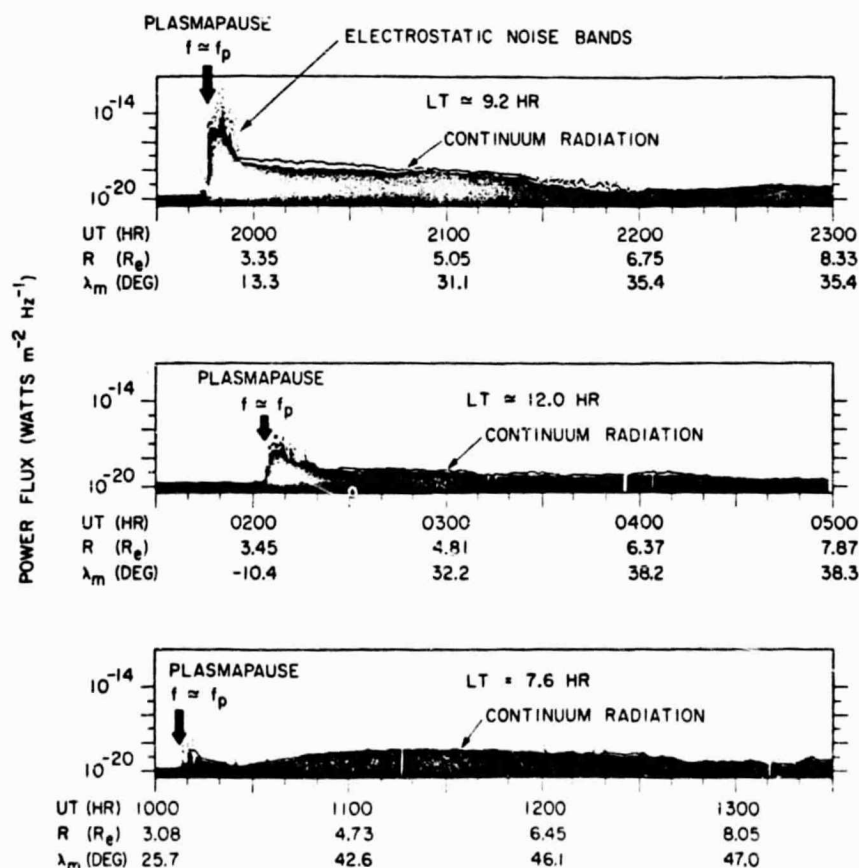


Fig. 13. The radial variation of intensity for three cases in which the intensity of the continuum radiation is well above the noise level of the Imp 6 experiment. In some cases the continuum radiation appears to be closely associated with the electrostatic noise bands at $f \approx f_p$ located near the plasmapause.

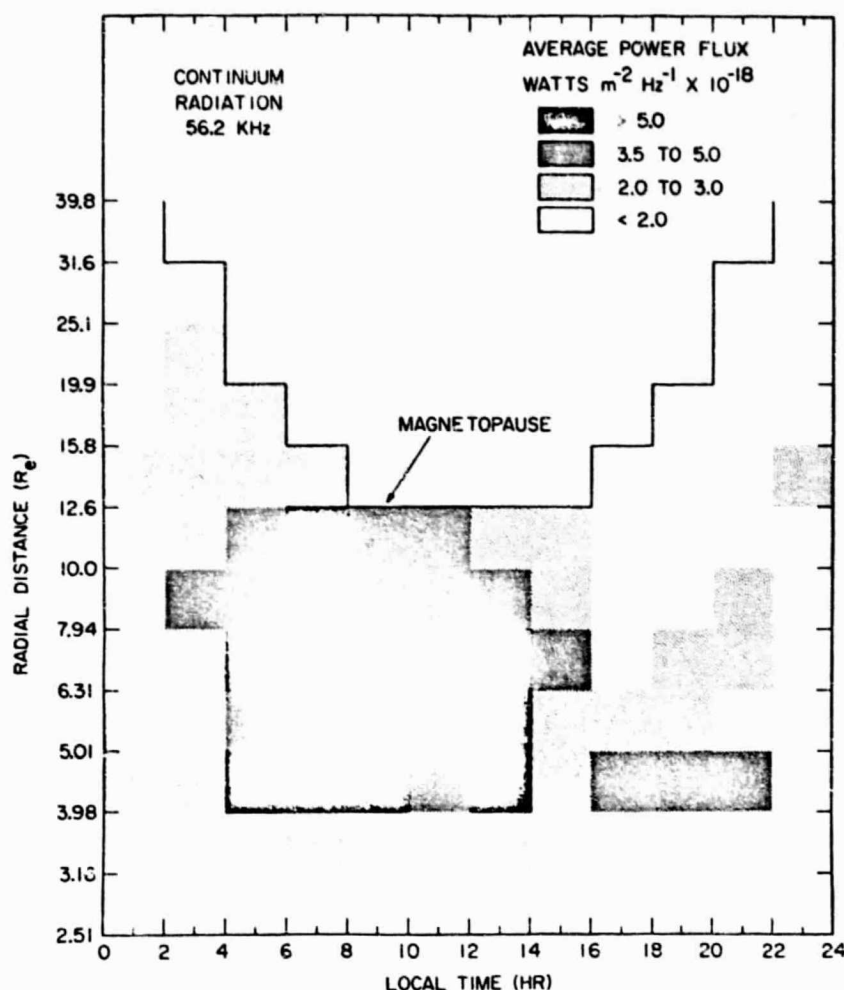


Fig. 14. The distribution of intensity of the escaping continuum radiation at 56.2 kHz. Again, a distinct maximum is evident in the local time range from 4.0 to 14.0 hours just beyond the plasmapause.

source region indicated by the direction-finding measurements in Figure 11 and is also consistent with the region of maximum intensity found for the trapped continuum radiation. On the basis of these results it is concluded that the source region of the continuum radiation is located in a broad region beyond the plasmapause boundary (where $f \approx f_p$) in the morning and early afternoon at local times from about 4.0 to 14.0 hours. Since the continuum radiation is often observed immediately beyond the plasmapause near the magnetic equator, as in the top two examples of Figure 13, it is also concluded that the continuum radiation is generated near the magnetic equator and is not primarily a high-latitude auroral zone emission. A qualitative illustration of the generation region suggested by these results is shown in Figure 15. The propagation cutoff surface at $f \approx f_p$ tends to follow the shape of the plasmapause because of the rapid change in the electron density near this boundary. The distinct outward bulge in the plasmasphere in the local evening is a well-known feature of the plasmapause [Carpenter, 1970].

RADIATION ASSOCIATED WITH THE BOW SHOCK AND/OR MAGNETOSHEATH

As is shown in Figure 10 and discussed earlier, a small but significant fraction of the direction-finding measurements at 56.2 kHz indicate source locations well outside of the magnetosphere with transverse source positions greater than 8

R_E and sometimes as large as 20 R_E . These apparently anomalous cases have been carefully examined to make certain that the direction-finding measurements are not being influenced by some spurious effect such as telemetry errors or interference from solar radio noise bursts. No such effect could be found. In many of these cases the computed uncertainty in the null direction is very small, less than 1° , indicating that a very reliable fit was obtained to the observed spin modulation.

Figure 16 shows the ray path directions, projected into the ecliptic plane, for the anomalous direction-finding measurements at 56.2 kHz. The most striking feature of this plot is that most of the ray paths appear to come from the general region of the bow shock and/or magnetosheath, particularly from the morning side of the magnetosphere. Similar direction-finding measurements of continuum radiation at 31.1 kHz show an even larger fraction of anomalous cases with the radiation also appearing to come from the general region of the bow shock and/or magnetosheath.

In studying possible origins for this anomalous radiation, two possible explanations have been considered. First, the radiation may be generated in the bow shock and/or magnetosheath and therefore not related to the magnetospheric continuum radiation. Second, it is possible that the anomalous direction-finding results may be the results of scattering, reflection, or partial obscuration of the magnetospheric continuum by the magnetosheath at times

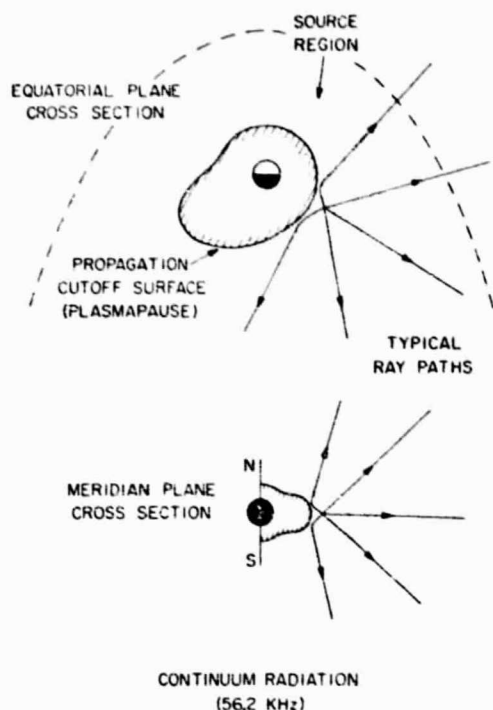


Fig. 15. A qualitative sketch of the source region of the continuum radiation indicated by the direction-finding measurements in Figure 11 and the intensity distributions in Figures 9 and 14.

when the solar wind and magnetosheath plasma frequencies are unusually high, near 56.2 kHz. The present indications are that the anomalous radiation is actually generated near the bow shock and is not associated with the nonthermal continuum from the magnetosphere. Although it is usually very weak, the frequency spectrum of the anomalous radiation sometimes exhibits a distinct enhancement in a single frequency channel, suggestive of a line emission rather than a

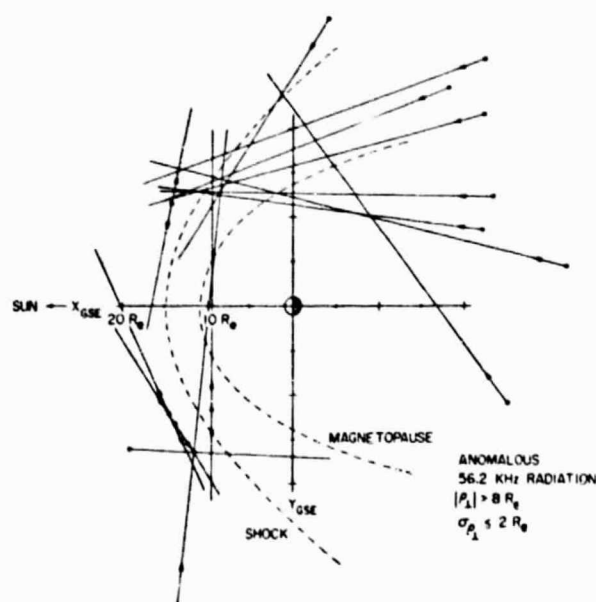


Fig. 16. The ray path directions for the anomalous direction-finding measurements at 56.2 kHz. Note that many of the ray paths appear to intersect near the bow shock on the morning side of the earth.

continuum. Since 56.2 kHz is approximately twice the solar wind plasma frequency, the most likely possibility is that this radiation is produced at twice the solar wind plasma frequency by nonlinear interactions with electrostatic electron plasma oscillations, as suggested by Ginzburg and Zheleznyakov [1958] for type 3 radio noise bursts. The source location of the anomalous 56.2-kHz radiation, near the bow shock on the morning side of the magnetosphere, is consistent with the favored region for electron plasma oscillations excited by energetic electrons streaming into the solar wind from the bow shock [Scarf et al., 1971; Fredricks et al., 1971]. Electromagnetic emissions of this type, at the second harmonic of the plasma frequency, have been previously observed near the bow shock region by Dunckel [1973].

DISCUSSION

We have shown that a weak nonthermal continuum is produced by the earth's magnetosphere extending over a very broad range of frequencies, from as low as 500 Hz in the low-density regions of the magnetotail to greater than 100 kHz. The intensity of this continuum decreases rapidly with increasing frequency and is usually not detectable above the galactic noise background at frequencies greater than about 100 kHz. At frequencies below the solar wind plasma frequency, which is typically about 20 kHz, the continuum radiation is trapped within the magnetospheric cavity and cannot escape. The Q of the cavity is evidently quite low because only a small, factor of 2-5, increase in intensity is observed as the frequency changes from the free escape to the trapped regimes. Direction-finding measurements indicate a distinct directionality to the trapped continuum radiation in the distant magnetotail, the ray paths being aligned roughly along the earth-sun line; this finding suggests that the day side magnetopause boundary acts as a giant parabolic reflector directing radiation from near the earth into the downstream tail region.

The spatial distribution of intensity for both the trapped and the freely escaping continuum radiation and the direction-finding measurements for the escaping component all indicate that the radiation is generated in a broad region located outside of the plasmapause at radial distances from 4.0 to 8.0 R_E and extending through the local morning and early afternoon from about 4.0 to 14.0 hours local time. In contrast to auroral kilometric radiation, which is generated in the high-latitude auroral zone regions, the continuum radiation appears to be generated at low to moderate latitudes, including the magnetic equator. The continuum radiation is often observed immediately beyond the propagation cutoff at $f \approx f_p$ near the magnetic equator with no evidence of an equatorial shadow zone such as is observed for auroral kilometric radiation [Gurnett, 1974].

Frankel [1973] has proposed that the nonthermal continuum radiation from the earth's magnetosphere is produced by gyro-synchrotron radiation from energetic electrons in the outer radiation zone. In many respects the results of this study are in reasonably good agreement with Frankel's calculations. The frequency spectrum of the escaping continuum radiation, the radial location of the source, and the power flux (within a factor of 5-15, depending on the model) are all in tolerable agreement with the gyro-synchrotron radiation model. No calculations are available for comparison with the trapped continuum radiation. However, some problems are presented by these new data. As is shown by the intensity measurements in Figures 9 and 14, a pronounced local time asymmetry is evident in the source intensity with a distinct maximum in the

range from 4.0 to 14.0 hours local time. Since most of the energy radiated by the gyrosynchrotron mechanism comes from electrons with energies from 100 to 500 keV, it is hard to see how this local time asymmetry can occur for these very high energies. The dawn to dusk electric field within the magnetosphere does tend to increase the electron energies in the local morning region by ~ 10 keV; however, this energy change is essentially trivial for the electrons contributing to the gyrosynchrotron radiation. It is possible that the evening bulge in the plasmasphere may be able to account for part of this asymmetry, although it seems unlikely that the bulge can account for the large asymmetry actually observed.

The radial intensity profiles of the continuum radiation, such as the profile in Figure 13, also do not agree with what would be expected for the gyrosynchrotron mechanism. For the synchrotron mechanism one would expect the intensity to increase gradually with increasing radial distance beyond the plasmopause with the maximum intensity occurring near the center of the emitting region. Instead, the maximum intensity sometimes occurs almost immediately after crossing the plasmopause (as in the top two panels of Figure 13), directly in the region where the electrostatic noise bands at $f \geq f_p$ are observed. Cases of this type strongly suggest that the electrostatic noise bands at $f \geq f_p$ are in some way closely associated with the generation of the continuum radiation.

Recently, Shaw and Gurnett [1975] completed a study of the electrostatic noise bands of the type illustrated in Figure 13. These noise bands are shown to consist of high-order $(n + 1/2)f_g$ harmonics of the electron gyrofrequency which become strongly enhanced at frequencies near the local plasma frequency. These noise bands are essentially a permanent feature of the magnetosphere and, interestingly, have maximum intensity in the same local time range in which the continuum radiation appears to be generated. Since the power radiated by the incoherent gyrosynchrotron mechanism is about a factor of 5–15 too small [Frankel, 1974], it may be that electrostatic waves of this type play an important role in the generation of electromagnetic radiation at frequencies above the local plasma frequency.

Acknowledgments. I wish to extend my thanks to S. Hame and M. Montgomery who provided the solar wind plasma density data from the Los Alamos plasma experiment on Imp 7 and to M. Baumbach and R. Anderson for their assistance in the data analysis. This work was supported in part by the National Aeronautics and Space Administration under contracts NAS5-11074 and NAS5-11431 and grants NGL-16-001-043 and NGL-16-001-002 and by the Office of Naval Research under grant N00014-68-A-0196-0009.

The Editor thanks R. A. Helliwell for his assistance in evaluating this paper.

REFERENCES

- Brown, L. W., The galactic radio spectrum between 130 kHz and 2600 kHz, *Astrophys. J.*, **180**, 359, 1973.
- Carpenter, D. I., Whistler evidence of the dynamic behavior of the dusk side bulge in the plasmasphere, *J. Geophys. Res.*, **75**, 3837, 1970.
- Dunckel, N., Plasma oscillations in the solar wind (abstract), *Eos Trans. AGU*, **54**, 442, 1973.
- Frankel, M. S., LF radio noise from the earth's magnetosphere, *Radio Sci.*, **8**, 991, 1973.
- Fredricks, R. W., F. L. Scarf, and L. A. Frank, Nonthermal electrons and high-frequency waves in the upstream solar wind, 2, Analysis and interpretation, *J. Geophys. Res.*, **76**, 6691, 1971.
- Ginzburg, V. L., and V. V. Zheleznyakov, On the possible mechanisms of sporadic radio emission (radiation in an isotropic plasma), *Sov. Astron.*, **2**, 653, 1958.
- Gurnett, D. A., The earth as a radio source: Terrestrial kilometric radiation, *J. Geophys. Res.*, **79**, 4227, 1974.
- Gurnett, D. A., and R. R. Shaw, Electromagnetic radiation trapped in the magnetosphere above the plasma frequency, *J. Geophys. Res.*, **78**, 8136, 1973.
- Kaiser, M. L., and R. G. Stone, Observations of the earth at low frequencies, paper presented at 1974 URSI meeting, Union Rad. Sci. Int., Boulder, Colo., Oct. 14–17, 1974.
- Kurth, W. S., M. M. Baumbach, and D. A. Gurnett, Direction-finding measurements of auroral kilometric radiation, *J. Geophys. Res.*, **81**, this issue, 1975.
- Scarf, F. L., R. W. Fredricks, L. A. Frank, and M. Neugebauer, Nonthermal electrons and high-frequency waves in the upstream solar wind, 1, Observations, *J. Geophys. Res.*, **76**, 5162, 1971.
- Shaw, R. R., and D. A. Gurnett, Electrostatic noise bands associated with the electron gyrofrequency and plasma frequency in the outer magnetosphere, *J. Geophys. Res.*, **80**, in press, 1975.

(Received January 6, 1975;
accepted March 7, 1975)

Continuum Radiation Associated With Low-Energy Electrons in the Outer Radiation Zone

D. A. GURNETT AND L. A. FRANK

Department of Physics and Astronomy, University of Iowa, Iowa City, Iowa 52242

A weak nonthermal continuum radiation is generated by the earth's magnetosphere in the frequency range from about 500 Hz to greater than 100 kHz. During magnetically disturbed periods the intensity of this continuum radiation increases significantly, by as much as 20 dB during large disturbances. In this paper we present a series of observations obtained by the Hawkeye 1 and Imp 8 spacecraft during a period of greatly enhanced continuum radiation intensity which occurred from October 14-21, 1974. The enhanced continuum radiation intensities observed during this event are found to be closely correlated with the injection of very intense fluxes of energetic, ~ 1 -30 keV, electrons into the outer radiation zone. Direction-finding measurements of the continuum radiation observed during this event show that the radiation is primarily coming from the dawn side of the magnetosphere, in agreement with the observed dawn-dusk asymmetry in the 1- to 30-keV electron distribution. These results suggest that the continuum radiation may be generated by a coherent plasma instability involving relatively low-energy, ~ 1 to 30 keV, electrons rather than by gyrosynchrotron radiation from very energetic, 200 keV to 1 MeV, electrons as has been previously suggested.

INTRODUCTION

Two principal types of radio emissions can be distinguished coming from the earth's magnetosphere at frequencies above the local plasma frequency: auroral kilometric radiation and continuum radiation. Auroral kilometric radiation consists of very intense and highly variable emissions with peak intensities in the frequency range from about 100 to 300 kHz [Gurnett, 1974]. This radiation is closely associated with the occurrence of aurora and is generated at altitudes of 1-2 R_E in the nighttime auroral zones [Kurth *et al.*, 1975]. Continuum radiation is a much weaker and slowly varying emission which extends over a broad range of frequencies, from as low as 500 Hz to greater than 100 kHz. Continuum radiation is thought to be generated at much higher altitudes in the outer radiation zone [Gurnett, 1975]. Figure 1 shows typical spectrums of these two types of radio emissions, as observed by a spacecraft about 30 R_E from the earth.

Recently, Kaiser and Stone [1975] have identified a third type of radio emission which appears to be generated in the day side auroral region. This radiation is very weak, with intensities only slightly above the galactic background, and occurs in a narrow frequency band with peak intensity slightly below 200 kHz. It seems likely that this weak narrow band emission is simply the day side analogue of the much more intense nighttime auroral kilometric radiation. However, at this time the exact relationship of this weak narrow band emission to auroral kilometric radiation has not been clearly established.

Continuum radiation from the earth's magnetosphere was first identified by Brown [1973] at frequencies from about 30 to 100 kHz using radio measurements from the Imp 6 satellite. Further studies by Gurnett [1975] have shown that the continuum radiation comprises two components: one that is permanently trapped within the low-density regions of the magnetospheric cavity at frequencies below the solar wind plasma frequency and one that can propagate freely away from the earth at frequencies above the solar wind plasma frequency. Direction-finding measurements show that the continuum

radiation is generated in a broad region on the dawn side and early afternoon side of the magnetosphere, as is shown in Figure 1. Whereas the intensity of auroral kilometric radiation sometimes varies by as much as 60-80 dB in only a few minutes, the intensity of the continuum radiation varies over a much smaller range, usually not more than 20 dB, and on a longer time scale, usually several hours or more. Frankel [1973] has shown that enhancements in the continuum radiation intensity, by as much as 20 dB above the quiescent intensity, occur during periods of geomagnetic disturbance. These periods of enhanced continuum radiation intensity sometimes last for several days.

Frankel [1973] proposed that the continuum radiation is generated by gyrosynchrotron radiation from energetic electrons, 200 keV to 1 MeV, injected into the outer radiation zone during the magnetic storm. Spectrums of the gyrosynchrotron radiation intensity computed by Frankel for a typical distribution of high-energy electrons injected into the outer radiation zone during a magnetic storm are in reasonably good qualitative agreement with the observed spectrum, but the absolute intensity is about a factor of 5-15 too small.

The purpose of this paper is to present a series of observations from the Hawkeye 1 satellite during a period of enhanced continuum radiation intensity which occurred from October 14-21, 1974. This event commenced during a geomagnetically disturbed period following a magnetic storm on October 14, 1974. The enhanced continuum radiation intensities occur in association with intense fluxes of low-energy electrons, ~ 1 -30 keV, injected deep into the outer radiation zone during this storm. The energy range of the electrons responsible for the continuum radiation and possible mechanisms for producing the radiation are considered.

The observations used in this study were gained primarily from the Hawkeye 1 spacecraft, which was launched on June 3, 1974. Hawkeye 1 is in a highly eccentric polar orbit with initial perigee and apogee geocentric radial distances of 6847 km and 130,856 km, respectively, an orbital inclination of 89.77°, and a period of 49.94 hours. The initial argument of perigee is 274.6°, so that the apogee is located almost directly over the north pole. The plasma wave experiment on Hawkeye 1 uses an electric dipole antenna with a tip-to-tip length of

C-675-310

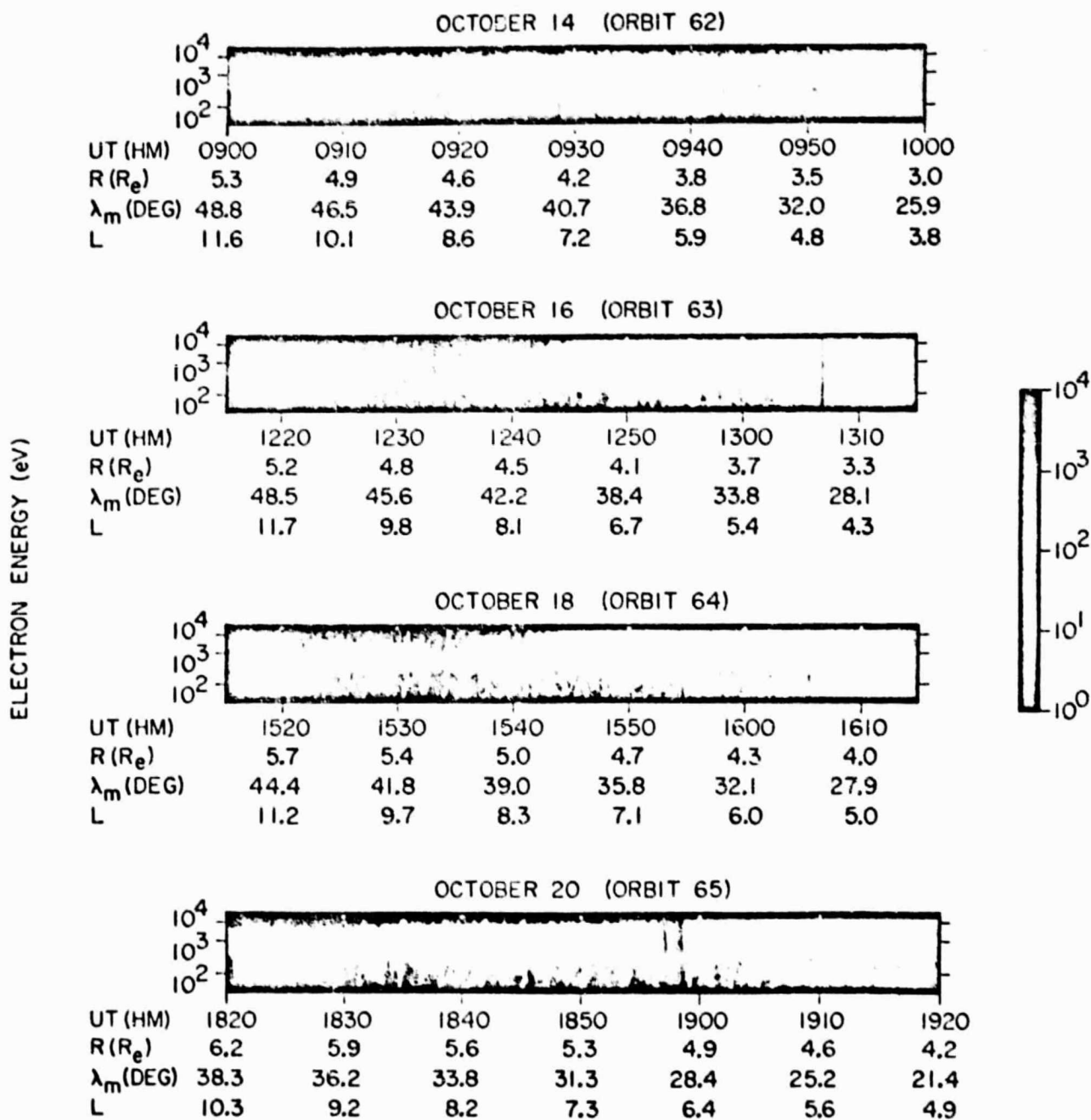


Plate 1. A series of electron energy-time spectrograms gained with the Lepedea instrument on Hawkeye i during the October 14-21 event. These spectrograms are for inbound passes through the outer radiation zone at local morning. Note the substantial increase in the electron intensities for $1 \leq E \leq 30$ keV over $4 < L < 8$ commencing with orbit 63, after the onset of the enhanced continuum radiation.

B-G75-311

ELECTRON ENERGY (eV)

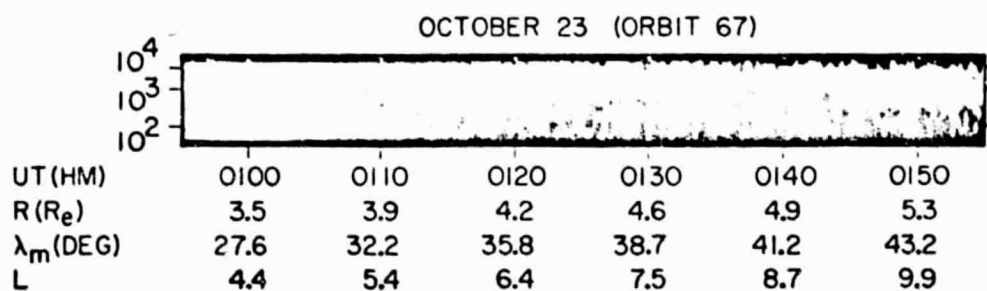
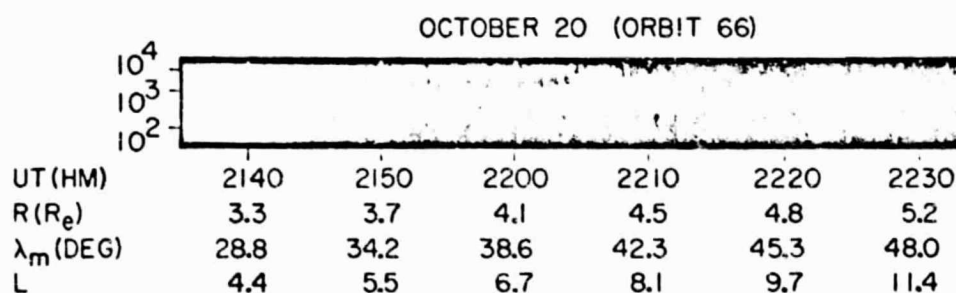
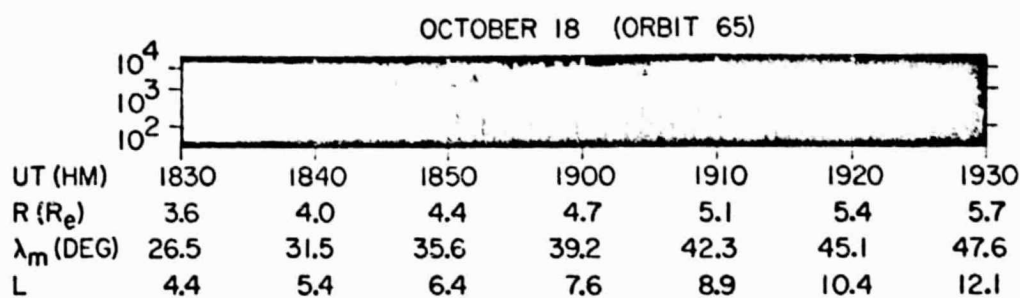


Plate 2. The spectrograms corresponding to those in Plate 1 for the outbound passes at local evening. Note the substantial decreases of both the electron energy and the intensities and lesser depth of penetration into the outer zone compared to those for the corresponding passes at local morning in Plate 1.

ORIGINAL PAGE IS
OF POOR QUALITY

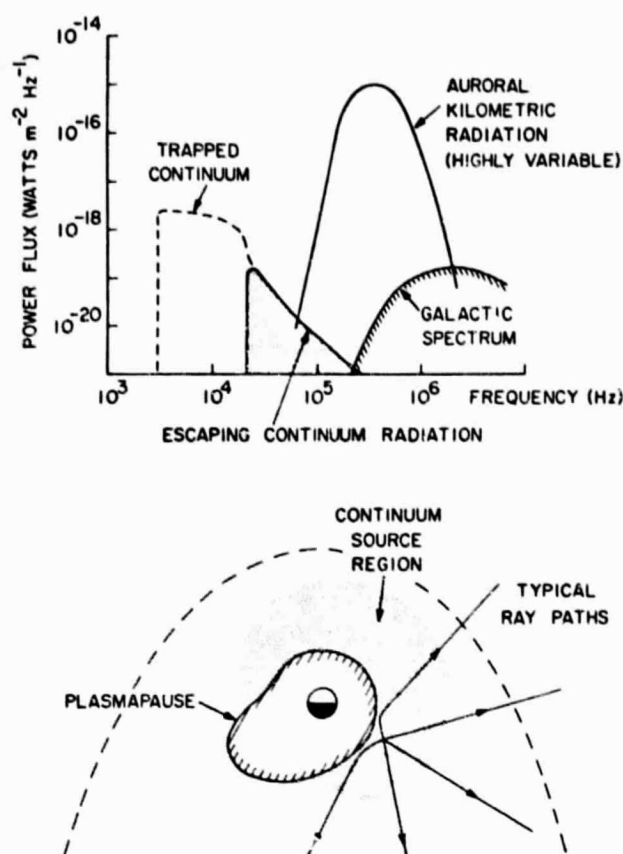


Fig. 1. Representative spectra of the galactic background, auroral kilometric radiation, and the trapped and escaping continuum radiation as would be observed by a satellite about $30 R_E$ from the earth. The continuum radiation is generated in a broad region beyond the plasmapause in the local morning and local noon sectors of the magnetosphere.

42.45 m for electric field measurements and a search coil magnetometer for magnetic field measurements. Electric field spectrum measurements are made in 16 frequency channels extending from 1.78 Hz to 178 kHz, and the magnetic field spectrum measurements scan the frequency range 1.78–5.62 kHz in 8 frequency channels. Plasma measurements were acquired with a low-energy proton-electron differential energy

analyzer (Lepede) similar to previous instruments of this type flown on the Imp and Injun satellites [Frank, 1967]. The Lepede instrument on board Hawkeye 1 provides measurements of the directional differential intensities of protons and electrons within the energy range $50 \text{ eV} \leq E \leq 40 \text{ keV}$. A collimated, thin-windowed Geiger-Mueller tube which responds primarily to electrons with $E > 45 \text{ keV}$ over most of the Hawkeye 1 orbit is also included within the Lepede instrumentation.

THE CONTINUUM RADIATION EVENT OF OCTOBER 14–21, 1974

Because of the relatively short electric antenna used on Hawkeye 1, continuum radiation can only be detected when the intensity is well above the normal quiescent level. During the first 6 months of in-flight operation, only one event, from October 14–21, 1974, has been found for which continuum radiation could be detected by Hawkeye 1 during a prolonged period. This event occurred following a magnetic storm which commenced at about 1700 UT on October 14. The hourly equatorial *Dst* magnetic disturbance index for this event is shown in Figure 2 [Sugiura and Poros, 1974]. Two abrupt depressions are evident in the *Dst* index near the start of the event: the first at about 0100 UT on October 13 and the second at about 1700 UT on October 14. Although the largest magnetic disturbance is associated with the October 13 storm, both the Hawkeye 1 and the Imp 8 observations show that the onset of the enhanced continuum radiation intensities during this event is associated with the October 14 magnetic disturbance.

The electric field intensities obtained from a series of Hawkeye 1 passes through the magnetosphere during the October 14–21 event are shown in Figures 3 and 4. The intensities are given in eight frequency channels from 13.3 to 178 kHz. The ordinate for each channel is proportional to the logarithm of the electric field strength. The interval from the base line of one channel to the base line of the next higher channel represents a dynamic range of 100 dB. The receiver noise level is located slightly above the base line of each channel. With the exception of orbit 67 these passes are all for the inbound portion of the orbit in the local morning, at about 0600 ± 1.0 hours magnetic local time. Usually, the continuum radiation is completely masked by intense auroral kilometric radiation on the outbound passes in the local evening. The outbound pass on orbit 67 is shown because no observations are available for the immediately preceding inbound pass. The start times are

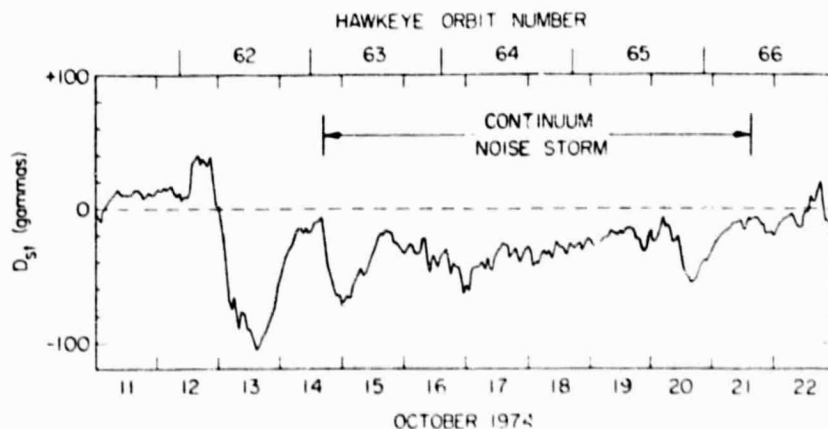


Fig. 2. The geomagnetic *Dst* index during the October 14–21, 1974, continuum radiation event. The times for the Hawkeye 1 orbits analyzed in this paper are shown at the top of this plot.

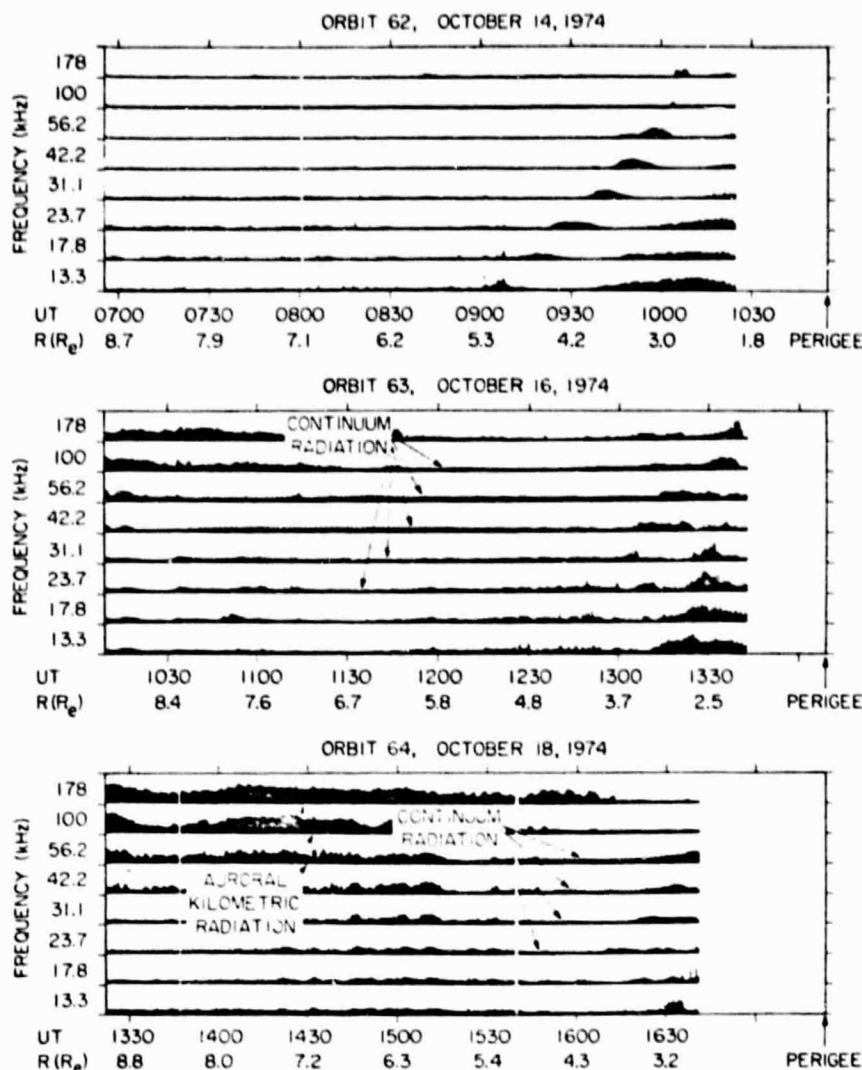


Fig. 3. The electric field intensities obtained during a series of three successive inbound Hawkeye 1 passes in the local morning. The intensity of the continuum radiation is only slightly above the receiver noise level but is easily recognized by the ~ 2 -min spin modulation caused by the electric antenna rotation. The dynamic range for each intensity plot is 100 dB.

adjusted so that the perigee is located at the right-hand edge of each plot, except for orbit 67, where perigee is on the left. The spacecraft coordinates are therefore similar for each plot. The universal time (UT) and geocentric radial distance to the spacecraft, in earth radii (R_E), are given at the bottom of each plot. The radial distance in these graphs varies from about 9.0 R_E at 60° magnetic latitude over the northern polar region to about 1.4 R_E at perigee over the southern polar cap.

The first pass shown in Figure 3, on October 14 (orbit 62), occurs shortly before the onset of the October 14 magnetic storm. The electric field noise levels are very low throughout this entire pass, the only significant noise being the $(n + \frac{1}{2})f_0$ noise bands of the type described by Shaw and Gurnett [1975] near the plasmapause. A representative power spectrum is shown in the top panel of Figure 5 at a radial distance of 5.93 R_E for this pass. Except for a very small enhancement at 31.1 kHz no continuum radiation is detectable. The second pass shown in Figure 3, orbit 63, occurs approximately 2 days later, on October 16. On this pass, several types of radio emissions are present. At high frequencies, in the 56.2- to 178-kHz channels, moderately intense auroral kilometric radiation is evident

during the first part of the pass, before about 1200 UT. At somewhat lower frequencies, from about 23.7 to 100 kHz, an almost constant amplitude broad band noise is present slightly above the receiver noise level. Even though this noise is very weak, it is easily distinguished from the receiver noise level by the spin modulation caused by the antenna rotation. The period of this modulation is about 2 min, which is the beat period between the spacecraft rotation rate and the telemetry sampling rate.

A representative spectrum of the broad band noise observed on orbit 63 is shown at a radial distance of 5.63 R_E in the center panel of Figure 5. This spectrum is qualitatively similar to the continuum radiation spectrums observed by the Imp 6 and Imp 8 satellites at $\sim 30 R_E$. However, the intensities are about 20 dB greater than the continuum radiation intensities normally observed by Imp 6 and Imp 8 during quiet times, even after correcting for the expected $1/R^2$ variation with radial distance. These high intensities are consistent with the continuum radiation intensities reported by Frankel [1973] for geomagnetically disturbed periods ($Kp > 5$). On the basis of these comparisons we identify the broad band noise observed

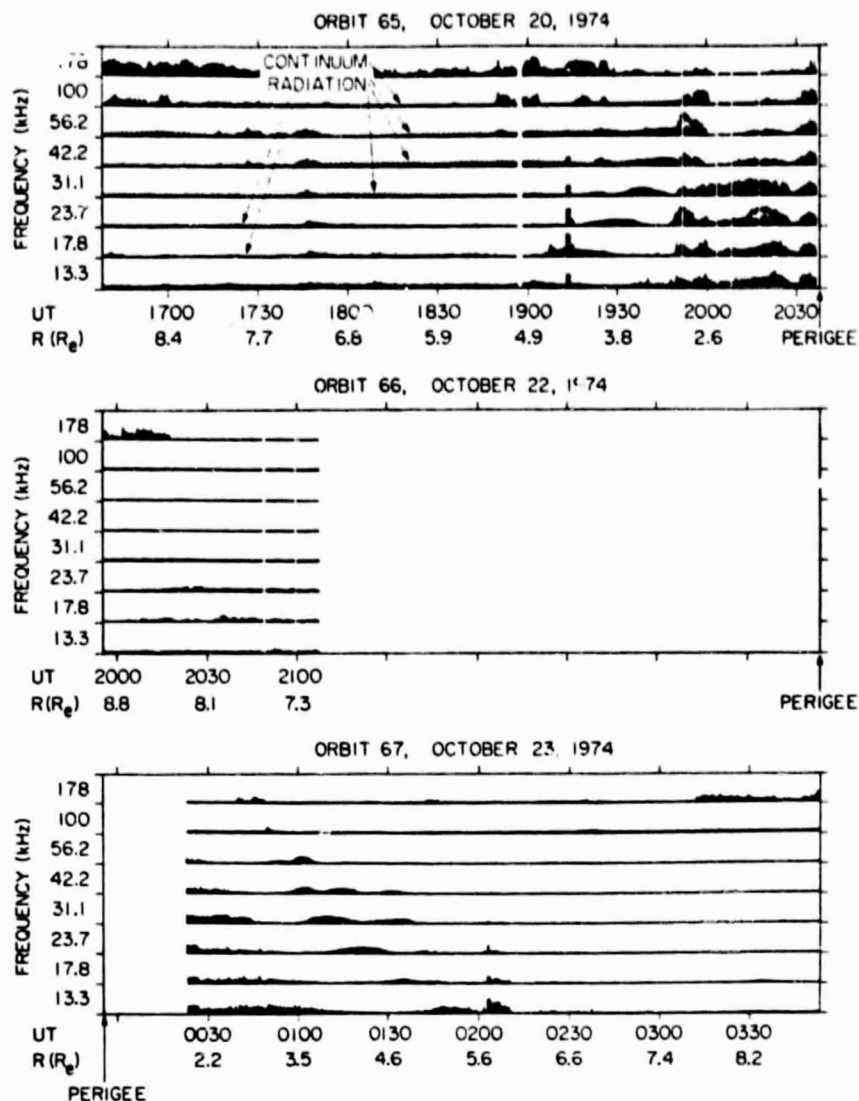


Fig. 4. Continuation of the sequence of Hawkeye 1 passes from Figure 3. Orbit 67 is an outbound pass in the local evening. This pass is shown because of the large data gap on the immediately preceding (orbit 66) inbound pass.

on this pass as continuum radiation of the type discussed by Frankel [1973] and Gurnett [1975].

Continuum radiation of comparable intensity is observed again 2 days later, on October 18 (orbit 64), and again 4 days later, on October 20 (orbit 65). However, 6 days later, on October 22 (orbit 66), the intensity has decreased to essentially undetectable levels at all frequencies above about 30 kHz. A power spectrum for the inbound pass of October 22 is shown in the bottom panel of Figure 5 at a radial distance of 7.16 R_E . No telemetry was received after about 2110 UT on this pass, so measurements are not available at radial distances less than about 7.0 R_E . During the immediately following outbound pass of October 23 (orbit 67 in Figure 4), only a few hours later, no continuum radiation is detectable at any radial distance.

The enhanced continuum radiation during this event was also detected by the University of Iowa plasma wave experiment on the Imp 8 spacecraft (for details of this experiment, see Gurnett [1975]). During the first few days of the event, Imp 8 was at a radial distance of about 28–46 R_E on the day side of the earth and in an excellent position to monitor the contin-

uum radiation without excessive interference from the night side auroral kilometric radiation. The radiation intensities detected by Imp 8 at frequencies from 31.1 to 178 kHz are shown in Figure 6 for this period. Since the continuum radiation intensities are only slightly above the receiver noise level, it is difficult to clearly identify the continuum radiation at all times during the event. The onset of the enhanced continuum radiation is, however, clearly evident at about 1700 UT on October 14, essentially coincident with the onset of the October 14 magnetic disturbance (see Figure 2). At 56.2 kHz the intensity increases about 20 dB above the normal quiescent level present before the onset of the event. The rise to maximum intensity takes place in approximately 1 hour, from 1700 to 1800 UT. The enhanced continuum radiation remains easily detectable for at least 3 days, through October 17. During this period the intensity varies by as much as 10 dB, typically on a time scale of a few hours. After October 17 the continuum radiation is almost completely masked by intense auroral kilometric radiation as the spacecraft progresses into the local evening region.

The spin modulation of the continuum radiation observed by Imp 8 during this event has been analyzed to determine the

location of the source of this noise. Details of the analysis procedure are given by Kurth *et al.* [1975]. Figure 7 shows the direction-finding measurements obtained from Imp 8 for the continuum radiation observed at 56.2 kHz during the October 14-21 event. The spacecraft position for each measurement is shown as a dot, and the line extended from each dot indicates the direction of the source projected into the ecliptic (X_{GSE} , Y_{GSE}) plane. Since the rotation axis of the Imp 8 electric antenna is directed perpendicular to the ecliptic plane, it is only possible to determine the direction to the source projected onto the ecliptic plane. Only certain selected periods are ana-

lyzed because of interference from other types of noise. Each direction-finding measurement in Figure 7 represents a 1- to 6-hour integration interval.

By assuming that the source distribution remained constant during the event the apparent center of the source region can be estimated from the intersection of the ray paths observed at various local times. It is evident from Figure 7 that most of the continuum radiation during this event appears to come from the dawn side of the magnetosphere at a radial distance, projected onto the ecliptic plane, of about 2-5 R_E from the center of the earth. Modulation index measurements also show that

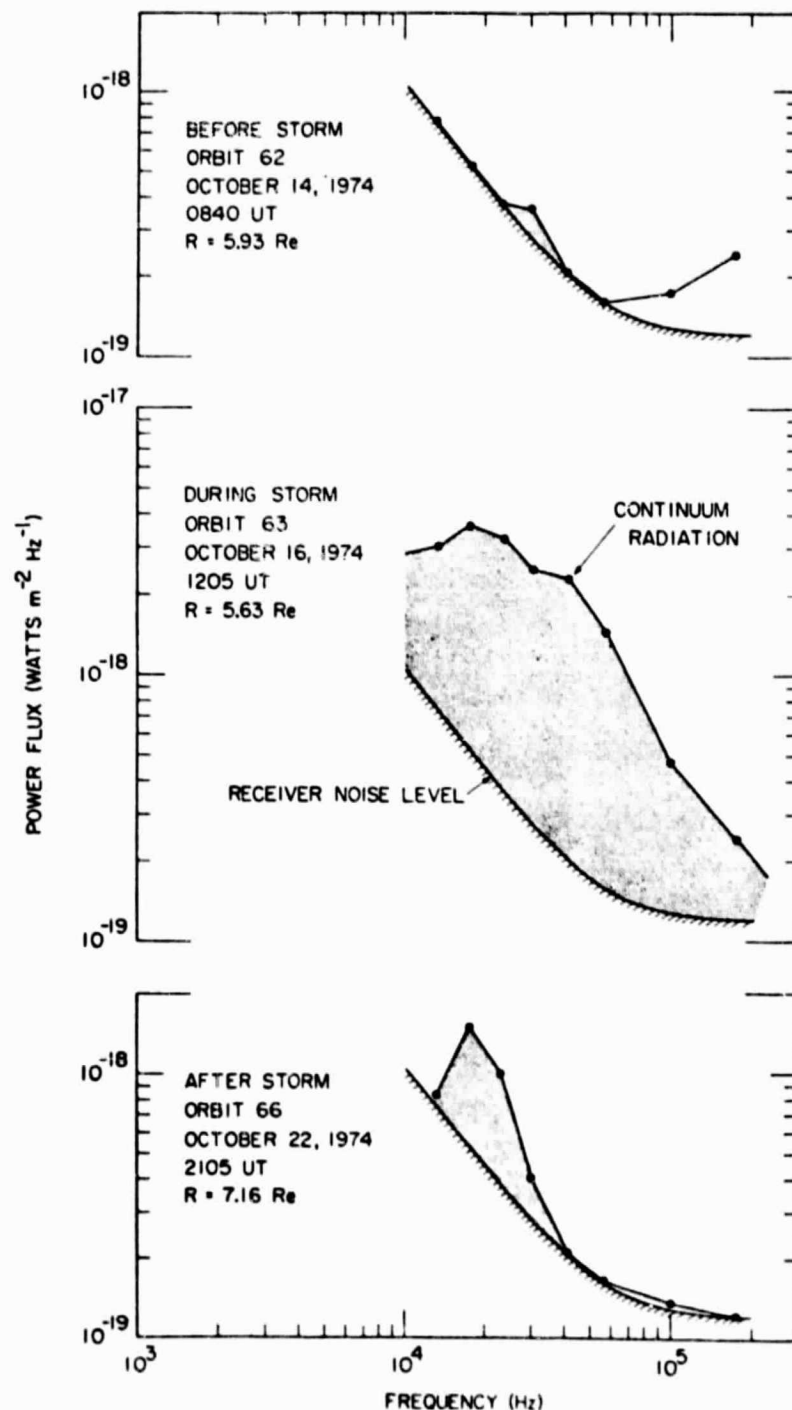


Fig. 5. Selected spectra of the received power flux before, during, and after the continuum radiation event at comparable radial distances from the earth. All three spectra are from inbound passes in the local morning.

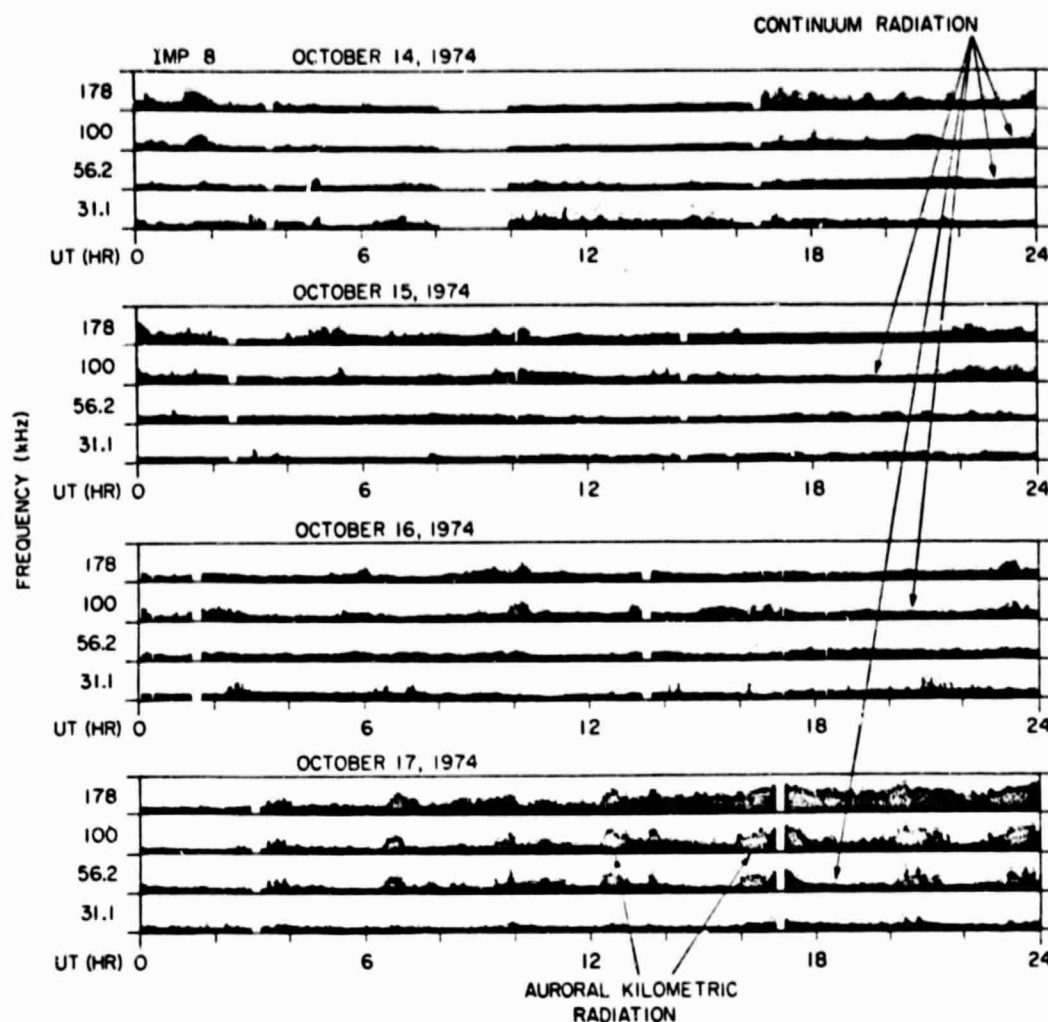


Fig. 6. Electric field intensities observed by Imp 8 during the period from October 14 to October 17, 1974. The onset of the enhanced continuum radiation is clearly evident from about 1700 to 1800 UT on October 14, shortly after the October 14 magnetic disturbance (see Figure 2).

the source is very broad, several earth radii in diameter. These results are similar to previous directing-finding measurements of continuum radiation during less disturbed periods [Gurnett, 1975].

OUTER ZONE ELECTRON INTENSITIES DURING THE EVENT OF OCTOBER 14-21, 1974.

To try to identify the charged particles responsible for the enhanced continuum radiation during this event, we have analyzed observations of the electron and proton intensities for each pass of Hawkeye 1 through the outer radiation zone during the October 14-21 event.

Plates 1 and 2 summarize the electron energy spectrums obtained with the Lepedeau on Hawkeye 1 before, during, and after the period of enhanced continuum radiation. These measurements were gained with the ramp operational mode (high temporal resolution) of the Lepedeau and cover the energy range 70 eV to 27 keV. Each spectrogram shows the responses of the electron electrostatic analyzer as a function of energy and time for a 1-hour period as the spacecraft passes through the outer radiation zone at L values ranging from about 4 to 10. The ordinate of each spectrogram gives the electron energy on an approximately logarithmic scale from 70

eV to 27 keV. The analyzer responses are color coded according to the logarithmic scale on the right-hand sides of these figures, the high responses being red and the lowest responses being blue. For these series of spectrograms the satellite spin axis is aligned approximately parallel to the local magnetic field direction. Since the axes of the fields of view of the Lepedeau are directed perpendicular to the spin axis, the pitch angles sampled by the instrument are $\sim 90^\circ$. The starting times of the spectrograms are chosen to provide a set of measurements corresponding to approximately the same range of L values for each pass. The spectrograms of Plate 1 are for inbound passes in the local morning sector of the magnetosphere, and the spectrograms of Plate 2 are for outbound passes during local evening. Because of telemetry coverage limitations, observations are usually not available for consecutive inbound and outbound passes through the outer radiation zone. To study temporal variations over a several-day period, it is therefore necessary to intercompare measurements on the inbound (local morning) and outbound (local evening) passes.

The inbound pass on October 14 (orbit 62) in Plate 1 occurs approximately 7 hours before the onset of the enhanced continuum radiation as determined by Imp 8. The electron in-

intensities during this pass are typical of quiet conditions in the outer radiation zone in the local morning. Moderate intensities of low-energy, ~ 1 keV, electrons are present at large L values, $L \geq 8$, but the intensities of these electrons decrease rapidly with decreasing L . These electrons are believed to be injected from the night side plasma sheet and are convected through the dawn and day side magnetosphere by the combined effect of gradient drift and the dawn-dusk electric field. The quiescent electron intensities observed during this pass show that the magnetic disturbance on October 13 did not produce a durable injection of low-energy electrons into the outer radiation zone.

The next inbound pass occurs on October 16 (orbit 63), approximately 2 days after the onset of the enhanced continuum radiation. The outer zone electron intensities encountered during this pass have changed radically since the preceding pass. A very substantial increase of electron intensities within the energy range from ~ 1 to 30 keV is evident deep within the magnetosphere at L values from about 4 to 8. The energy spectrums of these electron intensities are very broad and exhibit peak differential intensities at energies from about 1 to 10 keV. Representative electron energy spectrums at $L \approx 5.8$ for the inbound passes of orbit 62 (prior to electron injection) and orbit 63 (first pass after injection) are compared in Figure 8. Prestorm electron intensities are similar to those reported by Lyons and Williams [1975] at these L values near the magnetic equator. There is some evidence of satellite charging at these L values when the spin modulation of electron intensities at $E \leq 400$ eV is examined, a topic which will be discussed more thoroughly in a future paper (see, for example, the time period 1240–1300 UT of the spectrogram for orbit 63 of plate 1). Specifically, the electron spectrums at these lower electron energies exhibit peak intensities only once per satellite spin period, these maxima being closely centered at the minimum solar aspect angle relative to the instrument fields of view. The

Lepede is sampling pitch angles at about 90° for the entire spin period. Hence only differential electron intensities at $E > 900$ eV have been shown in Figure 8. The electron spectrums at $E > 900$ eV are not significantly affected by these charging events. The electron intensities on orbit 63 are among the highest encountered to this date for this region of the outer zone.

Subsequent passes on October 18 (inbound orbit 64 and outbound orbit 65) and on October 20 (inbound orbit 65 and outbound orbit 66) continue to reveal the presence of this energetic electron distribution deep within the outer zone. During the 4-day period from October 16 to October 20 the intensity of these electrons gradually decreases, and the spatial distribution slowly spreads over a broader range of L values. A striking dawn-dusk asymmetry in electron intensities is also evident upon examination of plate 1 (local morning) and Plate 2 (local evening). By comparing the inbound and outbound passes on October 18 and October 20 one can see that both the intensities and the average energies are greater in the local morning than in the local evening. Electron intensities are also found on significantly lower L shells during local morning. By October 23 (orbit 67) the electron intensities for $5 < L < 8$ have decreased to about the prestorm values.

These observations show that extremely high electron intensities were injected deep into the outer radiation zone sometime between approximately 0930 UT on October 14 and 1245 UT on October 16. Most likely this injection took place during the magnetic storm on October 14. After this injection the electron intensities slowly decreased over a several-day period, through October 20, and subsided to prestorm intensities by October 23.

DISCUSSION

We have shown that unusually intense fluxes of low-energy, 1 to 30 keV, electrons were observed deep in the outer radi-

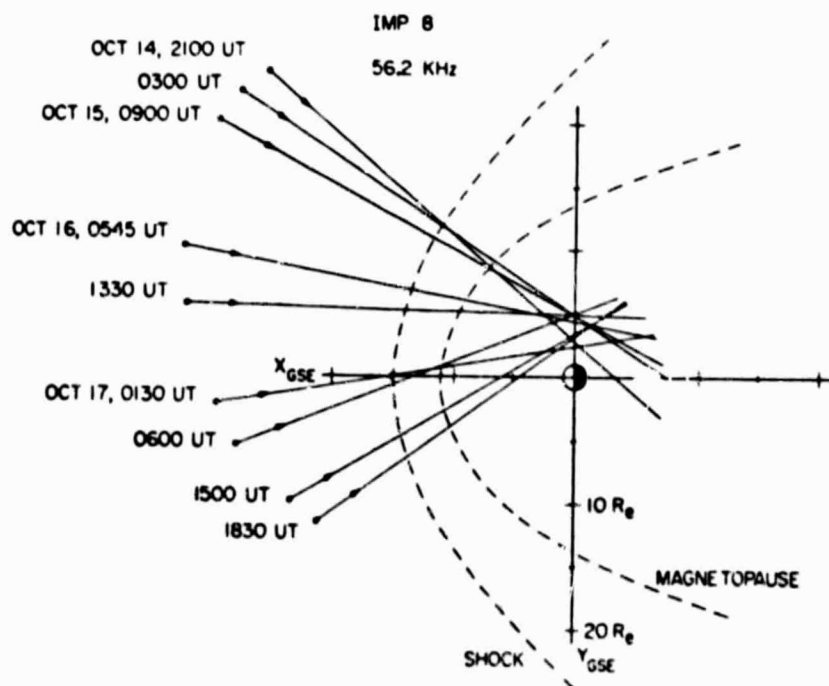


Fig. 7. A series of direction-finding measurements obtained from the Imp 8 spacecraft at various times during the October 14–21 event. The continuum radiation appears to be coming from a broad region centered in the dawn sector of the magnetosphere about 2–5 R_E from the center of the earth.

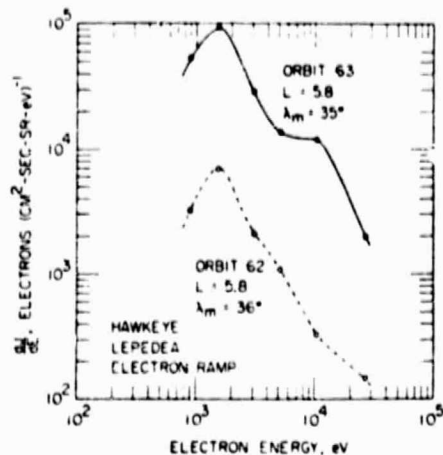


Fig. 8. Electron energy spectra at $L \approx 5.8$ in the local morning before (orbit 62) and after (orbit 63) the onset of the enhanced continuum radiation. The electron intensities on orbit 63 are among the highest reported to date for this region deep inside the outer radiation zone. The corresponding continuum radiation spectrum for this pass is shown in the center panel of Figure 5.

ation zone during a period of greatly enhanced continuum radiation intensities which occurred from October 14–21, 1972. The injection of these low-energy electrons into the outer radiation zone took place some time in the 2-day period between about 0950 UT on October 14 and 1245 UT on October 16. The occurrence of a large magnetic disturbance at 1700 UT on October 14 strongly suggests that these electrons were injected into the magnetosphere during this storm. The onset of the enhanced continuum radiation intensities occurred coincident with this magnetic disturbance on October 14. Af-

ter this magnetic disturbance, both the enhanced continuum radiation and the intense low-energy electron fluxes were observed through October 20, with a qualitatively similar rate of decay of the respective intensities. Direction-finding measurements showed that the continuum radiation originated primarily from the morning side of the magnetosphere. The low-energy electron intensities also showed a strong dawn-dusk asymmetry, the largest intensities occurring on the morning side of the magnetosphere. These observations all suggest that the enhanced continuum radiation is associated with the intense fluxes of low-energy electrons injected into the magnetosphere during this event.

Although the enhanced continuum radiation occurs during the same interval in which the intense fluxes of low-energy electrons were detected, it is still not immediately certain just what range of electron energies is primarily responsible for the continuum radiation or just what mechanism is involved in the generation of the noise. If the radiation is produced by the incoherent gyrosynchrotron process, as was proposed by Frankel [1973], then most of the radiation must come from high-energy, 200 keV to 1 MeV, electrons, since the mechanism requires relativistic energies to produce significant power fluxes. However, if the radiation is associated with lower electron energies, 10 keV or less, then a coherent plasma instability is required to explain the observed intensities. Because Hawkeye 1 does not provide measurements of the electron energies involved in the gyrosynchrotron process and since we know of no other spacecraft which can provide suitable measurements during this event, the gyrosynchrotron mechanism cannot be tested directly.

Although Hawkeye 1 does not have adequate measurements of the high-energy electron intensities to test the gyrosynchrotron mechanism directly, several factors suggest that a coherent plasma instability, involving interactions with low

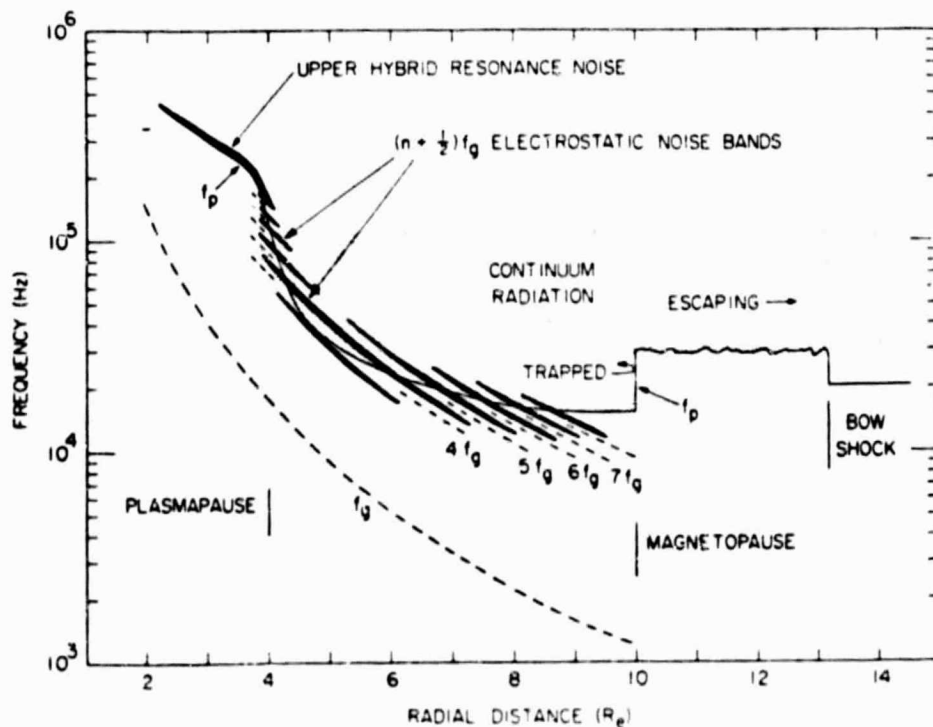


Fig. 9. A magnetospheric model showing the qualitative radial variation and region of occurrence of the electrostatic $(n + \frac{1}{2})f_g$ noise bands and the continuum radiation. The continuum radiation often appears to be generated in the region near the electrostatic noise bands.

energies, ~ 10 keV or less, should be seriously considered to explain continuum radiation events of this type. First, the temporal variation of the continuum radiation intensity during the storm corresponds closely with the observed temporal variation of the low-energy, ~ 10 keV, electron intensities but not with the expected temporal variation of the high-energy, ~ 500 keV, electron intensities. After the onset of the October 14 magnetic storm the intensity of the continuum radiation increased almost immediately, within a few hours or less. This time scale is comparable with the time scale in which electrons with energies of ~ 10 keV are injected deeply into the outer zone during a magnetic storm. The intensities of electrons with higher energies, ~ 500 keV, however, usually decrease dramatically during the initial phase of a magnetic disturbance on these L shells and then gradually increase to maximum intensity several days after the onset of the storm [Owens and Frank, 1968]. Since the primary electron injection into the outer radiation zone during this event probably took place in association with the October 14 magnetic storm, enhanced ~ 500 keV intensities are not expected until several days after the onset of the continuum radiation. Second, from examination of the radial variation of the electric field intensities, such as is seen in Figures 3 and 4, it often appears that the continuum radiation is closely associated with intense bands of electrostatic noise which occur just outside the plasmopause. Two excellent examples of relationships of this type are shown in Figure 13 of Gurnett [1975]. Our Figure 4 shows a similar case in which intense bands of electrostatic noise are evident near the low-altitude cutoff of the continuum radiation at $f \approx f_p$ (from about 1945–2000 UT in the 42.2-, 56.2-, and 100.0-kHz channels). These electrostatic noise bands occur at high-order $(n + \frac{1}{2})f_e$ harmonics of the electron gyrofrequency f_e and are particularly intense at frequencies near the electron plasma frequency f_p [Shaw and Gurnett, 1975]. The relationship between the continuum radiation and the $(n + \frac{1}{2})f_e$ noise bands suggested by these observations is illustrated in Figure 9, which shows an idealized radial profile of the frequency spectrums for both types of noise. Usually, the electrostatic noise bands at $(n + \frac{1}{2})f_e \approx f_p$ are most intense near and immediately outside of the plasmopause, although in some cases these bands extend almost to the magnetopause. Third, as was discussed by Frankel [1973], the power radiated by the incoherent gyrosynchrotron mechanism is about a factor of 5–15 too small to explain the observed continuum radiation intensity for a typical distribution of high-energy electrons injected into the outer radiation zone during a magnetic storm. A coherent radiation process could easily account for the power flux of the continuum radiation.

Several processes occur by which coherent plasma waves could produce electromagnetic emissions such as the continuum radiation. If the electric field amplitude of the plasma waves is sufficiently large, nonlinear interactions can cause the generation of electromagnetic radiation. Nonlinear interactions of this type are thought to be the mechanism by which type 3 radio noise bursts are produced from electrostatic plasma oscillations [Ginzburg and Zheleznyakov, 1958]. Gurnett and Shaw [1973] proposed that the trapped continuum radiation (referred to as $f > f_p$ electromagnetic noise) is produced by coherent cyclotron radiation from the high-order, nf_e , rotating charge distributions associated with the electrostatic $(n + \frac{1}{2})f_e$ electrostatic noise bands. Essentially, the electrostatic wave acts to organize the phases of the electrons, thereby greatly increasing the power radiated at the high harmonics of the cyclotron frequency. Scarf [1974], using a similar mechanism, proposed that wave-wave coupling between the $(n + \frac{1}{2})f_e$ electrostatic noise bands is involved in the generation of decametric radio emissions from Jupiter. These various mechanisms suggest that it is entirely possible, on theoretical grounds, that the enhanced continuum radiation is generated by low-energy, 1 to 30 keV, electrons via interactions with electrostatic plasma waves. Further investigation of similar events with instrumentation suitable for directly testing the gyrosynchrotron mechanism is needed to definitely establish the mechanism by which this radiation is produced.

Acknowledgments. This work was supported by the National Aeronautics and Space Administration under contracts NAS1-11257, NAS1-13129, NAS5-11074, and NAS5-11431 and grants NGL-16-001-002 and NGL-16-001-043 and by the Office of Naval Research. The Editor thanks M. L. Kaiser and two other referees for their assistance in evaluating this paper.

REFERENCES

- Brown, L. W., The galactic radio spectrum between 130 kHz and 2600 kHz, *Astrophys. J.*, **180**, 359, 1973.
- Frank, L. A., Initial observations of low-energy electrons in the earth's magnetosphere with Ogo 3, *J. Geophys. Res.*, **72**, 185, 1967.
- Frankel, M. S., LF radio noise from the earth's magnetosphere, *Radio Sci.*, **8**, 991, 1973.
- Ginzburg, V. L., and V. V. Zheleznyakov, On the possible mechanism of sporadic radio emission (radiation in an isotropic plasma), *Sov. Astron.*, **2**, 653, 1958.
- Gurnett, D. A., The earth as a radio source: Terrestrial kilometric radiation, *J. Geophys. Res.*, **79**, 4227, 1974.
- Gurnett, D. A., The earth as a radio source: The nonthermal continuum, *J. Geophys. Res.*, **80**, 2751, 1975.
- Gurnett, D. A., and R. R. Shaw, Electromagnetic radiation trapped in the magnetosphere above the plasma frequency, *J. Geophys. Res.*, **78**, 8136, 1973.
- Kaiser, M. L., and R. G. Stone, Earth as an intense planetary radio source: Similarities to Jupiter and Saturn, *Science*, **189**, 285, 1975.
- Kurth, W. S., M. M. Baumbach, and D. A. Gurnett, Direction-finding measurements of auroral kilometric radiation, *J. Geophys. Res.*, **80**, 2764, 1975.
- Lyons, L. R., and D. J. Williams, The quiet time structure of the energetic (30–560 keV) radiation belt electrons, *J. Geophys. Res.*, **80**, 943, 1975.
- Owens, H. D., and L. A. Frank, Electron omnidirectional intensity contours in the earth's outer radiation zone at the magnetic equator, *J. Geophys. Res.*, **73**, 199, 1968.
- Scarf, F. L., A new model for the high-frequency decametric radiation from Jupiter, *J. Geophys. Res.*, **79**, 3835, 1974.
- Shaw, R. R., and D. A. Gurnett, Electrostatic noise bands associated with the electron gyrofrequency and plasma frequency in the outer magnetosphere, *J. Geophys. Res.*, **80**, 4259, 1975.
- Sugiura, M., and D. J. Poros, Provisional hourly values of equatorial D_{st} , World Data Center A for Rockets and Satellites, Nat. Space Sci. Data Center, Greenbelt, Md., Oct. 1974.

(Received May 5, 1975;
accepted April 1, 1976.)

DIRECTION-FINDING MEASUREMENTS OF TYPE III RADIO BURSTS OUT OF THE ECLIPTIC PLANE*

MARK M. BAUMBACK, WILLIAM S. KURTH, and DONALD A. GURNETT

Department of Physics and Astronomy, The University of Iowa, Iowa City, Iowa 52242, U.S.A.

(Received 6 January, 1976)

Abstract. Direction-finding measurements with the plasma wave experiments on the HAWKEYE 1 and IMP 8 satellites are used to find the source locations of type III solar radio bursts in heliocentric latitude and longitude in a frequency range from 31.1 kHz to 500 kHz. IMP 8 has its spin axis perpendicular to the ecliptic plane; hence, by analyzing the spin modulation of the received signals the location of the type III burst projected into the ecliptic plane can be found. HAWKEYE 1 has its spin axis nearly parallel to the ecliptic plane; hence, the location of the source out of the ecliptic plane may also be determined. Using an empirical model for the emission frequency as a function of radial distance from the sun the three-dimensional trajectory of the type III radio source can be determined from direction-finding measurements at different frequencies. Since the electrons which produce these radio emissions follow the magnetic field lines from the Sun these measurements provide information on the three-dimensional structure of the magnetic field in the solar wind. The source locations projected into the ecliptic plane follow an Archimedean spiral. Perpendicular to the ecliptic plane the source locations usually follow a constant heliocentric latitude. When the best fit magnetic field line through the source locations is extrapolated back to the Sun this field line usually originates within a few degrees from the solar flare which produced the radio burst. With direction-finding measurements of this type it is also possible to determine the source size from the modulation factor of the received signals. For a type III event on June 8, 1974, the half angle source size was measured to be $\sim 60^\circ$ at 500 kHz and $\sim 40^\circ$ at 56.2 kHz as viewed from the Sun.

1. Introduction

Broadband radio emissions of solar origin characterized by a rapid decrease in frequency with increasing time were first reported by Wild and McCready (1950) and designated type III radio bursts. These first observations of type III bursts were made in the frequency range from 70 to 130 MHz. In addition to being characterized by a rapid frequency drift, type III bursts have lifetimes which increase with decreasing frequency and have shorter rise times than decay times. The amplitude of the bursts during the decay is proportional to e^{-kt} (Wild 1950), where k is the decay constant and t is time. For a general review of ground-based type III radio burst observations see Kundu (1965).

Wild *et al.* (1954) speculated that the rapid frequency drift is caused by charged particles moving outward through the solar corona emitting electromagnetic radiation at a frequency characteristic of the solar wind. Solar flare electrons with energies of ~ 40 keV were first observed in the interplanetary medium and identified to be of solar origin by Van Allen and Krimigis (1965). A high correlation between the onset of solar flare electrons in the energy range of 1 to

* Presented at Workshop on "Mechanisms for Solar Type III Radio Bursts", Berkeley, California, May 8-9, 1975; see *Solar Phys.* **46**, 433.

100 keV and type III emission near 1.0 AU indicates that these electrons generate the type III bursts (Lin, 1970; Alvarez *et al.*, 1972; Frank and Gurnett, 1972; Lin *et al.*, 1973; Alvarez *et al.*, 1975; Gurnett and Frank, 1975).

Measurements of the frequency drift rates of type III bursts provide information on the solar wind density, if the frequency of emission as a function of heliocentric radial distance is assumed to be related to the local plasma frequency. The velocity of the exciter electrons may also be determined from the frequency drift rates. Exciter velocities ranging from 0.2 to 0.8 times the velocity of light with an average velocity of $0.45c$ were calculated for frequencies between 60 and 45 MHz (Wild *et al.*, 1959). The average exciter velocity calculated from measurements by the RAE 1 satellite for frequencies between 0.7 MHz and 2.8 MHz was $0.38c$ (Fainberg and Stone, 1970). Other drift rate measurements give similar results (Hartz, 1964, 1969; Alexander *et al.*, 1969; Haddock and Graedel, 1970; Fainberg and Stone, 1971). These drift rate measurements give electron velocities that are in agreement with the energy range of the solar electrons observed in the interplanetary medium by the satellite experiments.

Ginzberg and Zhelezniakov (1958) suggested that type III bursts are generated by a coherent Cerenkov process. The energetic particles generate plasma waves at a frequency near the local plasma frequency by a two-stream instability. Then the plasma waves scatter off ion density inhomogeneities to produce electromagnetic radiation near the plasma frequency and also scatter off other plasma waves to produce radiation near the second harmonic. The theory has since been revised but the process is basically the same (Smith, 1970, 1974).

Models of the density of the solar wind can be used to determine the radial distances from the sun at which type III bursts radiate at different frequencies. Kaiser's (1975) study of the solar elongation of type III bursts indicates that the density of the solar wind from approximately 0.1 AU to 1.0 AU varies as $R^{-\gamma}$ where $2 \leq \gamma \leq 3$. Measurements of several thousand events were used to formulate the RAE emission level scale (Fainberg *et al.*, 1972; Fainberg and Stone, 1974). The RAE emission level scale relates the frequency of emission of a type III burst to the radial distance of the burst from the Sun. A solar wind density model can be computed from the RAE emission level scale if it is assumed that the radiation occurs at the fundamental or second harmonic of the plasma frequency. Initially the radiation was assumed to be at the fundamental of the plasma frequency (Fainberg *et al.*, 1972). The solar wind density models formulated from the analysis of type III bursts assuming emission at the fundamental of the plasma frequency usually disagreed with the observed plasma densities at 1.0 AU (Newkirk, 1967). Evidence now exists that radiation is predominantly at the second harmonic for low frequencies (Fainberg *et al.*, 1972; Fainberg and Stone, 1974; Lin *et al.*, 1973; Haddock and Alvarez, 1973; Alvarez *et al.*, 1975; Kaiser, 1975). The assumption of second harmonic emission brings densities calculated from the RAE emission level scale to better agreement with solar wind density measurements at 1.0 AU. For a model of the solar wind plasma density this paper uses the

RAE emission level scale with the assumption of second harmonic emission. For a review of density measurements see Newkirk (1967).

Since the electrons that generate type III bursts travel along the solar magnetic field lines, information can be obtained about the structure of the interplanetary magnetic field by analyzing the direction of arrival of a type III burst as a function of frequency. The source location of the type III burst can be determined from the direction-finding measurements and the radial distance of the emission from the Sun can be computed from a model of the solar density. The source location of the burst as a function of frequency, and hence radial distance, traces the magnetic field out from the Sun.

The first direction-finding measurements of type III bursts were made by Slysh (1967) using spin modulation and lunar occultations of the Luna 11 and 12 satellites to determine the source locations. Direction-finding measurements on the IMP 6 spacecraft confirmed that the type III emission regions as a function of frequency, and hence the electrons generating the type III bursts, follow the Archimedean spiral structure of the solar magnetic field (Lin *et al.*, 1973; Fainberg *et al.*, 1972; Fainberg and Stone, 1974; Stone, 1974).

Up to the present time direction-finding measurements of type III radio bursts have only provided one coordinate, in the plane of rotation of the antenna, of the direction of arrival. These one-dimensional measurements therefore only give a projection of the source location and do not provide a unique determination of the trajectory of the radio burst. Measurements of the source size from the spin modulation are similarly ambiguous for such one-dimensional measurements since the modulation of the received signal is also a function of the unknown elevation angle of the source above the plane of rotation of the antenna.

The purpose of this paper is to present a series of two-dimensional direction-finding measurements of type III radio bursts using spin modulation measurements from two satellites (IMP 8 and HAWKEYE 1) which have their spin axes nearly perpendicular to each other. Simultaneous direction-finding measurements from these satellites provide a unique determination of the direction of arrival (along a line) and the angular size of the source. This two-dimensional direction-finding technique is used, together with a model for the solar wind plasma density, to provide determinations of type III source locations out of the ecliptic plane and information on the three-dimensional structure of the solar magnetic field at radial distances of 0.2 to 1.0 AU from the Sun.

2. Description of Instrumentation

Data from two satellites, IMP 8 and HAWKEYE 1, are used in the direction-finding analysis. The three events analyzed occurred during June and July, 1974. All of the data presented in this paper were taken while the satellites were in the solar wind. Therefore, it was possible to analyze events down to frequencies near the solar wind plasma frequency, which is typically about 25 kHz at 1.0 AU.

The IMP 8 spacecraft was launched into earth orbit from the Eastern Test

Range on 26 October, 1973. The orbit is slightly eccentric with initial perigee and apogee geocentric radial distances of 147434 km and 295054 km, respectively, inclination of 28.6° , and period of 11.98 days. The spacecraft is spin stabilized with its spin axis oriented very nearly perpendicular to the ecliptic plane with a spin period of about 2.59 sec.

The University of Iowa plasma wave experiment on IMP 8 measures the average electric field intensity in a frequency range from 40 Hz to 2 MHz and the average magnetic field intensity from 40 Hz to 1.78 kHz. The electric field receiver is connected to a dipole antenna with a nominal tip-to-tip length of 121.8 m extended perpendicular to the spin axis, and the magnetic field receiver is connected to a triaxial search coil magnetometer. Electric field spectral measurements are made in 15 fixed frequency channels extending from 40 Hz to 178 kHz and in one channel with selectable frequency. The selectable frequency channel may be tuned to measure the average electric field intensity at 31.1 kHz, 500 kHz, or 2 MHz with a bandwidth of ± 1.0 kHz.

The HAWKEYE 1 spacecraft was launched into polar earth orbit on June 3, 1974 from the Western Test Range. The orbit is highly eccentric with initial perigee and apogee geocentric radial distances of 6847 km and 130856 km, respectively, inclination of 89.79° , and period of 49.94 hours. The initial argument of perigee is 274.6° ; thus, apogee is almost directly over the north pole. The spacecraft is spin stabilized with a spin period of about 11.0 sec. The spin axis lies in the plane of the orbit and is nearly parallel to the equatorial plane with a right ascension of 300.7° and declination of 6.8° .

The HAWKEYE 1 plasma wave experiment is similar to the IMP 8 plasma wave experiment. The electric field receiver is connected to a dipole antenna with a nominal tip-to-tip length of 42.45 m extended perpendicular to the spin axis. The magnetic field receiver is connected to a search coil magnetometer that is oriented parallel to the spin axis. Electric field spectral measurements are made in 16 fixed frequency channels extending from 1.78 Hz to 178 kHz, and magnetic field spectral measurements are made in 8 frequency channels extending from 1.78 Hz to 5.62 kHz.

3. Direction-Finding Technique

A. CALCULATION OF THE DIRECTION OF ARRIVAL

The amplitude of the detected signals from each satellite has a modulation caused by the rotation of electric dipole antenna. The angular position of the null in the modulation pattern can be used to determine a component of the source direction. The null in the modulation pattern occurs when the antenna is most nearly parallel to the wave propagation vector, and the maximum occurs when the antenna axis is perpendicular to the propagation vector. The depth of the null is determined by the size of the source and the elevation angle, α , between the plane of rotation of the antenna and the source direction. As α increases or as the source size increases the depth of the null decreases.

For both HAWKEYE 1 and IMP 8 the data sampling intervals are comparable to the spin period; thus, many rotations of the satellite are required to obtain a uniform angular distribution of samples through 360° . The time period necessary to collect a complete set of samples through 360° will be referred to as a sampling cycle.

The direction-finding routines used for analysis normalize the data to reduce the effects of amplitude changes that take place in a time interval that is long compared to the spin period. This normalization is performed by subtracting the average of all samples in the sampling cycle from each of the individual samples. Since the samples are proportional to the logarithm of the electric field intensity the normalization process is equivalent to dividing each sample by the geometric average intensity during the sampling cycle.

To determine the null direction, δ , data is accumulated over the duration of the type III event at each frequency and is then fit by the method of least squares to the theoretical modulation envelope given by

$$\left(\frac{E}{E_0}\right)^2 = \left(1 - \frac{m}{2}\right) - \frac{m}{2} \cos[2(\delta_y - \delta)], \quad (1)$$

where E/E_0 is the normalized intensity and δ_y is the orientation angle of the electric antenna axis in the plane of rotation of the antenna. The null direction, δ , is the direction to the centroid of the source projected onto the spin plane of the antenna. The modulation factor, m , provides a quantitative measure of the null depth: m is zero for no spin modulation, and m is one for the maximum modulation. The null direction computed represents the least squares fit δ over the duration of the event. Each sample receives an equal weighting in the analysis. Since the dipole pattern is assumed to be symmetric, the data from $90^\circ \leq \delta_y < 270^\circ$ is shifted into the range from $-90^\circ \leq \delta_y < 90^\circ$ by subtracting 180° .

Another direction-finding routine used for IMP 8 computes the null direction averaged over 10 minute intervals, rather than the average null direction for the entire event. For this routine samples from the current sampling cycle receive a weight of 1 while samples from previous sampling cycles are multiplied by a weighting factor that decreases exponentially for earlier times. The exponential weighting factors make it possible to compute δ averaged over a shorter pre-selected time interval in order to study changes in the direction of arrival during an event.

B. GEOMETRY IN THE ANALYSIS

The null direction computed from each satellite locates a plane in which the source must lie. The source lies along the intersection of the source planes determined by the two satellites. Figure 1 shows the geometry of the source planes and the angles and vectors used for the computation of the source location. The spin plane is the plane in which the antenna rotates. The spin axis, S , is perpendicular to the spin plane. The source plane is the plane in which both the

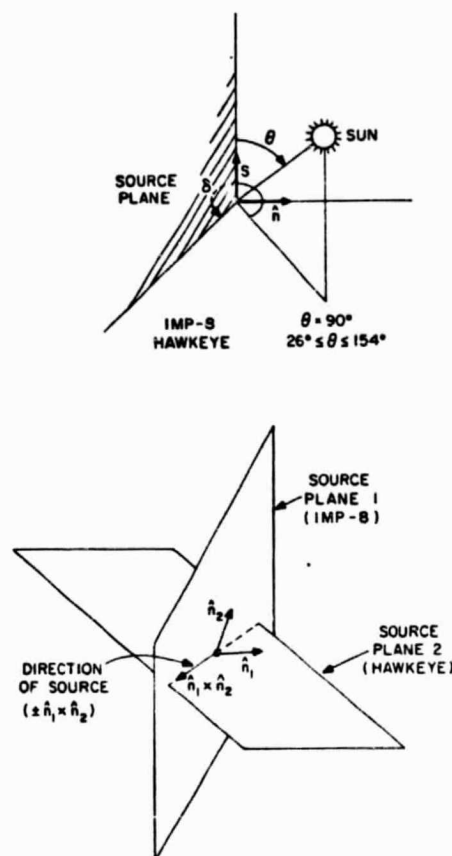


Fig. 1. The position of the source plane relative to the satellite spin axis, null position (δ), and the Sun for HAWKEYE 1 and IMP 8. The vector \hat{n} is perpendicular to the source plane, and the spin axis (S) is perpendicular to the spin plane. The source planes for IMP 8 and HAWKEYE 1 intersect, and the source is located along this intersection. The source location is computed by taking the cross product between \hat{n}_1 , a vector normal to the IMP 8 source plane, and \hat{n}_2 , a vector normal to the HAWKEYE 1 source plane. θ is the angle between the spin axis of the satellite and the Sun-satellite line.

spin axis of the satellite and the source lie. The angle between the satellite-Sun line projected into the spin plane and the intersection between the spin plane and the source plane is δ . Normals to both source planes are constructed. \hat{n}_1 is normal to IMP 8's source plane and \hat{n}_2 is normal to HAWKEYE 1's source plane. The source location vector is given by $\hat{n}_1 \times \hat{n}_2$. There is, however, a 180° ambiguity in the source location. At high frequencies this ambiguity is decided by assuming that the source is in the direction toward the Sun. At lower frequencies, where the source could be located at radial distances beyond 1.0 AU if the emission is at the second harmonic of the plasma frequency, the ambiguity is decided by requiring the source position to be in agreement with an extrapolation of the measurements

at higher frequencies. The source direction computed from $\hat{n}_1 \times \hat{n}_2$, after deciding the ambiguity, is given in geocentric solar ecliptic coordinates, λ_{GSE} and ϕ_{GSE} . The angle λ_{GSE} is the geocentric solar ecliptic latitude of the source, measured positive northward from the ecliptic plane. The angle ϕ_{GSE} is the solar ecliptic longitude of the source, measured positive counter-clockwise from the Sun-satellite line as viewed from the north ecliptic pole. Since the IMP 8 spin axis is perpendicular to the ecliptic plane the null angle δ , which is referenced to the Sun direction, is identical to the geocentric solar ecliptic longitude of the source.

4. Characteristics of Type III Bursts Observed by IMP 8 and HAWKEYE 1

At frequencies below 1 MHz, type III bursts have several readily observed features. Type III bursts are characterized by a rapid decrease in frequency with increasing time. The modulation factor of the burst varies with frequency and time. The direction of arrival is also observed to vary in time for any one frequency. Figure 2 shows a type III event observed simultaneously by both IMP 8 and HAWKEYE 1. This figure is a plot of the logarithm of the electric field intensity measured by the plasma wave experiments on board the two satellites. The data from seven frequency channels of each experiment are displayed as a function of time. Notice that in addition to a type III event, other naturally occurring radio signals such as auroral kilometric radiation and magnetosheath electrostatic noise are observed. The characteristic frequency drift is evident in the type III event shown in Figure 2.

The modulation factor observed at a particular frequency is usually greater near the start of the burst than near the end of the burst. The modulation factor also decreases with decreasing frequency. At 500 kHz the modulation is usually greater than 0.80 while at frequencies on the order of the local plasma frequency at 1.0 AU the modulation disappears completely. Figure 3 shows data from the 100 kHz channel of the IMP 8 experiment. In the top panel the logarithm of the electric field intensity is plotted as a function of time. The modulation of the received electric field intensity caused by the rotation of the dipole antenna is seen as a periodic amplitude fluctuation with a periodicity of about 100 sec. The bottom panel of Figure 3 displays the modulation factor calculated from Equation (1) as a function of time. The modulation factor at the start of the burst is about 0.65 while near the end of the burst the modulation factor is about 0.25.

At a particular frequency the direction of arrival changes systematically during the duration of the burst, usually starting near the Sun and deviating away from the Sun later in the event. The direction of arrival usually varies over a wider range at the lower frequencies. At 500 kHz there is a shift in ϕ_{GSE} of the source of about 10° , while at 56.2 kHz the ϕ_{GSE} shifts by as much as 60° . An example of this angle drift at 100 kHz is shown in the center panel of Figure 3. ϕ_{GSE} is initially near 0° (in the direction of the Sun), but then changes to approximately

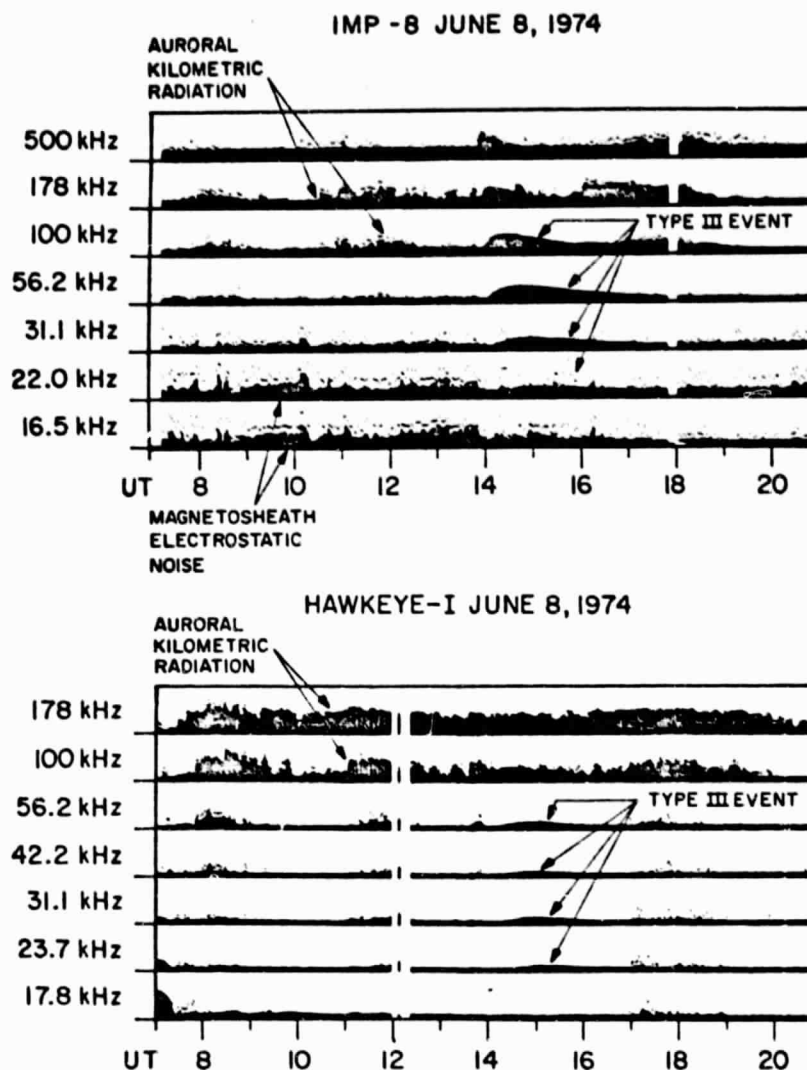


Fig. 2. A type III burst observed simultaneously by HAWKEYE 1 and IMP 8. The type III burst is characterized by a rapid decrease in frequency with increasing time, and at each frequency the intensity has a rapid rise time followed by a slower exponential decay.

45° at the end of the event. To compute the source locations for the events analyzed in this paper, the direction of arrival is the least squares fit δ computed over the duration of the event.

5. Plasma Density and Solar Magnetic Field Modes

Models of the solar wind density and the solar magnetic field are necessary to determine the source locations of the type III burst in three-dimensions. Since data from only two satellites are used in the analysis, only two components of the

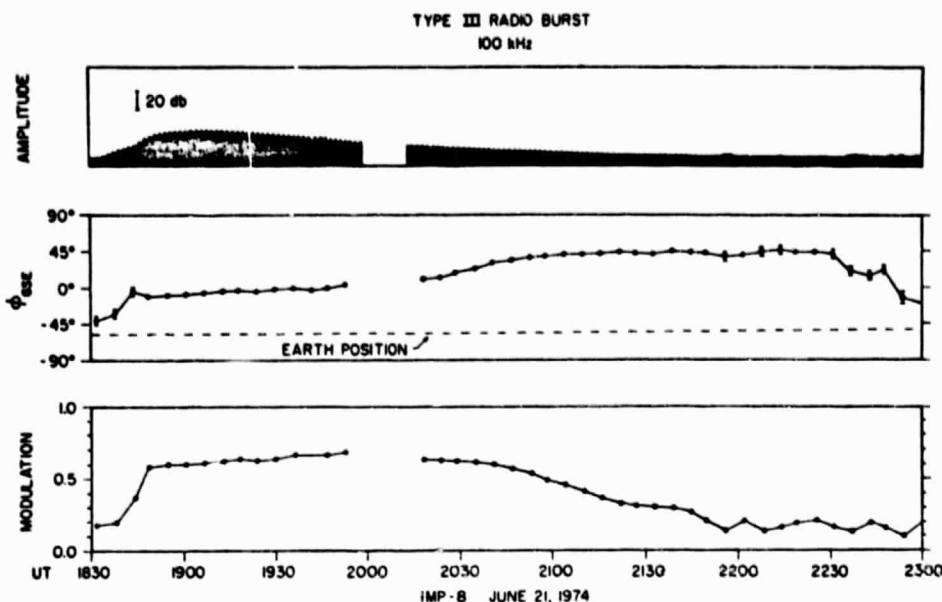


Fig. 3. The amplitude, geocentric solar ecliptic longitude, and modulation factor for a type III burst detected by IMP 8 on June 21 at 100 kHz. The spin modulation is evident as a small amplitude, periodic change in the observed intensity. The longitude drifts from near zero degrees near the beginning of the event to about 45° near the end. The modulation factor near the beginning of the event averages about 0.65, dropping to about 0.25 at the end of the event. The apparent shift in source location could be caused by polarization effects, density inhomogeneities, or by radiation from different source regions at both the fundamental and second harmonic of the plasma frequency.

source locations can be determined. A model of the solar wind plasma density provides the information required to determine the third component of the source locations.

A. RAE EMISSION LEVEL SCALE

The frequency of emission of type III bursts is a function of solar wind density; therefore, if a density scale of the solar wind as a function of heliocentric radial distance is assumed, it is possible to calculate the distance from the Sun to the type III burst emission region. The RAE emission level scale (Fainberg and Stone, 1970, 1974; Fainberg *et al.*, 1972) gives the frequency of emission as a function of heliocentric radial distance, independent of any assumption of the solar wind density. A density scale for the solar wind can be computed by assuming that the frequency of emission is at either the plasma frequency or at a harmonic of the plasma frequency. The density scale shown in Figure 4 is based on the RAE emission level scale and assumes emission at the second harmonic of the plasma frequency.

Since the RAE emission level scale is an average of many thousands of bursts, it is desirable on an individual basis to adjust the RAE emission level scale so that

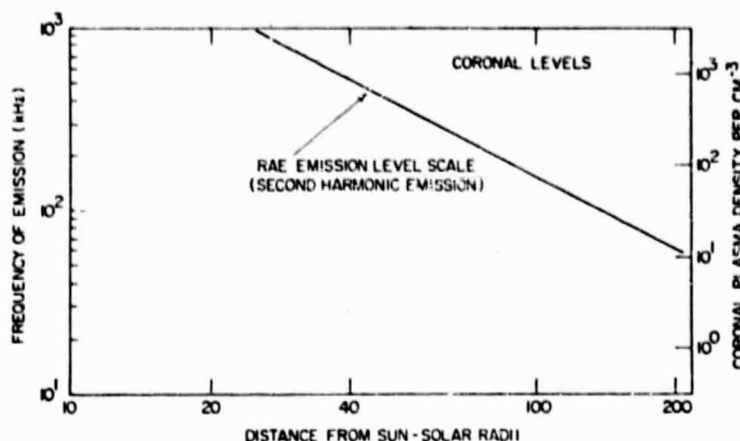


Fig. 4. The RAE emission level scale gives the average radial distance of a type III burst from the Sun as a function of frequency of emission. The density scale assumes emission at the second harmonic of the plasma frequency. For one of the events analyzed the RAE emission level scale was adjusted so that the density at 1.0 AU agreed with *in situ* measurements at 1.0 AU.

the density scale agrees with the plasma density measured at 1.0 AU in the solar wind. When the trajectory of the exciter electrons passes near the earth and *in situ* measurements of the solar wind density are available, the RAE emission level scale is adjusted to agree with the density measurements.

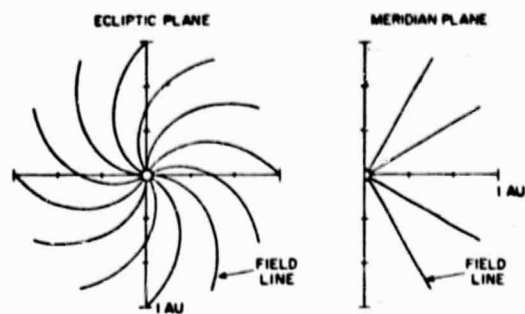
B. SOLAR MAGNETIC FIELD LINE CONFIGURATION IN THE ECLIPTIC PLANE

In the interplanetary medium the magnetic fields are constrained to move with the solar wind plasma flow. For the simplest model, the solar wind plasma flows radially out of the Sun at a constant velocity of approximately 400 km/sec^{-1} . Since the Sun is rotating the resulting magnetic field projected into the ecliptic plane corresponds to an Archimedean spiral (Parker, 1963, 1964, 1965). Measurements in the ecliptic plane confirm the general spiral structure of the magnetic field (Schatten *et al.*, 1968; and review by Schatten, 1972); however, the magnetic field is usually distorted from a perfect spiral configuration. For example, changes in the velocity of the solar wind will produce kinks in the spirals. Other distortions may be caused by variations in the magnetic field near the Sun and by magnetic field loops in which the field lines near the Sun reconnect back to the Sun (Schatten, 1972).

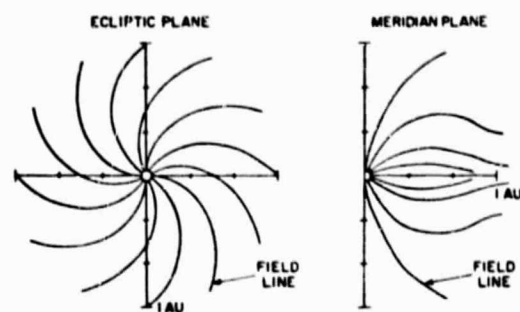
C. SOLAR MAGNETIC FIELD LINE STRUCTURE IN THE MERIDIAN PLANE

No direct measurements have been made of the solar magnetic field configuration out of the ecliptic plane, in the interplanetary medium. The structure of the solar magnetic field may be deduced by indirect measurements, such as the analysis of type III bursts, because the trajectory of the electrons that generate type III bursts is along the solar magnetic field lines.

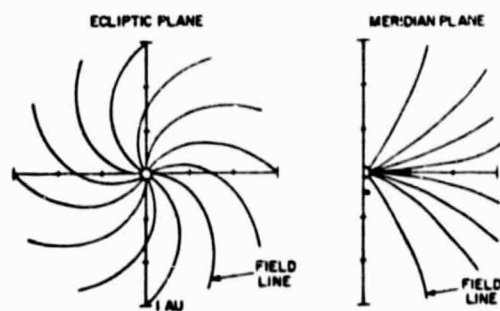
SOLAR MAGNETIC FIELD MODELS



CONSTANT LATITUDE MODEL



CONVERGENT FIELD LINE MODEL



DIVERGENT FIELD LINE MODEL

Fig. 5. Three models of the solar magnetic field. *Constant latitude*: Archimedean spirals wound on cones of constant heliocentric latitude. *Convergent field line model*: Archimedean spiral field lines which extend to lower heliocentric latitude with increasing radial distance. *Divergent field line model*: Archimedean spiral field lines which extend to higher heliocentric latitudes with increasing radial distance.

The simplest model of the solar magnetic field out of the ecliptic plane is the constant latitude model shown in Figure 5, which corresponds to a uniform radial flow of the solar wind plasma away from the Sun. Projected into the ecliptic plane the field lines are Archimedean spirals, while in a meridian plane the magnetic field lines are at a constant latitude. The constant latitude model corresponds to Archimedean spirals wound on cones of constant heliocentric latitudes.

The structure of the solar corona photographed during solar eclipses indicates that high latitude polar fields may extend to low latitudes at 1.0 AU (Schatten, 1972). The convergent field line model shown in Figure 5 is suggested by these observations. For this model the solar magnetic field projected into the ecliptic plane follows the Archimedean spiral but in the meridian plane the magnetic field lines extend to lower heliocentric latitudes with increasing radial distances.

Magnetic field measurements near 1.0 AU show a consistent skewing of the magnetic field away from the equatorial plane (Coleman and Rosenberg, 1971; Rosenberg and Winge, 1974). Such skewing may be caused by magnetic field diffusion in the interplanetary medium (Schatten, 1972). Stream interactions may contribute to an azimuthal velocity component in the solar wind or to a net divergence of mass and magnetic flux away from the equatorial plane (Suess *et al.*, 1975). The divergence of the magnetic field away from the equator could also be caused by magnetic pressure. The magnetic field spiral angle and, therefore, the magnetic pressure changes with heliocentric latitude. The magnetic pressure is greatest near the equator, causing mass and magnetic flux to be carried away from the equatorial plane (Suess, 1974; Suess and Nerney, 1975). These observations suggest the divergent field line model shown in Figure 5. The magnetic field projected into the ecliptic plane follows an Archimedean spiral, but in the meridian plane the magnetic field lines extend to higher heliocentric latitudes with increasing radial distances.

Coronal photographs and *in situ* measurements of the solar magnetic field each suggest different models of the solar magnetic field. It is the purpose of this paper to test these various solar magnetic field models.

6. Analysis of Events

Twenty type III events were initially chosen from the first 43 orbits of HAWKEYE 1 and from the same time period for IMP 8 (June through August, 1974). Of the initial 20 events only three events were analyzed in detail, while the others were thrown out for various reasons. Some events were multiple events originating from different regions of the Sun. Other events did not have adequate coverage with both satellites and for some events the modulation factor was too low to determine the direction of arrival accurately.

A. DIRECTION OF ARRIVAL ANALYSIS

Figures 6, 7, and 8 show the source locations for the three events that were analyzed as determined by simultaneous direction-finding measurements from

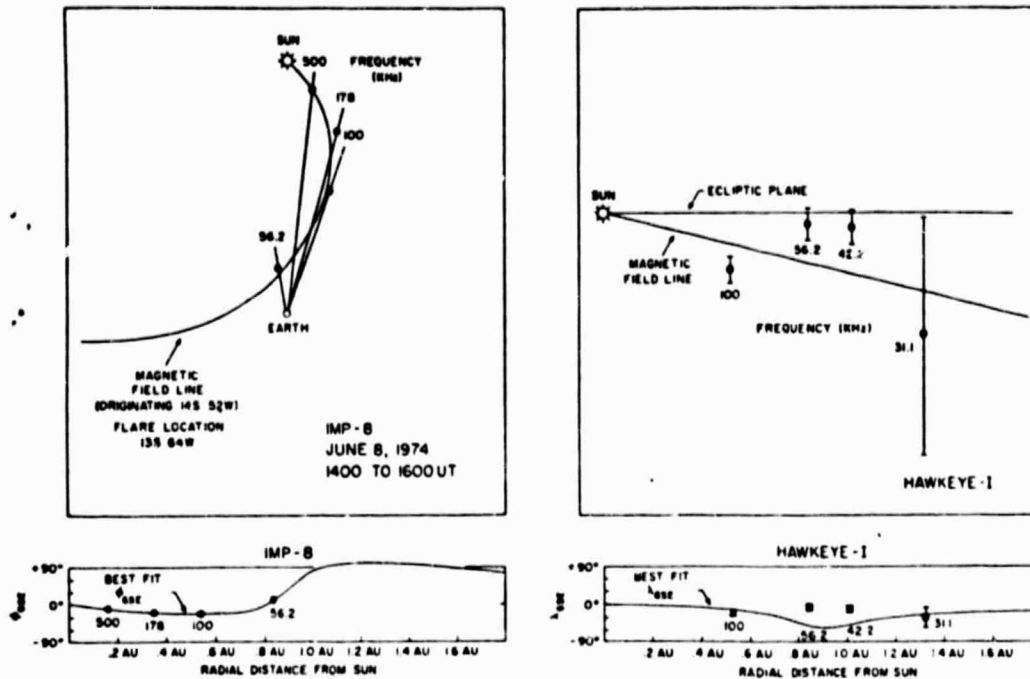


Fig. 6. Source locations for a type III event (June 8). The source locations follow an Archimedean spiral configuration in the ecliptic plane. The source locations out of the ecliptic are shown as a function of heliocentric latitude and radial distance. The bottom panels show the geocentric longitude and latitude of the source predicted by a least squares fit of the constant latitude field line model to the observed geocentric longitudes and latitudes. Note that this event deviates from the constant latitude model at 56.2 kHz and 42.2 kHz implying that the magnetic field lines may extend to lower heliographic latitudes with increasing radial distance. The predicted flare location is found by extrapolating the least squares fit field line back to the Sun.

HAWKEYE 1 and IMP 8 data, the RAE emission level scale, and the assumption of emission at the second harmonic of the plasma frequency. Since the trajectory of the burst in the first event (shown in Figure 6) was near the Earth the RAE emission level scale was adjusted so that the density scale agreed with *in situ* measurements of the solar wind density at 1.0 AU (M. Montgomery, personal communication, 1975). The RAE emission level scale was not adjusted for the last two events (shown in Figures 7 and 8) because the trajectory of the bursts were so far from the Earth that the densities measured by IMP 8 could not be considered representative of the density at 1.0 AU along the trajectories of the bursts.

For each event an Archimedean spiral is fit through the source locations projected into the ecliptic plane. Since HAWKEYE 1's spin plane is not oriented exactly perpendicular to the ecliptic plane it is necessary to know the ϕ_{GSE} coordinate of the source position before λ_{GSE} can be determined. If ϕ_{GSE} could not be determined from the IMP 8 data it was computed from the Archimedean spiral fit

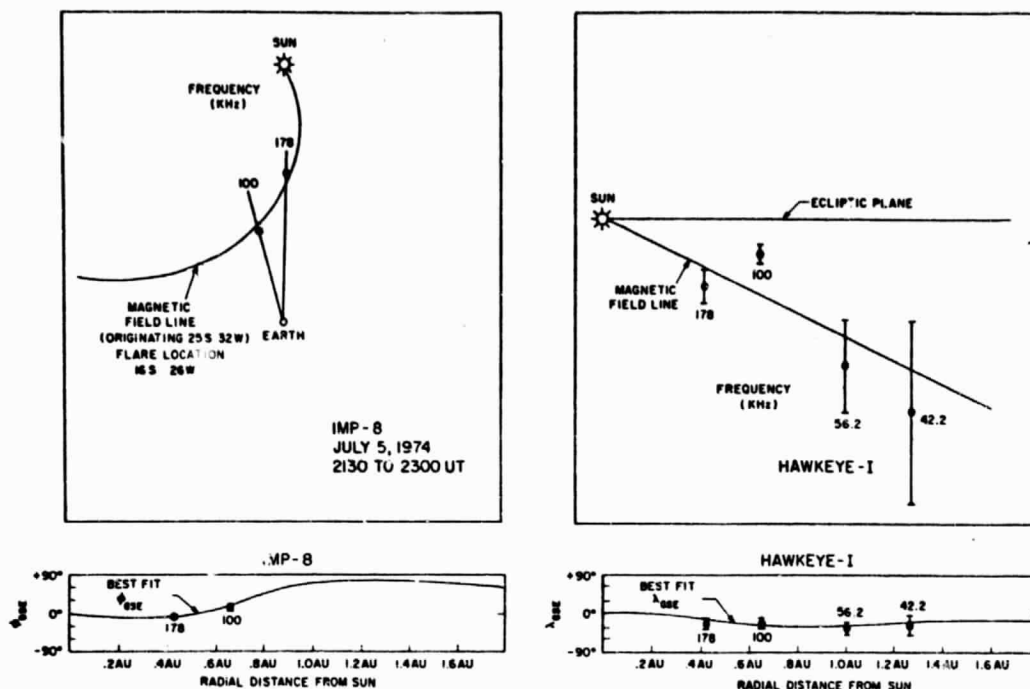


Fig. 7. Direction-finding measurements for another type III event (July 5). Projected into the ecliptic plane the source locations follow an Archimedean spiral configuration. Out of the ecliptic plane the source locations are at nearly constant heliocentric latitudes. Except for the 100 kHz emission the data is consistent with the constant latitude model.

through the available data points. Errors in λ_{GSE} caused by computing ϕ_{GSE} are estimated to be smaller than 3° . The GSE latitudes (λ_{GSE}) and GSE longitudes (ϕ_{GSE}) for the three events are summarized in Table I. Any λ_{GSE} in Table I that required the Archimedean spiral fit to compute ϕ_{GSE} is indicated by an asterisk.

The upper left-hand panel in Figures 6, 7, and 8 shows the source locations projected into the ecliptic plane and the best fit Archimedean spiral through the source locations. A solar wind velocity of 400 km s^{-1} was used to construct the Archimedean spiral. The lower left-hand panel shows the Geocentric Solar Ecliptic longitude (ϕ_{GSE}) of the least squares fit Archimedean spiral as viewed from Earth as a function of heliocentric radial distance. The experimental values of ϕ_{GSE} are also shown. The upper right-hand panel shows the heliocentric latitude of the source location as a function of frequency, and the least squares fit magnetic field line using the constant latitude model. The lower right-hand panel shows the geocentric solar ecliptic latitudes (λ_{GSE}) of the best fit field line as a function of heliocentric radial distance and the observed λ_{GSE} of the source locations.

The most probable flare location for each event is found by extrapolating the magnetic field line obtained from the constant latitude model back to the Sun. For

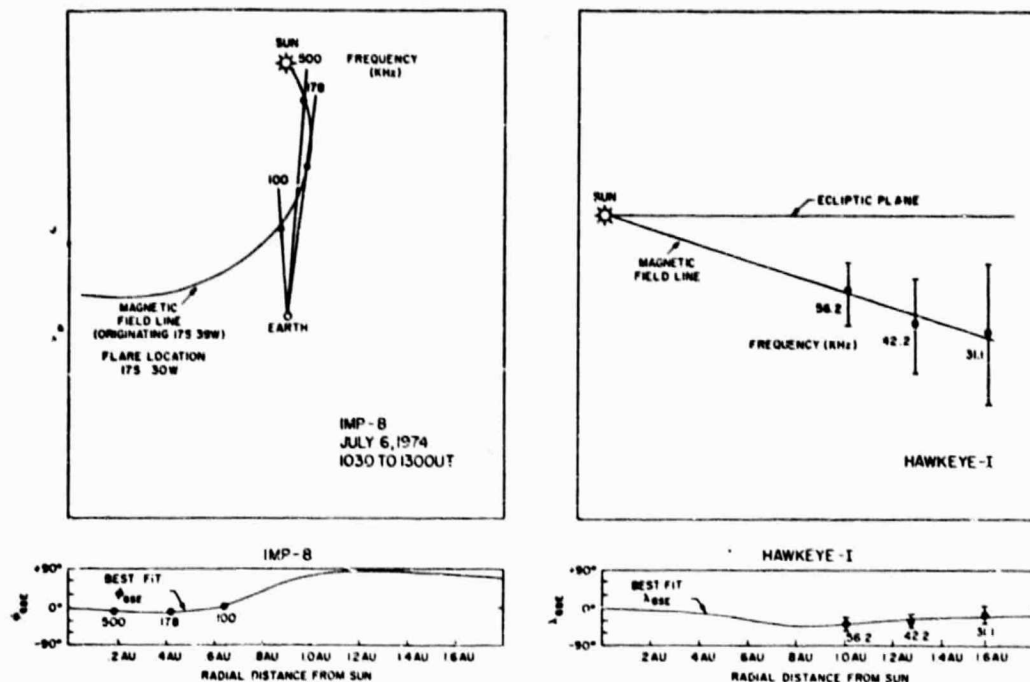


Fig. 8. Direction-finding measurements for the third type III event (July 6). Projected into the ecliptic plane the source regions follow an Archimedean spiral configuration. Out of the ecliptic the source locations are at very nearly constant latitude, which is in excellent agreement with the constant latitude model for the solar magnetic field.

the three events analyzed the differences between the actual flare location (NOAA, 1974, 1975) and the flare location computed from the least squares fit magnetic field line are in all cases less than 9° in heliocentric latitude and less than 12° in the heliocentric longitude. The first event, shown in Figure 6, deviates significantly from the constant latitude model of the magnetic field. The heliocentric latitude of the 100 kHz, 56.2 kHz, and 42.2 kHz source locations suggest that the convergent field line model may best represent this event. The other two events (Figures 7 and 8) are best represented by the constant latitude model.

B. SOURCE SIZE OF TYPE III BURSTS

The modulation factor of the emissions can be used to estimate the source size when the elevation angle, α , of the source is known. For this analysis the half angle source size is defined as the angle between a line from the observer to the centroid of the source and a line from the observer to the edge of the source. The source is modeled as a thin, flat disk from which radiation is emitted with a uniform intensity. For a given source size the solid angle of the disk remains constant for all elevation angles, α . The calculated source sizes represent the longitudinal extent of the source.

TABLE I
Latitude and longitude of type III radio bursts
(geocentric solar ecliptic coordinates)

Frequency	Latitude	Longitude
June 8, 1974		
500 kHz	—	$-7^\circ \pm 1^\circ$
178 kHz	—	$-16^\circ \pm 1^\circ$
100 kHz	$-24^\circ \pm 6^\circ$	$-20^\circ \pm 1^\circ$
56.2 kHz	$-11^\circ \pm 7^\circ$	$9^\circ \pm 1^\circ$
42.2 kHz	$-10^\circ \pm 9^\circ$ ^a	—
31.1 kHz	$-32^\circ \pm 32^\circ$ ^a	—
July 5, 1974		
178 kHz	$-21^\circ \pm 7^\circ$	$-2^\circ \pm 1^\circ$
100 kHz	$-20^\circ \pm 2^\circ$	$15^\circ \pm 6^\circ$
56.2 kHz	$-30^\circ \pm 16^\circ$ ^a	—
42.2 kHz	$-32^\circ \pm 25^\circ$ ^a	—
July 6, 1974		
500 kHz	—	$-5^\circ \pm 1^\circ$
178 kHz	—	$-8^\circ \pm 1^\circ$
100 kHz	—	$4^\circ \pm 1^\circ$
56.2 kHz	$-31^\circ \pm 8^\circ$ ^a	—
42.2 kHz	$-25^\circ \pm 15^\circ$ ^a	—
31.1 kHz	$-11^\circ \pm 15^\circ$ ^a	—

^a Involves model fitting, not a direct measurement.

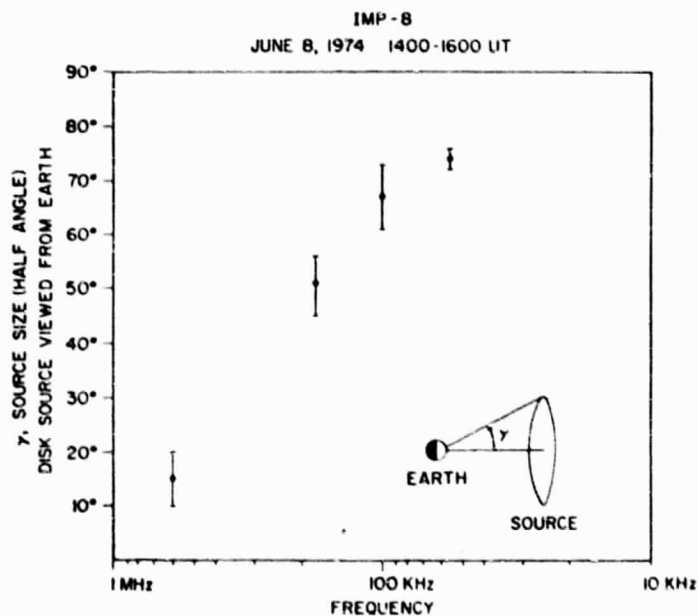


Fig. 9. The source size of a type III burst as a function of frequency as seen from the Earth using a thin, flat disk as the modeled source. As the source region approaches the earth the source size increases, as would be expected.

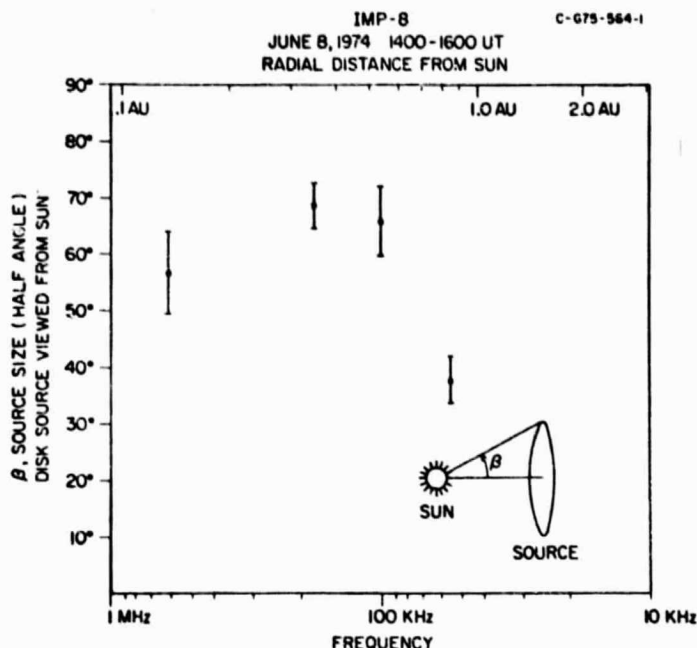


Fig. 10. Source sizes as a function of frequency for the same event as in Figure 9 viewed from the Sun. Note that the source size remains essentially constant in the range from 500 to 100 kHz. The source sizes are, however, larger than those previously determined from particle measurements.

Figure 9 shows the source sizes of the June 8 event as viewed from the Earth. As would be expected, the source size increases as the emission region nears the Earth. Figure 10 shows the source sizes for the same event, but, as viewed from the Sun. The source sizes at 500 kHz, 178 kHz and 100 kHz remain relatively constant with increasing radial distance; however, they are approximately twice as large as the 60° full-width-half-maximum values that Lin (1974) and Alvarez *et al.* (1975) report for particle fluxes associated with type III events. Scattering of the radio emissions may be responsible for the large apparent source sizes.

7. Discussion

Two of the three type III events presented in this paper are in agreement with the constant latitude model of the solar magnetic field. One event (June 8) is more consistent with the convergent field line model. However, the convergent field line model contradicts some measurements of the skewing of the magnetic field away from the equatorial plane which have been made at 1.0 AU (Coleman and Rosenberg, 1971; Rosenberg and Winge, 1974). None of the events presented indicates that the magnetic field lines cross the ecliptic plane or that the divergent field line model is valid. Additional evidence supporting the constant latitude model is that the predicted flare locations are in good agreement with the observed flare locations.

Three features of type III bursts presented in this study are of special interest. The source sizes measured are a factor of two larger than the angular sizes of the solar electron emissions from a flare reported by Lin (1974) and Alvarez *et al.* (1975). The modulation factor tends to be largest near the beginning of an event, and the direction of arrival of the radiation varies systematically during the event, usually starting near the Sun and deviating away from the Sun later in the event.

One possible explanation of all three features is a combination of emission at both the fundamental and the second harmonic of the plasma frequency. If a stream of particles generating a type III burst moves outward from the Sun and generates emission at both the fundamental and second harmonic of the plasma frequency the fundamental emission would be seen first in a particular frequency channel, followed by the second harmonic emission. The shift in the direction of arrival of the radiation could be explained by emission containing both fundamental and second harmonic radiation. The fundamental emission region would be closer to the Sun than the second harmonic emission region; therefore, for most Archimedean spiral positions the direction of the source would start near the Sun and drift away from the Sun in a systematic way, as is observed in many cases. A larger angle shift would be seen in the lower frequency channels because the source locations are closer to the earth. The source size would be smaller for fundamental emission because the size of the source region grows larger with increasing radial distance from the Sun, and the source region for fundamental emission is usually farther from the Earth than the second harmonic source region; explaining the higher observed modulation factor near the start of the event. With simultaneous emission of both fundamental and second harmonic radiation the apparent source sizes would be much larger than the individual source sizes for fundamental and second harmonic emission.

There are other possible explanations for the systematic drifts in source location and variations in the modulation factor which should also be considered. Irregularities in the solar wind density could cause different regions to radiate at the same frequency at different times thus causing the observed changes in the angular position of the source. If the radiation is not circularly or randomly polarized, changes in the polarization could affect the direction-finding measurements and produce effects of this type. However, polarization effects are least important in the direction-finding analysis when the source location is near the spin plane of the antenna. For the IMP 8 measurements the source is usually very near the spin plane, which minimizes errors of this type.

Although irregularities in the solar wind density or polarization effects may cause the systematic drift in the direction of arrival of radiation from a type III event at one frequency, there is currently no completely adequate explanation of the drift in source position. Although the changes in the direction of arrival could be caused by a combination of fundamental and second harmonic emission there is still no direct evidence that emission occurs at both frequencies. The effects of changes in the source position are thought to be reduced in this study since the

source locations are averaged over the duration of the event. However, the explanation of the drift may provide important insight into the type III emission processes in the solar wind and should be studied in detail.

The results of the analysis presented in this paper are model dependent. It is necessary to use a density scale to determine the heliocentric radial distance at which the radiation is generated. The requirement to assume a density model can be eliminated if the source position is determined by triangulation. For example, simultaneous direction-finding measurements from three spacecraft, two located near the Earth to establish the Earth-source line and one located far from the Earth to determine the source position along the line, can provide measurements of this type. We hope that simultaneous radio direction-finding measurements from the HELIOS 1 and 2 spacecraft, which are now in orbit around the Sun, and from the IMP 8 and HAWKEYE 1 satellites near the earth will be able to provide such measurements. If successful, these multi-spacecraft direction-finding measurements will make it possible to study the three-dimensional structure of the magnetic field in the solar wind completely independent of any modeling assumptions.

Acknowledgements

The authors thank Dr M. Montgomery for providing the solar wind density measurements from IMP 8. The authors wish to express their gratitude to Drs C. K. Goertz and R. R. Shaw for their invaluable comments on this paper.

This work was supported in part by the National Aeronautics and Space Administration under Contracts NAS1-13129 and NAS5-11431 and Grant NGL-16-001-043 and by the Office of Naval Research.

References

- Alexander, J. K., Malitson, H. H., and Stone, R. G.: 1969, *Solar Phys.* **8**, 388.
- Alvarez, H., Haddock, F. T., and Lin, R. P.: 1972, *Solar Phys.* **26**, 468.
- Alvarez, H., Lin, R. P., and Bame, S. J.: 1975, *Solar Phys.* **44**, 485.
- Coleman, P. J., Jr. and Rosenberg, R. L.: 1971, *J. Geophys. Res.* **76**, 2917.
- Fainberg, J., Evans, L. G., and Stone, R. G.: 1972, *Science* **178**, 743.
- Fainberg, J. and Stone, R. G.: 1970, *Solar Phys.* **15**, 433.
- Fainberg, J. and Stone, R. G.: 1971, *Solar Phys.* **17**, 392.
- Fainberg, J. and Stone, R. G.: 1974, *Space Sci. Rev.* **16**, 145.
- Frank, L. A. and Gurnett, D. A.: 1972, *Solar Phys.* **27**, 446.
- Ginzburg, V. L. and Zhelezniakov, V. V.: 1958, *Sov. Astron.-AJ* **2**, 653.
- Gurnett, D. A. and Frank, L. A.: 1975, *Solar Phys.* **45**, 477.
- Haddock, F. T. and Alvarez, H.: 1973, *Solar Phys.* **29**, 183.
- Haddock, F. T. and Graedel, T. E.: 1970, *Astrophys. J.* **160**, 293.
- Hartz, T. R.: 1964, *Ann. Astrophys.* **27**, 831.
- Hartz, T. R.: 1969, *Planet. Space Sci.* **17**, 267.
- Kaiser, M. L.: 1975, *The Solar Elongation Distribution of Low Frequency Radio Bursts*, Goddard Space Flight Center preprint X-693-75-99.
- Kundu, M. R.: 1965, *Solar Radio Astronomy*, Interscience, New York.

- Lin, R. P.: 1970, *Solar Phys.* **12**, 266.
- Lin, R. P.: 1974, *Space Sci. Rev.* **16**, 189.
- Lin, R. P., Evans, L. G., and Fainberg, J.: 1973, *Astrophys. Lett.* **14**, 191.
- Newkirk, G., Jr.: 1967, *Ann. Rev. Astron. Astrophys.* **5**, 213.
- NOAA: December 1974, *Solar-Geophysical Data* **364**, Part II.
- NOAA: January 1975, *Solar-Geophysical Data* **365**, Part II.
- Parker, E. N.: 1963, *Interplanetary Dynamical Processes*, Interscience, New York.
- Parker, E. N.: 1964, 'The penetration of Galactic Cosmic Rays into the Solar System', in *The Solar Wind*, Pergamon Press, Oxford.
- Parker, E. N.: 1965, *Space Sci. Rev.* **4**, 666.
- Rosenberg, R. L. and Winge, C. R., Jr.: 1974, 'The Latitude Dependencies of the Solar Wind', *Solar Wind Three*, Institute of Geophysics and Planetary Physics, UCLA, 300.
- Schatten, K. H.: 1972, 'Large-scale properties of the interplanetary Magnetic Field', *Solar Wind*, NASA publication SP-308, 65.
- Schatten, K. H., Ness, N. F., and Wilcox, J. M.: 1968, *Solar Phys.* **5**, 240.
- Slysh, V. I.: 1967, *Cosmic Research* (English transl.) **5**, 759.
- Smith, D. F.: 1970, *Adv. Astron. Astrophys.* **7**, 147.
- Smith, D. F.: 1974, *Space Sci. Rev.* **16**, 91.
- Stone, R. G.: 1974, 'Traveling Solar Radio Bursts', in *Solar Wind Three*, Institute of Geophys. and Planetary Phys., UCLA, 72.
- Suess, S. T.: 1974, 'Three Dimensional Modeling', in *Solar Wind Three*, Institute of Geophys. and Planetary Phys., UCLA, 311.
- Suess, S. T., Hundhausen, A. F., and Pizzo, V.: 1975, *J. Geophys. Res.* **80**, 2023.
- Suess, S. T. and Nerney, S. F.: 1975, *Geophys. Res. Lett.* **2**, 75.
- Van Allen, J. A. and Krimigis, S. M.: 1965, *J. Geophys. Res.* **70**, 5737.
- Wild, J. P.: 1950, *Aust. J. Sci. Res.* **A3**, 541.
- Wild, J. P. and McCready, L. L.: 1950, *Aust. J. Sci. Res.* **A3**, 387.
- Wild, J. P., Murray, J. D., and Rowe, W. C.: 1954, *Aust. J. Phys.* **7**, 439.
- Wild, J. P., Sheridan, K. V., and Neylan, A. A.: 1959, *Aust. J. Phys.* **12**, 369.

THE EARTH AS A RADIO SOURCE

DONALD A. GURNETT*

*Max-Planck-Institut für Physik und Astrophysik, Institut für extraterrestrische Physik,
8046 Garching b. München, Germany*

Abstract. Satellite low frequency radio measurements have revealed that the Earth is a very intense and interesting radio source with characteristics similar to other astronomical radio sources such as Jupiter, Saturn and the Sun. In this paper we summarize the primary characteristics of radio emissions from the Earth's magnetosphere, consider the origin of these emissions, and discuss the similarities to other astronomical radio sources.

1. Introduction

The Earth is usually not thought of as an intense radio source. However, in the past few years low frequency radio measurements by satellites have revealed that the Earth's magnetosphere is a very intense radio emitter, with characteristics similar to other astronomical radio sources such as Jupiter, Saturn and the Sun. In this paper we consider only radio emissions which can propagate freely away from the Earth at frequencies above the local electron plasma frequency. We do not discuss the many other types of whistler-mode waves and plasma instabilities which are present at frequencies below the electron plasma frequency.

The first clear evidence of intense radio emissions from the Earth's magnetosphere was obtained from satellite measurements by Benediktov *et al.* (1965, 1968) in which radio emissions at 725 kHz and 2.3 MHz were detected in association with geomagnetic storms. Later Duncel *et al.* (1970) reported similar observations of intense radio emissions, also associated with magnetic disturbances, at frequencies below 100 kHz. Only recently, however, with radio and plasma wave instruments on the IMP-6 and IMP-8 satellites, have measurements been made over a sufficiently broad frequency range and with adequate sensitivity, dynamic range and directional resolution to provide a comprehensive picture of radio emissions from the terrestrial magnetosphere (Stone, 1973; Brown, 1973; Frankel, 1973; Gurnett, 1974, 1975).

As currently understood two principal types of radio emissions can be identified coming from the terrestrial magnetosphere. We refer to these radio emissions as auroral kilometric radiation and continuum radiation. The characteristic spectrums of these two types of radio emissions are illustrated in Fig. 1. In addition to these two principal types of radiation several other types of radio emissions of lower intensity and/or infrequent occurrence are known to occur which have not yet been studied in much detail. The purpose of this paper is to summarize the present state of knowledge concerning these radio emissions and discuss their origin and relationship to other astronomical radio sources.

* Permanent address: The Department of Physics and Astronomy, The University of Iowa, Iowa City, Iowa 52242, U.S.A.

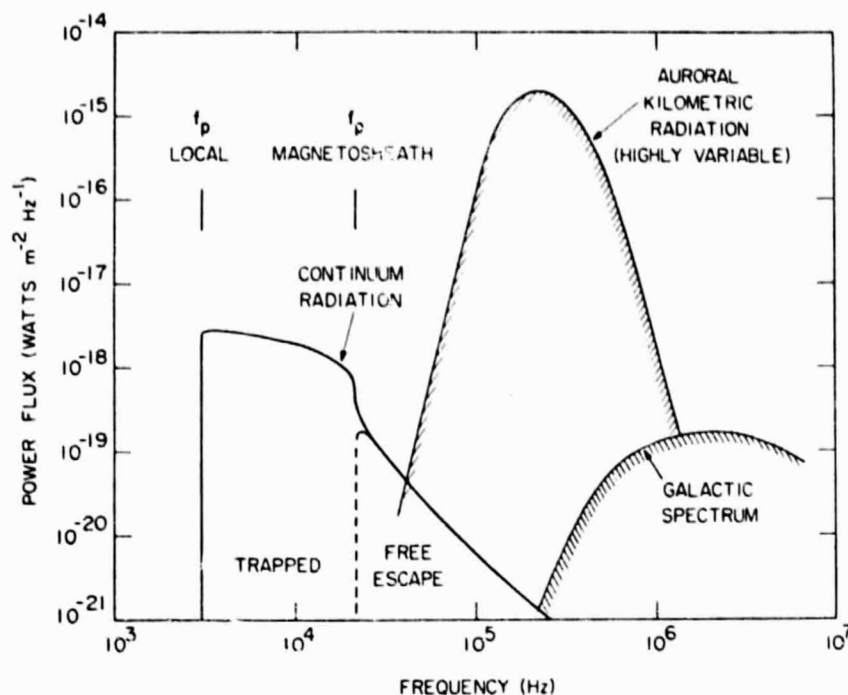


Fig. 1. The spectrums of the galactic background, the auroral kilometric radiation and the non-thermal continuum radiation as would be observed by a satellite $30 R_E$ from the Earth.

2. Auroral Kilometric Radiation

As shown in Figure 1 auroral kilometric radiation is characterized by a very intense peak in the frequency spectrum at about 100 to 300 kHz. The intensity of this radiation is highly variable. Sometimes the radiation intensity is below the galactic background and completely undetectable, while at other times the intensity is six to seven orders of magnitude above the galactic background at $30 R_E$ from the Earth. At peak intensity the total power radiated by the Earth exceeds 10^9 W (Gurnett, 1974). The Earth is therefore a very intense planetary radio source with a total power output comparable to the decametric radio emission from Jupiter. For comparison the total power of the decametric radiation from Jupiter has been estimated by Warwick (1963) to be about 2×10^7 W. More recent measurements indicate, however, that the power radiated by Jupiter may be somewhat larger than given by Warwick.

Auroral kilometric radiation has been previously called 'high-pass' noise by Dunkel *et al.* (1970) and 'midfrequency' noise by Brown (1973). Because of the close association of this radiation with the occurrence of auroral arcs (Gurnett, 1974) and the kilometer wavelength of the radiation we chose to refer to the radiation as auroral kilometric radiation. The close association of this radiation with the occurrence of auroral arcs is

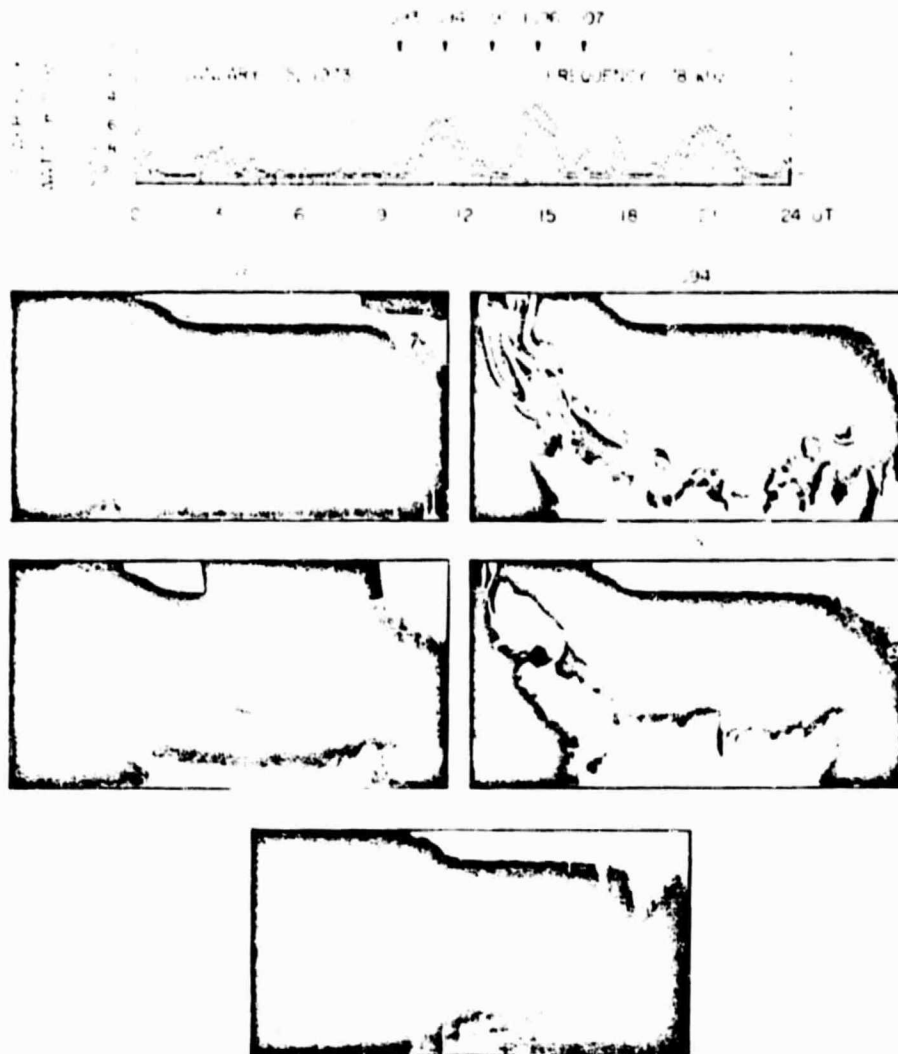


Fig. 2. The intensity of auroral kilometric radiation at 178 kHz and a sequence of photographs of the aurora over the northern polar region taken by the DAPP satellite. The intense bursts of auroral kilometric radiation are seen to be closely correlated with the occurrence of auroral arcs.

illustrated in Figure 2. The top panel of this illustration shows the radio noise intensity at 178 kHz for a 24 h period while the spacecraft (IMP-6) is about $30 R_E$ from the Earth. The bottom panels show a series of auroral photographs obtained during the same 24 h period by the low altitude polar-orbiting DAPP spacecraft as it passes over the northern polar region. Three intense bursts of auroral kilometric radiation occurred during this day, centred on approximately 1120, 1450, and 2100 UT. Each intense burst of auroral kilometric radiation is seen to be closely associated with the occurrence of bright discrete

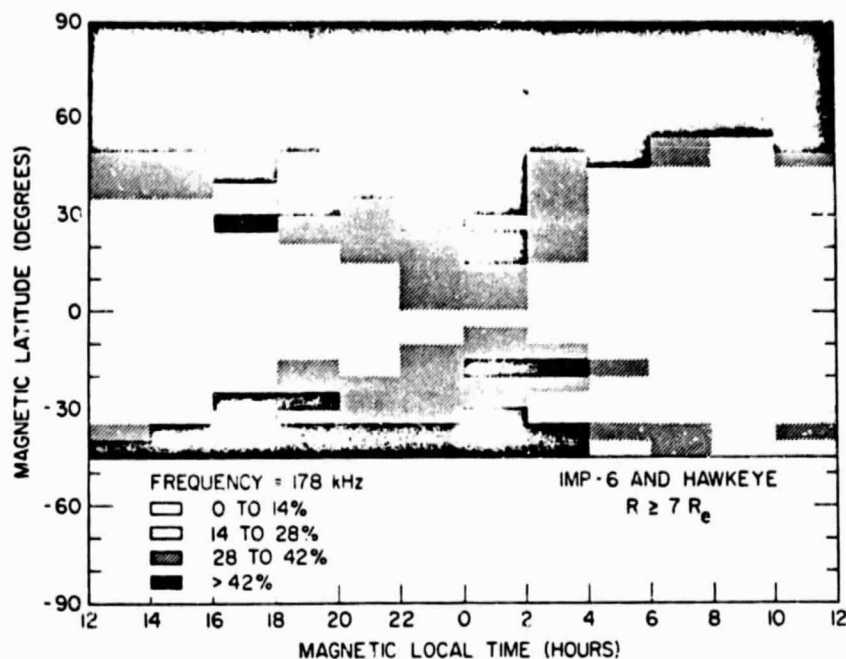


Fig. 3. The angular distribution of auroral kilometric radiation in magnetic coordinates.

auroral arcs in the DAPP photographs (one photograph for each orbit). Direction-finding measurements by Kurth and Gurnett (1975) show that the apparent center of the source of the auroral kilometric radiation is in the nighttime auroral region at a distance of about $0.75 R_E$ from the polar axis of the Earth. The association of this radiation with auroral arcs and the location of the source in the high latitude auroral regions strongly suggest that this radiation is produced by the same low energy electrons which produce the auroral light emissions. The association of the radio emissions with discrete auroral arcs rather than the diffuse aurora specifically implies that the noise is associated with intense 'inverted V' electron precipitation bands of the type discussed by Frank and Ackerson (1971) and Ackerson and Frank (1972).

Further information on the generation and propagation of the auroral kilometric radiation can be provided by measurements of the angular distribution of the radiation escaping from the Earth. Figure 3 shows the angular distribution of auroral kilometric radiation at a frequency of 178 kHz as obtained from the IMP-6 and Hawkeye-1 satellites. IMP-6 provides measurements at magnetic latitudes below 55° and Hawkeye-1 provides measurements over the northern polar region. The contours in Figure 3 give the frequency of occurrence of events with a power flux exceeding a preset threshold which varies as R^{-2} to correct for the expected radial variation in the power flux. These measurements show that most of the radiation is observed poleward of a cone-shaped boundary which extends from latitudes near the magnetic equator in the local evening to

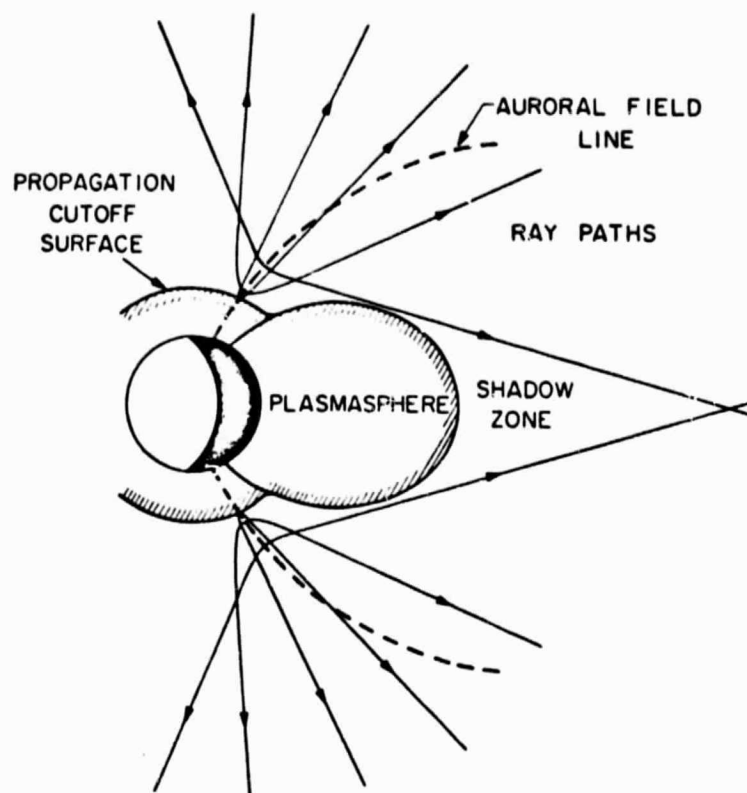


Fig. 4. A qualitative sketch of the ray paths and source region of auroral kilometric radiation. Note the distinct equatorial shadow zone caused by the plasmasphere.

latitudes of approximately 50° on the dayside of the Earth. Further studies (Green *et al.*, 1976) show that this cone-shaped boundary is frequency-dependent and rapidly shrinks poleward with decreasing frequency. This 'beaming' of the radiation is thought to be caused by the refraction of the radiation away from the ionosphere as illustrated in Figure 4. Since the index of refraction goes to zero at the propagation cutoff surface, which for these frequencies must occur at an altitude of about 1 to $1.5 R_E$ at 178 kHz, the ray path tends to be refracted upward away from the ionosphere. The frequency dependence of the cone-shaped boundary is qualitatively consistent with an essentially fixed source altitude at all frequencies, with the cone angle determined by the (frequency dependent) altitude of the propagation cutoff surface. A cone-shaped boundary, similar to that found for the auroral kilometric radiation, is observed for the Io related radio bursts from Jupiter and a similar beaming effect is a well known feature of radio emissions from pulsars.

Probably the most difficult feature of the auroral kilometric radiation which must be explained by any satisfactory theory is the very high efficiency with which this radiation

is produced. The maximum power dissipated by the aurora during an auroral substorm is about 10^{11} W (Akasofu, 1968). If the corresponding maximum power of the auroral kilometric radiation is 10^9 W, then the efficiency for generating this radiation must be at least 1%. From all present knowledge of magnetospheric radio emissions the generation of auroral kilometric radiation represents a very efficient conversion of charged-particle energy into radio waves. Interestingly, this efficiency is comparable to the efficiency by which a pulsar converts its rotational energy into radio emissions. Such high efficiencies cannot be obtained from an incoherent process, but must result from a coherent plasma instability. The location of the source, at an altitude of about 1 to $1.5 R_E$ along an auroral field line, coincides with the region where the auroral electron acceleration, anomalous resistivity and parallel electric fields are thought to occur (Mozer, 1976). Another type of intense whistler-mode radio emission called VLF auroral hiss is also thought to be generated in this same region (Gurnett and Frank, 1972).

Several theories have been developed which attempt to explain the principal features of the auroral kilometric radiation (Benson, 1975; Palmadesso *et al.*, 1976; Melrose, 1976). Most of these theories rely on the intermediate generation of electrostatic waves and the subsequent coupling of these waves to electromagnetic radiation to explain the observed intensities. At the present time no electric field measurements have been made in the source region which can confirm the existence of these electrostatic waves. Also, the polarization, which is a basic parameter that could help discriminate between the various theories, has not yet been determined.

5. Continuum Radiation

Brown (1973), using radio measurements from the IMP-6 satellite, has identified a weak continuum radiation coming from the Earth's magnetosphere in the frequency range from about 30 to 110 kHz. The intensity of this continuum decreases rapidly with increasing frequency, varying approximately as $f^{-2.8}$ (f is frequency). At about the same time Gurnett and Shaw (1973) identified another somewhat more intense continuum at even lower frequencies, from about 5 to 20 kHz. This radiation occurs at frequencies below the solar wind plasma frequency and is permanently trapped within the low density regions of the magnetospheric cavity. It now appears that these two types of radiation are simply different portions of a single non-thermal continuum spectrum which extends from frequencies as low as 500 Hz to greater than 100 kHz (Gurnett, 1975). This radiation, as implied by the term continuum, has a smooth monotonic frequency spectrum and a nearly constant intensity, seldom varying by more than 10 to 20 dB.

To illustrate the general features of the continuum radiation spectrum, Figure 5 shows five spectra obtained from IMP-8 at various local times around the Earth and at a nearly constant radial distance of from 28.2 to $40.4 R_E$. Four of these spectra were obtained in the solar wind and one (the center panel) was obtained in the low density region of the distant magnetotail. The spectra in the solar wind all show the same basic characteristics, consisting of a monotonically decreasing intensity with increasing frequency and a sharp cutoff near the solar wind plasma frequency at about 20 to 30 kHz.

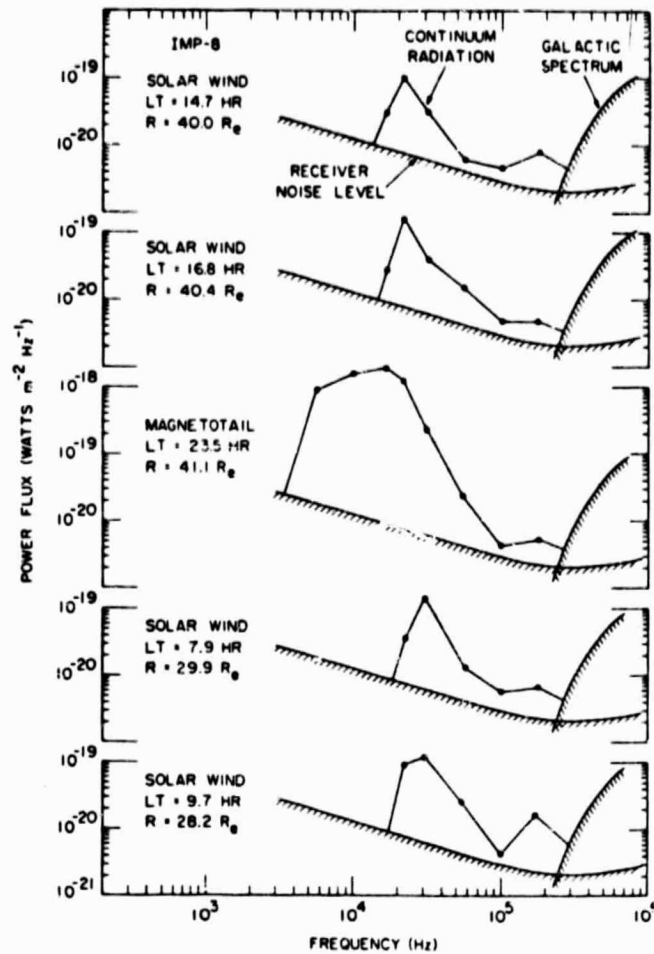


Fig. 5. Selected spectrum of continuum radiation observed by IMP-8 at various local times. The sharp cutoff in the solar wind spectra occur near the solar wind plasma frequency.

The low frequency cutoff is almost certainly caused by the propagation cutoff at the solar wind plasma frequency. The spectrum in the magnetotail, however, extends down to frequencies well below the solar wind plasma frequency. The continuity of the magnetotail spectrum with the spectra in the solar wind indicate that the radiation observed in both regions comes from the same source and that the spectrum observed in the solar wind represents that portion of the radiation which can escape into the solar wind above either the magnetosheath or solar wind plasma frequency, whichever is greater. The continuum radiation spectrum can therefore be divided into a trapped component and a freely escaping component as shown in Figure 1. At frequencies above the magnetosheath plasma frequency radiation from near the Earth can propagate directly to a distant

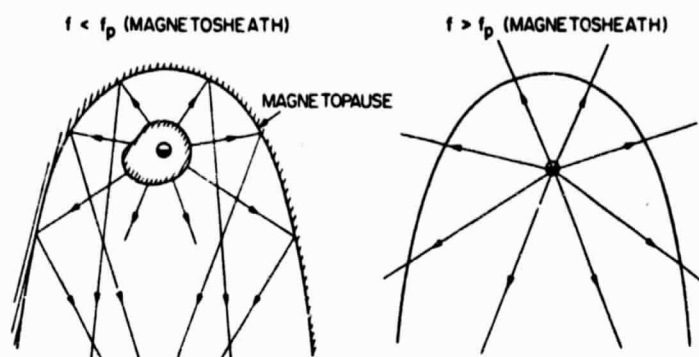


Fig. 6. A qualitative sketch of the ray paths from a source near the Earth at frequencies above and below the plasma frequency in the magnetosheath.

observer, whereas at frequencies below the magnetosheath plasma frequency the radiation is reflected into, and trapped in, the distant magnetotail as shown in Figure 6. Direction finding measurements (Gurnett, 1975) clearly show the transition from the free escape to the trapped regions and detailed ray path calculations exhibiting these effects have been performed by Jones and Grard (1975). Because the magnetosheath plasma frequency is largest near the nose of the magnetospheric cavity and decreases to approximately the solar wind value in the downstream region, the transition from the free escape to the trapped regions is not abrupt. Evidence showing the scattering of the escaping continuum radiation as it passes through the magnetosheath has been presented by Vesecky and Frankel (1975). Since only a slight, factor of 2, increase in the intensity occurs as the frequency varies from the free escape to the trapped region it can be concluded that the Q of the magnetospheric cavity is very low for this trapped radiation. Evidently a substantial portion of the radiation is reabsorbed in the distant downstream tail region.

Because of the complicated reflections which take place at frequencies below the magnetosheath plasma frequency it is nearly impossible to make a reliable determination of the source region from measurements of the trapped component. At frequencies well above the magnetosheath plasma frequency the source position can be determined directly from direction finding measurements. Gurnett (1975) using direction-finding measurements from the IMP-8 spacecraft has shown that the apparent center of the continuum radiation source is located on the morning side of the Earth at a radial distance, projected into the ecliptic plane, of about 2 to $3R_E$ from the center of the Earth. From studies of individual passes it is also evident that the radiation extends all the way to the propagation cutoff at the plasmapause, even near the equatorial plane, with no evidence of an equatorial shadow zone as observed for the auroral kilometric radiation (see Figure 4). It is therefore concluded that at least some of the continuum radiation is generated near the equatorial plane and that this radiation is not a high latitude auroral zone emission. On the basis of these data a qualitative model of the

ORIGINAL PAGE IS
OF POOR QUALITY

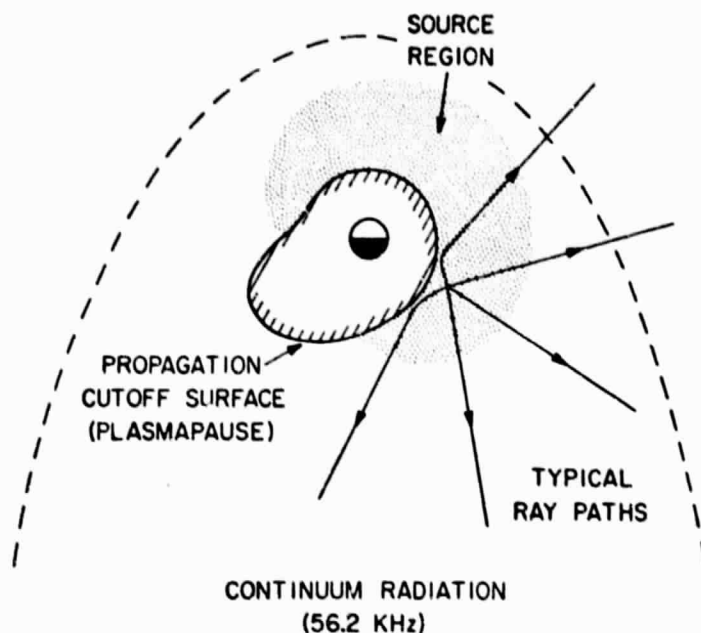


Fig. 7. A qualitative sketch of the source region of the continuum radiation as indicated by the direction-finding measurements in Figure 7.

source region of the continuum radiation is shown in Figure 7. This model is for a frequency of 56.2 kHz. At lower frequencies the propagation cutoff surface must extend to progressively larger radial distances into the outer magnetosphere.

At the present time the only comprehensive theory which attempts to explain the origin of the continuum radiation is by Frankel (1973), who proposed that the radiation is caused by gyro-synchrotron radiation from mildly relativistic, $E \approx 100$ to 500 keV, electrons injected into the outer radiation zone during magnetic storms. In many respects the observed characteristics are in reasonably good agreement with Frankel's calculations. The frequency spectrum of the escaping continuum radiation, the radial location of the source, and the local time asymmetry are all in tolerable agreement with the gyro-synchrotron model. However, the gyro-synchrotron model also has several difficulties which remain to be explained. First, the power flux calculated from the gyro-synchrotron model is about a factor of 5 to 15 too small. Second, although the gyro-synchrotron model does account for the high frequency, ~ 100 kHz, portion of the spectrum which is generated deep within the magnetosphere at $L \sim 3$, it is difficult to see how this mechanism can account for the much more intense low frequency, ~ 10 kHz, portion of the spectrum which must be generated far out in the magnetosphere at $L > 6$, where the energetic electron intensities are much lower. Third, as shown by an event recently analyzed by Gurnett and Frank (1976), the continuum radiation is closely correlated with the injection of electrons with energies of 1 keV to 10 keV into the magnetosphere.

These energies are much too small to produce significant levels of gyro-synchrotron radiation. Also, in a related observation by Gurnett and Frank the intensity of the continuum radiation is observed to increase within an hour following the onset of a magnetic storm, much too quick to be accounted for by variations of the energetic, ~ 500 keV, electron intensities, which usually do not increase until several days after the onset of a magnetic storm (Owens and Frank, 1968).

3. Other Magnetospheric Radio Emissions

Several other types of magnetospheric radio emissions are known to occur at frequencies above the local plasma frequency, but which have not yet been studied in as much detail as the auroral kilometric radiation and continuum radiation. The characteristics of these radio emissions are summarized below.

3.1. DAYSIDE KILOMETRIC RADIATION

Kaiser and Stone (1975) have reported a weak quasi-continuous radiation with a sharply defined peak in the spectrum at about 200 kHz which is thought to be generated at high latitudes on the dayside of the Earth. The distinct peak at 178 kHz in the selected continuum radiation spectrums of Figure 5 is probably from this source. Because of the similarity in the shape of the spectrum to the nightside auroral kilometric radiation it is thought that this dayside radiation may be basically of the same origin as the nightside auroral kilometric radiation except that it is produced by the much less energetic, ~ 100 eV, polar cusp electrons.

3.2. RADIATION FROM UPSTREAM OF THE BOW SHOCK

From direction finding measurements with IMP-8 it is virtually certain that some radiation is detected from the region near the bow shock (Gurnett, 1975). At least one component of this radiation appears to be a narrow band emission, first detected by Dunkel (1973), at the harmonic, $2f_p$, of the solar wind plasma frequency. Radiation is also sometimes observed at the fundamental, f_p .

The radiation at $2f_p$ is thought to be generated by non-linear interactions of the electron plasma oscillations upstream of the bow shock (Scarf *et al.*, 1971) which are generated by electrons from the bow shock. Although this radiation is very weak it is of considerable interest because of the possible similarity to the generation of type II and type III solar radio bursts by electron plasma oscillations (Ginzburg and Zheleznyakov, 1958).

3.3. DISCRETE BURSTS

Very narrow bandwidth radio bursts, with bandwidths of less than 100 Hz and durations from a few tenths of a second to several seconds, are sometimes observed at frequencies above the local plasma frequency (Gurnett and Shaw, 1973). The center frequency of a given burst tends to decrease rapidly after the onset of the burst, similar to the so-called 'S bursts' from Jupiter at frequencies in the 10 MHz range (Warwick, 1967). The

occurrence of narrowband emissions of this type is clear evidence of a resonant plasma instability operative at frequencies above the local plasma frequency, possibly comparable to the resonant whistler-mode instability which produces chorus and other discrete VLF emissions.

4. Discussion

It is evident that the Earth's magnetosphere produces a variety of complex and very interesting radio emissions at frequencies above the local plasma frequency. Since these waves can escape from the Earth's magnetosphere these radio emissions can be expected to have close similarities to radio emissions produced by other astronomical radio sources. Already certain close similarities are evident. The auroral kilometric radiation has features very similar to the Io-related decametric radiation from Jupiter and the recently discovered decametric radiation from Saturn (Brown, 1975). The radiation at f_p and $2f_p$ upstream of the bow shock appears to be generated by the same mechanism as type II and type III solar radio bursts. The beaming of the auroral kilometric radiation into a cone-shaped region over the polar cap has some similarity to the angular distribution of radiation from Io and to the beaming of radio emissions from pulsars.

At the present time the mechanisms by which most of these radio emissions are generated are rather poorly understood and the proper explanation of these radio emissions represents a significant challenge to the theorists. It should however be possible to arrive at a reasonably clear understanding of how these radio emissions are generated since a great deal is known about the charged particle distributions and processes which occur in the Earth's magnetosphere. Because a comparable detailed knowledge of the charge particle distribution will probably never be known for most other radio sources in the universe the study of these terrestrial radio emissions provides a unique opportunity to extend our understanding of radio emissions from other planets and astronomical objects.

Acknowledgments

The research at the University of Iowa was supported in part by the National Aeronautics and Space Administration under contracts NAS1-11257, NAS5-11074, NAS1-13129, and NAS5-11431 and grant NGL-16-001-043 and by the Office of Naval Research.

The research at the Max-Planck-Institut für extraterrestrische Physik was supported by the Alexander von Humboldt Foundation.

References

- Ackerson, K.L. and Frank, L.A.: 1972, *J. Geophys. Res.* 77, 1128.
Akasofu, S.-I.: 1968, *Polar and Magnetospheric Substorms*, p. 223.
Benediktov, E.A., Getmantsev, G.G., Sazonov, Yu.A., and Tarasov, A.F.: 1965, *Kosm. Issled.* 3, 614.
Benediktov, E.A., Getmantsev, G.G., Mityakov, N.A., Rapoport, V.O., and Tarasov, A.F.: 1968, *Kosm. Issled.* 6, 946.

- Benson, R.F.: 1975, *J. Geophys. Res. Letters* 2, 52.
Brown, L.W.: 1973, *Astrophys. J.* 180, 359.
Brown, L.W.: 1975, *Astrophys. J.* 198, 189.
Dunckel, N.: 1973, *EOS Trans. AGU* 54, 442.
Dunckel, N.B., Ficklin, B., Rorden, L., and Helliwell, R.A.: 1970, *J. Geophys. Res.* 75, 1854.
Frank, L.A. and Ackerson, K.L.: 1971, *J. Geophys. Res.* 76, 3612.
Frankel, M.S.: 1973, *Radio Sci.* 8, 991.
Ginzburg, V.L. and Zheleznyakov, V.V.: 1958, *Sov. Astron.* 2, 653.
Green, J.: 1976, (submitted for publication), *J. Geophys. Res.*
Gurnett, D.A.: 1974, *J. Geophys. Res.* 79, 4227.
Gurnett, D.A.: 1975, *J. Geophys. Res.* 80, 2751.
Gurnett, D.A., and Frank, L.A.: 1972, *J. Geophys. Res.* 77, 172.
Gurnett, D.A. and Frank, L.A.: 1976, *J. Geophys. Res.*, in press.
Gurnett, D.A. and Shaw, R.R.: 1973, *J. Geophys. Res.* 78, 8136.
Jones, D. and Grard, R.J.L.: 1975, *J. Roy. Astron. Soc.*, in press.
Kaiser, M.L. and Stone, R.G.: 1975, *Science* 189, 285.
Kurth, W.S. and Gurnett, D.A.: 1975, *J. Geophys. Res.* 80, 2764.
Melrose, D.B.: 1976, in press.
Mozer, F.S.: 1976, this volume, p. 125.
Owens, H.D. and Frank, L.A.: 1968, *J. Geophys. Res.* 73, 199.
Palmadesso, P., Coffey, T.P., Ossakow, S.L., and Papadopoulos, K.: 1976, in press.
Scarf, F.L., Fredricks, R.W., Frank, L.A. and Neugebauer, M.: 1971, *J. Geophys. Res.* 76, 5162.
Stone, R.G.: 1973, *Space Sci. Rev.* 14, 534.
Vesecky, J.F. and Frankel, M.S.: 1975, *J. Geophys. Res.* 80, 2771.
Warwick, J.: 1963, *Astrophys. J.* 137, 41.
Warwick, J.: 1967, *Space Sci. Rev.* 6, 841.

Plasma Waves in the Distant Magnetotail

D. A. GURNETT¹

Max-Planck-Institut für Physik und Astrophysik, Institut für extraterrestrische Physik
Garching, West Germany

L. A. FRANK

Department of Physics and Astronomy, University of Iowa, Iowa City, Iowa 52242

R. P. LEPPING

Laboratory for Extraterrestrial Physics, NASA Goddard Space Flight Center, Greenbelt, Maryland 20771

In this study we identify the principal types of plasma waves which occur in the distant magnetotail, and we investigate the relationship of these waves to simultaneous plasma and magnetic field measurements made on the same spacecraft. The observations used in this study are from the Imp 8 spacecraft, which passes through the magnetotail at radial distances ranging from about 23.1 to 46.3 R_E . Three principal types of plasma waves are detected by Imp 8 in the distant magnetotail: broad band electrostatic noise, whistler mode magnetic noise bursts, and electrostatic electron cyclotron waves. The electrostatic noise is a broad band emission which occurs in the frequency range from about 10 Hz to a few kilohertz and is the most intense and frequently occurring type of plasma wave detected in the distant magnetotail. This noise is found in regions with large gradients in the magnetic field near the outer boundaries of the plasma sheet and in regions with large plasma flow speeds, 10^3 km s⁻¹, directed either toward or away from the earth. The whistler mode magnetic bursts observed by Imp 8 consist of nearly monochromatic tones which last from a few seconds to a few tens of seconds. These noise bursts occur in the same region as the broad band electrostatic noise, although much less frequently, and are thought to be associated with regions carrying substantial field-aligned currents. Electrostatic electron cyclotron waves are seldom detected by Imp 8 in the distant magnetotail. Although these waves occur very infrequently, they may be of considerable importance, since they have been observed in regions near the neutral sheet when the plasma is extremely hot.

1. INTRODUCTION

It is widely recognized that processes occurring in the distant magnetotail are of fundamental importance to the understanding of the interaction of the earth's magnetosphere with the solar wind. The intense plasma heating which takes place in the plasma sheet region of the magnetotail is usually attributed to the merging of oppositely directed magnetic fields at one or more x type neutral lines, with the subsequent conversion of magnetic field energy into kinetic energy [Dungey, 1961; Axford *et al.*, 1965; Speiser, 1965]. Although the overall configuration of the magnetic fields and plasmas in the magnetotail is reasonably well understood, the detailed microscopic processes which occur in this region and their relationship to auroras and substorms are not. Classical magnetohydrodynamics requires a finite conductivity in the merging region. Since the plasma is essentially collisionless, an important question arises as to how this finite conductivity can occur. Piddington [1967], Dungey [1972], Syrovatskii [1972], and others have suggested that plasma wave turbulence produces an anomalous resistivity in the merging region and thereby provides the mechanism for dissipating the magnetic field energy. Similar plasma wave turbulence processes are thought to occur in regions of field-aligned currents associated with auroral precipitation [Kindel and Kennel, 1971]. The sudden onset of enhanced plasma wave turbulence, either in the

merging region or along the auroral field lines, has been suggested as the triggering mechanism for magnetospheric substorms [Piddington, 1967]. On the other hand, turbulence free processes have also been suggested to explain the merging process and the triggering of auroral substorms [Schindler, 1974]. Because of the possible role of plasma waves in these processes it is of considerable general interest to investigate the plasma wave phenomena which occur in the distant magnetotail.

At the present time, few plasma wave observations have been reported in the plasma sheet and neutral sheet regions of the distant magnetotail. Using data from the Ogo 1, 3, and 5 satellites, which provide measurements only in the near-earth regions of the plasma sheet (at radial distances $R \lesssim 17 R_E$), Brody *et al.* [1968] have reported observations of brief bursts of whistler mode magnetic noise near the neutral sheet. Early electric field measurements on Ogo 5 by F. L. Scarf revealed no VLF electric field oscillations in the tail with the exception of substorm-associated waves in the near-earth plasma sheet at radial distances of less than 12 R_E [Russell, 1972]. More recently, Scarf *et al.* [1974], using measurements from the Imp 7 spacecraft at a radial distance of about 30 R_E , have reported observations of moderately intense electric field oscillations in the region immediately outside the plasma sheet and very intense (160 mV) low-frequency magnetic noise in the high-density region of the plasma sheet.

The purpose of this paper is to present the results of an extensive study of plasma waves in the distant magnetotail using measurements from the Imp 8 spacecraft. These plasma wave measurements are compared with plasma and magnetic

¹ Now at Department of Physics and Astronomy, University of Iowa, Iowa City, Iowa 52242.

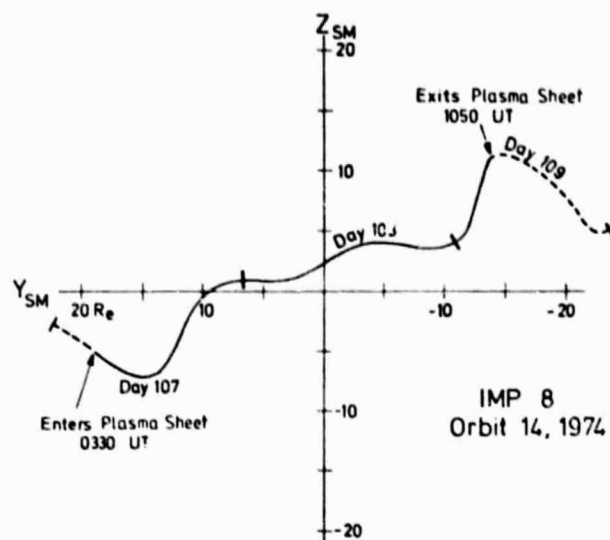


Fig. 1. Solar magnetospheric coordinates Y_{SM} and Z_{SM} for the magnetotail pass on days 107, 108, and 109, 1974. During this pass, X_{SM} varies from about -23.4 to $-35.6 R_E$.

field measurements presented in a companion paper by Frank *et al.* [1976] to study the relationship of the plasma waves to the various plasma regimes found in the distant magnetotail.

2. SPACECRAFT ORBIT AND INSTRUMENTATION

All of the measurements employed in this study were obtained with instrumentation on the Imp 8 (Explorer 50) spacecraft. This spacecraft is in a low-eccentricity orbit with initial perigee and apogee geocentric radial distances of 25.1 and $46.3 R_E$, respectively, and an orbit inclination of 41.5° with respect to the ecliptic plane. Because of the large orbit inclination, Imp 8 provides essentially complete coverage in 1 year of a cross section of the magnetotail at distances of about 25 – $35 R_E$ from the earth. Approximately 20 passes occur through the magnetotail each year. However, of these, only about 6 or 7 passes provide crossings of the neutral sheet. For this study we have examined all of the plasma wave data, and selected portions of the plasma and magnetic field data, for a 15-month period from December 22, 1973, to March 22, 1974. These data include a total of 26 passes through the magnetotail of which 8 have clearly defined neutral sheet crossings.

Measurements are shown from three instruments on Imp 8, the University of Iowa plasma wave experiment, the University of Iowa low-energy proton and electron differential energy analyzer (Lepede), and the Goddard Space Flight Center (GSFC) magnetometer. The plasma wave experiment on Imp 8 provides electric field measurements from 40 Hz to 2.0 MHz and magnetic field measurements from 40 Hz to 1.78 kHz. Electric field measurements are obtained by using a 'long' (121.5 m from tip to tip) electric dipole antenna which is extended outward perpendicular to the spacecraft spin axis. The spin axis is oriented perpendicular to the ecliptic plane. Magnetic field measurements are obtained by using a triaxial search coil magnetometer. Further details of the Imp 8 plasma wave experiment are given by Gurnett [1974].

The Lepede on Imp 8 provides measurements of the differential energy spectrums and angular distributions of protons and electrons over the energy range 50 eV to 45 keV. Electron and proton energy spectrums are obtained in 16 energy passbands and in 16 directions (sun-sectored) for each passband.

The Lepede also includes a Geiger-Mueller tube which is sensitive to electrons with energies $E \geq 45$ keV and protons with energies $E \geq 650$ keV. The fields of view of both the Lepede and the Geiger-Mueller tube are oriented perpendicular to the spacecraft spin axis. Further details of the Lepede instrumentation are given by Frank *et al.* [1976].

The magnetometer on Imp 8 is a triaxial flux gate magnetometer with a range of about $\pm 36 \gamma$ and a resolution of 0.3γ . Further details of this instrument are given by Scarce *et al.* [1976].

3. A TYPICAL IMP 8 PASS THROUGH THE NEUTRAL SHEET

To illustrate the general features of the Imp 8 plasma wave measurements, we first discuss a representative pass through the neutral sheet. The solar magnetospheric coordinates Y_{SM} and Z_{SM} , for this pass, which occurred on days 107, 108, and 109, 1974, are shown in Figure 1. Both the plasma and the magnetic field data, which are discussed later, show that the spacecraft enters the plasma sheet at about 0330 UT on day 107 and leaves the plasma sheet at about 1050 UT on day 109. This pass was selected for discussion because the magnetic field data show a very clear transition from the southern to the northern lobes of the magnetotail with an extended period (on day 108) in the vicinity of the neutral sheet.

The magnetic field and plasma wave measurements obtained during this pass are shown in Figures 2, 3, and 4. The corresponding plasma data for this pass are shown in Plates 1, 2, and 3. The top panels of Figures 2, 3, and 4 show the magnetic field measurements from the GSFC magnetometer, and the middle and bottom panels show the plasma wave magnetic and electric field intensities. The angles θ_{SM}^B and ϕ_{SM}^B of the magnetic field direction are given in solar magnetospheric coordinates, and the magnetic field magnitude is in gammas. The plasma wave magnetic field intensities are shown in seven frequency channels from 40 Hz to 1.78 kHz, and the electric field intensities are shown in 15 frequency channels from 40 Hz to 178 kHz. The ordinate for each channel is proportional to the logarithm of the field strength, with a range of 100 dB from the base line of one channel to the base line of the next higher channel. The vertical bars plotted for each channel give the average field strengths, averaged over intervals of 163.8 s, and the dots give the peak field strengths.

The magnetic field data show that after the spacecraft enters the plasma sheet at about 0330 UT on day 107 (Figure 2) it is located in the southern lobe of the magnetotail, with the magnetic field directed away from the sun ($\phi_{SM}^B \approx 180^\circ$). The spacecraft remains in the southern lobe of the magnetotail with a relatively steady magnetic field of about 15 – 20γ until about 0200 UT on day 108 (Figure 3). Starting at this time and continuing for the next 24 hours until about 0230 UT on day 109 (Figure 4), the magnetic field magnitude undergoes a series of depressions and directional changes which indicate multiple encounters and crossings of the neutral sheet. After about 0230 UT on day 109 and until the spacecraft leaves the plasma sheet at about 1050 UT the magnetic field is directed toward the sun ($\phi_{SM}^B \approx 0^\circ$) with a relatively steady magnitude of about 20γ , indicating that the spacecraft is in the northern lobe of the magnetotail.

Several types of plasma waves are evident in the magnetotail during this pass. In the electric field channels above about 50 kHz, many sporadic bursts of auroral kilometric radiation are evident throughout the pass (see Figure 2). Since this type of radiation is generated close to earth [Gurnett, 1974] and does

not interact with the plasma in the distant magnetotail, it will not be considered further in this paper. This radiation does, however, provide a useful index of auroral and magnetospheric substorm activity.

At lower frequencies, from about 5 to 50 kHz, a nearly steady level of continuum radiation is present for the entire duration of the pass through the magnetotail. As has been shown by Gurnett and Shaw [1973], this radiation is permanently trapped in the low-density regions of the magnetospheric cavity at frequencies below the solar wind plasma frequency. The abrupt cutoff of the trapped continuum radiation at the magnetopause crossings on days 107 and 109 is clearly evident in the 10.0- and 16.5-kHz channels. In the inner regions of the magnetosphere the low-frequency cutoff of the trapped continuum radiation is at the local electron plasma frequency, f_p , and can be used to make very accurate determinations of the local electron density [Gurnett and Frank, 1974]. It was initially thought that this cutoff could be used to determine the electron density in the very low density high-latitude regions of the magnetotail, where it is very difficult to measure the plasma density with other techniques. However, as was shown by this pass and by detailed analysis of many other passes, the low-frequency cutoff of the continuum radiation is essentially constant, independent of the spatial position within the magnetotail. The cutoff must therefore be determined by the plasma frequency in the source (or somewhere else in the magnetosphere) and not by the local plasma frequency. Since this radiation is also thought to be generated relatively close to the earth [Gurnett, 1975], this noise will not be discussed further in this paper.

In the region near the neutral sheet on day 108 (Figure 3), many intense bursts of low-frequency (40 Hz to 1.78 kHz) electric field noise are observed. This type of noise is detected on all passes which come close to the neutral sheet region and is the most intense type of plasma wave detected by Imp 8 in the distant magnetotail. Because the spectrum of this noise extends over a very broad frequency range and because no comparable noise is detected by the magnetic field sensor, we refer to this noise as broad band electrostatic noise. The detailed characteristics of this noise are discussed in section 4.

Another type of plasma wave is also evident in the low-frequency (40–562 Hz) magnetic field channels in Figure 3. This noise occurs much less frequently than the broad band electrostatic noise and is most clearly evident in the peak measurements, indicating that the noise consists of many short bursts. Since this noise is detected by a magnetic antenna and occurs at frequencies below the electron gyrofrequency, which is typically a few hundred hertz in these regions, the noise must consist of whistler mode waves. We refer to this noise as whistler mode magnetic noise bursts. The detailed characteristics of these magnetic noise bursts are discussed in section 5.

The one remaining type of plasma wave observed by Imp 8 in the distant magnetotail consists of electrostatic waves near harmonics of the electron gyrofrequency. Waves of this type are frequently observed in inner regions of the magnetosphere [Kennel et al., 1970] and are called electron cyclotron waves. Electron cyclotron waves of this type are seldom observed in the distant magnetotail and did not occur during the pass illustrated in Figures 2, 3, and 4. The detailed characteristics of this noise are discussed in section 6.

4. BROAD BAND ELECTROSTATIC NOISE

The pass illustration in Figures 2, 3, and 4 provides an excellent example of the typical characteristics of the broad

band electrostatic noise detected by Imp 8. The noise usually occurs over a broad range of frequencies extending from about 10 Hz to 1 kHz and with intensities ranging from about $50 \mu\text{V m}^{-1}$ to 5 mV m^{-1} . A typical spectrum of this noise, selected during an interval of relatively high intensity, from 1056 to 1059 UT on day 108, is shown in Figure 5. These electric field spectral densities are computed from the average field strength measurements and assume that the effective length of the electric antenna is one half of the tip-to-tip length. The rms electric field amplitude, integrated from 40 Hz to 10 kHz, is about 1.23 mV m^{-1} in this case. The peak electric field strengths for this same interval are about a factor of 3–5 times larger than the average field strengths. Usually, the intensity of the broad band electrostatic noise is less than that shown in Figure 5. However, on every pass close to the neutral sheet, several intervals of half an hour or more are usually encountered with intensities comparable to those in Figure 5.

To illustrate the fine structure of the broad band electrostatic noise, a high-resolution frequency-time spectrogram of this noise is shown in Figure 6. Two different frequency scales are shown to provide good resolution over the entire frequency range. The spectrum of the broad band electrostatic noise is seen to consist of many discrete bursts lasting from a few seconds to several minutes. These bursts often have a characteristic V shaped frequency-time variation, first decreasing and then increasing in frequency with increasing time. The spectrum also shows a marked decrease in intensity at frequencies above about 400 Hz. This upper cutoff frequency agrees well with the local electron gyrofrequency f_{ce} , which varies from about 400 to 500 Hz during the interval shown in Figure 6. Some weak bursts do, however, extend up to frequencies of several kilohertz, well above the electron gyrofrequency. This same quasi-cutoff effect near the electron gyrofrequency is evident in the spectrum of Figure 5, where the electron gyrofrequency was about 300 Hz. The wide band spectrograms in Figure 6 also show a well-defined lower cutoff frequency at about 10 Hz. This low-frequency cutoff is believed to correspond to the local lower hybrid resonance frequency f_{LHR} . If $f_p \gg f_{ce}$, which is usually the case in the regions where this noise is observed, the lower hybrid resonance frequency is given by $f_{LHR} = (f_{ce}^2 - f_{ce}^2)^{1/2}$ [Stix, 1962]. For the spectrum in Figure 6, $(f_{ce}^2 - f_{ce}^2)^{1/2}$ varies from about 10.5 to 11.6 Hz (assuming that the ions are protons).

To help establish the mode of propagation of the broad band electrostatic noise, it is useful to determine the orientation of the electric field relative to the static magnetic field. The direction of the electric field in the plane of rotation of the electric antenna can be obtained from the spin modulation of the noise intensity. To provide a meaningful interpretation in terms of the local magnetic field direction, measurements of this type must be made when the magnetic field lies close to the plane of rotation of the antenna. Fortunately, for the case shown in Figure 6 the magnetic field is in a satisfactory direction ($\varphi_{SR} \approx 165^\circ$ and $\theta_{SR} \approx 5^\circ$) for this type of analysis. Because the intensity of the noise fluctuates considerably, the intensity must be sector averaged over many rotations to determine the modulation pattern. The spin modulation observed for the event in Figure 6, averaged from 1037 to 1106 UT, is illustrated in Figure 7. These data show that a very distinct null occurs when the electric antenna axis is parallel to the local magnetic field. The depth and angular position of the null indicate that the electric field must be oriented within about $\pm 20^\circ$ from perpendicular to the magnetic field.

To clearly establish the region of the magnetotail in which

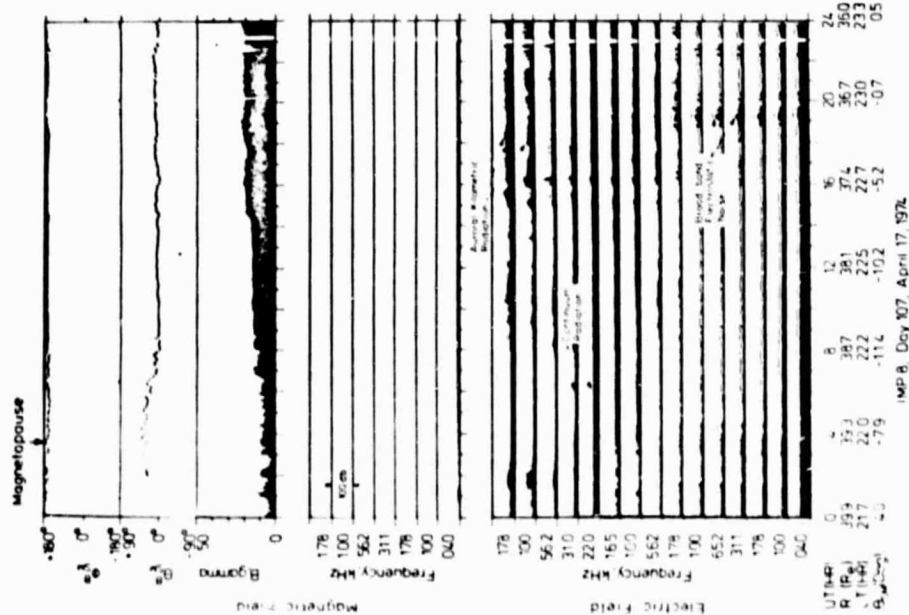


Fig. 2. Magnetic field and plasma wave measurements for day 107. After entering the plasma sheet at about 0330 UT the spacecraft is in the southern lobe of the magnetotail ($\phi_{\text{sw}} \approx 180^\circ$). In the high-frequency electric field channels, many sporadic bursts of auroral kilometric radiation and a nearly constant level of continuum radiation are present throughout this pass. At lower frequencies, several brief periods of intense broad-band electrostatic noise are evident near the end of the day, at about 1930 and 2230 UT.

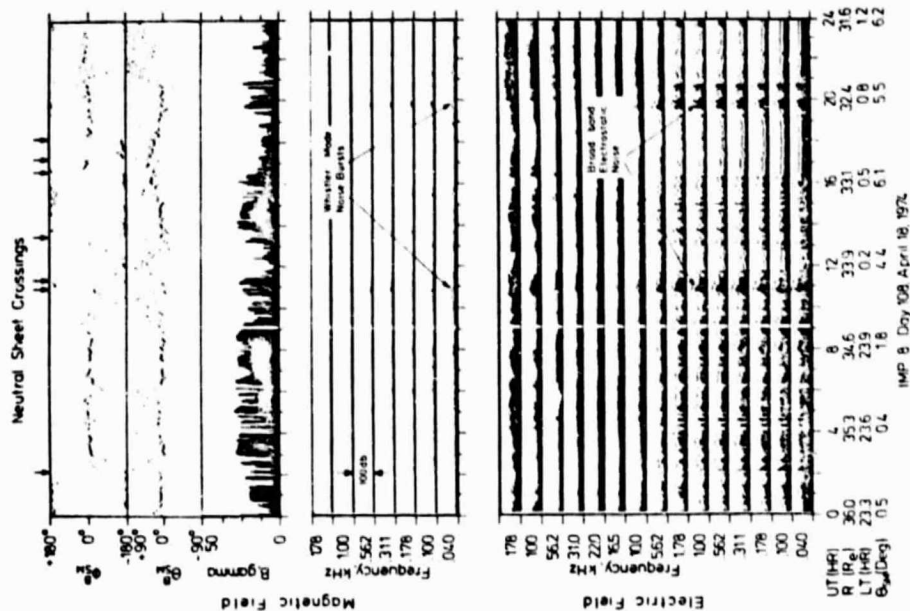


Fig. 3. Continuation of the measurements in Figure 2 for day 108. During most of this day the spacecraft is within the plasma sheet, and several clearly defined crossings of the neutral sheet are evident. Many intense bursts of broad band electrostatic noise and several intervals with whistler mode magnetic noise bursts occur in this region.

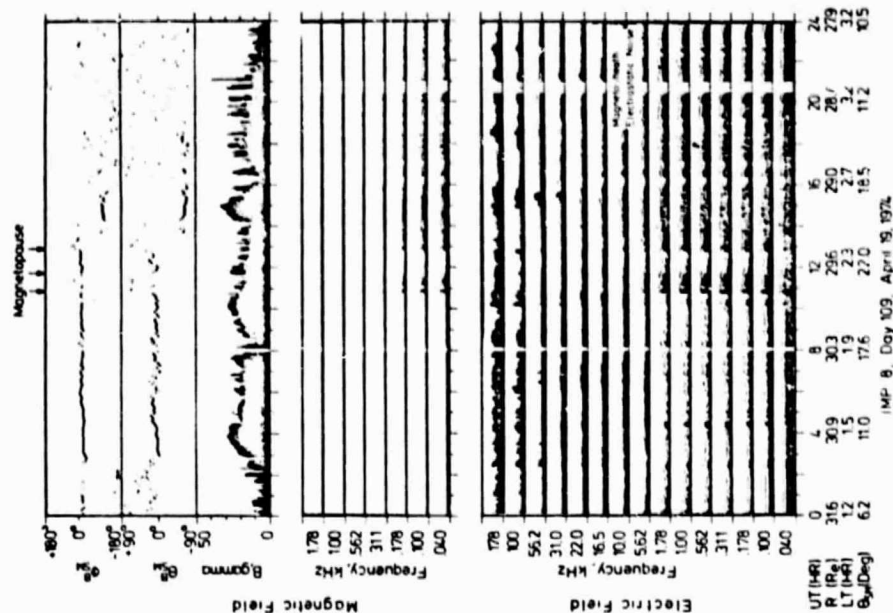


Fig. 4. Continuation of the measurements in Figure 3 for day 109. After about 0200 UT until the exit from the plasma sheet at about 1050 UT the spacecraft is in the northern lobe of the magnetotail. The plasma wave intensities in this region are quite low, comparable to the intensities in the southern lobe of the magnetotail in Figure 2.

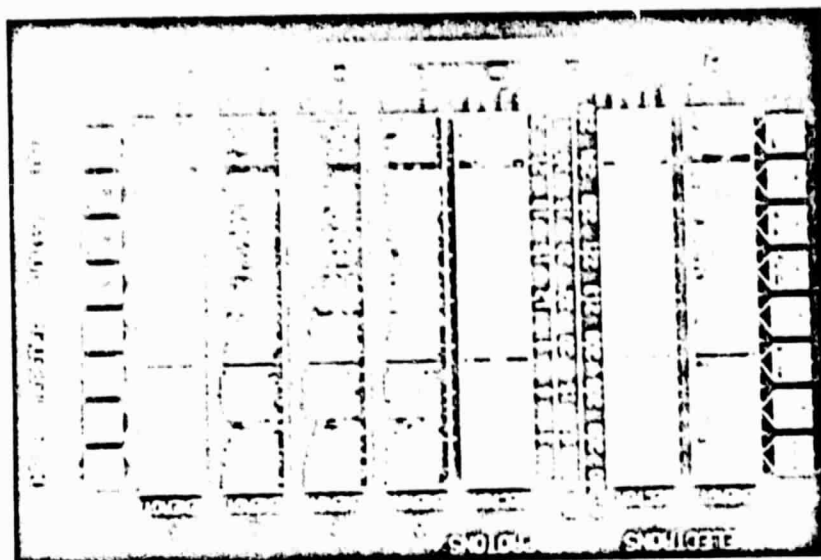


Plate 3. Lepedea observations for day 109. The corresponding plasma wave data are shown in Figure 4. The spacecraft remains in the nearly isotropic high-density region of the plasma sheet with very little plasma wave activity until the satellite's exit from the plasma sheet at about 1050 UT.

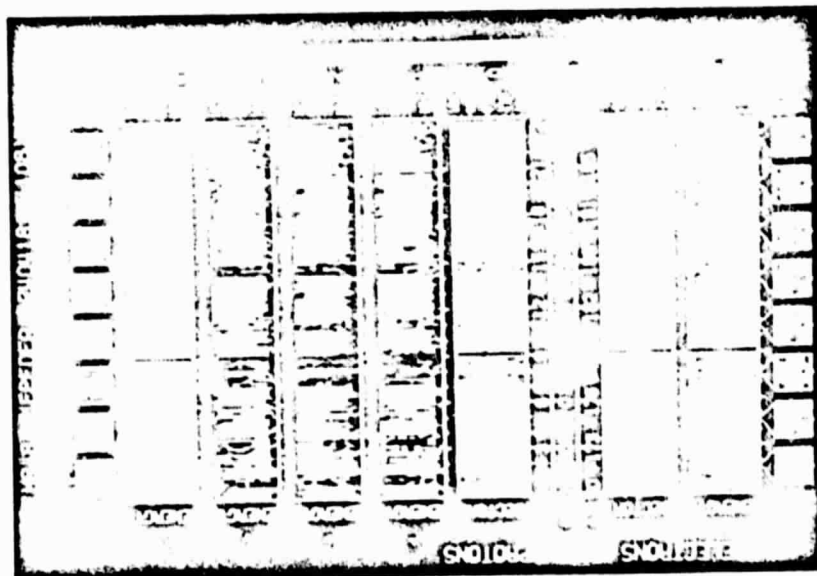


Plate 2. Lepedea observations for day 108. The corresponding plasma wave data are shown in Figure 3. The intense broad band electrostatic noise present from about 0200 to 1200 UT occurs in a region of sporadic sunward proton flow near the boundary of the plasma sheet. In the more isotropic regions deeper within the plasma sheet, from 1700 to 1900 UT and from 2100 to 2400 UT, for example, the broad band electrostatic noise is completely absent.

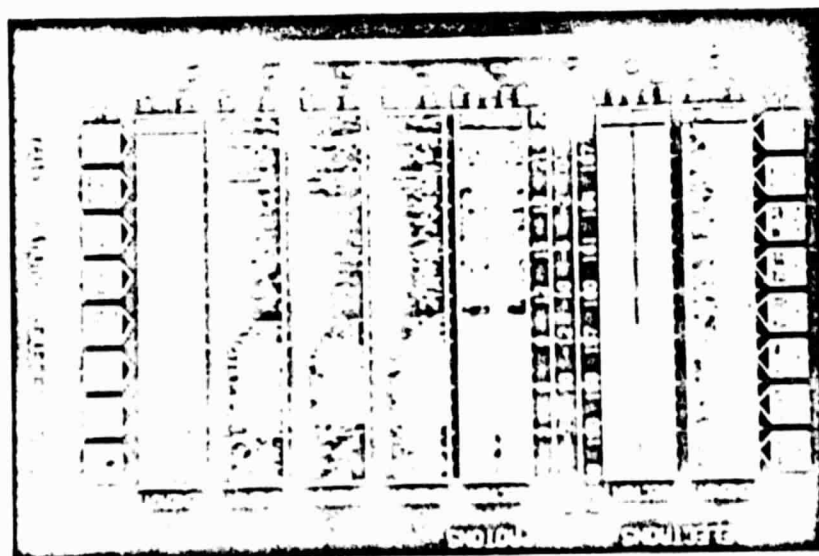


Plate 1. Lepedea observations for day 107. The corresponding plasma wave data are shown in Figure 2. Entry into the plasma sheet is clearly indicated by the change in the proton energy spectrum and angular distribution at about 0330 UT. The broad band electrostatic noise at about 1930 UT occurs in a region of intense sunward proton flow (see the proton sector spectrogram at this time).

ORIGINAL FILED IN
OF HAWAII

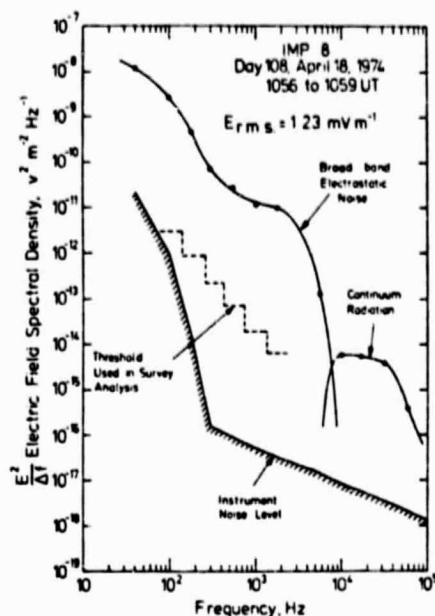


Fig. 5. A typical spectrum of the broad band electrostatic noise during a period of relatively high intensity, from 1056 to 1059 UT on day 108. The electron gyrofrequency during this period is about 300 Hz.

the broad band electrostatic noise is most frequently observed, we have analyzed all of the available Imp 8 magnetotail passes to determine the frequency of occurrence of this noise as a function of Y_{SM} and Z_{SM} . To compute the frequency of occurrence, events are counted only when the electric field spectral density simultaneously exceeds the thresholds indicated by the dashed lines in Figure 5. The results of this analysis are shown in Figure 8. It is evident that the broad band electrostatic noise is observed over a very broad region of the magnetotail. The

largest frequency of occurrence is clearly in the region near the neutral sheet; however, the noise is often detected at distances of as much as 10–15 R_E from the neutral sheet. Comparisons of individual events with switches in the magnetic field direction between $\varphi_{SM} \approx 0^\circ$ and $\varphi_{SM} \approx 180^\circ$ clearly show that although the broad band electrostatic noise occurs in the general region near the neutral sheet, it is not uniquely associated with crossings of the neutral sheet.

To identify the plasma region associated with the broad band electrostatic noise, the Lepedea data have been investigated on several selected passes through the neutral sheet. To illustrate the relationships typically observed, the Lepedea data for the pass discussed earlier, on days 107, 108, and 109 of 1974, are shown in Plates 1, 2, and 3. The details of these spectrogram displays of the Lepedea data are given in the companion paper by Frank *et al.* [1976]. In summary, the top four panels of each plate give (from top to bottom) the energy spectrums of protons in four viewing directions, toward the sun, toward local evening, away from the sun, and toward local morning, and the bottom panel gives the energy spectrum of electrons averaged over all sectors. The panels labeled 'sector' give the angular distributions of protons and electrons averaged over all energies.

In comparing the plasma measurements with the broad band electrostatic noise intensities, several relationships are apparent. First, the noise is usually observed near the boundaries of the plasma sheet. For example, many crossings of the plasma sheet boundary are evident from about 1900 UT on day 107 to about 1600 UT on day 108, and the broad band electrostatic noise intensity is correspondingly very large during this period. The noise intensity variations often show a very clear relationship to brief encounters with the plasma sheet, as from 1900 to 2000 UT and from 2215 to 2345 UT on day 107. Normally, the noise is completely absent in the very low density (~ 0.01 protons cm^{-3}) regions characteristic of the high-latitude magnetotail and in the high-density regions deep

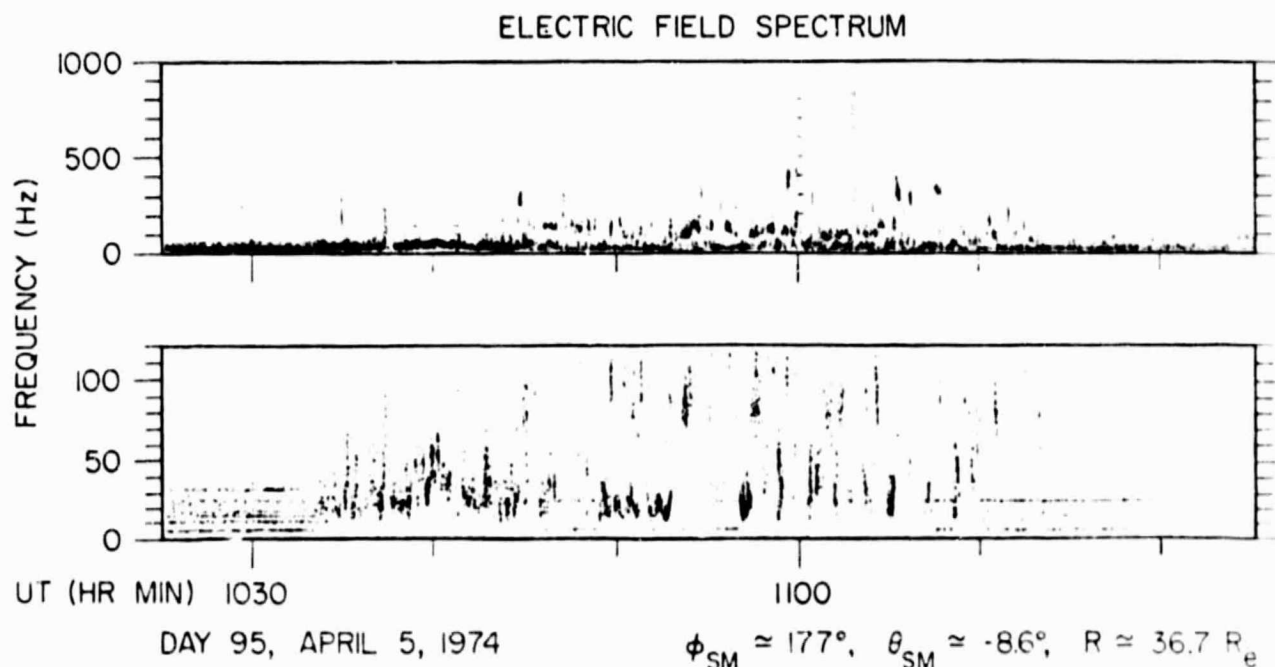


Fig. 6. Frequency-time spectrogram of the broad band electrostatic noise. Note the low-frequency cutoff at about 10 Hz and the marked decrease in the intensity above about 400 Hz. The electron gyrofrequency during this period varies from about 400 to 500 Hz.

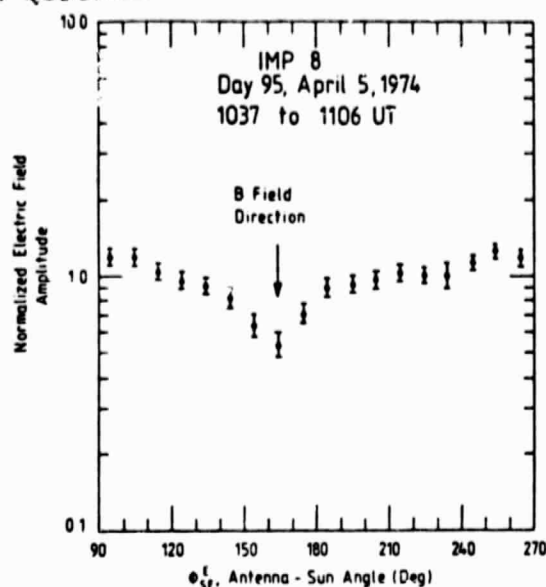


Fig. 7. Normalized electric field amplitude as a function of antenna orientation angle for the broad band electrostatic noise shown in Figure 6. The null in the electric field amplitude occurs when the antenna axis is approximately parallel to the local magnetic field.

within the plasma sheet. For example, when an extended period of several hours occurs where little or no plasma can be detected, as from about 1100 to 1900 UT on day 107, the noise intensities are very low. Similarly, when the spacecraft is within the high-density region of the plasma sheet for an extended period, as from about 1630 to 1900 on day 108, the intensities are very low.

Further evidence of the association of the broad band electrostatic noise with the boundaries of the plasma sheet is provided by the magnetic field data. Usually, the largest broad band noise intensities are observed in regions where large gradients occur in the magnetic field magnitude, particularly as the magnetic field changes from the relatively steady field characteristic of the high-latitude magnetotail to the depressed and more variable field in the plasma sheet. Because of the obvious difficulty in separating temporal variations from spatial variations it is not certain just how far these waves may extend inside or outside the plasma sheet boundaries. Measurements by two spacecraft are needed to eliminate some of these uncertainties.

Second, in most cases the broad band electrostatic noise occurs in regions which have highly anisotropic fluxes of protons streaming either toward or away from the sun, of the type discussed by Frank *et al.* [1976]. A good example of this association occurs from about 1900 to 2000 UT on day 107 in Figure 2. During this interval, which corresponds to a period of enhanced broad band noise intensity, both the proton energy spectrogram viewing away from the sun and the proton sector spectrogram (see Plate 1) show an intense flux of protons with energies of several keV streaming toward the sun. Another example of this relationship occurs during the period of intense broad band noise from about 1900 to 2000 UT on day 108 in Figure 3. As shown by Frank *et al.* [1976, Figure 1] this interval is characterized by substantial plasma flows directed away from the sun with velocities as large as 600 km s^{-1} . In comparison, the preceding interval from about 1630 to 1900 UT has very low electric field intensities and correspondingly small flow velocities, less than 200 km s^{-1} . The most intense

broad band electrostatic noise encountered during this pass, from about 1045 to 1140 UT on day 108, occurs in a region of very large flow velocities, greater than 10^3 km s^{-1} , which Frank *et al.* [1976] identify as the 'fireball,' the region of primary charged particle acceleration in the magnetotail. The maximum electric field intensities in this region, at about 1056 UT, occur essentially coincident with the change in the B_z component of the magnetic field (solar magnetospheric coordinates) from northward to southward and a corresponding switch in the plasma flow velocity from earthward to tailward [see Frank *et al.*, 1976, Figure 4]. A detailed analysis by Frank *et al.* [1976] of the charged particle angular distributions provides substantial evidence that this region of intense electric field turbulence and large rapidly fluctuating plasma flow velocities represents an encounter with the merging region in the distant magnetotail.

Because of temporal variations associated with auroral substorms it is very difficult to separate temporal variations, such as could occur from the sudden onset of a plasma instability, from variations produced by movements of the plasma sheet boundaries. Simple inspection of the intensity variations of the broad band electrostatic noise strongly suggests that the intensity variations of this noise are often closely associated with temporal variations in auroral activity taking place near the earth. Abrupt increases or changes in the broad band electrostatic noise intensity are often associated with abrupt increases in the intensity of the auroral kilometric radiation generated in the auroral regions near the earth. An example of this type of association is shown in Figure 9 for another Imp 8 pass through the plasma sheet near local midnight. Several distinct periods of enhanced auroral kilometric radiation are evident in the 56.2-, 100-, and 178-kHz channels during this period, the most prominent starting at about 1205, 1830, and 2200 UT. The onset of each of these periods of intense auroral kilometric radiation occurs coincident with an abrupt increase in the intensity of the broad band electrostatic noise. Although this relationship does not always occur on a one-to-one basis,

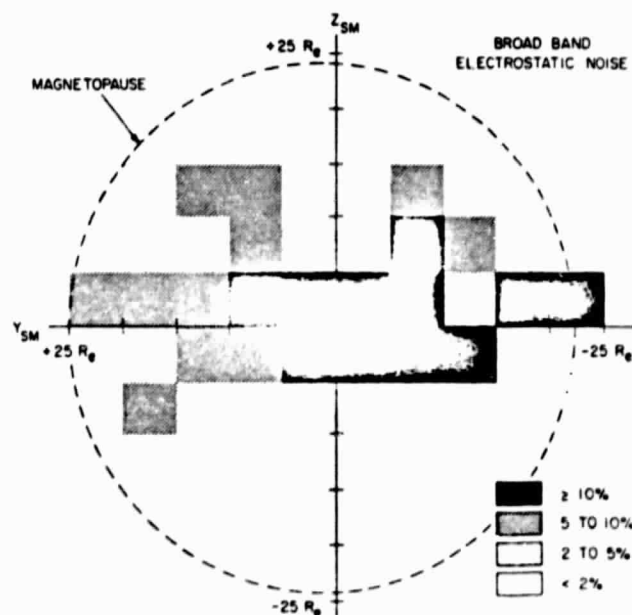


Fig. 8. Frequency of occurrence of the broad band electrostatic noise as a function of Y_{SM} and Z_{SM} . The thresholds used for this analysis are shown in Figure 5.

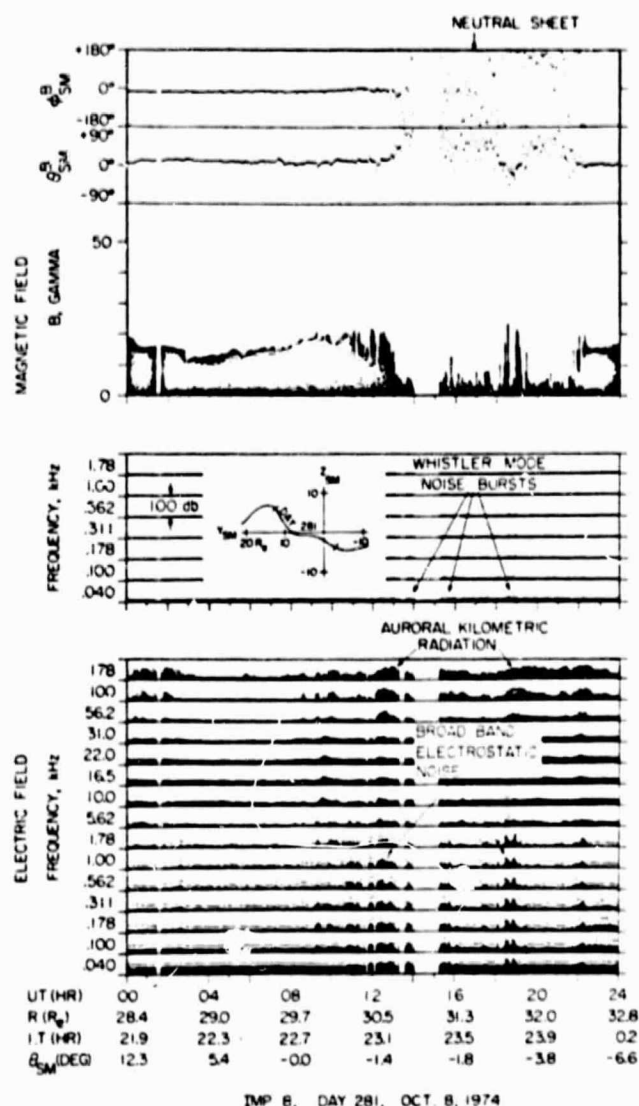


Fig. 9. Example of the association between abrupt increases in the intensity of auroral kilometric radiation generated near the earth (at about 1205, 1830, and 2200 UT in the 56.2-, 100-, and 178-kHz channels) and increases in the intensity of the broad band electrostatic noise in the distant magnetotail. Comparisons of these data with the corresponding plasma measurements of Frank et al. [1976, Figure 6] provide further examples of the association of the broad band electrostatic noise with the boundaries of the plasma sheet and with regions of large plasma flow velocities.

it occurs sufficiently often to suggest that the broad band electrostatic noise observed in the distant magnetotail by Imp 8 is closely associated with auroral activity taking place close to the earth.

In comparing the frequency-time spectra of the broad band electrostatic noise (Figure 6) with other types of plasma waves observed in the earth's magnetosphere one is immediately impressed with the close similarity to a type of broad band whistler mode noise called auroral hiss. Until now, auroral hiss has only been observed at low altitudes, up to a few thousand kilometers, over the auroral zone [Gurnett, 1966; Laaspere et al., 1971; Gurnett and Frank, 1972]. Although the frequency range of the auroral hiss observed by low-altitude satellites, about 1–100 kHz, is much different from the frequency range of the broad band electrostatic noise observed in the distant magnetotail by Imp 8, 10 Hz to a few kilohertz,

both types of noise have many characteristics in common. First, although the frequency ranges are quite different, both the auroral hiss and the broad band electrostatic noise occur in the same frequency range, $f_{LHR} < f < f_{UH}$, relative to the local characteristic frequencies of the plasma. The fact that some weak bursts of broad band electrostatic noise extend above the electron gyrofrequency can be attributed to Doppler shifts caused by the large streaming velocities (up to 10^3 km s⁻¹) observed in the region where the noise is detected. Second, both types of noise are nearly electrostatic, with the electric field oriented approximately perpendicular to the magnetic field. As discussed by Taylor and Shawhan [1974], auroral hiss is propagating in the whistler mode with the wave vector very close to the resonance cone. This wave normal direction results in a quasi-electrostatic type of propagation with a very small wave magnetic field. Because of the quasi-electrostatic mode of propagation, with the wave vector along the resonance cone, the electric field direction of auroral hiss is nearly perpendicular to the local magnetic field over most of the frequency range, similar to the electric field direction of the broad band electrostatic noise. Third, the detailed spectral characteristics of both the auroral hiss and the broad band electrostatic noise have a very similar appearance when the frequency scales are adjusted to account for the different frequency ranges in which these waves are observed. In particular, auroral hiss often has distinct V shaped spectral features, called 'V shaped hiss' and 'saucers' [see Gurnett and Frank, 1972], which bear a close similarity to the V shaped bursts evident in the broad band electrostatic noise. The frequency spectrum of the broad band electrostatic noise detected by Imp 8 in the distant mag-

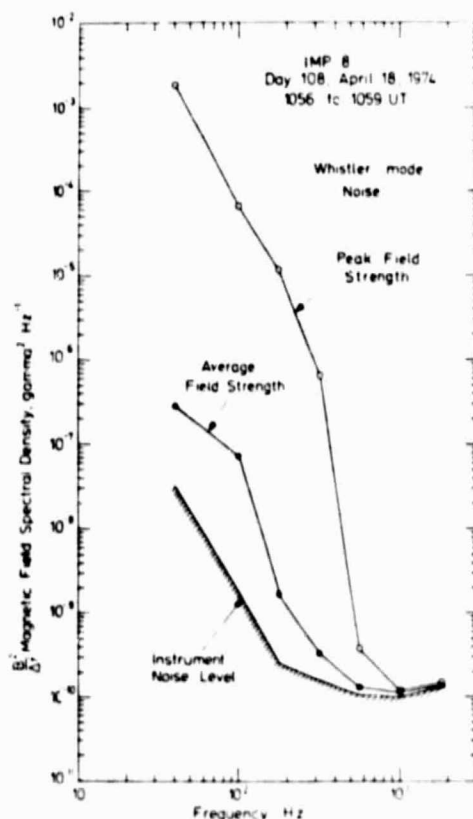


Fig. 10. Typical spectrum of the whistler mode magnetic noise bursts. The large ratio of peak to average field strength indicates that the noise consists of many short but intense bursts.

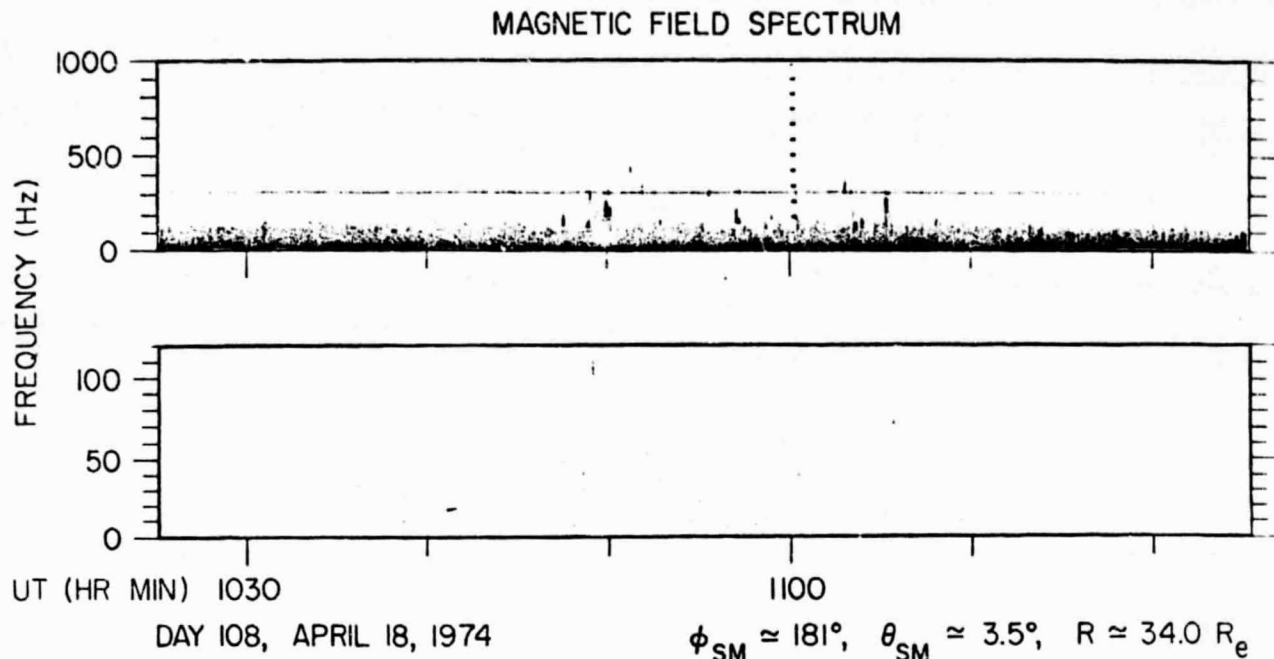


Fig. 11. Frequency-time spectrogram of the whistler mode magnetic noise burst. These bursts consist of many narrow bandwidth tones with rapidly varying frequencies lasting from a few seconds to a few tens of seconds.

netotail also shows a remarkable similarity to the moderately intense electrostatic noise detected throughout the magnetosheath, downstream of the earth's bow shock [Rodriguez and Gurnett, 1975]. The frequency range for the magnetosheath noise, a few hertz to about 1 kHz, is very similar to the frequency range of the broad band electrostatic noise, and the wide band spectrums of the magnetosheath noise have distinct V shaped spectral features which are remarkably similar to the broad band electrostatic noise (compare Figure 12 of Rodriguez and Gurnett [1975] with Figure 6 of this paper).

5. MAGNETIC NOISE BURSTS

During the pass illustrated in Figures 2, 3, and 4, several bursts of noise are evident in the low-frequency (40–311 Hz) magnetic field channels as the spacecraft passes through the region near the neutral sheet on day 108. These bursts are most clearly detected in the peak measurements and are particularly intense at about 0600, 1058, and 2000 UT (see Figure 3). Spectrums of the peak and average magnetic field spectral densities during one of the more intense bursts, from 1056 to 1059 UT, are shown in Figure 10. The peak field strengths are seen to be much larger than the average strengths. For example, the peak magnetic field strength in the 40-Hz channel during this interval is 126 mV, whereas the rms magnetic field strength determined from the average field strength measurements is only 4.6 mV. The large ratio of peak to average field strength indicates that the noise consists of many intense but brief bursts. To illustrate the detailed fine structure of this noise, a wide band frequency-time spectrogram from this same interval is shown in Figure 11. The bursts are seen to consist of nearly monochromatic tones, with rapidly changing frequencies, which last from a few seconds to a few tens of seconds. The frequency range of these bursts is always below the local electron gyrofrequency, which varies between about 300 and 500 Hz for the event shown in Figure 11. Since the only electromagnetic mode of propagation which occurs in this

frequency range is the whistler mode, these bursts are almost certainly propagating in the whistler mode.

Magnetic noise bursts of the type illustrated in Figures 10 and 11 occur much less frequently than the broad band electrostatic noise discussed in the previous section. A few such bursts are, however, observed on essentially every pass which comes close to the neutral sheet. To determine the region of the magnetotail in which these noise bursts are most frequently observed, the frequency of occurrence of this noise has been analyzed in the same way as was done for the broad band electrostatic noise. To compute the frequency of occurrence, any burst exceeding the noise level of any one of the magnetic field channels by more than 2 dB is counted as an event (see Figure 10 for the noise levels of the magnetic field sensor). The results of this frequency of occurrence analysis are shown in Figure 12. It is evident that the magnetic noise bursts occur in a region close to the neutral sheet ($|Z_{SM}| \lesssim 5 R_E$).

Comparison with the magnetic field and plasma data shows that although the magnetic noise bursts occur in the region near the neutral sheet, the bursts do not necessarily occur in the region where the spacecraft actually crosses the neutral sheet. As we have seen for the broad band electrostatic noise, the magnetic noise bursts tend to occur in regions with large gradients in the magnetic field near the boundaries of the plasma sheet. The bursts are often completely absent in regions of very small magnetic field, such as at about 1200 UT on day 108, and in the high-density inner region of the plasma sheet, as from 1600 to 1900 UT and from 2230 to 2400 UT on day 108. Frequently, the magnetic noise bursts are observed in the same region where the broad band electrostatic noise is unusually intense and where magnetic merging is thought to be taking place, for example, at about 1058 UT on day 108. Although it is possible that the weak average field intensities in these regions may be directly associated with the broad band electrostatic noise, the spectrums of these two types of noise are quite different (compare Figures 6 and 11). Thus although

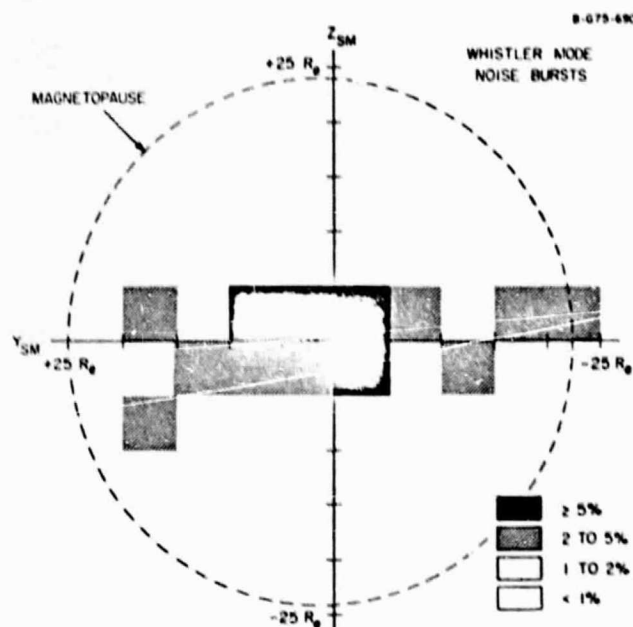


Fig. 12. Frequency of occurrence of the whistler mode magnetic noise bursts as a function of Y_{SM} and Z_{SM} . Any burst exceeding the noise level of the magnetic antenna by more than 2 dB is counted in this analysis.

the magnetic noise bursts sometimes occur in the same region as the broad band electrostatic noise, these bursts apparently constitute a completely different type of plasma instability. The electric field of the whistler mode magnetic noise bursts has not been detected, probably because the much more intense broad band electrostatic noise is usually present in the same region.

Although the magnetic noise bursts are observed in the same region and under similar conditions as the broad band electrostatic noise, the characteristics of these two different types of noise are quite different. It seems likely that these two types of noise are produced by distinctly different instability mechanisms, both of which occur for the same type of particle distribution function. The broad band electrostatic noise evidently has a lower instability threshold, since this noise is observed much more frequently and over a broader region than the magnetic noise bursts. Since both types of noise display characteristics of the whistler mode, the main difference is probably the wave normal angle at which the instability occurs. The large magnetic field amplitudes of the magnetic noise bursts are characteristic of whistler mode propagation at wave normal angles parallel to the magnetic field, whereas the large electric field amplitudes of the broad band electrostatic noise are characteristic of propagation at wave normal angles near the resonance cone.

In comparing these observations with previous studies it is almost certain that the magnetic noise bursts detected by Imp 8 are of the same type reported by Brody *et al.* [1968], using measurements from Ogo 1 in the near-earth region of the plasma sheet at radial distances of 15–20 R_E from the earth. The magnetic noise bursts detected by Imp 8 also have spectral characteristics similar to the whistler mode noise bursts called 'lion's roar,' which occur throughout the magnetosheath [Smith *et al.*, 1969]. Although the frequency range and duration of the magnetic noise bursts detected in the magnetotail are similar to lion's roar, the intensity is usually about a factor of 5 smaller.

Scarf *et al.* [1974] have reported observations of continuous high-intensity (160 mV) low-frequency magnetic field noise in the high-density regions of the distant plasma sheet. The brief intense magnetic field bursts discussed in this paper cannot correspond to this nearly continuous noise. Magnetic noise comparable to that discussed by Scarf *et al.* has not been detected in the distant magnetotail by the University of Iowa plasma wave instruments on either Imp 6 or Imp 8.

6. ELECTROSTATIC ELECTRON CYCLOTRON WAVES

The one remaining type of plasma wave detected in the distant magnetotail by Imp 8 consists of narrow band electrostatic emissions near harmonics of the electron gyro-frequency. This type of plasma wave did not occur during the pass illustrated in Figure 1 and has been observed only a few times in all of the available Imp 8 magnetotail data. A case in which this type of noise is observed is shown in Figure 13. During this pass a well-defined crossing from the southern to the northern lobe of the magnetotail takes place from about 0430 to 0440 UT, with ϕ_{SM}^B switching from 180° to 0°. During this entire period the magnetic field is directed northward, indicating that the spacecraft is on closed field lines within the plasma sheet. Starting at about 0345 UT, slightly before the neutral sheet crossing, and continuing to about 0545 UT, well

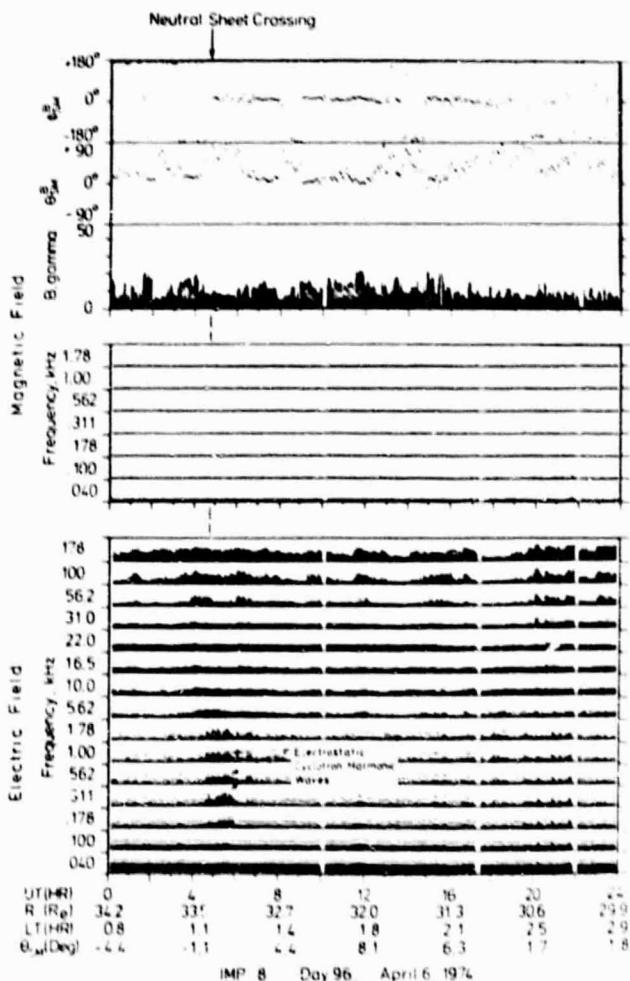


Fig. 13. Magnetic field and plasma wave intensities for a case where electrostatic electron cyclotron waves are observed. This event occurs near a neutral sheet crossing and in a region where the plasma is extremely hot.

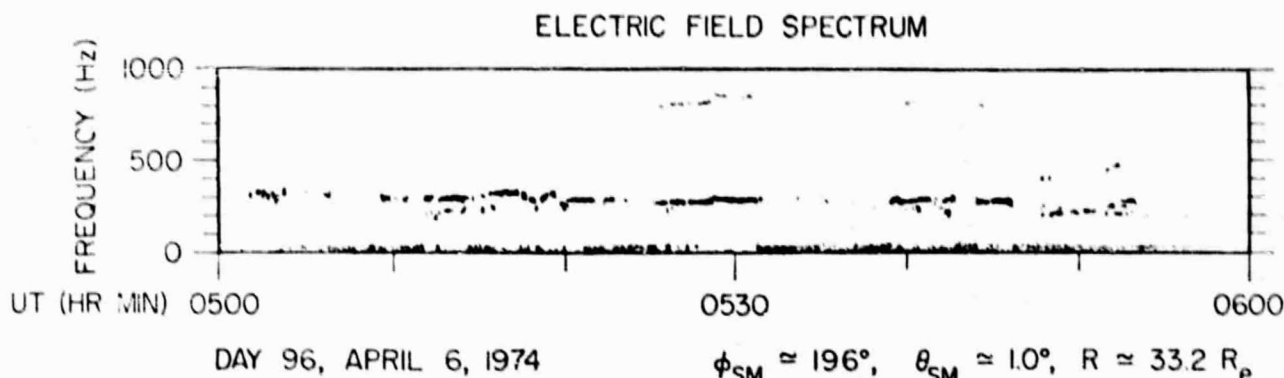


Fig. 14. Frequency-time spectrogram of the electron cyclotron waves shown in Figure 13. The fundamental emission frequency occurs at about 1.21 times the electron gyrofrequency.

after the neutral sheet crossing, a distinct enhancement is evident in the electric field channels from 311 Hz to 1.78 kHz. No comparable enhancement is evident in the corresponding magnetic field channels, indicating that the noise is electrostatic. The broad band electric field strength at the time of peak intensity, at about 0530 UT, is about $330 \mu\text{V m}^{-1}$.

A frequency-time spectrogram of the wide band data obtained during this event is shown in Figure 14. This spectrogram shows that the electrostatic noise consists of a strong narrow band emission at a frequency of about 280 Hz and weaker emissions at the second and third harmonics. Although the frequency spectrum of the fundamental is considered reliable, it is possible that the second and third harmonics may be due to nonlinearities in the wide band telemetry system. The existence of emissions above 280 Hz is, however, definitely confirmed by the enhanced electric field intensities in the 562-Hz, 1.0-kHz, and 1.78-kHz electric field channels (see Figure 13). During the interval from 0500 to 0600 UT the electron gyrofrequency varies from about 200 to 250 Hz. Detailed comparisons show that the fundamental frequency of the electrostatic emission occurs at about 1.21 times the electron gyrofrequency. The highest frequency detected, 1.78 kHz, corresponds to the seventh harmonic of the electron gyrofrequency. Because of unfavorable orientations and variations of the magnetic field it has not been possible, in this case or any of the other cases studied, to determine the orientation of the electric field relative to the local magnetic field.

Although electrostatic emissions near the electron gyrofrequency and its harmonics occur very infrequently and are not as intense as the broad band electrostatic noise, these emissions may be of considerable importance because they occur in the same region in which Frank *et al.* [1976] have reported the presence of an extremely hot plasma. For the event shown in Figure 13 the interval from about 0400 to 0630 UT is characterized by a very large increase in both the electron and the proton energies, with average energies greater than 10 keV and electron fluxes $J(E > 45 \text{ keV}) \geq 5 \times 10^9 \text{ el}(\text{cm}^2 \text{ s sr})^{-1}$. For further details and an analysis of this event, see Frank *et al.* [1976].

Electrostatic waves of this type, near harmonics of the electron gyrofrequency, have been previously observed in the inner regions of the earth's magnetosphere [Kennel *et al.*, 1970; Fredricks and Scarf, 1973; Shaw and Gurnett, 1975]. Usually, these waves occur near half-integral harmonics of the electron gyrofrequency, $(n + \frac{1}{2})f_e$. Scarf *et al.* [1974] have also interpreted observations of electrostatic waves detected by Imp 7 in

the distant magnetotail as being due to electrostatic waves at $\frac{1}{2}f_e$ and $\frac{3}{2}f_e$.

7. SUMMARY AND CONCLUSION

These observations have shown that three distinctly different types of plasma wave turbulence are detected by Imp 8 in the distant magnetotail. The first and most frequently occurring type of turbulence, called broad band electrostatic noise, consists of a broad band of electrostatic noise in the frequency range from about 10 Hz to a few kHz. This electric field noise is quite intense, with typical broad band electric field strengths of about 1 mV m^{-1} and occasional maximum intensities as large as 5 mV m^{-1} . The frequency range of this noise is bounded by the local lower hybrid resonance frequency f_{LHR} and (except for a few weak bursts) the electron gyrofrequency f_e . The electric field of this noise is oriented perpendicular (within $\pm 20^\circ$) to the local magnetic field, and the wave magnetic field is too small to be detected. Comparisons with the magnetic field and plasma data show that the noise occurs in regions with large magnetic field gradients near the outer boundary of the plasma sheet and is closely associated with large plasma flow velocities, both earthward and tailward, which occur in these regions. In a few cases this noise has also been observed with particularly large intensities directly in the region where the magnetic merge and charged particle acceleration are taking place. Intensity variations of this noise often appear to be closely associated with intense bursts of auroral kilometric radiation generated in the auroral regions near the earth. The second and less frequently occurring type of plasma wave turbulence detected in the distant magnetotail consists of intense (100 mV) bursts of low frequency (10–300 Hz) magnetic noise. These magnetic noise bursts, which must be propagating in the whistler mode, occur in regions with large magnetic field gradients near the outer boundaries of the plasma sheet and in the same general region in which the most intense broad band electrostatic noise is observed. The third and least frequently occurring type of plasma wave turbulence detected in the magnetotail consists of electrostatic waves near harmonics of the electron gyrofrequency. Electron cyclotron harmonic waves of this type have only been detected a few times in all of the available Imp 8 data. These waves are relatively weak, seldom exceeding intensities of about $300 \mu\text{V m}^{-1}$. Although these waves occur relatively infrequently and are very weak, they may be of considerable importance, since they have been observed in regions where the plasma is being heated to very high temperatures. In contrast to the broad band electrostatic

noise and the whistler mode magnetic noise bursts, the cyclotron harmonic emissions are observed very close to the neutral sheet, i.e., within the high-density region of the plasma sheet.

In considering the plasma wave modes which could be responsible for these different types of noise it is reasonably certain that the magnetic noise bursts consist of whistler mode waves, and the electron cyclotron harmonic emissions consist of $(n + \frac{1}{2})f_c$ electrostatic waves of the type studied by Fredrick [1971], Young et al. [1973], Ashour-Abdalla and Kennel [1976], and others. The exact identification of the plasma wave mode associated with the broad band electrostatic noise is more uncertain. As discussed earlier, this noise has certain spectral characteristics similar to auroral hiss and to the electrostatic noise detected throughout the magnetosheath. The similarity to auroral hiss suggests that this noise consists of short-wavelength quasi-electrostatic whistler mode waves propagating with wave normal directions near the resonance cone. Since hot plasma effects must almost certainly be involved in the generation of this noise, it seems more likely that this electrostatic turbulence consists of ion sound waves or electrostatic ion cyclotron waves of the type discussed by Kindel and Kennel [1971] and Syrovatskii [1972], which couple with, or are closely associated with, the whistler mode. Coupling effects of this type have been considered by Sizonenko and Stepanov [1967] and Maggs [1976]. The observed electric field direction of the broad band electrostatic noise, perpendicular to the magnetic field, would appear to favor the identification of this noise with the electrostatic ion cyclotron (Bernstein) modes.

Because substantial field-aligned currents are thought to occur near the outer boundary of the plasma sheet [Aubry et al., 1972; Fairfield, 1973] where the broad band electrostatic noise and the whistler mode magnetic noise bursts are observed, it seems most likely that these waves are produced by a current-driven plasma instability. Other instability mechanisms must also be considered, since the exact feature of the charged particle distribution function responsible for the instability remains unknown. The fact that the broad band electrostatic noise is usually detected in regions with large proton streaming velocities suggests that the instability may be driven by some characteristic feature of the proton stream rather than by a current produced by the differential motion with respect to the electrons. If, for example, the streaming protons interact with another more slowly moving ion distribution, such as from the ionosphere, or if multiple peaks occurred in the proton distribution function, then strong two-stream instabilities would be expected. Inspection of the proton velocity distribution function, such as appears in Figure 7 of Frank et al. [1976], does not show any evidence of double-peaked distributions. However, these distribution functions require a relatively long time, seconds, to accumulate compared to the short time scales of <1 s evident in the plasma wave spectrums, and it is possible that two-stream interactions of this type could occur within the proton stream, particularly in the highly turbulent region near the fireball. Further detailed studies are needed to clearly identify the instability mechanism involved in the generation of this noise.

When the possible role of this plasma wave turbulence is considered, many questions remain to be investigated. The issue of particular importance is whether the electric field turbulence is sufficiently intense to account for the anomalous resistivity often invoked to explain the existence of merging in an essentially collisionless plasma. We do not attempt to an-

swer this question of theoretical interpretation. However, the measurements in this paper together with the associated plasma and magnetic field measurements of Frank et al. [1976] provide the essential experimental parameters (electric and magnetic field frequency spectrums, flow velocities, and particle distribution functions) needed to proceed with a theoretical investigation of the role of anomalous resistivity in the merging region. These measurements also provide evidence that plasma wave turbulence in the distant magnetotail is often closely associated with enhanced auroral activity near the earth (in particular, the auroral kilometric radiation). Whether this relationship can be interpreted as evidence of a plasma wave instability acting to trigger the merging process by increasing the anomalous resistivity, as has been suggested by Piddington [1967], Syrovatskii [1972], and others, cannot be decided on the basis of these data. The essential interpretational difficulty is that with measurements from a single satellite it is not possible to distinguish spatial variations from temporal variations. Hopefully, measurements from dual spacecraft such as ISEE-A and ISEE-B will help resolve this question.

Acknowledgments. The authors wish to express their thanks to R. Anderson, G. Voots, and R. West for their assistance in the data processing and preparation of illustrations. The research at the University of Iowa was supported by the National Aeronautics and Space Administration under contracts NAS1-11257, NAS1-13129, NAS5-11074, NAS5-11064, and NAS5-11431 and grants NGL-16-001-002 and NGL-16-001-043 and by the Office of Naval Research under grant N00014-76-C-0016. The research performed by D. Gurnett while he was on leave at the Max-Planck-Institut für extraterrestrische Physik was supported by the Alexander von Humboldt Foundation.

The Editor thanks W. Bernstein and R. M. Thorne for their assistance in evaluating this paper.

REFERENCES

- Ashour-Abdalla, M., and C. F. Kennel, Convective cold upper hybrid instabilities, in *Magnetospheric Particles and Fields*, edited by B. M. McCormac, D. Reidel, Dordrecht, Netherlands, in press, 1976.
- Aubry, M. P., M. G. Kivelson, R. L. McPherron, C. T. Russell, and D. S. Colburn, Outer magnetosphere near midnight at quiet and disturbed times, *J. Geophys. Res.*, **77**, 5487, 1972.
- Axford, W. I., H. E. Petschek, and G. L. Siscoe, Tail of the magnetosphere, *J. Geophys. Res.*, **70**, 1231, 1965.
- Brody, K. L., R. E. Holzer, and E. J. Smith, Magnetic field fluctuations between 2 and 1000 Hz in the magnetotail (abstract), *Eos Trans. AGU*, **49**, 280, 1968.
- Dungey, J. W., Interplanetary magnetic field and the auroral zones, *Phys. Rev. Lett.*, **6**, 47, 1961.
- Dungey, J. W., Theory of neutral sheets, in *Earth's Magnetospheric Processes*, edited by B. M. McCormac, p. 210, D. Reidel, Dordrecht, Netherlands, 1972.
- Fairfield, D. H., Magnetic field signatures of substorms on high-latitude field lines in the nighttime magnetosphere, *J. Geophys. Res.*, **78**, 1553, 1973.
- Frank, L. A., K. L. Ackerson, and R. P. Lepping, On hot tenuous plasmas, fireballs, and boundary layers in the earth's magnetotail, *J. Geophys. Res.*, **81**, this issue, 1976.
- Fredricks, R. W., Plasma instability at $(n + \frac{1}{2})f_c$ and its relationship to some satellite observations, *J. Geophys. Res.*, **76**, 5344, 1971.
- Fredricks, R. W., and F. L. Scarf, Recent studies of magnetospheric electric field emission above the electron gyrofrequency, *J. Geophys. Res.*, **78**, 310, 1973.
- Gurnett, D. A., A satellite study of VLF hiss, *J. Geophys. Res.*, **71**, 5599, 1966.
- Gurnett, D. A., The earth as a radio source: Terrestrial kilometric radiation, *J. Geophys. Res.*, **79**, 4227, 1974.
- Gurnett, D. A., The earth as a radio source: The nonthermal continuum, *J. Geophys. Res.*, **80**, 2751, 1975.
- Gurnett, D. A., and L. A. Frank, VLF hiss and related plasma observations in the polar magnetosphere, *J. Geophys. Res.*, **77**, 172, 1972.
- Gurnett, D. A., and L. A. Frank, Thermal and suprathermal plasma

- densities in the outer magnetosphere, *J. Geophys. Res.*, **79**, 2355, 1974.
- Gurnett, D. A., and R. R. Shaw, Electromagnetic radiation trapped in the magnetosphere above the plasma frequency, *J. Geophys. Res.*, **78**, 8136, 1973.
- Kennel, C. F., F. L. Scarf, R. W. Fredricks, J. H. McGhee, and F. V. Coroniti, VLF electric field observations in the magnetosphere, *J. Geophys. Res.*, **75**, 6136, 1970.
- Kindel, J. M., and C. F. Kennel, Topside current instabilities, *J. Geophys. Res.*, **76**, 3055, 1971.
- Laaspere, T., W. C. Johnson, and L. C. Semprebon, Observations of auroral hiss, LHR noise, and other phenomena in the frequency range 20 Hz to 540 kHz on Ogo 6, *J. Geophys. Res.*, **76**, 4477, 1971.
- Maggs, J. E., Coherent generation of VLF hiss, *J. Geophys. Res.*, **81**, 1707, 1976.
- Piddington, J. H., Magnetic field annihilation in current pinches, *Planet. Space Sci.*, **15**, 33, 1967.
- Rodriguez, P., and D. A. Gurnett, Electrostatic and electromagnetic turbulence associated with the earth's bow shock, *J. Geophys. Res.*, **80**, 19, 1975.
- Russell, C. T., Noise in the geomagnetic tail, *Planet. Space Sci.*, **20**, 1541, 1972.
- Scarf, F. L., L. A. Frank, K. L. Ackerson, and R. P. Lepping, Plasma wave turbulence at distant crossings of the plasma sheet boundaries and the neutral sheet, *Geophys. Res. Lett.*, **1**, 189, 1974.
- Scearce, C. S., C. V. Moyer, R. P. Lepping, and N. F. Ness, GSFC magnetic field experiment, Explorers 47 and 50, *NASA GSFC X Doc. 695-76-191*, Oct. 1976.
- Schindler, K., A theory of the substorm mechanism, *J. Geophys. Res.*, **79**, 2803, 1974.
- Shaw, R. R., and D. A. Gurnett, Electrostatic noise bands associated with the electron gyrofrequency and plasma frequency in the outer magnetosphere, *J. Geophys. Res.*, **80**, 4259, 1975.
- Sizonenko, V. L., and K. N. Stepanov, Plasma instability in the electric field of an ion-cyclotron wave, *Nucl. Fusion*, **7**, 131, 1967.
- Smith, E. J., R. E. Holzer, and C. T. Russell, Magnetic emission in the magnetosphere at frequencies near 100 Hz, *J. Geophys. Res.*, **74**, 3027, 1969.
- Speiser, T. W., Particle trajectories in model current sheets, I, Analytical solutions, *J. Geophys. Res.*, **70**, 4219, 1965.
- Stix, T. H., *The Theory of Plasma Waves*, p. 32, McGraw-Hill, New York, 1962.
- Syrovatskii, S. I., Origin of the geomagnetic tail and neutral sheet, in *Critical Problems of Magnetospheric Physics*, edited by E. R. Dyer, p. 35, IUCSTP Secretariat, Washington, D. C., 1972.
- Taylor, W. W. L., and S. D. Shawhan, A test of incoherent Cerenkov radiation for VLF hiss and other magnetospheric emissions, *J. Geophys. Res.*, **79**, 105, 1974.
- Young, P. S., J. D. Callen, and J. E. McCune, High-frequency electrostatic waves in the magnetosphere, *J. Geophys. Res.*, **78**, 1082, 1973.

(Received March 19, 1976;
accepted June 18, 1976.)

A Region of Intense Plasma Wave Turbulence on Auroral Field Lines

D. A. GURNETT¹

Max-Planck-Institut für extraterrestrische Physik, 8046 Garching/Munich, West Germany

L. A. FRANK

Department of Physics and Astronomy, University of Iowa, Iowa City, Iowa 52242

Plasma wave measurements from the Hawkeye 1 and Imp 6 satellites show that a broad region of intense plasma wave turbulence occurs on the high-latitude auroral field lines at altitudes ranging from a few thousand kilometers in the ionosphere to many earth radii in the distant magnetosphere. This turbulence occurs in an essentially continuous band on the auroral *L* shells at all local times around the earth and is most intense during periods of auroral activity. The electric field intensity of this turbulence is often quite large, with maximum field strengths of about 10 mV m^{-1} and peak intensities in the frequency range 10–50 Hz. Magnetic field perturbations indicative of field-aligned currents and weak bursts of whistler mode magnetic noise are also observed in the same region as the electric field turbulence. In the local afternoon and evening the electric field turbulence is closely associated with V-shaped auroral hiss emissions. In some cases the electric field turbulence appears as a lowering and intensification of the low-frequency portion of the auroral hiss spectrum. Comparisons with plasma measurements and with similar measurements from other satellites strongly suggest that this plasma wave turbulence occurs on magnetic field lines which connect with regions of intense inverted V electron precipitation at low altitudes and with regions of intense earthward plasma flow in the distant magnetotail. The plasma instabilities which could produce this turbulence and the possible role which this turbulence may play in the heating and acceleration of the auroral particles are considered.

INTRODUCTION

Recent studies of plasma wave measurements obtained from the Hawkeye 1 and Imp 6 satellites have revealed the existence of a broad region of plasma wave turbulence on auroral field lines at altitudes ranging from a few thousand kilometers in the auroral ionosphere to many earth radii in the distant magnetosphere. The electric field intensity of this turbulence is often quite large, with maximum field strengths of about 10 mV m^{-1} . The frequency range of the electric field noise typically extends from about 10 Hz to several kilohertz, the maximum intensity occurring at about 10–50 Hz. The electric field turbulence sometimes appears to be closely associated with whistler mode auroral hiss emissions which are frequently observed on the high-latitude auroral field lines. Weak bursts of magnetic noise are also detected in the same region as the electric field turbulence, although these magnetic noise bursts do not appear to be directly associated with the electric field noise. In this paper we present a detailed study of the plasma wave turbulence observed by Hawkeye 1 and Imp 6 on high-latitude auroral field lines, and we investigate the relationship of this turbulence to magnetic field and plasma measurements obtained in the same region.

The importance of studying plasma wave turbulence on auroral field lines arises from the possible role that this turbulence may play in producing regions of 'anomalous' resistivity in the field-aligned currents which flow between the auroral oval and the distant magnetosphere. For many years it has been suggested [Sagdeev and Galeev, 1966] that intense electric fields produced by current-driven instabilities can interact with the current-carrying particles to produce an effective resistivity many orders of magnitude larger than the resistivity produced by Coulomb collisions. Kindel and Kennel [1971] have consid-

ered the possible current-driven instabilities which could occur in the auroral zone and have concluded that the electrostatic ion cyclotron and ion acoustic modes should be unstable in the regions of field-aligned currents associated with the auroral electron precipitation. If the electric field turbulence produced by these instabilities grows to sufficiently large amplitudes, the associated anomalous resistivity can produce large potential differences of several kilovolts along the magnetic field in these regions. Several investigators, including Coroniti and Kennel [1972, 1973], Sato and Holzer [1973], Holzer and Sato [1973], Papadopoulos and Coffey [1974], Møzer [1977], and others, have considered the possibility that the resulting parallel electric field could accelerate runaway electrons to energies of several keV, thereby accounting for the intense electron precipitation commonly observed in the auroral regions. Since other turbulence free acceleration mechanisms have also been proposed [Carlqvist, 1972], it is of considerable importance to establish whether intense electric field turbulence occurs in the regions of field-aligned current associated with the auroral electron precipitation.

Scarfi et al. [1973, 1975] have previously reported observations of electrostatic plasma wave turbulence associated with field-aligned currents for a few cases in which the Ogo 5 spacecraft reached sufficiently high magnetic latitudes to obtain measurements on auroral field lines, at $L > 7-8$, in the region close to the earth. During magnetically disturbed periods in the local afternoon and evening the electrostatic turbulence detected by Ogo 5 usually consisted of a few abrupt transient bursts with frequencies extending from about 1 kHz to about 10 kHz and with durations of a few seconds. The individual bursts tended to correlate with gradients in the magnetic field caused by field-aligned currents. Scarfi et al. [1972] and Fredricks et al. [1973] discussed similar observations of enhanced electrostatic wave turbulence detected by Ogo 5 at the boundaries of the dayside polar cusp.

In comparison with the Ogo 5 results, both the Hawkeye 1 and the Imp 6 spacecraft provide measurements at higher

¹ Permanent address: Department of Physics and Astronomy, University of Iowa, Iowa City, Iowa 52242.

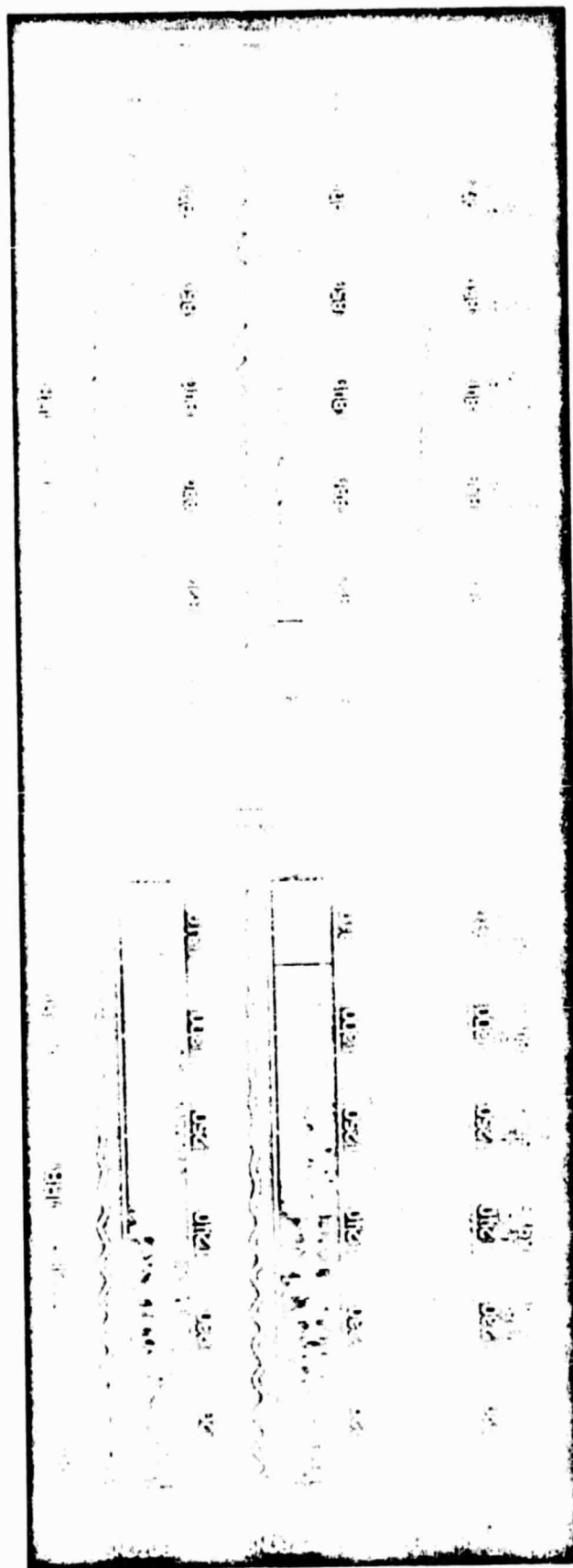


Plate 1. The Lepedea and GM tube data for the inbound Hawkeye 1 pass in Figure 2. The two spectrograms display the color-coded responses of the Lepedea as functions of the logarithm to the base 10 of the energy (ordinate) and universal time (abscissa). The color bar at the right-hand side of the figure displays the color coding (\log_{10} of the analyzer responses). Each spectrogram is topped with a plot of the instantaneous pitch angles as determined with the on-board magnetometer. The most intense broad-band electrostatic noise and magnetic noise bursts occur from about 1234 to 1244, just before the rapid increase in the GM tube counting rate and in a region characterized by low-energy magnetosheathlike proton intensities.

Plate 2. The Lepedea and GM tube data for the inbound Hawkeye 1 pass in Figure 3. The onset of the broad-band electrostatic noise and magnetic noise bursts and the cutoff of the continuum radiation at 13.3 kHz occur as the spacecraft enters the region of low energy after about 1825 UT.

ORIGINAL PAGE IS
OF POOR QUALITY

magnetic latitudes than were possible with Ogo 5. In this study it is therefore possible to obtain a much more comprehensive survey of phenomena occurring on auroral field lines at all local times and for both quiet and magnetically disturbed conditions. The plasma wave instrumentation on Hawkeye 1 and Imp 6 also provides measurements over a broader frequency range, particularly at lower frequencies, and with greater electric field sensitivity. As will be shown, the electric field turbulence detected by Hawkeye 1 and Imp 6 differs considerably from the Ogo 5 results. The electric field turbulence occurs with a relatively steady intensity over a broad region for a substantial fraction of the time (20–50%), rather than a few intense bursts, and the most intense component of the noise occurs at frequencies well below the lower frequency limit of the Ogo 5 electric field experiment.

SPACECRAFT ORBITS AND EXPERIMENT DESCRIPTIONS

To aid in interpreting the measurements presented in this paper, we briefly describe the orbits of Hawkeye 1 and Imp 6 and the regions of the magnetosphere sampled by these two satellites. Hawkeye 1 is in a highly eccentric polar orbit with initial perigee and apogee geocentric radial distances of 6,847 km and 130,856 km, respectively. The apogee is located almost directly over the north pole, so Hawkeye 1 provides extensive coverage of the high-latitude region of the magnetosphere. Since the region of primary interest for this study is relatively close to the earth ($R \leq 10 R_E$), the coordinates used throughout this paper are the magnetic latitude λ_m , the magnetic local time MLT, and the geocentric radial distance R . A typical magnetic meridional plane (R, λ_m) trajectory of Hawkeye 1 is shown in Figure 1. Because of the 11° tilt of the earth's magnetic dipole axis and the long-term secular changes in the orbit, measurements can be obtained over a broad range of magnetic latitudes if a sufficiently large quantity of data is used. For this study we have used Hawkeye 1 data from a period of approximately 14 months starting at launch on June 3, 1974, and continuing until August 29, 1975. The shaded area labeled

'Region sampled by Hawkeye 1' in Figure 1 indicates the region of the magnetic meridional plane sampled by Hawkeye 1 for a representative range of magnetic local times (2300–0100) near local midnight. In the northern hemisphere, Hawkeye 1 provides measurements on a typical auroral field line ($L = 8$) at radial distances ranging from about 4 to 6 R_E . In the southern hemisphere, measurements are obtained at radial distances ranging from about 1.1 to 1.8 R_E . Because of the increasing perigee altitude, data obtained during later periods of operation will extend the measurements on auroral field lines in the southern hemisphere to altitudes of about 2.6 R_E , so that eventually, observations will be provided over a very wide range of altitudes. The data set currently available for this study, however, has a distinct gap in the altitude coverage (at $L = 8$) from about 1.8 to 4.0 R_E .

The Imp 6 spacecraft is in a highly eccentric orbit with initial perigee and apogee geocentric radial distances of 6,613 and 212,630 km, respectively. In contrast to the Hawkeye 1 orbit the apogee of Imp 6 is located at a low latitude, close to the equatorial plane of the earth. However, the inclination of the orbit plane is sufficiently large to provide measurements at relatively high magnetic latitudes, up to about 55° , in the region near the earth. A typical magnetic meridional plane trajectory for Imp 6 is shown in Figure 1. As with Hawkeye 1, the tilt of the earth's magnetic dipole axis and orbital perturbations greatly extend the range of magnetic latitudes at low altitudes which are sampled during the lifetime of the spacecraft. For this study we have analyzed all of the available telemetry during the 3.5-year lifetime of Imp 6, from March 13, 1971, to October 1, 1974. The region of the magnetic meridional plane sampled by Imp 6 during this period is shown in Figure 1 for a representative range of magnetic local times (2300–0100) near local midnight. It is evident from Figure 1 that the Hawkeye 1 and Imp 6 spacecraft together provide coverage over a very broad region. The detailed coverage tends to vary somewhat with local time, but in general, along the auroral field lines, all altitudes above about 4 R_E are sampled by these two spacecraft. In some local time ranges a small hole in the coverage occurs near the magnetic equator at radial distances of about 4–5 R_E . This small hole in the coverage is not particularly relevant for the region of interest in this study.

Since the details of both the Hawkeye 1 and the Imp 6 plasma wave experiment have been described in previous reports [Kurth *et al.*, 1975; Gurnett and Shaw, 1973], only a few brief comments are made concerning the plasma wave instrumentation. Both experiments use long electric antennas, 42.45 m from tip to tip for Hawkeye 1 and 92.5 m from tip to tip for Imp 6. Magnetic field measurements are obtained from a search coil antenna on Hawkeye 1 and from a single turn loop antenna on Imp 6. The frequency range of the Hawkeye 1 instrumentation, 1.78 Hz to 178 kHz, is somewhat larger than the frequency range of the Imp 6 instrumentation, 36 Hz to 178 kHz. Both experiments provide electric field intensities in 16 frequency channels, extending with an approximately constant fractional frequency spacing over the entire frequency range, and wide-band wave form measurements for high-resolution frequency-time spectrograms.

Plasma measurements were acquired with an electrostatic analyzer, a low-energy proton and electron differential energy analyzer (Lepede) [cf. Frank, 1967], on board Hawkeye 1. Directional differential intensities of positive ions and electrons over the energy range 50 eV $\leq E \leq 40$ keV are telemetered for directions perpendicular to the spacecraft spin

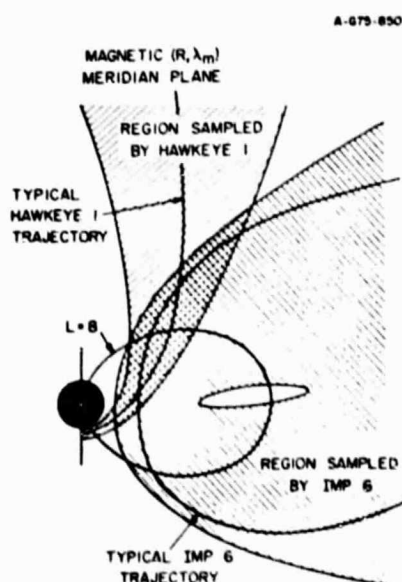


Fig. 1. Typical trajectories and the boundaries of the region sampled by Hawkeye 1 and Imp 6 in the magnetic meridional plane (geocentric radial distance and magnetic latitude coordinates). Secular changes in the orbit provide coverage over a wide range of magnetic latitudes. The measurements analyzed include 14 months of data from Hawkeye 1 and 3.5 years of data from Imp 6.

axis. A collimated thin-windowed Geiger-Mueller (GM) tube was employed for determining directional intensities of electrons with $E > 45$ keV.

The Hawkeye 1 magnetometer is a three-orthogonal-axis flux gate instrument constructed by the Schonstedt Instrument Company. The sensor package is mounted at the end of a boom 1.22 m from the closest face of the spacecraft and 1.57 m from its rotational axis. The magnetometer has four sensitivity ranges on each axis, selectable by ground command: ± 150 , ± 450 , $\pm 1,500$, and $\pm 25,000$ γ . Instrumental accuracy is $\pm 0.5\%$ of full range on each axis in each range. The frequency response is flat from 0 to 1 Hz and down 3 dB at 10 Hz, rolling off at higher frequencies at 6 dB/octave. The analog outputs of

the three axes are sampled simultaneously, at approximately equal intervals of 1.92 s, with 8-bit resolution.

SOME REPRESENTATIVE PLASMA WAVE OBSERVATIONS AT HIGH LATITUDES

To illustrate the main characteristics of the plasma wave observations obtained by Hawkeye 1 and Imp 6 on the auroral L shells, we first discuss four typical passes through the high-latitude region of the magnetosphere. These passes, which are shown in Figures 2-5, were selected to illustrate the variety of plasma wave phenomena detected in this region at various local times. The data in Figures 2, 3, and 4 are from Hawkeye 1 passes in the local dawn, local morning, and local afternoon,

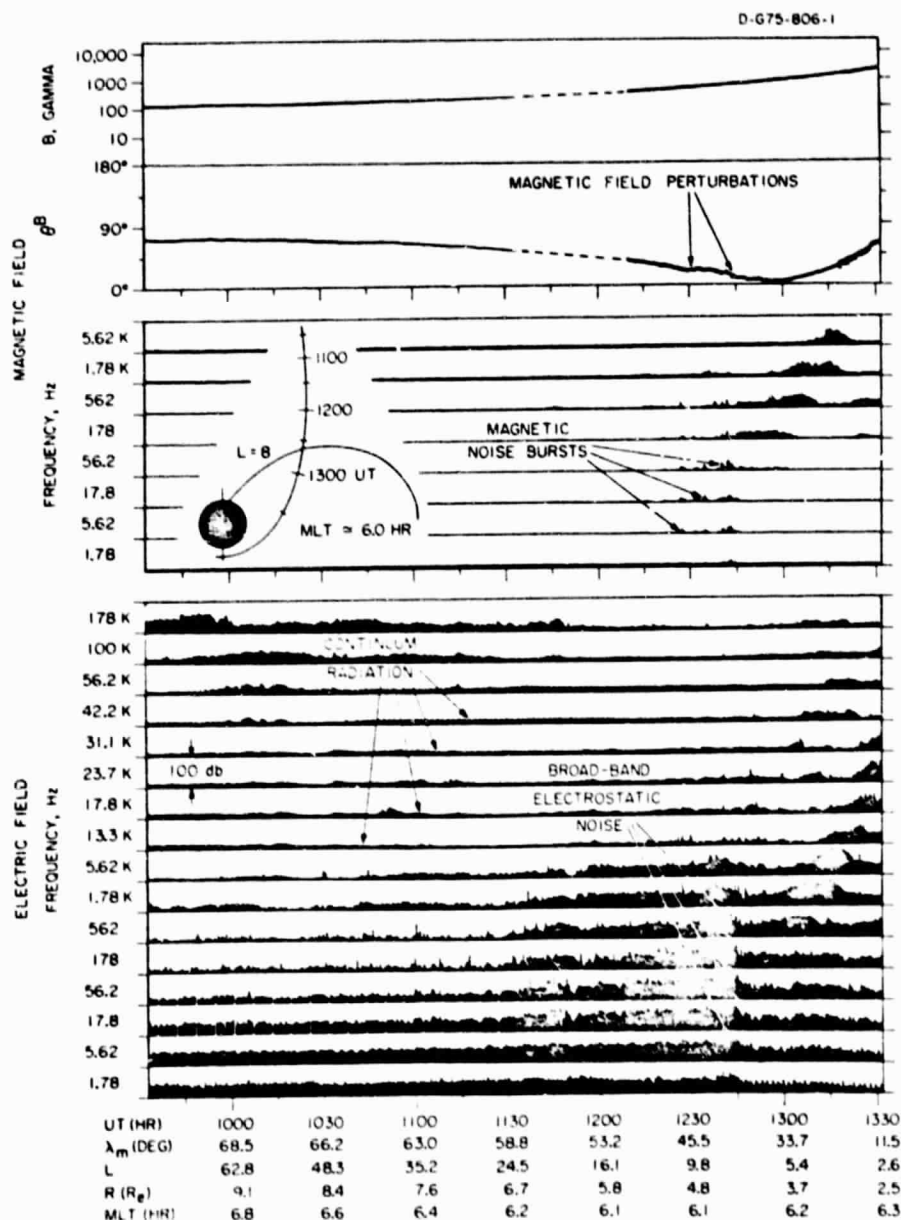
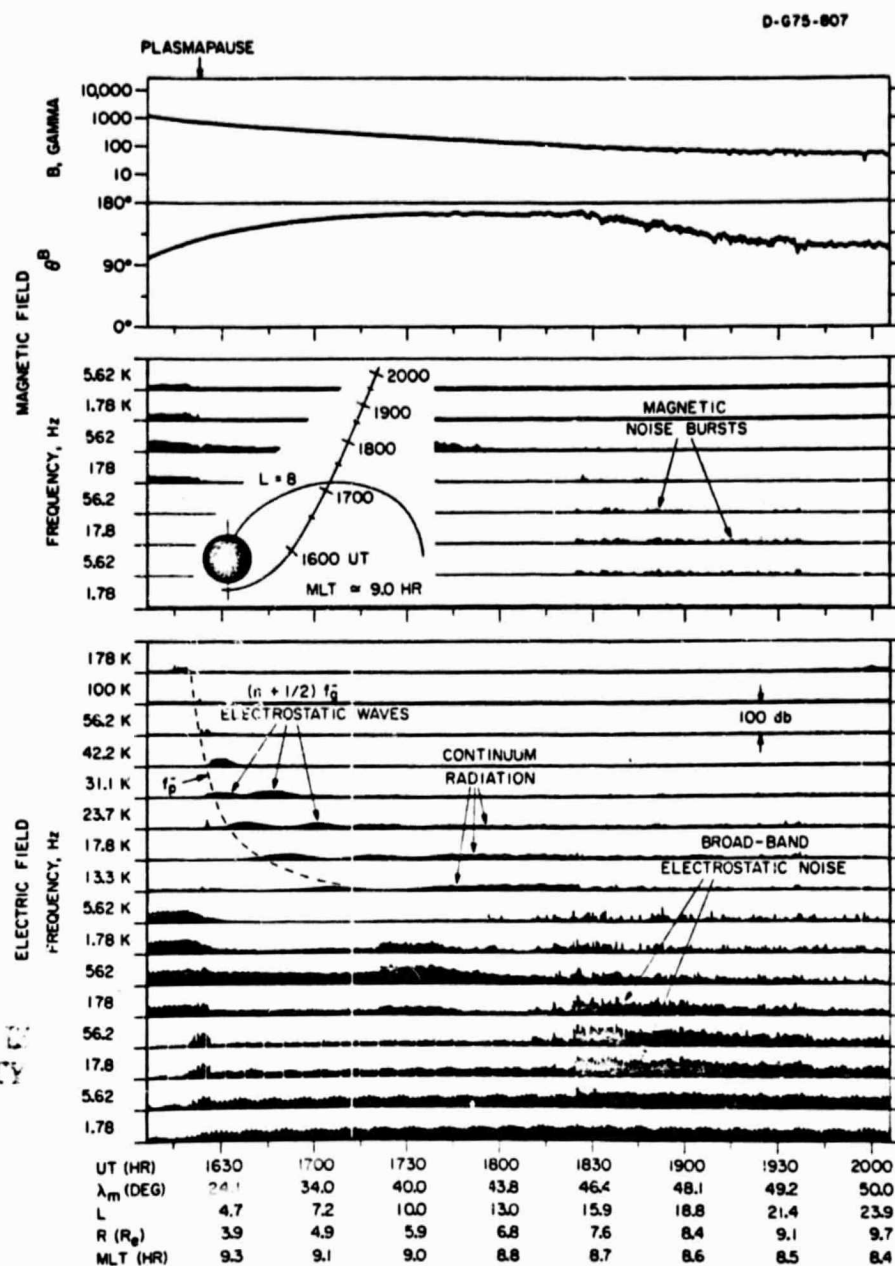


Fig. 2. A representative Hawkeye 1 pass near local dawn. A region of intense broad-band electrostatic noise and magnetic noise bursts is evident from about 1225 to 1244 UT. Perturbations in the magnetic field direction θ^B indicate the presence of field-aligned currents in this region.



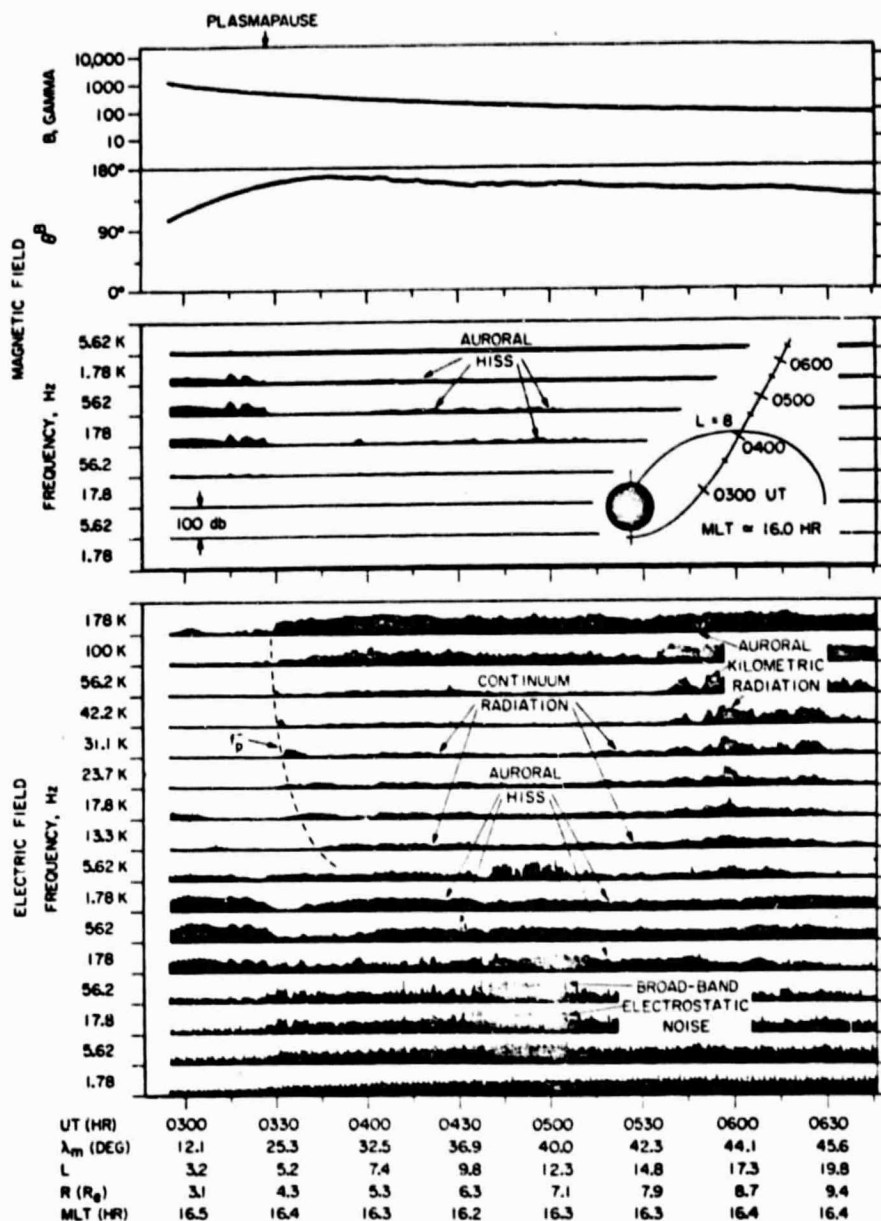
HAWKEYE 1, DAY 50, FEB 19, 1975

Fig. 3. A representative Hawkeye 1 pass at local morning. A broad region of intense broad-band electrostatic noise and magnetic noise bursts is evident from about 1825 to 1940 UT, which accompanies a distinct skewing in the magnetic field direction and magnetic fluctuations. The distinct cutoff in the continuum radiation at about 1825 UT indicates an abrupt increase in the plasma density at this time.

respectively, and the data in Figure 5 are from an Imp 6 pass near local midnight. The top panel of each illustration shows the magnetic field magnitude and direction, and the center and bottom panels show the plasma wave magnetic and electric field intensities. The angle θ^B in Figures 2, 3, and 4 is the angle between the magnetic field and spacecraft spin axis, and the angle ϕ^B in Figure 5 is the azimuthal direction of the magnetic field in solar magnetospheric coordinates. Because of a failure in the Hawkeye 1 attitude determination system after 3 months in flight, θ^B is the only magnetic field orientation angle that is available at present for the periods shown in Figures 2, 3, and 4. (This shortcoming is being remedied in subsequent work using data from the scientific instruments themselves to

reconstruct the spacecraft attitude.) The wave magnetic field intensities are shown in 8 frequency channels, from 1.78 Hz to 5.62 kHz for Hawkeye 1 and from 36.0 Hz to 1.78 kHz for Imp 6, and the electric field intensities are shown in 16 frequency channels, from 1.78 Hz to 178 kHz for Hawkeye 1 and from 36.0 Hz to 178 kHz for Imp 6. The intensity scale for each channel is proportional to the logarithm of the field strength, with a range of 100 dB from the base line of one channel to the base line of the next higher channel. For the Hawkeye 1 measurements, every sample is plotted. For the Imp 6 data the dots give the peak field strengths, and the vertical bars give the average field strengths over intervals of 81.92 s.

The first representative pass (in Figure 2) is an inbound



HAWKEYE I, DAY 313, NOV 9, 1974

Fig. 4. A representative Hawkeye I pass at local afternoon. The broad-band electrostatic noise in this case occurs centered on a region of auroral hiss emission, similar to Figure 14. No magnetic noise bursts are detected during this pass.

Hawkeye I pass near local dawn at about 0600 magnetic local time. The spacecraft trajectory in the magnetic meridian plane (R, λ_m coordinates) for this pass is shown by the small sketch in the center panel of Figure 2. Several types of plasma wave emissions are present during this pass. In the high-frequency (13.3–178 kHz) electric field channels, two types of electromagnetic emissions called auroral kilometric radiation and continuum radiation [Gurnett, 1974, 1975] are detected throughout most of this pass. These electromagnetic emissions occur at frequencies above the local plasma frequency and are generated in regions of higher plasma density near the earth. Deep within the magnetosphere, at L values less than 4, plasmaspheric hiss [Russell *et al.*, 1969] is evident in both the electric and the magnetic field channels at frequencies from

about 562 Hz to 5.62 kHz, increasing in frequency toward lower L values. At lower frequencies, from about 5.62 Hz to 1.78 kHz, a region of very intense electric field noise can be seen from about 1145 to 1245 UT. The intensity of this noise increases gradually with decreasing radial distance and reaches peak intensity in the 17.8- and 56.2-Hz channels at about 1240 UT ($L \approx 8.1$), followed by a very abrupt decrease in the intensity at about 1244 UT. At the time of maximum intensity this noise is very intense, with a broad-band rms electric field strength of 10.8 mV m^{-1} and a peak intensity of about 35 mV m^{-1} . Since this noise occurs over a broad range of frequencies and is most evident in the electric field data, we refer to this noise as broad-band electrostatic noise. This name is the same as was used for a similar type of noise detected by the Imp 8

D-675-891-3

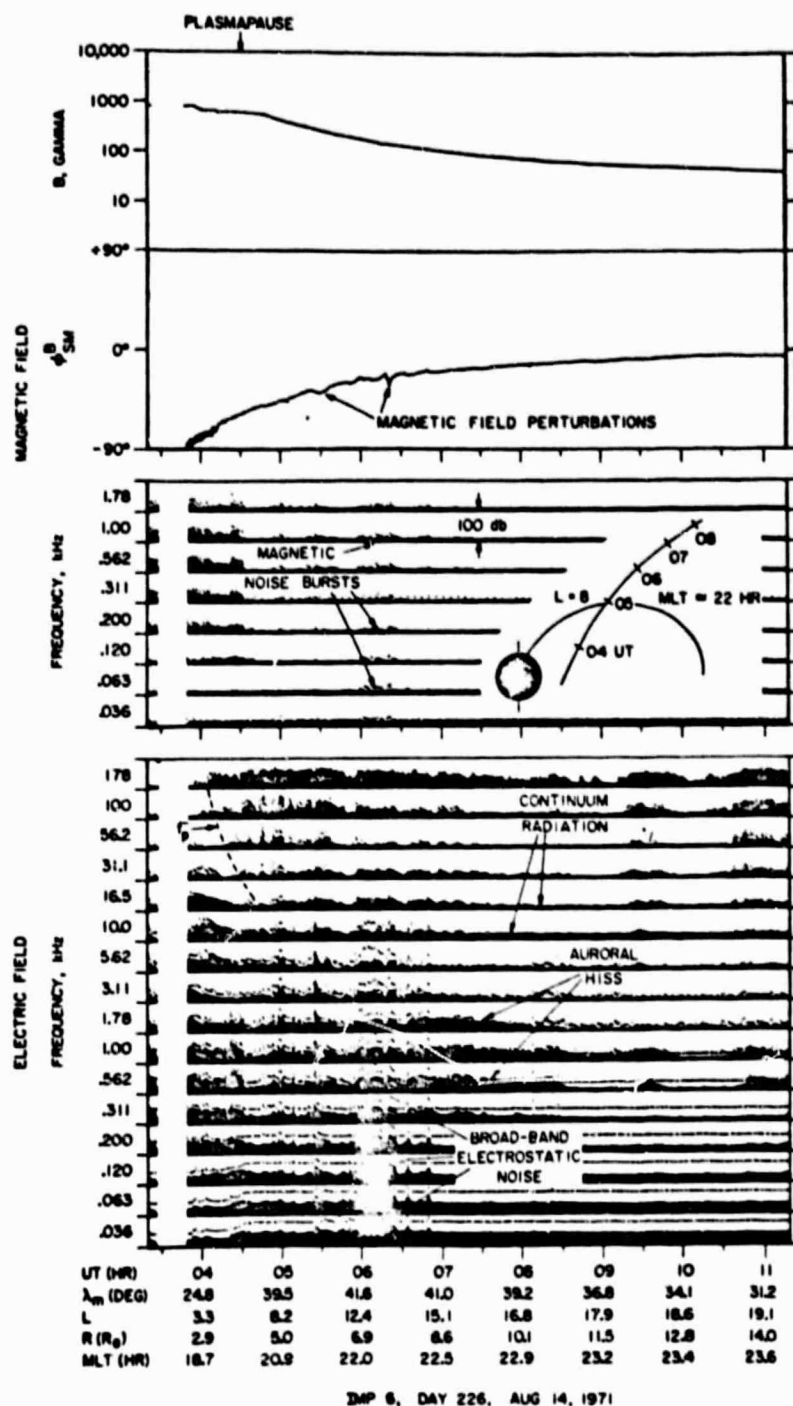


Fig. 5. A representative Imp 6 pass, again at local evening. The dots and vertical bars give the peak and average field intensities, respectively. The broad-band electrostatic noise is very intense in the low-frequency electric field channels, ≤ 120 Hz, and extends with detectable intensities to frequencies above 10 kHz.

spacecraft in the distant magnetotail [Gurnett *et al.*, 1976]. As will be discussed later, these two types of noise are believed to be essentially identical, which justifies the use of the same terminology, although this association remains a matter of later interpretation. The term electrostatic is used because, as will be shown, the electric to magnetic field ratio is much larger than would be expected for any of the usual electromagnetic modes which occur in a plasma. Broad-band electrostatic noise of the type shown in Figure 2 is frequently detected by

Hawkeye 1 and Imp 6 on the high-latitude auroral field lines and is the main topic of this paper.

In the same region as the broad-band electrostatic noise, numerous bursts of low-frequency (1.78–562 Hz) magnetic field noise are also evident in Figure 2. As will be shown, the spectrum of these magnetic noise bursts is distinctly different from the spectrum of the broad-band electrostatic noise. The temporal variations are also quite different. The magnetic noise usually consists of many short transient bursts, whereas

the broad-band electrostatic noise has a more nearly constant amplitude. Thus even though both types of noise occur in the same region and in the same general frequency range, these emissions apparently consist of two distinctly different plasma instabilities. In this paper the low-frequency magnetic noise of the type shown in Figure 2 will be called magnetic noise bursts.

The second representative pass (Figure 3) is an outbound Hawkeye 1 pass in the local morning at about 0900 MLT. No auroral kilometric radiation is detectable in the high-frequency electric field channels during this pass. A very weak level of continuum radiation is evident in the 13.3- to 23.7-kHz channels at radial distances beyond about $6.0 R_E$. In the region beyond the plasmapause, after about 1555 UT, several distinct noise bands are evident, sweeping downward in frequency from about 56.2 to 13.3 kHz. These noise bands are $(n + \frac{1}{2})f_{ce}$ electrostatic cyclotron harmonic emissions of the type discussed by Shaw and Gurnett [1975]. As indicated by the dashed line in Figure 3, the local electron plasma frequency f_{pe} can be estimated from the frequency at which these emissions occur. Inside the plasmapause, before about 1555 UT, plasmaspheric hiss is evident in both the electric and the magnetic field channels from about 178 Hz to 5.62 kHz. Starting at about 1825 UT and extending to about 1940 UT, a region of intense broad-band electrostatic noise is evident, with characteristics very similar to the example in Figure 2. In this same region, many distinct magnetic noise bursts are also clearly evident in the low-frequency (1.78–178 Hz) magnetic field channels.

The third representative pass (Figure 4) is an outbound Hawkeye 1 pass in the local afternoon at about 1600 magnetic local time. The plasma wave activity during this pass is more complicated than that for the two preceding examples. In the high-frequency electric field channels, above about 10 kHz, very high intensities of auroral kilometric radiation are present throughout most of this pass. At the plasmapause, which is located at about 0330 UT, an abrupt cutoff is evident in the auroral kilometric radiation. This cutoff occurs when the local electron plasma frequency f_{pe} exceeds the wave frequency. In this same region, some rather poorly defined $(n + \frac{1}{2})f_{ce}$ electron cyclotron harmonics, similar to those in Figure 3, can be seen sweeping downward in frequency near the electron plasma frequency, indicated by the dashed lines in Figure 4. Beyond the plasmapause, continuum radiation can be seen extending down to frequencies of about 5 kHz. Although not evident in Figure 4, the wide-band wave form data show a distinct low-frequency cutoff at a frequency which varies from about 5 kHz at 0430 UT to about 2 kHz at 0600 UT. This cutoff has been used to estimate the electron plasma frequency in this region, as indicated in Figure 4. At slightly lower frequencies, in the 178-Hz to 1.78-kHz channels, a relatively steady band of noise is evident, extending over a broad region beyond about 0345 UT. On the basis of detailed examinations of high-resolution spectrograms of the wide-band wave form data, as will be discussed in a later section, this noise is identified as auroral hiss, a type of whistler mode emission which is commonly observed in the auroral zone by low-altitude satellites [Gurnett, 1966; Laaspere et al., 1971; Gurnett and Frank, 1972a]. The magnetic field of the auroral hiss is also evident in the corresponding magnetic field channels. At even lower frequencies, in the 17.8- and 56.2-Hz electric field channels, a distinct enhancement can be seen in the electric field intensity from about 0437 to 0505 UT. This noise is identified as broad-band electrostatic noise of the same type as that shown in Figures 2 and 3. No magnetic noise bursts comparable to those shown in Figures 2 and 3 are observed during this pass.

The fourth representative pass (Figure 5) is an outbound Imp 6 pass near local midnight at about 2330 magnetic local time (at $R = 4.9 R_E$). The plasma wave phenomena occurring during this pass are even more complicated and difficult to analyze than the preceding example. Although essentially the same plasma wave phenomena (auroral kilometric radiation, continuum radiation, plasmaspheric hiss, auroral hiss, and broad-band electrostatic noise) occur during this pass, in some cases it is very difficult to distinguish the different types of emissions. However, several distinct regions with intense broad-band electrostatic noise can be easily identified, the first at about 0527 UT, followed by several broad regions from about 0558 to 0625 UT, and the last at about 0650 UT. The enhanced electric field intensities associated with these regions are very clear and distinct, particularly in the peak field strength measurements. Again the maximum electric field intensities occur at low frequencies, from about 36 to 120 Hz, although some bursts of noise can be detected at frequencies as high as 10 kHz. At high frequencies, particularly in the 5.62-kHz channel, the ratio of peak to average field strengths is quite large (~ 50 dB), indicating that at these frequencies the broad-band electrostatic noise is very impulsive, consisting of many brief but intense bursts. Magnetic noise bursts are also clearly evident in the same region in which the broad-band electrostatic noise occurs.

The four passes which have just been discussed are intended to illustrate the types of plasma waves observed by Hawkeye 1 and Imp 6 in the high-latitude region of the magnetosphere. It is evident in these passes and many other similar passes which have been examined that a distinct, easily identified region of low-frequency electric field turbulence is present on the high-latitude auroral field lines at essentially all local times. The main observational characteristics of this turbulence, which has been called broad-band electrostatic noise, are that (1) it is very intense, with electric field strengths up to 10 mV m^{-1} and occasionally larger, (2) it is most intense in the frequency range of about 10–50 Hz, and (3) it occurs over a relatively wide region, usually several degrees in magnetic latitude, at L values of typically 8–12. The detailed characteristics of this noise are described in the following sections.

FREQUENCY SPECTRUMS

A typical frequency spectrum of the broad-band electrostatic noise is shown in Figure 6. This spectrum was selected from the Hawkeye 1 pass in Figure 2 at about the time of peak intensity, from 1240 to 1243 UT. The two spectrums shown in Figure 6 give the peak and average electric field spectral densities from each frequency channel during this interval. The rms electric field strength obtained by integrating the average electric field spectral density over all frequencies is 10.8 mV m^{-1} , and the corresponding peak electric field strength is about 35.6 mV m^{-1} . The main contribution to the rms electric field strength comes from the frequency range of about 10–50 Hz. At high frequencies, above about 100 Hz, the electric field intensity decreases very rapidly with increasing frequency, and a moderately sharp cutoff is evident at about 10 kHz. This upper cutoff occurs near the local electron gyrofrequency f_{ce} . At low frequencies, below about 10 Hz, the electric field intensity decreases with decreasing frequency, and a distinct maximum occurs in the frequency spectrum at about 20 Hz. As indicated in Figure 6, this maximum is in the frequency range between the local proton gyrofrequency f_{cp} and the hybrid frequency $(f_{ce} f_{cp})^{1/2}$. The exact shape of the spectrum at frequencies below about 10 Hz is somewhat uncertain because of the high levels of spacecraft-generated interference

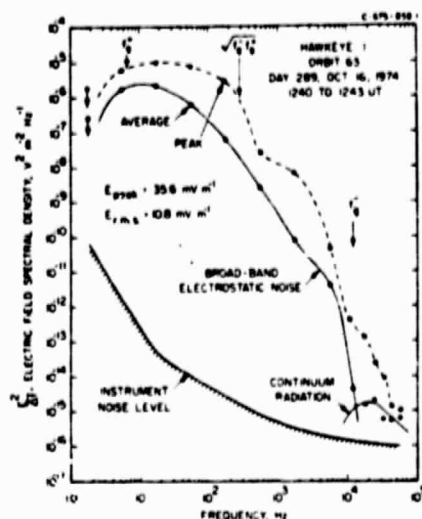


Fig. 6. An electric field spectrum of the broad-band electrostatic noise at about the time of maximum intensity for the pass shown in Figure 2. This event is typical of the most intense events of this type detected by either Hawkeye 1 or Imp 6.

(from the solar panels) at these low frequencies. Usually, the broad-band electrostatic noise is not detectable in the 1.78-Hz electric field channel, and the largest field strengths are detected in either the 17.8- or the 56.2-Hz channel.

To compare the electric field and magnetic field spectrums, the magnetic field spectrum for the same interval is shown in Figure 7. Again both peak and average spectrums are shown. The magnetic noise intensities are seen to be significantly above the instrument noise levels for all frequencies below about 1.0 kHz. Both the peak and the average magnetic field intensities show a distinct maximum in the spectrum at about 50 Hz. This maximum is associated with the magnetic noise bursts indicated in Figure 2. The rms and peak magnetic field strengths of this noise, integrated from 5.6 Hz to 1.78 kHz, are about 5.8 and 36.8 mV, respectively. The large difference between the peak and average field strengths is caused by the large fluctuations in the field strengths which are clearly evident in Figure 2. The ratio of the average electric field energy density to the average magnetic field energy density in this case is $E^2/C^2B^2 \approx 39$, which confirms the electrostatic (or at least quasi-electrostatic) character of the broad-band electrostatic noise detected in this region. Below about 10 Hz, a weak low-frequency component is evident slightly above the receiver noise level, increasing in intensity toward lower frequencies. This monotonic low-frequency component is probably associated with the magnetic field perturbations evident in the θ^B angle at about this time (see Figure 2). Whether this low-frequency component represents an ambient wave spectrum, as is almost certainly the case for the magnetic noise bursts detected at higher frequencies, or simply the spacecraft motion through spatial gradients in the magnetic field cannot be determined.

Further details regarding the frequency-time structure of these emissions can be obtained from the wide-band wave form data. High-resolution frequency-time spectrograms of the broad-band electrostatic noise and magnetic noise bursts observed during the Imp 6 pass in Figure 5 are shown in Figure 8. Two different frequency scales, 0–1 kHz and 0–200 Hz, are used to provide good frequency resolution over the entire frequency range. For the mode of operation being used

during this pass the wave form receiver alternately switches between the electric and magnetic antennas once every 20.48 s. The electric field spectrums of the broad-band electrostatic noise in Figure 8 show remarkably little temporal structure. The rapid decrease in the intensity with increasing frequency is clearly evident. A few impulsive bursts can be seen extending to frequencies above 1 kHz. At low frequencies a distinct low-frequency cutoff is evident at a frequency which varies from about 20 to 50 Hz. Although this cutoff is near the low-frequency limit of the wave form receiver, the temporal variations show that this cutoff is not caused by instrumental effects. At certain times, for example, at about 0619:25 and 0620:10 UT, the noise becomes very intense near this cutoff and develops into a strong emission at about 50 Hz. Comparisons between successive electric and magnetic spectrograms show that the magnetic field spectrum is quite different from the electric field spectrum. Generally, the magnetic field intensities are very low, and it is very difficult to clearly identify the magnetic noise bursts evident in the magnetic field channels of Figure 5. The magnetic noise bursts usually comprise poorly defined emissions lasting only a few seconds at about 50–100 Hz, as evident, for example, at about 0619:55 and 0620:34 UT in Figure 8. Occasionally, as at about 0620:33 UT, a diffuse burst with a rapidly varying center frequency can be seen extending to frequencies above 1 kHz. In some cases it appears that the strong electric field enhancements near the lower cutoff frequency of the broad-band electrostatic noise may be directly associated with the quasi-monochromatic magnetic noise bursts. Unfortunately, we do not have suitable simultaneous electric and magnetic field spectrograms to definitely establish this relationship.

REGION OF OCCURRENCE

The examples of broad-band electrostatic noise which have been shown have all been at L values typical of the auroral field lines. We would now like to definitely establish the region of occurrence of this noise, using the extensive measurements obtained by Hawkeye 1 and Imp 6. Since an extremely large number of measurements are to be surveyed (14 months of data from Hawkeye 1 and 3.5 years of data from Imp 6), a simple criterion must be used to provide automatic computer identification of the broad-band electrostatic noise. As has

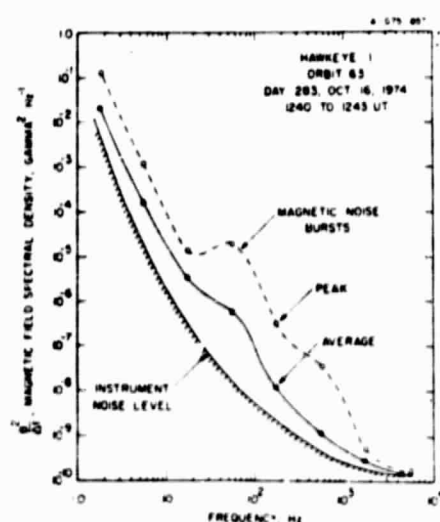


Fig. 7. A magnetic field spectrum of the magnetic noise bursts detected during the same interval as the spectrum in Figure 6.

ORIGINAL PAGE IS
PHOTOCOPIED

C-676-8-2

IMP-6, ORBIT 38, AUGUST 14, 1971

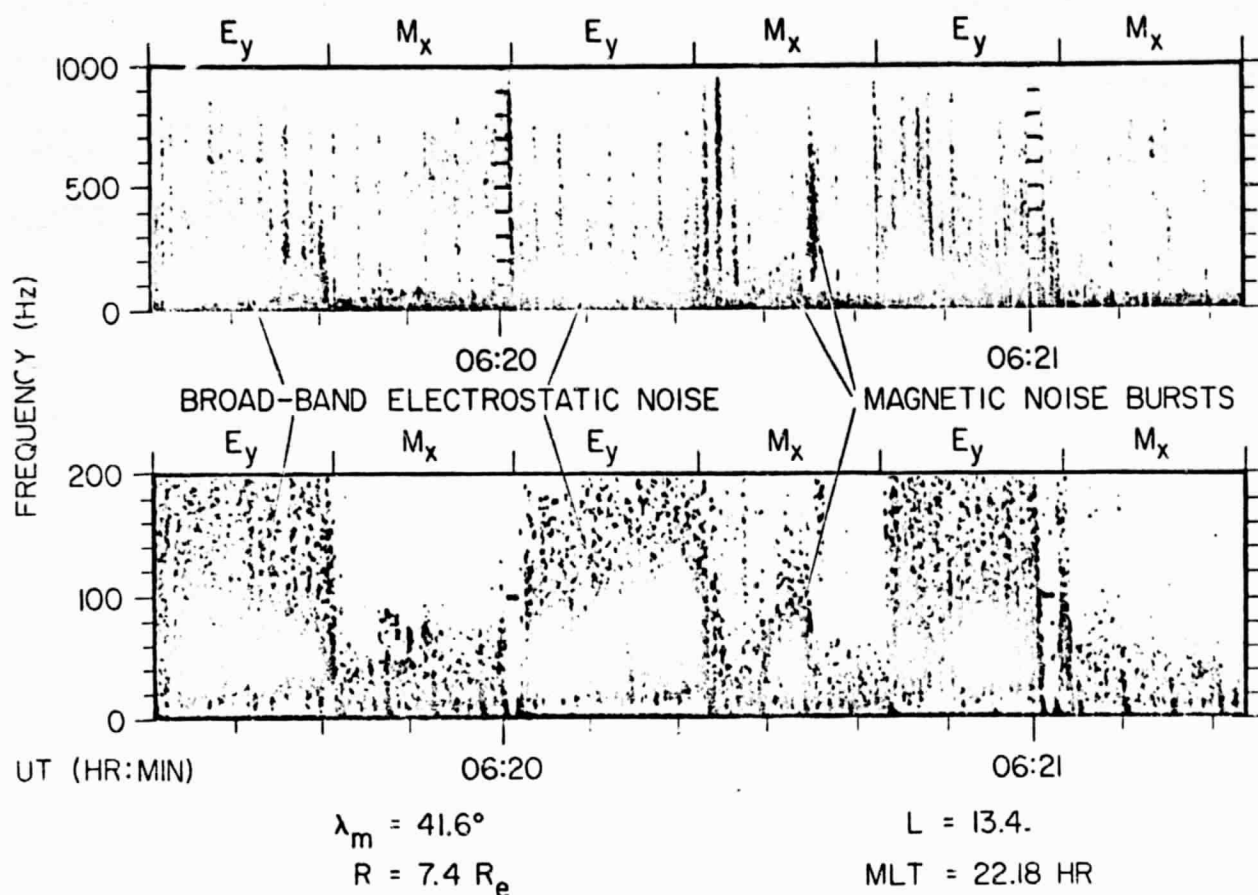


Fig. 8. Wide-band frequency-time spectra of the electric (E_y) and magnetic (M_x) fields detected by Imp 6 during a period of enhanced broad-band electrostatic intensity during the pass shown in Figure 5. The spectrum of the broad-band electrostatic noise shows little structure at low frequencies except for a distinct low-frequency cutoff at about 20–50 Hz. The magnetic noise bursts are also very diffuse and difficult to identify.

been previously discussed, the broad-band electrostatic noise is usually most intense in the frequency range of about 10–50 Hz. Fortunately, except for the earth's bow shock, no other type of magnetospheric plasma wave emission has electric field intensities comparable to the broad-band electrostatic noise in this frequency range. The broad-band electrostatic noise can therefore be identified with good reliability on the basis of the low-frequency electric field intensities. For this study we have chosen to use the peak electric field intensities in the 56.2-Hz channel of Hawkeye 1 and in the 63.0-Hz channel of Imp 6 for identifying these events. Several electric field thresholds have been tried, and a threshold electric field spectral density of $1.4 \times 10^{-7} \text{ V}^2 \text{ m}^{-2} \text{ Hz}^{-1}$ has been selected. This threshold represents a reasonable compromise between obtaining too few events if the threshold is set too high and obtaining too many false identifications from other plasma wave phenomena if the threshold is set too low.

Figures 9 and 10 show the magnetic meridian plane (R, λ_m) coordinates of all of the events in the 14 months of Hawkeye 1 data and 3.5 years of Imp 6 data which exceed the selected

threshold. Figure 9 shows the events which occurred in magnetic local time quadrants centered on local noon (0900–1500 MLT) and local midnight (2100–0300 MLT), and Figure 10 shows the corresponding data for local dawn (0300–0900 MLT) and local dusk (1500–2100 MLT). Each point represents a specific interval, 184.3 s for Hawkeye 1 and 327.6 s for Imp 6, during which the electric field intensity exceeded the selected threshold. The approximate outline of the combined region sampled by the two spacecraft is indicated by the dashed lines in each quadrant. Although these plots do not provide a precise indication of the frequency of occurrence because of the difference in the number of data from each satellite and the complexity of the orbital coverage, they do provide a good qualitative picture of where the broad-band electrostatic noise is observed. Almost without exception the noise is observed on magnetic field lines which connect with the high-latitude auroral regions. The noise is observed over a large range of radial distances, from about $1.5 R_E$ to greater than $15 R_E$. Although most of the events are observed at radial distances greater than about $4 R_E$, this boundary is seen to be

D. 675-853

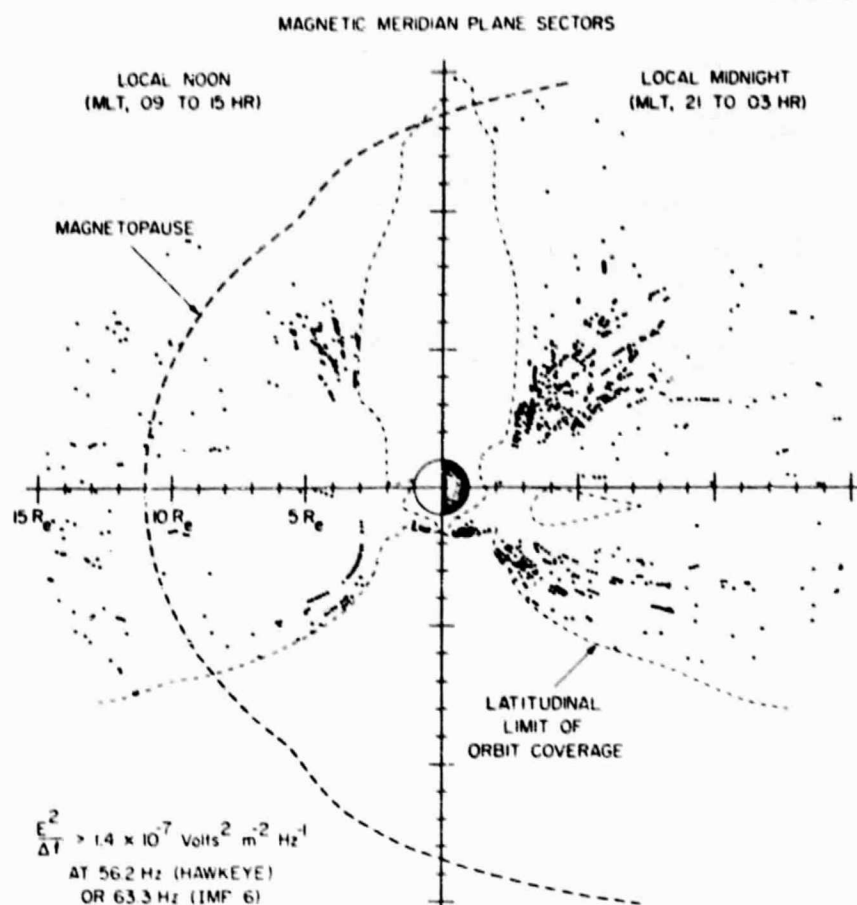


Fig. 9. Magnetic meridional plane (R, λ_m) plots for magnetic local times (MLT) near local noon and local midnight of all the Hawkeye 1 and Imp 6 electric field intensities which exceed a preset threshold. The threshold intensity and frequencies are chosen to provide reasonably reliable identification of intense broad-band electrostatic noise events. A few of the events beyond about $10 R_E$ in the local noon sector are caused by electrostatic noise associated with the bow shock and magnetosheath. Most of the events occur at high magnetic latitudes at L values typical of the auroral field lines.

primarily a limitation imposed by the orbital coverage, since essentially no measurements are obtained on auroral field lines at radial distances between about 1.8 and $4.0 R_E$. A very dense concentration of points can be seen over the southern auroral region at radial distances from about 1.5 to $1.8 R_E$. These data also show that the broad-band electrostatic noise is observed at all local times, although relatively few events are evident in the local noon quadrant. The widely scattered events evident beyond about $10 R_E$ in the local noon quadrant are caused by electrostatic noise associated with the bow shock and magnetosheath and not by broad-band electrostatic noise.

To take into account the effects of the orbital coverage, we have performed a detailed analysis of the frequency of occurrence of the events shown in Figures 9 and 10. For this analysis the R, λ_m and MLT coordinate system has been divided into boxes, and the number of events counted once per orbit and the number of orbits passing through each box are determined. The frequency of occurrence is given by the ratio of the number of events to the number of orbits counted in each box. The essential features of the frequency of occurrence distribution determined from this analysis are summarized in Figures 11 and 12. Figure 11 shows the frequency of occurrence as a function of radial distance and magnetic latitude for magnetic local times in the local midnight quadrant, from about 2100 to 0300 MLT. These data clearly show that the broad-band electrostatic noise occurs in two distinct latitudinally symmetric

regions, starting at high latitudes, $\sim 70^\circ$, near the earth and extending to progressively lower latitudes with increasing radial distance. The two regions appear to merge in the magnetotail at a radial distance of about $10 R_E$. The latitudinal width of the region of occurrence, approximately 20° at $R = 4.01$ and $6.31 R_E$, is several times larger than the latitudinal width typically observed on an individual pass. This increase in the apparent latitudinal width of the region of occurrence is almost certainly caused by the orbit-to-orbit variations of the L shell on which the noise occurs. The regions of occurrence shown in these illustrations must not be viewed as an instantaneous picture of the region in which the noise occurs. At large distances from the earth, $R \geq 10 R_E$, the ability of the magnetic field model (for λ_m and MLT) to represent the real field is also subject to large errors. The tendency of the latitudinal width of the region of occurrence to increase with increasing radial distance is probably due in part to errors of this type. For the threshold used in this analysis the maximum frequency of occurrence is about 20%. Because of temporal variations of the L shell on which the noise is detected a more meaningful parameter is probably the percentage occurrence of the broad-band electrostatic noise during a given pass across the auroral L shells. For the threshold used in Figures 11 and 12 this percentage occurrence is about 50–60% in the region near local midnight. The absolute frequency of occurrence should not be considered of fundamental importance.

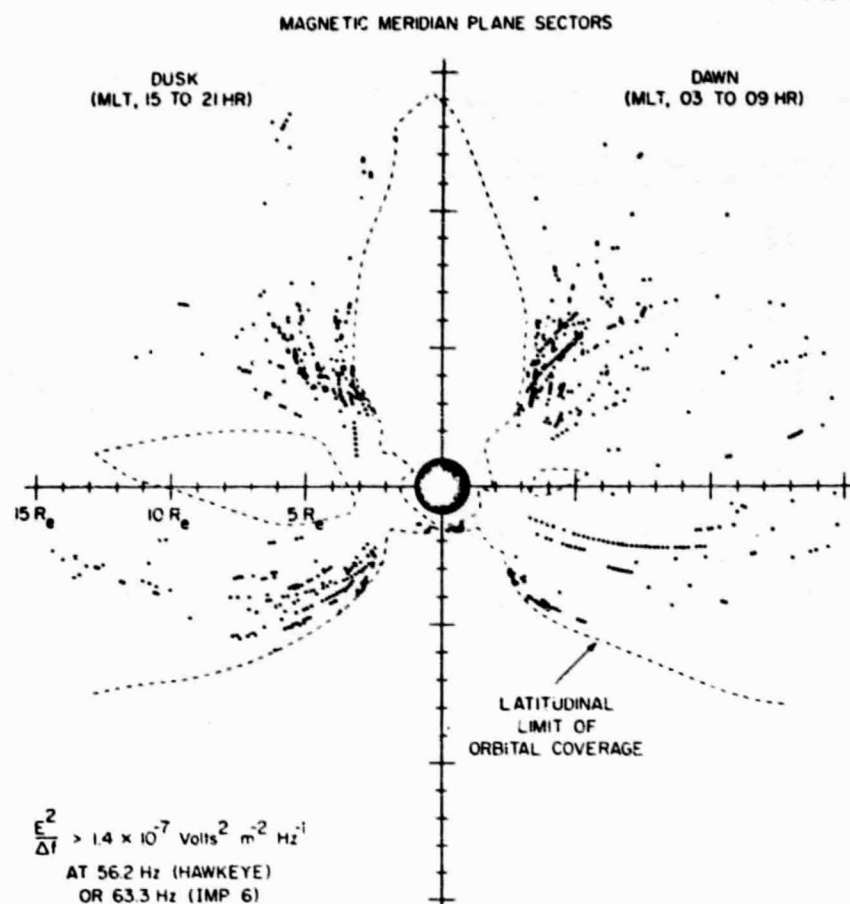


Fig. 10. Magnetic meridian plane plots comparable to Figure 9 for magnetic local times near local dawn and dusk.

since it depends somewhat on the choice of the threshold field strength. However, the region of occurrence on auroral field lines extending back into the distant magnetotail is relatively insensitive to this threshold.

To illustrate the variations in the region of occurrence with magnetic local time, Figure 12 shows the frequency of occurrence as a function of magnetic latitude and magnetic local time at a constant radial distance, $5.01 R_E \leq R < 6.31 R_E$. This range of radial distances was chosen because it is sufficiently far from the earth to provide measurements over a wide range of magnetic latitudes and still close enough for the magnetic field model to be reasonably accurate. For reference, the L value of the magnetic field passing through $R = 5.62 R_E$ is shown on the right side of Figure 12. The broad-band electrostatic noise is seen to occur in an essentially continuous band at all local times around the earth. The noise occurs at the lowest magnetic latitudes near local midnight and at systematically higher magnetic latitudes on the dayside of the earth. Near local midnight the maximum occurrence is at L values from about 8 to 12.

RELATIONSHIP TO AURORAL HISS

Observations

Auroral hiss is a broad-band whistler mode emission commonly observed in the auroral regions by low-altitude polar-orbiting satellites. As is indicated in Figures 4 and 5, auroral hiss has also been observed at high altitudes in the magnetosphere by Hawkeye 1 and Imp 6. Although the broad-band

electrostatic noise sometimes occurs in regions where no auroral hiss can be identified, as in Figures 2 and 3, in some cases these two types of noise occur in the same region of the magnetosphere and appear to be closely related. This relationship is illustrated by the two Hawkeye 1 passes in Figures 13 and 14. Both of these passes occur near local midnight, and the plasma wave phenomena observed are qualitatively similar to Figures 4 and 5. In both cases the auroral hiss emissions are easily identified in the wide-band spectrograms by the characteristic broad-band noise spectrum, with little temporal structure, extending from a few hundred hertz to several kilohertz. A distinct upper cutoff frequency is evident at a frequency slightly below the local electron gyrofrequency (indicated by the dashed lines marked f_{ce}). This cutoff occurs because the whistler mode cannot propagate at frequencies above the electron gyrofrequency. The spectrogram in Figure 13 also clearly shows the distinct gap between the auroral hiss and continuum emissions which is usually not apparent in the coarse frequency resolution measurements (as in Figure 4). The auroral hiss spectrum from about 1100 to 1230 UT in Figure 14, and to some extent in Figure 13, has a distinct V-shaped lower-frequency cutoff which bears an unmistakable similarity to the V-shaped low-frequency cutoff of the auroral hiss observed by low-altitude satellites [see Gurnett, 1966; Gurnett and Frank, 1972a].

In the top panel of Figure 13, several periods of enhanced electric field intensity, characteristic of the broad-band electrostatic noise, can be seen from about 1207 to 1300 UT, between the two regions where the auroral hiss is observed. In

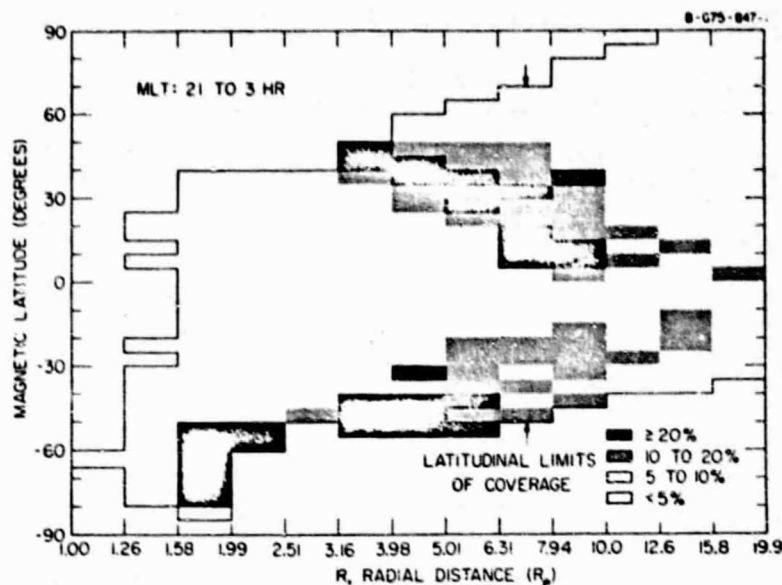


Fig. 11. The normalized frequency of occurrence of the broad-band electrostatic noise as a function of magnetic latitude and radial distance in the 2100-0300 magnetic local time sector near local midnight. The electric field threshold is the same as in Figures 9 and 10.

the wide-band spectrograms the broad-band electrostatic noise appears as a distinct increase in the intensity near the low-frequency limit of the spectrogram. Note that the wide-band spectrograms (which are obtained by using an automatic gain control receiver) show only the relative intensity at different frequencies, whereas the fixed frequency channels give the absolute intensity. Thus even though the wide-band spectrograms indicate that the auroral hiss has completely disappeared in the region where the broad-band electrostatic noise is observed, the fixed frequency channels (1.78 kHz, in particular) show that the auroral hiss intensity actually increases slightly in this region. The broad-band electrostatic noise therefore can be interpreted as a lowering and intensification of the low-frequency portion of the auroral hiss spectrum. This transition from the auroral hiss to the broad-

band electrostatic noise is shown even more clearly by the example in Figure 14. In this case the enhanced electric field intensities in the 56.2-Hz electric field channel place the region of broad-band electrostatic noise from about 1135 to 1200 UT. Inspection of the wide-band spectrograms shows that this noise is essentially indistinguishable from the auroral hiss.

Discussion

Because of the close relationship between the auroral hiss and the broad-band electrostatic noise the question arises whether there is any essential difference between these two types of noise. The auroral hiss detected by Hawkeye 1 and Imp 6 is clearly a whistler mode electromagnetic emission which propagates a considerable distance through the magnetosphere. The simultaneous detection of both the electric and

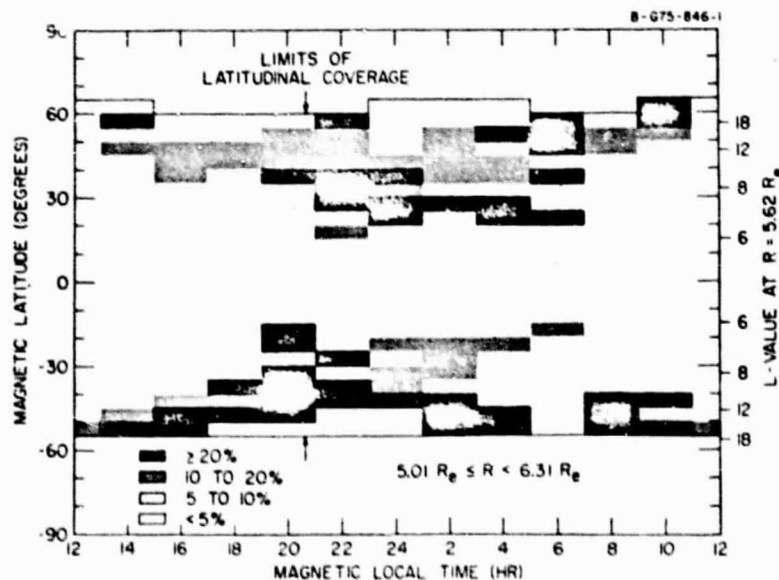
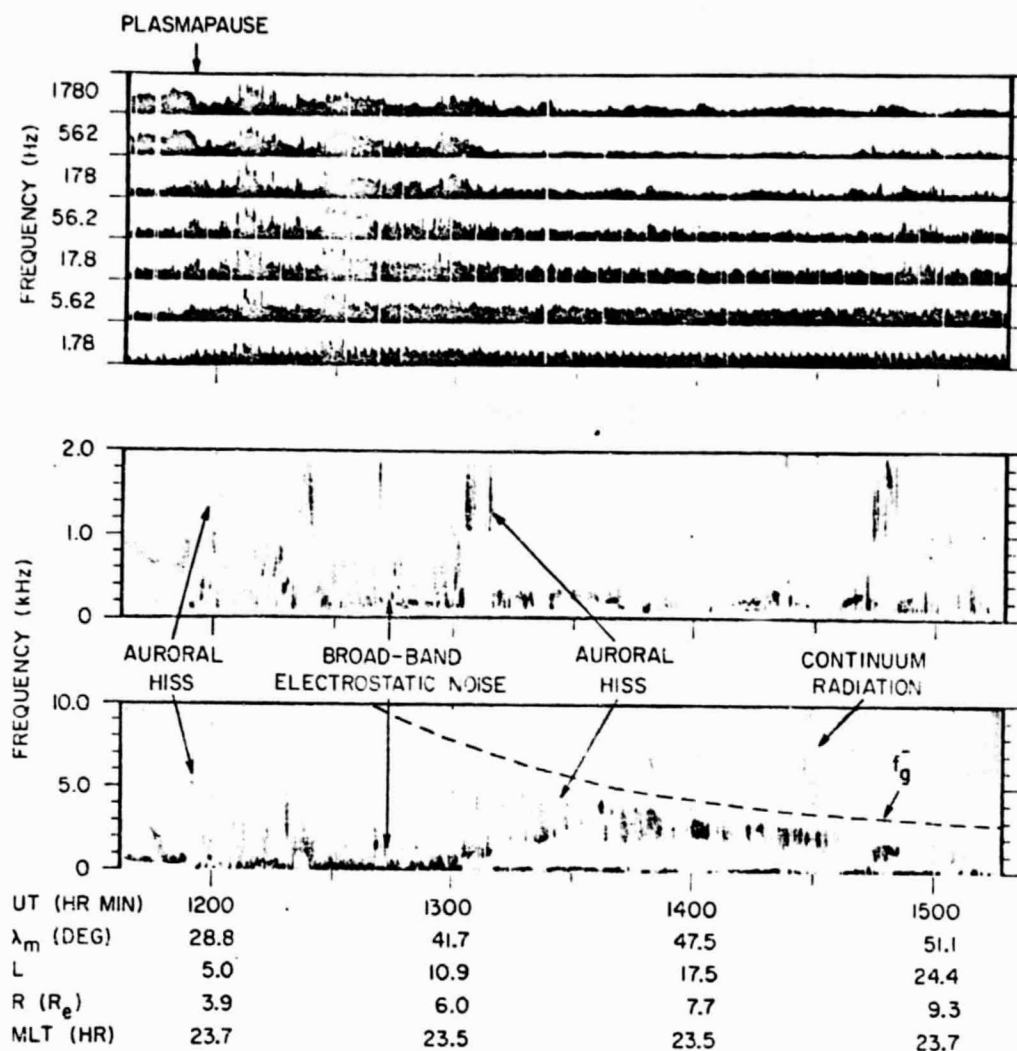


Fig. 12. The normalized frequency of occurrence of the broad-band electrostatic noise as a function of magnetic latitude and magnetic local time within the radial distance range $5.01 R_e$ – $6.31 R_e$. The L value of the magnetic field line which intersects $R = 5.62 R_e$ is shown on the right for comparison with low-altitude measurements.



HAWKEYE-1, DAY 193, JULY 12, 1974

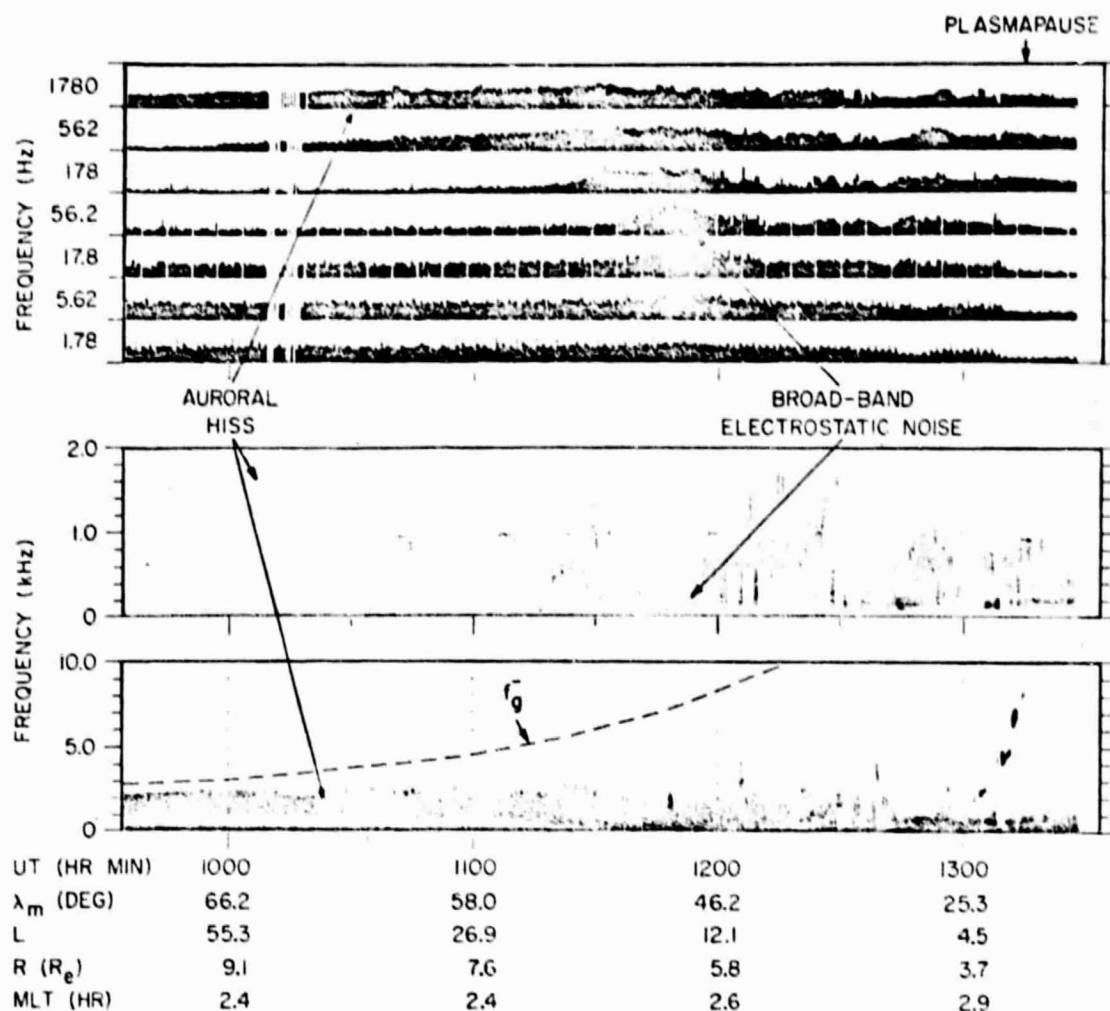
Fig. 13. Frequency-time spectrograms showing the relationship between auroral hiss and broad-band electrostatic noise during an outbound Hawkeye 1 pass near local midnight. The broad-band electrostatic noise sometimes appears as a lowering and intensification of the low-frequency cutoff of the auroral hiss spectrum. The distinct cutoff of the auroral hiss at a frequency slightly below the local electron gyrofrequency f_g^- and the gap between the auroral hiss ($f < f_g^-$) and continuum radiation ($f > f_g^-$) are clearly evident.

he magnetic field of the auroral hiss, as in Figure 4, shows that the emission is an electromagnetic wave, and the frequency range $f < f_g^-$ unmistakably identifies the mode of propagation as the whistler mode. The V-shaped low-frequency cutoff of the auroral hiss can be explained from simple ray path considerations if the noise is generated along an auroral field line below the spacecraft, as shown in Figure 15. It is a well-known characteristic of the whistler mode that the ray paths are guided somewhat along the magnetic field line and that this guiding effect is frequency dependent. If the emission is generated at wave normal directions near the resonance cone, as is thought to be the case for auroral hiss observed at low altitudes [Taylor and Shawhan, 1974], then the angle that the ray path makes with respect to the magnetic field increases with increasing frequency, varying from 0° at the lower hybrid resonance frequency f_{LH} to 90° at the electron gyrofrequency. This frequency dependence causes the ray paths to deviate

increasingly from the magnetic field line as the wave frequency approaches the electron gyrofrequency. The effect of this frequency dependence is to allow the emission to be observed over a larger spatial region at higher frequencies (compare f_1 and f_2 in Figure 15), thus producing the V-shaped low-frequency cutoff.

In contrast to the electromagnetic auroral hiss, which propagates large distances from the L shell on which it was generated, the broad-band electrostatic noise is observed in a very localized region and has no detectable magnetic field component, as would be expected for a local electrostatic plasma instability. Despite these marked differences the wide-band spectra, as in Figure 14, sometimes show a nearly continuous transition between the auroral hiss and the broad-band electrostatic noise. These observations strongly suggest that the electrostatic noise is closely related to the generation of the auroral hiss. Taylor and Shawhan [1974] have shown that for

ORIGINAL PAGE IS
OF POOR QUALITY



HAWKEYE-1, DAY 336, DEC 2, 1974

Fig. 14. Another case, similar to Figure 13, showing auroral hiss and broad-band electrostatic noise during an inbound Hawkeye 1 pass in the early morning. In this case, no clear distinction can be made between the auroral hiss and the broad-band electrostatic noise.

wave normal directions very close to the resonance cone the whistler mode takes on characteristics of a local electrostatic wave, with short wavelengths, small magnetic field components, and low phase velocities. If the broad-band electrostatic noise is closely coupled to these short-wavelength whistler mode waves or represents an extension of the same plasma wave mode, it seems entirely possible that the auroral hiss is generated directly from this electrostatic noise by changes in the wave normal direction at plasma boundaries and density irregularities. Processes of this type have already been suggested by Maggs [1976] for generation of auroral hiss.

RELATIONSHIP TO MAGNETOSPHERIC PLASMAS AND FIELD-ALIGNED CURRENTS

Observations

We now consider the relationship of the intense electric field turbulence detected by Hawkeye 1 and Imp 6 to the plasmas

and field-aligned currents which are present in the high-latitude auroral regions of the magnetosphere. To illustrate the plasma relationships which are typically observed, Plate 1 shows the charged particle intensities for the inbound Hawkeye 1 pass in Figure 2 during the period in which the intense broad-band electrostatic noise is detected. The top two panels of Plate 1 show the energy-time spectrograms of electron and proton intensities detected by the Lepedea, and the bottom panel gives the counting rate (\log_{10}) of the thin-windowed GM tube. The Lepedea on board Hawkeye 1 provides measurements of the differential energy spectrums of protons and electrons within the energy range $50 \text{ eV} \leq E \leq 40 \text{ keV}$, and the GM tube responds to electrons with energies $E > 45 \text{ keV}$ and protons with energies $E > 650 \text{ keV}$. In comparing Figure 2 and Plate 1 it is evident that the region of intense broad-band electrostatic noise observed during this pass, with maximum intensities from about 1234 to 1244 UT, occurs just before the rapid increase in the GM tube counting rate and in a region

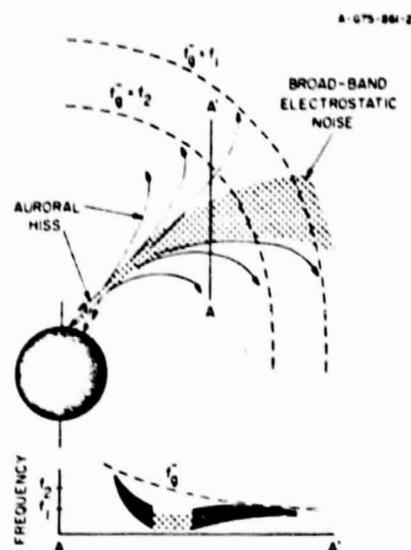


Fig. 15. A qualitative model showing the region of broad-band electrostatic noise and the ray paths of the auroral hiss suggested by events such as in Figure 14. The ray paths of the whistler mode auroral hiss tend to deviate from the local magnetic field direction as the wave frequency approaches the electron gyrofrequency. The frequency dependence of the ray path can account for the V-shaped low-frequency cutoff.

with substantial fluxes of low-energy (~ 1 keV) protons. The rapid increase in the GM tube counting rate at about 1242 UT, which is shown in more detail in Figure 16, marks the entrance into the stably trapped region of the outer radiation zone and is a characteristic boundary called the electron $E > 45$ keV trapping boundary. Low-altitude measurements of convection electric fields show that the $E > 45$ keV trapping boundary usually corresponds closely with the boundary between open and closed magnetic field lines [Frank and Gurnett, 1971; Gurnett and Frank, 1973]. The low-energy electron and proton spectrums in the region in which the broad-band electrostatic noise is observed are characteristic of the high-density plasma typically found in the magnetosheath and polar cusp. The relationship of the electrostatic noise to the $E > 45$ keV trapping boundary and to the low-energy plasma in this case is qualitatively similar to events of the type previously discussed by Scarf *et al.* [1973, 1975]. After crossing the trapping boundary a region of very intense (1–10 keV) electron intensities is encountered from about 1245 to 1310 UT. These more energetic and intense electron fluxes are characteristic of the outer radiation zone during magnetically disturbed periods (a magnetic storm occurred 2 days earlier, on October 14, 1974).

Examination of charged particle measurements similar to those in Plate 1 and Figure 16 for other local times shows that the region of broad-band electrostatic noise is consistently observed near and always on the poleward side of the electron $E > 45$ keV trapping boundary, outside the energetic (1–10 keV) electron intensities characteristic of the plasma sheet and outer radiation zone. The region of intense electric field turbulence is usually characterized by a distinct increase in the low-energy (100 eV to 1 keV) electron and proton intensities. Several types of measurements show that a distinctly different higher-density plasma is encountered in this region. In Figure 3 a sharp cutoff is evident in the continuum radiation (in the 13.3-kHz channel, in particular) at about the time, ~ 1825 UT, that the broad-band electrostatic noise is encountered. The cutoff is almost certainly caused by an abrupt increase in the

plasma frequency and hence plasma density in the region where the broad-band electrostatic noise is observed. This increase in the plasma density is directly confirmed by the Lepede data for this pass illustrated in Plate 2, which shows an abrupt increase in the low-energy (100 eV to 1 keV) electron and proton intensities characteristic of magnetosheath and polar cusp plasma at about 1825 UT. The static electric field measurement on Hawkeye 1, which is very sensitive to changes in the plasma density and temperature, also usually indicates an abrupt discontinuity at the boundaries of the region where the broad-band electrostatic noise is observed.

The Hawkeye 1 magnetic field data have been carefully examined in search of magnetic field perturbations caused by field-aligned currents in the region where the broad-band electrostatic noise is observed. In most cases, no corresponding magnetic field perturbations can be detected. However, in a few cases, magnetic field perturbations occur which are almost certainly associated with field-aligned currents. One of these cases is illustrated in Figure 2. The magnetic field measurements in Figure 2 clearly show numerous small perturbations in the angle θ^H as the spacecraft passes through the region in which the most intense broad-band electrostatic noise is detected. These magnetic field perturbations have not yet been analyzed in detail because of the previously mentioned problem of reconstructing the spacecraft attitude during the periods in question. However, the magnetic field signature given by the angle θ^H , when compared with similar measurements of this type by Aubry *et al.* [1972] and Fairfield [1973], provides convincing evidence that field-aligned currents are present in the region where the broad-band electrostatic noise occurs. Similar magnetic field perturbations indicative of field-aligned currents are also evident in Figure 5 and to a lesser extent in Figure 4. The magnetic field measurements in Figure 3 show a somewhat different magnetic field signature which has been observed several times on the dayside of the earth. In this case a marked change in the slope of θ^H versus time is evident as the spacecraft enters the region of broad-band electrostatic noise at about 1825 UT. As the spacecraft passes through the region of most intense electrostatic noise, from 1830 to 1930 UT, θ^H

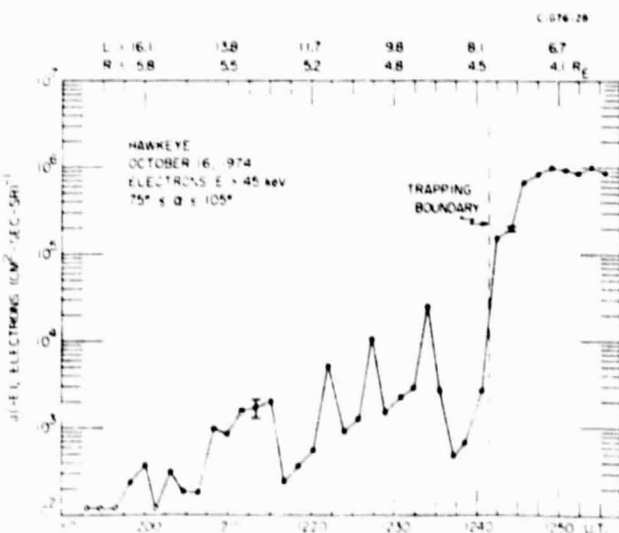


Fig. 16. The electron intensities with $E > 45$ keV, which were obtained with the GM tube for the pass shown in Plate 1. The electron $E > 45$ keV trapping boundary is located at about 1242 UT. This boundary marks the entrance into the stably trapped region of the outer radiation zone.

changes by about 45°, and many small amplitude fluctuations are evident in both the magnitude and the direction of the field. Both the skewing of the magnetic field direction and the small-scale fluctuations indicate that the spacecraft has entered a region of higher β (ratio of the plasma to magnetic field pressure) in which the plasma is producing significant local changes in the magnetic field. The abrupt increase in the low-energy (100 eV to 1 keV) proton intensities, shown in Plate 2, provides further evidence of the higher β in this region. The magnetic field in this region still remains sufficiently well ordered to rule out the possibility that the boundary at 1825 UT could be the magnetopause.

Discussion

It is evident that the broad-band electrostatic noise detected by Hawkeye 1 and Imp 6 corresponds to a distinct plasma region which extends along the magnetic field from low altitudes in the auroral zone into the distant magnetosphere. When these data are compared with low-altitude measurements in the local afternoon and evening, all of the available evidence indicates that the broad-band electrostatic noise occurs on magnetic field lines which connect with the region of intense inverted V electron precipitation observed by low-altitude polar-orbiting satellites [Frank and Ackerson, 1971]. This conclusion is supported by the following specific comparisons. (1) As was discussed in the previous section, the V-shaped auroral hiss events detected by Hawkeye 1 and Imp 6 appear to originate from the region in which the broad-band electrostatic noise is detected. At low altitudes, comparable V-shaped auroral hiss events are directly associated with inverted V events [Gurnett and Frank, 1972a] and can be reliably used to identify the inverted V electron precipitation region. (2) The low-frequency magnetic noise bursts detected by Hawkeye 1 and Imp 6, which occur in the same region as the broad-band electrostatic noise, appear to be the same as the whistler mode ELF noise bands reported by Gurnett and Frank [1972b] at low altitudes. These ELF noise bands also occur in the same region as the inverted V events and can be used as a good indicator of the inverted V electron precipitation region. (3) The broad-band electrostatic noise occurs in a region which is poleward of the electron $E > 45$ keV trapping boundary. At low altitudes the inverted V events have essentially the same relationship to the electron $E > 45$ keV trapping boundary [Frank and Ackerson, 1971]. (4) The broad-band electrostatic noise occurs in regions with substantial field-aligned currents. At low altitudes the inverted V events are also known to occur in regions with substantial field-aligned currents [Ackerson and Frank, 1972].

In the local morning the association of the broad-band electrostatic noise with the low-altitude inverted V electron precipitation is not as clearly established as in the local afternoon and evening. The location of the broad-band electrostatic noise, always immediately poleward of the $E > 45$ keV trapping boundary, suggests that the spatial relationship with the inverted V events is essentially the same in the local morning as in the local afternoon and evening. Unfortunately, in the local morning, most of the remaining methods of comparison either are absent or have not yet been adequately studied. For example, auroral hiss events with a distinct V-shaped low-frequency cutoff, which provide a method of identifying the inverted V region in the local afternoon and evening, are not observed in either the low-altitude or the high-altitude plasma wave measurements in the local morning. ELF noise bands, which also provide a method of identifying the

inverted V region, have not been studied sufficiently in the local morning region at low altitudes to provide a basis for comparison.

When the Hawkeye 1 and Imp 6 measurements are compared with other measurements in the distant magnetosphere, a very clear relationship is found with plasma waves detected in the distant magnetotail. Recently, Gurnett *et al.* [1976], using data from the Imp 8 spacecraft at geocentric radial distances from about 23.1 to 46.3 R_E , reported observations of broad-band electrostatic noise and magnetic noise bursts with characteristics essentially identical to the noise detected by Hawkeye 1 and Imp 6 much closer to the earth. Actually, Imp 6 also detects this noise in the distant magnetotail (see Figure 11); however, only the near-earth results, $R \leq 10 R_E$, are emphasized in this paper. In the distant magnetotail the broad-band electrostatic noise and magnetic noise bursts are detected by Imp 8 near the outer boundary of the plasma sheet in regions which have very large plasma streaming velocities, $> 10^3$ km s⁻¹, directed either toward or away from the earth. The electrostatic noise intensities are often greatly enhanced during periods of intense auroral activity. On the basis of these and other comparisons, Gurnett *et al.* [1976] suggested that the broad-band electrostatic noise and magnetic noise bursts occur in regions of field-aligned currents which develop at the outer boundaries of the plasma sheet during periods of increased auroral activity [Aubry *et al.*, 1972; Fairfield, 1973]. The very close similarity between the broad-band electrostatic noise and magnetic noise bursts detected by Hawkeye 1 and Imp 6 near the earth and by Imp 8 in the distant magnetotail provides strong evidence that this noise is associated with field-aligned currents which map into the inverted V electron precipitation regions observed at low altitudes. The relationships between the plasma waves, plasma regions, and field-aligned currents suggested by these data on the nightside of the earth are summarized in Figure 17.

At other local times the relationships between the broad-band electrostatic noise and the plasma regions of the distant magnetosphere are not as well understood. On the dayside of the earth the distinct skewing of the magnetic field direction in the region where the broad-band electrostatic noise is detected, as in Figure 3, strongly suggests that this region corresponds to the 'entry layer' discussed by Paschmann *et al.* [1976]. Since the investigation of the polar cusp region with Hawkeye 1 is still in a preliminary stage, further study is needed to establish the relationship of the broad-band electrostatic noise to the plasma regions observed on the dayside of the earth.

SUMMARY AND INTERPRETATION

In this study we have shown that a region of intense plasma wave turbulence occurs on high-latitude auroral field lines at altitudes ranging from a few thousand kilometers in the ionosphere to greater than 40 R_E in the distant magnetotail. Two distinctly different components are evident in the spectrum of this turbulence, (1) an intense quasi-electrostatic component called broad-band electrostatic noise and (2) a weak whistler mode electromagnetic component called magnetic noise bursts. The broad-band electrostatic noise occurs over a very broad frequency range, a few hertz to several kilohertz, with maximum electric field intensities in the frequency range of about 10–50 Hz and typical maximum broad-band rms electric field strengths of 10 mV m⁻¹. The magnetic noise bursts occur in the frequency range of about 10 Hz to a few hundred hertz (always with $f < f_{ce}$) and are usually most intense at frequencies of about 100 Hz, with typical broad-band magnetic field

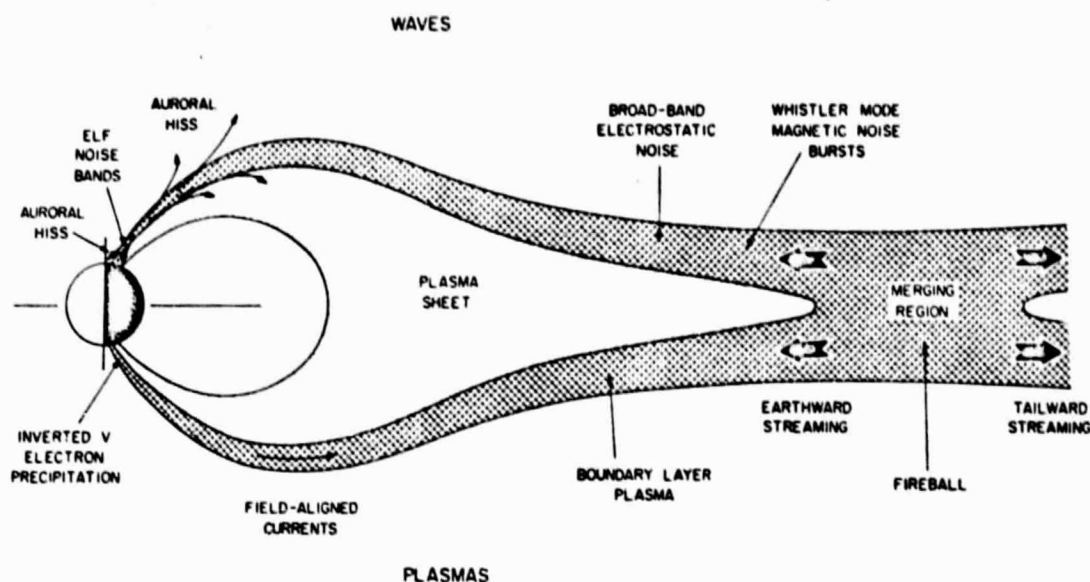


Fig. 17. The spatial relationships between the broad-band electrostatic noise, field-aligned currents, low-altitude inverted V electron precipitation, and earthward streaming protons in the distant magnetotail suggested by this study.

strengths of about 10 mV. The magnetic noise bursts are always observed in the same region as the broad-band electrostatic noise. In the local afternoon and evening the broad-band electrostatic noise appears to have a close relationship with auroral hiss emissions which occur in this local time region. Comparison with low-altitude measurements provides substantial evidence that the intense plasma wave turbulence detected by Hawkeye 1 and Imp 6 occurs on magnetic field lines which connect with regions of intense inverted V electron precipitation observed at low altitudes. In the distant magnetotail the same plasma wave turbulence is detected by the Imp 8 spacecraft in regions with intense fluxes of protons streaming toward the earth at velocities sometimes in excess of 10^4 km s⁻¹. At intermediate radial distances, magnetic field perturbations characteristic of field-aligned currents have been detected in the same region as the intense plasma wave turbulence.

When these results are compared with other previous electric field measurements, it is apparent that the broad-band electric field turbulence detected by Hawkeye 1 and Imp 6 has many close similarities to the electric field turbulence detected by the Ogo 5 spacecraft in the high-latitude regions of the magnetosphere [Scarfi et al., 1973, 1975]. In both cases, intense electric field turbulence is observed near the energetic ($E \geq 50$ keV) electron trapping boundary and in regions with large field-aligned currents. However, substantial differences are also evident. The most intense component of the broad-band electric field turbulence detected by Hawkeye 1 and Imp 6 occurs at frequencies (10–50 Hz) which are well below the low-frequency cutoff (~ 500 Hz) of the Ogo 5 plasma wave experiment and therefore not detectable. Within the frequency range of the Ogo 5 experiment the electrostatic turbulence usually consists of a few very impulsive bursts with durations of only a few seconds. In contrast, the low-frequency component of the electrostatic noise detected by Hawkeye 1 and Imp 6 occurs over a broad region, usually several degrees in magnetic latitude, with a nearly constant intensity. Frequently, short duration bursts can be seen in the Hawkeye 1 and Imp 6 wide-band

spectrograms, as in Figure 8, extending upward in frequency out of the intense low-frequency component. These brief bursts probably correspond to the intense short duration bursts detected by Ogo 5.

Although most of the general features of this plasma wave turbulence are now known, many questions remain concerning the plasma wave modes involved in this turbulence and the role which these waves play in the plasma processes which occur along the auroral field lines. Although the mode of propagation of the magnetic noise bursts can be clearly identified as the whistler mode, the plasma wave mode associated with the broad-band electrostatic noise is poorly understood. The nearly continuous transition of the whistler mode auroral hiss spectrum into the broad-band electrostatic noise (as in Figures 13 and 14) suggests that the broad-band electrostatic noise is closely associated with the whistler mode. As was discussed earlier, very short wavelength whistler mode waves, with wave normal directions close to the resonance cone, have many of the characteristics required to explain this noise (they are quasi-electrostatic, have a low-frequency cutoff near f_{UH} , and have small phase velocities characteristic of a spatially localized plasma wave mode). Although the broad-band electrostatic noise has certain characteristics of the cold plasma whistler mode, hot plasma effects must certainly be involved in the generation of this noise. Most likely, this noise is associated with a hot plasma mode, such as the ion sound wave mode ($f < f_p^*$) or the electrostatic ion cyclotron modes ($f \geq nf_p^*$), which couple strongly with the whistler mode at frequencies near f_{UH} . Electrostatic instabilities and whistler mode coupling effects of this type have been discussed by several investigators [e.g., Sazonenko and Stepanov, 1967; James, 1976; Maggs, 1976]. Since both the broad-band electrostatic noise and the whistler mode magnetic noise bursts occur in regions with substantial field-aligned currents, it seems almost certain that both of these waves are produced by a current-driven instability. Although several current-driven instabilities are known which could possibly account for these waves [e.g., Kindel and Kennel, 1971], further detailed studies

of the charged particle distribution functions are needed to identify the plasma instabilities involved in the generation of these waves.

Since the broad-band electrostatic noise is believed to occur on the same magnetic field lines as the inverted V electron events, it is of interest to consider how this plasma wave turbulence may be associated with the inverted V electron acceleration and heating. As was discussed by Frank and Ackerson [1971], Evans [1974], and others, the inverted V electron acceleration is believed to take place relatively close to the earth, at radial distances of only a few earth radii. Numerous other phenomena, such as auroral hiss [Gurnett and Frank, 1972a] and auroral kilometric radiation [Gurnett, 1974], clearly show that some distinctly nonthermal process is taking place along the nighttime auroral field lines at altitudes from about 5,000 to 20,000 km. On the same magnetic field lines as the inverted V events, intense field-aligned currents are known to flow between the distant magnetosphere and the ionosphere, and intense fluxes of protons are detected streaming toward the earth in the distant magnetotail [Frank et al., 1976]. In considering the possible role of the plasma wave turbulence detected by Hawkeye 1 and Imp 6 on the acceleration and heating of the auroral particles, two main questions can be identified: (1) whether the waves act to thermalize the earthward streaming protons and in the process heat the electrons to the high temperatures characteristic of the inverted V events, and (2) whether the waves cause an anomalous resistivity sufficiently large to account for field-aligned potential differences thought to be involved in the primary acceleration of the inverted V electrons.

Since only a small fraction of the protons streaming toward the earth in the distant magnetotail are observed to return from the direction of the earth, Frank [1972] has suggested that the energy carried by these protons is transferred to the electrons at some point along the magnetic field line closer to the earth, thereby accounting for the inverted V electron precipitation and the absence of comparable intense proton fluxes at low altitudes. Since the plasma at these altitudes is nearly collisionless, some mechanism is needed to transfer the energy and momentum from the electrons to the protons. The occurrence of intense plasma wave turbulence along the field lines where the inverted V events are observed strongly suggests that this turbulence is involved in heating these electrons. In many respects the process could be similar to the earth's bow shock, where plasma waves play the dominant role in the plasma heating. For the observed electric field spectrum the primary interactions with the protons would be expected at the harmonics $n f_{pe}$ of the proton gyrofrequency. The electron heating could occur by either Landau damping or cyclotron damping of the waves generated by the earthward streaming protons.

In addition to the heating caused by the generation and reabsorption of plasma waves, energy exchange can also occur in regions of field-aligned currents because of the anomalous resistivity caused by the plasma wave turbulence. Estimates of the field-aligned potential differences caused by anomalous resistivity in regions of field-aligned currents have been previously given by Fredricks et al. [1973]. Assuming an rms broad-band electric field strength of 90 mV m^{-1} , Fredricks et al. estimate that field-aligned potential differences of the order of 2 kV can be expected. In the region surveyed by Hawkeye 1 and Imp 6 the rms electric field strength of the broad-band electrostatic noise is seldom larger than about $10\text{--}30 \text{ mV m}^{-1}$, and in the distant magnetotail the electric field strength of this noise is even smaller, seldom exceeding about $1\text{--}2 \text{ mV m}^{-1}$ [see

Gurnett et al., 1976]. Since the anomalous resistivity varies as the square of the electric field strength [Sagdeev and Galeev, 1966], the field-aligned potential differences in the regions surveyed by Hawkeye 1 and Imp 6 are less than those estimated by Fredricks et al., probably not more than about 200 V, assuming that the other parameters are similar. Potential differences of this order are too small to account for the electron energies of $\sim 10 \text{ keV}$ observed in the inverted V electron precipitation at low altitudes. However, it should be noted that the Hawkeye 1 and Imp 6 measurements do not include the radial distance range of about $1.8\text{--}4.0 R_E$ (at $L = 8$), and the electric field intensity may be significantly larger in this altitude range. Comparisons between Imp 8 and Hawkeye 1 in fact suggest that the electric field intensity of the broad-band electrostatic noise increases at lower altitudes (compare Figure 5 from Gurnett et al. [1976] with Figure 6 of this paper). The possibility that the electric field intensities may increase with decreasing altitude is further supported by the Ogo 5 observations of Scarf et al. [1973], in which electric field strengths as large as $\sim 200 \text{ mV m}^{-1}$ were observed at a radial distance of $2.5 R_E$. Broad-band electric field strengths this large have not yet been observed by Hawkeye 1 and Imp 6. The absence of such large field strengths in the Hawkeye 1 and Imp 6 data is not considered to be in disagreement with the Ogo 5 measurements because of the previously mentioned limitations in the orbital coverage, which has not yet provided measurements at radial distances near $2.5 R_E$ on the auroral field lines. Hopefully, data obtained later in the Hawkeye 1 lifetime can provide the measurements necessary to extend the results of the present study into the region from 1.8 to $4.0 R_E$ along the auroral field lines.

Since the wavelength of the electric field turbulence detected by Hawkeye 1 and Imp 6 may be very short, consideration must also be given to the possibility that the wavelengths may be shorter than the antenna lengths (42.45 and 92.50 m for Hawkeye 1 and Imp 6, respectively). If wavelengths λ occur which are shorter than the antenna length L , then the electric field strength will be underestimated, possibly by a large factor if $\lambda \ll L$. The shortest wavelength which can occur in a plasma is approximately $\lambda_m = 2\pi\lambda_D = 46.6(T/n)^{1/2} \text{ m}$, where λ_D is the Debye length, T is the electron temperature in electron volts, and n is the electron density in units per cubic centimeter. In the high-altitude region ($R > 4.0 R_E$) surveyed by Hawkeye 1 and Imp 6 a reliable upper limit to the electron density can be obtained from the low-frequency cutoff of the continuum radiation, which must occur at frequencies greater than the local electron plasma frequency $f > f_{pe} \approx 9(n)^{1/2} \text{ kHz}$. In the region where the broad-band electrostatic noise is observed the continuum radiation cutoff is typically about 15 kHz and almost never greater than 30 kHz, which implies densities of typically 3 cm^{-3} and almost never more than 10 cm^{-3} . The electron temperature is more difficult to estimate. Because substantial fluxes of electrons with energies of several hundred electron volts are usually present in these regions, it is estimated that the electron temperature is almost certainly of the order of 100 eV or more. When $n = 10 \text{ cm}^{-3}$ and $T = 100 \text{ eV}$, the minimum wavelength is $\lambda_m = 147.4 \text{ m}$, which is longer than either the Hawkeye 1 or the Imp 6 antenna by a significant factor. We conclude that errors due to short wavelength effects are not likely to be present in the high-altitude ($R > 4.0 R_E$) measurements presented in this paper. This conclusion has been verified in a few cases by comparing measurements obtained with antennas of different lengths on Imp 6, which show the expected proportionality of the signal strength with in-

creasing antenna length which should be observed when $\lambda \gg L$.

For the low-altitude region ($R < 1.8 R_E$) surveyed by Hawkeye I it is certain that the minimum wavelength can be much less than the antenna length because of the larger electron density and lower electron temperature in the ionosphere. Whether the broad-band electric field turbulence detected at low altitudes actually has wavelengths sufficiently short to cause serious errors in the electric field measurements is difficult to determine and has not been investigated in detail, since the primary emphasis of this study has been on the high-altitude observation. On the basis of earlier studies by Kelley and Mozer [1972], in which wavelengths of the low-altitude electric field turbulence were directly measured, Kintner [1976] has presented arguments showing that the wavelengths of the broad-band electrostatic noise are sufficiently long to preclude the possibility of serious errors in the electric field spectrum even at low altitudes.

Acknowledgments. The Hawkeye I program at the University of Iowa is under the supervision of J. A. Van Allen, to whom the authors are further indebted for the magnetic field data used herein. The authors also wish to express their thanks to K. Ackerson, R. Shaw, R. Anderson, R. West, and W. Kurth for their assistance in data processing and the preparation of illustrations. The research at the University of Iowa was supported by the National Aeronautics and Space Administration through grants NGL-16-001-002 and NGL-16-001-043, contracts NAS1-11257 and NAS1-13129 with the Langley Research Center, and contracts NAS5-20539, NAS5-11074, and NAS5-11431 with the Goddard Space Flight Center and by the U.S. Office of Naval Research. The research at the Max-Planck-Institut was supported by the Alexander von Humboldt Foundation.

The Editor thanks R. W. Fredricks and T. Laaspere for their assistance in evaluating this paper.

REFERENCES

- Ackerson, K. L., and L. A. Frank, Correlated satellite measurements of low-energy electron precipitation and ground-based observations of a visible auroral arc, *J. Geophys. Res.*, **77**, 1128, 1972.
- Aubry, M. P., M. G. Kivelson, R. L. McPherron, C. T. Russell, and D. S. Colburn, Outer magnetosphere near midnight at quiet and disturbed times, *J. Geophys. Res.*, **77**, 5487, 1972.
- Carlqvist, P., On the formation of double layers in plasmas, *Cosmic Electrodynamics*, **3**, 377, 1972.
- Coroniti, F. V., and C. F. Kennel, Polarization of the auroral electrojet, *J. Geophys. Res.*, **77**, 2835, 1972.
- Coroniti, F. V., and C. F. Kennel, Can the ionosphere regulate magnetospheric convection?, *J. Geophys. Res.*, **78**, 2837, 1973.
- Evans, D. S., Precipitating electron fluxes formed by a magnetic field aligned potential difference, *J. Geophys. Res.*, **79**, 2853, 1974.
- Fairfield, D. H., Magnetic field signatures of substorms on high latitude field lines in the nighttime magnetosphere, *J. Geophys. Res.*, **78**, 1553, 1973.
- Frank, L. A., Initial observations of low-energy electrons in the earth's magnetosphere with Ogo 3, *J. Geophys. Res.*, **72**, 185, 1967.
- Frank, L. A., Plasma entry into the earth's magnetosphere, in *Critical Problems of Magnetospheric Physics*, edited by E. R. Dyer, p. 35, IUCSTP Secretariat, Washington, D. C., 1972.
- Frank, L. A., and K. L. Ackerson, Observations of charged particles precipitated into the auroral zone, *J. Geophys. Res.*, **76**, 3612, 1971.
- Frank, L. A., and D. A. Gurnett, Distributions of plasmas and electric fields over the auroral zones and polar caps, *J. Geophys. Res.*, **76**, 6829, 1971.
- Frank, L. A., K. L. Ackerson, and R. P. Lepping, On hot tenuous plasmas, fireballs, and boundary layers in the earth's magnetotail, *J. Geophys. Res.*, **81**, 5859, 1976.
- Fredricks, R. W., F. L. Scarf, and C. T. Russell, Field-aligned currents, plasma waves, and anomalous resistivity in the disturbed polar cusp, *J. Geophys. Res.*, **78**, 2133, 1973.
- Gurnett, D. A., A satellite study of VLF hiss, *J. Geophys. Res.*, **71**, 5599, 1966.
- Gurnett, D. A., The earth as a radio source: Terrestrial kilometric radiation, *J. Geophys. Res.*, **79**, 4227, 1974.
- Gurnett, D. A., The earth as a radio source: The nonthermal continuum, *J. Geophys. Res.*, **80**, 2751, 1975.
- Gurnett, D. A., and L. A. Frank, VLF hiss and related plasma observations in the polar magnetosphere, *J. Geophys. Res.*, **77**, 172, 1972a.
- Gurnett, D. A., and L. A. Frank, ELF noise bands associated with auroral electron precipitation, *J. Geophys. Res.*, **77**, 3411, 1972b.
- Gurnett, D. A., and L. A. Frank, Observed relationships between electric fields and auroral particle precipitation, *J. Geophys. Res.*, **78**, 145, 1973.
- Gurnett, D. A., and R. R. Shaw, Electromagnetic radiation trapped in the magnetosphere above the plasma frequency, *J. Geophys. Res.*, **78**, 8136, 1973.
- Gurnett, D. A., L. A. Frank, and R. P. Lepping, Plasma waves in the distant magnetotail, *J. Geophys. Res.*, **81**, 6059, 1976.
- Holzer, T. E., and T. Sato, Quiet auroral arcs and electrodynamic coupling between the ionosphere and the magnetosphere, *J. Geophys. Res.*, **78**, 7330, 1973.
- James, H. G., VLF saucers, *J. Geophys. Res.*, **81**, 501, 1976.
- Kelley, M. C., and F. S. Mozer, A satellite survey of vector electric fields in the ionosphere at frequencies of 10 to 500 Hz, *J. Geophys. Res.*, **77**, 4158, 1972.
- Kindel, J. M., and C. F. Kennel, Topside current instabilities, *J. Geophys. Res.*, **76**, 3055, 1971.
- Kintner, P. M., Jr., Observations of velocity shear driven plasma turbulence, *J. Geophys. Res.*, **81**, 5114, 1976.
- Kurth, W. S., M. M. Baumbach, and D. A. Gurnett, Direction-finding measurements of auroral kilometric radiation, *J. Geophys. Res.*, **80**, 2764, 1975.
- Laaspere, T., W. C. Johnson, and L. C. Semprebon, Observations of auroral hiss, LHR noise, and other phenomena in the frequency range 20 Hz to 540 kHz on Ogo 6, *J. Geophys. Res.*, **76**, 4477, 1971.
- Maggis, J. E., Coherent generation of VLF hiss, *J. Geophys. Res.*, **81**, 1707, 1976.
- McEwen, D. J., and R. E. Barrington, Some characteristics of the lower hybrid resonance noise bands observed by the Alouette 1 satellite, *Can. J. Phys.*, **45**, 13, 1967.
- Mozer, F. S., Anomalous resistivity and parallel electric fields, in *Magnetospheric Particles and Fields*, edited by B. M. McCormac, D. Reidel, Dordrecht, Netherlands, in press, 1977.
- Papadopoulos, K., and T. Coffey, Anomalous resistivity in the auroral plasma, *J. Geophys. Res.*, **79**, 1558, 1974.
- Paschmann, G., G. Haerendel, N. Sckopke, H. Rosenbauer, and P. C. Hedgecock, Plasma and magnetic field characteristics of the distant polar cusp near local noon, *J. Geophys. Res.*, **81**, 2883, 1976.
- Russell, C. T., R. E. Holzer, and E. J. Smith, Ogo 3 observations of ELF noise in the magnetosphere. I. Spatial extent and frequency of occurrence, *J. Geophys. Res.*, **74**, 755, 1969.
- Sagdeev, R. Z., and A. A. Galeev, Non-linear plasma theory, *Tech. Rep. IC/66/64*, Int. Center for Theor. Phys., Trieste, Italy, 1966.
- Sato, T., and T. E. Holzer, Quiet auroral arcs and electrodynamic coupling between the ionosphere and the magnetosphere. I, *J. Geophys. Res.*, **78**, 7314, 1973.
- Scarf, F. L., R. W. Fredricks, I. M. Green, and C. T. Russell, Plasma waves in the dayside polar cusp, *J. Geophys. Res.*, **77**, 2274, 1972.
- Scarf, F. L., R. W. Fredricks, C. T. Russell, M. Kivelson, M. Neugebauer, and C. R. Chappell, Observation of a current-driven plasma instability at the outer zone-plasma sheet boundary, *J. Geophys. Res.*, **78**, 2150, 1973.
- Scarf, F. L., R. W. Fredricks, C. T. Russell, M. Neugebauer, M. Kivelson, and C. R. Chappell, Current-driven plasma instabilities at high latitudes, *J. Geophys. Res.*, **80**, 2030, 1975.
- Shaw, R. R., and D. A. Gurnett, Electrostatic noise bands associated with the electron gyrofrequency and plasma frequency in the outer magnetosphere, *J. Geophys. Res.*, **80**, 4259, 1975.
- Sizonenko, V. L., and K. N. Stepanov, Plasma instability in the electric field of an ion-cyclotron wave, *Nucl. Fusion*, **7**, 131, 1967.
- Taylor, W. W. L., and S. D. Shawhan, A test of incoherent Cerenkov radiation for VLF hiss and other magnetospheric emissions, *J. Geophys. Res.*, **79**, 105, 1974.

(Received April 29, 1976;
accepted September 17, 1976)

ELECTROSTATIC TURBULENCE IN THE MAGNETOSPHERE

Donald A. Gurnett[†]
Department of Physics and Astronomy
The University of Iowa
Iowa City, Iowa 52242

Plasma wave measurements from the IMP-6, IMP-8 and Hawkeye-1 satellites show that a broad region of intense low-frequency electric field turbulence occurs on the high latitude auroral field lines at altitudes ranging from a few thousand kilometers in the ionosphere to many earth radii in the distant magnetosphere. A qualitatively similar, but less intense, type of electric field turbulence is also observed at the plasmopause during magnetic storms. In the auroral regions the turbulence occurs in an essentially continuous band on the auroral L-shells at all local times around the earth and is most intense during periods of auroral activity. In this paper we summarize the basic characteristics of this electric field turbulence and consider the possible role this turbulence may play in the heating and acceleration of plasma in the magnetosphere.

I. INTRODUCTION

Recent studies of plasma wave measurements obtained from the IMP-6, IMP-8 and Hawkeye-1 satellites have revealed the existence of a broad region of low frequency electric field turbulence on auroral field lines at altitudes ranging from a few thousand kilometers in the auroral ionosphere to many earth radii in the distant magnetosphere [Gurnett and Frank, 1976; Gurnett et al., 1976]. A similar region of electric field turbulence with somewhat lower intensities is also detected near the plasmopause during magnetic storms [Anderson and Gurnett, 1973]. The electric field intensity of the turbulence on the auroral field lines is often quite large, with maximum field strengths of about 30 mV m^{-1} . The frequency range of the electric field noise typically extends from about 10 Hz to a few kHz, with the maximum intensity at about 10 to 50 Hz. Weak bursts of magnetic noise are also detected in the same region as the electric field turbulence.

For many years it has been suggested that intense electric fields produced by current-driven instabilities can interact with the current-carrying particles in a plasma to produce an effective resistivity many orders of

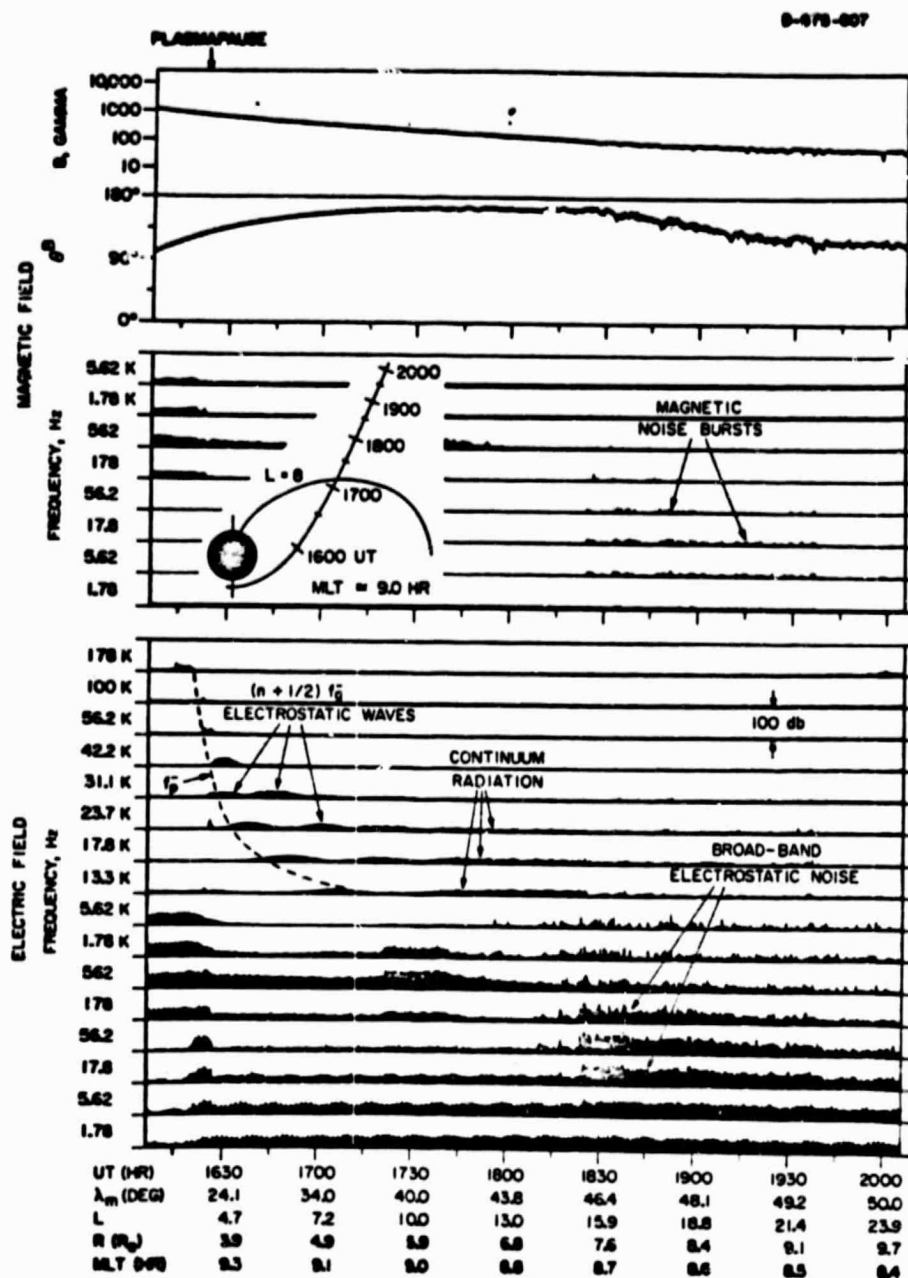
[†]Research performed while on leave at the Max-Planck-Institut für Extraterrestrische Physik, 8046 Garching, West Germany.

magnitude larger than the Coulomb resistivity. (See for example the recent review by Mozer, 1976). Kindel and Kennel [1971] have considered the possible current-driven instabilities which could occur in the auroral zone and have concluded that the electrostatic ion cyclotron and ion acoustic modes should be unstable in the regions of field-aligned currents associated with the auroral electron precipitation. If the electric field turbulence produced by these instabilities grows to sufficiently large amplitudes the associated anomalous resistivity can produce large electrostatic potential differences along the magnetic field line, with an associated acceleration of some of the particles to high energies. In the distant magnetotail anomalous resistivity produced by plasma wave turbulence has also been suggested as a mechanism to control the merging rate of oppositely directed magnetic fields at X-type neutral lines [Piddington, 1967; Dungey, 1972]. In this paper we summarize the observed characteristics of the electric field turbulence detected by the IMP and Hawkeye satellites and consider the possible role of this turbulence in the heating and acceleration of auroral particles.

II. ELECTROSTATIC TURBULENCE ON AURORAL FIELD LINES

To illustrate the principal characteristics of the intense low frequency electric field turbulence which occurs on the high latitude auroral field lines we first discuss the plasma wave measurements on three representative passes of the Hawkeye-1, IMP-6 and IMP-8 spacecraft. The Hawkeye-1 and IMP-6 passes in Figures 1 and 2 cut across the auroral L-shells relatively close to the earth (5 to 10 R_E) in the local morning and evening, respectively, and the IMP-8 pass in Figure 3 crosses through the neutral sheet region of the distant magnetotail about 30 R_E from the earth. The top panel of each of these illustrations shows the magnetic field magnitude and direction and the middle and bottom panels show the plasma wave magnetic and electric field intensities. The intensity scale for each channel is proportional to the logarithm of the field strength, with a range of 100 db from the baseline of one channel to the baseline of the next higher channel. For the IMP data the dots give the peak field strength and the vertical bars give the average field strength. For further details of the plasma wave instrumentation on these spacecraft see Gurnett [1974] and Kurth *et al.* [1975].

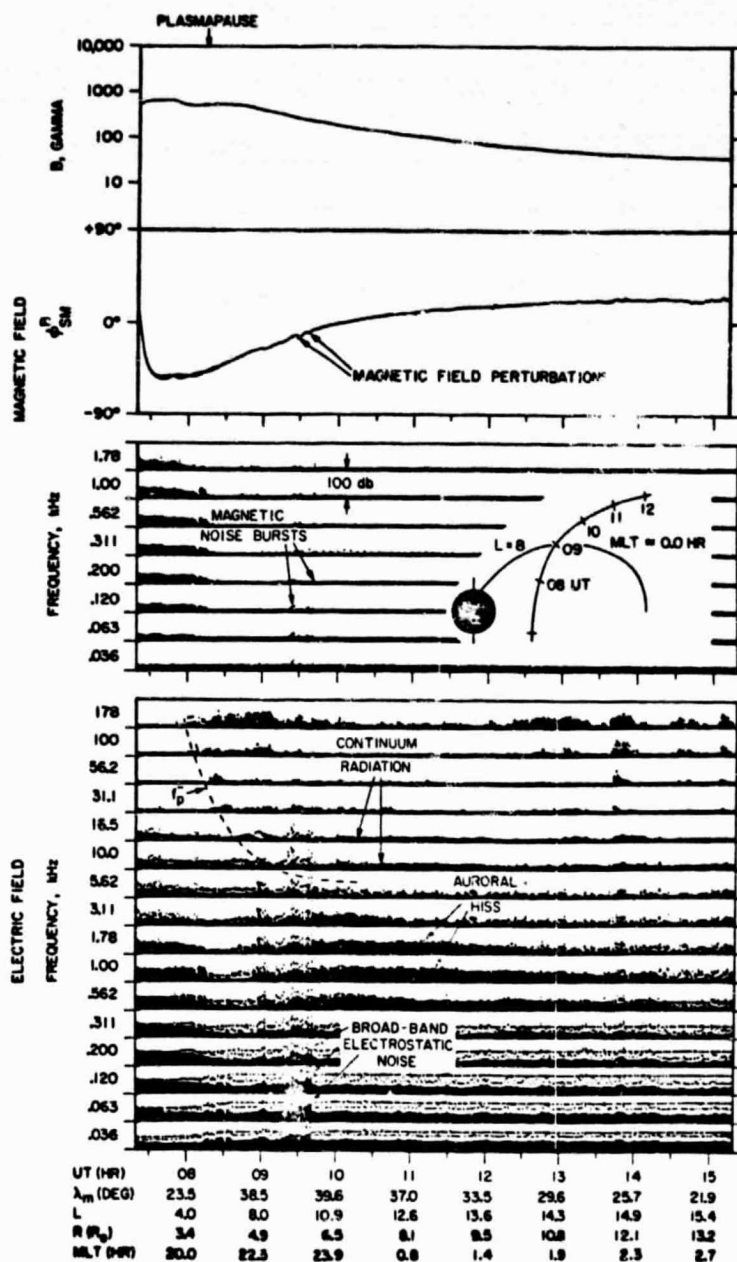
The first representative pass (in Figure 1) is an outbound Hawkeye-1 pass in the local morning at about 0900 magnetic local time. Several types of plasma waves are present during this pass. Within the plasmasphere, before about 1525 UT, plasmaspheric hiss is evident in both the electric and magnetic field channels at frequencies from 178 Hz to 5.62 kHz. At slightly higher frequencies outside of the plasmapause a series of $(n + 1/2)f_c$ electrostatic cyclotron harmonic emissions and a band of continuum radiation can be seen extending over a large range of radial distances. Starting at about 1825 UT, and extending to about 1940 UT, a region of intense low-frequency electric field noise is evident in the frequency range from about 10 Hz to 10 kHz. Since this noise occurs over a broad range of frequencies and is most evident in the electric field data we refer to this noise as broad-band electrostatic noise [Gurnett *et al.*, 1976; Gurnett and Frank, 1976]. Some



HAWKEYE-1, DAY 50, FEB 19, 1975

Figure 1. A Hawkeye-1 pass near local dawn. Intense electrostatic turbulence occurs near the plasmopause, from 1620 to 1625 UT and along the auroral field lines, from about 1825 to 1940 UT.

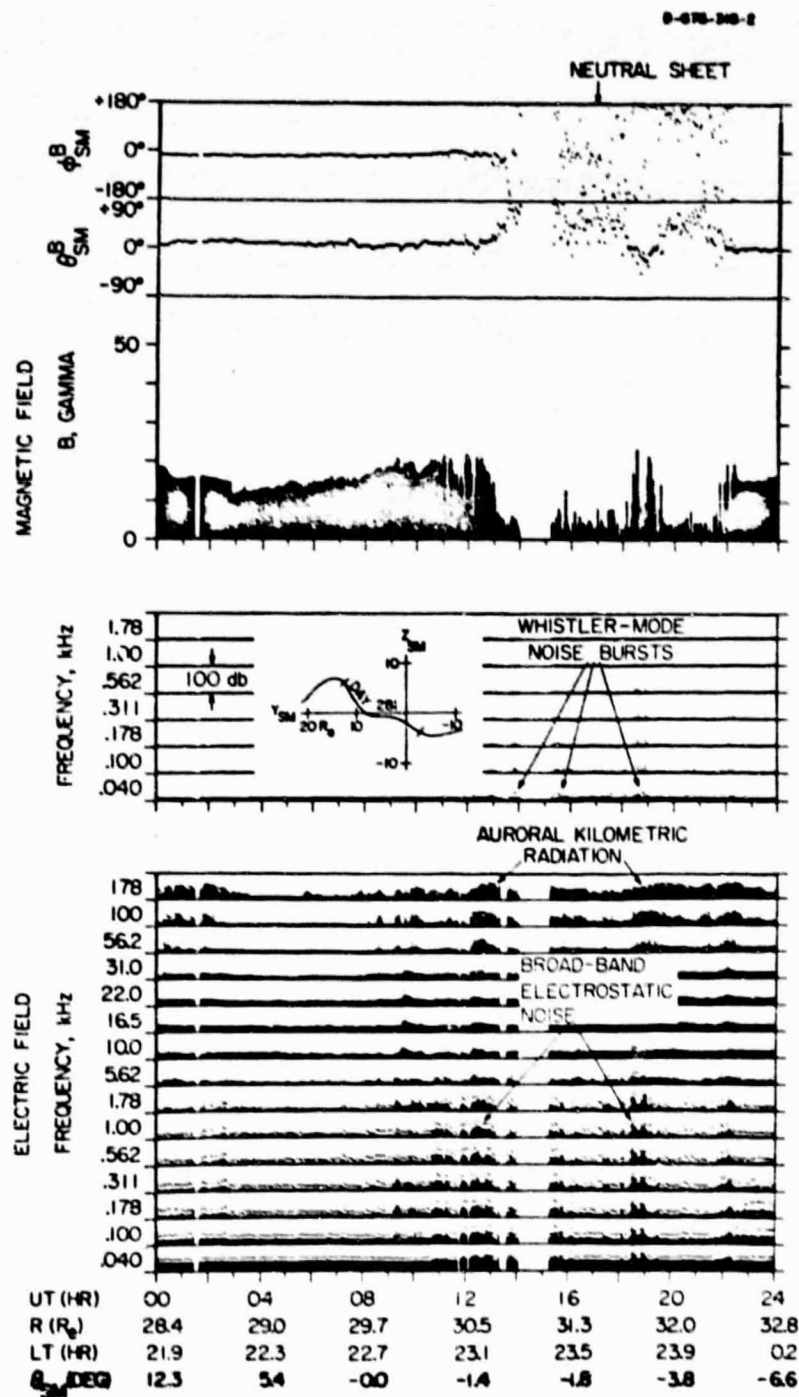
weak bursts of magnetic noise are also observed in the same region as the broad-band electrostatic noise. Simultaneous with the onset of the broad-band electrostatic noise in Figure 1 (at 1825 UT) an abrupt cutoff occurs in the continuum radiation in the 13.3 and 17.8 kHz channels. This cutoff



IMP-6, DAY 192, JULY 11, 1973

Figure 2. An IMP-6 pass near local midnight showing the occurrence of several regions of intense broad-band electrostatic noise.

indicates that the spacecraft has entered a region of distinctly higher plasmas density (with $f_p \approx 17.8$ kHz) in the region where the broad-band electrostatic noise occurs. At the same time a distinct skewing of the magnetic field direction, θ^D , and an increase in the magnetic field fluctuations are evident. Both the skewing of the magnetic field direction and the increase



TMP-R DAY 281 OCT. 8 1974

Figure 3. An IMP-8 pass through the plasma sheet in the distant magnetotail showing the occurrence of broad-band electrostatic noise near the outer boundary of the plasma sheet.

ORIGINAL PAGE IS
OF IMP-8 DATA

in the plasma density indicate that the spacecraft has entered a region of higher β (ratio of plasma to magnetic pressure) characteristic of the polar cusp or entry layer [Frank, 1971; Paschmann et al., 1976] on the day side of the magnetosphere.

On the night side of the magnetosphere a qualitatively similar type of plasma wave turbulence is also observed, both near the earth and in the distant magnetotail. Figure 2 shows a typical IMP-6 pass through the high-latitude region of the magnetosphere near the earth in the local evening, at about 2300 magnetic local time. During this pass several distinct regions with intense broad-band electrostatic noise can be identified, the first at about 0900 UT, followed by a broad region from about 0920 to 0940 UT. The enhanced electric field intensities within these regions, at L-values from about 8 to 10, are very clear and distinct, particularly in the peak field strength measurements. Magnetic noise bursts are also evident in the low frequency, 36 Hz to 200 Hz, magnetic field channels. Several distinct perturbations in the magnetic field direction, ϕ_{SM}^B , indicative of field-aligned currents, are also present in the region where the broad-band electrostatic noise is observed. Figure 3 shows an IMP-8 pass through the plasma sheet in the distant magnetotail for which the same type of broad-band electrostatic noise is observed at a radial distance of over $30 R_E$ from the earth. During this pass the transition from the northern to the southern lobes of the magnetotail is indicated by the change in the magnetic field direction from $\phi_{SM}^B \approx 0^\circ$ to $\phi_{SM}^B \approx 180^\circ$ and the high energy density $\beta \approx 1$ region of the plasma sheet can be identified by the region of depressed magnetic field intensity from about 1300 to 2200 UT. Comparing the electric field intensities with the magnetic field magnitude B it is seen that the intense broad-band electrostatic noise tends to occur near the boundaries of the plasma sheet in the region where the magnetic field changes from the relatively steady field characteristic of the high latitude magnetotail to the depressed and more variable field in the plasma sheet. Detailed comparisons with the plasma measurements of Frank et al. [1976] for this same period show that the intense broad-band noise occurs in regions with large flow velocities, $> 10^3$ km sec $^{-1}$, associated with the merging region (fireball) in the distant magnetotail. Magnetic noise bursts, comparable to the events in Figures 1 and 2, are also evident in the regions of intense broad-band electrostatic noise. The onset of the broad-band electrostatic noise bursts at 1205, 1830 and 2200 UT, also occurs coincident with the onset of intense bursts of auroral kilometric radiation, a type of radio emission generated at low altitudes near the earth. This association strongly suggests that the plasma wave turbulence in the distant magnetosphere plays an important role in controlling or influencing the auroral particle precipitation near the earth.

Typical peak and average spectrums of the electric and magnetic fields in a region of intense broad-band electrostatic noise are shown in Figure 4. These spectrums show that the ratio of the average electric field energy density to the average magnetic field energy density is much greater than one, $E^2/c^2 B^2 \approx 39$, which illustrates the essentially electrostatic (or quasi-electrostatic) character of the turbulence. The electric field spectrum in Figure 4 also shows that the frequency range of this turbulence extends from near the proton gyrofrequency, f_g^+ , to the electron gyrofrequency, f_g^- . The largest electric field intensities occur at low frequencies, from about 10 to

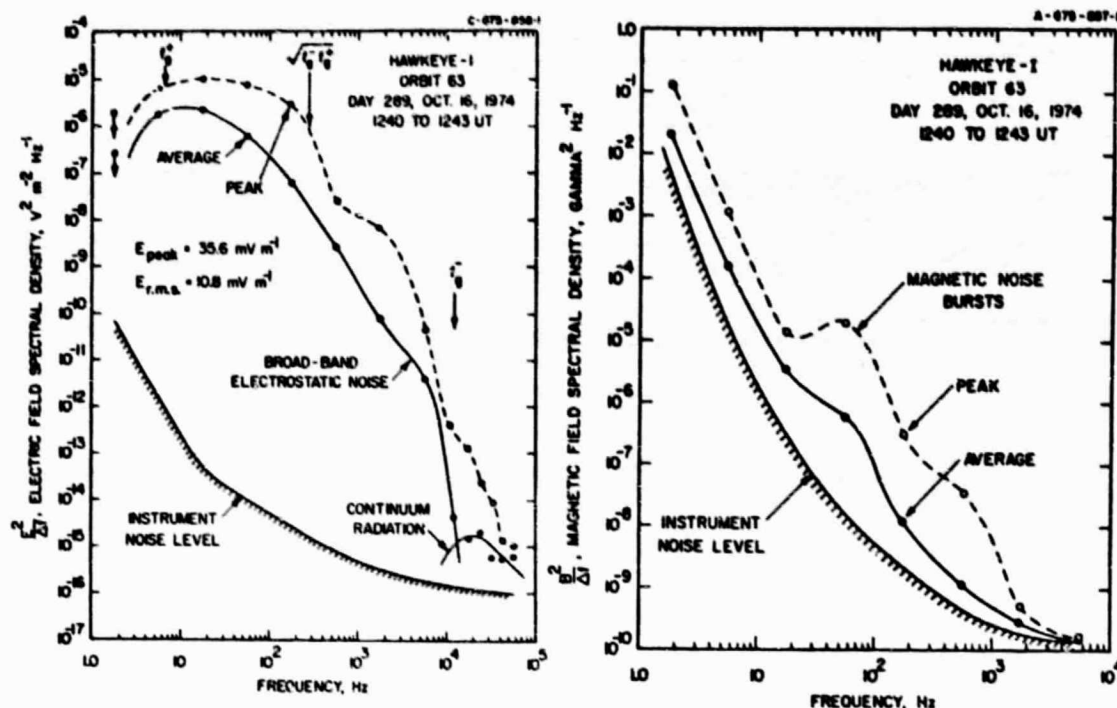


Figure 4. Representative electric and magnetic field spectrums in a region of intense broad-band electrostatic noise.

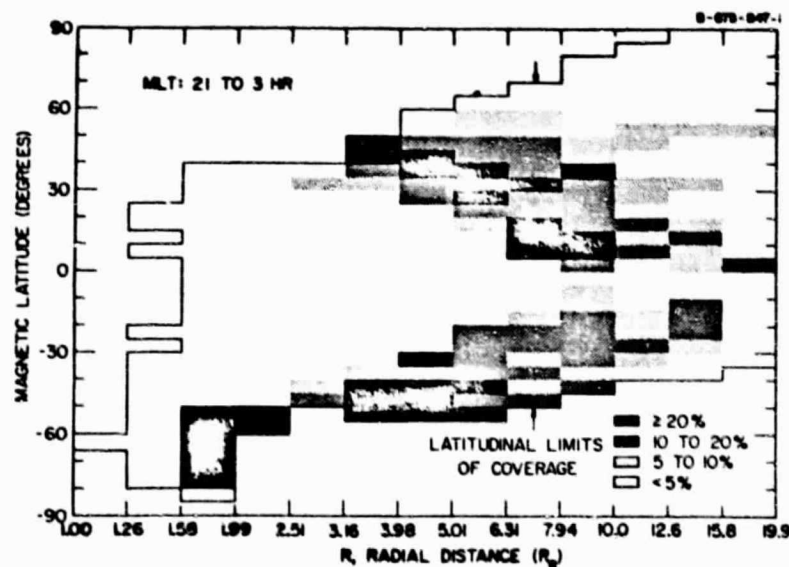


Figure 5. The frequency of occurrence of broad-band electrostatic noise in the region near local midnight.

8

50 Hz, in the range between f_g^+ and the hybrid frequency $\sqrt{f_g^+ f_g^-}$. The r.m.s. broad-band electric field strength for this case is 10.8 mV m^{-1} and the peak broad-band field strength is 35.6 mV m^{-1} .

Using the extensive measurements available from the IMP-6 and Hawkeye-1 spacecraft a detailed study has been made of the region of occurrence of the broad-band electrostatic noise. The essential features of the frequency of occurrence distribution are shown in Figures 5 and 6. For this frequency of occurrence distribution events are identified on the basis of the low-frequency electric field intensity (56.2 Hz for Hawkeye-1 and 63.0 Hz for IMP-6). The threshold electric field spectral density used for defining an event is $1.4 \times 10^{-7} \text{ volt}^2 \text{ m}^{-2} \text{ Hz}^{-1}$. Figure 5 shows the frequency of occurrence as a function of radial distance, R , and magnetic latitude, λ_m , for magnetic local time in the local midnight quadrant, from about 21 to 03 Hr. MLT. These data show that the broad-band electrostatic noise occurs in two distinct latitudinally symmetric regions, starting at high latitudes, $\sim 70^\circ$, near the earth and extending to progressively lower latitudes with increasing radial distance. The two regions appear to merge in the distant magnetotail at a radial distance of about $10 R_e$. The latitudinal width of the region of occurrence, approximately 20° at $R = 5.01$ to $6.31 R_e$, is several times larger than the latitudinal width typically observed on an individual pass. This increase in the apparent latitudinal width of the region of occurrence is almost certainly caused by the orbit-to-orbit variations of the L-shell on which the noise occurs. On the basis of passes through the plasma sheet, as in Figure 3, in which the noise is observed near the outer boundaries of the plasma sheet, it seems likely that at any given time the northern and southern regions of occurrence remain distinctly separated to much larger distances ($R \gg 10 R_e$) in the magnetotail than are indicated by the statistical survey in Figure 5.

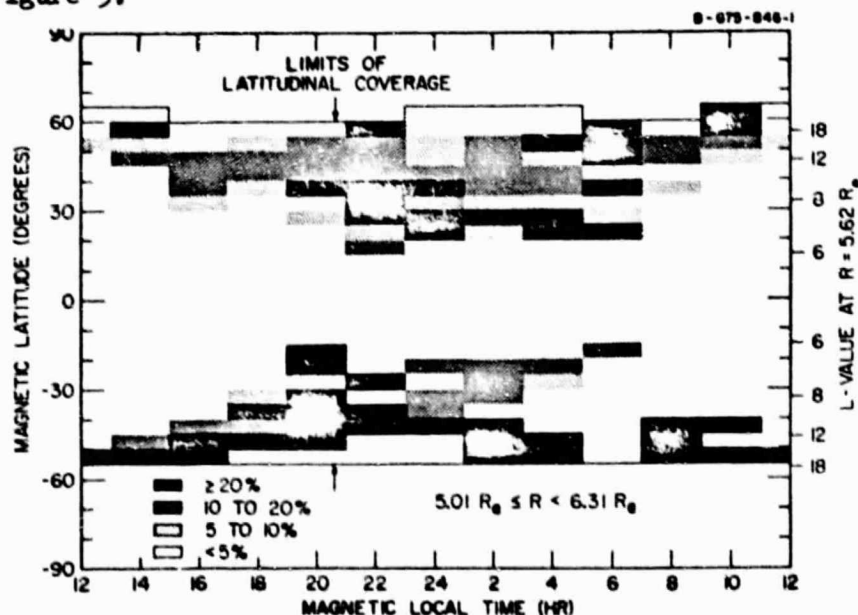


Figure 6. The frequency of occurrence of broad-band electrostatic noise on a shell of constant radial distance from 5.01 to $6.31 R_e$.

7

To illustrate the variations in the region of occurrence with magnetic local time Figure 6 shows the frequency of occurrence as a function of magnetic latitude and magnetic local time at a constant radial distance, $5.01 R_e \leq R < 6.31 R_e$. This range of radial distance was chosen because it is sufficiently far from the earth to provide measurements over a wide range of magnetic latitudes and still close enough for the magnetic field model to be reasonably accurate. For reference, the L-value of the magnetic field passing through the center of this region at $R = 5.62 R_e$ is shown on the right side of Figure 6. The broad-band electrostatic noise is seen to occur in an essentially continuous band at all local times around the earth. The noise occurs at the lowest magnetic latitudes near local midnight and at systematically higher magnetic latitudes on the day side of the earth. The frequency of occurrence (and also the average intensity, not shown) is significantly higher on the night side of the earth. Near local midnight the maximum occurrence is at L-values from about 8 to 12.

III. ELECTROSTATIC TURBULENCE NEAR THE PLASMAPAUSE

Electrostatic turbulence similar to the intense broad-band electrostatic noise observed along the auroral field lines is also observed near the plasmopause during magnetic storms. A good example of this electrostatic turbulence is evident in the 17.8 and 56.2 Hz electric field channels of Figure 1 as the spacecraft crosses the plasmopause, from about 1620 to 1625 UT. The broad-band field strength of this noise is relatively weak, only about $250 \mu V m^{-1}$. No magnetic field can be detected in the corresponding magnetic field channels. As with the broad-band electrostatic noise in the auroral zone the electric field energy density of the plasmopause noise greatly exceeds the magnetic field energy density (for example, compare this noise with the electromagnetic plasmaspheric hiss emissions in the 178 Hz channel at 1615 UT).

Electrostatic noise of the type illustrated in Figure 1 has been previously observed on the S³-A spacecraft [Anderson and Gurnett, 1973] near the equatorial plane during a magnetic storm and similar electrostatic waves have also been observed at low altitudes near the plasmopause in association with a stable red arc [Nagy et al., 1972]. The Hawkeye-1 observations indicate that this plasmopause electrostatic turbulence occurs all along the magnetic field line, from the equator to low altitudes in the ionosphere. At the present time relatively little is known in detail about the occurrence of this electrostatic turbulence, or its relationship to the plasma interactions occurring at the plasmopause during a magnetic storm.

IV. SUMMARY AND DISCUSSION

Intense low-frequency electrostatic turbulence is observed in two distinct regions of the magnetosphere: along the auroral field lines and near

the plasmopause. Along the auroral field lines this electric field turbulence, which has been called broad-band electrostatic noise, is very intense with maximum broad-band electric field strengths sometimes as large as 30 mV m^{-1} . This turbulence occurs in an essentially continuous band on the auroral L-shells at all local times around the earth and extends to large distances ($> 40 R_e$) in the distant magnetotail near the outer boundary of the plasma sheet. Weak bursts of magnetic noise are also observed in the same region as the broad-band electrostatic field and comparisons with magnetic field and plasma measurements show that this noise occurs on field lines which carry significant field-aligned currents between the distant magnetosphere and the ionosphere and in regions of the distant magnetotail which have large plasma flow velocities, $> 10^3 \text{ km sec}^{-1}$ [Gurnett et al., 1976]. At low altitudes evidence has been presented [Gurnett and Frank, 1976] indicating that this low frequency electric field turbulence occurs on the same magnetic field lines as the intense inverted-V electron precipitation events responsible for a major fraction of the auroral energy dissipation in the local evening. These relationships are summarized in Figure 7. Near the plasmopause a lower intensity type of electrostatic turbulence is observed which has many characteristics (broad-band, quasi-electrostatic, peak intensity from 10 to 50 Hz) similar to the broad-band electrostatic noise observed in the auroral regions. This noise occurs relatively infrequently and is apparently associated with the interaction of the hot ring current plasma with the plasmasphere during magnetic storms.

C-676-43-1

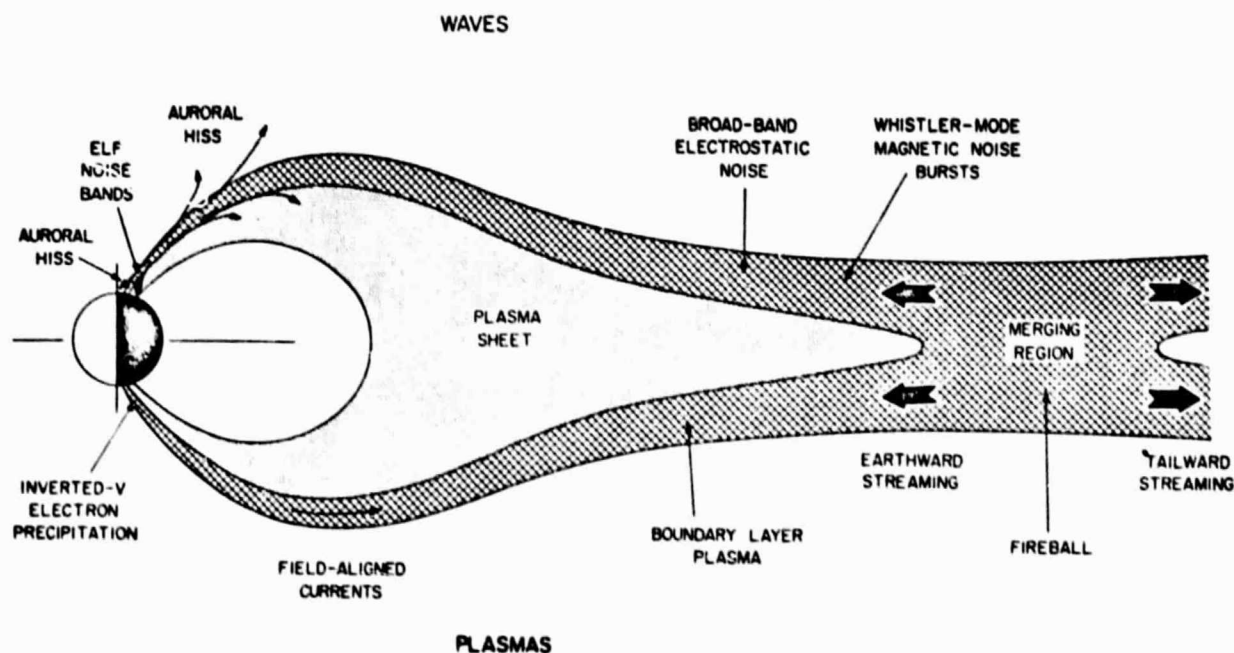


Figure 7. A qualitative model showing the region where the broad-band electrostatic noise occurs in relation to the plasma sheet near local midnight.

Although most of the general features of the electric field turbulence which occurs in the auroral regions and distant magnetotail are now known many questions remain concerning the plasma wave modes involved in this turbulence and the role which these waves play in the plasma heating and acceleration which occur along the auroral field lines. Since this turbulence occurs in regions with substantial field-aligned currents it seems most likely that these waves are produced by a current driven instability, such as the ion sound wave mode ($f < f_p^+$) or the electrostatic ion cyclotron modes ($f \approx n f_g^+$). Current driven instabilities of this type have been studied by several investigators (see for example, Kindel and Kennel, 1971). Further detailed studies of the charged particle distribution functions are needed to identify the plasma instabilities involved in the generation of these waves. Rough estimates of the anomalous resistivity produced by the broadband electric field turbulence detected in regions of field-aligned currents at high altitudes ($R > 4R_e$), indicate that this turbulence could only account for potential differences of about 100 volts between $R \approx 4.0 R_e$ and the distant magnetosphere [Gurnett and Frank, 1976]. Unless the turbulence becomes stronger at lower altitudes these potential differences are too small to account for the acceleration of auroral electrons to energies of 10 keV. Measurements are still needed in the altitude range from about 1.8 to $4.0 R_e$ to provide a conclusive evaluation of the role of this turbulence on the acceleration of auroral particles.

ACKNOWLEDGMENTS

The author wishes to thank Dr. J. A. Van Allen for providing the magnetic field data from Hawkeye-1 and Dr. R. P. Lepping for providing the magnetic field data from IMP-8.

The research at the University of Iowa was supported by the National Aeronautics and Space Administration through Grants NGL-16-001-002 and NGL-16-001-043, through Contracts NAS1-11257 and NAS1-13129 with Langley Research Center and through Contracts NAS5-11074 and NAS5-11431 with the Goddard Space Flight Center; and by the U. S. Office of Naval Research. The research at the Max-Planck-Institut was supported by the Alexander von Humboldt Foundation.

REFERENCES

- Anderson, R. R., and D. A. Gurnett (1973): Plasma wave observations near the plasmapause with the S³-A satellite. J. Geophys. Res., 78:4756.
- Dungey, J. W. (1972): Theory of neutral sheets. In: Earth's Magnetospheric Processes, Ed. by B. M. McCormac, Reidel, Dordrecht-Holland, 210.

- Frank, L. A. (1971): Plasma in the earth's polar magnetosphere. J. Geophys. Res., 76:5202.
- Frank, L. A., K. L. Ackerson and R. P. Lepping (1976): On hot tenuous plasmas, fireballs and boundary layers in the earth's magnetotail. Submitted to J. Geophys. Res.
- Gurnett, D. A. (1974): The earth as a radio source: terrestrial kilometric radiation. J. Geophys. Res., 79:4227.
- Gurnett, D. A., and L. A. Frank (1976): A region of intense plasma wave turbulence on auroral field lines. Submitted to J. Geophys. Res.
- Gurnett, D. A., L. A. Frank, and R. P. Lepping (1976): Plasma waves in the distant magnetotail. Submitted to J. Geophys. Res.
- Kindel, J. M., and C. F. Kennel (1971): Topside current instabilities. J. Geophys. Res., 76:3055.
- Kurth, W. S., M. M. Baumbach, and D. A. Gurnett (1975): Direction-finding measurements of auroral kilometric radiation. J. Geophys. Res., 80:2764.
- Mozer, F. S. (1976): Anomalous resistivity and parallel electric fields. In: Magnetospheric Particles and Fields, Ed. by B. M. McCormac, Reidel, Dordrecht-Holland (in press).
- Nagy, A. F., W. B. Hanson, T. L. Aggson, and R. J. Hoch (1972): Satellite and ground-based observations of a red arc. J. Geophys. Res., 77:3613.
- Paschmann, G., G. Haerendel, N. Sckopke, H. Rosenbauer, and P. C. Hedgecock (1976): Plasma and magnetic field characteristics of the distant polar cusp near local noon. Submitted to J. Geophys. Res.
- Piddington, J. H. (1967): Magnetic field annihilation in current pinches. Planet. and Space Sci., 15:733.

The Angular Distribution of Auroral Kilometric Radiation

JAMES LAUER GREEN, DONALD A. GURNETT, AND STANLEY D. SHAWHAN

Department of Physics and Astronomy, University of Iowa, Iowa City, Iowa 52242

Measurements of the angular distribution of auroral kilometric radiation (AKR) are presented by using observations from the Hawkeye 1, Imp 6, and Imp 8 satellites. The University of Iowa plasma wave experiments on Hawkeye 1 and Imp 6 provide electric field measurements of AKR in narrow frequency bands centered at 178, 100, and 56.2 kHz, and the Imp 8 experiment provides measurements at 500 kHz. From a frequency of occurrence survey, at radial distances greater than $7 R_E$ (earth radii) it is shown that AKR is preferentially and instantaneously beamed into solid angles of approximately 3.5 sr at 178 kHz, 1.8 sr at 100 kHz, and 1.1 sr at 56.2 kHz, directed upward from the nighttime auroral zones. Simultaneous multiple satellite observations of AKR in the northern hemisphere show that the radiation occurs simultaneously throughout these solid angles and that the plasmopause acts as an abrupt propagation cutoff on the nightside of the earth. No comparable cutoff is observed at the plasmopause on the dayside of the earth.

The results of computer ray tracing calculations for both the right-hand ($R-X$) and left-hand ($L-O$) polarized modes are also presented in an attempt to understand the propagation characteristics of the AKR. These calculations assume that a small source emits radiation at various frequencies along a magnetic field line at 70° invariant latitude near local midnight. The approximate altitude of the source can be determined for each of the two modes of propagation by adjusting the source altitude to give the best fit to the observed angular distributions. The $R-X$ mode is found to give the best agreement with the observed angular distributions.

INTRODUCTION

Recent satellite observations have revealed two distinctly different nonthermal radio emissions associated with the earth's magnetosphere. Both types of emissions occur at kilometric wavelengths in the radio spectrum. One of these types of radiation has a relatively constant intensity and is very weak. This radiation has been called the 'nonthermal continuum' and is generated between the plasmopause and the magnetopause, the greatest intensity being on the dayside of the earth [Gurnett, 1975]. The other type of radiation, which has been called 'terrestrial kilometric radiation' by Gurnett [1974] and by Kaiser and Alexander [1976], consists of intense sporadic bursts of electromagnetic radiation generated over a wide range of distances ($2-15 R_E$) above the auroral zones [Kaiser and Alexander, 1976]. Since the most intense and frequently occurring kilometric radio emissions originate from the nighttime auroral regions and are closely correlated with the occurrence of aurora, Kurth *et al.* [1975] have called these emissions 'auroral kilometric radiation.' The present study only considers satellite observations of auroral kilometric radiation (AKR).

Dunckel *et al.* [1970] first showed that AKR was correlated with the auroral electrojet index AE . Using photographs produced from the optical scanner aboard the Dapp satellite, Gurnett [1974] demonstrated a close association of AKR with discrete auroral arcs. Since Ackerson and Frank [1972] had previously showed that intense 'inverted V' electron precipitation events are correlated with discrete auroral arcs, Gurnett [1974] concluded that AKR is closely associated with the inverted V electron precipitation.

The power spectrum of AKR has a large degree of variability with time. Gurnett [1974] presented a power spectrum of a typical auroral kilometric burst as observed by Imp 8 that had a peak power flux of about $10^{-14} \text{ W m}^{-2} \text{ Hz}^{-1}$ at 178 kHz. On either side of the peak the spectrum decreased rapidly in intensity, decreasing to the receiver noise level at about 30 kHz and to near the cosmic background at 2 MHz. Kaiser and

Stone [1975] presented a similar power spectrum with peak frequency near 500 kHz, and they also indicated that the peak may sometimes be as low as 130 kHz. Gurnett [1974] estimated that at peak intensity the total power of AKR is sometimes as high as 10^6 W .

Preliminary evidence presented by Gurnett [1974] at 178 kHz indicated that AKR is generated at radial distances as low as $2.8 R_E$ (earth radii) in the evening auroral zone from a source that 'subtends a small angular size.' Direction finding measurements from Imp 8 and Hawkeye 1 were used by Kurth *et al.* [1975] to locate the average source region of AKR projected onto the equatorial plane at the frequency of 178 kHz. From Imp 8 observations the average source region was found to be at a local time of 21.25 hours and at a distance of $0.835 R_E$ from the polar axis. These measurements would place the source at a geocentric radial distance of about $2 R_E$ along an auroral field line (70° invariant latitude). The Hawkeye 1 observations presented by Kurth *et al.* [1975] also gave similar results.

Using RAE 2 in orbit about the moon, Kaiser and Alexander [1976] produced two-dimensional source location measurements of AKR from lunar occultations. They found that although the average source location at 250 kHz is between 2 and $3 R_E$ above the polar regions, a number of events indicated that the radiation may occasionally be generated at large radial distance ($>7 R_E$). From single lunar occultations, Alexander and Kaiser [1976] have observed several source regions at the same frequency. The most intense component of the multiple sources is almost always closest to the earth, and the weakest component is the most distant. A preliminary investigation by Alexander and Kaiser [1976] of the variation of source positions with observing frequency indicated that AKR emission at frequencies above 300 kHz came from closer to the earth than the emissions at frequencies less than 250 kHz. In addition, the sources in the northern hemisphere, on the nightside, appear to trace out a 70° invariant latitude magnetic field line.

The purpose of this paper is to determine the angular distribution of auroral kilometric radiation at different frequencies

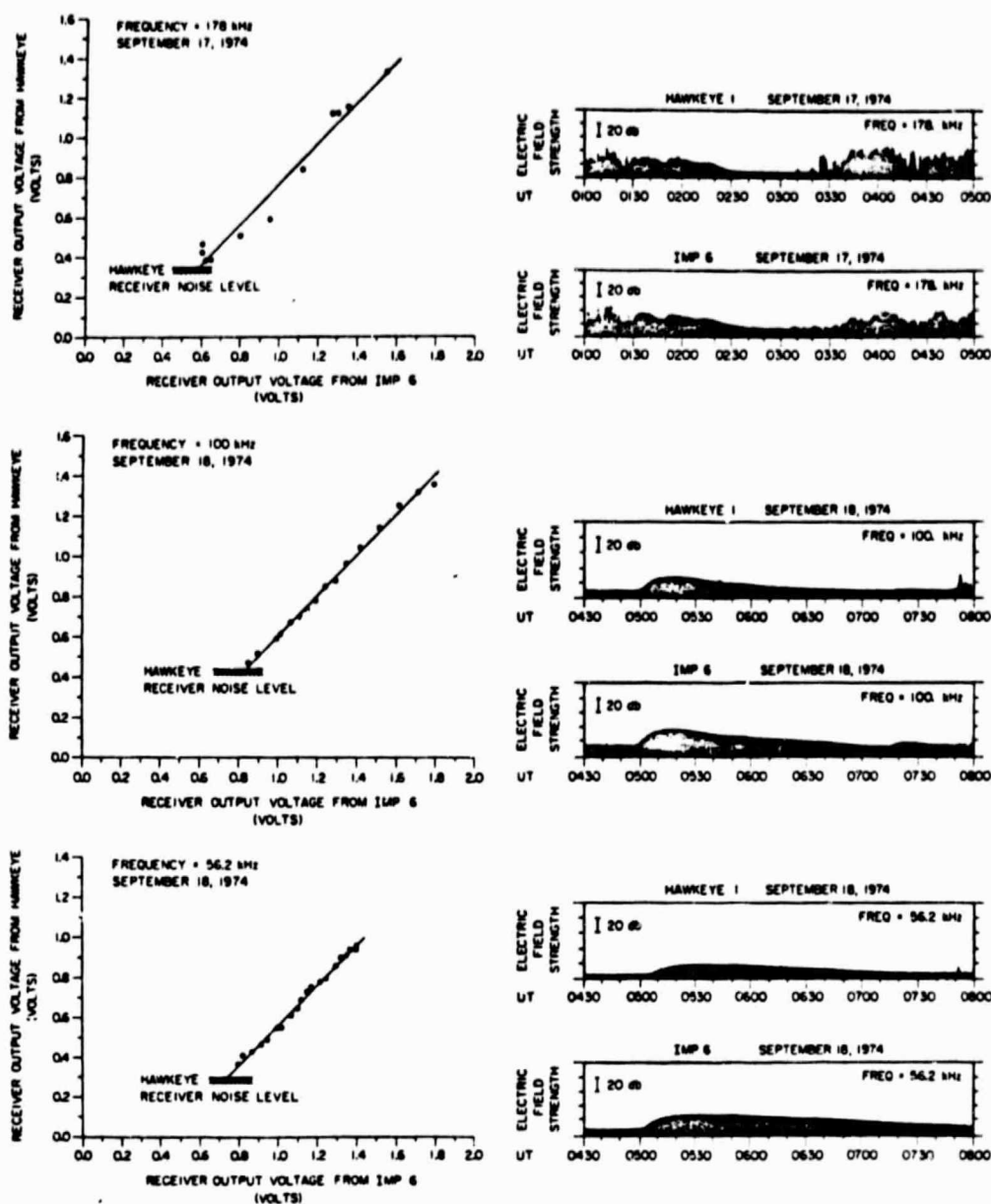


Fig. 1. Cross calibration of the receiver responses of the plasma wave experiments on Hawkeye 1 and Imp 6 using simultaneous observations of a type III radio burst.

by making use of observations from three satellites over a period of several years. Variations in these observed angular distributions as a function of frequency are then explored by using ray tracing calculations in order to obtain more information on the spatial position and characteristics of the source region of AKR. The ray tracing calculations also indicate the most probable polarization of this electromagnetic radiation.

METHOD OF ANALYSIS

Instrumentation

The University of Iowa has nearly identical plasma wave experiments on board Hawkeye 1, Imp 6, and Imp 8. Imp 6 and Hawkeye 1 are in highly elliptical earth orbits. The apogee of Hawkeye 1 is over the north polar region at a radial distance of 130,856 km. The apogee of Imp 6 is near the equatorial plane (orbit inclination of 28.7°) at a radial distance of 212,630 km. Imp 8 is in a low-eccentricity earth orbit near the equa-

torial plane with initial perigee and apogee radial distances of 147,434 and 295,054 km, respectively, and an orbit inclination of 28.6° .

Each of the three satellites has a long dipole antenna for electric field measurements. The Hawkeye 1 antenna is the shortest, measuring 42.45 m from tip to tip. The Imp 6 and Imp 8 antennae are longer, 92.5 and 121.8 m from tip to tip, respectively. To determine the electric field intensity at various frequencies, the antenna signals are periodically analyzed with spectrum analyzers. The Imp 6 spectrum analyzer has 16 frequency bands with center frequencies from 36 Hz to 178 kHz. For this experiment the filter bandwidths range from about $\pm 10\%$ of the center frequency at high frequencies to $\pm 20\%$ at low frequencies. The electric field spectrum analyzers on board Hawkeye 1 and Imp 8 also have 16 narrow band frequency channels with center frequencies from 1.78 Hz to 178 kHz ($\pm 10\%$) and 40 Hz to 178 kHz ($\pm 10\%$), respectively. In addition, Imp 8 has a tunable wide band receiver which measures

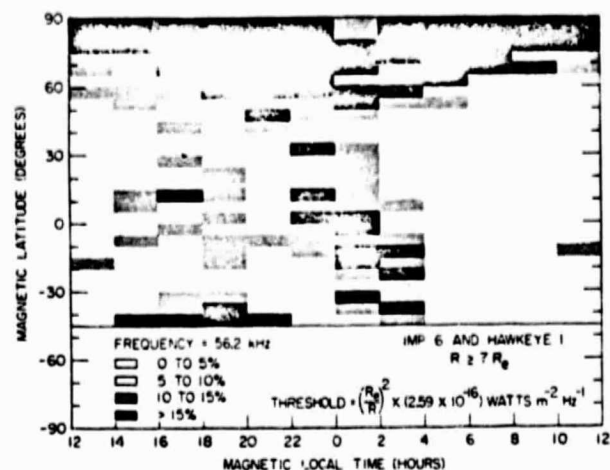


Fig. 2. The frequency of occurrence diagram of AKR as observed from the Imp 6 and Hawkeye 1 spacecraft at 56.2 kHz as a function of MLT and magnetic latitude.

the electric field intensity at 2 MHz, 500 kHz, 125 kHz, or 31.1 kHz with a bandwidth of ± 1 kHz. The dynamic range of each of these instruments is about 100 dB. The raw data from the spectrum analyzer channels are transmitted as voltages which range from 0 to 5 V and are approximately proportional to the logarithm of the electric field intensity.

In 6 months, Hawkeye 1 covers 24 hours of magnetic local time and provides observations over essentially the entire northern polar regions. Complete coverage of magnetic latitudes between -45° and $+45^\circ$ at all magnetic local times (out to $33 R_E$) is accomplished by Imp 6 after 1 year in orbit. The magnetic latitudinal coverage of Imp 6 and Imp 8 is quite similar, but a larger body of data is now available from Imp 6. Consequently, observations from Imp 6 and Hawkeye 1 will be combined to determine the angular extent of AKR at 56.2, 100, and 178 kHz in the northern hemisphere. Additional coverage by Imp 8 at 500 kHz is also presented to extend the analysis to higher frequencies.

Cross Calibration of Hawkeye 1 and Imp 6

Since data from two different satellites, Imp 6 and Hawkeye 1, are to be combined in a single frequency of occurrence

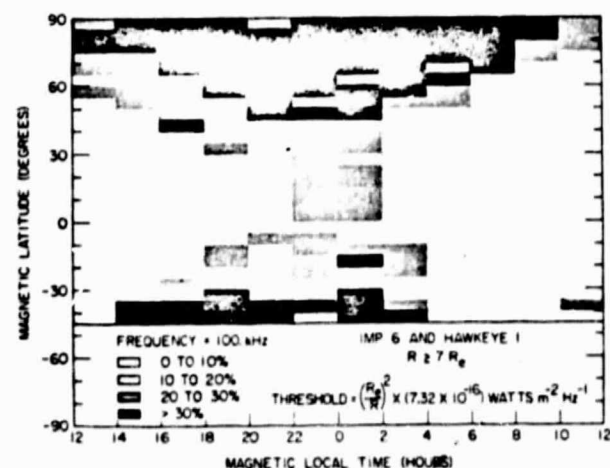


Fig. 3. The frequency of occurrence diagram of AKR as observed from the Imp 6 and Hawkeye 1 spacecraft at 100 kHz as a function of MLT and magnetic latitude.

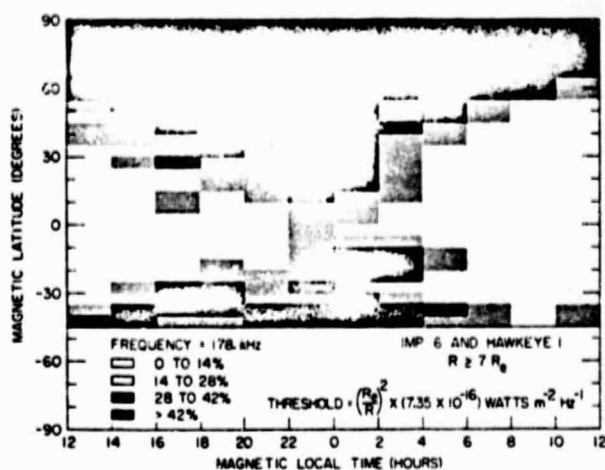


Fig. 4. The frequency of occurrence diagram of AKR as observed from the Imp 6 and Hawkeye 1 spacecraft at 178 kHz as a function of MLT and magnetic latitude.

analysis, it is necessary to perform a cross calibration of the two instrument sensitivities to make certain that no systematic differences are present in the calibrations. A convenient method of performing such a cross calibration is to compare simultaneous observations of a type III solar radio burst. Type III bursts are radio emissions from superthermal electrons emitted by the sun during a flare [Lin, 1970]. The use of the type III bursts to provide a cross calibration of Hawkeye 1 and Imp 6 is based on the assumption that the distance between the satellites is small compared to the distance the radiation has to travel from the source to the two satellites. Both satellites are then subjected to the same power flux.

Figure 1 shows a series of simultaneous observations of type III solar radio bursts by Imp 6 and Hawkeye 1 at 56.2 and 100 kHz on September 18, 1974, and at 178 kHz on September 17, 1974. The signature of the type III burst at these frequencies can be recognized easily by the smooth rapid increase in signal strength to a maximum on a time scale of a few minutes followed by a gradual decrease to the receiver noise level on a time scale of several tens of minutes. Note the multiple type III event on September 17, 1974, in the 178-kHz channels. The large sporadic intensity fluctuations on either side of the multiple type III events in Figure 1 are bursts of AKR. Close

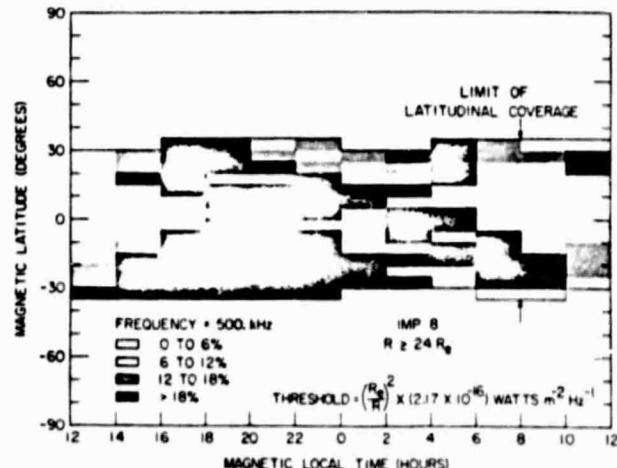


Fig. 5. The frequency of occurrence diagram of AKR as observed from the Imp 8 spacecraft at 500 kHz as a function of MLT and magnetic latitude.

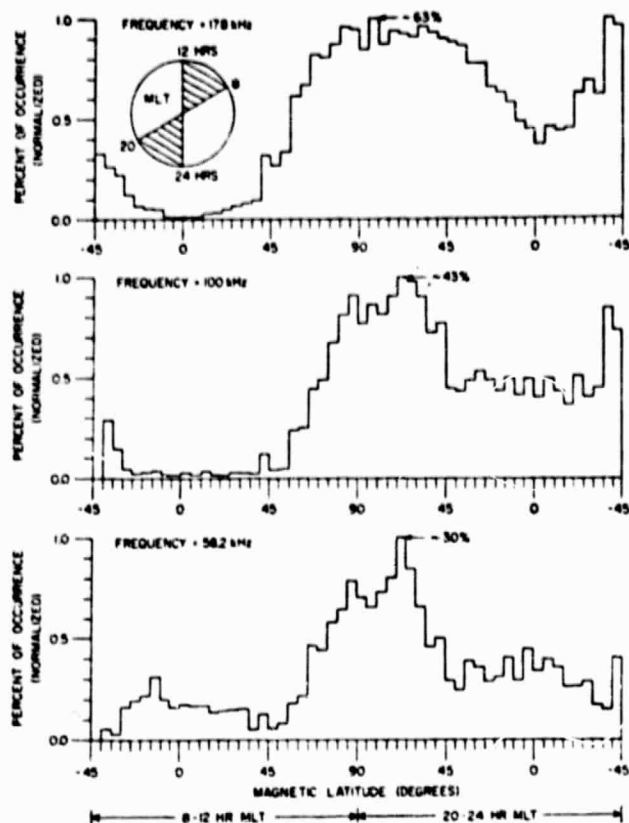


Fig. 6. The normalized percentage of occurrence of AKR in magnetic meridian sections between 8 and 12 hours and 20 and 24 hours MLT.

examination shows that both satellites are receiving the same AKR bursts, as is evident by the closely correlated variation of the electric field strengths in the 178-kHz channels.

The cross calibration graphs on the left of Figure 1 are obtained by plotting the raw voltage output of the Hawkeye spectrum analyzer versus the raw voltage output of the Imp 6 analyzer for these type III bursts. Each point is a measurement from both satellites taken at the same time and at the same frequency during the slowly decreasing part of the type III radio burst. Only the peak intensities were used in these comparisons to take into account any spin modulation effects. From the straight line fits in each graph the relationship between the output voltage from the receivers on Hawkeye 1 and Imp 6 can be found. In every case the slope of each straight line fit is one, confirming that the sensitivities of the receivers are identical. The absolute magnitudes of the intensities determined from the preflight calibrations agree within 2 dB.

THE OBSERVED ANGULAR DISTRIBUTION

Information on the angular distribution of AKR can be obtained by examining where the satellites have observed the highest frequency of occurrence of radiation above a preset threshold. A two-dimensional frequency of occurrence diagram of AKR can be constructed in magnetic latitude (λ_m) and magnetic local time (MLT) by using a $1/R^2$ power flux threshold criterion to correct for the expected $1/R^2$ radial variations of the power flux [see Gurnett, 1974]. Although the source is not located at the center of the earth, this radial

variation corrects for the first-order radial dependence of the power flux, provided the source is located relatively close to the earth.

On the basis of a survey of 10 months of Hawkeye 1 data at 178, 100, and 56.2 kHz and 1½ years of Imp 8 data at 500 kHz a power flux threshold was chosen 25 dB below the maximum power flux observed for each frequency. This threshold was a compromise resulting from the conflicting requirements to obtain enough data points above the threshold for good statistical accuracy, and at the same time assure that the threshold is well above the receiver noise for each spacecraft and for each frequency analyzed. The thresholds selected are as follows:

$$\begin{aligned} (500 \text{ kHz}) \text{ threshold} &= (R_E/R)^2 \times (2.17 \times 10^{-16}) \text{ W m}^{-2} \text{ Hz}^{-1} \\ (178 \text{ kHz}) \text{ threshold} &= (R_E/R)^2 \times (7.35 \times 10^{-16}) \text{ W m}^{-2} \text{ Hz}^{-1} \\ (100 \text{ kHz}) \text{ threshold} &= (R_E/R)^2 \times (7.32 \times 10^{-16}) \text{ W m}^{-2} \text{ Hz}^{-1} \\ (56.2 \text{ kHz}) \text{ threshold} &= (R_E/R)^2 \times (2.59 \times 10^{-16}) \text{ W m}^{-2} \text{ Hz}^{-1} \end{aligned}$$

Since the distance from the spacecraft to the source of AKR is not known during the initial reduction of data, the R value used in calculating the power flux threshold is the geocentric radial distance to the spacecraft. To reduce the error caused by the uncertainty in the radial distance to the source and to avoid complications due to near-earth propagation effects, only measurements obtained at $R > 7 R_E$ are used in the analysis. If the source is near the earth ($R < 3 R_E$), then the margin of error in the radial distance correction of the threshold is at most ± 4 dB, which is small in comparison with the amplitude range (~ 100 dB) over which the intensity of AKR varies.

The frequency of occurrence diagram determined from the frequency of occurrence analysis for 56.2 kHz is shown in Figure 2. The measurements used comprise 3.5 years of Imp 6 data and 10 months of Hawkeye 1 data. Blocks of 5° increments in λ_m and 2-hour increments of MLT are used. The magnetic coordinates of the spacecraft determine the block within which an observation is counted. In each block the total number of 3-min observations of AKR above the threshold are counted. This number is divided by the total number of 3-min observations in that block to give the frequency of occurrence. The black shading in Figure 2 represents the highest percentage of times that AKR was detected above the power flux threshold. The distinct emission cone (black shading) of AKR is clearly evident in Figure 2 in the northern hemisphere. The emission cone appears to be completely filled and is symmetric, centering around 22 hours MLT, indicating that the preferred direction of AKR is in the local evening, in agreement with direction finding measurements of the average source locations by Kurth *et al.* [1975] and Kaiser and Stone [1975]. Near local midnight the latitudinal boundary of the emission cone extends to near the magnetic equator and is rather poorly defined, as is indicated by the complicated variations of the frequency of occurrence in this region. At high magnetic latitudes on the dayside of the earth (6–10 hours MLT) the frequency of occurrence of AKR changes by at least a factor of 4 at $\lambda_m = 65^\circ \pm 10^\circ$. This rapid change in the frequency of occurrence indicates that a relatively stable boundary to the AKR angular distribution occurs on the dayside of the earth.

The frequency of occurrence diagrams at 100 and 178 kHz, shown in Figures 3 and 4, respectively, were produced in the same manner as those of Figure 2. AKR is observed with

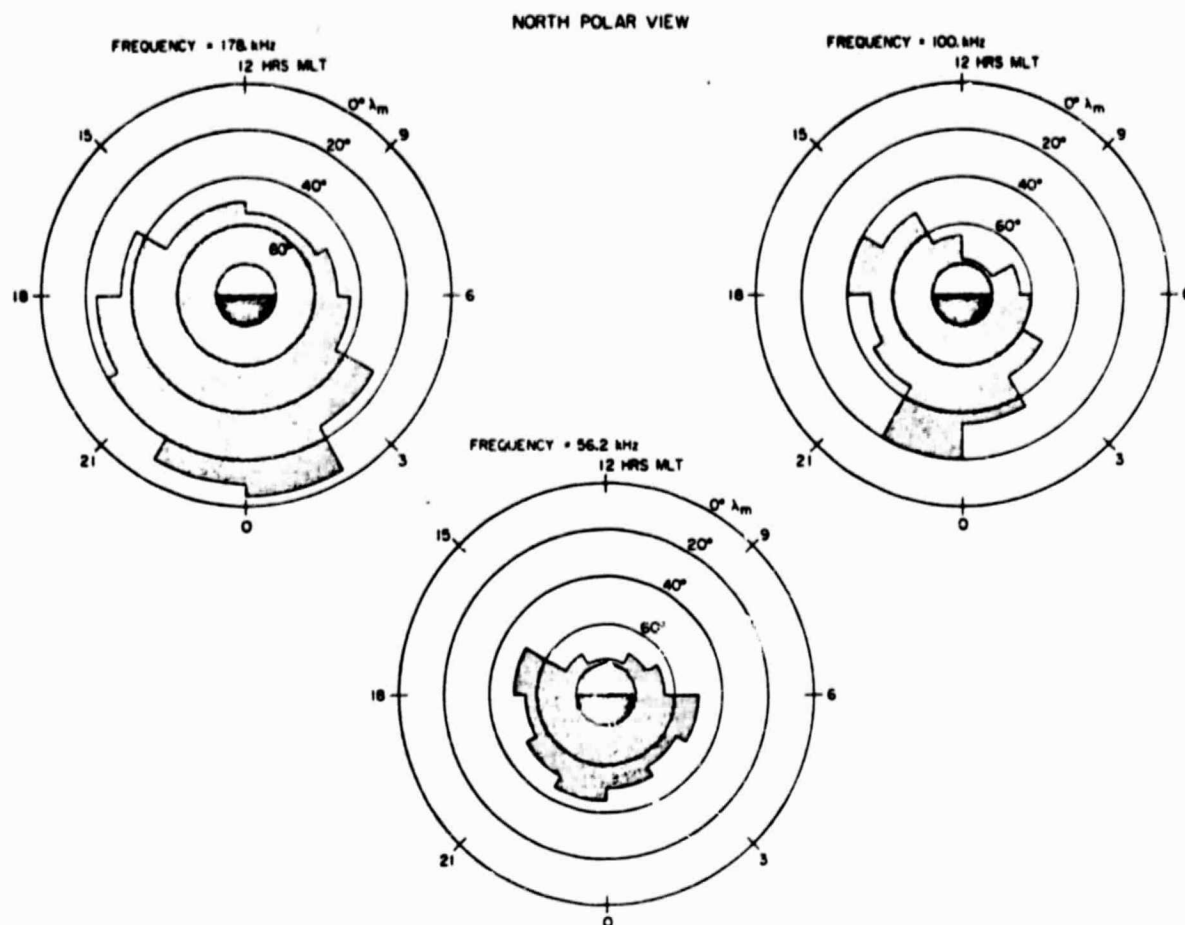


Fig. 7. A north polar view of the latitudinal boundary of the AKR emission cones at 178, 100, and 56.2 kHz in magnetic coordinates. The decreasing angular size of the emission region with decreasing frequency is clearly evident.

almost equal frequency throughout the emission cones (black shading) at 100 kHz and 178 kHz. Similarities with Figure 2 include (1) a rapid change in the frequency of occurrence at high λ_m on the dayside of the earth, (2) a complicated poorly defined latitudinal boundary at low latitudes on the nightside of the earth, and (3) symmetry about 22 hours MLT. At higher frequencies (particularly 178 kHz) the emission cones extend closer to the magnetic equator in the local evening.

Figure 5 shows the frequency of occurrence of AKR at 500 kHz from 1½ years of Imp 8 data. Hawkeye 1 and Imp 6 do not have a 500-kHz channel, and consequently we are limited in latitudinal coverage to $\pm 45^\circ \lambda_m$. Figures 2, 3, 4, and 5 are consistent with the general picture that from 56.2 to 500 kHz the solid angle of the emission cones increases as the frequency increases. At 500 kHz the northern and southern emission cones appear to overlap substantially in the region near local midnight.

To obtain a better impression of the latitudinal variation of the frequency of occurrence, we can normalize each of these frequency of occurrence diagrams. The normalization is accomplished by changing the scale of each frequency of occurrence diagram to a scale that ranges from zero to one with the maximum percentage of occurrence equals one. Figure 6 shows the normalized percentage of observed AKR for the three frequencies 178, 100, and 56.2 kHz versus magnetic

latitude. All observations on the dayside of the earth with MLT between 8 and 12 hours are on the left side of each panel. The right side shows observations on the nightside of the earth from 20 to 24 hours MLT. The observations are organized by magnetic latitude, the north magnetic pole being located directly at the center of each plot. Starting at the pole, the normalized occurrence decreases rapidly with decreasing latitude on the dayside of the earth, with a sharp boundary at about $\lambda_m = 65^\circ \pm 10^\circ$ for all frequencies. On the nightside of the earth the normalized occurrence decreases less rapidly with decreasing latitude and has a nearly constant plateau from about $+45^\circ$ to -45° in the 56.2- and 100-kHz channels. The 178-kHz distribution extends closer to the equator than the 100- and 56.2-kHz distribution. The day-night skewness in the normalized occurrence of AKR evident in Figure 6 could be produced by an angular distribution that would be variable in time on the nightside of the earth and spatially fixed in time on the dayside.

A north polar view of the angular distribution of AKR can be constructed by noting the magnetic latitude of the normalized half-occurrence points at all MLT. The boundaries of the shaded areas in Figure 7 show the position of these normalized half-occurrence points in magnetic coordinates. This illustration shows that AKR is preferentially beamed into larger solid angles at higher frequencies, approximately 1.1 sr at 56.2 kHz.

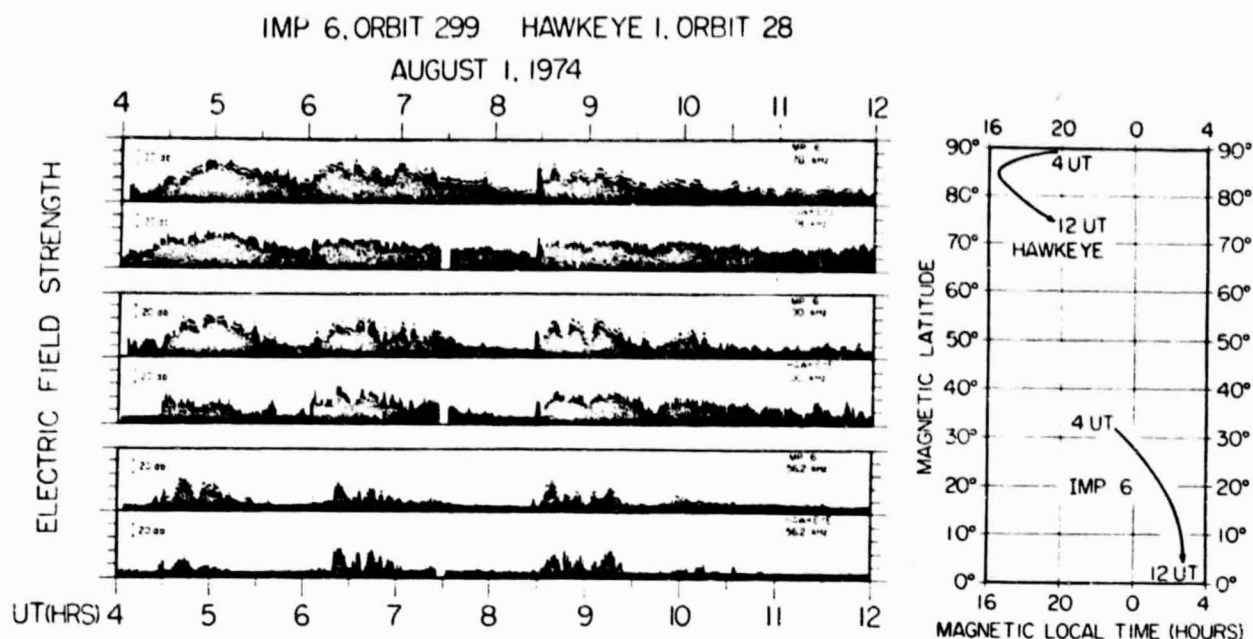


Fig. 8. Simultaneous observations from the Hawkeye 1 and Imp 6 spacecraft of AKR at widely separated magnetic latitudes. In this case the intensity variations are closely correlated, indicating that the radiation occurs simultaneously over a large solid angle. In addition, the absolute power fluxes are approximately the same at both spacecraft.

1.8 sr at 100 kHz, and 3.5 sr at 178 kHz. On the assumption that the angular distribution at 500 kHz is completely filled in over the polar regions, Figure 5 shows that the solid angle at 500 kHz is approximately 5.3 sr, in agreement with the general trend toward larger solid angles at higher frequencies.

SIMULTANEOUS OBSERVATIONS AT WIDELY SEPARATED LOCATIONS

Simultaneous observations from two satellites at widely separated locations reveal many important characteristics of AKR that cannot be discerned with a single satellite. One of the most important questions which can be investigated is whether or not individual bursts of AKR simultaneously and uniformly illuminate the large solid angles depicted in Figure 7 or whether these frequency of occurrence distributions could be the result of a much narrower instantaneous beam or cone which varies in time.

To illustrate, Figure 8 presents simultaneous electric field data from Imp 6 and Hawkeye 1 for the same auroral kilometric storms. On the left side of this figure the corresponding frequencies from each satellite are individually compared in plots of electric field intensity versus time. It is easy to see that both satellites are observing radiation originating from the same source. On the right side the satellite trajectories are shown in MLT and λ_m coordinates for the corresponding time period. Figure 8 illustrates that individual AKR bursts radiate into large solid angles and that the frequency of occurrence diagrams are not representations of small solid angle beams of AKR that have moved in time. In addition, the absolute power fluxes of AKR observed by both satellites are nearly identical (to within about 2 dB). This important observation indicates that the source of AKR uniformly illuminates the entire region within the emission cones.

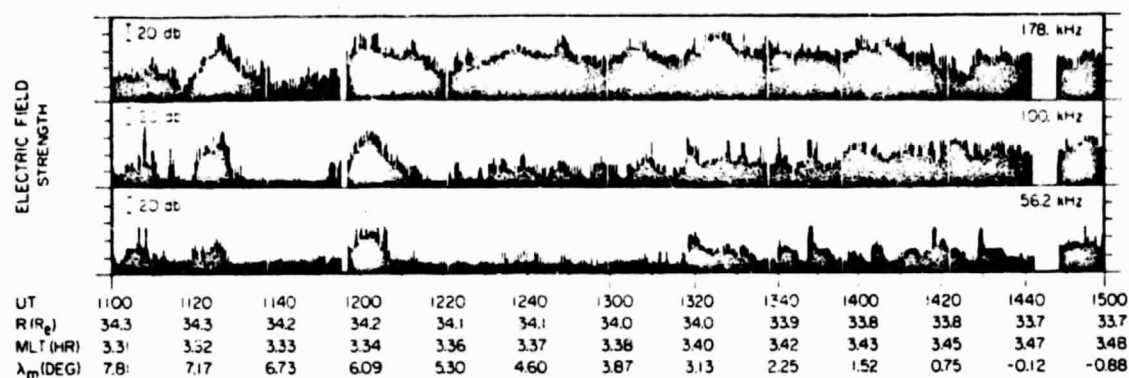
Simultaneous observations of electric field data from Imp 8 and Hawkeye 1 can be used to investigate propagation cutoff characteristics of AKR. In Figure 9, for instance, Imp 8 is near

3 hours MLT at large radial distances and is observing intense storms of AKR during the entire time period shown. Hawkeye 1 also observes these intense storms of AKR but only in certain regions of its orbit. This is evidently a spatial effect and not a temporal effect, since Imp 8 still observes AKR when Hawkeye 1 is not detecting the radiation.

The position of the plasmapause in Figure 9 has been identified by the change in the low-frequency (17.8 Hz) electric field intensity and the plasmaspheric hiss cutoff, similar to the observations of Shaw and Gurnett [1975]. The identification of the upper hybrid resonance (UHR) noise in Figure 9 also provides an indication of the location of the plasmapause boundary. As is evident in Figure 9, the position of the plasmapause at 1152 UT (universal time) closely corresponds to the abrupt drop in intensity of AKR as observed from Hawkeye 1 near local midnight. The times of the signal loss for the different frequencies (178, 100, and 56.2 kHz) are not the same. At higher frequencies the propagation cutoff tends to occur closer to the earth. This propagation cutoff characteristic of AKR at low altitudes on the nightside has been previously reported by Gurnett [1974] from Imp 6 data and is assumed to occur when the local electron plasma frequency exceeds the wave frequency. Gurnett [1974] notes that the propagation cutoffs of AKR are consistent with the expected rapid increase in the plasma density, and hence plasma frequency, at the plasmapause. These observations imply that the extent of the propagation of AKR on the nightside is limited by the local plasma characteristics at the plasmapause.

At 1403 UT in Figure 9, Hawkeye 1 again leaves the plasmapause, but it is now on the dayside of the earth. As the spacecraft travels upward in its trajectory, the intensity of the AKR gradually begins to increase over a distance of several earth radii and does not exhibit a sharp propagation cutoff such as was observed on the nightside of the earth. Imp 8 meanwhile observes many large amplitude bursts of AKR at its position on the nightside, confirming that AKR is present

IMP 8 ORBIT 39 FEB. 2, 1975



HAWKEYE 1 ORBIT 115 FEB. 2, 1975

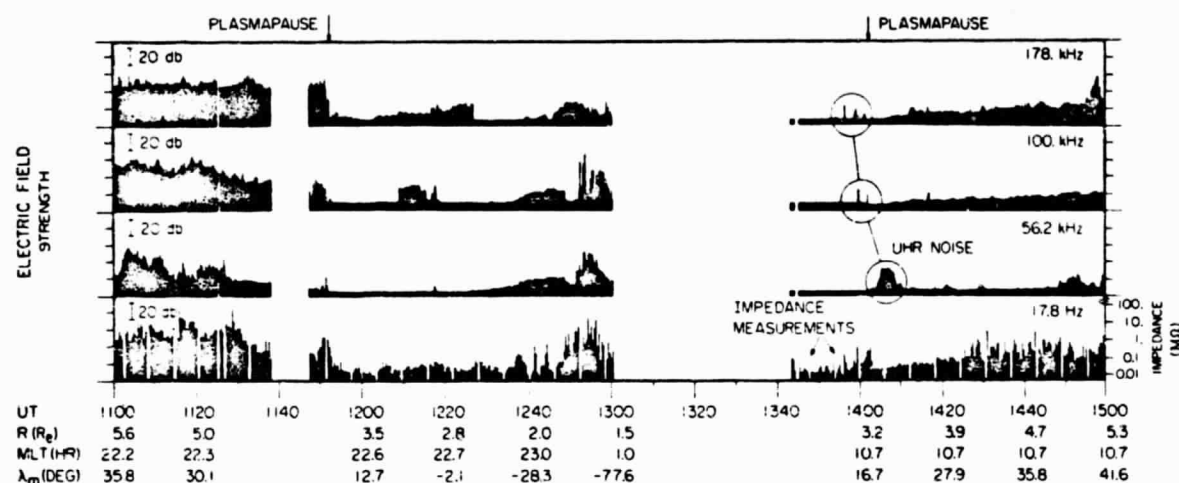


Fig. 9. Simultaneous observations from Imp 8 and Hawkeye 1. Imp 8 is at large radial distances on the nightside in the northern hemisphere observing intense bursts of AKR. Meanwhile, Hawkeye 1 moves in and out of the emission cones of AKR as it passes through the inner regions of the earth's magnetosphere near the noon-midnight meridian. As observed from Hawkeye 1, the plasmapause acts as an abrupt propagation cutoff to AKR only on the nightside. On the dayside, AKR does not propagate down to the plasmapause. The 17.8-Hz channel is used to determine the position of the plasmapause.

during this period. The absence of an abrupt propagation cutoff indicates that the latitudinal boundary of the illumination region on the dayside of the earth is not determined by the plasma characteristics near the plasmapause, in direct contrast with what is observed on the nightside. This asymmetry in the angular distribution in the noon-midnight meridian provides important information about the propagation of AKR at low altitudes (3–5 R_E). Any meaningful model of AKR ray paths must describe this effect.

COMPARISON OF COMPUTED RAY PATHS WITH OBSERVED ANGULAR DISTRIBUTIONS

Introduction

From cold plasma theory it is known that the only modes which can escape into 'free space' (where the magnetic field and plasma density are small compared to the source region) are the right-hand polarized extraordinary ($R-X$) mode and the left-hand polarized ordinary ($L-O$) mode. Mechanisms which lead to radiation primarily in the left-hand mode have

been proposed by Benson [1975], Palmadesso et al. [1976], and Jones [1976]. Right-hand polarized radiation will be produced by the generation mechanisms proposed by Scarf [1974], Gurnett [1974], and Melrose [1976]. In addition, Barbosa [1976] suggests a process which produces both $R-X$ and $L-O$ components. At the present time there is no direct experimental evidence on the polarization of AKR or the exact height at which the radiation is generated.

Ray tracing calculations can be used in comparisons with the observed angular distributions to provide information on the polarization of AKR and on the region in which the radiation is generated. It will be shown from such comparisons that the ray paths are very sensitive to the source location and to the polarization.

The Electron Density and Magnetic Field Models

In order for a valid comparison to be made the magnetospheric models which are used in the ray tracing must be acceptable representations of the physical environment that

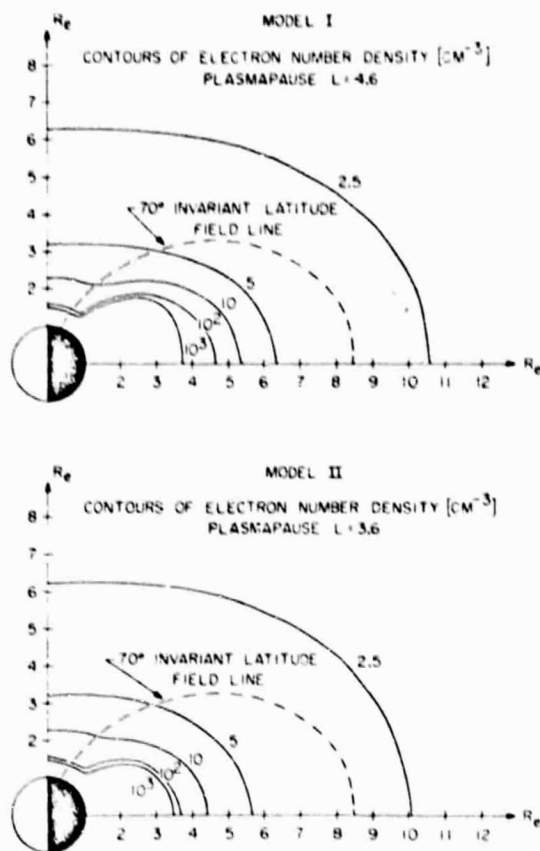


Fig. 10. Two model magnetospheres used in the ray tracing of AKR. The main difference between the models is the size of the plasmapause. Model I has a plasmapause L value of 4.6 and represents the earth's magnetosphere in times of moderate geomagnetic activity. Model II has a plasmapause L value of 3.6 for times of severe geomagnetic activity. Only the electron distributions in the northern hemisphere on the nightside are shown in this figure.

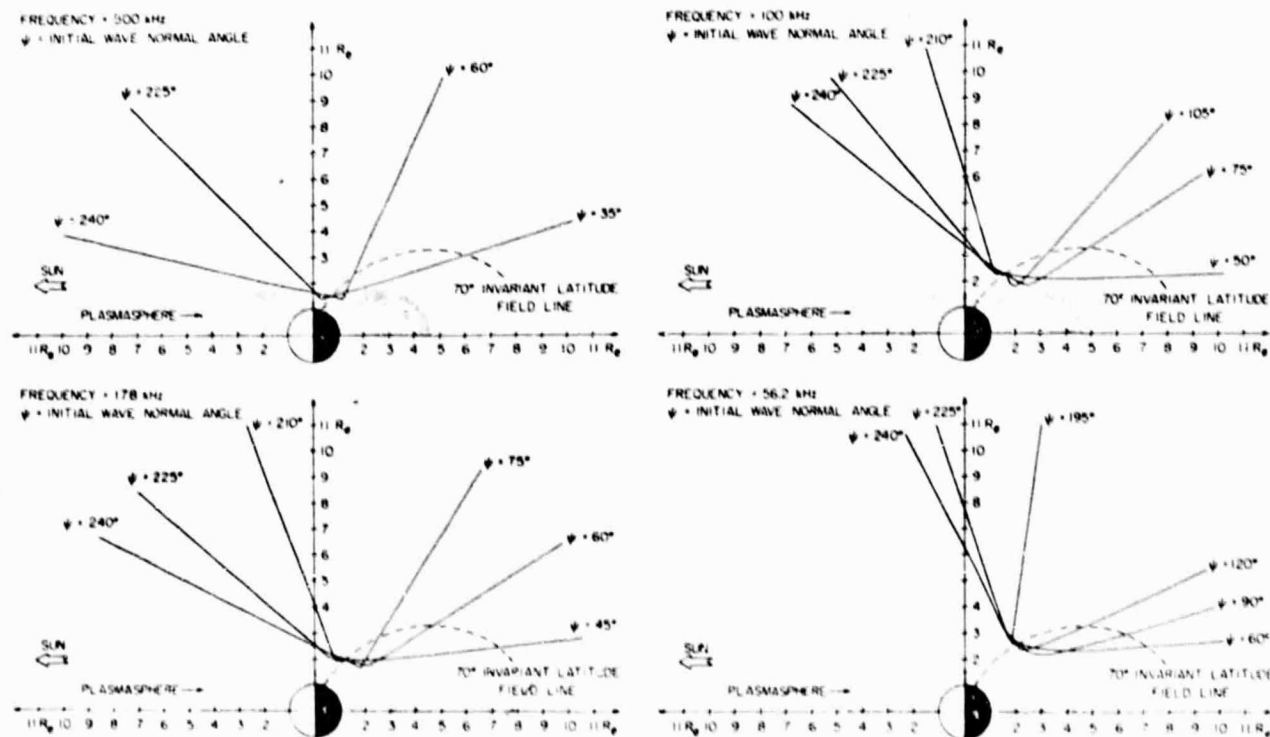


Fig. 11. Ray tracing examples of radiation in the R - A mode in the model I magnetosphere at 500, 178, 100, and 56.2 kHz.

influences the radiation. The polar magnetosphere and plasmapause are known to be strongly dependent on geomagnetic activity. AKR is observed most frequently during times of disturbed geomagnetic activity [Dunckel et al., 1970; Gurnett, 1974; Voots et al., 1976]. Since the plasmapause position plays an important role in controlling the angular extent of the AKR on the nightside of the earth, it is important that a suitable model of the plasmapause position be used. During moderate magnetic activity the plasmapause is located at about $4.5 R_E$ geocentric radial distance in the equatorial plane near local evening [Carpenter, 1963]. At times of severe magnetic storms the plasmapause contracts inward to about $3.5 R_E$ [Carpenter, 1963]. The plasmapause is believed to be closely aligned along the magnetic field.

For these ray tracing studies, two models, shown in Figure 10, have been used for the electron density near the plasmapause. For model I the plasmapause is located at $L = 4.6$, and for model II the plasmapause is at $L = 3.6$. For both models the electron density is 100 cm^{-3} at the plasmapause. In all cases it is assumed that the radio emission is generated along a magnetic field line which intersects the earth at 70° invariant latitude ($L = 8.55$). Since the earth's magnetic field closely resembles a dipole field at the relatively low altitudes where the AKR is believed to be generated, an ideal dipole field is used with a surface magnetic field strength of 0.62 G at the poles. The electron density is assumed to decrease very rapidly with increasing radial distance over the polar regions, reaching a density of about 10 cm^{-3} at $2.25 R_E$ (essentially the modified polar wind model used by Gurnett [1974]).

Experimental justification for some of the main features of the density contours in models I and II can be found in Figure 9. The UHR noise band in Figure 9 has a frequency range that extends between the local plasma frequency and the local UHR frequency [Shaw and Gurnett, 1975]. From the plasmapause determined by the peak in the 17.8-Hz channel and the

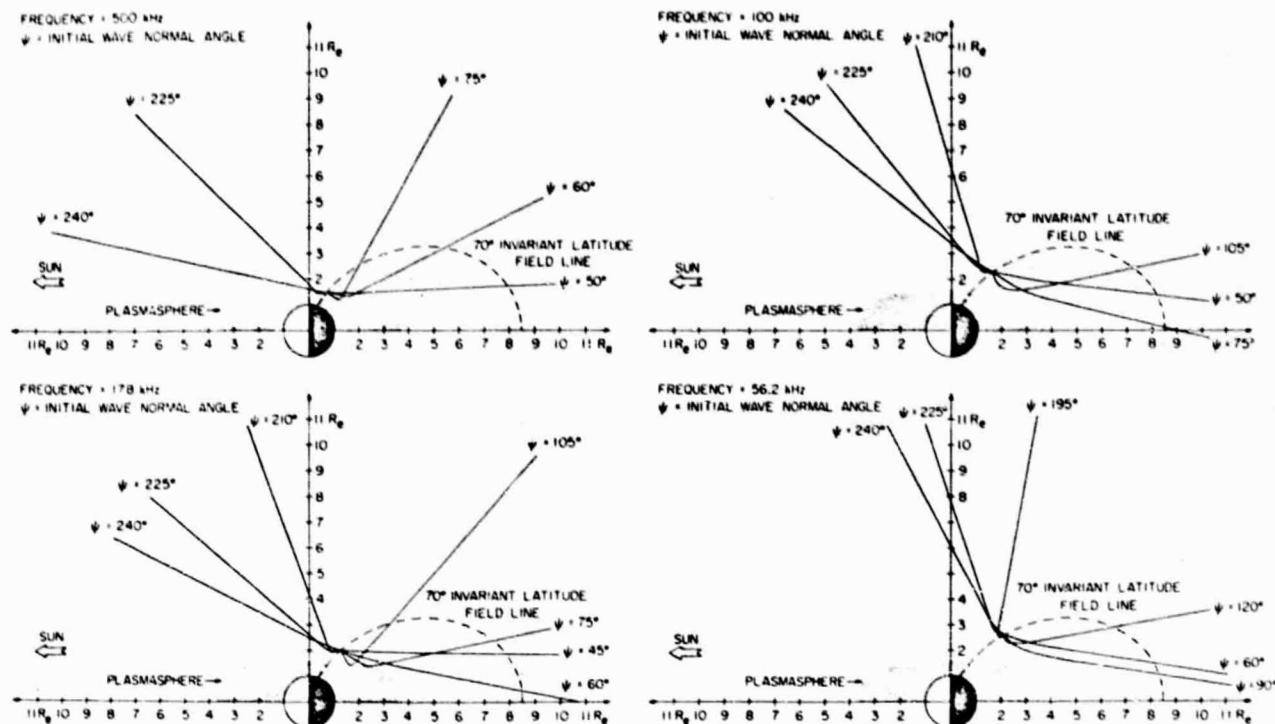


Fig. 12. Additional $R-X$ mode ray tracing examples in the model II magnetosphere at 500, 178, 100, and 56.2 kHz. The source locations are the same as those used in Figure 11. Note the effect that a contracted plasmapause has on the angular extent of this radiation when this figure is compared to Figure 11. The contracted plasmapause allows the $R-X$ radiation to propagate to the equator at lower altitude while the dayside distribution remains unchanged.

frequency range of the UHR noise the plasma frequency associated with the plasmapause is between 56.2 and 100 kHz. The plasmapause density of 100 cm^{-3} used in models I and II gives an electron plasma frequency of about 90 kHz, which is consistent with these observations. In Figure 9 the position of the plasmapause on the dayside is approximately $3.3 R_E$ at $\lambda_m = 18.6^\circ$. The plasmapause (100-cm^{-3} density contour) in model II at $\lambda_m = 18.6^\circ$ is also $3.3 R_E$. In Figure 9 on the nightside the

plasmapause is at approximately $3.87 R_E$ at $\lambda_m = 17.8^\circ$, which is halfway between the model I and II plasmapause positions.

Program Description

The ray tracing computer program used in this study was initially developed by Shawhan [1966, 1967a, b]. The program is based on a closed set of first-order differential equations in spherical polar coordinates derived by J. Haselgrove [1955]

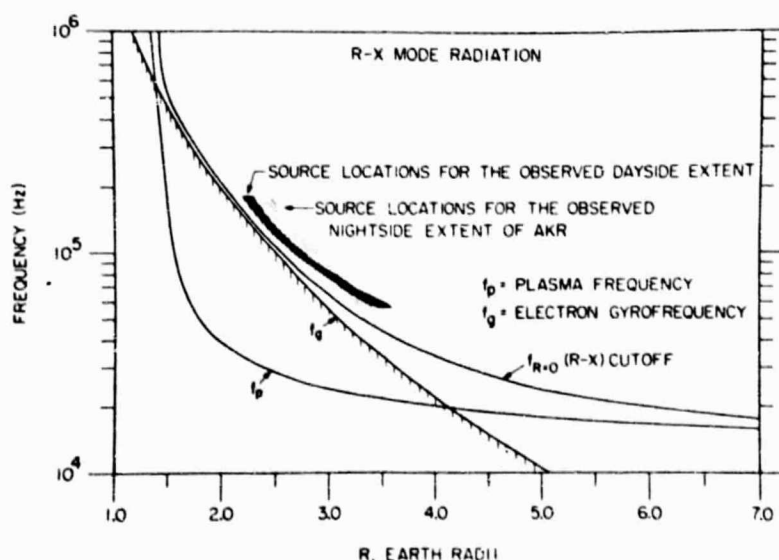


Fig. 13. Radial variation of the $R-X$ cutoff frequency along the 70° invariant latitude magnetic field line in the model I or II magnetosphere. The cross-hatching indicates the source region determined from matching the dayside latitudinal cutoff of AKR to the $R-X$ mode ray paths in the model I or II magnetosphere. The dot pattern indicates the $R-X$ mode source region determined from the nightside latitudinal cutoff of AKR by using the model II magnetosphere.

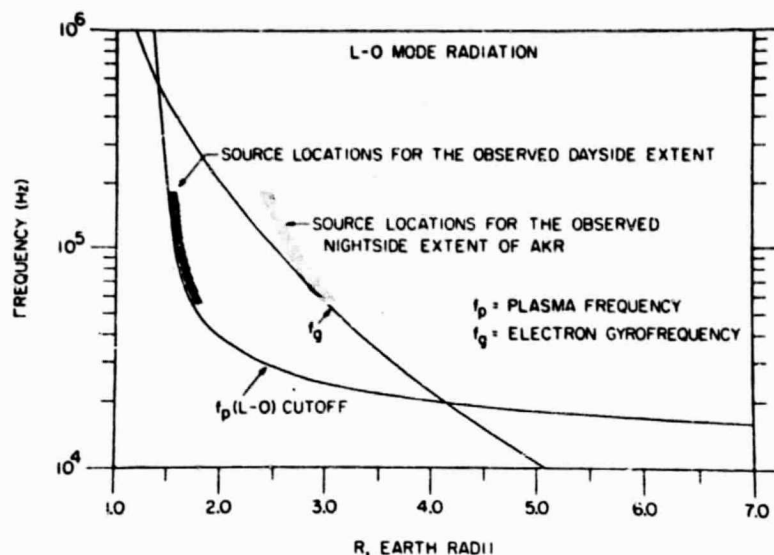


Fig. 14. Source regions in the midnight meridian (along a 70° invariant latitude field line) which produce rays of frequencies 178–56.2 kHz in the L - O mode whose latitudinal cutoffs are consistent with the observed AKR angular distribution. The cross-hatching indicates the source region in model I or model II determined from only the dayside latitudinal cutoff of AKR. The dot pattern indicates the source region in model II determined from only the nightside latitudinal cutoff of AKR.

and C. G. Haselgrove and J. Haselgrove [1960]. The equations were specialized by Shawhan [1966] for ray tracing in a magnetic meridian for a model magnetosphere. The expressions for the phase index of refraction and its derivatives are from the cold plasma formulation by Stix [1962]. The behavior of a ray path is determined by the frequency of the wave, the initial wave normal angle, the initial latitude, the initial altitude, the propagation mode, and the magnetospheric model.

Ray Tracing Results

All ray tracing calculations and source locations presented here are in the noon-midnight meridian. Since the source of AKR at a particular frequency 'subtends a small angular size' [Gurnett, 1974], all rays at a particular frequency are assumed to emanate from a point source along a 70° invariant latitude field line. The 70° invariant latitude field line is used to be consistent with observations of actual AKR source locations made by Alexander and Kaiser [1976]. Each source location is assumed to emit electromagnetic radiation at all wave normal angles ψ . For any given source location, two specific wave normal directions will give the most extreme dayside and nightside latitudinal limits to the ray directions at large radial distances, all of the other wave normal angles giving intermediate ray directions. By varying the source latitude along the magnetic field line a unique altitude can be found for each frequency which will give a limiting ray direction in agreement with the observed dayside (or nightside) latitudinal limit. By performing this analysis as a function of frequency a unique determination can be obtained for the source altitude as a function of frequency which can be compared with the various theories for AKR generation.

To demonstrate some of the basic ray path effects involved in this analysis, Figure 11 shows R - X mode rays calculated in the model I magnetosphere (plasmapause L value of 4.6) for various selected wave normal angles. The wave normal angles shown include those which give the most extreme dayside and nightside latitudinal limits to the ray paths, as well as other rays at intermediate wave normal angles. The dayside latitudinal

limits are in good agreement with what is qualitatively observed: the higher the frequency, the lower the magnetic latitude at which the radiation can be observed. Rays on the nightside penetrate the topside plasmapause to depths qualitatively consistent with those in Figure 9. These ray paths show that the plasmapause presents a refracting layer. The ray behavior (R - X mode) in the model II magnetosphere (plasmapause L value of 3.6) for the same source region is illustrated in Figure 12. The latitudinal extent of the dayside rays is the same as that for Figure 11, which shows that the dayside rays are relatively unaffected by the plasmapause. The substantial change in the angular distribution on the nightside demonstrates that the position of the plasmapause for this assumed source region strongly determines the latitudinal extent of the ray paths on the nightside of the earth. The smaller plasmapause has allowed the rays to propagate down to the equatorial plane on the nightside.

The assumed radial variation of the frequency of the R - X cutoff ($R = 0$) along a 70° invariant latitude field line in the model magnetospheres is illustrated in Figure 13. The $R = 0$ cutoff is the same for both plasma models because the size of the plasmasphere is not thought to affect the electron densities significantly at high latitudes. By adjusting the source altitude so that the limiting ray angles agree with the observed latitudinal limits of the angular distribution (within specified limits) a range of source altitudes can be found which would produce the observed angular distribution at each frequency. For instance, the crosshatched region in Figure 13 shows the relationship found between source altitudes and frequencies which would result in dayside R - X rays whose latitudinal limit at large radial distance agreed (to within $\pm 5^\circ$) with the observed angular distributions on the dayside of the earth. On the dayside the source region is essentially identical for models I and II because of the previously mentioned insensitivity to the plasmapause location in this region. On the nightside of the earth the corresponding source region required to obtain agreement with the nighttime angular distribution is indicated by the dot pattern in Figure 13. This source region was calcu-

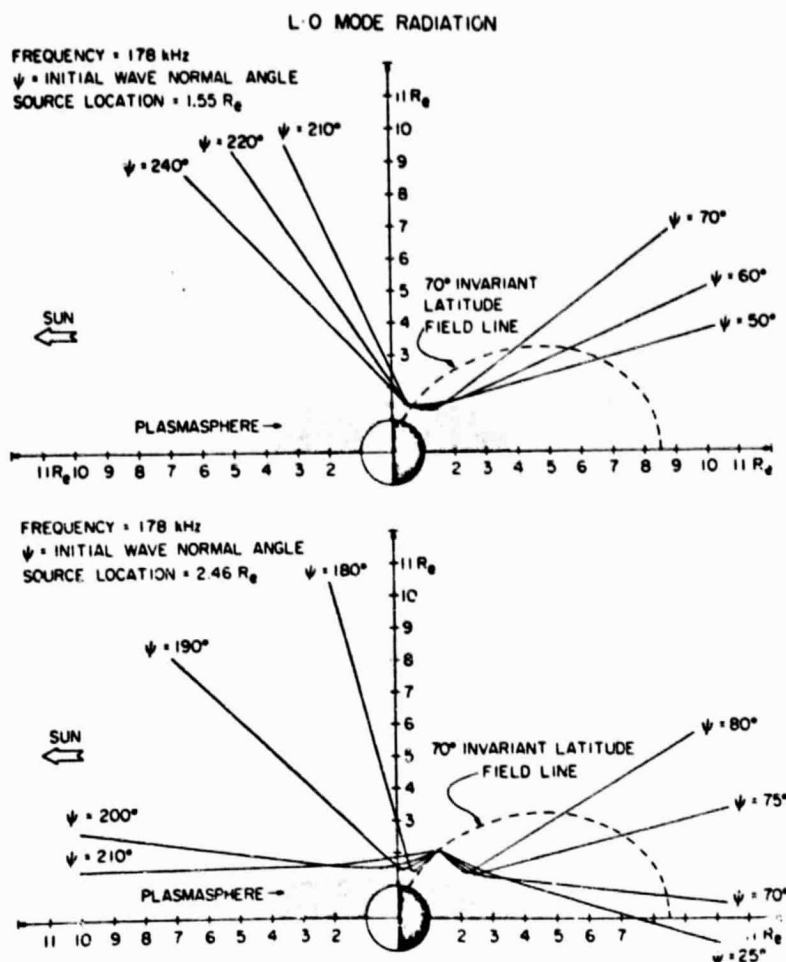


Fig. 15. *L-O* mode ray paths in the model II magnetosphere at 178 kHz. The top panel has a source location that lies within the cross-hatched region of Figure 14 and thus produces rays on the dayside whose latitudinal cutoffs are consistent with the observed angular distribution of AKR. The bottom panel has a source location from the dotted region of Figure 14 and produces rays on the nightside whose latitudinal cutoffs are consistent with the nightside extent of AKR at this frequency. Note that the dayside rays from such a source extend almost down to the dayside plasmapause. Angular distributions of this type are never observed on the dayside of the earth.

lated by using model II and is slightly different for model I (not shown) because of the dependence on the size of the nightside plasmapause.

The *L-O* mode radiation can propagate only in regions where the wave frequency is greater than the electron plasma frequency f_p . Since the electron plasma frequency is less than the $R = 0$ cutoff frequency in the frequency range where the AKR is observed, *L-O* mode radiation must be generated closer to the earth than the *R-X* mode to produce the same angular distribution. The ray tracing results for the *L-O* mode are summarized in Figure 14, which shows the computed source regions and their relationship to the electron plasma frequency. The crosshatched region again shows the source altitudes that produce *L-O* rays consistent with the observed dayside latitudinal limits of the AKR angular distribution. The dot pattern shows the corresponding source altitudes which produce *L-O* rays consistent with the observed nightside latitudinal limits. The source regions which account for the dayside and nightside angular distributions in Figure 14 are seen to be much further apart than the corresponding regions for the *R-X* rays in Figure 13. The origin of the inconsistency in the angular distribution of the dayside and nightside *L-O* rays is illustrated in the top panel of Figure 15. Source posi-

tions which give good agreement with the observed dayside latitudinal limits are shielded by the topside of the plasmapause on the nightside and never reach the equator at the low latitudes observed on the nightside of the earth. If the altitude of the source is moved up, as in the bottom panel of Figure 15, to account for the nightside observations, the rays penetrate to much lower latitudes than they do on the dayside of the earth.

SUMMARY AND DISCUSSION

This study has shown that the intense kilometric radio emissions generated over the nightside auroral regions are beamed into a cone-shaped region whose axis of symmetry is tilted away from the magnetic axis of the earth, toward local evening, by about 20°. The solid angle of this emission cone increases systematically with increasing frequency, varying from approximately 1.1 sr at 56.2 kHz to approximately 3.5 sr at 178 kHz. Simultaneous measurements from two satellites show a good correlation between the radio emission intensities observed over a wide range of angular separations within the emission cone, indicating that the kilometric radiation source simultaneously illuminates the entire region within the emission cone with comparable intensities. A clear day-night asymmetry is observed in the propagation cutoffs at the plasma-

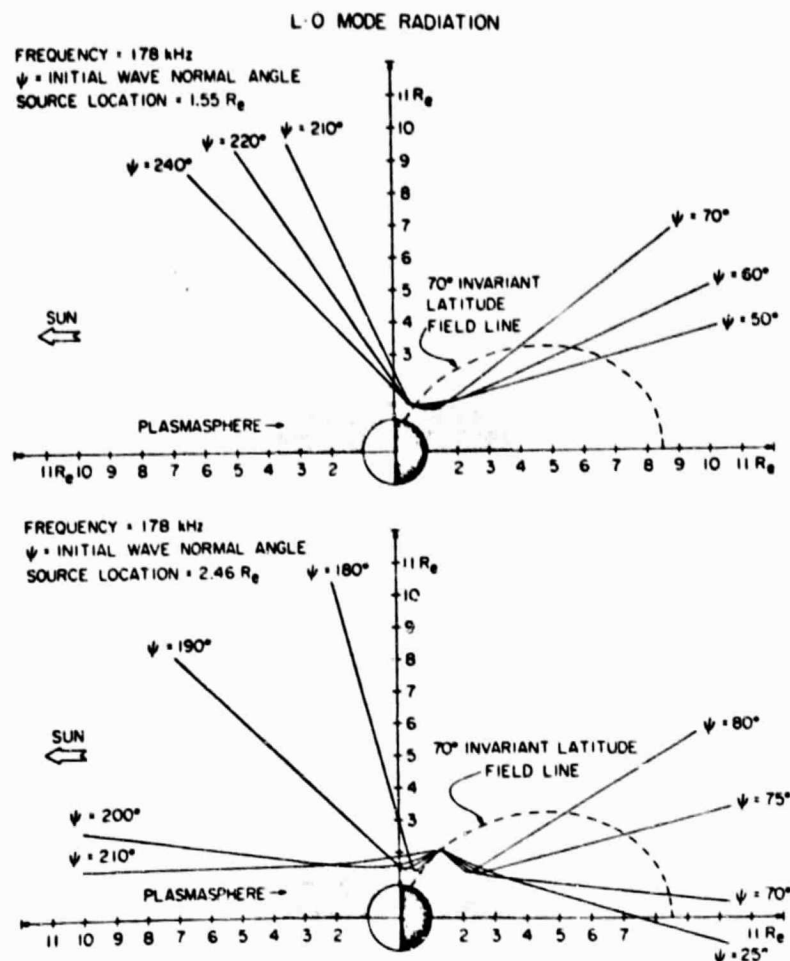


Fig. 15. *L-O* mode ray paths in the model II magnetosphere at 178 kHz. The top panel has a source location that lies within the cross-hatched region of Figure 14 and thus produces rays on the dayside whose latitudinal cutoffs are consistent with the observed angular distribution of AKR. The bottom panel has a source location from the dotted region of Figure 14 and produces rays on the nightside whose latitudinal cutoffs are consistent with the nightside extent of AKR at this frequency. Note that the dayside rays from such a source extend almost down to the dayside plasmapause. Angular distributions of this type are never observed on the dayside of the earth.

lated by using model II and is slightly different for model I (not shown) because of the dependence on the size of the nightside plasmapause.

The *L-O* mode radiation can propagate only in regions where the wave frequency is greater than the electron plasma frequency f_p . Since the electron plasma frequency is less than the $R = 0$ cutoff frequency in the frequency range where the AKR is observed, *L-O* mode radiation must be generated closer to the earth than the *R-X* mode to produce the same angular distribution. The ray tracing results for the *L-O* mode are summarized in Figure 14, which shows the computed source regions and their relationship to the electron plasma frequency. The crosshatched region again shows the source altitudes that produce *L-O* rays consistent with the observed dayside latitudinal limits of the AKR angular distribution. The dot pattern shows the corresponding source altitudes which produce *L-O* rays consistent with the observed nightside latitudinal limits. The source regions which account for the dayside and nightside angular distributions in Figure 14 are seen to be much further apart than the corresponding regions for the *R-X* rays in Figure 13. The origin of the inconsistency in the angular distribution of the dayside and nightside *L-O* rays is illustrated in the top panel of Figure 15. Source posi-

tions which give good agreement with the observed dayside latitudinal limits are shielded by the topside of the plasmapause on the nightside and never reach the equator at the low latitudes observed on the nightside of the earth. If the altitude of the source is moved up, as in the bottom panel of Figure 15, to account for the nightside observations, the rays penetrate to much lower latitudes than they do on the dayside of the earth.

SUMMARY AND DISCUSSION

This study has shown that the intense kilometric radio emissions generated over the nightside auroral regions are beamed into a cone-shaped region whose axis of symmetry is tilted away from the magnetic axis of the earth, toward local evening, by about 20° . The solid angle of this emission cone increases systematically with increasing frequency, varying from approximately 1.1 sr at 56.2 kHz to approximately 3.5 sr at 178 kHz. Simultaneous measurements from two satellites show a good correlation between the radio emission intensities observed over a wide range of angular separations within the emission cone, indicating that the kilometric radiation source simultaneously illuminates the entire region within the emission cone with comparable intensities. A clear day-night asymmetry is observed in the propagation cutoffs at the plasma-

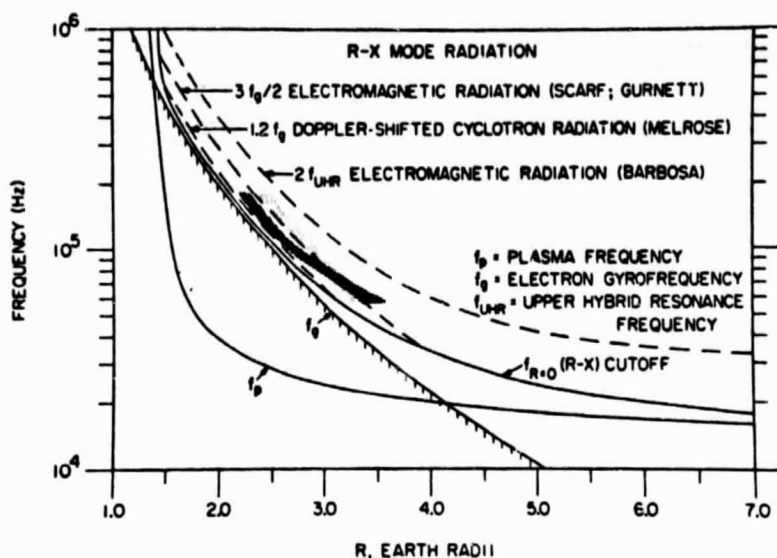


Fig. 16. Source locations (dashed lines) for three proposed R - X mode generation mechanisms as a function of emission frequency, shown in comparison to the AKR source regions determined from ray tracing calculations. Electromagnetic waves generated at $3f_p/2$ [Sarf, 1974; Gurnett, 1974] would originate from a region which produced an angular distribution qualitatively consistent with that observed for AKR. Radiation at $1.2f_u$ [Melrose, 1976] and $2f_{uH}$ [Barbosa, 1976] would not produce a consistent angular distribution.

pause, with sharp cutoffs on the nightside of the earth and no corresponding cutoff on the dayside.

In an attempt to understand the essential features of the angular distribution of the AKR a detailed study of ray paths was performed for various source positions along a magnetic field line at 70° invariant latitude. Two magnetospheric density models were used which reflected the range of plasma-pause locations encountered during moderately disturbed and disturbed magnetic conditions. By adjusting the altitude of the source to agree with the observed latitudinal cutoffs of the emission cone on the dayside and nightside of the earth a range of source positions were obtained as a function of frequency. These calculations were performed for both the R - X and the L - O mode of propagation.

In interpreting these ray tracing results it is essential that the uncertainties and limitations of the ray tracing analysis be carefully examined. Three main areas of uncertainty can be identified: (1) the spatial distribution of the source, (2) the distribution of initial wave normal angles, and (3) the plasma density models. For the ray tracing results presented we have assumed that the source is a point source at each frequency. Although height variations of the source have been considered, no attempt has been made to consider a spatially extended source in MLT and latitude. The assumption of a point source is primarily due to the lack of adequate information on the actual spatial extent of the source in local time and latitude. Conceptually, one can visualize the angular distribution from a spatially extended source by superposing the ray paths from an equivalent distribution of point sources. Even though very extreme source locations have been observed in some situations (at radial distances greater than $7 R_E$ and in the polar cusp on the dayside of the earth), these extreme cases are believed to occur so infrequently that they do not make a significant contribution to the long-term average results presented in this study. From our previous direction finding studies [Kurth et al., 1975] and from those of Kaiser and Stone [1975] it is clear that the dominant component of the high-intensity ($\geq 2 \times 10^{-16} \text{ W m}^{-2} \text{ Hz}^{-1}$ at $30 R_E$) kilometric radi-

ation comes from the nightside auroral regions. The fact that the ray tracing calculations for the R - X mode fit the average features of the angular distribution is considered further confirmation that the source is relatively small and that the average position is on the nightside relatively close (2.25 – $3.5 R_E$) to the earth.

The ray tracing results presented have assumed that the radiation is generated over a wide range of wave normal angles. This assumption is justified mainly by the fact that the radiation appears to be almost uniformly distributed throughout the emission cone. If the radiation were generated within a narrow range of wave normal angles, then the angular distribution should be sharply peaked at a well-defined angle with respect to the local magnetic field, such as it is for the decametric radiation generated by Jupiter's moon Io. Even when the possible smearing effect caused by a spatially extended source is taken into consideration, it seems unlikely that the near-uniformity of the illumination throughout the emission cone can be explained if the wave normal direction is sharply limited to a narrow range of angles. This conclusion is confirmed by the ray tracing calculations of Jones and Grard [1976], who assumed that the wave normal directions are either parallel or perpendicular (within 10°) to the magnetic field. Their calculations give quite different limiting ray paths from our results and do not appear to be in good agreement with the observed angular distributions. Since virtually all theories of the terrestrial kilometric and Jovian decametric radiation lead to a preferred wave normal direction for the emitted radiation, these conclusions may appear to conflict with the theoretical expectations. However, this difficulty could be explained if there is a substantial amount of scattering in the source region which could act to spread the angular distribution of the emitted radiation. The presence of such scattering would be entirely consistent with the large density fluctuations typically observed in the auroral electron precipitation at high altitudes.

Probably the primary uncertainty in the ray tracing comparisons with the observed angular distributions is the electron density models used in these calculations. Although the den-

sity models used are believed to be reasonably representative on the basis of certain general considerations, such as matching the observed ionospheric densities and scale heights at low altitudes and the low densities ($< 1 \text{ cm}^{-3}$) at large distances in the magnetotail, there are essentially no adequate density measurements at intermediate radial distances (from about 2 to $10 R_E$) over the polar regions to confirm these models. The effect of errors in the density model on the ray tracing results is quite different for the two modes of propagation. In the region of primary interest from about 2.0 to $3.5 R_E$ one can be reasonably confident that the plasma frequency is substantially less than the electron gyrofrequency ($f_p \ll f_g$). Under these conditions the index of refraction for the $R-X$ mode (and the $R = 0$ cutoff, as in Figure 13) is mainly determined by the magnetic field strength and is relatively independent of the plasma density. The ray paths for the $R-X$ mode are therefore relatively insensitive to changes in the plasma density model. For the $L-O$ mode of propagation, however, the propagation cutoff occurs at the local plasma frequency, and the ray paths and source altitudes are very sensitive to changes in the plasma density. Even small horizontal gradients, which change the slope of the constant density contours, cause marked changes in the angle of reflection and the angular distribution at large radial distances. Indirectly, the sensitivity of the $L-O$ mode to horizontal gradients in the plasma density, which must almost certainly occur near the auroral field lines, provides additional evidence that the AKR is not propagating in the $L-O$ mode. As was mentioned earlier, the dayside latitudinal cutoff at $\lambda_m = 65^\circ \pm 10^\circ$ is very sharp and consistent. Considering the probable variability of the horizontal gradients in the plasma density near the reflection point, it is hard to see how this dayside cutoff can be so stable and consistent if the radiation is emitted in the $L-O$ mode. In contrast, the magnetic control of the $R-X$ mode provides a relatively stable reflecting surface (at the $R = 0$ cutoff) which would result in a nearly constant limiting ray path at a given frequency, independent of the electron density variations near the reflecting region.

From these ray tracing considerations it is our conclusion that the $R-X$ mode provides the best and most consistent agreement with the observed angular distribution of the AKR. Because of the many uncertainties involved in the detailed ray tracing models and the mechanism by which this radiation is generated it is obvious that this conclusion cannot be considered firm. Direct measurements of the polarization or other techniques are needed to provide the final determination of the polarization. However, it is of interest to note that the Jovian decametric radiation, which is generally thought to be equivalent to the intense terrestrial kilometric radiation, has been determined by Warwick and Dulk [1963] to be emitted in the $R-X$ mode, in agreement with the conclusions of this study.

The limitations placed on the source regions of AKR which are illustrated in Figures 13 and 14 can be used to test the validity of proposed emission mechanisms. Since the ray tracing calculations favor the generation of AKR in the $R-X$ mode, we will consider only those mechanisms proposed by Scarf [1974], Gurnett [1974], Melrose [1976], and Barbosa [1976]. Scarf [1974] and Gurnett [1974] proposed that planetary emissions such as AKR may be produced from electrostatic plasma instabilities (set up by precipitating electrons) that couple into electromagnetic waves at $3f_g/2$. As is shown in Figure 16, electromagnetic waves at $3f_g/2$ would originate from a region which produced an angular distribution qualitatively consistent with that observed for AKR. Another mechanism which is gyro related was proposed by Melrose. In

his theory, $R-X$ cyclotron radiation from precipitating electrons is Doppler-shifted upward in frequency, above the $R = 0$ cutoff, so that the radiation can escape. For an energy of 10 keV, typical of the auroral electron precipitation, the Doppler shift is about 20%, which would produce radiation at $f = 1.2f_g$. The source region for the Doppler-shifted cyclotron radiation mechanism would then correspond to frequencies of about $1.2f_g$ along a 70° invariant latitude field line. As is illustrated in Figure 16, radiation at $f = 1.2f_g$ would originate from a region below the region determined by our ray tracing analysis. Electron energies of at least 50 keV are needed to produce Doppler shifts sufficiently large to be in agreement with the observed angular distribution. Although electrons with energies greater than 50 keV are occasionally observed in the auroral electron precipitation, these electrons do not constitute a very large fraction of available energy and would not be expected to play a significant role in the generation of the intense AKR. Barbosa's [1976] mechanism produces $R-X$ radiation near twice the UHR frequency ($2f_{UH}$). Radiation at $2f_{UH}$ originates from a region at larger radial distances than those indicated by the dot pattern of Figure 16. Much larger emission cones than those observed for AKR would result from $R-X$ mode radiation of $2f_{UH}$ in the model magnetospheres presented in this study.

CONCLUSIONS

Analysis of spacecraft data from Hawkeye 1, Imp 6, and Imp 8 has led to the following conclusions concerning the propagation characteristics of AKR:

1. AKR in the northern hemisphere is beamed into a cone-shaped region whose solid angle increases with increasing frequency, varying from approximately 1.1 sr at 56.2 kHz to approximately 3.5 sr at 178 kHz.
2. There is simultaneous illumination with nearly constant intensities over the entire solid angle.
3. The symmetry axis of the emission cone is tilted toward local evening by about 20° with respect to the magnetic axis of the earth.
4. There is a day-night asymmetry in the topside plasma-pause cutoffs, with sharp cutoffs on the nightside of the earth and no corresponding cutoff on the dayside.
5. Ray tracing calculation for the escaping modes $R-X$ and $L-O$ using two magnetospheric density models leads to the following conclusions:
 5. Variability in the size of the nightside plasmopause can account for the nightside variability in the angular distribution of AKR, as is suggested by Figures 2, 3, 4, and 5.
 6. Rays in either of the $R-X$ or $L-O$ modes exhibit the day-night asymmetry in the topside plasmopause cutoffs.
 7. The angular distribution of AKR can best be reproduced from low-altitude source regions (from 2 to $3.5 R_E$) in the nighttime auroral zone if the emission is in the $R-X$ mode.

Acknowledgments. The research at the University of Iowa was supported by the National Aeronautics and Space Administration through grants NGL-16-001-002 and NGL-16-001-043, contracts NAS1-11257 and NAS1-13129 with Langley Research Center, and contracts NAS5-11074 and NAS5-11431 with Goddard Space Flight Center, by the Office of Naval Research, and by the Atmospheric Sciences Section of the National Science Foundation.

The Editor thanks J. K. Alexander and W. Bernstein for their assistance in evaluating this paper.

REFERENCES

- Ackerson, K. L., and L. A. Frank, Correlated satellite measurements of low-energy electron precipitation and ground-based observations

- of a visible auroral arc, *J. Geophys. Res.*, **77**, 1128, 1972.
- Alexander, J. K., and M. L. Kaiser, Terrestrial kilometric radiation. I. Spatial structure studies, *J. Geophys. Res.*, **81**, 5948, 1976.
- Barbosa, D. D., Electrostatic mode coupling at $2\omega_{UH}$: A generation mechanism for auroral kilometric radiation, Ph.D. dissertation, Dep. of Phys., Univ. of Calif., Los Angeles, 1976.
- Benson, R. F., Source mechanism for terrestrial kilometric radiation, *Geophys. Res. Lett.*, **2**, 52, 1975.
- Carpenter, D. L., Whistler evidence of a 'knee' in the magnetospheric ionization density profile, *J. Geophys. Res.*, **68**, 1675, 1963.
- Dunckel, N., B. Ficklin, L. Rorden, and R. A. Helliwell, Low-frequency noise observed in the distant magnetosphere with Ogo 1, *J. Geophys. Res.*, **75**, 1854, 1970.
- Gurnett, D. A., The earth as a radio source: Terrestrial kilometric radiation, *J. Geophys. Res.*, **79**, 4227, 1974.
- Gurnett, D. A., The earth as a radio source: The nonthermal continuum, *J. Geophys. Res.*, **80**, 2751, 1975.
- Haselgrove, C. G., and J. Haselgrove, Twisted ray paths in the ionosphere, *Proc. Roy. Soc. London*, **75**, 357, 1960.
- Haselgrove, J., Ray theory and a new method for ray tracing, Report of Conference on the Physics of the Ionosphere, p. 355, Phys. Soc., London, 1955.
- Jones, D., Mode-coupling of z-mode waves as a source of terrestrial kilometric and Jovian decametric radiation, submitted to *Astron. Astrophys.*, 1976.
- Jones, D., and R. J. L. Garrd, Propagation characteristics of electromagnetic waves in the magnetosphere, in *The Scientific Satellite Programme During the Magnetospheric Study*, edited by K. Knott and B. Battrock, p. 293, D. Reidel, Dordrecht, Netherlands, 1976.
- Kaiser, M. L., and J. E. Alexander, Source measurements of terrestrial kilometric radiation obtained from lunar orbit, *Geophys. Res. Lett.*, **3**, 37, 1976.
- Kaiser, M. L., and R. G. Stone, Earth as an intense planetary radio source: Similarities to Jupiter and Saturn, *Science*, **189**, 285, 1975.
- Kurth, W. S., M. M. Baumbach, and D. A. Gurnett, Direction finding measurements of auroral kilometric radiation, *J. Geophys. Res.*, **80**, 2764, 1975.
- Lin, R. P., The emission and propagation of ~ 40 keV solar flare electrons, *Solar Phys.*, **12**, 266, 1970.
- Melrose, D. B., An interpretation of Jupiter's decametric radiation and the terrestrial kilometric radiation as direct amplified gyro-emission, *Astrophys. J.*, **207**, 651, 1976.
- Palmadesso, P., T. P. Coffey, S. L. Ossakow, and K. Papadopoulos, Generation of terrestrial kilometric radiation by a beam-driven electromagnetic instability, *J. Geophys. Res.*, **81**, 1762, 1976.
- Scarf, F. L., A new model for the high-frequency decametric radiation from Jupiter, *J. Geophys. Res.*, **79**, 3835, 1974.
- Shaw, R. R., and D. A. Gurnett, Electrostatic noise bands associated with the electron gyrofrequency and plasma frequency in the outer magnetosphere, *J. Geophys. Res.*, **80**, 4259, 1975.
- Shawhan, S. D., VLF ray tracing in a model ionosphere, *Res. Rep. 66-33*, Dep. of Phys. and Astron., Univ. of Iowa, Iowa City, 1966.
- Shawhan, S. D., A computer program for VLF ray tracing in a model ionosphere, *Res. Rep. 67-12*, Dep. of Phys. and Astron., Univ. of Iowa, Iowa City, 1967a.
- Shawhan, S. D., Behavior of VLF ray paths in the ionosphere, *Res. Rep. 67-25*, Dep. of Phys. and Astron., Univ. of Iowa, Iowa City, 1967b.
- Stix, T. H., *The Theory of Plasma Waves*, McGraw-Hill, New York, 1962.
- Voots, G., D. A. Gurnett, and S.-I. Akasofu, Auroral kilometric radiation as an indicator of auroral magnetic disturbances, submitted to *J. Geophys. Res.*, 1976.
- Warwick, J. W., and G. A. Dulk, Faraday rotation on decametric radio emissions from Jupiter, *Science*, **145**, 380, 1963.

(Received September 13, 1976;

accepted January 27, 1977.)

Auroral Kilometric Radiation as an Indicator of Auroral Magnetic Disturbances

G. R. VROOTS AND D. A. GURNETT

Department of Physics and Astronomy, University of Iowa, Iowa City, Iowa 52242

S.-I. AKASOFU

Geophysical Institute, University of Alaska, College, Alaska 99701

Satellite low-frequency radio measurements have shown that an intense radio emission from the earth's auroral regions called auroral kilometric radiation is closely associated with auroral and magnetic disturbances. In this paper we present a detailed investigation of this relationship, using the auroral electrojet (AE) index as an indicator of auroral magnetic disturbances and radio measurements from the Imp 6 spacecraft. This study indicates that the mean power flux of the 178-kHz radiation tends to be proportional to $(AE)^{1.2}$ for $AE > 100 \gamma$ and, with less certainty, to $(AE)^2$ for $AE < 100 \gamma$. The correlation coefficient between $\log AE$ and the logarithm of the power flux is 0.514. Occasionally, a kilometric radiation event is detected which is not detected by the ground magnetometer stations, even though an auroral substorm is in progress. This study shows that the remote detection of kilometric radio emissions from the earth can be used as a reasonably reliable indicator of auroral substorm activity.

INTRODUCTION

In the past several years, low-frequency radio measurements have shown that the earth's magnetosphere is a very intense radio emitter, having characteristics very similar to those of other astronomical radio sources, such as Jupiter and Saturn [Kaiser and Stone, 1975]. From the very earliest measurements by Benediktov *et al.* [1968] and Dunkel *et al.* [1970] it was discovered that intense radio emissions in the several hundred kHz frequency range were closely associated with magnetic disturbances in the high-latitude auroral regions of the earth. Later studies by Gurnett [1974] showed that these radio emissions are closely associated with the occurrence of auroral arcs on the nightside of the earth. Direction-finding measurements and the angular distribution of the emitted radiation [Gurnett, 1974; Green *et al.*, 1977] indicate that the intense (up to 10^9 W of total radiated power) radiation is generated at relatively low altitudes ($\sim 3 R_E$ radial distance) over night and evening auroral regions. The radiation is presumably produced by the same intense fluxes of several keV electrons which cause the aurora and the currents responsible for the magnetic disturbances. Because of the close association with auroral phenomena and the wavelengths in the kilometer range these radio emissions have been called auroral kilometric radiation (AKR) [Kurth *et al.*, 1975].

Although auroral kilometric radiation is known to be associated with high-latitude magnetic disturbances, little has been done to study this relationship in detail. It is of interest to determine just how good the correlation is and whether there are any exceptions to the observed relationship. The relationship of the radio emission intensity to the currents flowing through the auroral zone may, for example, be helpful in developing a better understanding of how the auroral kilometric radiation is generated. Furthermore, since radio emissions from the entire auroral zone can be easily monitored by a single spacecraft, there is the question of whether the auroral kilometric radiation intensity could provide, on a near real time basis, a parameter which is comparable to the auroral

electrojet index AE without the need for a large array of ground stations with the attendant problems of information retrieval and processing. In this paper we present a detailed study of the relationship between the auroral kilometric radiation intensities observed by the Imp 6 spacecraft and the AE index computed from a series of high-latitude magnetometer stations. A description of the Imp 6 plasma and radio wave experiment is given by Gurnett [1974].

QUALITATIVE COMPARISON OF SOME TYPICAL EVENTS

Figure 1 shows the radio emission intensities detected by the Imp 6 spacecraft at 178 kHz and the corresponding variations in the auroral electrojet index AE for four 24-hour periods selected to illustrate the relationships typically observed between these two parameters. Since Imp 6 is in a highly eccentric orbit with an apogee radial distance of $33 R_E$, this spacecraft provides observations for long periods far from the earth where the auroral kilometric radiation intensities can be monitored nearly continuously without interruption. All of the enhanced radio emission intensities in Figure 1 are attributed to auroral kilometric radiation. The magnetic latitude, local time, and radial distance coordinates of Imp 6 are shown at the bottom of each panel.

The data in Figure 1 show the general type of correlation which is typically observed between the auroral kilometric radiation and auroral magnetic disturbances. Essentially every period of substantial magnetic activity, indicative of an auroral substorm, can be associated with a distinct period of enhanced auroral kilometric radiation intensity. Even during relatively quiet days, such as December 27, 1972, small magnetic disturbances are associated with an enhancement in the radio emission at 178 kHz.

Although the magnetic disturbances associated with an individual magnetic substorm usually have a close correspondence to a period of enhanced radio emission, the detailed short time scale (as 1 hour) intensity variations often do not have a close association with variations in the AE index. The onset time of the radio emission at the start of a magnetic substorm is sometimes significantly delayed with respect to the onset time of the magnetic disturbance. For example, delays of this type

ORIGINAL PAGE IS
OF POOR QUALITY

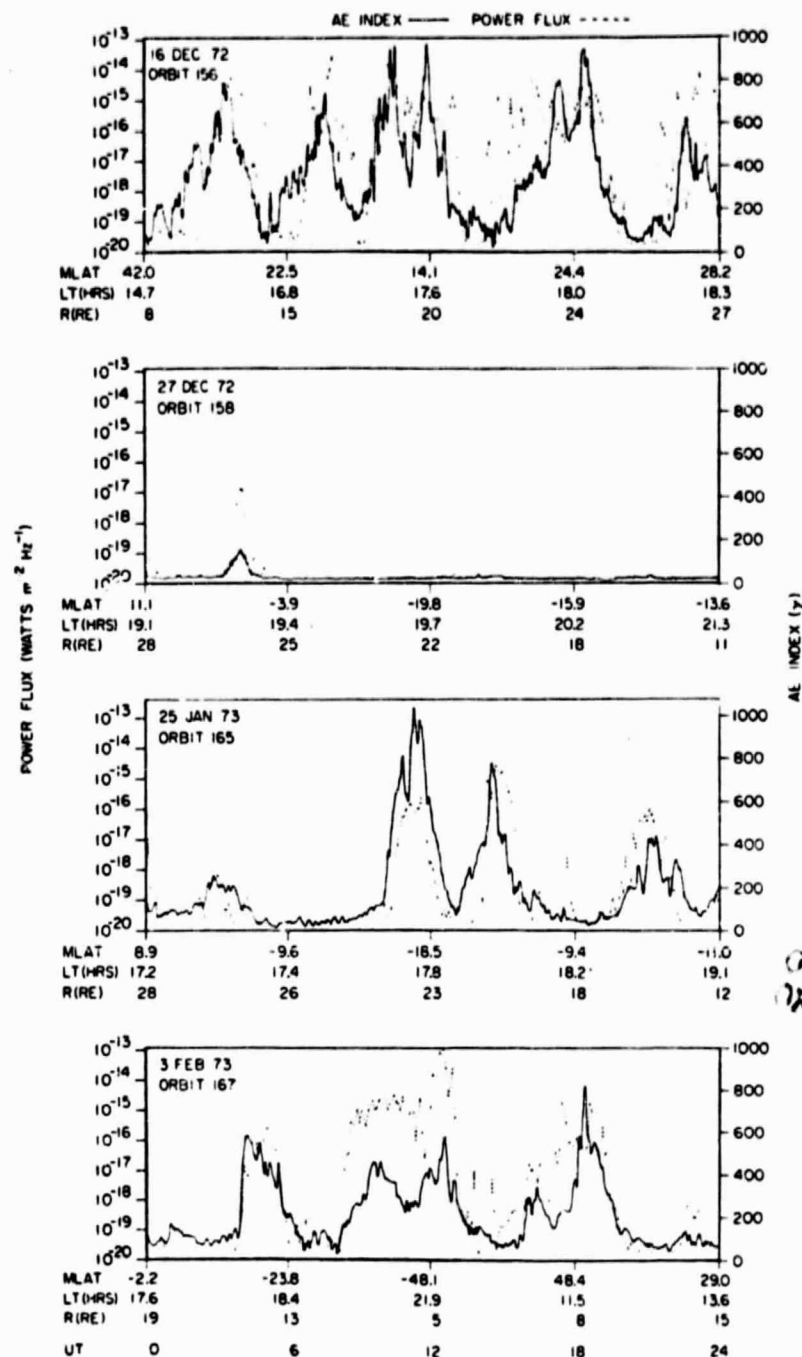


Fig. 1. Simultaneous measurements of the auroral kilometric radiation intensity at 178 kHz by the Imp 6 satellite and the auroral electrojet index AE for a selection of days in which a close correlation is observed. The coordinates of Imp 6 are shown at the bottom of each panel.

can be seen at about 0200 and 0600 UT on December 16, 1972, and at 1330 UT on January 25, 1973.

Occasionally, events can be found in which a large magnetic disturbance is clearly evident in the AE index but for which no corresponding radio emission is detectable and vice versa. Events of each of these types are shown in Figure 2. The event on March 31, 1973, at the top of Figure 2 illustrates a case in which a large magnetic disturbance ($AE > 1000-1500$) occurs with only a negligible enhancement in the radio emission. This type of event, consisting of a large magnetic disturbance characteristic of a substorm with only a small or undetectable

increase in the radio intensity, occurs most frequently when the spacecraft is on the dayside of the earth. The absence of a detectable radio emission in most of these cases is thought to be caused by a propagation cutoff effect which prevents the radiation generated in the nighttime auroral regions from being detected at low latitudes on the dayside of the earth. This propagation cutoff effect is illustrated in the bottom panel of Figure 3, from Green *et al.* [1977], which shows the frequency of occurrence of auroral kilometric radiation at 178 kHz as a function of magnetic latitude and magnetic local time. This frequency of occurrence distribution, which is analyzed in

greater detail by *Green et al.* [1977], shows that a distinct latitudinal cutoff occurs, below which the radiation is much less frequently detected. The magnetic latitude of this cutoff varies from about 60° on the dayside of the earth to about 20° on the nightside of the earth. The cutoff is not sharp but occurs over a transition region about 20° wide in latitude. This cutoff effect is almost certainly caused by refraction effects in the ionosphere which cause the radiation to be beamed into a conical-shaped region, with a half angle of about 60° , directed upward from the nighttime auroral region. Comparison of the magnetic latitude and local time (14.7° and 12.4 hours LT) of Imp 6 during the intense magnetic disturbance on March 31, 1973, in Figure 2 with the frequency of occurrence contours in Figure 3 shows that no radio emission should be detected during this event. The top panel of Figure 3 shows the approximate boundaries of the northern and southern illumination regions within which the auroral kilometric radiation at 178 kHz can be detected essentially free of propagation effects. It should be noted that the boundaries of the illumination region are frequency dependent [*Green et al.*, 1977], so that even

though the radiation cannot be detected at 178 kHz, it is still possible that the radiation could be detected at higher frequencies. Effects of this type may account for some of the local time variations of the emission frequency reported by *Kaiser and Alexander* [1976]. If all of the data are examined when the spacecraft is in the northern illumination region (about 40 days of data), no large AE index enhancements are evident unless a corresponding enhancement in AKR also occurs at some time during the event. There may be periods during an event when the AE index is high and the AKR values are low, but at some time during the event the AKR is also enhanced.

Events for which enhanced auroral kilometric radiation intensities occur with no clear enhancement in the AE index are not uncommon. In most cases some minor disturbances can be identified in the AE index for an enhanced radiation intensity, although they are far from typical in indicating the occurrence of substorms. Almost complete breakdown of the correlation occurs, however, very infrequently. Of a total of 146 days which have been examined, two substorm events of this type have been clearly identified. We suggest that the lack of corre-

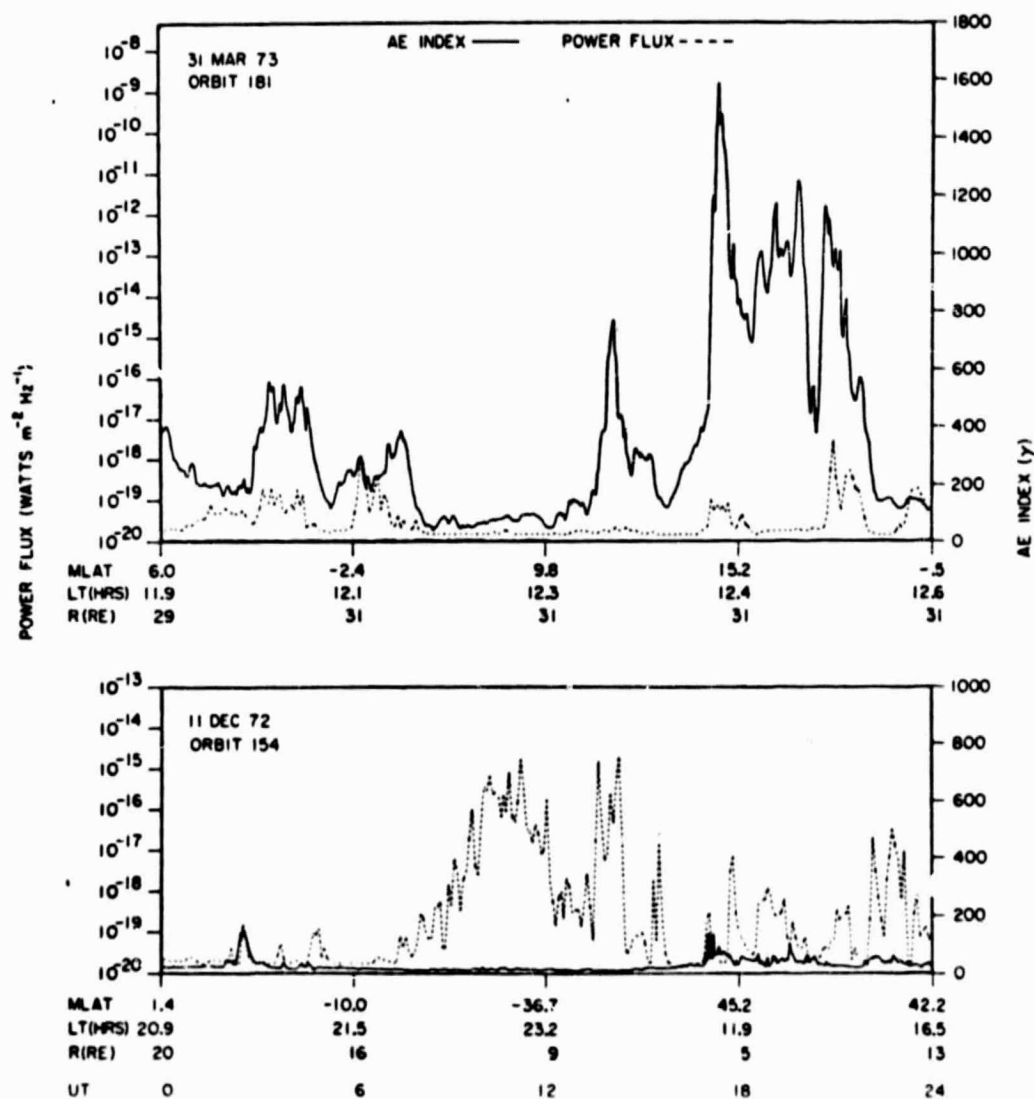


Fig. 2. Two days selected to illustrate cases in which no correlation is evident between the radio emission and the AE index. (Top) An intense auroral kilometric radiation event occurs with essentially no variation in the AE index. (Bottom) A large enhancement in the AE index occurs with only minor variations in the radio emission. Events of this type occur very infrequently.

lation in these cases results from the distribution of ground magnetometer stations being insufficiently dense to detect all the magnetic substorms which occur, in particular, small isolated disturbances at very high magnetic latitudes. This explanation is confirmed for the December 11, 1972, event at the bottom of Figure 2 by the photograph shown in Figure 4, which was taken by the Defense Meteorological Satellite Program (DMSP) spacecraft over the north pole near the time (1100 UT) of maximum radio emission intensity. Although no magnetic disturbance is evident in the *AE* index, the DMSP photograph clearly shows that an auroral substorm was occurring during this event. The intense surge apparent in Figure 4 is traveling westward and lies off the eastern Siberian coast.

High-quality DMSP photographs were not available for the other event, occurring at 1230–1330 UT on March 4, 1973 (not shown). All-sky camera photographs from the Alaska meridian chain (College, Fort Yukon, Inuvik, Sachs Harbour) indicate that auroral activity during that period was confined mostly between Fort Yukon (dip latitude 67°) and Inuvik. Auroras were quite active between 1130 and 1200 UT and then shifted poleward; they were seen near Inuvik until about 1440 UT (through clouds).

STATISTICAL ANALYSIS

To provide a quantitative evaluation of the correlation between the auroral kilometric radiation and the *AE* index, a

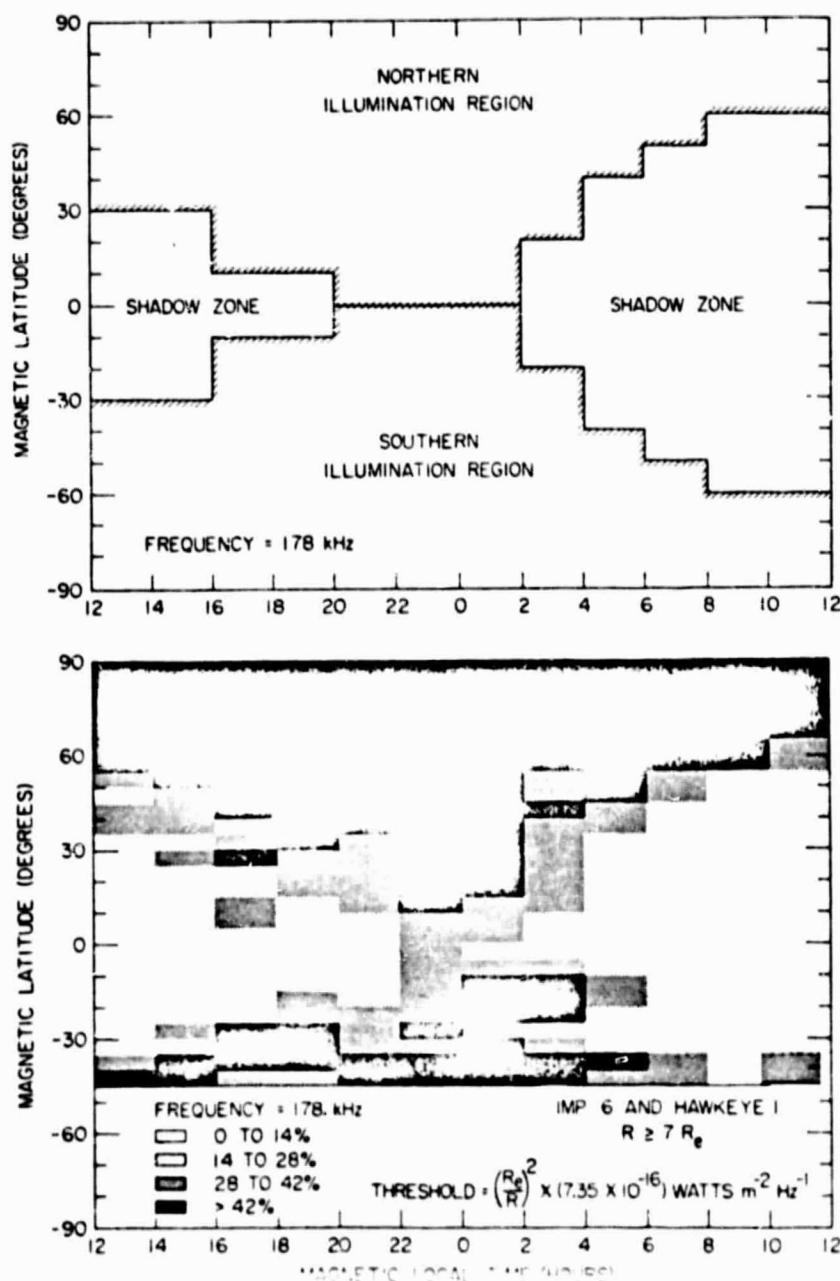


Fig. 3. (Bottom) Frequency of occurrence of auroral kilometric radiation at 178 kHz as a function of magnetic latitude and magnetic local time. A distinct latitudinal boundary is evident in the frequency of occurrence, most of the radiation being beamed into a conical-shaped region over the northern and southern polar regions. (Top) Approximate boundaries of the northern and southern illumination regions.

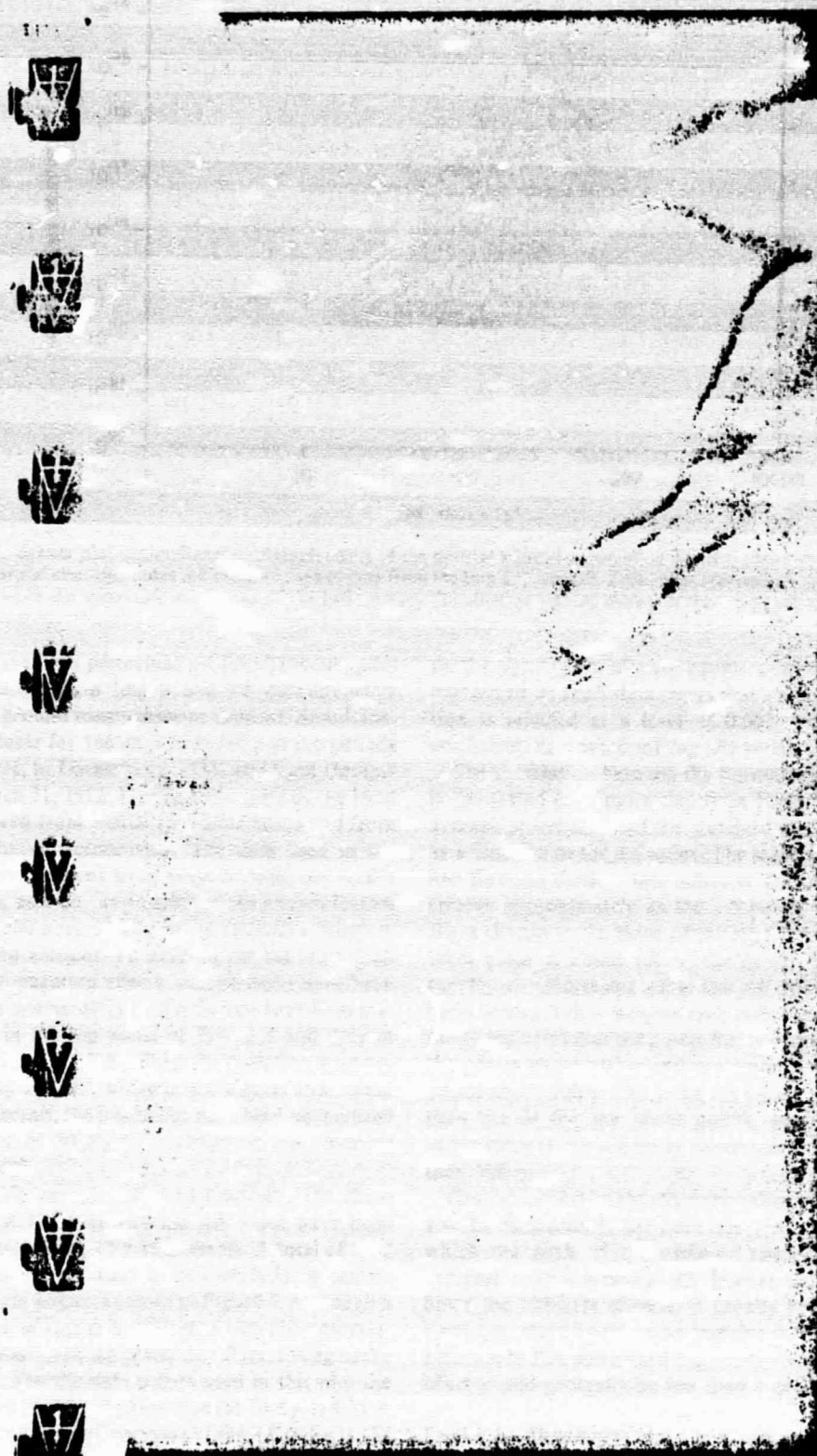


Fig. 4. DMSP 2 photograph (orbit 457) taken over the northern polar region for December 11, 1972, showing the occurrence of an auroral substorm during the auroral kilometric radiation event shown at the top of Figure 2. The absence of a detectable magnetic disturbance during this event is due to the limited spatial coverage of the ground magnetometer network.

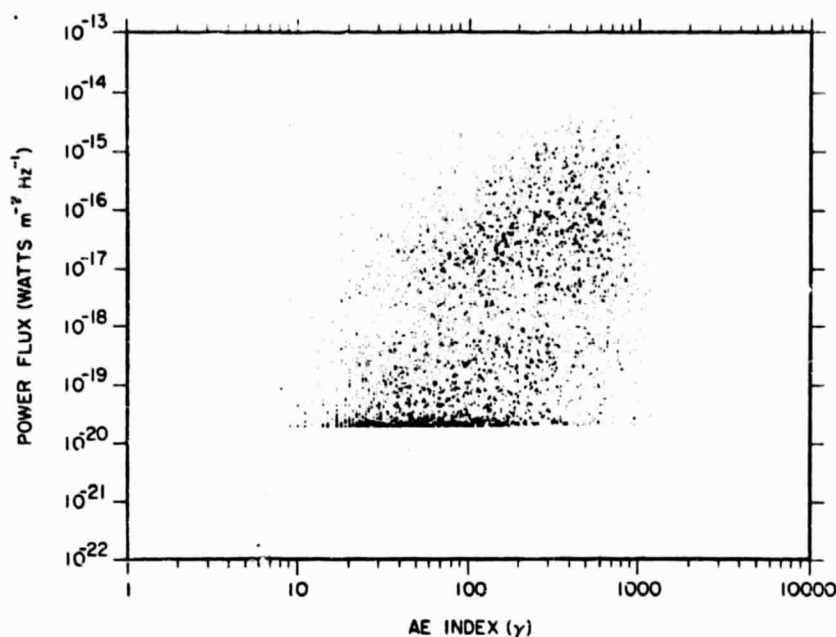


Fig. 5. Scatter plot of simultaneous measurements of the auroral kilometric radiation intensity (normalized to $30 R_E$) and the auroral electrojet index AE using 40 days of data from the Imp 6 spacecraft. Each point represents a 10-min average obtained while the spacecraft was in one of the two primary illumination regions shown in the top panel of Figure 3.

statistical analysis has been performed on simultaneous radio intensity measurements from Imp 6 and AE measurements from a network of ground magnetometer stations. Simultaneous data were available for 146 days, occurring in the periods from August 31, 1971, to December 3, 1971, and from December 1, 1972, to March 31, 1973. During these periods the local time of apogee moved from ~ 0100 to ~ 2000 hours and from ~ 2000 to ~ 1200 hours, respectively. The data used in the statistical analysis are selected from these periods. To obtain the best correlation, as many as possible of the known factors which could affect the auroral kilometric radiation intensity have been taken into account. To account for the latitudinal cutoff caused by propagation effects, comparisons have been made only when the spacecraft is within the northern illumination region shown in the top panel of Figure 3 and only at radial distances greater than $7 R_E$. Since the radiation intensity varies approximately as $1/R^2$, where R is the geocentric radial distance to the spacecraft, the intensities have been normalized to a radial distance of $30 R_E$ by multiplying the observed power flux by $(R/30)^2$.

To provide directly comparable measurements, the radio emission intensity at 178 kHz and the AE index have been averaged over corresponding 10-min intervals. A total of 5702 ten-minute intervals are included in this analysis. A scatter plot of all of these data points is shown in Figure 5. Although a considerable amount of scatter is evident, a very clear correlation can be seen, the mean of the power flux P increasing as the AE index increases. For the data points used in this plot the median value of the normalized power flux (at $30 R_E$) is $6.31 \times 10^{-19} \text{ W m}^{-2} \text{ Hz}^{-1}$, and the median value of the AE index is 158 γ . If AE is greater than 158 γ , then 69.2% of the power flux values are greater than $6.31 \times 10^{-19} \text{ W m}^{-2} \text{ Hz}^{-1}$; whereas if AE is less than 158 γ , then 68.7% of the power flux values are less than $6.31 \times 10^{-19} \text{ W m}^{-2} \text{ Hz}^{-1}$. The percentage distributions above and below the median values are summarized in Table 1. (For computational reasons the values used as the medians are not exactly the true medians, but this has no effect

on the significance of a chi-square analysis.) A chi-square test performed on these data shows that a hypothesis of no correlation is rejected at a level of 0.001. The linear correlation coefficient, computed for $\log(P)$ versus $\log(AE)$, is 0.514.

The correlation between the normalized power flux and AE is illustrated even more clearly in Figure 6, which shows the average power flux and the standard deviation of the average as a function of the AE index. The slope of the best-fit straight line through these points indicates that the power flux P increases approximately as the 1.5 power of the AE index. A slight change in the slope of the $\log(P)$ versus $\log(AE)$ curve takes place at about 100 γ , the power flux increasing more rapidly with increasing AE at low AE values. A computer fit to these averages that weights each point according to its uncertainty indicates that the power flux is proportional to $(AE)^2$ for the points under 100 γ and is proportional to $(AE)^{1.2}$ for the points above 100 γ . The fit for the higher points is much better than the fit for the lower points, possibly because of the uncertainty in the AE index determination for AE values less than 100 γ .

One factor that might affect the values of these slopes should also be discussed. It has been observed that the frequency at which the peak of the emission spectrum occurs tends to decrease with increasing AE [Kaiser and Alexander, 1976]. Since the 178-kHz channel is usually below the peak in the spectrum, there could be an increase in the power flux at 178 kHz due to this downward frequency shift. It appears that this effect would generally be less than 1 order of magnitude and

TABLE 1. Distribution of Power Flux Values as a Function of the Corresponding AE Index Value (%)

$P = 6.31 \times 10^{-19} \text{ W m}^{-2} \text{ Hz}^{-1}$	Below $AE = 158 \gamma$	Above $AE = 158 \gamma$	Entire Range of AE
Above P	31.3	69.2	48.4
Below P	68.7	30.8	51.6
Total	100	100	100

would make the slopes of the fitted lines in Figure 6 somewhat steeper than they might be if the data were taken at the peak of the spectrum.

DISCUSSION

This study has shown that satellite measurements of auroral kilometric radiation can be used as a sensitive and reliable indicator of auroral magnetic disturbances. Detailed comparisons of the auroral kilometric radiation intensity and AE index variations show that periods of enhanced radio emission intensities at 178 kHz are very closely associated with magnetic disturbances indicative of auroral substorms. Occasionally, events are detected in which no typical substorm features in the AE index can be detected even though greatly enhanced radio emission intensities are being observed. Investigation of cases of this type shows that the lack of correlation is usually due to a failure of the ground station magnetometer network to detect an auroral substorm because of the limited spatial coverage of the magnetometer network. Cases also occasionally occur in which a large magnetic disturbance is detected with no corresponding enhancement in the radio emission. Cases of this type usually occur because the spacecraft is located at a latitude too low to be within the primary illumination region of the auroral kilometric radiation. The number of such cases can be greatly reduced by using only measurements obtained when the spacecraft is within the illumination regions given at the top of Figure 3. A statistical analysis shows that if the auroral electrojet index AE exceeds the median value of 158 γ , then the auroral kilometric radiation intensity (normalized to $30 R_E$) has a 69% probability of exceeding the median value of $6.31 \times 10^{-19} \text{ W m}^{-2} \text{ Hz}^{-1}$. The correlation coefficient

between $\log P$ at 178 kHz and $\log AE$ is 0.514. This relatively low correlation coefficient, despite the qualitatively good association of individual radio emission events with magnetic substorms, is apparently due to the poor short time scale (<1 hour) correlation and to the variable proportionality factor between the radio emission intensity and the AE index from event to event. Long-term averages of the power flux show a very consistent correlation with AE , the power flux increasing approximately as the 1.5 power of the AE index overall. It appears that for lower values of AE the power flux increases as the 2.0 power of AE and for higher values of AE it increases as the 1.2 power of AE . Since AE is directly proportional to the auroral electrojet current, on the assumption that spatial effects average out, the change in the slope of $\log AE$ versus $\log P$ may suggest that some type of nonlinear saturation effect may occur in the AKR-generating mechanism in high electrojet currents.

The results of this study show that auroral kilometric radiation can be used with good reliability to identify magnetic substorms, provided the radio measurements are taken within the regions of primary illumination for the auroral kilometric radiation and at distances sufficiently remote ($R > 7 R_E$) from the earth to avoid local propagation cutoff effects. In certain situations, auroral kilometric radiation intensity measurements may provide a more useful index of auroral activity than some of the more conventional parameters, such as the AE index. This is particularly true when a near real time monitoring of global auroral activity is needed. Measurements of this type can be obtained on a limited basis from the presently operating Hawkeye 1, Rae 2, and Imp 8 satellites and should be possible on the forthcoming Isec-A, Isec-B, and Dynamic Explorer satellites.

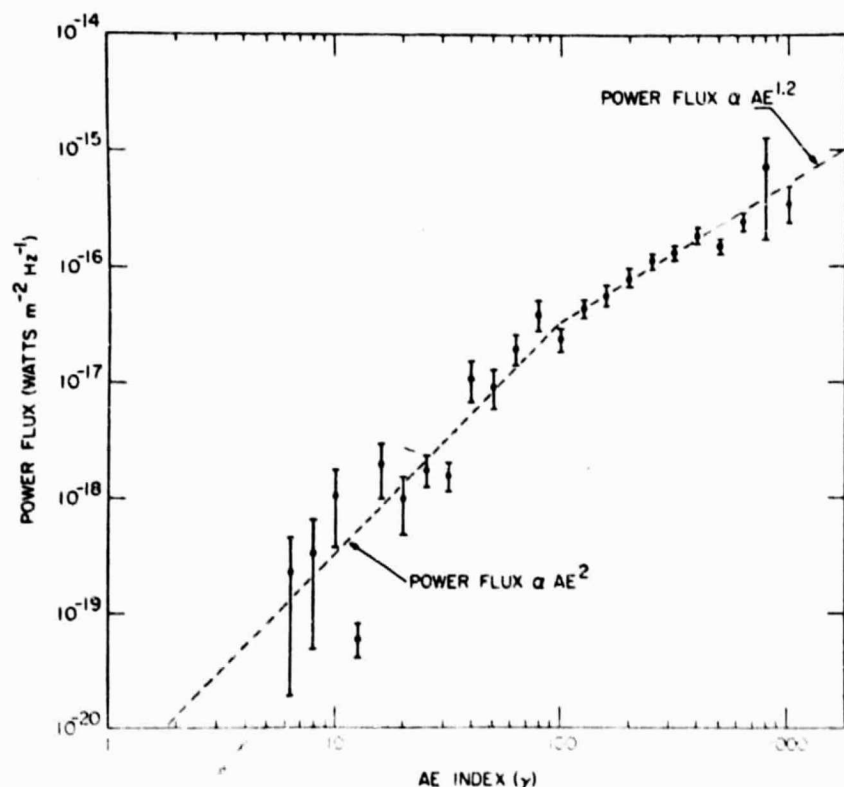


Fig. 6. The average power flux and the standard deviation of the average for the data points shown in Figure 5. The monotonic increase in the average auroral kilometric radiation intensity with increasing AE is clearly evident.

Acknowledgments. The authors wish to thank R. West for assistance in data analysis. The research at the University of Iowa was supported by the National Aeronautics and Space Administration under contracts NAS5-11431 and NAS1-13129 and grant NGL-16-001-043. The research at the University of Alaska was supported by the U.S. Air Force under contract F-19628-76-C-0074 and by the National Science Foundation.

The Editor thanks R. L. Arnoldy and M. L. Kuiser for their assistance in evaluating this paper.

REFERENCES

- Benediktov, E. A., G. G. Getmantsev, N. A. Mityakov, V. O. Rapoport, and A. F. Tarasov, Relation between geomagnetic activity and the sporadic radio emission recorded by the electron satellites, *Cosmic Res.*, Engl. Transl., 6, 791, 1968.
- Dunckel, N., B. Ficklin, L. Rorden, and R. A. Helliwell, Low-frequency noise observed in the distant magnetosphere with Ogo 1, *J. Geophys. Res.*, 75, 1854, 1970.
- Green, J. L., D. A. Gurnett, and S. D. Shawhan, The angular distribution of auroral kilometric radiation, submitted to *J. Geophys. Res.*, 1977.
- Gurnett, D. A., The earth as a radio source: Terrestrial kilometric radiation, *J. Geophys. Res.*, 79, 4227, 1974.
- Kuise, M. L., and J. K. Alexander, Terrestrial kilometric radiation: 3-average spectral properties, *NASA X Doc.* 695-76-255, 1976.
- Kuise, M. L., and R. G. Stone, Earth as an intense planetary radio source: Similarities to Jupiter and Saturn, *Science*, 189, 285, 1975.
- Kurth, W. S., M. M. Baumbach, and D. A. Gurnett, Direction-finding measurements of auroral kilometric radiation, *J. Geophys. Res.*, 80, 2764, 1975.

(Received October 29, 1976;
accepted February 28, 1977.)

sion frequency model have the correct qualitative characteristics, large errors can occur in individual events because of deviations of the solar wind density from the average model. Furthermore, comparisons of the emission frequency with the local electron plasma frequency cannot be performed with high accuracy because of the implicit requirement to assume a model for the emission frequency as a function of radial distance from the sun. As will be shown, the stereoscopic direction finding analyses used in this study completely eliminate the need for any a priori assumption regarding the emission frequency as a function of radial distance from the sun, thereby providing a more direct method for determining the relationship of the emission frequency to the local electron plasma frequency.

INSTRUMENTATION AND METHOD OF ANALYSIS

Radio wave and plasma density measurements from five spacecraft, Helios 1 and 2, Imp 7 and 8, and Hawkeye 1, are used in this study. Helios 1 and 2 are in eccentric solar orbits near the ecliptic plane with perihelion radial distances of 0.309 and 0.290 AU and aphelion radial distances of 0.985 and 0.983 AU, respectively. Imp 7 and 8 are in low-eccentricity earth orbits near the equatorial plane at geocentric radial distances ranging from about 23.1 to 46.3 R_E . Hawkeye 1 is in a highly eccentric earth orbit with the apogee located at a radial distance of 20.5 R_E over the north pole. The radio wave measurements presented are from very similar University of Iowa plasma wave instruments on the Helios 2, Imp 8, and Hawkeye 1 spacecraft. Details of these experiments are given by Kurth *et al.* [1975] and Gurnett and Anderson [1977].

The plasma density measurements used in this study are from the Max-Planck-Institut plasma experiments on Helios 1 and 2 and from the Los Alamos plasma experiments on Imp 7 and 8. Details of these instruments and the procedures used in the data analysis are given by Schwenn *et al.* [1975] and Asbridge *et al.* [1976].

In order to interpret the three-dimensional radio direction finding measurements presented in this study it is important to review briefly the method of analysis and the geometry used for determining the source position. The direction of arrival of a radio wave is determined by a least squares fit of the mea-

sured electric field intensities to a theoretical equation for a spin modulation envelope given by

$$\left(\frac{E}{E_0}\right)^2 = \left(1 - \frac{m}{2}\right) - \frac{m}{2} \cos [2(\varphi_A - \alpha)]$$

where E is the measured field strength and φ_A is the corresponding orientation angle of the electric antenna in the plane of rotation. The parameters determined by the fitting procedure, which is usually applied to a sequence of about 10 min of data, are the direction of arrival α , the modulation factor m , and the electric field strength E_0 . As was mentioned earlier, it is only possible to determine the direction of arrival projected onto a plane perpendicular to the spacecraft spin axis. The spin axis directions of both Helios and Imp 8 are oriented perpendicular to the ecliptic plane as shown in Figure 1. Simultaneous direction finding measurements from Helios and Imp 8 therefore give the angles α_1 and α_2 shown in Figure 1, which uniquely determines the position of the source projected onto the ecliptic plane. The spin axis direction of Hawkeye 1, on the other hand, is oriented nearly parallel to the ecliptic plane, which gives the angle of arrival β_1 above the ecliptic plane. As shown in Figure 1, these three angles, α_1 , α_2 , and β_1 , completely specify the position of the source. By performing this analysis as a function of frequency the three-dimensional trajectory of the type III burst can be determined.

ANALYSIS OF THE TYPE III RADIO BURST ON MARCH 23, 1976

Because of the low occurrence of solar flare activity during solar minimum and various geometrical constraints the number of type III radio bursts which are currently available for a detailed analysis is very small. One event for which all of the spacecraft involved were in particularly favorable positions for analysis occurred on March 23, 1976. The onset of time of this event is at about 0843 UT as determined by ground high-frequency radio measurements [VOAA, 1976]. No H α solar flare was detected at this time; however, a large X-ray flare and a solar electron event consistent with this onset time were detected by both Helios 1 and Helios 2 (J. Trainor and A. Richter, personal communication, 1976). The type III radio emission associated with this event was first detected by Helios 2 at about 0850 UT. The corresponding radio intensities detected by Helios 2, Hawkeye 1, and Imp 8 are shown in Figure 2. At the time of this event, Helios 2 was east of the earth-sun line, at an earth-sun-probe angle of 1.38° and a heliocentric radial distance of 0.56 AU, and Helios 1 was west of the earth-sun line, at an earth-sun-probe angle of 28.8° and a heliocentric radial distance of 0.34 AU. The positions of Helios 1 and 2 projected onto the ecliptic plane are shown in Figure 3. The type III burst was not detected by Helios 1.

The direction of arrival measurements obtained for this event are summarized in Table 1. The time intervals used to obtain the parameters given in Table 1 were selected on the basis of a sliding average analysis, and only those intervals which give a consistent direction of arrival for several contiguous intervals were used in computing the average directions of arrival. Reliable fits were obtained for three frequencies, 500, 178, and 100 kHz, from Imp 8, for two frequencies, 178 and 100 kHz, from Helios 2, and for one frequency, 178 kHz, from Hawkeye 1. Although Table 1 shows results from Hawkeye 1 for 100 kHz, the standard deviation and fluctuations in the direction of arrival for this frequency are so large that this measurement was not used in the subsequent analysis.

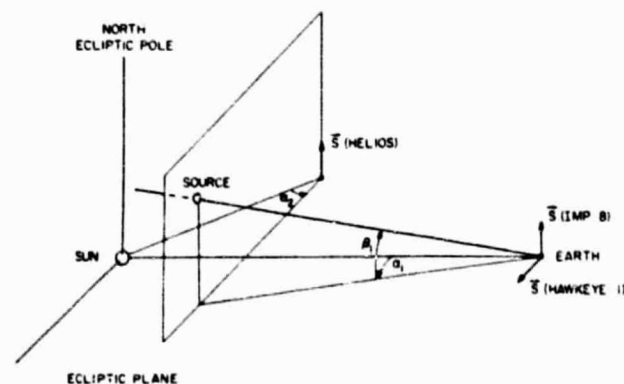


Fig. 1. The geometry used for the three-dimensional stereoscopic direction finding with Imp 8, Hawkeye 1, and Helios. The spin modulation gives the direction of arrival projected onto a plane perpendicular to the spacecraft spin axis. Imp 8 and Helios have their spin axes perpendicular to the ecliptic plane, which gives the angles α_1 and α_2 , thereby determining the source position projected onto the ecliptic plane. Hawkeye 1 has its spin axis nearly parallel to the ecliptic plane, which gives the angle β_1 , thereby determining the source position out of the ecliptic plane.

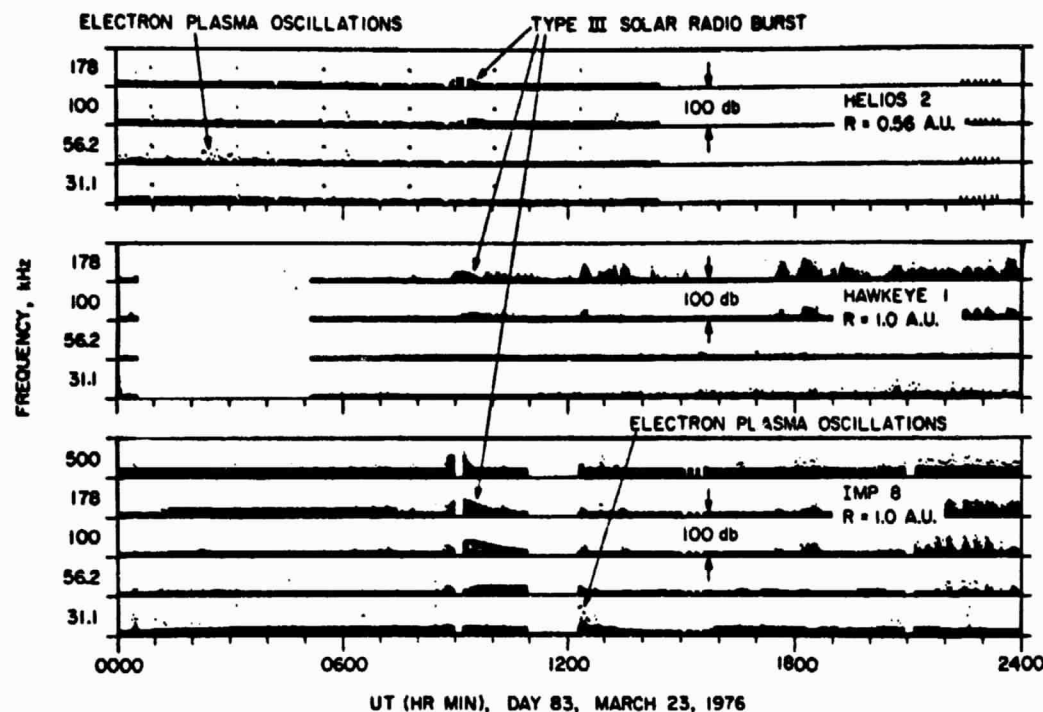


Fig. 2. The electric field intensities detected by Imp 8, Hawkeye 1, and Helios 2 for the type III radio burst on day 83, March 23, 1976. The larger intensities detected by Imp 8 are due to the longer antenna length, 121.8 m from tip to tip for the Imp 8 plasma wave experiment, compared to 42.45 m for Hawkeye 1 and 32.0 m for Helios 2.

For all frequencies below 100 kHz the intensities and modulation factors were too small to give a reliable fit.

The directions of arrival projected onto the ecliptic plane are shown in Figure 3 for each frequency analyzed. The source positions at 100 and 178 kHz are indicated by the corresponding intersections of the directions of arrival from Imp 8 and Helios 2 for these frequencies. The crosshatched regions give the uncertainty in the source positions as determined from the estimated errors in α_1 and α_2 (see Table 1). Both the Imp 8 and the Helios direction finding measurements clearly show a systematic eastward shift in the directions of arrival with decreasing frequency and increasing radial distance from the sun, characteristic of the typical Archimedean spiral trajectory of a type III burst. The best fit Archimedean spiral through the source positions is shown in Figure 3. The equation used for the Archimedean spiral is

$$\varphi = \varphi_0 - (\Omega/V_{sw})r$$

where φ and r are the heliographic longitude and radial distance, V_{sw} is the solar wind velocity, and Ω is the rotational velocity of the sun. The solar wind velocity is assumed to be 600 km s⁻¹. As will be discussed in the next section, this solar wind velocity is an approximate average value based on direct measurements by Helios 2 and Imp 8, with an appropriate delay to provide measurements in the source region. The trajectory of the type III burst in Figure 3 shows that the particles which produced the radio emission were emitted slightly east of the central meridian.

The trajectory of the type III burst out of the ecliptic plane, as determined by Hawkeye 1, is shown in the meridian plane projection of Figure 4. Unfortunately, accurate source positions in the meridian plane can only be obtained at one frequency, 178 kHz, for this event. Nevertheless, this measurement is important because it shows that the type III burst trajectory is very close to the ecliptic plane.

From the modulation factors given in Table 1 it is also possible to estimate the apparent size of the source. As can be easily shown, the modulation factor is sensitive to the angular width of the source projected in the plane of rotation of the antenna. The modulation factor is the largest for a point source and decreases monotonically with increasing source size. The modulation factor is also affected by the angular position of the source with respect to the spin plane of the

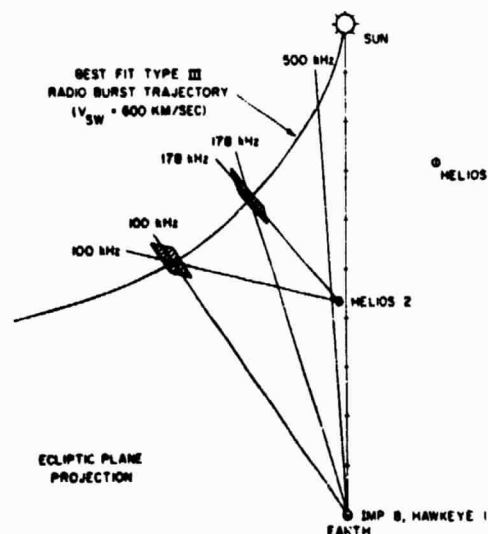


Fig. 3. The ecliptic plane projection of the source positions determined by triangulation from Imp 8 and Helios 2. The uncertainty in the centroid of the source position is indicated by the crosshatched regions at the intersections of the directions of arrival. The best fit trajectory is an Archimedean spiral through the observed source positions. The parameters of the Archimedean spiral have been selected to represent the expected configuration of the solar wind magnetic field for a solar wind velocity of 600 km s⁻¹.

TABLE 1. Direction of Arrival Measurements Obtained for the March 23, 1976, Type III Radio Burst

Frequency, kHz	Helios 2		Imp 8		Hawkeye 1	
	α_s , deg	m	α_i , deg	m	β_i , deg	m
500	3.9 ± 1.1	0.985
178	42.0 ± 0.4	0.444	17.4 ± 1.2	0.809	4.1 ± 0.6	0.448
100	78.0 ± 4.1	0.047	35.4 ± 0.6	0.521	24.7 ± 9.4	0.130

antenna. Since the detailed shape of the source cannot be determined from this type of analysis, some assumption must be made concerning the form of the source intensity distribution. For this analysis we have assumed that the source consists of a uniformly illuminated circular disk normal to the direction to the sun and centered on the source position determined from the triangulation measurements. Because of the geometric complexities the best fit source size must be determined by a computer fitting procedure which gives the best agreement with the measured modulation factors. For 178 and 500 kHz, which are the only frequencies analyzed, the half angles of the source regions as viewed from the earth are 36.5° and 10.5° . It is evident that the source region of the type III radio emission at these frequencies is quite large. These source sizes are probably larger than the true size of the radiating region because of scattering in the interplanetary medium.

COMPARISON WITH THE SOLAR WIND DENSITY

Since the trajectory of the radio burst has been determined without reference to any specific model for the emission frequency, these results can now be compared with the in situ plasma density measurements to determine the relationship of the emission frequency to the local electron plasma frequency. Fortunately, the trajectory of the type III burst passed very close to the ecliptic plane, since this is the only region in which plasma density measurements are available. For this event, plasma densities can be obtained over a wide range of heliocentric radial distances. Densities are available from Imp 7 and 8 at 1.0 AU, from Helios 2 at about 0.55 AU, and from Helios 1 at about 0.32 AU. As is shown in Figure 3, the trajectory of

the type III burst passed eastward of all of these spacecraft. Therefore it is not possible to determine the plasma densities in the source region at the time of the burst. Instead the comparisons must be made a few days later, after the appropriate time delays for the solar rotation to bring the magnetic field line through the source region into coincidence with the spacecraft positions. The geometric considerations required to determine these time delays are illustrated in Figure 5, which shows the trajectories of Imp 7 and 8, Helios 2, and Helios 1 in a coordinate system fixed to the sun. The appropriate time delays are approximately 3.9 days for Imp 7 and 8, 2.6 days for Helios 2, and 8 days for Helios 1. Since the large-scale rotational structure of the solar wind is usually quite consistent and repeatable for several solar rotations during solar minimum conditions, it is believed that any temporal changes which may have occurred in the plasma density during this few-day period should be small. Fortunately, the shortest delay is for Helios 2, which passes the closest to the observed source locations (compare Figures 3 and 5).

The solar wind plasma densities obtained from Imp 7 and 8, Helios 2, and Helios 1 are shown in Figure 6. Although the plasma instruments actually measure ion densities, the measurements shown are equivalent electron densities computed assuming the plasma to be electrically neutral. The time scales in Figure 6 are adjusted so that measurements obtained at the same heliographic longitude are aligned vertically. The points A, B, and C correspond to times when the spacecraft cross the best fit trajectory of the type III burst. Although large variations in the electron density are evident, particularly in the Imp 7 and 8 data, the density is relatively smooth and constant in the region near the type III burst trajectory. The density enhancement evident at all three radial distances (day 87 at Helios 1, days 83 and 84 at Helios, and days 85 and 86 at Imp 7 and 8) is evidently a corotating structure which has an Archimedean spiral structure similar to the type III burst but displaced approximately 20° westward in longitude. Comparisons with solar wind velocity measurements show that this density compression precedes the onset of a high-speed stream, following the well-known pattern discussed by Hundhausen [1973].

When the electron plasma frequencies obtained from these plasma densities are compared with the observed emission frequencies, consideration must be given to the uncertainties in the position of the source and the apparent size of the source. Although points A, B, and C in Figure 6 represent the best estimate of the type III trajectory, based on the Archimedean spiral fit, these intersections are somewhat uncertain because of our lack of knowledge of the exact structure of the solar wind magnetic field. Point C probably has the largest error because it represents an extrapolation by several tenths of an astronomical unit into a region where the Archimedean spiral angle is quite sensitive to the solar wind velocity. The solar wind velocity, $V_{sw} = 600 \text{ km s}^{-1}$, used in the Archimedean spiral fit is in close agreement with the velocities measured by

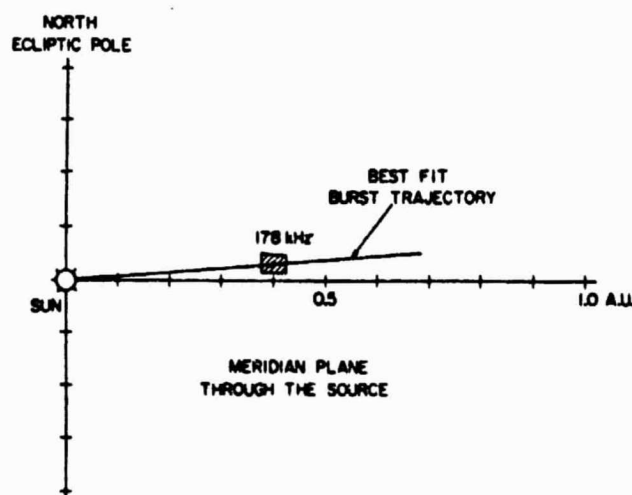


Fig. 4. The observed source position of the type III burst in the meridian plane. Unfortunately, reliable direction finding measurements can only be obtained for one frequency, 178 kHz, from Hawkeye 1 during this event. This one measurement does, however, show that the trajectory of the type III was very close to the ecliptic plane.

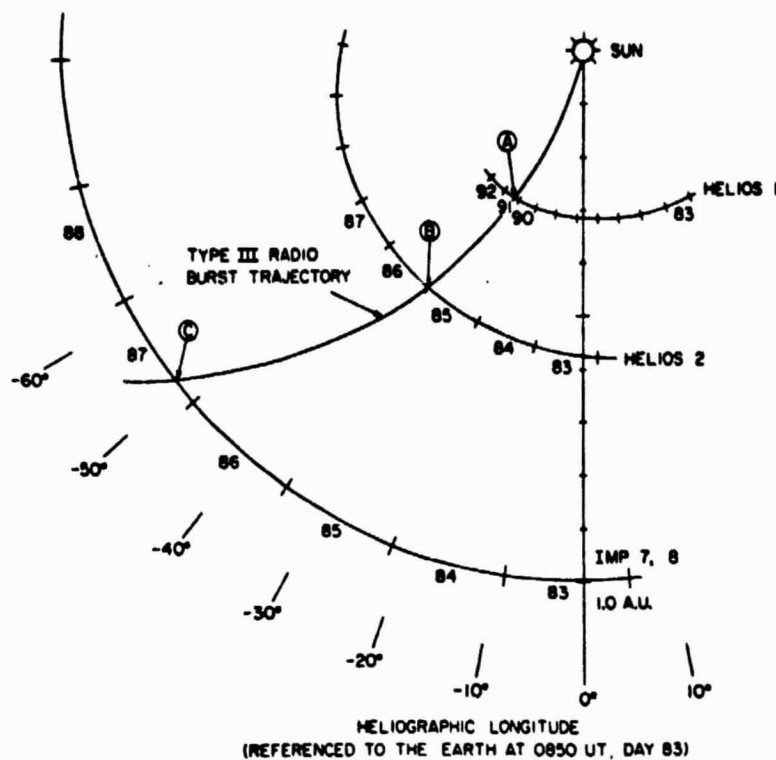


Fig. 5. The trajectories of Imp 7 and 8, Helios 2, and Helios 1 in a coordinate system fixed to the sun. The spacecraft intersect the best fit trajectory of the type III burst at the points marked A, B, and C. Point B represents the best position for comparisons with the local plasma frequency, since this intersection is the closest to the observed source positions (compare with Figure 3) and occurs at the shortest time (2.6 days) after the event.

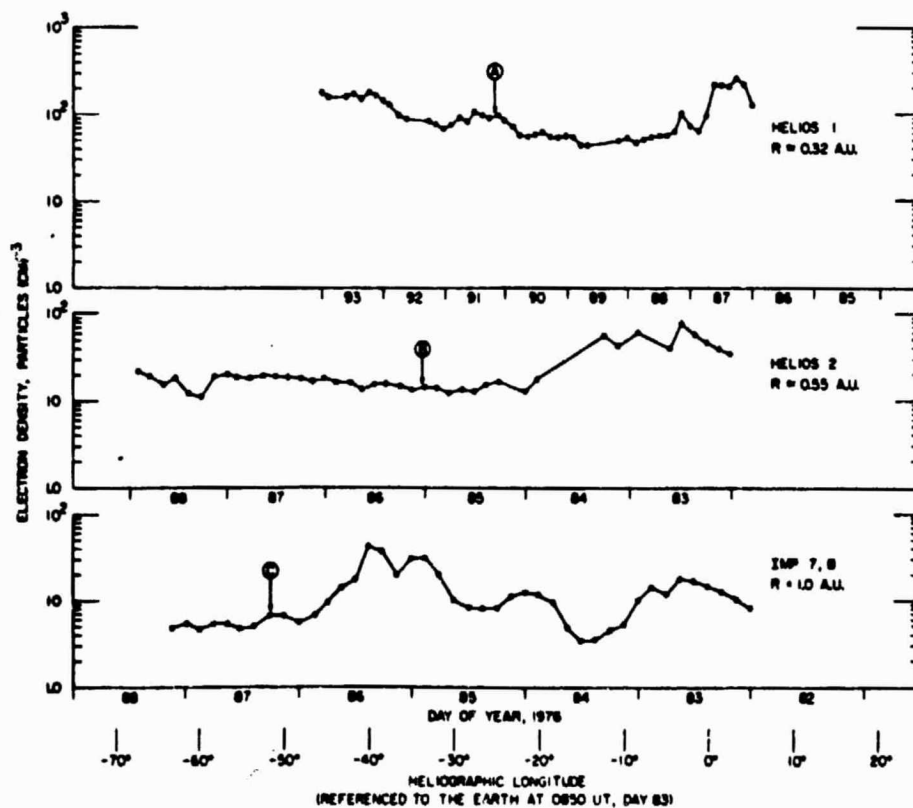


Fig. 6. The electron densities observed by Imp 7 and 8, Helios 2, and Helios 1 for the several-day period after the type III event on day 83. The intersections with the best fit trajectory occur at points A, B, and C, as determined from Figure 5.

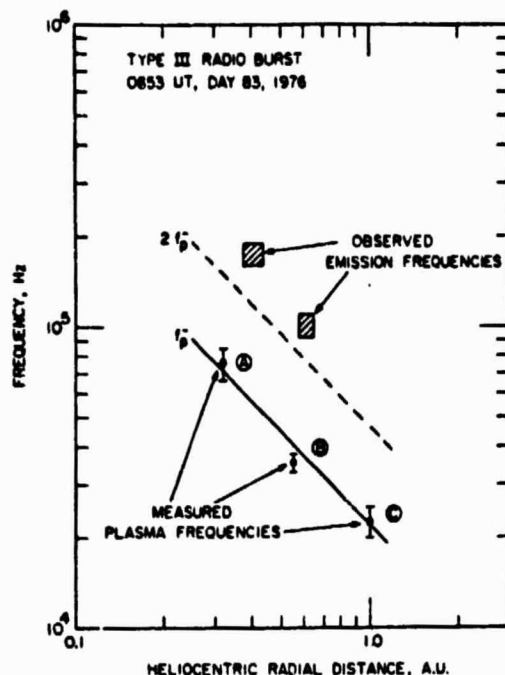


Fig. 7. A comparison of the observed emission frequencies of the type III burst and the measured electron plasma frequencies as a function of radial distance from the sun. Since the angular size of the source is rather large, as viewed from the earth, the electron plasma frequencies have been averaged over a longitude range of $\pm 10^\circ$ centered on the points A, B, and C in Figure 6. The error bars give the standard deviation of the electron plasma frequency over this interval.

Helios 2 and Imp 7 and 8. Point B, on the other hand, is probably very accurate, since it is determined by an interpolation between measured source positions less than 0.2 AU apart. Point A is also considered to be reasonably accurate, since the Archimedeian spiral model for the magnetic field is less subject to errors close to the sun. Also, in the region close to the sun the direction finding measurements (500 kHz in Figure 3) show good qualitative agreement with the best fit Archimedeian spiral, even though exact source positions cannot be determined by triangulation.

Because of the large apparent source size a choice must be made concerning the size of the region over which the electron densities are to be compared. Although the Imp 8 and Hawkeye 1 spin modulation measurements indicate that the source subtends a half angle of about 40° , as viewed from the sun, this source size is almost certainly determined by scattering and is too large. This viewpoint is supported by the Helios 2 measurements at 178 kHz which still have a sizable spin modulation ($m = 0.44$, which corresponds to a half angle of about 46° for a uniformly illuminated disk), even though the spacecraft is only 18° in heliographic longitude from the center of the source. These results suggest that the angular size of the source is of the order of 10° – 15° half angle, as viewed from the sun, or possibly even smaller. On the basis of these estimates of the source size we have averaged the electron density measurements over a region of $\pm 10^\circ$ heliographic longitude on either side of the centroid of the source as determined by the points A, B, and C in Figure 6.

The average electron plasma frequencies within the $\pm 10^\circ$ regions centered on points A, B, and C are shown in Figure 7, plotted as a function of heliocentric radial distance. The standard deviation of the plasma frequency in each region is also shown by the error bars in Figure 7, to indicate the range of

variability of the plasma frequency in the assumed source region. The electron plasma frequency is also considered to be uncertain by about $\pm 15\%$ because of instrumental limitations in the absolute density determination. Also shown in Figure 7 are the observed type III emission frequencies and their corresponding heliocentric radial distances, as determined from the triangulation measurements in Figure 3. The error limits on the emission frequencies and radial distances, indicated by the cross-hatched regions, are determined by the filter bandwidths ($\pm 7.5\%$) and the uncertainties in the triangulation measurements.

The systematic decrease in the solar wind plasma frequency and the type III emission frequency with increasing heliocentric radial distance is clearly evident in Figure 7. The electron plasma frequencies are seen to be in good agreement with the expected $1/R$ variation with radial distance, as indicated by the solid line. The emission frequencies are in all cases substantially above the local electron plasma frequency, too far removed to be consistent with generation of the radiation at f_p . For comparison the second harmonic of the electron plasma frequency, $2f_p$, is shown by the dashed line in Figure 7, based on the $1/R$ curve through the average plasma frequencies. The observed emission frequencies are seen to be in reasonably good agreement with the second harmonic, $2f_p$, much better than for the fundamental, f_p .

SUMMARY AND DISCUSSION

By using long base line stereoscopic direction finding measurements from the Imp 8, Hawkeye 1, and Helios 2 spacecraft the three-dimensional trajectory of a type III solar radio burst has been determined and analyzed. In contrast to previous direction finding analyses of type III radio bursts the trajectory in this case was obtained completely independent of any modeling assumptions regarding the radial dependence of the emission frequency. Comparisons of the observed emission frequencies with the plasma densities measured along the trajectory were used to determine whether the radiation is generated at the fundamental, f_p , or second harmonic, $2f_p$, of the local electron plasma frequency. For the event analyzed the results show that the radio emission is generated near the second harmonic, $2f_p$, and not at the fundamental.

In considering possible uncertainties in our result, several factors must be considered. The primary uncertainties in the analysis are concerned with (1) the constancy of the solar wind density distribution from the time the event occurred until the time that the density measurements were obtained, (2) the size of the source, and (3) the plasma densities out of the ecliptic plane. The temporal stability of the rotating solar wind structure during the period of interest is supported by the close agreement between the solar wind velocity and density variations observed by Imp 7 and 8 near the earth and by Helios 1 and 2 closer to the sun and by the fact that the solar wind sector structure is relatively steady and repeatable for several solar rotations during solar minimum. The uncertainty regarding the source size arises because of the necessity for comparing a large-scale average property, the emission frequency, with a series of local measurements. Because of the presently unknown role of scattering in the interplanetary medium the actual source size is not easily related to the apparent source size given by the modulation factor measurements. Since the actual source size is not well known, except for an upper limit, the size of the region over which the electron density must be averaged to compute the 'average' electron plasma frequency is not accurately known. Fortunately, the spatial variations in

the plasma frequency are not so large that the basic conclusion is affected by the assumed size of the source region. Even if the source size is increased by a factor of 2 or more, the electron plasma frequencies detected by Helios 1 and 2 are not changed sufficiently to be consistent with generation of the radiation at the fundamental. Another limitation is that in situ plasma density measurements are only available near the ecliptic plane. It is of course possible that the plasma density is unexpectedly large in the region away from the ecliptic plane, in which case the radiation could be generated at the fundamental and still be consistent with our measurements. Since the centroid of the source is located very close to the ecliptic plane (see Figure 4), this hypothesis is not considered very likely, since it would require that the average plasma density increase symmetrically, by at least a factor of 4, within a few degrees on either side of the ecliptic plane. Considering the observed range of longitudinal variations, such large latitudinal variations of the plasma density away from the ecliptic plane seem quite unlikely.

The conclusion of this investigation, that the low-frequency type III radio emission is generated at $2f_p$, is consistent with and confirms the earlier results of Fainberg et al. [1972], Haddock and Alvarez [1973], Fainberg and Stone [1974], Alvarez et al. [1975], and Kaiser [1975]. The main advantage of this study is that the relationship is determined directly by comparisons with in situ measurements rather than relying on an assumed model for the radial dependence of the emission frequency and/or average statistical properties of the solar wind.

Acknowledgments. The authors express their thanks to William Feldman from the Los Alamos Scientific Laboratory for providing the Imp 7 and 8 plasma densities and velocities used in this study. The research at the University of Iowa was supported in part by NASA under contracts NASS-11431, NAS1-13129, and NASS-11279 and grant NGL-16-001-043 and by the Office of Naval Research.

The Editor thanks D. F. Smith for his assistance in evaluating this paper.

REFERENCES

- Alvarez, H., F. T. Haddock, and R. P. Lin, Evidence for electron excitation of type III radio burst emission, *Solar Phys.*, 26, 468, 1972.
- Alvarez, H., R. P. Lin, and S. J. Bame, Fast solar electrons, interplanetary plasma and km-wave type-III radio bursts observed from the Imp-6 spacecraft, *Solar Phys.*, 44, 485, 1975.
- Asbridge, J. R., S. J. Bame, W. C. Feldman, and M. D. Montgomery, Helium and hydrogen velocity differences in the solar wind, *J. Geophys. Res.*, 81, 2719, 1976.
- Baumback, M. M., W. S. Kurth, and D. A. Gurnett, Direction finding measurements of type III radio bursts out of the ecliptic plane, *Solar Phys.*, 48, 361, 1976.
- Fainberg, J., and R. G. Stone, Satellite observations of type III solar radio bursts at low frequencies, *Space Sci. Rev.*, 16, 145, 1974.
- Fainberg, J., L. G. Evans, and R. G. Stone, Radio tracking of solar energetic particles through interplanetary space, *Science*, 178, 743, 1972.
- Fitzenreiter, R. J., J. Fainberg, R. R. Weber, H. Alvarez, F. T. Haddock, and W. H. Potter, Radio observations of interplanetary magnetic field structures out of the ecliptic, *Solar Phys.*, 52, 477, 1977.
- Frank, L. A., and D. A. Gurnett, Direct observations of low-energy solar electrons associated with a type III solar radio burst, *Solar Phys.*, 27, 446, 1972.
- Ginzburg, V. L., and V. V. Zheleznyakov, On the possible mechanism of sporadic solar radio emission (radiation in an isotropic plasma) (in Russian), *Sov. Astron. AJ*, 2, 653, 1958.
- Gurnett, D. A., and R. R. Anderson, Electron plasma oscillations associated with type III radio bursts, *Science*, 194, 1159, 1976.
- Gurnett, D. A., and R. R. Anderson, Plasma wave electric fields in the solar wind: Initial results from Helios 1, *J. Geophys. Res.*, 82, 632, 1977.
- Haddock, F. T., and H. Alvarez, The prevalence of second harmonic radiation in type III bursts observed at kilometric wavelengths, *Solar Phys.*, 29, 183, 1973.
- Hundhausen, A. J., Nonlinear model of high-speed solar wind streams, *J. Geophys. Res.*, 78, 1528, 1973.
- Kaiser, M. L., The solar elongation distribution of low frequency radio bursts, *Solar Phys.*, 45, 181, 1975.
- Kurth, W. S., M. M. Baumback, and D. A. Gurnett, Direction-finding measurements of auroral kilometric radiation, *J. Geophys. Res.*, 80, 2764, 1975.
- Lin, R. P., L. G. Evans, and J. Fainberg, Simultaneous observations of fast solar electrons and type III radio burst emission near 1 AU, *Astrophys. J.*, 14, L191, 1973.
- NOAA, Solar Geophysical Data, vol. 385, part II, p. 22, Sept. 1976.
- Papadopoulos, K., M. L. Goldstein, and R. A. Smith, Stabilization of electron streams in type III solar radio bursts, *Astrophys. J.*, 190, 175, 1974.
- Parker, E. N., Dynamics of the interplanetary gas and magnetic fields, *Astrophys. J.*, 128, 664, 1958.
- Schwenn, R., H. Rosenbauer, and H. Miggenrieder, Das Plasmaexperiment auf Helios (E1), *Raumfahrtforschung*, 19(5), 226, 1975.
- Smith, D. F., Type III radio bursts and their interpretation, *Space Sci. Rev.*, 16, 91, 1974.
- Sturrock, P. A., Spectral characteristics of type III solar radio bursts, *Nature*, 192, 58, 1961.
- Wild, J. P., Observations of the spectrum of high-intensity solar radiation at metre wavelengths, III. Isolated bursts, *Aust. J. Sci. Res.*, A3, 541, 1950.
- Wild, J. P., M. D. Murray, and W. C. Rowe, Harmonics in the spectra of solar radio disturbances, *Aust. J. Phys.*, 7, 439, 1954.

(Received April 4, 1977;
accepted August 30, 1977.)

Ion Acoustic Waves in the Solar Wind

D. A. GURNETT AND L. A. FRANK

Department of Physics and Astronomy, University of Iowa, Iowa City, Iowa 52242

Plasma wave measurements on the Helios 1 and 2 spacecraft have revealed the occurrence of electric field turbulence in the solar wind at frequencies between the electron and ion plasma frequencies. Wavelength measurements with the Imp 6 spacecraft now provide strong evidence that these waves are short-wavelength ion acoustic waves which are Doppler-shifted upward in frequency by the motion of the solar wind. Comparison of the Helios results with measurements from the earth-orbiting Imp 6 and 8 spacecraft shows that the ion acoustic wave turbulence detected in interplanetary space has characteristics essentially identical to those of bursts of electrostatic turbulence generated by protons streaming into the solar wind from the earth's bow shock. In a few cases, enhanced ion acoustic wave intensities have been observed in direct association with abrupt increases in the anisotropy of the solar wind electron distribution. This relationship strongly suggests that the ion acoustic waves detected by Helios far from the earth are produced by an electron heat flux instability, as was suggested by Forslund. Possible related mechanisms which could explain the generation of ion acoustic waves by protons streaming into the solar wind from the earth's bow shock are also considered.

INTRODUCTION

Plasma wave measurements on the solar-orbiting Helios 1 and 2 spacecraft [Gurnett and Anderson, 1977] have recently revealed the occurrence of significant levels of electric field turbulence in the solar wind at frequencies from about 1 to 10 kHz, between the electron and ion plasma frequencies. In this paper we expand the initial investigation of this turbulence and present evidence that this turbulence consists of short-wavelength ion acoustic waves below the ion plasma frequency which are Doppler-shifted upward in frequency by the motion of the solar wind. Measurements are presented both in interplanetary space, from Helios 1 and 2, and in the solar wind upstream of the earth's bow shock, from Imp 6 and 8. These data provide a comprehensive description of the spectrum, polarization, wavelength, and other essential characteristics of the turbulence. Comparisons are also made with the ambient plasma parameters under a variety of conditions to identify the origin of these waves. In interplanetary space, far away from the earth, the primary mechanism for producing the ion acoustic waves is believed to be the electron heat flux instability suggested by Forslund [1970]. Near the earth, however, the same types of waves are often observed to be associated with low-energy (1–10 keV) protons streaming toward the sun from the earth's bow shock. Thus more than one mechanism is apparently operative in the solar wind to destabilize the ion acoustic mode. As will be discussed, similar mechanisms, based on an induced drift between the solar wind electrons and protons, are believed to account for both the heat flux and the proton streaming instabilities.

In the initial description of the ion acoustic wave turbulence by Gurnett and Anderson [1977] this turbulence was called $f_p^+ < f < f_p^-$ noise. This terminology was chosen on a strictly observational basis, since the largest intensities usually occur in the frequency range between the electron and ion plasma frequencies f_p^- and f_p^+ . As detected by Helios 1 and 2, the maximum single-channel ($\pm 10\%$ bandwidth) electric field amplitudes of the $f_p^+ < f < f_p^-$ noise are typically a few hundred microvolts per meter. The electric field strength of this noise is very impulsive, consisting of many brief bursts lasting for only a few seconds. When it is viewed on a time scale of several hours or more, the $f_p^+ < f < f_p^-$ noise is present a large

fraction (30–50%) of the time. The noise is observed over the entire range of the Helios orbits from about 0.3 to 1.0 AU. The frequency spectrum of the $f_p^+ < f < f_p^-$ noise shows a systematic variation with radial distance from the sun, shifting toward higher frequencies closer to the sun. Spin modulation measurements show that the electric field of the noise tends to be aligned along the direction of the magnetic field in the solar wind. Gurnett and Anderson discussed the possible plasma wave modes which could account for the $f_p^+ < f < f_p^-$ noise and concluded that the noise could be produced by either the Buneman [1958] mode or the ion acoustic mode, the ion acoustic mode being the most likely.

HELIOS OBSERVATIONS IN INTERPLANETARY SPACE

Since more data have now been analyzed from the Helios plasma wave experiments, a much more detailed analysis of the $f_p^+ < f < f_p^-$ noise detected by Helios in the interplanetary medium can be provided than was given in the initial survey by Gurnett and Anderson [1977]. For details of the Helios 1 and 2 plasma wave instrumentation, see the paper by Gurnett and Anderson [1977]. A typical example of the $f_p^+ < f < f_p^-$ noise detected by Helios 2 is shown in Figure 1. Helios 2 at this time is near the earth-sun line at a heliocentric radial distance of about 0.45 AU. The solid lines for each frequency channel in Figure 1 show the peak electric field intensities over 40.0-s intervals, and the vertical bars (solid black areas) indicate the corresponding average electric field intensities. The intensity scales are logarithmic with a total range of 100 dB from the bottom of one channel to the bottom of the next adjacent channel. The $f_p^+ < f < f_p^-$ noise is evident as a broad band of noise extending from about 1.0 to 17.8 kHz, roughly between the electron and ion plasma frequencies f_p^- and f_p^+ , as indicated on the right-hand side of Figure 1. A typical spectrum, selected from Figure 1 at a time of nearly maximum intensity, is shown in Figure 2. The broad peak in the spectrum between the electron and ion plasma frequencies is clearly evident. The relationship to the local electron and ion plasma frequencies $f_p^+ < f < f_p^-$ is believed to be mainly fortuitous, since as will be shown later, the frequency spectrum is strongly Doppler-shifted by the motion of the solar wind. Both Figure 1 and Figure 2 show that the peak field strengths of the $f_p^+ < f < f_p^-$ noise are much larger than the average field strengths, indicating that the noise is very impulsive. The detailed temporal

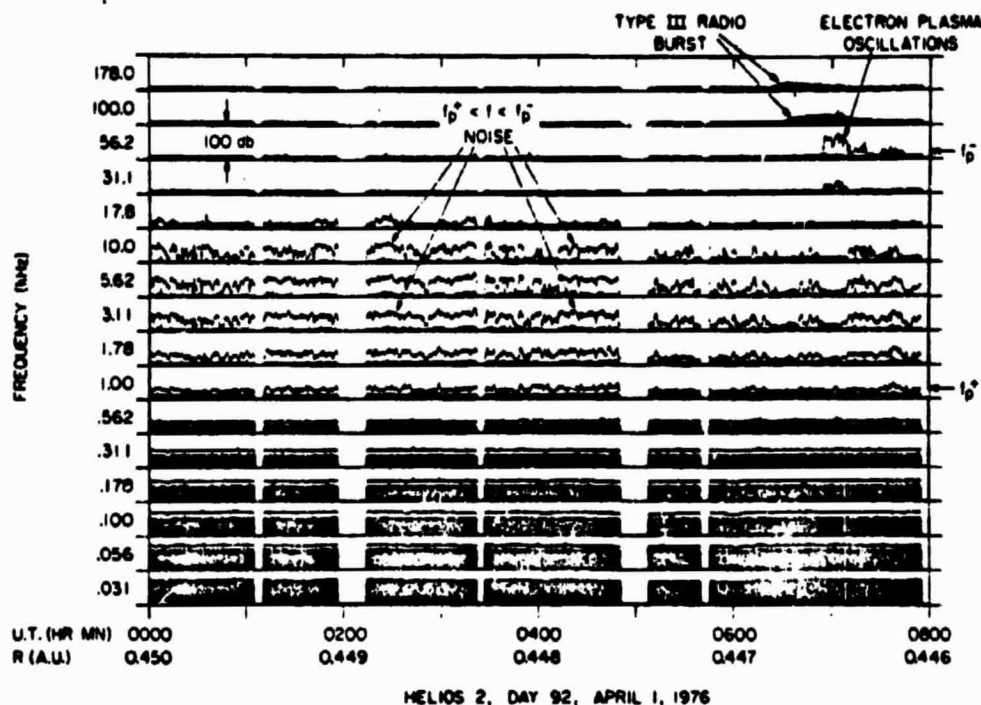


Fig. 1. Typical example of the $f_p^+ < f < f_p^-$ noise detected by the Helios 2 spacecraft at about 0.45 A.U. The solid lines and the vertical bars (solid black areas) indicate the peak and average electric field strengths. The intense noise at low frequencies, ≤ 311 Hz, is caused by interference from the spacecraft solar array.

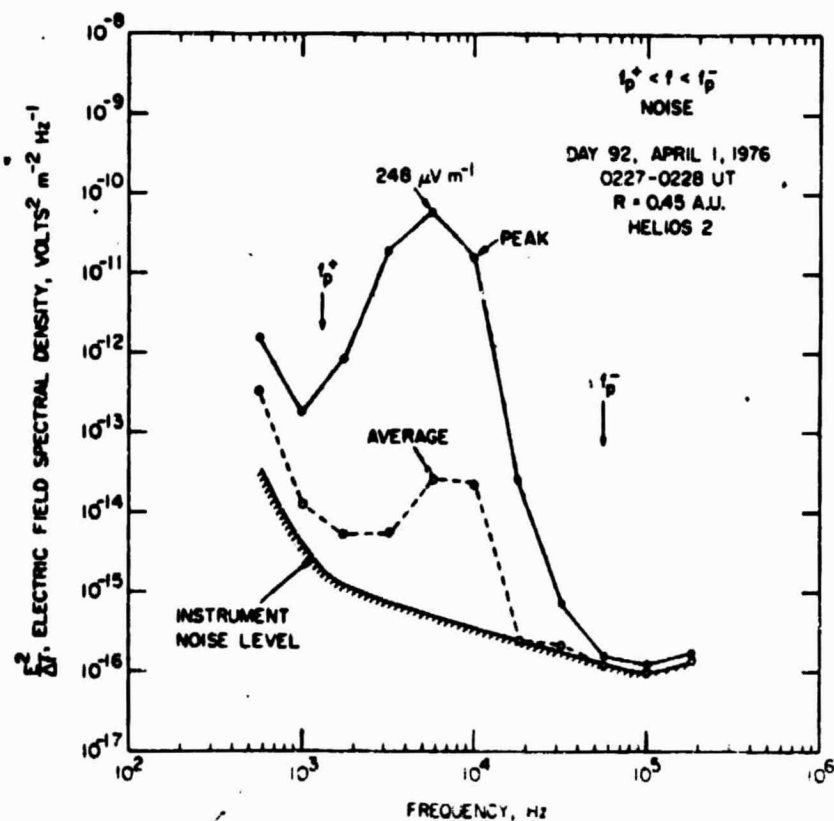


Fig. 2. Typical spectrum of the $f_p^+ < f < f_p^-$ noise at a selected interval from Figure 1. Note the distinct peak in the spectrum at about $(2-10)f_p^-$ and the large ratio of the peak to the average electric field strength, indicative of very impulsive temporal variations.

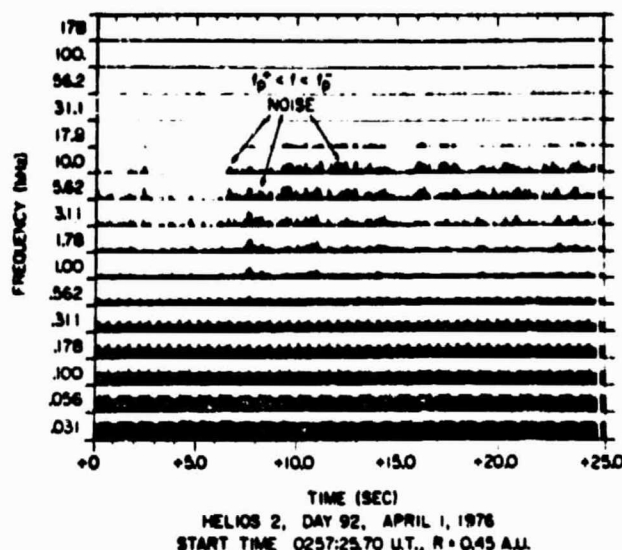


Fig. 3. Very high time resolution measurements from Figure 1, showing the impulsive burstlike temporal structure of the $f_p^+ < f < f_p^-$ noise.

variations are illustrated in Figure 3, which shows a very high time resolution snapshot of the electric field intensities stored in the spacecraft memory from the event in Figure 1, at about 0257 UT. These high time resolution measurements show that the $f_p^+ < f < f_p^-$ noise consists of many short bursts lasting only a few tenths of a second. The individual bursts have a very broad bandwidth and tend to occur simultaneously across a broad range of frequencies. Occasionally, high time resolution measurements, such as those in Figure 3, show distinct evidence of spin modulation caused by the rotation of the electric antenna. A brief period in which such spin modulation is apparent occurs from about +12 to +15 s in the 1.78-kHz channel in Figure 3. The spin modulation consists of two maxima and two minima in each 1-s rotation of the spacecraft. In most cases the extremely rapid temporal variations make it very difficult to determine the phase of the spin modulation accurately. However, by averaging a long series of measurements the detailed spin modulation pattern can usually be identified. An example of one such series of measurements is illustrated in Figure 4, which shows the electric field intensity distribution above a fixed percentage occurrence level (10 and 20%) as a function of the antenna orientation angle ϕ_{SE} . A long (1 hour) analysis interval is used to reduce statistical fluctuations. These data show that the maximum electric field intensity occurs when the antenna is oriented approximately parallel to the solar wind magnetic field. Individual high time resolution measurements of the spin modulation, such as those in Figure 3, also show the same relationship. From these measurements it is concluded that the electric field of the $f_p^+ < f < f_p^-$ noise is oriented approximately parallel to the static magnetic field in the solar wind.

To illustrate the approximate fraction of the time that the $f_p^+ < f < f_p^-$ noise is present in the solar wind, Figure 5 shows the peak and average field strengths for one complete solar rotation. The four frequencies shown in Figure 5 are selected to cover the range of frequencies in which the $f_p^+ < f < f_p^-$ noise is normally observed. Here, as in Figure 1, the peak and average field strengths are shown by lines and vertical bars. A time interval of 36.0 min is used for both the peak and the

average field strength calculations. It is evident from Figure 5 that peak electric field amplitudes of a few hundred microvolts per meter are present in the frequency range from 1.78 to 5.62 kHz a substantial fraction of the time. Occasionally, bursts of $f_p^+ < f < f_p^-$ noise are seen to extend into the 562-Hz and 17.8-kHz channels. Because of the long interval for the peak determination the compressed time scale presentation in Figure 5 tends to enhance the apparent occurrence of the $f_p^+ < f < f_p^-$ noise, since even one short burst during any given 36-min interval will register in the peak measurements. Nevertheless, these data show that bursts of $f_p^+ < f < f_p^-$ noise are a common feature of the solar wind, since during any given 36-min interval a few bursts are normally detected. Occasionally, quiet periods occur. However, some turbulence is usually detected in any given 36-min interval. Sometimes, distinct enhancements are evident for periods of several days, for example, from November 21 to November 23 and from November 27 to November 29.

To investigate the variation in the spectrum of the $f_p^+ < f < f_p^-$ with radial distance from the sun, a detailed statistical analysis has been performed on all of the available Helios 1 data, consisting of approximately two complete orbits around the sun. The results of this analysis are summarized in Figure 6, which shows the distribution of electric field strengths detected in each frequency channel as a function of radial distance. The electric field strengths used in this analysis are 36-min peak values, comparable to those in Figure 5. The electric field strength contours shown in Figure 6 correspond to intensities which are exceeded a fixed fraction (5 and 10%) of the time. The portion of the overall spectrum attributed to the $f_p^+ < f < f_p^-$ noise is indicated by the shaded areas. The steeply rising spectrum at low frequencies (≤ 500 Hz) is caused by interference from the spacecraft solar array (also evident in Figure 1). The isolated peaks in the spectrum at high frequencies (≥ 30 kHz) are caused by narrow-band electron plasma

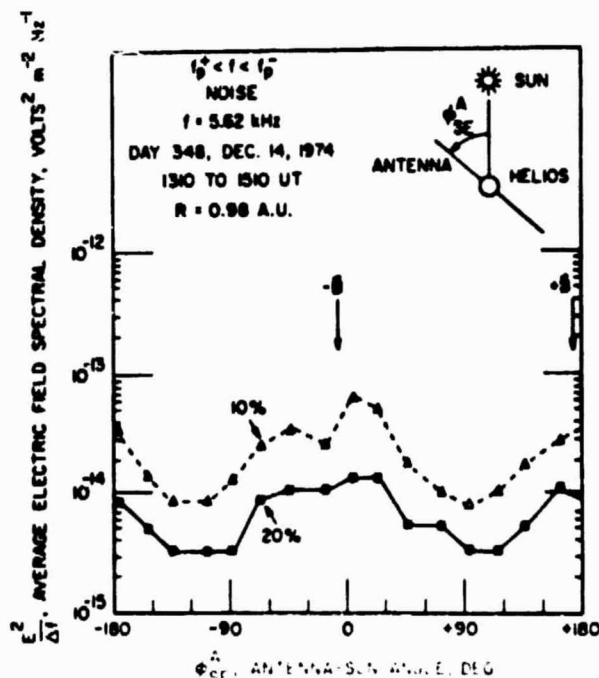


Fig. 4. Angular distribution of the electric field intensity of the $f_p^+ < f < f_p^-$ noise, showing that the electric field of this noise is oriented approximately parallel to the solar wind magnetic field.

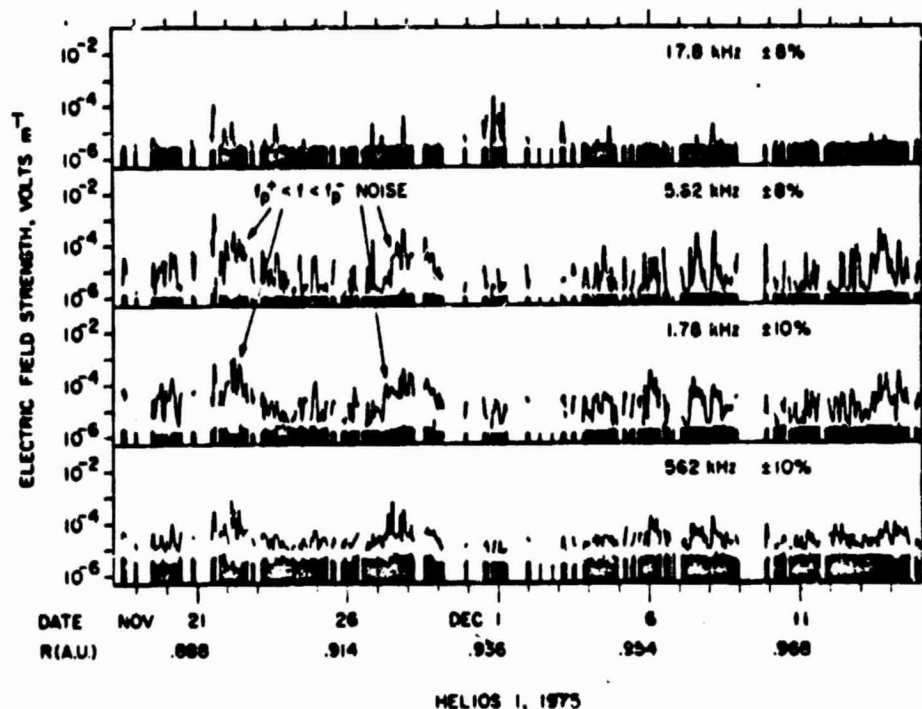


Fig. 5. Compressed time scale plot showing the electric field intensities for one solar rotation. Each peak and each average point represent a 36-min interval. These data show that a low level of $f_p^+ < f < f_p^-$ noise, at amplitudes of $10\text{--}100 \mu\text{V m}^{-1}$, is present in the solar wind a substantial fraction of the time.

oscillations comparable to the event in Figure 1 at about 0700 UT. These plasma oscillations are directly associated with energetic electrons streaming outward from the sun [Gurnett and Frank, 1975] and are often directly associated with type III solar radio bursts [Gurnett and Anderson, 1976]. Although narrow-band electron plasma oscillations are easily distinguished from the $f_p^+ < f < f_p^-$ noise, no attempt was made to separate the two types of waves for the statistical analysis in Figure 6, since the plasma oscillations occur very infrequently. Figure 6 clearly shows that both the upper cutoff-frequency and the intensity of the $f_p^+ < f < f_p^-$ noise increase with decreasing radial distance from the sun. A rough analysis indicates that the upper cutoff frequencies of the $f_p^+ < f < f_p^-$ noise and the frequency of the electron plasma oscillations vary approximately as $1/R$, where R is the heliocentric radial distance. The radial variation of the $f_p^+ < f < f_p^-$ noise intensity is shown in more detail in Figure 7, which gives the distribution of broadband electric field strengths as a function of the radial distance from the sun. The broadband electric field strengths used in this analysis are calculated by integrating the individual 36-min peak electric field spectrums from 562 Hz to 31.1 kHz. As can be seen from Figure 5, the main contribution to the $f_p^+ < f < f_p^-$ noise spectrum usually occurs in this frequency range. The frequency of occurrence contours in Figure 7 clearly show the increase in the $f_p^+ < f < f_p^-$ noise intensity with decreasing radial distance from the sun. A best fit analysis of the broadband field strength as a function of the radial distance, a power law radial distance dependence being assumed, indicates that the electric field strength also varies approximately as $1/R$.

IMP 6 AND 8 OBSERVATIONS UPSTREAM OF THE EARTH'S BOW SHOCK

Waves essentially identical to the $f_p^+ < f < f_p^-$ noise detected by Helios are also commonly observed by the Imp 6 and

8 spacecraft in the solar wind upstream of the earth's bow shock. See the description by Gurnett [1974] of the plasma wave instrumentation on Imp 6 and 8. As will be shown, some of the $f_p^+ < f < f_p^-$ noise bursts detected by Imp 6 and 8 are clearly of terrestrial origin, whereas others appear to be of interplanetary origin, as is true in the Helios observations. Figures 8, 9, and 10 illustrate some typical examples of the $f_p^+ < f < f_p^-$ noise detected by Imp 8 upstream of the bow shock. Figure 8 shows an example of an earth-related event in which a burst of $f_p^+ < f < f_p^-$ noise, from about 0920 to 1115 UT, is closely associated with the arrival of a stream of low-energy protons from the earth's bow shock. The corresponding charged particle measurements from the University of Iowa low-energy proton-electron differential energy analyzer (Lepede) on Imp 8 are shown in Plate 1. Details of this spectrogram display of the charged particle intensities and the Lepede instrumentation are given by Frank *et al.* [1976]. The sunward streaming 1- to 10-keV protons associated with the $f_p^+ < f < f_p^-$ noise are clearly evident in the second, third, and fourth spectrograms from the top in Plate 1, between about 0920 and 1115 UT, in almost exact coincidence with the burst of $f_p^+ < f < f_p^-$ noise. These spectrograms represent viewing directions looking toward local evening, local midnight, and local morning, respectively. The direction of motion of the protons can also be seen from the sector spectrogram in Plate 1, which shows that the protons are streaming toward the sun with directions of arrival in the range $120^\circ \leq \psi_{\text{sc}} \leq 300^\circ$ (solar ecliptic coordinates). Imp 8 at this time is located upstream of the earth at a local time of about 14.5 hours and a geocentric radial distance of about $41 R_E$. The observed directions of arrival correspond closely with the expected directions of motion for particles originating from the vicinity of the earth. The velocity distribution function for these protons, measured along directions approximately parallel to the earth-sun line, is shown in Figure 11, along with the ambient solar

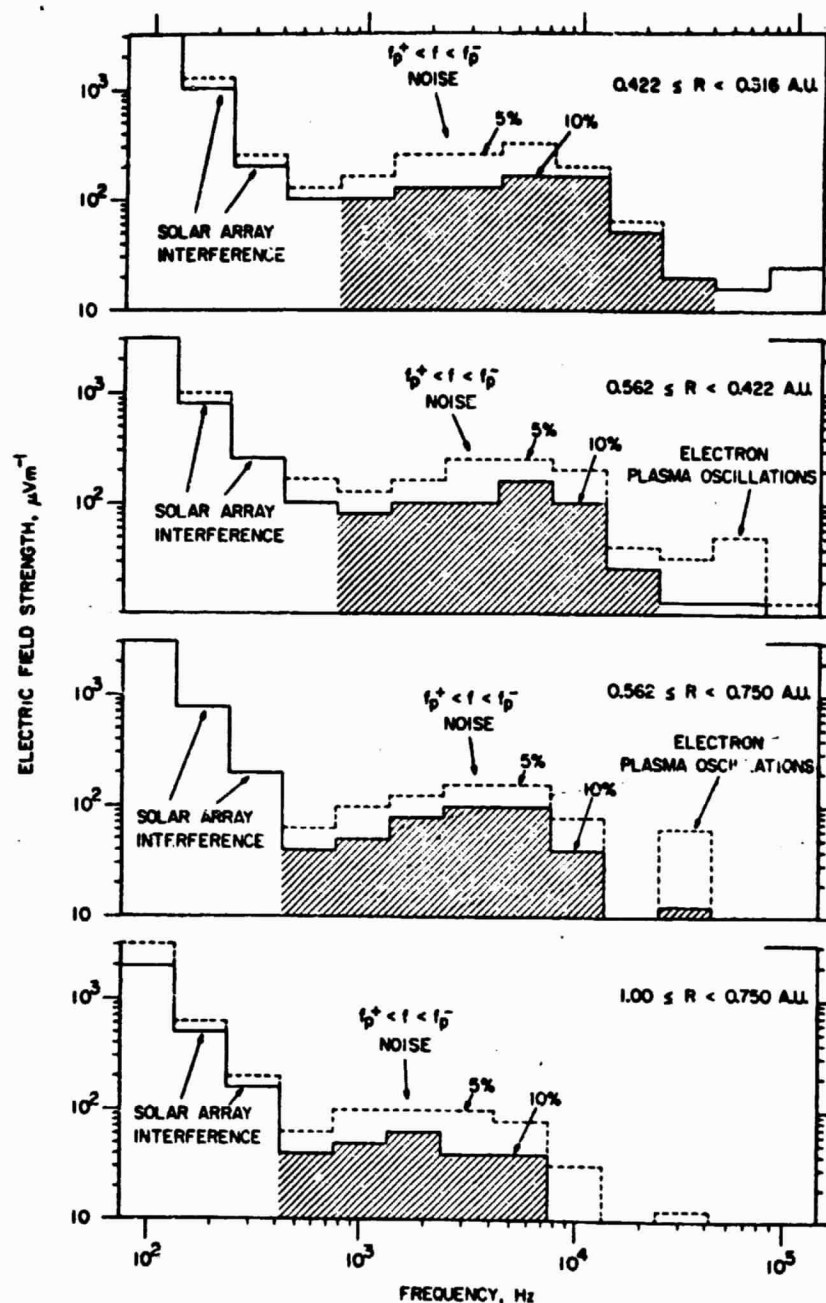


Fig. 6. Statistical survey of the 36-min peak field strength measurements of the type shown in Figure 5 for a total of two complete orbits around the sun. These data show that both the frequency and the amplitude of the $f_p^+ < f < f_p^-$ noise increase systematically with decreasing radial distance from the sun, with $f_{\max} \propto 1/R$.

wind distribution determined from the Los Alamos plasma instrument on Imp 8 (W. Feldman, personal communication, 1977). As can be seen in Figure 11, the protons streaming into the solar wind produce a very pronounced double peak in the proton distribution function. Possible mechanisms by which these sunward streaming protons can generate $f_p^+ < f < f_p^-$ noise are considered later.

The upstream $f_p^+ < f < f_p^-$ noise associated with protons arriving from the earth's bow shock, such as that in Figure 8, almost certainly corresponds to the electrostatic noise first reported by Scarf *et al.* [1976] upstream of the bow shock from Ogo 5. In comparison to the $f_p^+ < f < f_p^-$ noise detected by Helios the upstream waves detected by Imp 8 have essentially

identical characteristics. In both cases the noise is electrostatic and extends with comparable intensities from about 562 Hz to 10 kHz, between the electron and ion plasma frequencies. The peak electric field strengths are much greater than the average electric field strengths, as is true in the Helios measurements, and angular distributions, such as those in Figure 12, show that the wave electric field is aligned approximately parallel to the solar wind magnetic field, also in agreement with the Helios observations. From all available evidence the electrostatic waves generated upstream of the earth by protons arriving from the bow shock are essentially identical to the $f_p^+ < f < f_p^-$ noise detected by Helios far from the earth. These comparisons indicate that the same basic plasma wave mode is

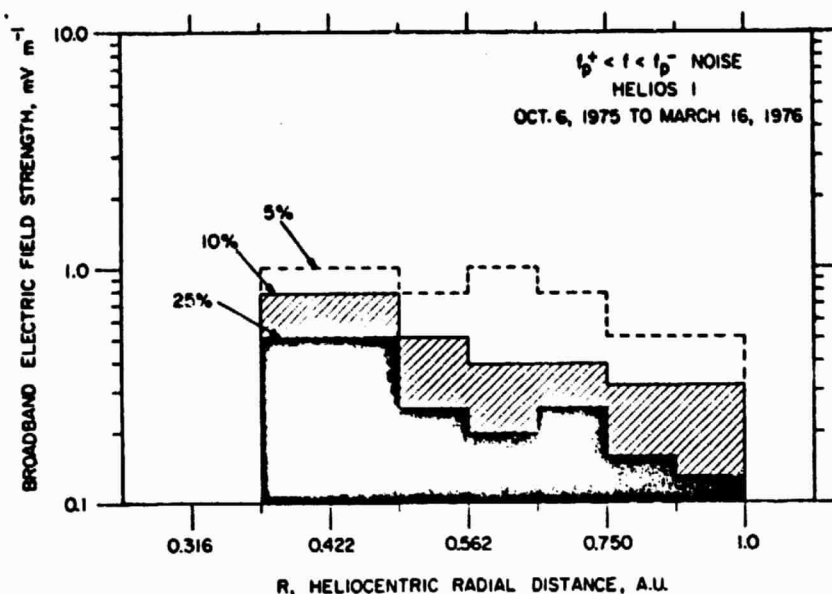


Fig. 7. More detailed analysis of the broadband electric field intensity as a function of the radial distance from the sun. The radial distance is plotted on a logarithmic scale, so that a power law dependence will be a straight line. The electric field amplitude varies approximately as $1/R$.

involved in both types of noise. The detailed mechanisms by which the noise is generated must, however, be quite different in the two cases, since protons from the earth's bow shock cannot possibly produce the waves detected by Helios far from the earth.

Not all of the $f_p^+ < f < f_p^-$ noise bursts detected by Imp 8 are associated with protons arriving from the bow shock. Figure 9, for example, shows a sequence of $f_p^+ < f < f_p^-$ noise events extending over an entire day which are not related to upstreaming protons. The corresponding Lepede spectrograms in Plate 2 for the same day demonstrate that no sunward streaming protons are detectable during these events, except possibly for the event around 1300–1400 UT. The magnetic field during this day is often close to the ecliptic plane, so there is no possibility that the Lepede, which scans viewing directions in the ecliptic plane, would not be able to detect protons streaming along the magnetic field from the bow shock. The corresponding electron spectrograms in Plate 2 also show no abrupt changes in the electron distribution function which can be clearly related to variations in the $f_p^+ < f < f_p^-$ noise intensity. Events of this type, for which no earth-related source can be identified, constitute about 30–50% of all of the $f_p^+ < f < f_p^-$ noise events detected by Imp 8 upstream of the bow shock. These events evidently correspond to the interplanetary $f_p^+ < f < f_p^-$ noise commonly detected by Helios far from the earth, since no earth-related source can be identified.

To try to identify the feature of the solar wind charged particle distribution which produces the interplanetary (non earth related) $f_p^+ < f < f_p^-$ noise, the Imp 8 Lepede and plasma wave data have been examined for correlated events which would indicate the origin of the instability. Several events have been identified which strongly indicate that the anisotropy associated with the electron heat flux in the solar wind plays an important role in producing the $f_p^+ < f < f_p^-$ noise. One such event, which occurred during a disturbed period on July 5, 1974, is illustrated in Figure 10 and Plate 3. In this case a pronounced burst of $f_p^+ < f < f_p^-$ noise occurs

from about 1645 to 1930 UT, preceded by a shorter burst from about 1540 to 1600 UT. The Lepede spectrograms in Plate 3 clearly show that no protons are arriving from the earth's bow shock during this time, so these waves must correspond to the interplanetary $f_p^+ < f < f_p^-$ noise. The enhanced background, evident in the proton spectrogram throughout the period shown in Plate 3, is caused by an energetic solar cosmic ray event. Close examination of the electron sector spectrogram in the second panel from the bottom in Plate 3 shows that the $f_p^+ < f < f_p^-$ noise occurs during a period when a substantial anisotropy is present in the solar wind electron distribution. The maximum intensities occur for Lepede viewing directions in the range $0^\circ \leq \varphi_{SE}^L \leq 90^\circ$, which are approximately symmetrical with respect to the magnetic field direction, $\varphi_{SE}^B \approx 45^\circ$, during this period. This anisotropy is representative of a substantial streaming of electrons along the magnetic field away from the sun. The electron velocity distribution indicates that these electrons correspond to the high-temperature 'halo' electrons which provide the main contribution to the heat flux in the solar wind [Feldman et al., 1974]. The anisotropy evident in Plate 3 corresponds to an unusually large electron heat flux away from the sun, directed along the solar wind magnetic field. The detailed variations of the electron velocity distribution function at a fixed energy and the corresponding 1.78-kHz electric field intensity variations are shown in Figure 13 near the beginning of the event. The electron distribution function is shown in two directions, $\varphi_{SE}^L = 34^\circ$ and 12° , which are approximately parallel and perpendicular, respectively, to the average magnetic field directions projected onto the ecliptic plane during this period. The interpretation of these data is somewhat complicated by variations in the magnetic field direction. Before about 1610 UT the magnetic field is too far out of the ecliptic plane, $\theta \gtrsim 60^\circ$, for accurate measurements of the anisotropy parallel and perpendicular to the magnetic field. However, after about 1610 UT the magnetic field is sufficiently close to the ecliptic plane, $\theta_{SE}^B \lesssim 30^\circ$, for good anisotropy measurements. As can be seen from Figure 13, after about 1650 the intensities at $\varphi_{SE}^L = 34^\circ$, looking along

the magnetic field toward the sun, increase substantially above the intensities at $\varphi_{SE}^L = 124^\circ$, perpendicular to the magnetic field. Comparisons with the 1.78-kHz electric field intensities show that the onset of the $f_p^+ < f < f_p^-$ noise is closely correlated with the increase in the anisotropy of the electron distribution. The burst of noise at about 1550 UT is also seen to be correlated closely with the increase of electron intensities in the direction $\varphi_{SE}^L \approx 34^\circ$ at about 1552 UT. Even though θ_{SE}^B is large at this time, this burst must be associated with an anisotropic component streaming along the magnetic field, since the intensity perpendicular to the magnetic field, $\varphi_{SE}^L = 124^\circ$, shows no comparable increase. The evidence that the $f_p^+ < f < f_p^-$ noise is associated with the magnetic-field-aligned anisotropy in the electron flux is further supported by the velocity distributions shown in Figure 14, which are selected for times when $\theta_{SE}^B \approx 0^\circ$ and for viewing direction parallel ($\varphi_{SE}^L = 304^\circ$ and 34°) and antiparallel ($\varphi_{SE}^L = 124^\circ$ and 214°) to the magnetic field. The electron intensity measurements at 1252 UT (triangles), before the onset of the $f_p^+ < f < f_p^-$ noise, show that the anisotropy is typically small, $\leq 20\%$, at all velocities. However, the measurements at 1720 UT (circles), after the onset of the $f_p^+ < f < f_p^-$ noise, show that the anisotropy is very large, typically a factor of 3-5, over a broad range of velocities. These velocity distributions also show that other than the change in the anisotropy the electron distribution functions are nearly identical in the two regions, before and after onset of the noise. Comparison of these velocity distributions with the measurements of Feldman *et al.* [1975] clearly identifies this anisotropy with a greatly enhanced heat flux of the halo electrons, directed along the magnetic field line away from the sun. These and other similar observations provide strong evidence that the anisotropy associated with the electron heat flux in the solar wind plays an essential role in the generation of these waves. Close inspection of the electron angular distributions in Plate 2 also shows, for example, that a similar electron anisotropy is present during the period when the ion acoustic waves in Figure 9 are being observed. The variations in the $f_p^+ < f < f_p^-$ noise intensity are not, however, as easily associated with changes in the electron distribution function in this case, possibly because the plasma is close to marginal stability, so that only very minor changes in the electron distribution or other parameters can trigger the growth or decay of the waves.

IDENTIFICATION OF THE $f_p^+ < f < f_p^-$ NOISE AS SHORT-WAVELENGTH ION ACOUSTIC WAVES

Some of the factors involved in the identification of the plasma wave mode associated with the $f_p^+ < f < f_p^-$ noise detected by Helios have already been discussed by Gurnett and Anderson [1977]. From the electrostatic character of the noise, all of the well-known electromagnetic modes of propagation, such as the whistler and magnetosonic modes, can be eliminated from consideration. The electric field orientation, parallel to the static magnetic field, further restricts the possibilities, eliminating, for example, the various types of ion cyclotron and Bernstein modes which propagate nearly perpendicular to the static magnetic field. Essentially only two plasma wave modes are known which could account for all of the observed characteristics. These modes are the ion acoustic mode at $f \leq f_p^+$ and the Buneman [1958] mode at $f_B \approx (m^+/m^-)^{1/2} f_p^-$. We also note that Scarf *et al.* [1970] identified the same modes as the best candidates for explaining the upstream electrostatic noise, which is now believed to be the same basic plasma wave mode detected by Helios far from the earth. Although Gurnett and Anderson [1977] argue that it is unlikely that the proper conditions exist in the solar wind for generating the Buneman

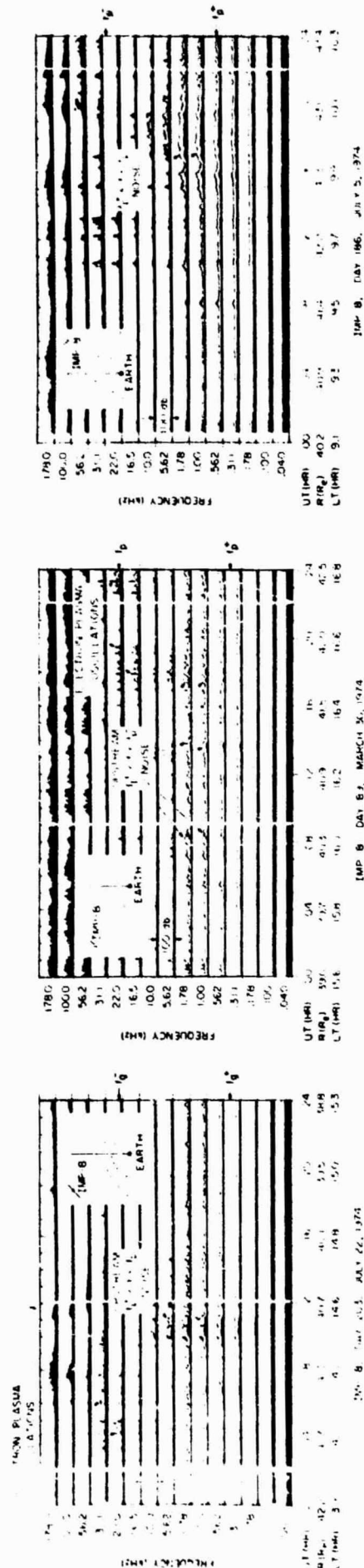


Fig. 8. Example of $f_p^+ < f < f_p^-$ noise detected upstream of the earth's magnetosphere in association with an intense burst of 1- to 10-kV protons streaming into the solar wind from the bow shock (see Plate 1).

Fig. 9. Series of $f_p^+ < f < f_p^-$ noise bursts detected by Imp 8 for which no protons can be detected arriving from the bow shock (see Plate 2). These waves evidently correspond to the interplanetary $f_p^+ < f < f_p^-$ noise detected by Helios far from the earth.

Fig. 10. Intense burst of $f_p^+ < f < f_p^-$ noise detected during a period when a substantial anisotropy is evident in the low-energy electron distribution (see Plate 3).

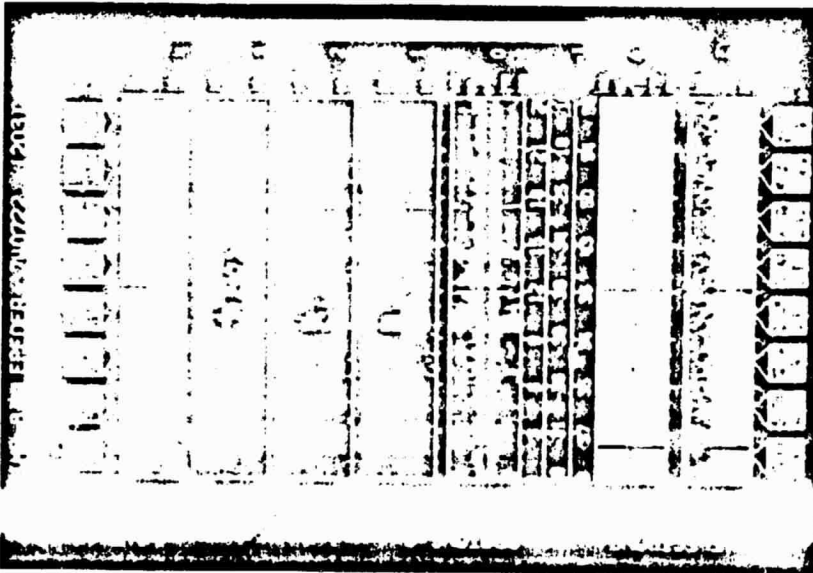


Plate 1. The Lepedea data corresponding to the electric field measurements in Figure 8, showing the occurrence of an intense burst of protons streaming toward the sun in direct correspondence with the burst of f_p^+ noise from about 0920 to 1115 UT. These protons propagate from the earth's bow shock.

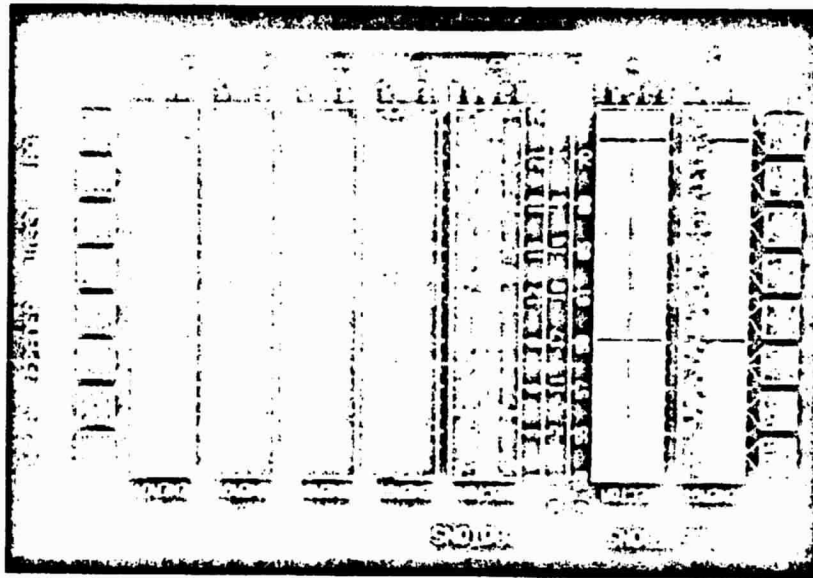


Plate 2. The Lepedea data corresponding to the electric field measurements in Figure 9, showing a series of f_p^+ noise bursts for which no significant enhancement in either the electron or the proton intensities can be identified in association with the f_p^+ noise.

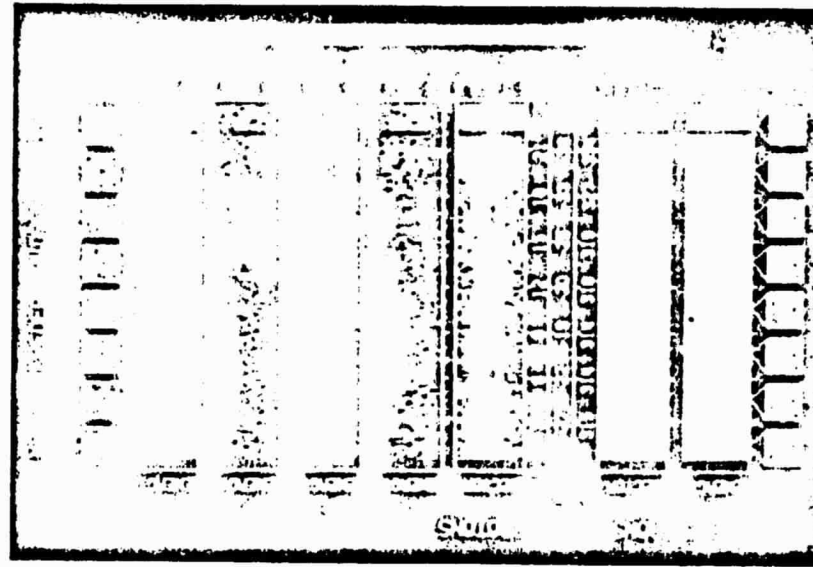


Plate 3. The Lepedea data corresponding to the electric field measurements in Figure 10, showing an event in which the f_p^+ noise (from about 1540 to 1930 UT) is closely correlated with the occurrence of a greatly enhanced anisotropy in the low-energy solar wind electron distribution. This anisotropy is clearly evident in the electron sector spectrogram from about 1540 to 1900 UT.

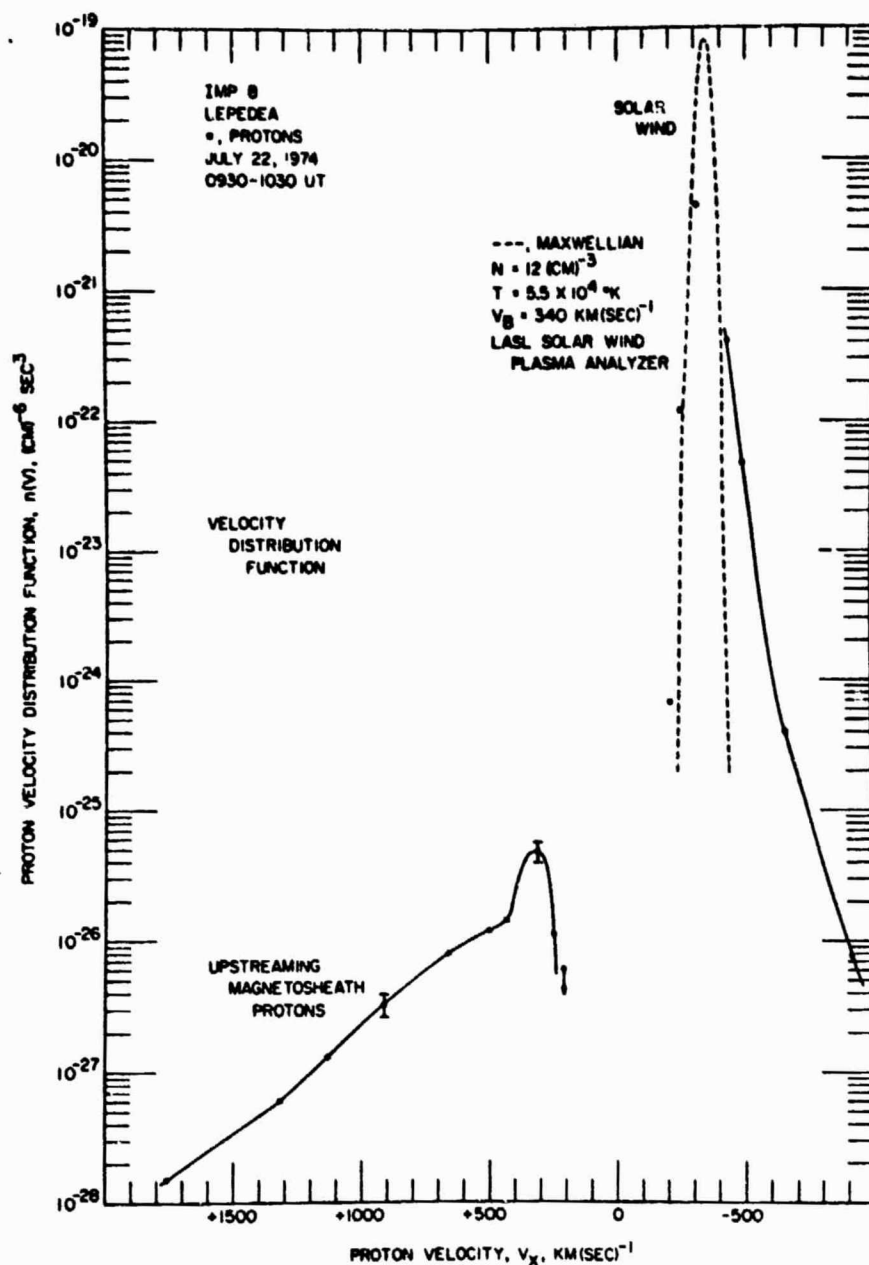


Fig. 11. Distribution function for the intense burst of protons observed streaming into the solar wind from the earth's bow shock from 0930 to 1030 UT in Plate 1. The $+V_x$ velocity axis is directed toward the sun. The dashed line gives the solar wind proton distribution function as determined from the Los Alamos plasma analyzer on Imp 8.

instability, no method was available to distinguish clearly between these two modes of propagation.

One way of distinguishing the Buneman mode from the ion acoustic mode is to measure the wavelength. The two modes differ fundamentally in the wavelengths required to account for the observed frequency spectrums. Since ion acoustic waves only occur at frequencies less than f_p^* in the rest frame of the plasma, large Doppler shifts and correspondingly short wavelengths of tens to hundreds of meters are required to account for the frequency range, $(2-10)f_p^*$, in which the noise is usually observed. The Buneman mode, on the other hand, occurs at a frequency $f_B \approx 3.49f_p^*$, which requires no Doppler shift to account for the observed frequency spectrum, implying wavelengths of several hundred meters or more.

Since only a single electric dipole antenna is used on Helios,

the wavelength cannot be determined. However, the Imp 6 spacecraft, which also detects the same waves upstream of the bow shock, has two antennas of different lengths which can be used to estimate wavelengths. The technique used consists of comparing the measured antenna voltages V with the tip-to-tip lengths L of the antennas. For wavelengths longer than the antenna length, so that the computed electric field strength $E = 2V/L$ is the same for both antennas. However, for wavelengths λ comparable to or shorter than the antenna this proportionality no longer holds. In general, we expect that when $\lambda \lesssim L$, the measured electric field strength will be underestimated.

On Imp 6 the electric field antennas consist of two orthogonal dipoles with tip-to-tip lengths of $L_y = 92.5$ m and $L_z =$

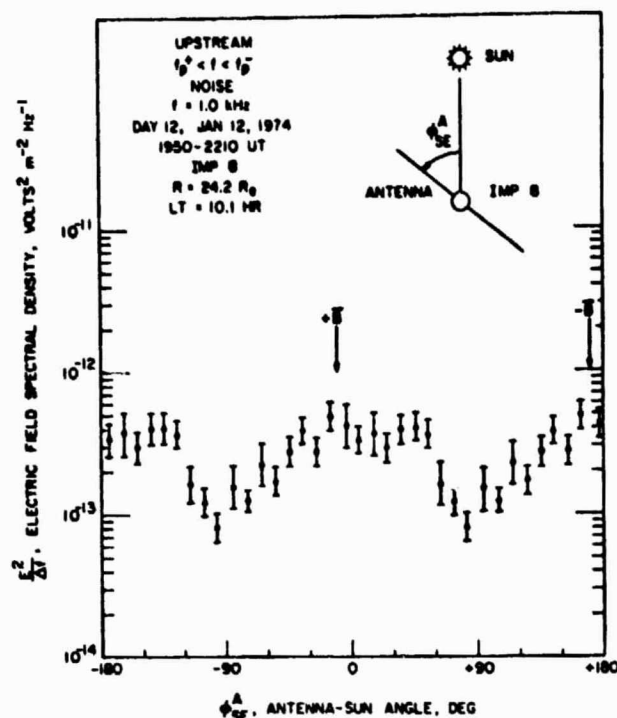


Fig. 12. Angular distribution of the electric field intensity for a burst of $f_p^+ < f < f_p^-$ noise produced by upstreaming magnetosheath protons. These data show that the electric field of the proton-driven $f_p^+ < f < f_p^-$ noise is parallel to the solar wind magnetic field, essentially identical to the $f_p^+ < f < f_p^-$ noise detected by Helios far from the earth (compare with Figure 4).

53.5 m [Gurnett, 1974]. The two antennas are mounted orthogonally to each other and to the spacecraft spin axis. The spin axis is directed normal to the ecliptic plane. Simultaneous measurements of the voltage spectrums from the two antennas are made with two identical spectrum analyzers. Because of their orientation the two antennas do not detect the same component of the electric field. However, for a steady state wave spectrum, comparisons can be made by averaging over many rotations of the spacecraft.

A case for which the wavelength of the interplanetary $f_p^+ < f < f_p^-$ noise has been estimated by using this technique is shown in Figure 15. During this period, Imp 6 is upstream of the bow shock at geocentric radial distances from about 19 to 26 R_E and local times from about 9.8 to 10.2 hours. A substantial level of $f_p^+ < f < f_p^-$ noise is present during this period. Some of these events can be associated with low-energy protons arriving from the bow shock, whereas other events, such as the intense bursts from about 0520 to 0610 UT, are of interplanetary origin. This period of enhanced activity occurs shortly after an abrupt increase in the solar wind density at about 0500 UT (see the top panel of Figure 15), which preceded the onset of a high-speed solar wind stream a few hours later (W. Feldman, personal communication, 1977).

The electric field spectrums obtained from the E_y and E_z antennas during the interval from about 0530 to 0602 UT are shown in the bottom panel of Figure 16. These spectrums give the median values of all of the peak intensities obtained during this interval, computed by using $E = 21/L$. Each point represents the median of approximately 700 individual peak measurements. Because of the impulsive temporal fluctuations a large number of measurements are needed to reduce the statis-

tical fluctuations to an acceptable level. The ratio of the E_y to the E_z field strengths, computed from these spectrums, is shown in the top panel of Figure 16, with estimates of the corresponding error limits (one standard deviation). As can be seen, the E_y/E_z ratio is approximately 1 at low frequencies, $f \leq 3$ kHz, but deviates substantially below 1 at high frequencies, $f \geq 10$ kHz. The decrease in the E_y/E_z ratio at high frequencies indicates that the longer, E_y antenna is significantly underestimating the field strengths in comparison to the shorter, E_z antenna. This deviation of the E_y/E_z ratio indicates that wavelengths shorter than $L_y = 92.5$ m are being detected at frequencies above about 3 kHz.

To demonstrate the overall accuracy and reliability of this technique, a corresponding analysis was performed on a band of whistler mode plasmaspheric hiss detected in the earth's magnetosphere a few hours later. It is easily shown that the wavelengths of these whistler mode waves are very large, much larger than the dimensions of the Imp 6 electric antennas. The results of this analysis are shown in Figure 17. As can be seen, the E_y/E_z ratio stays very close to 1 at all frequencies, thereby confirming that the wavelengths are longer than the antenna length. These and many other similar comparisons for a wide variety of plasma wave phenomena demonstrate that significant deviations of the E_y/E_z ratio below 1, such as the deviation in Figure 16, are not instrumental effects and can only be attributed to wavelengths shorter than the antenna length.

Since the accuracy of the method has been confirmed, it is now of interest to compare the measurements in Figure 16 with the wavelengths to be expected if the waves are ion acoustic waves. For typical solar wind parameters $T \approx 1.5 \times 10^6$ °K it is readily shown that the ion acoustic speed $C_s = (kT/m)^{1/2} \approx 35.2$ km s⁻¹ is much less than the solar wind velocity. For these conditions the frequency detected in the spacecraft frame of reference is, to a good approximation, given entirely by the Doppler shift (valid for $f \gg f_p^+$),

$$f = (V_{sw}/\lambda) \cos \theta_{kv} \quad (1)$$

where θ_{kv} is the angle between the propagation vector \mathbf{k} and the solar wind velocity \mathbf{V}_{sw} . Even though the ion acoustic mode can propagate at a substantial angle to the magnetic field [Stix, 1962], the $f_p^+ < f < f_p^-$ noise is evidently generated with \mathbf{k} vectors nearly parallel to the static magnetic field, since the electric field is always observed to be nearly parallel to the static magnetic field. Thus θ_{kv} can be determined from the measured magnetic field direction; i.e., $\theta_{kv} \approx \theta_{bv}$. By solving (1) for λ by means of the appropriate solar wind speed $V_{sw} \approx 360$ km s⁻¹ from Figure 15 and by means of $\theta_{bv} \approx 22^\circ$ from the Imp 6 magnetometer data (D. Fairfield, personal communication, 1977) the wavelengths corresponding to each frequency can be calculated. These wavelengths are shown by the wavelength scale at the top of Figure 16 along with the lengths L_y and L_z of the two electric antennas. As can be seen, the E_y/E_z ratio starts to deviate below 1 as soon as the computed wavelength becomes significantly shorter than the antenna. These comparisons show that the wavelength computed from the Doppler shift formula is in excellent quantitative agreement with the wavelength estimated from the E_z/E_y ratio ($\lambda \approx 92.5$ m at $f \approx 3$ kHz).

Further evidence of short wavelengths is provided by the upper cutoff of the observed frequency spectrum and the variation of this cutoff with radial distance from the sun. It is well known that the shortest wavelength which can occur in a plasma is determined by the onset of strong Landau damping

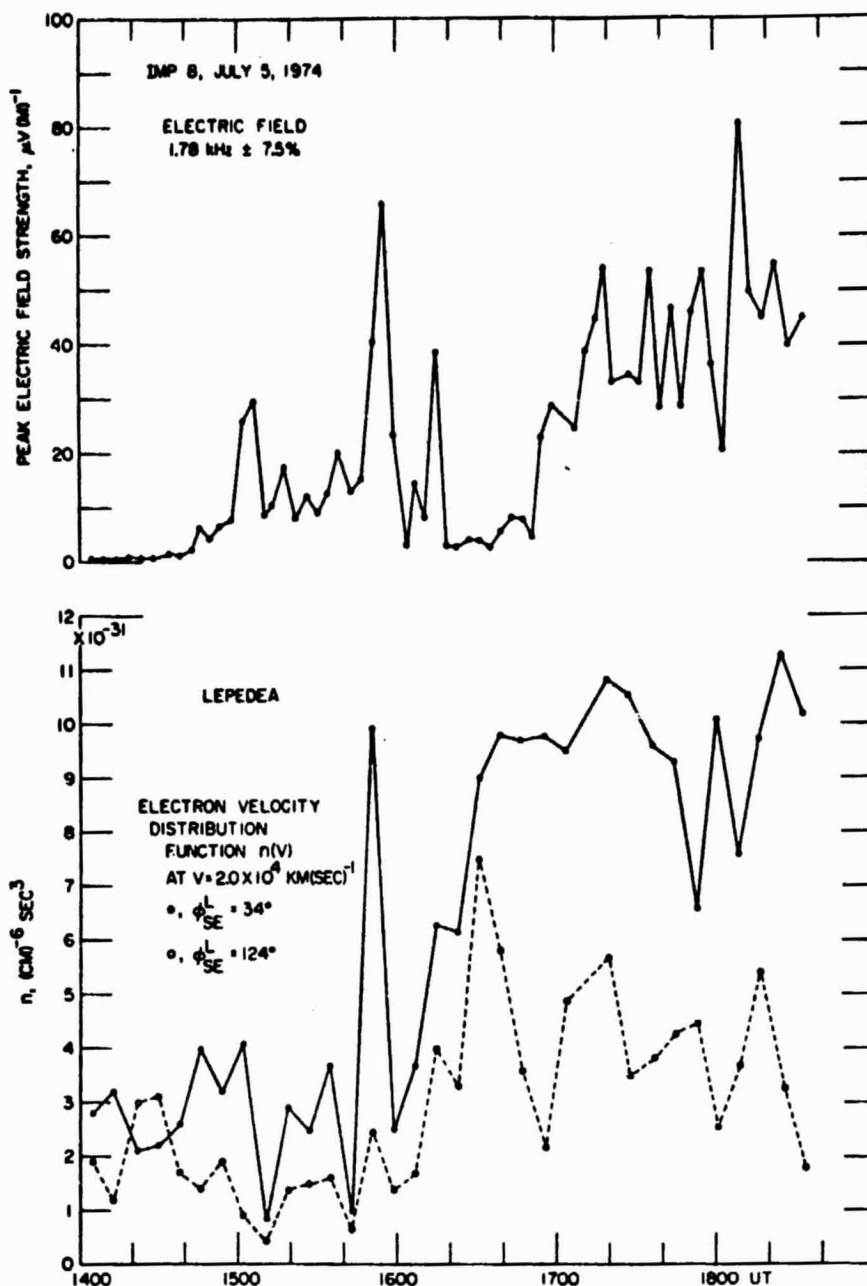


Fig. 13. Low-energy electron intensity variations associated with the burst of $f_p^+ < f < f_p^-$ noise shown in Figure 10. The dashed curve at $\phi_{SE}^L = 124^\circ$ gives the electron intensities perpendicular to the magnetic field, and the solid curve at $\phi_{SE}^L = 34^\circ$ gives the intensities looking generally toward the sun and along the ecliptic plane projection of the magnetic field. The $f_p^+ < f < f_p^-$ noise occurs during periods of substantial anisotropy in the low-energy electron intensities associated with the electron heat flux in the solar wind.

at a wavelength of about $2\pi\lambda_D$, where $\lambda_D^2 = \epsilon_0 kT/ne^2$ is the Debye length. The minimum wavelength $\lambda_{min} = 2\pi\lambda_D$, computed from the measured plasma density $n \approx 35 \text{ cm}^{-3}$ and the temperature $T = 1.4 \times 10^6 \text{ }^\circ\text{K}$, is approximately 27.5 m, as is shown at the top of Figure 16. As can be seen, this minimum wavelength is in excellent agreement with the observed upper cutoff frequency of the electric field spectrum. The dependence of the minimum wavelength on the plasma density, $\lambda_{min} \propto \lambda_D \propto 1/n^{1/2}$, furthermore explains the tendency for the upper cutoff frequency $f_{max} \approx (V_{sw}/\lambda_{min}) \propto n^{1/2}$ to increase with decreasing radial distance from the sun (see Figure 6), since the plasma density increases closer to the sun. When the

plasma density scaling law $n \propto 1/R^2$ appropriate for the solar wind far from the sun, is used, the upper cutoff frequency should vary approximately as $f_{max} \propto 1/R$, which is seen to be in good agreement with the observed radial variation of the upper cutoff frequency illustrated in Figure 6. All these comparisons provide strong evidence that the low-frequency electrostatic waves detected in the solar wind by Imp 6, Imp 8, and Helios have short wavelengths and Doppler shifts consistent with the identification of these waves as ion acoustic waves.

Although short wavelengths are clearly evident for the event in Figure 16, in most cases the $f_p^+ < f < f_p^-$ noise detected by Imp 6 does not show these effects. The event in Figure 16 is

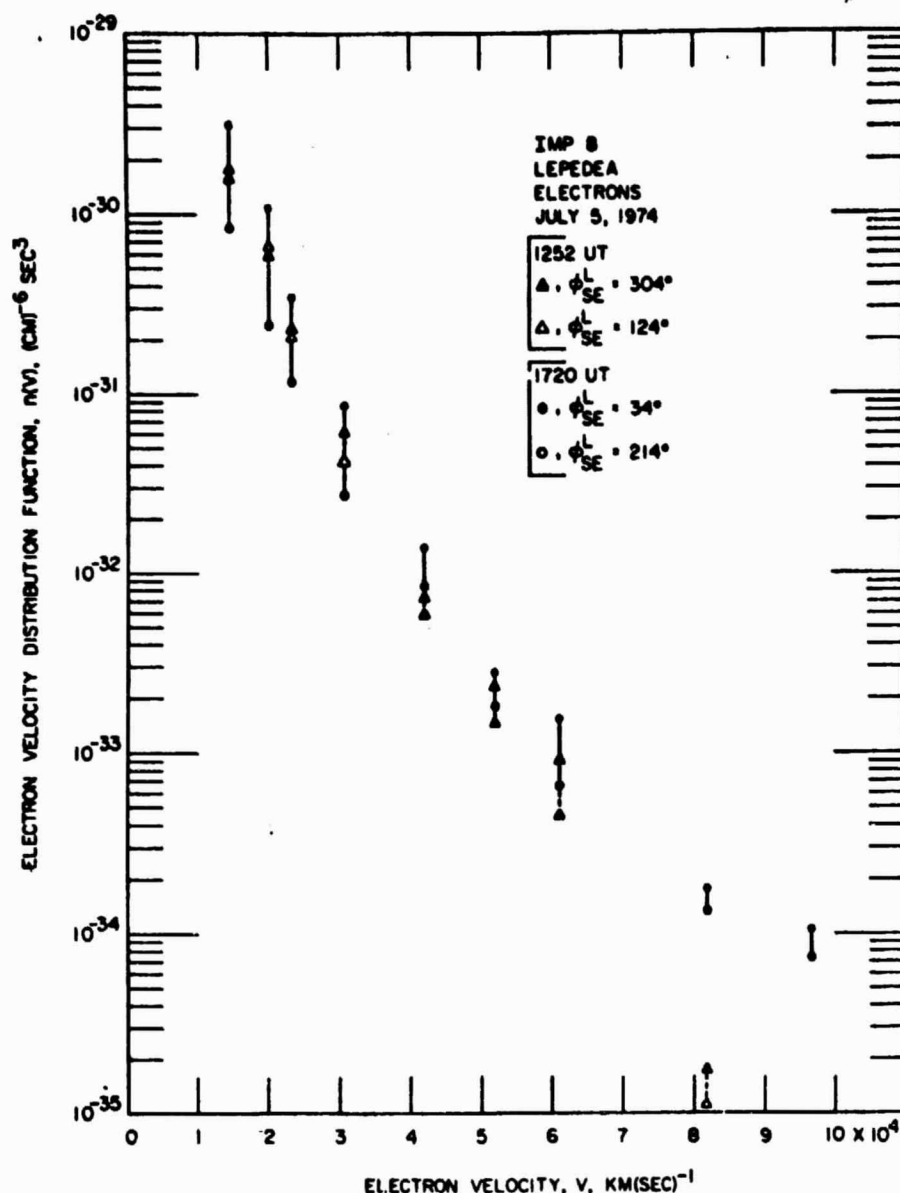


Fig. 14. Further details of the anisotropic electron distribution associated with the burst of $f_p^+ < f < f_p^-$ noise shown in Figure 10, selected for times when the magnetic field is aligned parallel to the viewing direction of the Lepedeu. At 1252 UT the anisotropy is very small, and no $f_p^+ < f < f_p^-$ noise is present. At 1720 UT the anisotropy is large, particularly at the lower velocities, and the $f_p^+ < f < f_p^-$ noise intensities are correspondingly large.

unusual in that the plasma density is very large, $n = 35 \text{ cm}^{-3}$, and results in a minimum wavelength substantially less than the antenna length. For typical solar wind plasma densities at 1 AU, $n \approx 5 \text{ cm}^{-3}$, the minimum wavelength is approximately $\lambda_m = 72 \text{ m}$, which is evidently sufficiently large to make short-wavelength effects undetectable even though wavelengths shorter than the Imp 6 antenna length, $L_a = 92.5 \text{ m}$, could occur. Note from Figure 16 that most of the wave energy occurs at wavelengths substantially larger than $\lambda_{\min} = 2\pi\lambda_D$ and that the intensity is strongly attenuated for wavelengths approaching λ_{\min} . It should also be noted that because of the shorter length of the Helios antennas ($L = 16 \text{ m}$ for Helios 1, and $L = 32 \text{ m}$ for Helios 2), errors due to short-wavelength effects are not normally expected to be significant for the Helios measurements, except for unusually high densities.

ORIGIN OF THE SOLAR WIND ION ACOUSTIC WAVES

Having established that the $f_p^+ < f < f_p^-$ noise consists of short-wavelength ion acoustic waves, we now consider the mechanisms for generating these waves, both in the interplanetary medium and in the region upstream of the bow shock. The observed triggering of the ion acoustic waves by an increase in the electron heat flux provides strong evidence that the ion acoustic mode is being driven unstable by the electron heat flux in the solar wind, as was first suggested by Forslund [1970].

The basic mechanism proposed by Forslund [1970] is illustrated schematically in Figure 18, which shows the general form of the reduced one-dimensional electron and proton distribution functions in the solar wind. The reduced one-

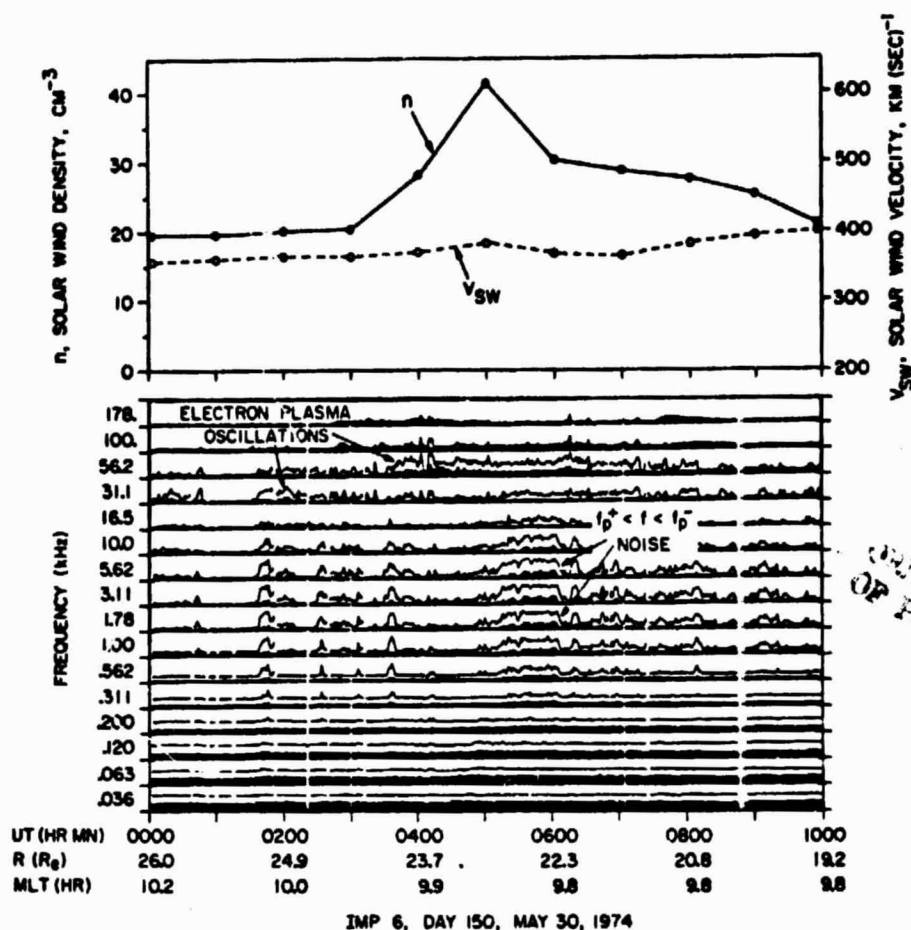


Fig. 15. Series of $f_p^+ < f < f_p^-$ noise bursts detected by Imp 6 in association with a density compression preceding a high-speed solar wind stream.

dimensional distribution function $F(V)$ is defined by $F(V) = \int dV_{\perp} f(V)$, where $f(V)$ is the three-dimensional distribution function and dV_{\perp} represents an integration over velocities perpendicular to the magnetic field. As is indicated, a substantial anisotropy is produced in the high-energy, or 'halo,' electrons by the electron heat flux flowing outward away from the sun [Feldman et al., 1974, 1975]. Since the net current in the solar wind is essentially zero, except at discontinuities, the electron current associated with the antisunward drift of the energetic 'halo' electrons must be compensated by a sunward drift of the low-energy 'core' electrons. This drift velocity V_d is indicated in Figure 18. If the double peak in the combined velocity distribution function $F(V) = F^-(V) + (m^-/m^+)F^+(V)$ produced by this drift is sufficiently large, then the ion acoustic mode is unstable. Since the drift is parallel to the static magnetic field, the waves produced by this instability are expected to have their wave vectors and electric fields oriented approximately parallel to the static magnetic field. The condition for instability is given by the Penrose criterion

$$\int \frac{F(V) - F(V_0)}{(V - V_0)^2} dV > 0 \quad (2)$$

where V_0 is the velocity of the minimum in $F(V)$ [Penrose, 1960]. For equal electron and ion temperatures $T^- = T^+$ the threshold drift velocity is very large, approximately $V_i = (kT^-/$

$m^-)^{1/2}$, which is too large to be exceeded in the solar wind. However, if $T^- \gg T^+$, which is sometimes satisfied in the solar wind, then the threshold drift velocity for instability is greatly reduced, to approximately

$$V_i \approx (kT^+/m^+)^{1/2} \quad (3)$$

[Krall and Trivelpiece, 1973]. For a solar wind ion temperature of $T^+ \approx 4.0 \times 10^4$ °K the threshold drift velocity is, for example, only $V_i = 18$ km s⁻¹ ($T^- \gg T^+$ being assumed). For electron temperatures only moderately larger than the ion temperature the threshold drift velocity is larger than (3) by a factor which depends on T^-/T^+ [see Krall and Trivelpiece, 1973]. On the basis of his analysis, Forslund [1970] concluded that the ion acoustic mode should be driven unstable by the electron heat flux whenever the electron to ion temperature ratio is sufficiently large.

Both the observed electric field orientation and the association of enhanced ion acoustic wave activity with increases in the electron anisotropy provide substantial evidence for the mechanism proposed by Forslund [1970]. The detailed arguments in support of this mechanism are, however, more involved, since all other types of double-peaked distribution functions which could possibly generate ion acoustic waves must be eliminated from consideration. Charged particle measurements, such as those in Plates 2 and 3, clearly show that ion

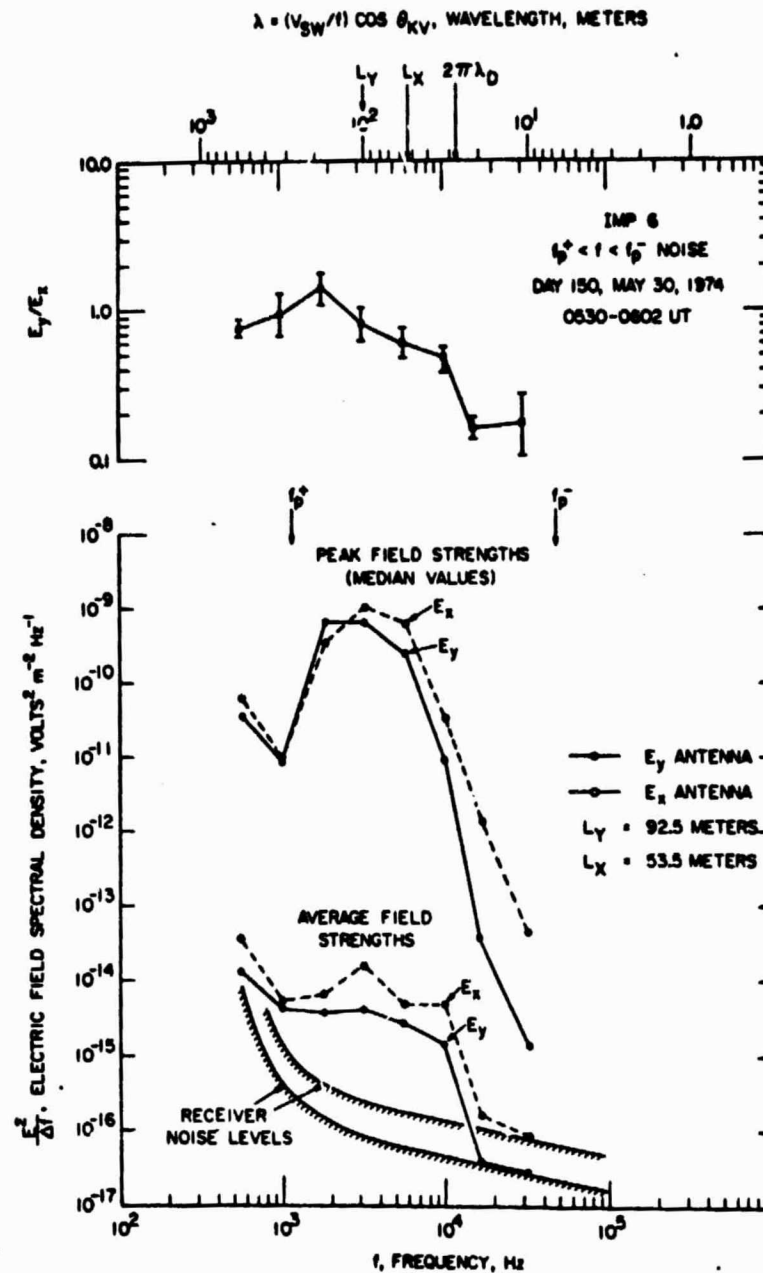


Fig. 16. Comparison of the electric field amplitudes for the burst of $f_p^+ < f < f_p^-$ noise from 0530 to 0602 UT in Figure 15 using antennas of two different lengths. The deviation of the E_y/E_x ratio below 1 indicates that the wavelengths of the waves are shorter than the longest antenna, $L_y = 92.5$ m, at frequencies above about 3 kHz. The scale at the top of the illustration indicates the wavelength which would occur if the observed frequencies were entirely due to Doppler shifts. Note the close correspondence of the upper frequency cutoff to the minimum wavelength $2\pi\lambda_D$ caused by Landau damping.

acoustic waves occur during times when no secondary peak is detectable in either the electron or the proton distribution functions, within the energy range ($50 \text{ eV} \leq E \leq 45 \text{ keV}$) and resolution of the Lepedea. Although electron energies less than 100 eV were not investigated, it is almost completely certain, on the basis of the results of Feldman *et al.* [1975], that double peaks do not occur in the electron distribution function at energies less than 100 eV. It is possible that closely spaced double peaks could occur in the ion distribution, such as the double proton streams reported by Feldman *et al.* [1973a], and still be unresolved in the Lepedea data. Comparisons with published examples of double proton streams [Feldman *et al.*,

1973a] do not show a close correspondence with the occurrence of ion acoustic waves; however, further detailed studies are needed to investigate whether double proton streams can under some circumstances generate ion acoustic waves. On the assumption that the ion distribution functions do not generally have the double-peaked form required to produce an instability, essentially the only possibility left is the double peak produced by a velocity shift between the peaks in the electron and ion distributions, as illustrated in Figure 18. The presence of such a velocity shift in the solar wind has now been amply demonstrated by Feldman *et al.* [1974, 1975]. It only remains to be demonstrated that this shift is sufficiently large to exceed

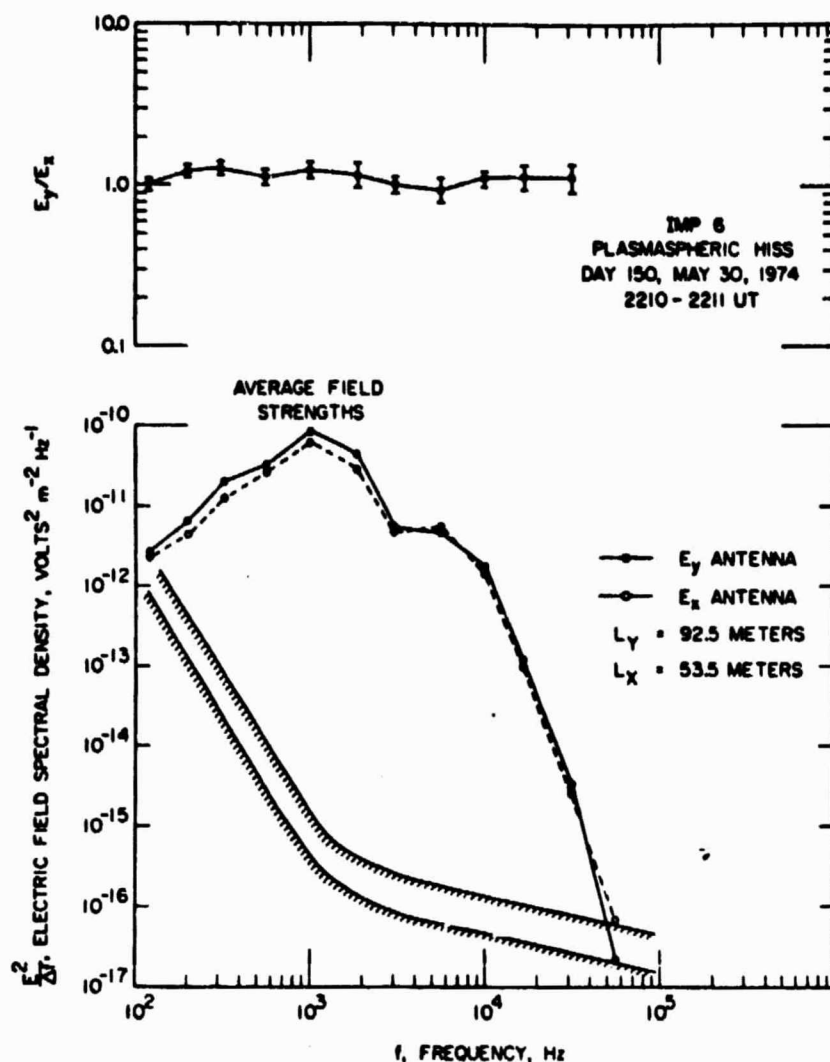


Fig. 17. Comparison of the E_y/E_x ratio for a broadband plasmaspheric hiss emission observed a few hours after the event in Figure 16. Plasmaspheric hiss has wavelengths much longer than the antenna length. The close correspondence of the E_y/E_x ratio to 1 confirms the overall accuracy of this technique for detecting short-wavelength effects.

the threshold for generating ion acoustic waves. The magnitude of the velocity shift, which is difficult to measure directly, can be estimated from the anisotropy in the halo electron distribution. For the event in Figure 14 at 1720 UT the flux of electrons along the magnetic field (first moment) is estimated to be 1.50×10^8 el $(\text{cm}^2 \text{s})^{-1}$. When the measured local plasma density of $n = 10.1$ el cm^{-3} is used, this flux must be compensated by a sunward drift of the core electrons at a velocity of about 150 km s^{-1} . The ratio of this drift velocity to the electron thermal speed ($T^- = 1.5 \times 10^6$ °K being used) is about 0.1. Whether this drift velocity exceeds the threshold drift velocity for the ion acoustic wave instability is critically dependent on the electron to ion temperature ratio. For the period of interest the ion temperature measured by the Los Alamos plasma probe on Imp 8 is $T^+ = 7.1 \times 10^4$ °K. When a typical temperature of $T^- = 1.5 \times 10^6$ °K is used for the core electrons, the temperature ratio is $T^-/T^+ = 2.14$. For this relatively low electron to ion temperature ratio the ion acoustic mode should be stable according to the curves given by Stringer [1964]. On the other hand, if a typical halo temperature of $T^- = 7.0 \times 10^6$ °K is used, which gives $T^-/T^+ = 10$,

the threshold drift velocity given by equation (3), $V_t = 23 \text{ km s}^{-1}$ (valid when $T^- \gg T^+$), is exceeded by a substantial factor. Since no computer calculations of the threshold drift velocity are available for a realistic combination of core and halo electron distributions, the stability of the ion acoustic mode cannot be accurately determined. However, since the correct effective electron to ion temperature ratio is probably somewhere in between the two extremes given by the core and halo temperatures, it seems likely that the ion acoustic mode is unstable in this case. Further detailed analyses of the exact instability conditions are needed for realistic models of the solar wind electron distribution to answer this question clearly.

For the ion acoustic waves generated by protons streaming into the solar wind from the bow shock there is no question about which particles are responsible for the instability. However, considerable uncertainty still remains concerning the detailed mechanism by which the proton stream produces the instability. In considering the origin of the instability, two distinctly different mechanisms can be identified: (1) the instability may be caused directly by the double peak in the proton

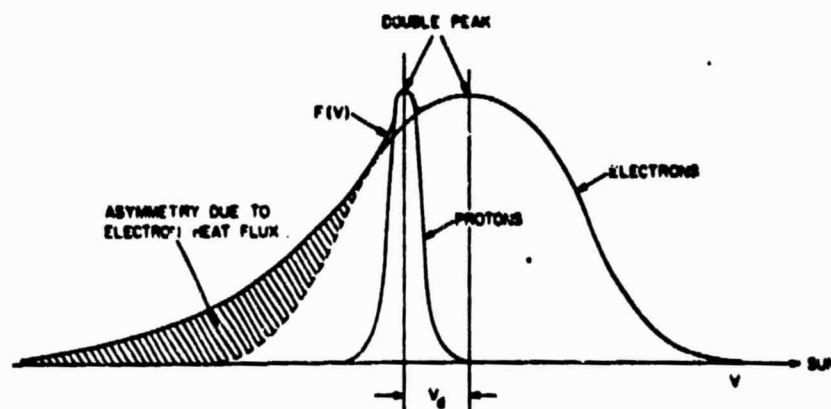


Fig. 18. Illustration showing the velocity shift V_e between the low-energy electrons and the solar wind protons, required to maintain zero net current when a substantial electron heat flux is present. If the velocity shift is sufficiently large, the resulting double peak in the combined electron and proton distribution function $F(V)$ can cause the ion acoustic mode to become unstable.

distribution (see Figure 11), or (2) the instability may be caused indirectly by the shift in the velocity of the core electrons required to maintain zero net current, similar to the heat flux mechanism. Of these two possibilities the second mechanism is believed to be dominant. For the first mechanism, rough estimates show that the peak in the proton distribution function due to the upstreaming protons is simply too small to be unstable according to the Penrose criterion. Note that the contribution of the proton stream to $F(V)$ is greatly reduced by the factor (m^-/m^+) in the combined one-dimensional distribution function, in addition to the fact that the distribution function for this stream is nearly 6 orders of magnitude below the peak due to the solar wind beam (see Figure 11). On the other hand, the proton flux associated with the upstreaming protons can be quite substantial, $\sim 5 \times 10^6$ protons $(\text{cm}^2 \text{ s})^{-1}$. The upstreaming protons must therefore cause a shift in the velocity of the core electrons with respect to the solar wind protons in order to maintain zero net current. If this shift is large enough to produce instability, this mechanism will explain why the ion acoustic waves driven by the upstreaming protons are so similar to the interplanetary ion acoustic waves, since the mechanisms are essentially identical. Note that halo electrons streaming away from the sun and sunward streaming protons both contribute in the same sense to the current imbalance. Detailed comparisons, however, often show that the intensities of the upstreaming protons are too small, by factors of 10–100, to produce velocity shifts exceeding the threshold for the ion acoustic wave instability using a simple Maxwellian distribution for the core electrons. The detailed explanation of this discrepancy is not known; however, one possibility is that the electron heat flux maintains the plasma near marginal stability for ion acoustic waves, so that only a small current imbalance is needed to trigger the instability. Also, *Feldman et al.* [1973b] have shown that protons streaming into the solar wind from the earth's bow shock produce substantial perturbations in the ambient solar wind electron distribution. These perturbations and their effect on the instability condition given by the Penrose criterion must be studied in greater detail before the generation mechanism of the upstream ion acoustic waves can be completely resolved.

Numerous investigators have suggested possible roles which ion acoustic turbulence may play in determining the large-scale properties of the solar wind. It has been suggested that plasma waves can heat the solar wind ions [*Fredricks, 1969*],

regulate the electron heat flux in the solar wind [*Forstlund, 1970; Schulz and Evciatar, 1972*], and thermally couple the electron and ion distributions [*Perkins, 1973*]. The extent to which the ion acoustic waves detected by Helios and Imp 6 and 8 play any significant role in these processes remains to be determined. At 1 AU the maximum intensities of the ion acoustic turbulence are relatively small, energy density ratios being approximately $\epsilon_0 E^2 / 2nkT \approx 10^{-4}$. The turbulence is, however, present a large fraction of the time and increases rapidly in intensity with decreasing radial distance from the sun. These factors all suggest that the presence of these waves must be given serious consideration in the overall understanding of the solar wind, particularly in relation to the regulation of the solar wind heat flux.

SUMMARY AND CONCLUSION

Plasma wave measurements on the solar-orbiting Helios spacecraft have previously shown that sporadic bursts of electrostatic turbulence are commonly observed in the solar wind at frequencies between the electron and ion plasma frequencies [*Gurnett and Anderson, 1977*]. In this paper we have expanded the earlier investigation of these waves using the Helios data and have compared the Helios results with similar measurements from the earth-orbiting Imp 6 and 8 spacecraft. Wavelength measurements with the Imp 6 spacecraft now provide strong evidence that these waves are short-wavelength ion acoustic waves at $f \leq f_p^+$ which are Doppler-shifted upward in frequency by the motion of the solar wind. The upper cutoff frequency and the variation of this cutoff frequency with radial distance from the sun, $f_{\text{max}} \propto 1/R$, are in close agreement with the short-wavelength cutoff expected for ion acoustic waves.

Comparison with the Imp 6 and 8 data reveals that a substantial fraction, 50–70%, of the ion acoustic wave turbulence detected in the solar wind near the earth is caused by suprathermal protons streaming into the solar wind from the earth's bow shock. These waves, which correspond to the upstream electrostatic waves first reported by *Scarf et al.* [1970], are observationally indistinguishable from the ion acoustic waves detected by Helios. Although both the upstream proton-driven waves and the waves detected by Helios are evidently ion acoustic waves, some distinctly different source is required to explain the Helios observations, since protons from the earth's bow shock cannot possibly account for the waves detected by Helios far from the earth. Examina-

tion of the Imp 6 and 8 data reveals many examples of ion acoustic turbulence during periods when no protons can be detected coming from the earth's bow shock. These events evidently correspond to the waves detected by Helios far from the earth. Usually in these cases there is no evidence of significant suprathermal electron or proton fluxes other than the quiescent solar wind distribution. In a few events, variations in the ion acoustic wave intensity were found which are closely correlated with changes in the anisotropy of the solar wind electron distribution. These events suggest that the ion acoustic turbulence is driven by the anisotropy associated with the electron heat flux in the solar wind, as was suggested by Forslund [1970]. Although it seems reasonably certain that the electron heat flux is in some cases involved in the generation of the interplanetary ion acoustic waves, the association of ion acoustic waves with suprathermal protons from the bow shock suggests that the solar wind ion distributions should be investigated in greater detail to see if double ion streams and other nonthermal solar wind ion distributions could also be involved in the generation of these waves.

Acknowledgments. The authors express their thanks to William Feldman from the Los Alamos Scientific Laboratory for providing the Imp 8 plasma density and temperature measurements used in this report. The research at the University of Iowa was supported in part by NASA under contracts NASS-11279, NASS-11431, and NASS-11064 and grants NGL-16-001-002 and NGL-16-001-043 and by the Office of Naval Research.

The Editor thanks W. Bernstein and F. L. Scarf for their assistance in evaluating this paper.

REFERENCES

- Buneman, O., Instability, turbulence and conductivity in a current-carrying plasma, *Phys. Rev. Lett.*, **1**, 8, 1958.
- Feldman, W. C., J. R. Asbridge, S. J. Bame, and M. D. Montgomery, Double ion streams in the solar wind, *J. Geophys. Res.*, **78**, 2017, 1973a.
- Feldman, W. C., J. R. Asbridge, S. J. Bame, and M. D. Montgomery, Solar wind heat transport in the vicinity of the earth's bow shock, *J. Geophys. Res.*, **78**, 3697, 1973b.
- Feldman, W. C., M. D. Montgomery, J. R. Asbridge, S. J. Bame, and H. R. Lewis, Interplanetary heat conduction—Imp 7 results, in *Solar Wind Three*, p. 334, Institute of Geophysics and Planetary Physics, University of California, Los Angeles, Calif., 1974.
- Feldman, W. C., J. R. Asbridge, S. J. Bame, M. D. Montgomery, and S. P. Gary, Solar wind electrons, *J. Geophys. Res.*, **80**, 4181, 1975.
- Forslund, D. W., Instabilities associated with heat conduction in the solar wind and their consequences, *J. Geophys. Res.*, **75**, 17, 1970.
- Frank, L. A., K. L. Ackerson, and R. P. Lepping, On hot tenuous plasmas, fireballs, and boundary layers in the earth's magnetotail, *J. Geophys. Res.*, **81**, 5859, 1976.
- Fredricks, R. W., Electrostatic heating of solar wind ions beyond 0.1 AU, *J. Geophys. Res.*, **74**, 2919, 1969.
- Gurnett, D. A., The earth as a radio source: Terrestrial kilometric radiation, *J. Geophys. Res.*, **79**, 4227, 1974.
- Gurnett, D. A., and R. R. Anderson, Electron plasma oscillations associated with type III radio bursts, *Science*, **194**, 1159, 1976.
- Gurnett, D. A., and R. R. Anderson, Plasma wave electric fields in the solar wind: Initial results from Helios 1, *J. Geophys. Res.*, **82**, 632, 1977.
- Gurnett, D. A., and L. A. Frank, The relationship of electron plasma oscillations to type III radio emission and low-energy solar electrons, *Solar Wind*, **45**, 477, 1975.
- Krall, N. A., and A. W. Trivelpiece, *Principles of Plasma Physics*, p. 482, McGraw-Hill, New York, 1973.
- Penrose, O., Electrostatic instability of a uniform non-Maxwellian plasma, *Phys. Fluids*, **3**, 258, 1960.
- Perkins, F., Heat conduction, plasma instabilities, and radio star scintillations in the solar wind, *Astrophys. J.*, **179**, 637, 1973.
- Scarf, F. L., R. W. Fredricks, L. A. Frank, C. T. Russell, P. J. Coleman, Jr., and M. Neugebauer, Direct correlations of large-amplitude waves with suprathermal protons in the upstream solar wind, *J. Geophys. Res.*, **75**, 7316, 1970.
- Schulz, M., and A. Eviatar, Electron-temperature asymmetry and the structure of the solar wind, *Cosmic Electrodynamics*, **2**, 402, 1972.
- Stix, T. H., *The Theory of Plasma Waves*, p. 215, McGraw-Hill, New York, 1962.
- Stringer, T. E., Electrostatic instabilities in current-carrying and counterstreaming plasmas, *Plasma Phys.*, **6**, 267, 1964.

(Received April 4, 1977;
accepted August 1, 1977.)

Electromagnetic Plasma Wave Emissions from the Auroral Field Lines

Donald A. GURNETT

*Department of Physics and Astronomy, The University of Iowa,
Iowa City, Iowa, U.S.A.*

(Received October 17, 1977)

Several types of electromagnetic waves are known to be emitted by charged particles on the auroral field lines. In this paper we review the most important types of auroral radio emissions both from a historical perspective as well as considering the latest results. Particular emphasis is placed on four types of electromagnetic emissions which are directly associated with the plasma on the auroral field lines. These emissions are (1) auroral hiss, (2) saucers, (3) ELF noise bands, and (4) auroral kilometric radiation. Ray tracing and radio direction finding measurements indicate that both the auroral hiss and auroral kilometric radiation are generated along the auroral field lines relatively close to the earth, at radial distances from about 2.5 to 5 R_E , probably in direct association with the acceleration of auroral particles by parallel electric fields. The exact mechanism by which these radio emissions are generated has not been firmly established. For the auroral hiss the favored mechanism appears to be amplified Cerenkov radiation. For the auroral kilometric radiation several mechanisms have been proposed, usually involving the intermediate generation of electrostatic waves by the precipitating electrons.

1. Introduction

For many years it has been known that certain types of electromagnetic emissions from the earth's magnetosphere are closely associated with the occurrence of auroras. As early as 1933, BURTON and BOARDMAN (1933) reported observations of bursts of very-low-frequency (VLF) 'static' which were closely correlated with flashes of auroral light. Later investigations using ground based VLF radio receivers firmly established that auroral disturbances at high latitudes are often accompanied by intense bursts of broad-band radio noise at frequencies from a few hundred Hz to over 100 kHz (ELLIS, 1957; DUNCAN and ELLIS, 1959; DOWDEN, 1959; MARTIN *et al.*, 1960; JORGENSEN and UNGSTRUP, 1962; MOROZUMI, 1963; HARANG and LARSEN, 1964). Because of the close association of these radio emissions with aurora and their broad bandwidth these emissions came to be known as auroral hiss, following the classification scheme of HELLWELL (1965). The first satellite observations of auroral hiss were reported by GURNETT (1966) who showed that auroral hiss is closely correlated with intense fluxes of precipitating electrons with energies less than 10 keV. Subsequent studies have firmly established that auroral hiss is generated along the auroral field lines by intense fluxes of electrons precipitating into the ionosphere with

energies in the range from a few hundred eV to several keV (HARTZ, 1970; GURNETT and FRANK, 1972a; HOFFMAN and LAASPERE, 1972). Since the auroral hiss emissions occur at frequencies below the local electron gyrofrequency these waves must be propagating in the whistler mode. Simple ray tracing considerations show that the auroral hiss appears to be propagating downward from a source at an altitude of about 5,000 to 10,000 km. Poynting flux measurements by MOSIER and GURNETT (1969) showed that another type of emission, called a saucer, also occurs on the auroral field lines, propagating upward from a source at altitudes of approximately 1,400 km. These VLF saucer emissions have been studied in greater detail by JAMES (1976). Other electromagnetic emissions have been observed along the auroral field lines at even lower frequencies, from 100 to 300 Hz, by GURNETT and FRANK (1972b). These emissions, which are called ELF noise bands, have a very narrow bandwidth and are also closely associated with the auroral electron precipitation.

Since the auroral hiss, saucers, and ELF noise bands consist of internally trapped plasma wave modes these emissions cannot escape from the earth's magnetosphere. At higher frequencies, above the local characteristic frequencies of the plasma, radio emissions of auroral origin have been observed escaping from the earth. Since the ionosphere effectively blocks all radiation at frequencies below the local electron plasma frequency from reaching the earth's surface, escaping electromagnetic emissions of this type can only be observed by a satellite above the ionosphere. The first evidence of intense auroral-related radio emissions escaping from the earth's magnetosphere was obtained from the Elektron 2 and 4 satellites by BENEDIKTOV *et al.* (1965, 1968). These observations showed that bursts of radio noise at 725 kHz and 2.3 MHz were originating from the earth in close association with geomagnetic storms. Later DUNCKEL *et al.* (1970) reported similar bursts of radio noise, also associated with high-latitude magnetic disturbances, at frequencies below 100 kHz. The first complete determination of the spectrum of these radio emissions was provided by the IMP-6 spacecraft which showed that the maximum intensities are in the frequency range from about 100 to 500 kHz (STONE, 1973; BROWN, 1973) and that the total power radiated from the earth is sometimes as large as 10^9 watts (GURNETT, 1974), comparable to the decametric (3.0 to 30 MHz) radio emission from Jupiter. It was also determined that the intense radio bursts from the earth are directly associated with the occurrence of discrete auroral arcs and that the angular distribution of the escaping radiation is consistent with generation along the auroral field lines on the night side of the earth. Because of the close association of these radio emissions with auroral processes and the kilometer wavelength of the radiation, KURTH *et al.* (1975) have referred to this radiation as auroral kilometric radiation, which is the terminology that will be used in this paper. Other names for this radiation include 'high pass noise' (DUNCKEL *et al.*, 1970), 'mid-frequency noise' (BROWN, 1973), and 'terrestrial kilometric radiation' (GURNETT, 1974; ALEXANDER and KAISER, 1976).

These four types of electromagnetic emissions (auroral hiss, saucers, ELF noise bands, and auroral kilometric radiation) constitute all of the known electromagnetic plasma wave emissions from the auroral field lines. The purpose of this paper is to

review the
and to di

review the present state of knowledge of these electromagnetic plasma wave emissions and to discuss the mechanisms by which these waves are thought to be generated.

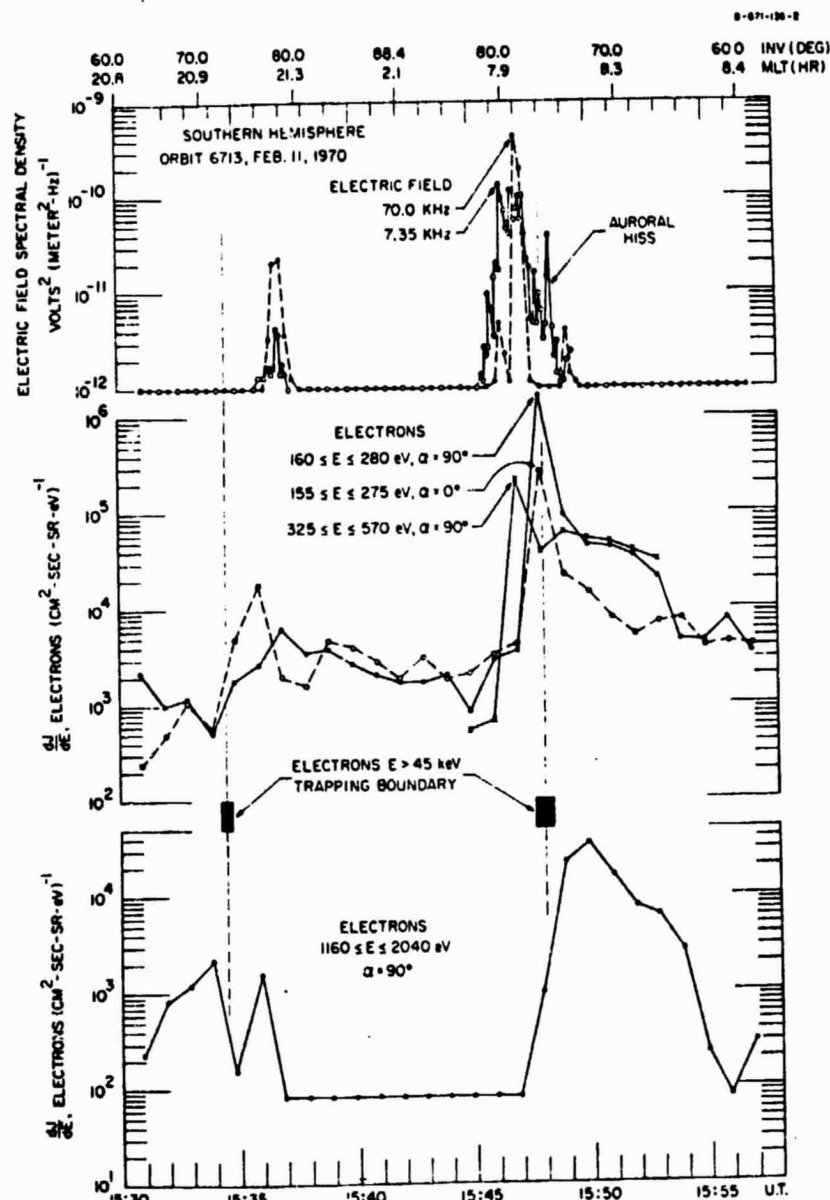


Fig. 1. An example of an intense broad-band auroral hiss emission associated with intense fluxes of low energy, a few hundred eV, auroral electrons. The auroral hiss is indicated by the enhanced 7.35 and 70.0 kHz electric field intensities from about 1546 to 1549 UT, slightly poleward of the $E > 45 \text{ keV}$ electron trapping boundary.

ORIGINAL PAGE IS
OF POOR QUALITY

2. Auroral Hiss, Saucers and ELF Noise Bands

A typical example of an auroral hiss event detected by a low-altitude polar-orbiting satellite is shown in Fig. 1. This event illustrates the primary identifying characteristics of auroral hiss, consisting of (1) the very broad frequency range of the emission, usually from a few kHz to several tens of kHz, (2) the large electric field intensities, often exceeding 1 mV m^{-1} broad band electric field strength, (3) the occurrence in a narrow latitudinal band centered on the auroral zone, typically only 5 to 10° wide, and (4) the close association with intense fluxes of low energy, 100 eV to 1 keV , electrons. The spatial distribution of the auroral hiss over the polar region is illustrated in Fig. 2 (from HUGHES *et al.*, 1971), which shows the frequency of occurrence of VLF magnetic field intensities greater than $10^{-12} \text{ gamma}^2 \text{ Hz}^{-1}$ at 9.6 kHz . The maximum occurrence of auroral hiss closely follows the auroral oval, varying from about 80° invariant latitude on the day side of the earth to about 72° invariant latitude on the night side of the earth. A pronounced dawn-dusk asymmetry is clearly evident, with a distinct minimum in the auroral hiss occurrence in the local morning from about 2 to 8 hr magnetic local time. This dawn-dusk asymmetry is probably related to the dawn-dusk asymmetry in the spectrum and intensity of the precipitating auroral electrons, in particular to the low intensity and diffuse character of inverted-V electron precipitation events in the local morning (FRANK and ACKERSON, 1972). The relationship of the auroral hiss emission to the spectrum of the auroral electron precipitation is illustrated in further detail by the event in Fig. 3 (from GURNETT and FRANK, 1972a), which shows that the auroral hiss emission

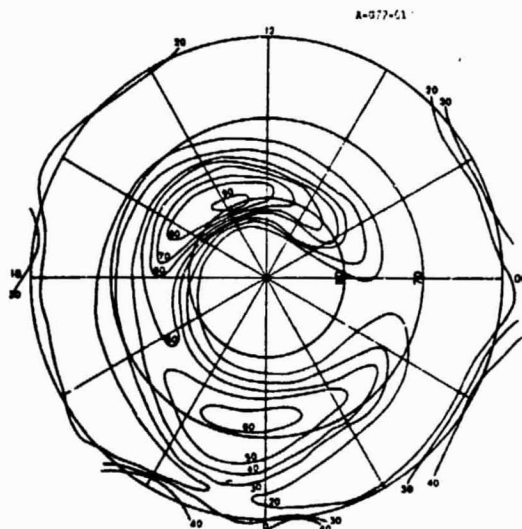


Fig. 2. The frequency of occurrence distribution of auroral hiss at 9.6 kHz as a function of invariant latitude and magnetic local time. Only events with magnetic field intensities greater than $10^{-12} \text{ gamma}^2 \text{ Hz}^{-1}$ are counted (from HUGHES *et al.*, 1971).

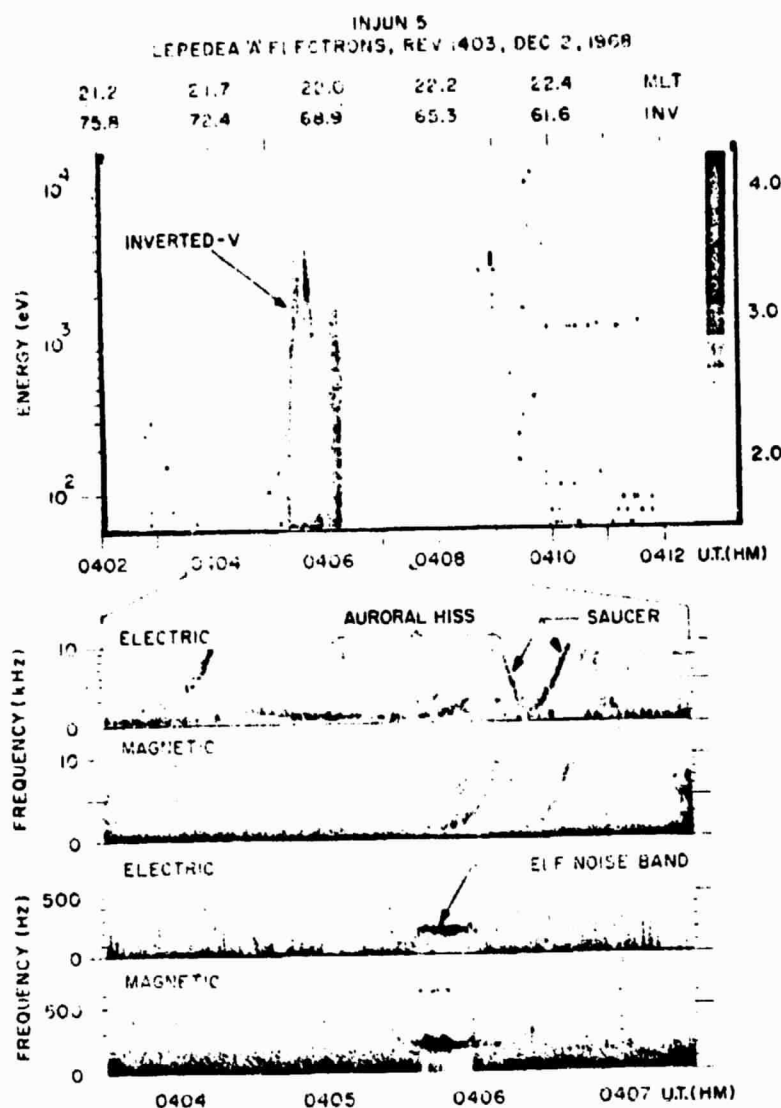


Fig. 3. High resolution frequency-time spectrograms of electric and magnetic fields detected by the Injun 5 spacecraft at an altitude of about 2,500 km showing the occurrence of auroral hiss, saucer emissions and an ELF noise band in close association with an inverted-V electron precipitation event (from GURNETT and FRANK, 1972a).

occurs in direct association with an intense inverted-V electron precipitation event of the type first discussed by FRANK and ACKERSON (1971). A VLF saucer emission is also evident near the low-latitude boundary of the electron precipitation region. Both the auroral hiss and the saucer emissions are characterized by a V-shaped

ORIGINAL PAGE IS
OF POOR QUALITY

frequency-time structure. This characteristic frequency-time variation is a spatial effect caused by the frequency-dependent limiting ray direction of the whistler mode at large wave normal angles (MOSIER and GURNETT, 1969). Essentially the source illuminates a region along the magnetic field with a beam-width which increases with increasing frequency. As the spacecraft approaches the auroral field lines the highest frequencies are encountered first, since these rays can propagate at the largest angle to the magnetic field. The essential distinction between the auroral hiss and the saucer emissions is the direction of propagation, which is downward for the auroral hiss and upward for the saucers. Although the particles responsible for the downward propagating auroral hiss have been identified as inverted-V electrons, the particles responsible for the saucer emissions have not yet been established. It seems most likely that the upward propagating saucer emissions are produced by upward streaming ionospheric electrons of very low energy, \sim few eV, which constitute the return current for the nearby inverted-V electron precipitation. This relationship is illustrated schematically in Fig. 4. For observing altitudes in the range from about 1,500 to 3,000 km the latitudinal width of the saucer emissions, 10 to 100 km, is usually somewhat smaller than the width of the auroral hiss, 100 to 500 km. The saucers also have very sharp spectral structure, indicating a very small source region, whereas the auroral hiss is much more diffuse, indicating a broader more extended source.

The event in Fig. 3 also illustrates the occurrence of ELF noise bands in the same region as the inverted-V electron precipitation and the auroral hiss. The electromagnetic character of these narrow band emissions is clearly indicated by their detection with both the electric and magnetic antennas. Poynting flux measurements indicate the presence of both upgoing and downgoing components. These emissions occur near but below the local proton gyrofrequency. Since the polarization of these waves has never been measured it is not known whether these emissions are propagating in the whistler mode or the ion cyclotron mode.

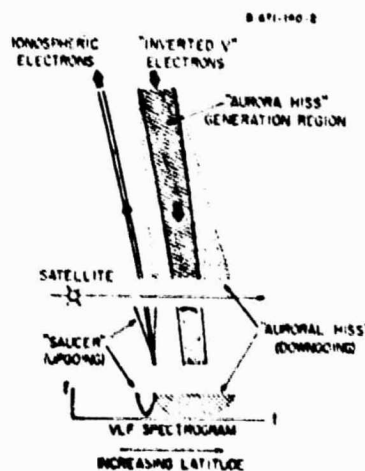


Fig. 4. A schematic illustration showing the spatial relationships between the downward propagating auroral hiss and the upward propagating saucer emissions for events such as in Fig. 3. The association of the saucer emissions with upward streaming ionospheric electrons has not yet been confirmed.

3. Auroral hiss

The auroral hiss is a broadband emission at frequencies between 1 and 10 MHz. It is intense in the auroral region and is closely related to the quiet time background. The power of the auroral hiss is of the order of 10³ to 10⁴ W m⁻² at 178 kHz.

(1) MEDIAN FLUX DENSITY AT 25 MHz (W m⁻² Hz⁻¹)

3. Auroral Kilometric Radiation

The intense radio emissions escaping outward from the earth's auroral regions at frequencies above the local electron plasma frequency are characterized by a very intense peak in the frequency spectrum from about 100 to 500 kHz. Figure 5 shows the median power flux spectrums of this radiation at various local times around the earth, as measured from the IMP-6 spacecraft at radial distances greater than $25 R_E$ (KAISER and ALEXANDER, 1977). The intensity of this noise is highly variable and is closely correlated with the auroral electrojet index, AE . During geomagnetically quiet times the radiation intensity at $25 R_E$ is often completely below the galactic background, whereas at other times the intensity can be as much as six to eight orders of magnitude above the galactic background. Power fluxes as large as 10^{-14} watts $m^{-2} Hz^{-1}$ have been observed at $30 R_E$, with even larger intensities closer to the earth (GURNETT, 1974). The occurrence of intense bursts of kilometric radiation is closely associated with the occurrence of auroral arcs. This association is illustrated in Fig. 6, which shows the occurrence of intense bursts of kilometric radiation at 178 kHz during periods (passes 1094 and 1096) when discrete auroral arcs are present

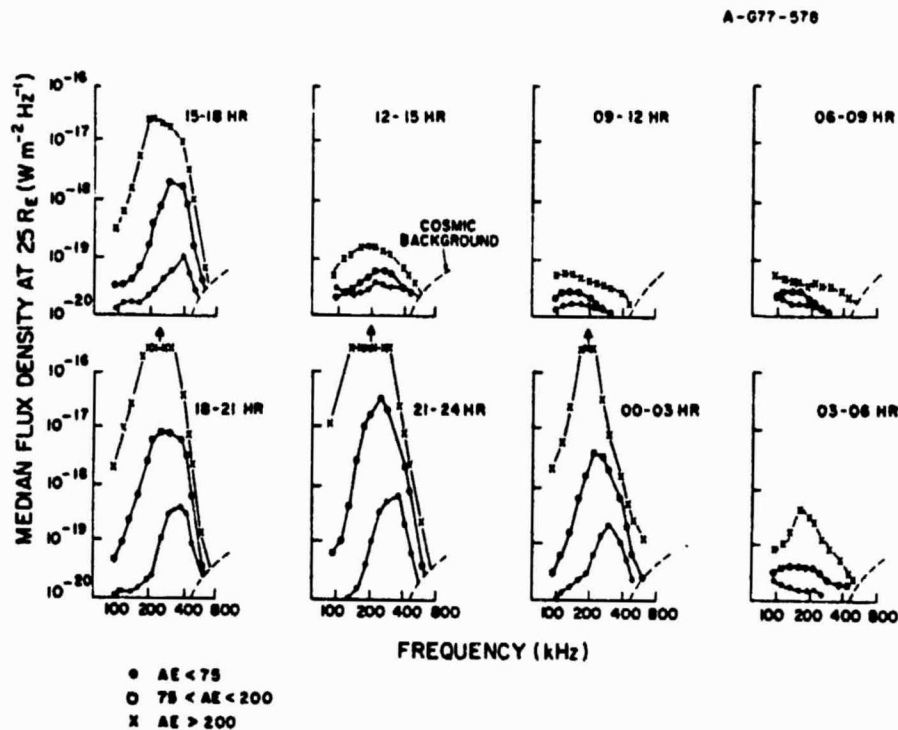


Fig. 5. Median spectrums of auroral kilometric radiation observed at various local times around the earth by the IMP-6 spacecraft at radial distances $R > 25 R_E$. The three spectrums in each plot are for various ranges of the auroral electrojet, AE , index. The kilometric radio emissions from the earth are closely correlated with auroral zone currents as indicated by the AE index (from KAISER and ALEXANDER, 1977).

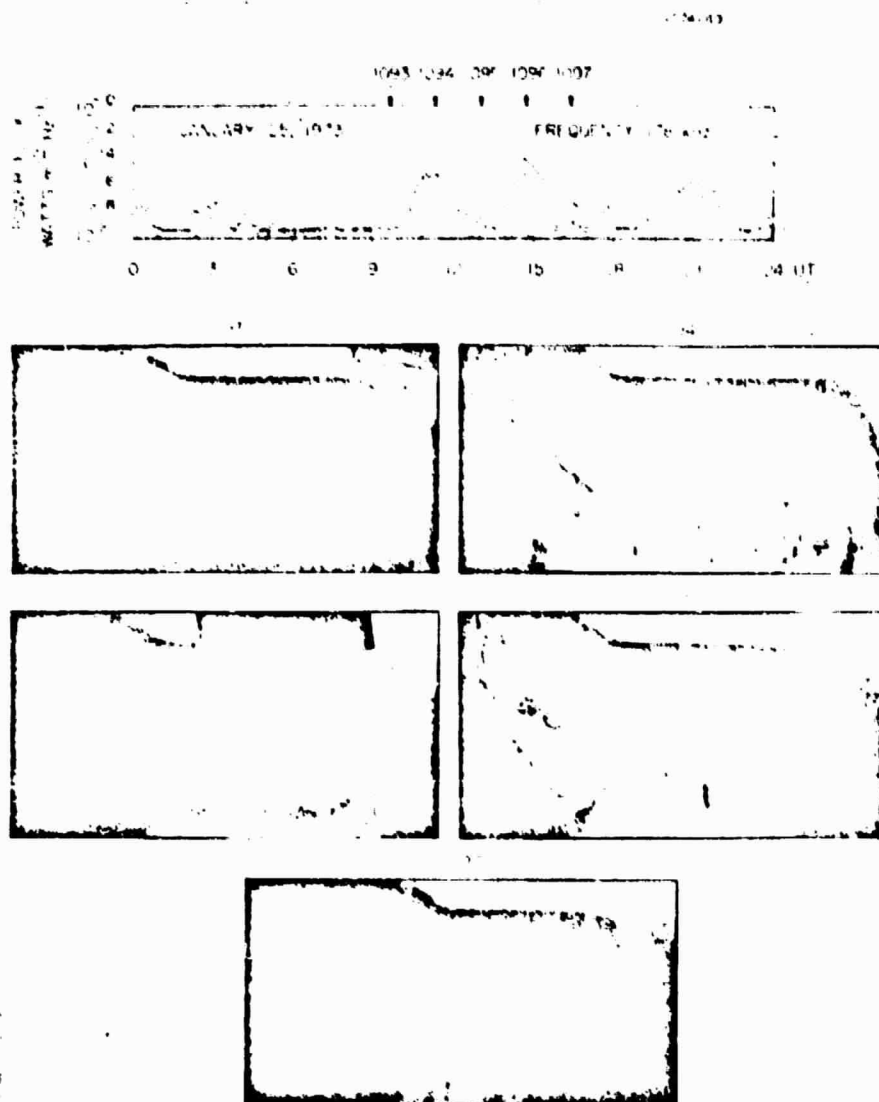


Fig. 6. The intensity of auroral kilometric radiation at 178 kHz observed about 30 R_E from the earth and a sequence of photographs of the aurora taken by a low-altitude satellite over the northern polar region. The intense bursts of auroral kilometric radiation are seen to be closely correlated with the occurrence of discrete auroral arcs.

and no radiation during periods (passes 1093, 1095 and 1097) when no discrete arcs are present. The association with discrete arcs provides substantial evidence that the generation of auroral kilometric radiation is closely associated with inverted-V events, since the inverted-V electron precipitation is associated with discrete arcs. Both direction finding measurements (KURTH *et al.*, 1975; KAISER and STONE, 1975) and lunar occultation measurements (ALEXANDER and KAISER, 1976) show that the

most intense bursts of kilometric radiation come from the auroral field lines on the night side of the earth at radial distances ranging from 2 to 5 R_E . These results are illustrated in Fig. 7, which shows a series of source positions obtained by occultation measurements from the RAE-2 spacecraft in orbit around the moon. The moon in this case was in the dusk meridian plane (magnetic local time ~ 17.5 hr) so that the day-night position of the source can be resolved. The occultation measurements at 1255, 1635 and 2020 UT indicate the occurrence of multiple sources located at various points along a magnetic field line at about 70 to 75° invariant latitude. Occasionally day-side sources are also observed (ALEXANDER and KAISER, 1976, 1977), apparently associated with the day-side polar cusp region. The day-side sources occur less frequently and are less intense than the night-side sources. Angular distribution measurements by GREEN *et al.* (1977) are also consistent with a night-side, high-latitude source for the intense auroral kilometric radiation. A typical angular distribution is illustrated in Fig. 8, which shows the frequency of occurrence of auroral kilometric radiation intensities above a preset threshold at 178 kHz as a function of the magnetic latitude and magnetic local time of the observing point. A sharp low-latitude boundary is evident, varying from about 45° on the day side of the earth to near the equator on the night side of the earth. At large distances from the earth this cutoff forms a cone-shaped boundary, with the axis of the cone tipped toward local evening (~ 22 hr, magnetic local time) by about 20° . The radiation is confined

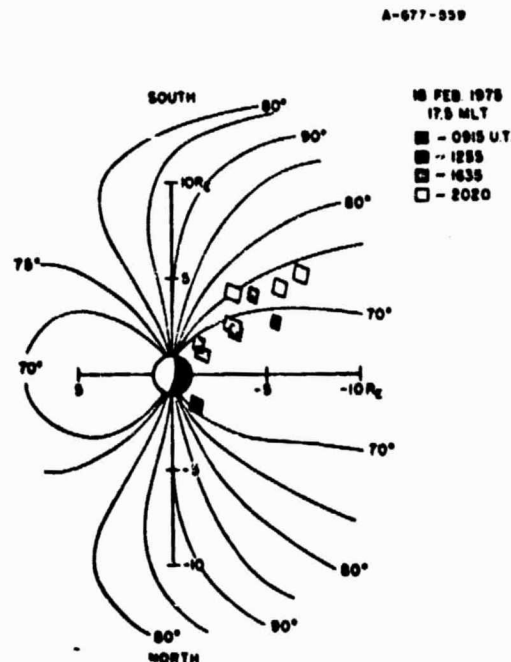


Fig. 7. Source positions for auroral kilometric radiation as determined by lunar occultation measurements with the RAE 2 spacecraft in orbit around the moon (from ALEXANDER and KAISER, 1976).

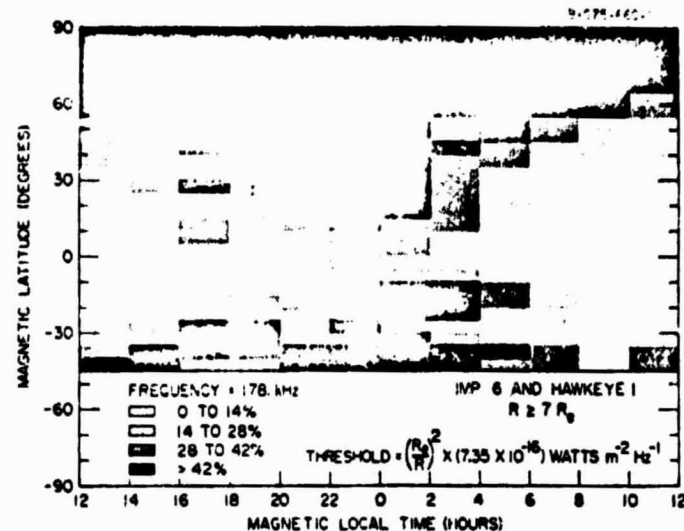


Fig. 8. The angular distribution of auroral kilometric radiation with intensities above a given threshold as a function of magnetic latitude and magnetic local time.

almost entirely to the poleward side of this boundary. Symmetrical cone-shaped boundaries are present in the northern and southern hemispheres, evidently corresponding to sources in the northern and southern auroral regions, respectively. Detailed studies have shown that these cone-shaped boundaries are strongly frequency dependent, with the solid angle of the emission region increasing with increasing frequency. Multiple satellite studies have also shown that the entire region poleward of the cone-shaped boundary is illuminated with comparable radiation intensities.

Ray tracing studies show that the general features of the angular distribution of the auroral kilometric radiation can be explained by relatively simple propagation considerations if the radiation is generated by a small localized source at about 2 to 3 R_E along an auroral field line on the night side of the earth. Some typical ray tracing results are illustrated in Fig. 9, which shows the distribution of ray paths at various frequencies for a representative model of the polar ionosphere. Because the index of refraction decreases with decreasing altitude the general effect is for the ray paths to be refracted upward away from the ionosphere, thus producing a low-latitude cutoff in the region accessible to the radiation. Detailed calculations of the distribution of intensity within the accessible region cannot be performed without a more detailed understanding of the generation mechanism. However, the overall features of the angular distribution can be understood from propagation considerations of this type. At the present time the polarization of the auroral kilometric radiation has not been directly measured. Several indirect methods indicate that the polarization is right hand with respect to the magnetic field in the generation region. For example, comparison of ray paths for the right and left hand modes of propagation, as in Fig. 9, with observed angular distributions, as in Fig. 10, give the best fit and

ORIGINAL PAGE IS
OF POOR QUALITY

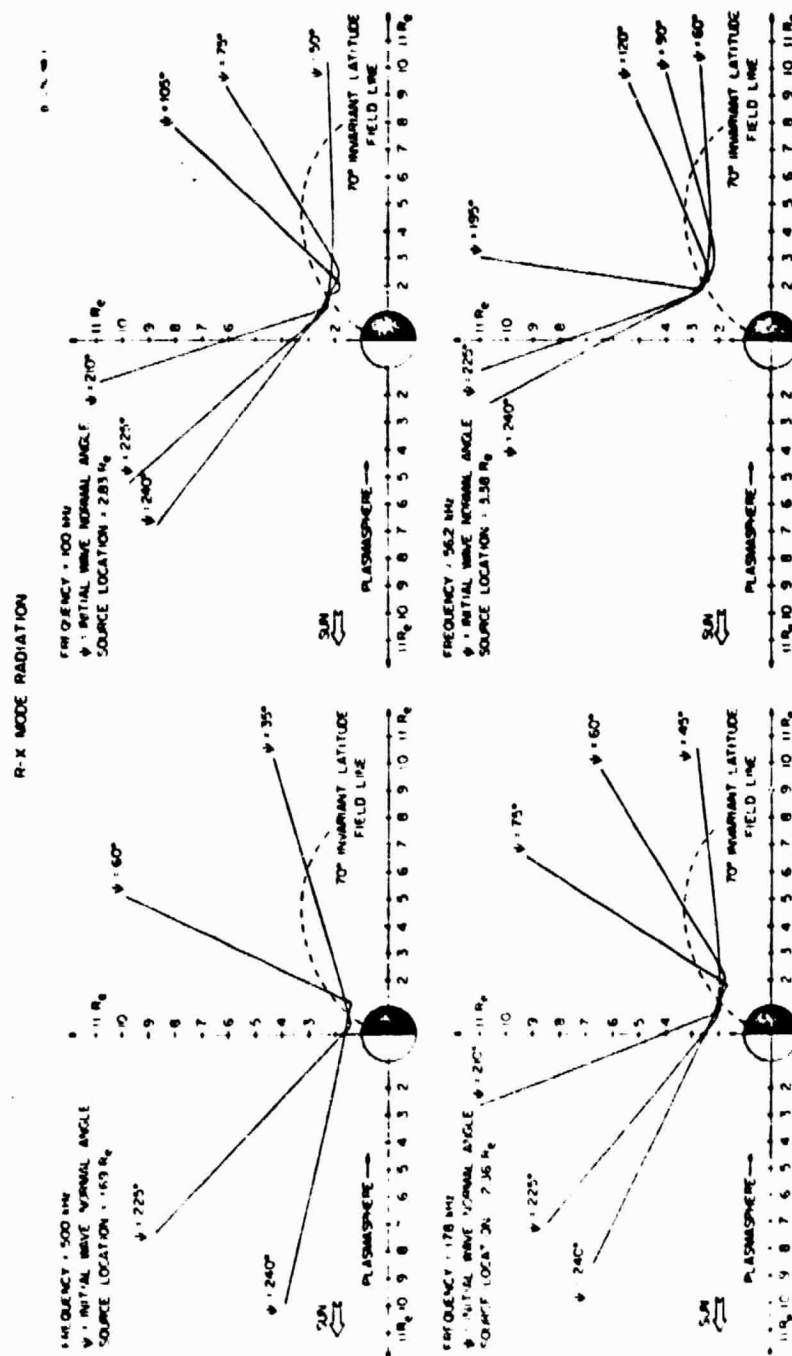


Fig. 9. Ray paths computed for various initial wave normal angles for a point source located at various points along an auroral field line at 70° invariant latitude. The cone shaped latitudinal cutoff evident in Fig. 8 is the result of refraction of the radiation upward away from the ionosphere in the region near the source (from GREEN *et al.*, 1977).

C-674-992-1

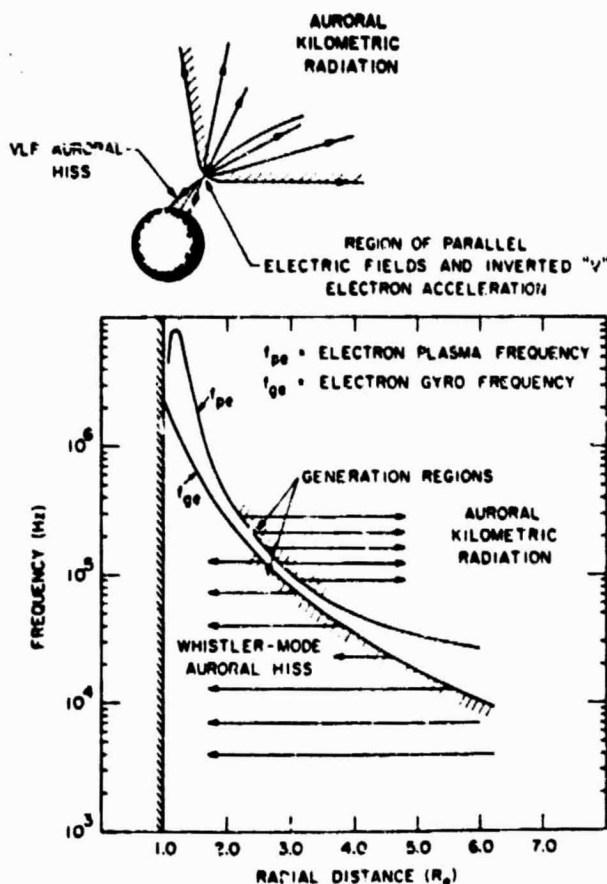


Fig. 10. Both the auroral hiss and auroral kilometric radiation appear to originate from a common region at about 2.0 to 5.0 R_E along the auroral field line. This region is believed to correspond to the region of parallel electric fields responsible for the auroral electron acceleration.

consistency if the radiation is right-hand polarized. Furthermore, recent observations by GURNETT and GREEN (1978) of a cutoff in the spectrum of the auroral kilometric radiation at the local electron gyrofrequency are consistent with the expected propagation cutoff of the right-hand polarized extraordinary (R-X) mode. Right-hand polarization is also consistent with the polarization of the decametric radiation from Jupiter (WARWICK, 1967), which is thought to be fundamentally similar to the terrestrial kilometric radiation.

4. Generation Mechanisms

When comparing these various auroral electromagnetic emissions one cannot help but be impressed by the close similarity of the spatial regions within which the

auroral hiss and the auroral kilometric radiation are generated. In both cases the radiation is believed to be generated in a relatively small region along the auroral field lines at about $3.0 R_E$ radial distance. Evidence that the source region is relatively small and localized is provided by the distinct V-shaped spectral features often observed in the auroral hiss and by the small angular size of the auroral kilometric radiation source obtained from the direction finding and lunar occultation measurements. Although no evidence exists showing that these two types of radiation originate from exactly the same region the evidence does strongly suggest that the two source regions overlap to a substantial extent. Since both the auroral hiss and the auroral kilometric radiation are closely associated with the inverted-V electron precipitation it seems most likely that the generation of these radio emissions is closely related to the acceleration of these electrons. Substantial evidence now exists (HAERENDEL *et al.*, 1976; MOZER *et al.*, 1977) showing that precipitating auroral electrons are accelerated by parallel electric fields at altitudes ranging from 5,000 to 15,000 km, in the same general region where these radio emissions are produced.

Although both the auroral hiss and the auroral kilometric radiation appear to originate from a common spatial region, distinctly different mechanisms are required to explain these two types of radiation since they are propagating in different plasma wave modes. As shown in Fig. 10, the whistler-mode auroral hiss must be generated at frequencies below the local electron gyrofrequency, whereas the auroral kilometric radiation must be generated at frequencies above the local electron plasma frequency. For many years it has been suggested that auroral hiss is produced by incoherent Cerenkov radiation from the precipitating auroral electrons (ELLIS, 1957; JORGENSEN, 1968; LIM and LAASPERE, 1972; TAYLOR and SHAWHAN, 1974). Although the Cerenkov mechanism has many desirable features, it is generally concluded that this mechanism produces power fluxes which are several orders of magnitude too low to explain the observed auroral hiss intensities. At the present time the best possibility for explaining the observed auroral hiss intensities appears to be the mechanism proposed by MAGGS (1976), in which incoherent Cerenkov radiation generated by the precipitating electron beam is amplified to higher intensities by a whistler-mode instability. Similar mechanisms also appear to be responsible for the generation of saucer emissions (JAMES, 1976), although the details have not been investigated as thoroughly as for the auroral hiss. Cerenkov radiation has also been considered as a mechanism for generating the auroral kilometric radiation and again the computed power fluxes are much too small. Rough estimates indicate that an overall efficiency of 0.1 to 1% is required for the generation of this radiation. Such high conversion efficiencies can only be produced by a coherent plasma instability. Instability mechanisms which have been proposed include the generation of escaping electromagnetic radiation by interactions between electrostatic waves at the upper hybrid resonance (BENSON, 1975; BARBOSA, 1976), by interactions of the precipitating electron beam with ion turbulence (PACIADESSO *et al.*, 1976), by electrostatic waves produced by energetic ions streaming outward from the auroral regions (BOSWELL, 1977), and by direct conversion via coherent electron cyclotron emission from the

precipitating electrons (MELROSE, 1976). At the present time, no consensus exists about which, if any, of these mechanisms can account for the intense kilometric radiation from the earth's auroral regions.

5. Conclusions

It is evident that the auroral particle distributions produce a variety of complex and very interesting electromagnetic emissions. At the present time the mechanisms by which these electromagnetic emissions are generated are rather poorly understood and the full explanation of these radio emission processes represents a significant challenge to both the theorists and the experimentalists. It should, however, be possible to arrive at a reasonably clear understanding of how these radio emissions are generated since a great deal is already known about the charged particle distributions and processes which occur along the auroral field lines and our understanding of these processes is advancing rapidly. Because a comparable detailed knowledge of the charged particle distribution will probably never be known for most other radio sources in the universe, the study of these terrestrial radio emissions provides a unique opportunity to extend our understanding of similar electromagnetic plasma wave emissions from other planets and astronomical objects.

This research was supported in part by the National Aeronautics and Space Administration under Contracts NAS1-11257, NAS1-13129 and NAS5-11431 and Grants NGL-16-001-002 and NGL-16-001-043.

REFERENCES

- ALEXANDER, J.K. and M.L. KAISER, Terrestrial kilometric radiation. 1. Spatial structure studies, *J. Geophys. Res.*, **81**, 5948-5956, 1976.
- ALEXANDER, J.K. and M.L. KAISER, Terrestrial kilometric radiation. 2. Emission from the magnetospheric cusp and dayside magnetosheath, *J. Geophys. Res.*, **82**, 98-104, 1977.
- BARBOSA, D.D., Electrostatic mode coupling at $2\omega_{UH}$: A generation mechanism for auroral kilometric radiation, Ph. D. dissertation, Dept. of Phys., Univ. of Calif., Los Angeles, 1976.
- BENEDIKTOV, E.A., G.G. GETMANTSEV, YU.A. SAZONOV, and A.F. TARASOV, Preliminary results of measurements of the intensity of distributed extraterrestrial radio-frequency emission at 725 and 1525-kHz frequencies by the satellite electron-2, *Kosm. Issled.*, **3**, 614-617, 1965.
- BENEDIKTOV, E.A., G.G. GETMANTSEV, N.A. MITYAKOV, V.O. RAPOPORT, and A.F. TARASOV, Relation between geomagnetic activity and the sporadic radio emission recorded by the elektron satellites, *Kosm. Issled.*, **6**, 946-949, 1968.
- BENSON, R.F., Source mechanism for terrestrial kilometric radiation, *Geophys. Res. Lett.*, **2**, 52-55, 1975.
- BOEWELL, R.W., Energetic ions and electromagnetic radiation in auroral regions, preprint, Max-Planck-Institut für Extraterrestrische Physik, Garching, Germany, 1977.
- BROWN, L.W., The galactic radio spectrum between 130 kHz and 2,600 kHz, *Astrophys. J.*, **180**, 359-370, 1973.
- BURTON, E.T. and E.M. BOARDMAN, Audio-frequency atmospherics, *Proc. IRE*, **21**, 1476-1494, 1933.
- DOWDEN, R.L., Low frequency (100 kc/s) radio noise from the aurora, *Nature*, **184**, 803, 1959.
- LYNCH, R.A. and G.R. ELLIS, Simultaneous occurrence of subvisual aurorae and radio noise bursts on 4.6 kc/s, *Nature*, **183**, 1618-1619, 1959.

- DUNCKEL, N., B. FICKLIN, L. RORDEN, and R.A. HELLIWELL, Low frequency noise observed in the distant magnetosphere with OGO 1, *J. Geophys. Res.*, **75**, 1854-1862, 1970.
- ELLIS, G. R., Low-frequency radio emission auroral, *J. Atmos. Terr. Phys.*, **10**, 302-306, 1957.
- FRANK, L.A. and K.L. ACKERSON, Observations of charged-particle precipitation into the auroral zone, *J. Geophys. Res.*, **76**, 3612-3643, 1971.
- FRANK, L.A. and K.L. ACKERSON, Local-time survey of plasma at low altitudes over the auroral zones, *J. Geophys. Res.*, **77**, 4116-4127, 1972.
- GREEN, J.L., D.A. GURNETT, and S.D. SHAWHAN, The angular distribution of auroral kilometric radiation, *J. Geophys. Res.*, **82**, 1825-1838, 1977.
- GURNETT, D.A., A satellite study of VLF hiss, *J. Geophys. Res.*, **71**, 5599-5615, 1966.
- GURNETT, D.A. and L.A. FRANK, VLF hiss and related plasma observations in the polar magnetosphere, *J. Geophys. Res.*, **77**, 172-190, 1972a.
- GURNETT, D.A. and L.A. FRANK, ELF noise bands associated with auroral electron precipitation, *J. Geophys. Res.*, **77**, 3411-3417, 1972b.
- GURNETT, D.A., The earth as a radio source: Terrestrial kilometric radiation, *J. Geophys. Res.*, **79**, 4227-4238, 1974.
- GURNETT, D.A. and J.L. GREEN, On the polarization and origin of auroral kilometric radiation, *J. Geophys. Res.*, **83**, 689-696, 1978.
- HAERENDEL, G., E. RIEGER, A. VALENZUELA, H. FÖPPL, H.C. STENBAEK-NIELSEN, and E.M. WESCOTT, First observation of electrostatic acceleration of barium ions into the magnetosphere, in *European Programmes on Sounding-Rocket and Balloon Research in the Auroral Zone*, European Space Agency Report ESA-SP115, pp. 203-211, August 1976.
- HARANG, L. and R. LARSEN, Radio wave emissions in the VLF band observed near the auroral zone. 1. Occurrence of emissions during disturbances, *J. Atmos. Terr. Phys.*, **27**, 481-497, 1964.
- HARTZ, T.R., Low frequency noise emissions and their significance for energetic particle processes in the polar ionosphere, in *The Polar Ionosphere and Magnetospheric Processes*, edited by G. Skovli, pp. 151-160, Gordon and Breach, New York, 1970.
- HELLIWELL, R.A., *Whistlers and Related Ionospheric Phenomena*, p. 207, Stanford University Press, Stanford, California, 1965.
- HOFFMAN, R.A. and T. LAASPERE, Comparison of very-low-frequency auroral hiss with precipitating low-energy electrons by the use of simultaneous data from two OGO 4 experiments, *J. Geophys. Res.*, **77**, 640-650, 1972.
- HUGHES, A.R.W., T.R. KAISER, and K. BULLOUGH, The frequency of occurrence of VLF radio emissions at high latitudes, in *Space Research*, Vol. XI, Akademie-Verlag, Berlin, 1323-1330, 1971.
- JAMES, H.G., VLF saucers, *J. Geophys. Res.*, **81**, 501-514, 1976.
- JØRGENSEN, T.S. and E. UNGSTRUP, Direct observation of correlation between aurorae and hiss in Greenland, *Nature*, **194**, 462-463, 1962.
- JØRGENSEN, T.S., Interpretation of auroral hiss measured on OGO 2 and at Byrd Station in terms of incoherent Cerenkov radiation, *J. Geophys. Res.*, **73**, 1055-1069, 1968.
- KAISER, M.L. and R.G. STONE, Earth as an intense planetary radio source: Similarities to Jupiter and Saturn, *Science*, **189**, 285-289, 1975.
- KAISER, M.L. and J.K. ALEXANDER, Terrestrial kilometric radiation: 3. Average spectral properties, *J. Geophys. Res.*, **82**, 3273-3280, 1977.
- KURTH, W.S., M.M. BAUMBACK, and D.A. GURNETT, Direction-finding measurements of auroral kilometric radiation, *J. Geophys. Res.*, **80**, 2764-2770, 1975.
- LIM, T.L. and T. LAASPERE, An evaluation of the intensity of Cerenkov radiation from auroral electrons with energies down to 100 eV, *J. Geophys. Res.*, **77**, 4145-4157, 1972.
- MAGGS, J.E., Coherent generation of VLF hiss, *J. Geophys. Res.*, **81**, 1707-1724, 1976.
- MARTIN, L.H., R.A. HELLIWELL, and K.R. MARKS, Association between aurorae and very-low-frequency hiss observed at Byrd Station, Antarctica, *Nature*, **187**, 751-753, 1960.
- MELROSE, D.B., An interpretation of Jupiter's decametric radiation and terrestrial kilometric radiation as direct amplified gyroemission, *Astrophys. J.*, **207**, 651-662, 1976.

- MOROZUMI, H.M., Semi-diurnal auroral peak and VLF emissions observed at the south pole, 1960, *Trans. Am. Geophys. Union*, **44**, 798-806, 1963.
- MOSIER, S.R. and D.A. GURNETT, VLF measurements of the Poynting flux along the geomagnetic field with the Injun 3 satellite, *J. Geophys. Res.*, **74**, 5675-5687, 1969.
- MOZER, F.S., C.W. CARLSON, M.K. HUDSON, R.B. TORBERT, B. PARADY, J. YATTEAU, and M.C. KELLEY, Observations of paired electrostatic shocks in the polar magnetosphere, *Phys. Rev. Lett.*, **38**, 292-295, 1977.
- PALMADESSO, P., T.P. COFFEY, S.L. OSSAKOW, and K. PAPADOPOULOS, Generation of terrestrial kilometric radiation by a beam-driven electromagnetic instability, *J. Geophys. Res.*, **81**, 1762-1770, 1976.
- STONE, R.G., Radio physics of the outer solar system, *Space Sci. Rev.*, **14**, 534-551, 1973.
- TAYLOR, W.W.L. and S.D. SHAWHAN, A test of incoherent Cerenkov radiation for VLF hiss and other magnetospheric emissions, *J. Geophys. Res.*, **79**, 105-117, 1974.
- WARWICK, J.W., Radiophysics of Jupiter, *Space Sci. Rev.*, **6**, 841-891, 1967.

The Heliocentric Radial Variation of Plasma Oscillations Associated With Type III Radio Bursts

D. A. GURNETT, R. R. ANDERSON, F. L. SCARF,¹ AND W. S. KURTH

Department of Physics and Astronomy, University of Iowa, Iowa City, Iowa 52242

A survey is presented of all of the electron plasma oscillation events found to date in association with low-frequency type III solar radio bursts using approximately 9 years of observations from the Imp 6 and 8, Helios 1 and 2, and Voyager 1 and 2 spacecraft. Plasma oscillation events associated with type III radio bursts show a pronounced increase in both the intensity and the frequency of occurrence with decreasing heliocentric radial distance. This radial dependence explains why intense electron plasma oscillations are seldom observed in association with type III radio bursts at the orbit of the earth. Possible interpretations of the observed radial variation in the plasma oscillation intensity are considered.

1. INTRODUCTION

The currently accepted model for the generation of type III solar radio bursts is that these radio emissions are produced by nonlinear processes involving electron plasma oscillations excited by solar flare electrons streaming outward through the solar corona. The electron plasma oscillation mechanism, first proposed by *Ginzburg and Zheleznyakov* [1958], has become the basic element of essentially all theories of type III radio bursts, with suitable refinements to account for various types of nonlinear interactions [*Sturrock*, 1961; *Tidman et al.*, 1966; *Papadopoulos et al.*, 1974; *Smith*, 1974]. Although the plasma oscillation mechanism has been widely accepted for many years, only in the past two years have measurements been obtained which definitely establish the existence of these electron plasma oscillations. Initially, studies by earth-orbiting satellites failed to detect electron plasma oscillations in association with type III radio bursts [*Kellogg and Lin*, 1976]. After searching through nearly 4 years of data from the earth-orbiting Imp 6 and 8 satellites, only one type III event was identified with clearly associated electron plasma oscillations [*Gurnett and Frank*, 1975]. However, the intensity of this event, $\sim 100 \mu\text{V m}^{-1}$, was much too small to account for the observed radio emission intensities. The first observations of electron plasma oscillations with intensities sufficiently large to explain type III radio emissions were obtained from the Helios 1 and 2 solar probes, in orbit around the sun at radial distances ranging from 0.29 to 1.00 AU [*Gurnett and Anderson*, 1976, 1977]. In the initial survey of the Helios 1 and 2 plasma wave data, three events were found with electron plasma oscillation intensities exceeding 1 mV m^{-1} . All of these events occurred relatively close to the sun, at heliocentric radial distances of less than 0.45 AU.

Since the initial survey of the Helios 1 and 2 data the quantity of data available for analysis has increased considerably, and several more intense electron plasma oscillation events have been identified in association with type III radio bursts. Approximately 12 months of plasma wave data are also available from the Voyager 1 and 2 spacecraft at radial distances of from 1.0 to 2.2 AU. A description of the plasma wave instrumentation on the Voyager 1 and 2 spacecraft is given by *Scarf and Gurnett* [1977]. From these data it is found that the most intense electron plasma oscillations, $\sim 1\text{--}10 \text{ mV m}^{-1}$, are

usually detected relatively close to the sun, at heliocentric radial distances of less than 0.5 AU, and that only weak events, $\sim 100 \mu\text{V m}^{-1}$, are detected near and beyond 1.0 AU. These observations indicate the presence of a strong radial variation in the electron plasma oscillation intensities associated with type III radio bursts, decreasing rapidly with increasing radial distance from the sun. The purpose of this paper is to survey the characteristics of all of the electron plasma oscillation events observed to date in association with type III bursts and to investigate the variation in intensity of these events with radial distance from the sun.

2. SURVEY OF EVENTS ANALYZED

Up to the present time a total of 18 type III solar radio bursts have been detected with clearly associated electron plasma oscillations. The total quantity of data surveyed to identify these events consists of approximately 4 years of observations from Imp 6 and 8 [*Gurnett and Frank*, 1975], 4 years of observations from Helios 1 and 2, and 12 months of observations from Voyager 1 and 2. These data include 153 type III radio bursts which were detectable at frequencies below 178 kHz. Since only 18 of these events occur in association with plasma oscillations, it is evident that the chance of detecting the plasma oscillations responsible for a type III radio burst is quite small, approximately 12%.

The typical characteristics of the events detected are illustrated in Figures 1 and 2, which show the electric field strength in four adjacent frequency channels for each of the 18 events. The solid line in each plot gives the maximum electric field strength, and the solid black area (or vertical lines in the case of days 208 and 209) gives the average electric field strength. The spectrum analyzers on Imp 6, Imp 8, Helios 1, and Helios 2 all have continuously active channels with peak detection so that any signal within the time resolution of the instrument ($\sim 50 \text{ ms}$) is always detected by the peak field strength measurement. The maximum field strength shown in each channel is the largest peak field strength in the interval since the previous point plotted. For Voyager 1, which does not have peak detection, the maximum field strength is computed from all of the average field strengths available in each interval plotted. The type III radio bursts in Figures 1 and 2 are in most cases easily identified by the smooth increase in the field strength over a period of several tens of minutes and by the characteristic decrease in the emission frequency with increasing time. The electron plasma oscillations associated with these events usually consist of a series of brief but very intense narrow band

¹ Now at TRW Defense and Space Systems Group, Redondo Beach, California 90278.

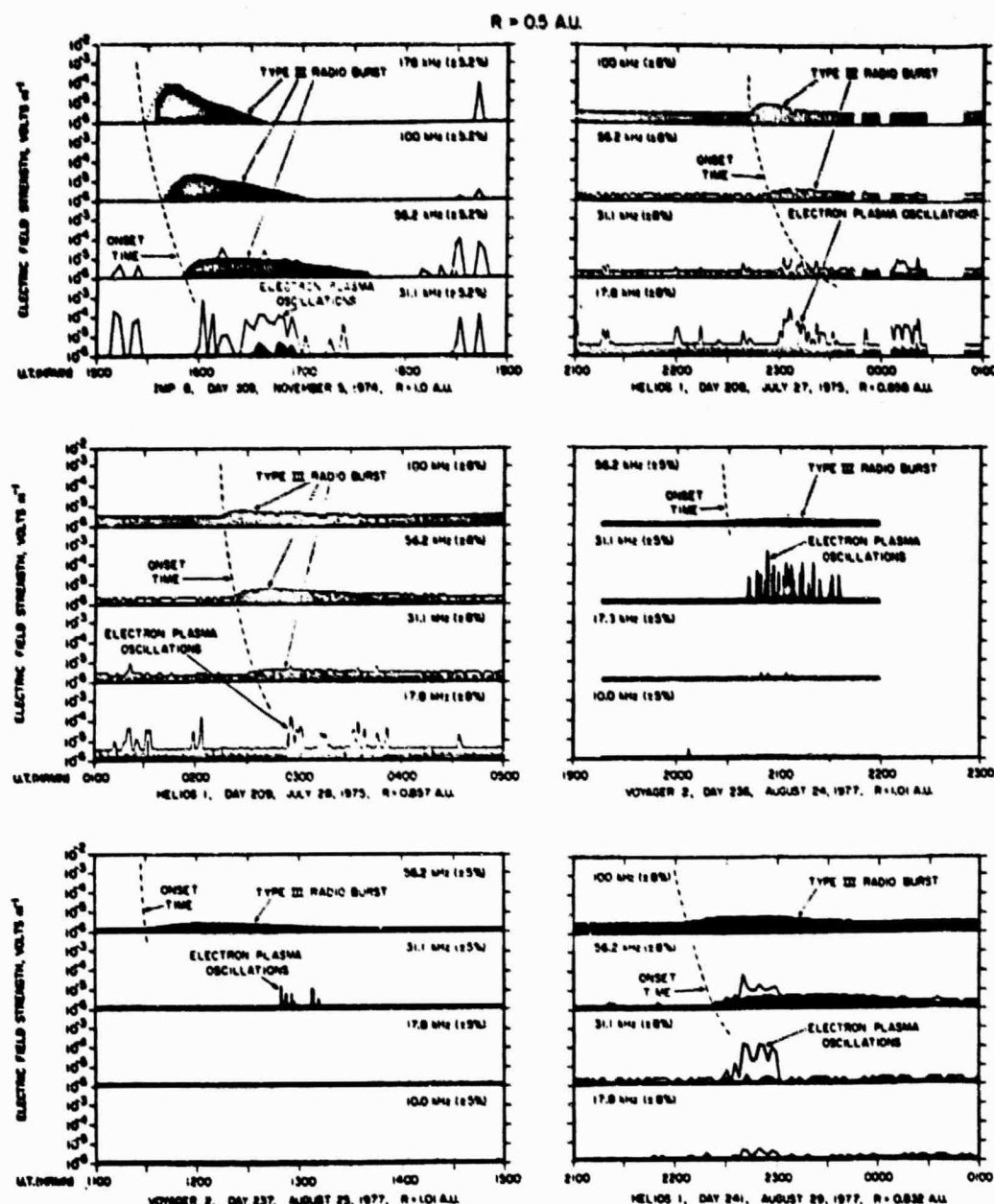


Fig. 1a

Fig. 1. All of the type III radio noise bursts and associated electron plasma oscillation events observed to date at heliocentric radial distances beyond 0.5 AU. The solid line gives the maximum electric field intensity, and the solid black areas (or vertical bars for days 208 and 209) give the average electric field intensity. The plasma oscillations beyond 0.5 AU are generally very weak, typically $\sim 100 \mu\text{V m}^{-1}$, and occur very infrequently in comparison with the total number of type III bursts.

bursts at the local electron plasma frequency. These bursts usually occur shortly after the onset of the type III radio emission in the next higher frequency channel. The maximum electric field intensity is always much larger than the average electric field intensity, indicating that the plasma oscillations consist of many short impulsive bursts. The impulsive intensity variations of the plasma oscillations are illustrated in greater detail in Figure 3, which shows a high-time resolution snapshot of the plasma oscillation intensities associated with the day 92, 1976, event. The most intense burst detected during this interval lasted only a few tenths of a second. Large temporal variations are evident on time scales comparable to the time resolution (50 ms) of the instrument.

To illustrate the variation in plasma oscillation intensity with heliocentric radial distance, the events in Figures 1 and 2 have been arranged with all of the events at radial distances greater than 0.5 AU in Figure 1 and all of the events at radial distances less than 0.5 AU in Figure 2. Comparison of these illustrations shows that the plasma oscillations are more intense in the region closer to the sun. Although more events have been detected beyond 0.5 AU than inside of 0.5 AU, considerations of the relative observing times in the two regions show that the frequency of occurrence of plasma oscillations is significantly higher in the region closer to the sun. Because of the eccentric orbits of the Helios spacecraft, with aphelion near 1.0 AU and perihelion near 0.3 AU, the frac-

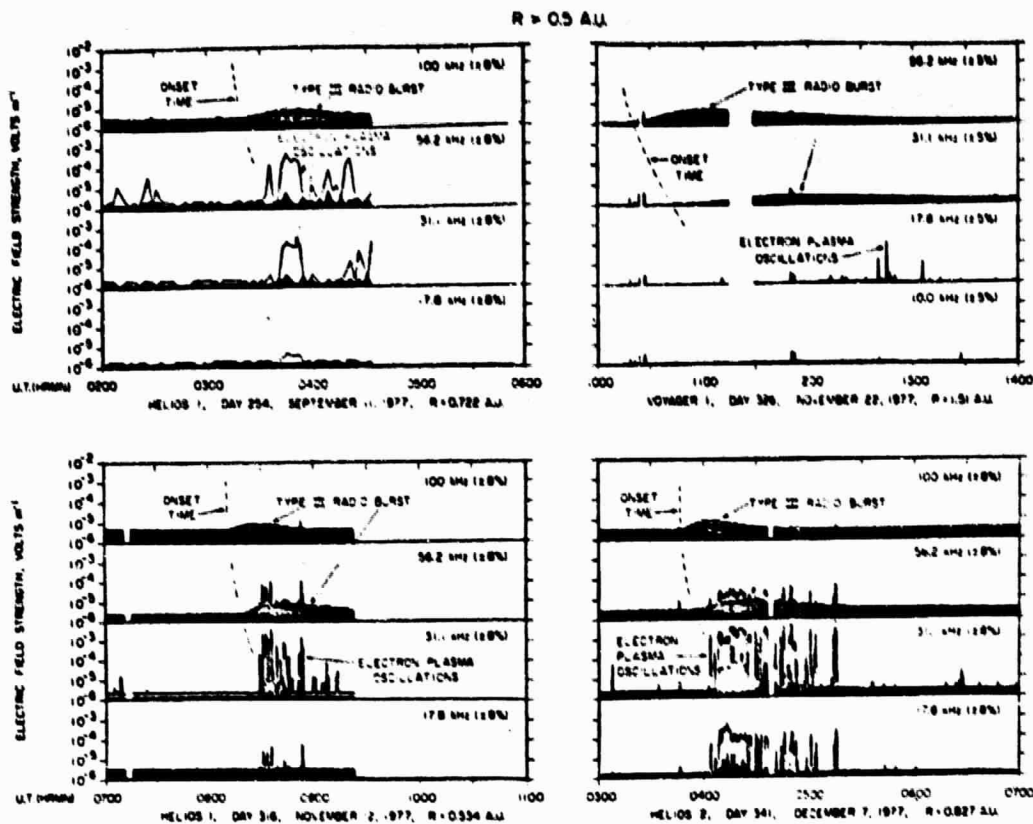


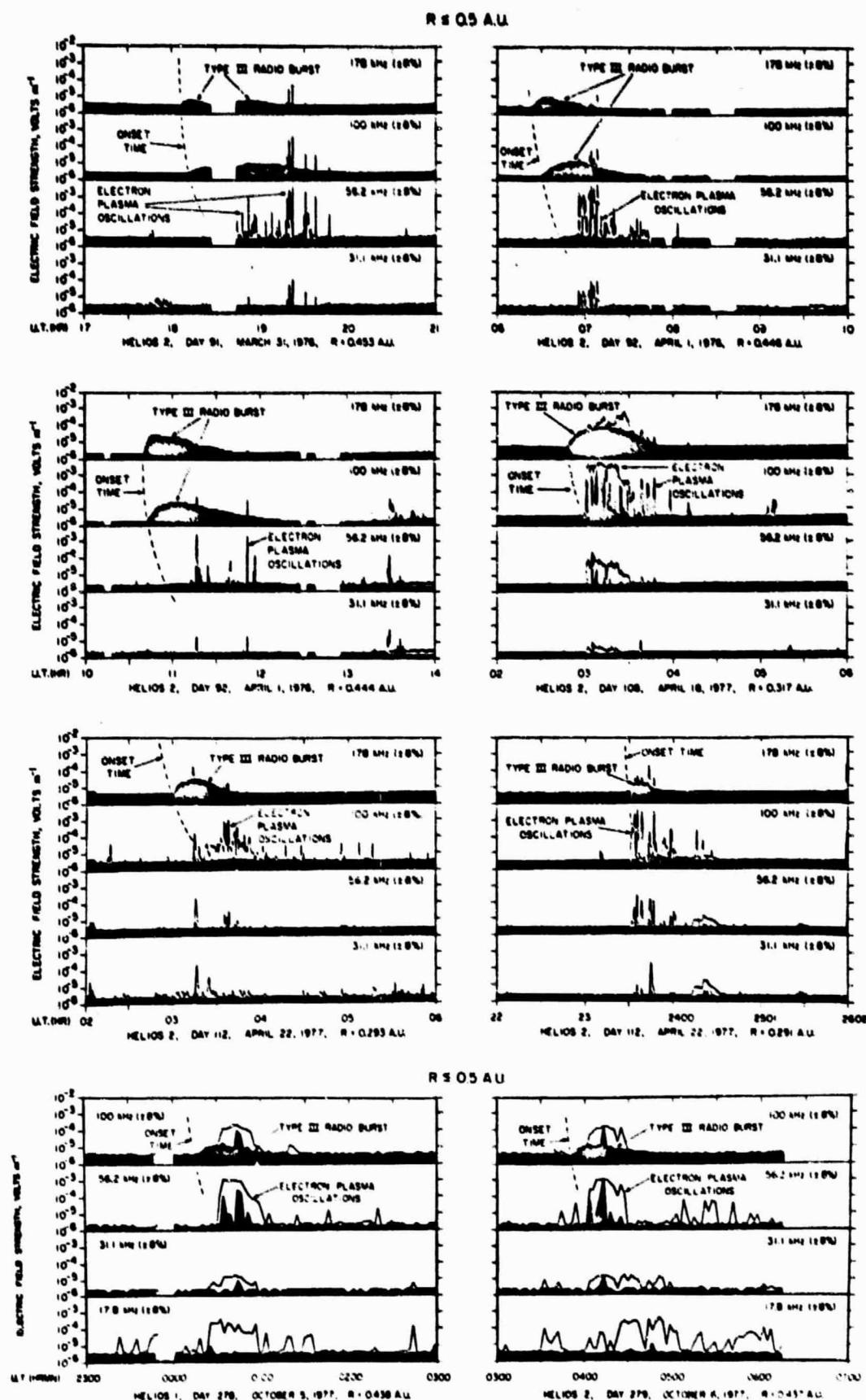
Fig. 1b

tional observing time inside of 0.5 AU is only about 25%. It is estimated that only about 1 year of total observing time is available inside of 0.5 AU, compared with 8 years of combined observing time outside of 0.5 AU. Since eight events have been detected in only 1 year at $R \leq 0.5$ AU, compared with ten events in 8 years at $R > 0.5$ AU, we estimate that the chance of detecting plasma oscillations in association with a type III radio burst is almost 10 times larger in the region inside of 0.5 AU than in the region beyond 0.5 AU.

As can be seen from Figure 1, most of the plasma oscillation events beyond 0.5 AU are quite weak, typically only a few hundred microvolts per meter. In many of these cases it is probably questionable whether these weak plasma oscillations could be responsible for the observed radio emission intensities, even though the close time coincidence indicates that they are produced by the same particles which are responsible for the type III radio emission. Probably the only events in Figure 1 which are strong enough to account for the observed type III radio emission intensities, according to current theories, are on days 316 and 341, 1977. As is evident in Figure 2, the plasma oscillations inside of 0.5 AU are generally much more intense, typically 1–10 mV m⁻¹. According to the estimates of Gurnett and Frank [1975], plasma oscillations in this intensity range are required to explain the observed type III radio emission intensities. For the intense events the onset of the plasma oscillations is usually very abrupt, as it is on days 92, 108, 112, 278, and 279, and consistently occurs about 10–30 min after the onset of the radio burst in the next higher frequency channel. Detailed comparisons show, however, that the onset time is usually a little too late to be consistent with generation of the type III radio emission at the second harmonic of the electron plasma frequency [Fainberg and Stone, 1974; Kaiser, 1975; Gurnett et al., 1978]. If the radiation is

generated at the second harmonic, as is widely believed, then the plasma oscillations should start when the frequency of the type III radio emission reaches the second harmonic, $2f_p$, of the local electron plasma frequency. As can be seen for the events on days 91, 92, 108, 112, and 341, the plasma oscillations start well after the frequency of the type III emission drops below $2f_p$. The disagreement in these cases may indicate that the radiation was being generated at the fundamental rather than the second harmonic, that plasma oscillations were present but on time scales too small (<50 ms) to be detected, or that the plasma oscillations were occurring in small regions or filaments which by chance were not encountered until well after the leading edge of the emission region had swept past the spacecraft. The events on day 341 in Figure 1 and day 108 in Figure 2 also show another interesting effect, which is a nearly constant peak electric field amplitude for time intervals of almost half an hour. These nearly constant electric field amplitudes are almost certainly the result of some nonlinear saturation mechanism which limits the maximum attainable electric field amplitude.

The radial variation of the maximum electric field amplitude with radial distance from the sun is shown in Figure 4. This illustration shows the maximum electric field amplitude for each of the 18 plasma oscillation events shown in Figures 1 and 2. A best fit power law through all of the points indicates that the electric field amplitude varies approximately as $(1/R)^{0.6}$. Although the limited number of events strongly restricts the accuracy with which the detailed radial dependence can be determined, the general trend toward decreasing field strength with increasing radial distance from the sun is unmistakable, especially when consideration is given to the much greater observing time near 1.0 AU compared with regions closer to the sun.



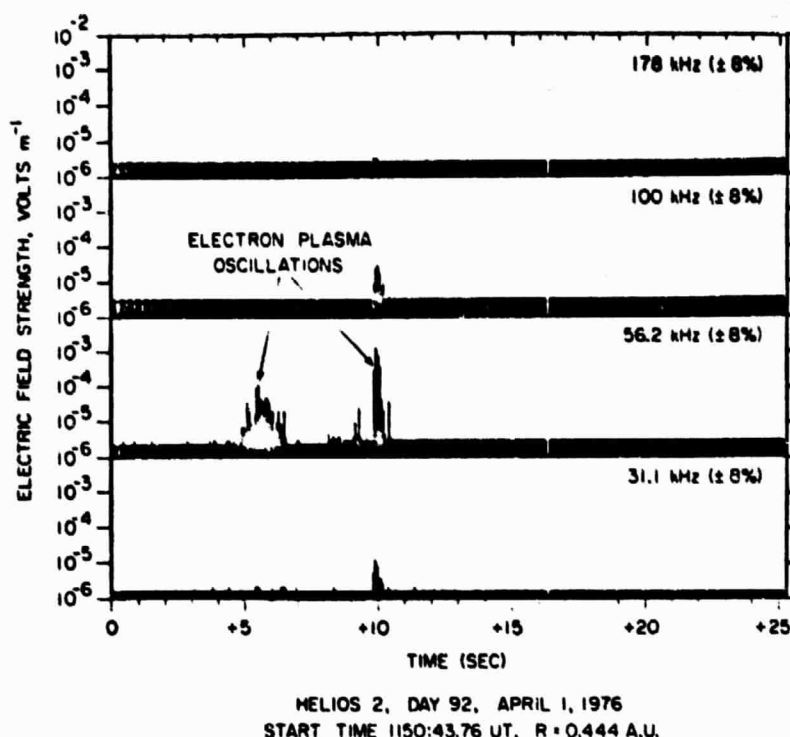


Fig. 3. A high-time resolution snapshot of the electron plasma oscillations associated with the event on day 92, 1976, in Figure 2. The plasma oscillations are seen to occur in short intense bursts lasting only a few tenths of a second. In some cases the temporal variations occur on time scales which approach the time resolution (50 ms) of the instrument.

3. DISCUSSION

These measurements show that the electric field strength of electron plasma oscillations associated with type III radio bursts decreases rapidly with increasing radial distance from the sun. This radial variation provides a partial answer to the question of why electron plasma oscillations are so seldom observed in association with type III radio bursts at the orbit of the earth. Evidently, by the time the beam of electrons which produces the type III radio emission reaches the earth, the velocity distribution function has evolved to the point that the plasma oscillations are only weakly unstable or not unstable at all. Closer to the sun the distribution function is evidently more unstable, leading to more intense plasma oscillations. The observed radial variation of plasma oscillation intensities is also consistent with the frequency spectrums of type III radio bursts, which usually decrease in intensity with decreasing frequency, indicating a decreasing emissivity (hence plasma oscillation intensity) with increasing radial distance from the sun.

Qualitatively, the decreasing plasma oscillation intensity with increasing distance from the sun fits in reasonably well with what one would expect, since the temporal dispersion of the emitted electron beam tends to intensify the unstable part of the electron velocity distribution function in the region closer to the sun, causing larger electric field amplitudes. A quantitative understanding of the observed radial variation, however, will require a detailed understanding of the nonlinear effects which saturate or limit the growth of the plasma oscillations and of the wave-particle interactions which influence the evolution of the electron beam as it propagates outward from the sun. Saturation effects are usually characterized by the dimensionless ratio of the electric field to plasma energy density, $E^2/8\pi nkT$, which for a given distribution function reaches an approximately constant asymptotic value after the instabil-

ity has grown into the nonlinear regime. Numerical simulations [Armstrong and Montgomery, 1967] for strongly unstable distributions typically show that after several hundred plasma periods the energy density ratio $E^2/8\pi nkT$ approaches a constant asymptotic value characteristic of the initial beam intensity. Since the plasma density increases with decreasing distance from the sun approximately as $n \propto (1/R)^2$ and the temperature T remains nearly constant, the electric field strength would be expected to vary as $E \propto (1/R)$ if the asymptotic energy density ratio remains constant, independent of the radial distance. On the basis of the results in Figure 4 it is seen that the electric field strength varies much more rapidly than $(1/R)$, which means that changes in the electron beam characteristics are significantly modifying the asymptotic value of the saturation energy density ratio between 0.3 and 1.0 AU. Typical values for the energy density ratio vary from about $E^2/8\pi nkT \approx 10^{-6}$ at 0.3 AU to about 5×10^{-6} at 1.0 AU.

Because of the complex evolution and interaction of the electron beam with the background plasma, numerical simulations are clearly needed to understand these radial dependences. Calculations of the propagation of solar electron streams have been performed by Magelssen and Smith [1977], assuming that the plasma oscillation intensities are controlled by quasi-linear interactions [Smith and Fung, 1971]. Overall, the results of Magelssen and Smith predict the correct general behavior, with approximately the right plasma oscillation amplitudes. However, detailed comparisons show significant disagreements with observations. The observed radial variation in the electric field energy density (in Figure 4) decreases more rapidly than predicted by the computer simulation, and the observed rapid spikelike variations in the plasma oscillation intensities have no resemblance to the smooth intensity variations predicted by the quasi-linear model. Further simulations using more complex models for the nonlinear beam plasma interactions, such as those discussed by Papadopoulos et al.

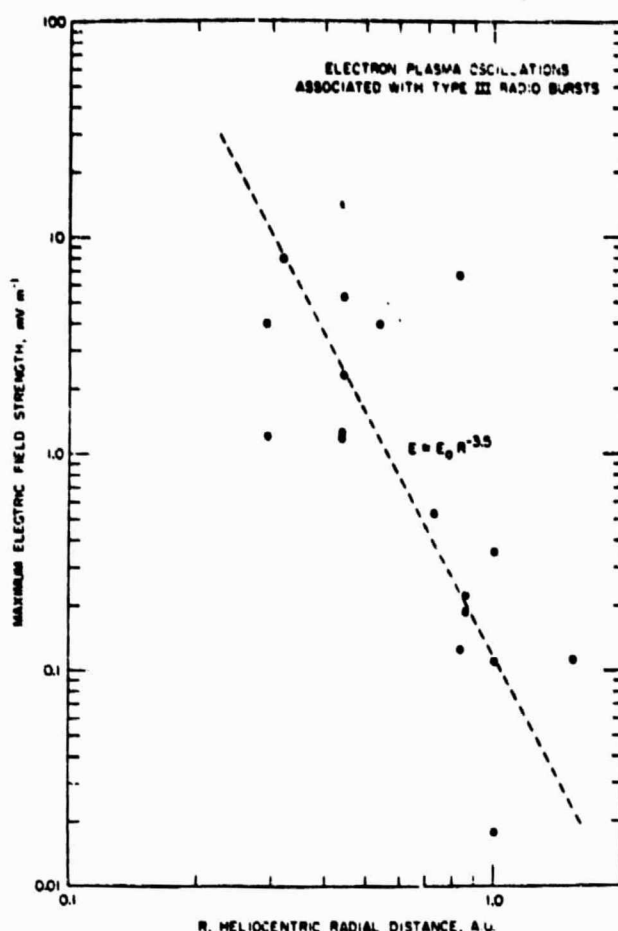


Fig. 4. A scatter plot of the maximum electric field strengths of the plasma oscillations in Figures 1 and 2 as a function of heliocentric radial distance. The electric field strength of the plasma oscillations decreases rapidly with increasing radial distance from the sun, varying approximately as $R^{-3.5}$.

[1974], Bardwell and Goldman [1976], and Rowland and Papadopoulos [1977], need to be performed to see if more complex models of the beam stabilization mechanism provide better agreement with the observations.

Acknowledgments. The research at the University of Iowa was supported by the National Aeronautics and Space Administration through grants NGL-16-001-002 and NGL-16-001-043 and through contract NAS5-11279 with Goddard Space Flight Center and contract 954013 with the Jet Propulsion Laboratory. The research at TRW was

supported by the National Aeronautics and Space Administration through contract 954012 with the Jet Propulsion Laboratory.

The Editor thanks R. G. Stone and P. Kellogg for their assistance in evaluating this paper.

REFERENCES

- Armstrong, T. P., and D. Montgomery, Asymptotic state of the two-stream instability, *J. Plasma Phys.*, **1**, 425, 1967.
- Bardwell, S., and M. W. Goldman, Three-dimensional Langmuir wave instabilities in type III solar radio bursts, *Astrophys. J.*, **209**, 912, 1976.
- Fainberg, J., and R. G. Stone, Satellite observations of type III solar radio bursts at low frequencies, *Space Sci. Rev.*, **16**, 145, 1974.
- Ginzburg, V. L., and V. V. Zheleznyakov, On the possible mechanism of sporadic radio emission (radiation in an isotropic plasma), *Sov. Astron., AJ*, **2**, 653, 1958.
- Gurnett, D. A., and R. R. Anderson, Electron plasma oscillations associated with type III radio bursts, *Science*, **194**, 1159, 1976.
- Gurnett, D. A., and R. R. Anderson, Plasma wave electric fields in the solar wind: Initial results from Helios 1, *J. Geophys. Res.*, **82**, 632, 1977.
- Gurnett, D. A., and L. A. Frank, The relationship of electron plasma oscillations to type III radio emissions and low-energy electrons, *Solar Phys.*, **45**, 477, 1975.
- Gurnett, D. A., M. M. Baumbach, and H. Rosenbauer, Stereoscopic direction finding analysis of a type III solar radio burst: Evidence for emission at $2f_p$, *J. Geophys. Res.*, **83**, 616, 1978.
- Kaiser, M. L., The solar elongation distribution of low frequency radio bursts, *Solar Phys.*, **45**, 181, 1975.
- Kellogg, P. J., and R. P. Lin, Generation of solar type III bursts at the second harmonic (abstract), *Solar Phys.*, **447**, 1976.
- Magelssen, G. R., and D. F. Smith, Nonrelativistic electron stream propagation in the solar atmosphere and type III radio bursts, *Solar Phys.*, **55**, 211, 1977.
- Papadopoulos, K., M. L. Goldstein, and R. A. Smith, Stabilization of electron streams in type III solar radio bursts, *Astrophys. J.*, **190**, 175, 1974.
- Rowland, H. L., and K. Papadopoulos, Simulations of nonlinearly stabilized beam-plasma interactions, *Phys. Rev. Lett.*, **39**, 1276, 1977.
- Scarf, F. L., and D. A. Gurnett, A plasma wave investigation for the Voyager mission, *Space Sci. Rev.*, **21**, 289, 1977.
- Smith, D. F., Type III radio bursts and their interpretation, *Space Sci. Rev.*, **16**, 91, 1974.
- Smith, D. F., and P. C. Fung, A weak turbulence analysis of the two-stream instability, *J. Plasma Phys.*, **5**, 1, 1971.
- Sturrock, P. A., Spectral characteristics of type III solar radio bursts, *Nature*, **192**, 58, 1961.
- Tidman, D. A., T. J. Birmingham, and H. M. Stainer, Line splitting of plasma radiation and solar radio outbursts, *Astrophys. J.*, **146**, 207, 1966.

(Received February 7, 1978;
revised April 17, 1978;
accepted April 17, 1978.)

Auroral Kilometric Radiation: Time-Averaged Source Location

DENNIS L. GALLAGHER AND DONALD A. GURNETT

Department of Physics and Astronomy, University of Iowa, Iowa City, Iowa 52242

The location of the average generation region of auroral kilometric radiation is found by studying average electric field strengths as a function of spacecraft position in narrow frequency bands centered at 178, 100, and 56.2 kHz. A combined 5 years of data from the University of Iowa plasma wave experiments on satellites Hawkeye 1 and Imp 6 provide the basis for determining the average electric field strengths. Hawkeye 1 was in a highly elliptical, polar orbit with an apogee near $21 R_E$ over the northern polar region, and Imp 6 was in a highly elliptical, near-equatorial orbit with an apogee of $33 R_E$. Together these satellites provide extensive coverage from 3 to $21 R_E$ in the northern hemisphere and inside of $3 R_E$ in the southern hemisphere. Intense sources of auroral kilometric radiation are found in the northern and southern hemispheres. Their locations are near 65° invariant latitude in their respective hemispheres, between 22 and 24 hours magnetic local time, and near $2.5 R_E$. The total time-averaged power generation is found to be about 10^7 W, assuming a spectral bandwidth of 200 kHz. Propagation effects limit the emission cone of auroral kilometric radiation in a given hemisphere to roughly 4.1 sr at 178 kHz, 2.2 sr at 100 kHz, and 1.5 sr at 56.2 kHz. Evidence that the polar cusp region is illuminated at distances as close as $4 R_E$ suggests the possibility that previously observed polar cusp sources are the result of scattering from field-aligned density irregularities.

1. INTRODUCTION

This study of electric field intensities has been undertaken to resolve uncertainties in the location of intense sources of earth-related kilometric radiation. From the earliest observations by Benediktov *et al.* [1965, 1968], evidence submitted by numerous investigators has pointed to widely varying locations for the origin of the very intense and sporadic kilometric radiation which has a sharply peaked spectrum between 100 and 300 kHz. Benediktov *et al.* [1965, 1968] correlated radio emissions between 0.725 and 2.3 MHz with geomagnetic activity and concluded that the source is near the earth. Dunkel *et al.* [1970] reported that this intense radiation is observed primarily in the local nighttime and is strongly correlated with the auroral electrojet (AE) index. A source location in the tail region of the magnetosphere for sporadic noise at 250 kHz was observed by Stone [1973]. Gurnett [1974] presented a frequency of occurrence study of kilometric radiation showing a conical radiation pattern centered at the earth, at high latitudes in the local evening, and referred to this intense radiation as terrestrial kilometric radiation. Gurnett demonstrated that the observed conical radiation pattern could be explained if the source location of the radiation was on an auroral field line at $\leq 3 R_E$ (earth radii). Gurnett also showed that the kilometric radiation was closely associated with discrete auroral arcs. The two-component source model proposed by Kaiser and Stone [1975] described a less intense, quasi-continuous dayside source in addition to the intense, sporadic nightside source described by Gurnett. Using the direction-finding technique of analyzing spin-modulated electric field intensities from satellites Hawkeye 1 and Imp 8, Kurth *et al.* [1975] reported the average source location of auroral kilometric radiation between 1 and $2 R_E$ and at about 20 hours magnetic local time. In another experiment, lunar occultations of intense kilometric radiation observed with Rae 2 were used by Kaiser and Alexander [1977] to locate apparent source origins. The most intense source observed was the auroral source described by Kurth *et al.* [1975]. Emissions were also observed in the region of the polar cusp and magnetosheath on the dayside of the earth.

Such diverse observations of the source locations of the intense kilometric radiation have produced the very difficult task of finding a single mechanism for the generation of the radiation, which will operate under widely varying plasma conditions. Toward resolving the dilemma, Alexander *et al.* [1978] have recently given strong evidence that kilometric radiation generated near the earth at auroral latitudes may be scattered at large distances in the magnetosheath and solar wind, thereby appearing to come from distant sources. Following this explanation of the observation of distant kilometric radiation sources, two types of terrestrial kilometric radiation observations remain to be examined. The strongest component is auroral kilometric radiation, which is known to originate within $5 R_E$ at auroral latitudes and in the local evening. Other less intense components discussed by Alexander *et al.* [1978] are observed between 5 and $15 R_E$ and appear to come from sources aligned along a specific family of geomagnetic field lines. An example is the polar cusp sources observed by Kaiser and Alexander [1977]. In summary, these studies have found source locations by lunar occultation techniques and by examining spin-modulated electric field intensities. The methods determine the instantaneous positions of apparent sources of intense kilometric radiation. Such an apparent source may represent a generation region of the radiation or scattering from localized inhomogeneities in plasma density.

The present study will determine which regions in the magnetosphere are strong sources of power at kilometric wavelengths. Time-averaged spectral power flux will first be integrated over earth-centered spherical shells. For shells of varying radius the integrals will give the spectral power and geocentric radial distance of regions of power generation. The latitudinal and local time dependences of the averaged spectral power flux will be examined along with a consequence of the $1/R^2$ radial dependence of spectral power flux observed by Gurnett [1974] for terrestrial kilometric radiation. As was postulated by Alexander *et al.* [1978], previously observed polar cusp sources may result from field-aligned scattering centers. Since this study utilizes extensive measurements in and near the source region, the resulting source locations are not as sensitive as remote direction-finding measurements to errors arising

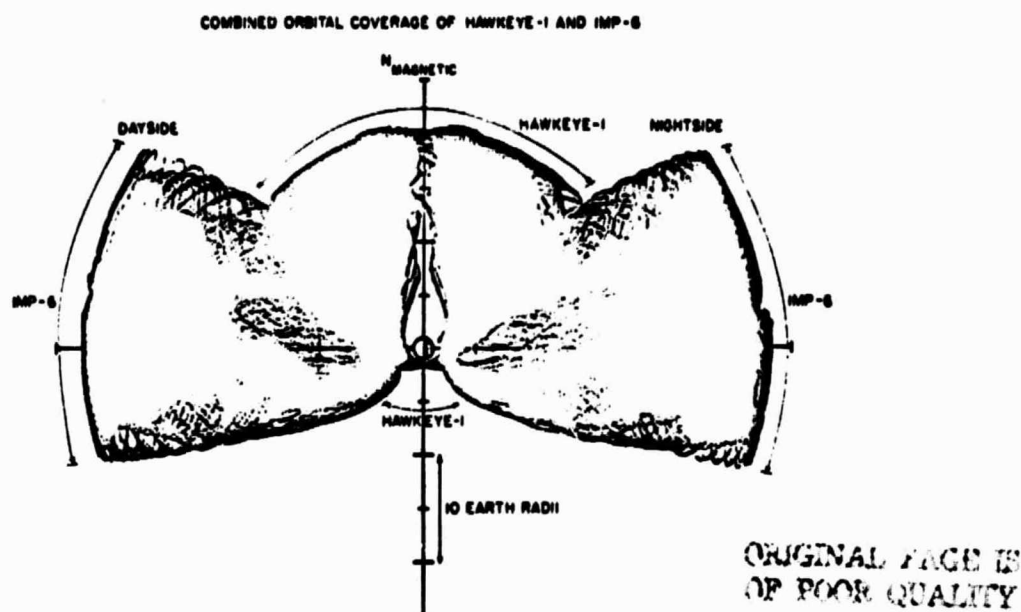


Fig. 1. Combined orbital coverage of Hawkeye 1 and Imp 6. All points on the nightside have been rotated in MLT to form the right side of the figure, and all points on the dayside have been rotated in MLT to form the left side of the figure.

ing from scattering or reflections. The dimensions of observed regions of power generation will also be a measure of the variation in the locations of instantaneous intense sources of kilometric radiation. To the extent that this study better defines those regions which contribute to the energy produced at kilometric wavelengths the generation mechanism for intense kilometric radiation may be sought using a more limited range of plasma parameters than has been possible in the past.

2. INSTRUMENTATION

The Hawkeye 1 and Imp 6 satellites have similar plasma wave experiments (described by Kurth *et al.* [1975] and Gurnett and Shaw [1973], respectively), which together provide about 5 years of electric field measurements. The combined orbital coverage of the satellites is shown in Figure 1. Locations where measurements are made on the nightside of the earth have been rotated in magnetic local time to form the right side of the figure; all points on the dayside have been rotated to form the left side of the figure. As is shown, northern hemisphere coverage is almost complete out to about $21 R_E$. There is no coverage, however, at small radial distances and at high latitudes above the northern pole. Southern hemisphere coverage is limited to latitudes greater than about -40° magnetic latitude except for Hawkeye 1 coverage within $2 R_E$.

The success of integrating spectral power flux over spherical shells to find regions of power generation depends strongly upon the completeness of the flux observations over each spherical surface. Such observations cannot satisfactorily be provided by the data from only one satellite. The orbital coverage of satellites Hawkeye 1 and Imp 6 are only partially overlapping. When taken together, the data from these satellites provide an extensive survey of electric field strengths in the vicinity of the earth. Although not shown in Figure 1, the combined orbital coverage extends uniformly throughout all magnetic local times.

3. DATA ANALYSIS

Integrating average power flux over earth-centered spherical shells will give an estimate of the geocentric radial dis-

tances of the sources of the most intense kilometric radiation and the value of the total average power generation. Using simultaneous observations of electric and magnetic fields by Imp 6, Gurnett [1974] showed that electric-to-magnetic field ratios of intense kilometric radiation correspond to that for electromagnetic waves in free space. On this basis an inverse dependence of power flux on the square of radial distance should be observed in the data obtained from satellites Hawkeye 1 and Imp 6. However, the $1/R^2$ dependence of power flux on distance should be seen only as a function of the distance from the origin of the radiation. This origin may be inferred by selecting a source region which yields the power flux dependence of $1/R^2$ that is expected for free space propagating electromagnetic radiation.

Measurements of electric field strength by each satellite are logarithmically compressed and available in the form of a voltage between 0 and 5 V (V_{out}). By using prelaunch calibration tables these measurements are converted to the actual voltages applied to the satellite antennas (V_{in}). From the known effective antenna lengths and filter bandwidths the electric field strength and spectral power flux, P , can be calculated for each measurement. In a study by Green *et al.* [1977] the calibrations on these two satellite instruments were compared through simultaneous observations of type III radio bursts. On the assumption that the satellites were equidistant from the source regions of type III radio bursts the observations of electric field strengths were found to be in close agreement; therefore no normalization is required in averaging measurements of spectral power flux by the two satellites.

For this study the electric field data from Hawkeye 1 and Imp 6 have been averaged over 3-min 4-s and 5-min 28-s intervals, respectively, and as a consequence, spin modulation effects are removed from the data. All data are then averaged into 72.5° increments of magnetic local time (MLT), 36.5° increments of magnetic latitude λ_m , and 15 equal logarithmic increments in geocentric radial distance. This produces a picture of time-averaged spectral power fluxes as a function of position in the vicinity of the earth. The resolution of the picture is limited only by the amount of data available from Hawkeye 1

and Imp 6. For the chosen resolution, there are 10-50 measurements of spectral power flux averaged into each volume element where satellite coverage exists. The objective is for the average of spectral power flux measurements within each volume element to be representative of the average kilometric radiation intensities at each corresponding location. Bursts of kilometric radiation last from tens of minutes to several hours. As a result, some observations within a given volume element will be made when kilometric radiation cannot be observed. By requiring many uncorrelated measurements within a volume element the error in the average intensity is reduced, approximately in proportion to $1/(n)^{1/2}$, where n is the total number of measurements.

As a result of using the electric field data from satellites Hawkeye 1 and Imp 6, over 600,000 measurements of spectral power flux are obtained. Because sources of radiation at kilometric wavelengths such as continuum radiation and type III radio bursts have been observed by Gurnett [1974] to be a minor source of energy when compared with terrestrial kilometric radiation, no lower threshold on measurements of spectral power flux will be used to exclude these other forms of kilometric radiation from the present study. An upper threshold can be estimated at respective receiver channel saturations and results in the omission of only four measurements.

Also important is how well measurements of spectral power flux represent the spectral components of the magnitude of the poynting flux. How well an average across the spin-modulated data corresponds to the magnitude of the poynting flux depends ideally on the polarization of the radiation and the orientation of the satellite's axis of rotation. The average of measurements of circularly polarized radiation will yield a result which varies approximately from a factor of 1-0.7 times the magnitude of the electric field component of the radiation. The larger result occurs when the poynting flux direction is along the satellite's axis of rotation. Auroral kilometric radiation is an R-X mode propagating radiation as predicted by Green *et al.* [1977] and observed by Gurnett and Green [1978] and by Kaiser *et al.* [1978]. Each electric field average will be in error by no more than a factor of about 1.4, and therefore spectral power flux measurements will be in error by no more than a factor of about 2.

The present study could also be influenced by seasonal and long-term variations in kilometric radiation intensities. Seasonal changes are sought by studying separate summer and winter averages of spectral power flux as a function of position. When plots along earth-centered radial vectors of spectral power flux versus distance are made separately for the summer and winter, no statistical differences are found. A possible source of long-term variations is the 11-year solar sunspot cycle. Data are taken from satellites Imp 6 and Hawkeye 1, which provide 7 years of almost nonoverlapping temporal coverage. A solar minimum occurred midway through those 7 years; therefore measurements from these two satellites were made during similar phases of the solar cycle. The effect is expected to mask solar cycle related variations in kilometric radiation intensities if such a variation exists. Consequently, the data examined in this study constitute, as well as possible, an unbiased representation of spectral power flux intensities in the vicinity of the earth.

Assume initially that the picture proposed by Gurnett [1974] is generally accurate in describing the locations of the most intense sources of kilometric radiation. The sources of intense kilometric radiation are shown in Gurnett's Figure 14 to be very close to the earth and at high latitudes on auroral field

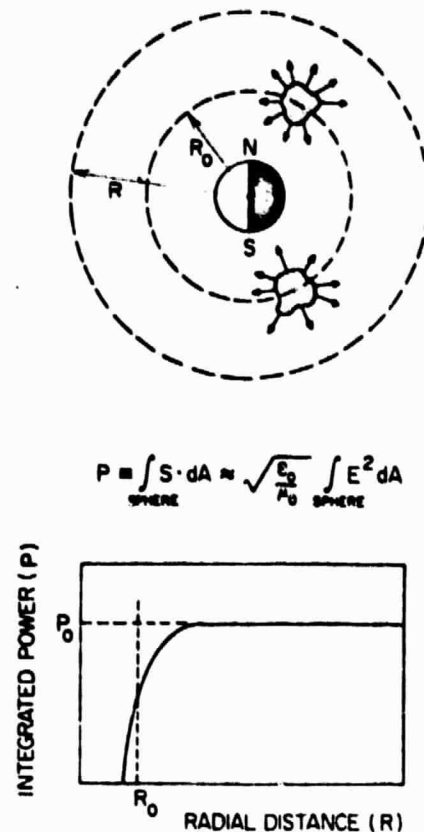


Fig. 2. The integration of poynting flux over concentric, earth-centered, spherical shells for model auroral kilometric radiation sources is shown. Poynting flux magnitudes must be approximated by measurements of spectral power flux. P_0 corresponds to the total power generated by the sources, and R_0 approximately marks the radial distance of the sources from the center of the earth.

lines. If these northern and southern sources of auroral kilometric radiation, as termed by Kurth *et al.* [1975], are well confined, then an integration of the poynting flux over spherical shells which completely enclose the source regions should yield a constant power as shown in Figure 2. If both sources could always be seen, this constant would be equal to the total spectral power generated at the frequency for which the data were chosen. As the radius of these concentric, spherical, earth-centered shells become small, a radius will be reached where they no longer completely enclose the generation regions. As this occurs, the integrated power will fall off at a rate which reflects how well, on the average, the source is confined within the shell of integration. The radii of shells during which this drop off occurs define the location of the source regions in earth-centered radial distance. Poynting flux, however, is not available from both satellites. Instead, measurements of average spectral power flux are used to perform the integrations:

$$\int_{\text{sphere}} \mathbf{S} \cdot d\mathbf{A} \approx \int P dA = \left(\frac{\epsilon_0}{\mu_0}\right)^{1/2} \int E^2 dA \quad (\epsilon_0/\mu_0)^{1/2} \approx 1/377$$

where \mathbf{S} is the spectral poynting vector and P is the spectral power flux. The effect of introducing this approximation will be discussed later.

To perform the integration, all volume elements must contain a measurement of spectral power flux. Orbital coverage, however, was not 100% complete, as shown in Figure 1. To compensate, those volume elements for which there are no

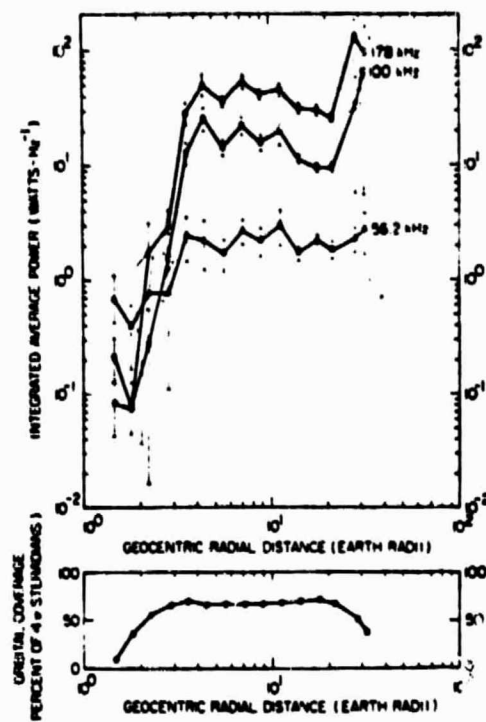


Fig. 3. The integration of observed spectral power flux across concentric, earth-centered, spherical shells is shown in the upper graph. The radial distances plotted horizontally correspond to radii of the spherical shells of integration. The lower graph gives the extent of orbital coverage for each spherical surface of integration.

satellite data are filled with the average spectral power flux calculated from all those volume elements which contain satellite data at the same radial distance. As was noted, incomplete orbital coverage occurred primarily in the southern hemisphere. The procedure for artificially filling volume elements with data therefore depends mostly upon the symmetry between the northern and the southern hemispheres. This filling procedure is used because symmetry is found between the northern and the southern hemisphere when existing spectral power flux measurements are examined. Finally, volume elements within each radial distance increment are treated as spherical shells with radii which are the average for all measurements within each radial group.

The integration was then performed for 178, 100, and 56.2 kHz, and the result is shown in Figure 3. Each of the radial distances plotted represents an average of the radial distances of the measurements in each corresponding radial distance group. The lower panel in Figure 3 shows the extent of satellite orbital coverage as a percentage of 4π sr. The error bars in the figure represent one standard deviation of the integration for each of 15 spherical shells at each frequency. An interpretation of Figure 3 will be made later in the discussion section of this paper.

Another approach is to examine the data for a $1/R^2$ radial dependence. Except for the plasmopause propagation effects discussed by Green *et al.* [1977], auroral kilometric radiation propagates away from the earth in free space. The radiation should therefore propagate away from the source region with a $1/R^2$ radial dependence. A plot of average power versus earth-centered radial distances along a radial vector that passes through the source region in a given hemisphere can easily be examined for the $1/R^2$ radial dependence. Prior to

selecting a radial vector direction for making this plot, the southern and northern hemispheres are examined for symmetry. As was discussed, they are found to be roughly equivalent in structure; therefore the southern hemisphere data can be reflected about the equatorial plane and averaged together with northern hemisphere data to produce a single hemisphere of data with increased orbital coverage.

Because these data are organized in earth-centered coordinates, average spectral power flux can not easily be examined for $1/R^2$ radial dependence until a solid angle is chosen which passes as near as possible to the source region. After the selection of such a solid angle the dependence of spectral power flux on distance may be examined in a single dimension along the corresponding radial vector. The solid angle direction is chosen by examining the MLT and λ_m dependence of the intensity of the radiation. Figure 4 shows intensity-modulated, polar plots of power flux for four radial distance groups. The logarithm of spectral power flux is used to determine the darkness of the plot. The more intense fluxes correspond to the darker regions in each plot. The plots appear to show a cone of emission originating from premidnight magnetic local times and at intermediate magnetic latitudes. The magnetic latitudes of the solid angle which must be determined are selected to range from 30° and 55° . This selection of magnetic latitudes is large enough to include the location of the source region and small enough to avoid the areas of poor orbital coverage at high latitudes.

The selection of a MLT direction is performed by plotting average power versus earth-centered radial distances in various MLT directions. The MLT which best corresponds to that of the source region will show the most intense and most sharply peaked plot because measurements along a radial vector in that MLT will pass closer to the source region than in any other MLT. Plots made in four MLT groups for spectral power fluxes averaged between 30° and 55° λ_m are shown in Figure 5. On the basis of the above discussion the plot between 22 and 24 hours MLT clearly represents the MLT direction of the source region. The peaks for plots in other magnetic local times are less intense and flattened because those points on a flattened peak represent locations which are separated and approximately equidistant from the source region. The solid angle has now been chosen to range from 22 to 24 hours MLT and from 30° to 55° λ_m . This selection best represents the direction of the source region from the center of the earth and avoids the influence of poor orbital coverage at high magnetic latitudes.

The plot of Figure 5 between 22 and 24 hours MLT can now be examined for $1/R^2$ radial dependence. A straight line fit to the trailing edge of the plotted curve for 178 kHz on this log-log graph has a slope of -3.47 . Radial distances plotted on the graph are geocentric rather than distances from the source region, thereby increasing the slope of the straight line fit. The distance of the actual source region from the center of the earth can indirectly be found by replotting spectral power flux where the radial distances used are with respect to various possible source locations. An assumed source location which produces the expected slope of -2.0 when spectral power flux is plotted as a function of the distance from this location would then correspond to the actual distance of the source from the center of the earth. An example of the effect of choosing source locations at 2, 3, and 4 R , for the frequencies examined is shown in Figure 6. The dashed line in each plot represents a $1/R^2$ slope. As possible source locations are cho-

POLAR PLOTS OF AVERAGE POWER AT 178 KHz

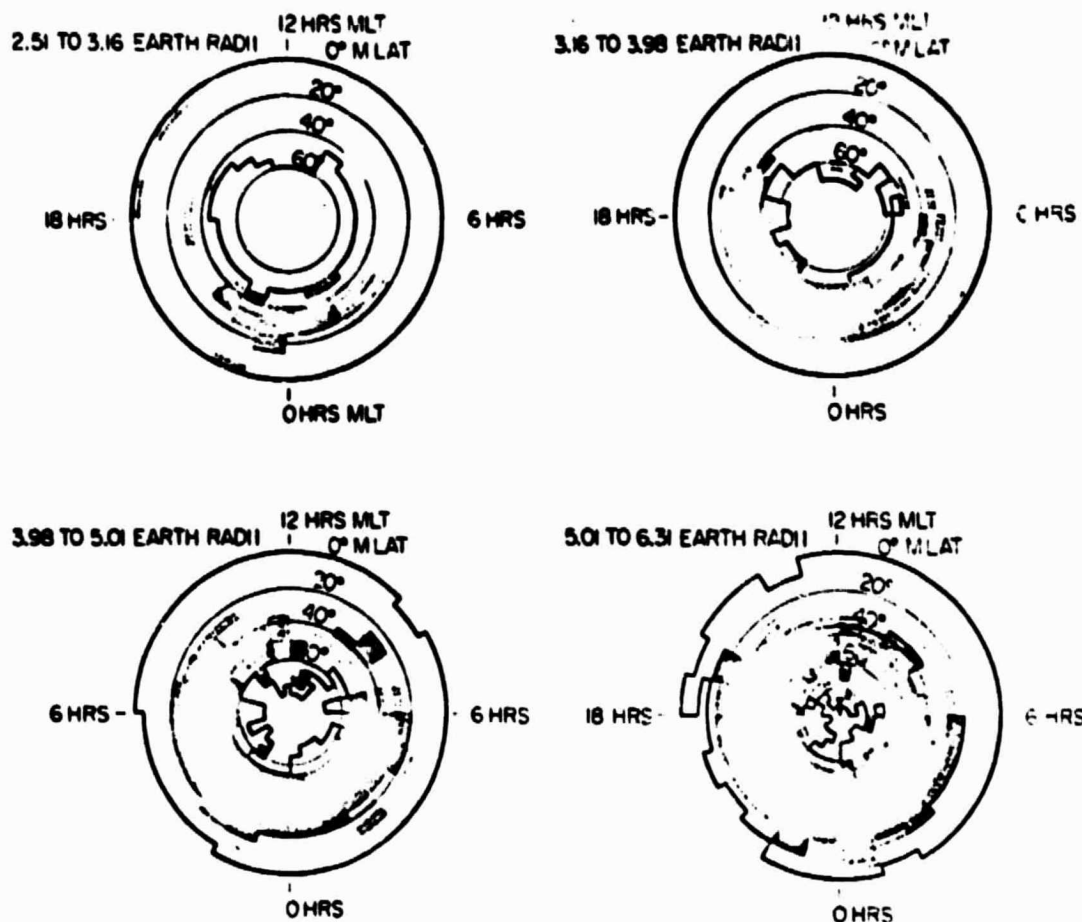


Fig. 4. These are intensity-modulated polar plots of the average spectral power flux observed in four consecutive, concentric, hemispherical shells at 178 kHz. Dark borders interior and exterior to each plot mark the limits of orbital coverage. Plotted intensities are derived from the logarithm of spectral power flux.

seen at consecutively larger distances from the center of the earth, the slope reduces on these log-log plots. A uniform plot of slope as a function of source location is shown in Figure 7. The horizontal dashed line representing a $1/R^2$ slope shows an inferred actual source location which ranges from 2 to 3 R_E .

4. DISCUSSION

The calculation of spectral power emitted at kilometric wavelengths by means of integrating over earth-centered, spherical shells was performed so that the radial distance of the most intense sources of kilometric radiation could be found. The result of the integration in Figure 3 agrees remarkably well with the idealized sketch shown in Figure 2. In many respects, however, the result shown in Figure 3 is not the product of ideal conditions. First, $S \cdot dA$ was approximated with the measured spectral power flux PdA or $(c_0/\mu_0)^{1/2} E^2 dA$. As a measurement of the spectral poynting flux magnitude $|S|$, the spectral power flux has been shown to be no more than about a factor of 2 too small. As a result of the approximation, the magnitude of the component of the poynting flux normal to the surface of integration is not known. This means that the total observed spectral power flux magnitude will be used in the integration at each surface element. When

the surface of integration has a large radius and completely encloses the source regions, the error associated with the approximation $S \cdot dA = |S|dA$ should be very small, and the result of the integration should be a constant function of radius. As the surfaces of integration no longer completely enclose the source regions, the integral will become roughly proportional to the area of the surface of integration. The important point is that the value of the integral will not be a constant when the radius of the surface of integration becomes less than the distance of the source positions from the center of the earth, independent of any other effects which may be present. The drop-off occurs in Figure 3 at approximately 4 R_E . An additional reduction in the value of the integral occurs due to measurements made inside the propagation cutoff surface, described by Gurnett [1974], which is located at about 2 R_E for high latitudes. For the radiation to be propagating in free space the source of intense kilometric radiation must be outside of the propagation cutoff surface, while the integration of spectral power flux places the source region inside of 4 R_E . The primary result of the integrations therefore locate well-confined intense sources of kilometric radiation at a distance of 2-4 R_E from the center of the earth. Effects, in addition to those described above, can cause the value of the integration

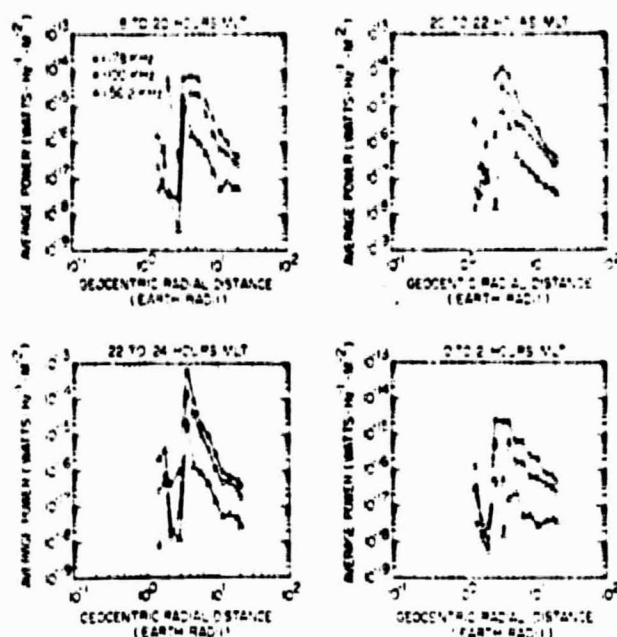


Fig. 5. Average spectral power flux is plotted against geocentric radial distance in four magnetic local time groups. Spectral power has been averaged between 30° and 55° λ_m in each magnetic local time group. The graph from 22 to 24 hours MLT best corresponds to the MLT of the source region of auroral kilometric radiation.

to reduce. The drop-off at $4 R_E$ is therefore an outer limit to the generation of intense kilometric radiation. No significant source of power at kilometric wavelengths is seen between 5 and $15 R_E$.

A measurement of the total power emitted as auroral kilometric radiation can also be determined. The significance of various features of the curves in Figure 3 must be examined before the emitted power can be obtained. Where orbital coverage becomes poor, the error in the integration becomes very large. The error for radial distances less than $3 R_E$ does not significantly effect the determination of source position because the reduction in the value of the integral remains clearly indicated near $4 R_E$. Owing to the large errors at distances beyond $21 R_E$, the sharp rise in the value of the integral cannot be reliably interpreted. It is likely that the sharp rise in the integrated power at distances beyond $21 R_E$ is caused by the sharply reduced orbital coverage (particularly from Hawkeye) and the simultaneous observation of both northern and southern hemispherical sources on the nightside of the earth. At this distance the solid angle where both sources are observable becomes a significant fraction of all solid angles where orbital coverage exists. An observation of spectral power flux is twice as large as that for the observation of only one source. Because the average of spectral power flux from those volume elements where coverage exists (primarily near the equator) is used to fill those volume elements where orbital coverage does not exist (primarily over the poles) the value of the in-

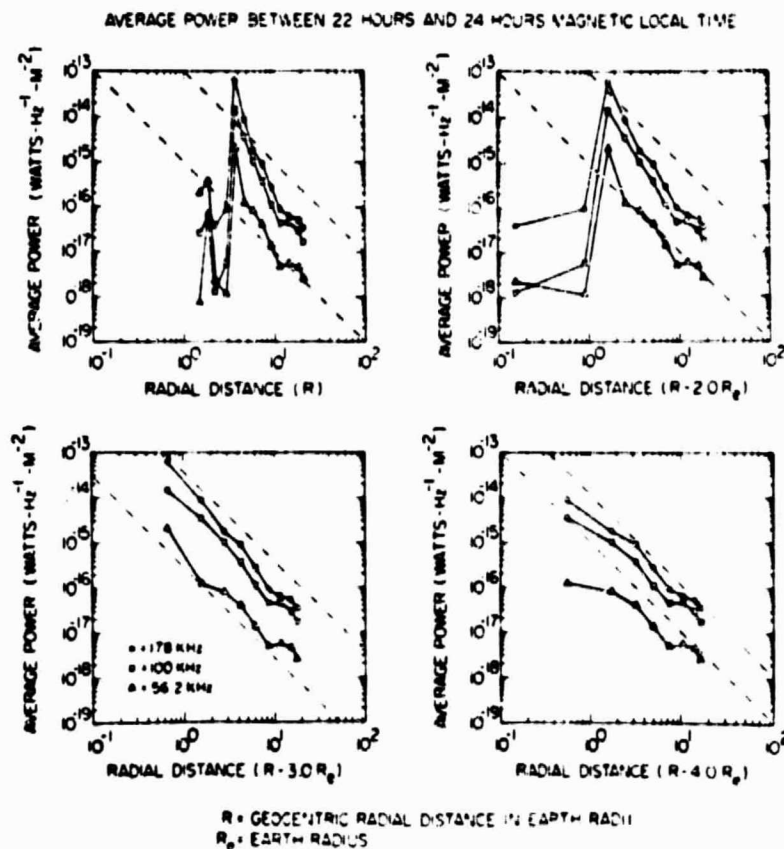


Fig. 6. Average spectral power flux is plotted against the distances from selected possible source locations. All four plots are for spectral power flux which has been averaged between 22 and 24 hours MLT and between 30° and 55° λ_m . Data in the upper left panel are plotted against geocentric radial distances. Points in the other three panels are plotted as a function of the distances away from model source locations at 2, 3, and $4 R_E$. The dotted lines which indicate a $1/R^2$ slope show that data plotted for a source location at $3 R_E$ most nearly follow the $1/R^2$ functional dependence.

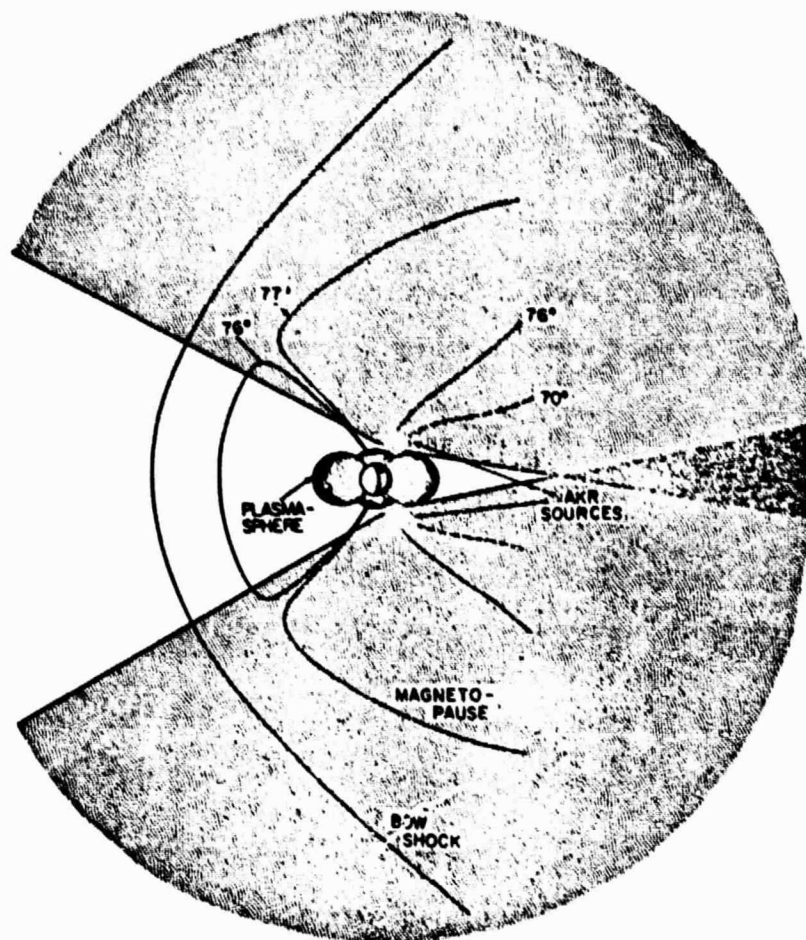


Fig. 8. The time-averaged extent of the conelike emission of auroral kilometric radiation is shown along with the Hawkeye magnetic field model of Chen and Van Allen [1978]. On the average, both sources are observable in the equatorial plane on the nightside of the earth at a distance of $12 R_E$ and beyond. The polar cusp is illuminated by auroral kilometric radiation at radial distances as close as $4 R_E$.

study. A more detailed study of the characteristics of the integration of spectral power flux is needed before the nature of kilometric radiation sources between 5 and $15 R_E$ can be determined. However, the observed illumination of the polar cusp at distances as small as $4 R_E$ allows observations of polar cusp sources, such as those by Alexander and Kaiser [1976], to be explained by scattering from field-aligned density irregularities.

5. CONCLUSIONS

Intense sources of power radiating at kilometric wavelengths are found near 65° invariant latitude in the northern and southern hemispheres, from 22 to 24 hours MLT, and between 2 and $4 R_E$. These dominant sources of power produce the electromagnetic radiation that has been described by Kurth *et al.* [1975] as auroral kilometric radiation. Each northern and southern hemisphere auroral kilometric radiation source is well confined and emits radiation into solid angles of about 4.1 sr at 178 kHz, 2.2 sr at 100 kHz, and 1.5 sr at 56.2 kHz. A lower limit for the spectral power generated by each source is found to be 37 W/Hz at 178 kHz, 16 W/Hz at 100 kHz, and 2 W/Hz at 56.2 kHz. For a bandwidth of 200 kHz the total time-averaged power emitted by the northern and southern sources of auroral kilometric radiation is found to be about 10^7 W.

Acknowledgments. We wish to extend special thanks to J. L. Green, W. S. Kurth, and R. R. Anderson for their valuable advice. This work was supported by NASA under grant NGL-16-001-043 and contracts NASS-11074, NASS-11431, and NAS1-13129.

The Editor thanks J. Alexander and M. S. Frankel for their assistance in evaluating this paper.

REFERENCES

- Alexander, J. K., and M. L. Kaiser, Terrestrial kilometric radiation, I. Spatial structure studies, *J. Geophys. Res.*, **81**, 5948, 1976.
- Alexander, J. K., M. L. Kaiser, and P. Rodriguez, Scattering of terrestrial kilometric radiation at very high altitudes, *J. Geophys. Res.*, **84**, 2619, 1979.
- Benediktov, E. A., G. G. Getmantsev, Yu. Al. Sazonov, and A. F. Tarasov, Preliminary results of measurement of the intensity of distributed extraterrestrial radio-frequency emission at 725 and 1525-kHz frequencies by the satellite Elektron-2, *Cosmic Res.*, English Transl., **3**, 492, 1965.
- Benediktov, E. A., G. G. Getmantsev, N. A. Mityakov, V. O. Papoport, and A. F. Tarasov, Radiation between geomagnetic activity and the sporadic radio emission recorded by the Elektron satellites, *Cosmic Res.*, Engl. Transl., **6**, 791, 1968.
- Chen, T.-F. and J. A. Van Allen, The earth's magnetic field at large radial distances as observed by Hawkeye 1, submitted to *J. Geophys. Res.*, 1978.
- Dunckel, N., B. Ficklin, L. Rorden, and R. A. Helliwell, Low-frequency noise observed in the distant magnetosphere with Ogo 1, *J. Geophys. Res.*, **75**, 1854, 1970.
- Green, J. L., D. A. Gurnett, and S. D. Shawhan, The angular distribution of

- bution of auroral kilometric radiation, *J. Geophys. Res.*, **82**, 1825, 1977.
- Gurnett, D. A., The earth as a radio source: Terrestrial kilometric radiation, *J. Geophys. Res.*, **79**, 4227, 1974.
- Gurnett, D. A., and J. L. Green, On the polarization and origin of auroral kilometric radiation, *J. Geophys. Res.*, **83**, 689, 1978.
- Gurnett, D. A., and R. R. Shaw, Electromagnetic radiation trapped in the magnetosphere above the plasma frequency, *J. Geophys. Res.*, **78**, 8136, 1973.
- Kaiser, M. L., and J. K. Alexander, Terrestrial kilometric radiation. 3, average spatial properties, *J. Geophys. Res.*, **82**, 3273, 1977.
- Kaiser, M. L., and R. G. Stone, Earth as an intense planetary radio source: Similarities to Jupiter and Saturn, *Science*, **189**, 285, 1975.
- Kaiser, M. L., J. K. Alexander, A. C. Riddle, J. B. Pearce, and J. W. Warwick, Direct measurements by Voyagers 1 and 2 of the polarization of terrestrial kilometric radiation, *Geophys. Res. Lett.*, **5**, 857, 1978.
- Kurth, W. S., M. M. Baumback, and D. A. Gurnett, Direction-finding measurements of auroral kilometric radiation, *J. Geophys. Res.*, **80**, 2764, 1975.
- Stone, R. G., Radio physics of the outer solar system, *Space Sci. Rev.*, **14**, 534, 1973.

(Received February 12, 1979;
revised May 17, 1979;
accepted June 21, 1979.)

**A Test of Two Theories for
the Low Frequency Cutoffs of
Non-Thermal Continuum Radiation**

by

**Robert R. Shaw
and
Donald A. Gurnett**

**Department of Physics and Astronomy
The University of Iowa
Iowa City, Iowa 52242**

April, 1980

Submitted to J. Geophys. Res.

**This work was supported in part by the National Aeronautics and
Space Administration and the Office of Naval Research under Contracts
NAS5-11431, NAS5-11074, NAS5-20093 and Grants NGL-16-001-043, N00014-
76-C-0016 and NGL-16-001-002.**

ABSTRACT

Two theories have been proposed that differently identify the frequencies of the low frequency cutoffs of nonthermal continuum radiation. The first of these theories states that the two low frequency cutoffs occur at the local plasma frequency and $R = 0$ cutoff frequency, with the continuum radiation propagating in the ordinary mode between the cutoffs and a mixture of ordinary and extraordinary mode above the upper cutoff. The second theory suggests that the two low frequency cutoffs occur at the local $L = 0$ cutoff frequency and plasma frequency, with the continuum radiation being generated by Cerenkov emission in the Z-mode between the local plasma frequency and upper hybrid resonance frequency. Mode coupling at the local plasma frequency is suggested to generate continuum radiation in the ordinary mode which freely propagates to remote regions of the magnetosphere. In this paper, several examples of continuum radiation observed in the outer magnetosphere by IMP 6 and ISEE 1 are analyzed in detail, and it is shown that these cutoff frequencies occur at the local plasma frequency and $R = 0$ cutoff frequency. In addition, no substantive evidence is found in the outer magnetosphere for a component of continuum radiation propagating in the Z-mode.

INTRODUCTION

Numerous observations of weak electromagnetic radiation emitted from the Earth's magnetosphere and from the Jovian magnetosphere have been made by several satellites, among them IMP 6, IMP 8, Hawkeye 1, ISEE 1 and 2, and Voyager 1 [Brown, 1973; Gurnett and Shaw, 1973; Gurnett, 1975; Scarf et al., 1979]. This radio emission, called the nonthermal continuum, consists of waves propagating in each of two high frequency modes possible in a magnetized plasma, which are commonly called the ordinary mode (O-mode) and the extraordinary mode (X-mode) [Allis, 1963].

Continuum radiation is observed in the Earth's magnetosphere at frequencies greater than the local plasma frequency. Because both the O-mode and the X-mode do not have access to regions where the wave frequency is less than the local plasma frequency, these waves are trapped within the Earth's magnetosphere at frequencies less than the solar wind plasma frequency, possibly escaping the magnetosphere through the geomagnetic tail [Gurnett, 1975; Melrose, 1980].

Direction-finding measurements have shown that continuum radiation from the Earth is emitted from a broad region several Earth radii thick outside the plasmapause on the dawn side of the magnetosphere. This region begins near local noon and extends through the local morning regions of the outer magnetosphere [Gurnett, 1975]. Frankel [1973] has

suggested that these waves could be generated by gyrosynchrotron radiation emitted by electrons in the 200 keV to 1 MeV energy range. Gurnett and Frank [1976], however, have observed the occurrence of a continuum radiation "storm" simultaneously with the injection of low-energy electrons, ~ 1 -30 keV, into the outer radiation zone, concluding that continuum radiation may be generated by some plasma instability involving electrons in this lower energy range. It has been suggested, for example, that continuum radiation may be generated by conversion of intense electrostatic waves into electromagnetic radiation [Gurnett, 1975; Gurnett and Frank, 1976; Kurth et al., 1979; Gurnett et al., 1979, and Melrose, 1980].

Continuum radiation in the Earth's magnetosphere is frequently observed to have two distinct lower frequency cutoffs that are sharp and well defined in high resolution frequency-time spectrograms obtained with the wideband receivers of the type flown on IMP 6, ISEE 1 and 2, and Voyager 1 and 2. Gurnett and Shaw [1973] previously identified the frequencies at which these two cutoffs occur using data from the IMP 6 plasma wave instrument. The lowest cutoff was determined to be at the local plasma frequency, f_p , and the upper cutoff at the local $R = 0$ cutoff frequency, $f_{R=0}$, where

$$f_{R=0} = \frac{f_g}{2} + \sqrt{f_p^2 + (f_g/2)^2} \quad , \quad (1)$$

and f_g is the local electron gyrofrequency [see Stix, 1962]. The plasma frequency and the $R = 0$ cutoff frequency are bounding frequencies below which no wave energy can exist in the O-mode and the X-mode, respectively.

The observation of the two lower frequency cutoffs is, thereby, readily explained by the propagation characteristics of O-mode and X-mode waves.

Recently, Jones [1976a; 1976b] proposed an alternative explanation for these lower frequency cutoffs. Jones suggested that energy is generated by Cerenkov emission from low-energy electrons at frequencies between the local upper-hybrid resonance frequency, f_{UHR} ,

$$f_{UHR} = \sqrt{f_p^2 + f_g^2} \quad , \quad (2)$$

and the greater of the plasma frequency or the electron gyrofrequency.

Similar radiation characterized by enhanced wave amplitudes in this frequency range has been observed by numerous investigators at lower altitudes in the ionosphere and plasmasphere [Walsh et al., 1964; Bauer and Stone, 1968; Gregory, 1969; Muldrew, 1970; Hartz, 1970; and Mosier et al., 1973]. These waves, called upper hybrid resonance noise, propagate in a third plasma wave mode at high frequencies in a cold, magnetized plasma. Waves in this mode, called the Z-mode, do not have access to regions where the wave frequency is greater than the local upper hybrid resonance frequency or less than the local $L = 0$ cutoff frequency, $f_{L=0}$.

$$f_{L=0} = \frac{-f_g}{2} + \sqrt{f_p^2 + (f_g/2)^2} \quad . \quad (3)$$

As a consequence, these waves are trapped in a limited region of space in the Earth's magnetosphere defined by bounding surfaces where the

$L = 0$ cutoff frequency and upper hybrid resonance frequency equal the wave frequency.

In contrast to upper hybrid resonance noise, continuum radiation is observed to extend over a much larger frequency range, consisting of waves at frequencies well above the local upper hybrid resonance frequency. Jones [1976a; 1976b] suggests that coupling between Z-mode waves and waves in the O-mode at frequencies near the local plasma frequency generates the nonthermal continuum, which subsequently propagates to remote regions in the magnetosphere at frequencies well above the local upper hybrid resonance frequency.

Based on this mechanism Jones has suggested that the identification of the lower frequency cutoffs of continuum radiation by Gurnett and Shaw [1973] was incorrect. Jones suggests that the lower cutoff actually occurs at the local $L = 0$ cutoff frequency instead of f_p , and that the upper cutoff occurs at f_p rather than at the $R = 0$ cutoff frequency.

Data are presented in this paper to demonstrate that these cutoffs are not at $f_{L=0}$ and f_p as suggested by Jones, hereafter called the $f_{L=0}/f_p$ theory, furthermore, that the original identification by Gurnett and Shaw, hereafter called the $f_p/f_{R=0}$ theory, is correct. Cutoff frequencies of the nonthermal continuum have been used to accurately measure the local plasma density in the low density regions of the Earth's magnetosphere [Gurnett and Frank, 1974] and Jupiter's magnetosphere [Scarf et al., 1979; Gurnett et al., 1979]; hence, the proper identification of these frequencies is important for confirming the accuracy of such measurements.

EXPERIMENTAL COMPARISONS OF THE $f_{R=0}/f_p$ THEORY
AND THE $f_p/f_{L=0}$ THEORY

Figure 1 is a frequency-time spectrogram of nonthermal continuum radiation observed by the plasma wave experiment on IMP 6 well beyond the plasmapause ($\sim 9 R_E$) near local morning. This spectrogram shows the wave electric field detected by one of the long electric dipole antennas on IMP 6. IMP 6 is spinning with a period of about eleven seconds, and the spin axis of the spacecraft is oriented normal to the ecliptic plane. The spectrogram in Figure 1 shows that the continuum radiation has two distinct low frequency cutoffs, labeled f_1 and f_2 in this figure. Waves at frequencies between f_1 and f_2 are observed to be highly spin modulated, while the waves at frequencies above f_1 have little, if any, spin modulation.

If the spacecraft spin axis is oriented perpendicular to the geomagnetic field, a single dipole antenna can be used to differentiate between wave electric fields aligned parallel and perpendicular to the magnetic field direction. This differentiation can be made because the antenna has a gain factor that is a maximum when the electric field vector is aligned parallel to the antenna elements and a minimum when the electric field vector is aligned perpendicular to the antenna elements. Accordingly, waves with electric fields parallel to the geomagnetic field will be spin modulated with nulls in the modulation occurring when

the antenna is perpendicular to the magnetic field direction. Similarly, waves with electric fields perpendicular to the magnetic field will have nulls in the spin modulation that occur when the antenna is parallel to the magnetic field direction.

For the data shown in Figure 1, the angle between the spin axis of IMP 6 and the geomagnetic field direction is 87 degrees. The components of the geomagnetic field were measured by the NASA/GSFC magnetometer experiment on IMP 6 and were provided by N. Ness and D. Fairfield of the Goddard Space Flight Center. Since the spacecraft spin axis is essentially perpendicular to the magnetic field direction, the orientation of the wave electric field vector can be determined for the data shown in Figure 1. The wave electric field between the two cutoff frequencies is oriented parallel to the geomagnetic field in each of these examples and also in all other cases that have been previously analyzed.

The cutoff frequencies shown in Figure 1 have been measured with an accuracy of ± 50 Hz, which is twice the bandwidth resolvable in the spectral analysis of these data. To test the $f_p/f_{R=0}$ theory it is assumed that $f_1 = f_{R=0}$ and that $f_2 = f_p$. Using (1) the electron gyrofrequency can be calculated from these two measurements by

$$f_g = f_1 \left(1 - \frac{f_2^2}{f_1^2} \right) \quad (4)$$

To test the $f_{L=0}/f_p$ theory it is assumed that $f_1 = f_p$ and that $f_2 = f_{L=0}$, and the electron gyrofrequency is calculated from (3) to be

$$f_g = f_2 \left(\frac{f_1^2}{f_2^2} - 1 \right) \quad (5)$$

These two equations, (4) and (5), yield different values for the electron gyrofrequency, which can be compared to the electron gyrofrequency derived from the value of the local magnetic field, B_0 , measured by the IMP 6 magnetometer ($f_g = 28 B_0$ where B_0 is in gamma). A comparison of the predictions of (4) and (5) with the measured gyrofrequency provides a definitive test for the validity of these two respective identifications of the cutoff frequencies.

The difference, Δf , between values of f_g obtained from (4) and (5) is often small, 10 to 20 percent of the measured gyrofrequency for most cutoff frequencies observed in the magnetosphere; therefore, high frequency resolution measurements are essential to unambiguously determine these cutoff frequencies. The value of Δf can be calculated by subtracting (4) from (5), and is given by (6)

$$\Delta f = \frac{(f_1 - f_2)^2 (f_1 + f_2)}{f_1 f_2} \quad (6)$$

Using (4) and (5) to calculate the value of f_g at about 2200:30 UT from the data shown in Figure 1 we have, including the measurement uncertainty,

$$1.62 \text{ kHz} < f_g < 1.96 \text{ kHz} \quad (f_{R=0}/f_p \text{ theory})$$

$$1.92 \text{ kHz} < f_g < 2.41 \text{ kHz} \quad (f_p/f_{L=0} \text{ theory})$$

$$f_g = 1.73 \text{ kHz} \quad (\text{NASA/GSFC Magnetometer})$$

It is apparent that the value of f_g calculated from the $f_p/f_{L=0}$ theory does not agree with the value of f_g measured by the IMP 6 magnetometer, even considering a conservative estimate of ± 30 Hz for the accuracy of the frequency measurement obtained by use of the high resolution IMP 6 wideband data. Furthermore, the value of f_g calculated from the $f_{R=0}/f_p$ theory is in agreement with the value of f_g measured by the IMP 6 magnetometer.

In order to demonstrate that this agreement is representative of more than one isolated example, a total of ten examples of continuum radiation exhibiting sharp low frequency cutoffs with spin modulation were selected for analysis. These examples were selected from wideband data collected from the IMP 6 spacecraft and the ISEE 1 spacecraft. The result of this analysis is shown in Figure 2.

Figure 2 contains two graphs that compare the measured electron gyrofrequency with the electron gyrofrequency calculated from the $f_{L=0}/f_p$ theory and the $f_p/f_{R=0}$ theory. It is evident that the values of the electron gyrofrequency calculated from the $f_{L=0}/f_p$ theory are not in general agreement with the magnetometer measurements made simultaneously with the plasma wave measurements. In particular, the only data for which any agreement is achieved are at low values of Δf , for which differentiation between the two theories would be expected to be difficult due to the experimental uncertainties in the measurement. In contrast with this result, the values of the electron gyrofrequency calculated from the $f_p/f_{R=0}$ theory agree with the magnetometer measurements for all ten examples selected. The results of the analysis shown in Figure 2 demonstrate that these cutoffs are at the local plasma frequency and $R = 0$ cutoff frequency as originally proposed by Gurnett and Shaw [1973]

and not at the $L = 0$ cutoff frequency and plasma frequency as suggested by Jones [1976a; 1976b].

In addition to the conclusive evidence already provided, several other observations also indicate that the theory proposed by Jones is not applicable to continuum radiation in the outer magnetosphere. Figures 3 and 4 show the amplitudes of two examples of continuum radiation plotted as a function of frequency. These plots contain a superposition of spectrum analyzer sweeps (0.05 seconds/sweep) obtained over the two second interval defined by the arrows pointing to the spectrogram in the top panel of Figures 3 and 4. Neither example shows any evidence of an increase in the wave amplitudes between f_p and f_{UHR} , where waves generated locally by Cerenkov radiation would be expected to be found. Enhancements greater than 20 db between f_p and f_{UHR} are characteristic of Z-mode waves produced by Cerenkov emission in the plasmasphere and ionosphere (see Figure 1 of Hartz [1970] and Figure 4 of Mosier et al. [1973] for examples).

The absence of an enhancement in amplitude between f_p and f_{UHR} strongly suggests that continuum radiation observed in the outer magnetosphere does not contain any substantive component locally generated in the Z-mode. Instead, it is apparent that these waves are predominantly O-mode and X-mode waves that appear to have propagated to the spacecraft from more distant sources. Occasionally cases are observed that contain more complicated frequency structures, which may be related to the generation of these waves. These structures usually resemble harmonic bands or discrete emissions, however, and appear to be considerably different

from structures expected for waves generated by Cerenkov emission in the Z-mode (see Gurnett and Shaw [1973] for representative examples).

In addition to the arguments already presented, an examination of the polarization of the wave electric field of the nonthermal continuum near these cutoff frequencies provides strong evidence that these waves are predominately O-mode and X-mode waves. It can be shown (see Stix [1962]) that the wave electric field vector for the X-mode is perpendicular to the magnetic field and circularly polarized, rotating around the magnetic field in the right-hand sense at the $R = 0$ cutoff frequency. The wave electric field vector for the O-mode is linearly polarized in the direction parallel to the magnetic field direction at the plasma frequency.

For waves in the Z-mode generated by Cerenkov emission, the wave electric field would be expected to be most intense in the direction of the resonance cone, which varies from an angle of 90 degrees with respect to the magnetic field at f_{UHR} to 0 degrees at the greater of f_p or f_g . At the $L = 0$ cutoff frequency the electric field is perpendicular to the magnetic field and circularly polarized rotating around the magnetic field in the left-hand sense. At f_{UHR} the wave electric field is linearly polarized perpendicular to the geomagnetic field.

The polarization of the continuum radiation near the two lower cutoffs is readily explained by the characteristics of the ordinary and extraordinary modes. Of the X-mode, the O-mode, and the Z-mode, only the O-mode is oriented parallel to the geomagnetic field direction at any bounding frequency. The X-mode is strongly polarized perpendicular to

the geomagnetic field at $f_{R=0}$. Consequently, if O-mode radiation is present between the two cutoffs and a mixture of O-mode and X-mode radiation is present above the upper frequency cutoff, the observed polarization can be explained in a straight forward manner by the characteristics of O-mode and X-mode radiation. If the lower cutoff occurred at the $f_{L=0}$ cutoff frequency, however, the observed polarization would be completely inconsistent with the characteristics of Z-mode radiation at the $L = 0$ cutoff frequency. In summary, the observed polarization is contrary to that predicted by the $f_{L=0}/f_p$ theory [Jones, 1976a; 1976b] and completely consistent with that predicted by the $f_p/f_{R=0}$ theory [Gurnett and Shaw, 1973].

DISCUSSION

We have shown, in some detail, that the characteristics of non-thermal continuum radiation observed in the outer magnetosphere are consistent with the expected characteristics of ordinary and extraordinary mode waves described by cold plasma theory. The alternate theory, proposed by Jones [1976a; 1976b], does not maintain consistency between theory and observation in several ways. First, this theory is not consistent with measurements of the local magnetic field made by the IMP 6 magnetometer. Second, there is no definite indication of a substantive component of continuum radiation observed in the Z-mode in the outer magnetosphere. If, as according to Jones, the continuum is produced in this region by Cerenkov radiation in the Z-mode, subsequently coupling into O-mode radiation at the local plasma frequency, significant wave electric fields would be expected to be observed in the Z-mode. Finally, the observed polarization of the wave electric field at the cutoff frequencies is inconsistent with that predicted using Jones' interpretation.

We wish to emphasize that, while we disagree completely with Jones' identification of these cutoff frequencies, which are commonly observed in the outer magnetosphere, we do not necessarily disagree with his hypothesis that mode coupling between the O-mode and the Z-mode may occur in some regions of the magnetosphere. In other regions, for example within the plasmasphere, energy generated by Cerenkov radiation in the Z-mode coupling into O-mode radiation might generate freely propagating radio

emissions at higher frequencies. In the outer magnetosphere, however, there is little evidence to indicate that substantial wave energy is generated by Cerenkov radiation at frequencies below about 30 kHz or that this mechanism contributes significantly to the generation of continuum radiation. Most of the local generation of waves near f_p and f_g in the outer magnetosphere appears to require generation mechanisms characteristic of other types of plasma instabilities, such as those proposed to explain $(n + 1/2)f_g$ harmonics [Fredricks, 1971; Young et al., 1973; Ashour-Abdalla and Kennel, 1978; Hubbard and Birmingham, 1978; Rönmark et al., 1978].

ACKNOWLEDGEMENTS

We thank Drs. N. Ness and D. Fairfield for providing measurements of the local geomagnetic field with the NASA/GSFC magnetometer on IMP 6 and Dr. C. Russell for providing measurements of the local geomagnetic field with the UCLA magnetometer on ISEE 1.

This work was supported in part by the National Aeronautics and Space Administration and The Office of Naval Research under Contracts NAS5-11431, NAS5-11074, NAS5-20093, and Grants NGL-16-001-043, N00014-76-C-0016, and NGL-16-001-002.

REFERENCES

- Allis, W. P., S. J. Buchsbaum, and A. Bers, Waves in Anisotropic Plasmas, MIT Press, Cambridge, MA, 30, 1963.
- Ashour-Abdalla, M., and C. F. Kennel, Nonconvective and convective electron cyclotron harmonic instabilities, J. Geophys. Res., 83, 1531, 1978.
- Bauer, S. J., and R. G. Stone, Satellite observations of radio noise in the magnetosphere, Nature, 218, 1145, 1968.
- Brown, L. W., The galactic radio spectrum between 130 kHz and 2600 kHz, Astrophys. J., 180, 359, 1973.
- Frankel, M. S., LF radio noise from the Earth's magnetosphere, Radio Sci., 8, 991, 1973.
- Fredricks, R. W., Plasma instability at $(n + 1/2)f_c$ and its relationship to some satellite observations, J. Geophys. Res., 76, 5344, 1971.
- Gregory, P. C., Radio emission from auroral electrons, Nature, 221, 350, 1969.

Gurnett, D. A., and R. R. Shaw, Electromagnetic radiation trapped in the magnetosphere above the plasma frequency, J. Geophys. Res., 78, 8136, 1973.

Gurnett, D. A., and L. A. Frank, Thermal and suprathermal plasma densities in the outer magnetosphere, J. Geophys. Res., 79, 2355, 1974.

Gurnett, D. A., The earth as a radio source: The nonthermal continuum, J. Geophys. Res., 80, 2751, 1975.

Gurnett, D. A., and L. A. Frank, Continuum radiation associated with low-energy electrons in the outer radiation zone, J. Geophys. Res., 81, 3875, 1976.

Gurnett, D. A., W. S. Kurth, and F. L. Scarf, Plasma wave observations near Jupiter: Initial results from Voyager 2, Science, 206, 987, 1979.

Hartz, T. R., Low frequency noise emissions and their significance for energetic particle processes in the polar ionosphere, The Polar Ionosphere and Magnetospheric Processes, Gordon Breach Publishing Co., New York, 151, 1970.

Hubbard, R. F., and T. J. Birmingham, Electrostatic emissions between electron gyroharmonics in the outer magnetosphere, J. Geophys. Res., 83, 4837, 1978.

Jones, D., Mode coupling of Cerenkov radiation as a source of noise above the plasma frequency, The Scientific Satellite Programme During the International Magnetospheric Study, ed. by K. Knott and B. Batrick, D. Reidel Publishing Co., Dordrecht, Holland, 281, 1976a.

Jones, D., Source of terrestrial nonthermal radiation, Nature, 260, 686, 1976b.

Kurth, W. S., J. D. Craven, L. A. Frank, and D. A. Gurnett, Intense electrostatic waves near the upper hybrid resonance frequency, J. Geophys. Res., 84, 4145, 1979.

Melrose, D. B., A theory for the nonthermal radio continua in the terrestrial and Jovian magnetospheres, J. Geophys. Res., (submitted for publication), 1980.

Mosier, S. R., M. L. Kaiser, and L. W. Brown, Observations of noise bands associated with the upper hybrid resonance by the IMP 6 radio astronomy experiment, J. Geophys. Res., 78, 1673, 1973.

Muldrew, D. B., Preliminary results of ISIS 1 concerning electron density variations, ionospheric resonances, and Cerenkov radiation, Space Research X, North-Holland Publishing Co., Amsterdam, Holland, 786, 1970.

Rönnmark, K., H. Borg, P. J. Christiansen, M. P. Gough, and D. Jones, Banded electron cyclotron harmonic instability - a first comparison of theory and experiment, Space Sci. Rev., 22, 401, 1978.

Scarf, F. L., D. A. Gurnett, and W. S. Kurth, Jupiter plasma wave observations: An initial Voyager 1 overview, Science, 204, 991, 1979.

Stix, T. H., The Theory of Plasma Waves, McGraw-Hill, New York, 27, 1962.

Walsh, D., F. T. Haddock, and H. F. Schulte, Cosmic radio intensities at 1.225 and 2.0 Mc measured up to an altitude of 1700 km, Space Research IV, North-Holland Publishing Co., Amsterdam, Holland, 935, 1964.

Young, T. S. T., J. D. Callen, and J. E. McCune, High-frequency electrostatic waves in the magnetosphere, J. Geophys. Res., 78, 1082, 1973.

13

FIGURE CAPTIONS

Figure 1

An example of continuum radiation containing two lower frequency cutoffs and spacecraft spin modulation. The lower frequency cutoffs, f_1 and f_2 , were measured at about 2200:30 UT as indicated by the dashed line. For this example:

$$1.62 \text{ kHz} < f_g < 1.96 \text{ kHz if } f_1 = f_{R=0} \text{ and } f_2 = f_p$$

$$1.92 \text{ kHz} < f_g < 2.41 \text{ kHz if } f_1 = f_p \text{ and } f_2 = f_{L=0}$$

$$f_g = 1.73 \text{ kHz (NASA/GSFC magnetometer)}$$

The identification $f_1 = f_p$ and $f_2 = f_{L=0}$ is inconsistent with the IMP 6 magnetometer measurements; however, the identification $f_1 = f_{R=0}$ and $f_2 = f_p$ is in agreement with the magnetometer measurements.

Figure 2

An analysis of ten examples of continuum radiation observed by IMP 6 and ISEE 1. Within the experimental accuracies of measurement, the electron gyrofrequency calculated from the $f_p/f_{R=0}$ theory, f_{gCALC} , agrees with the simultaneous magnetometer measurements, f_{gMEAS} . The electron gyrofrequency calculated from the $f_{L=0}/f_p$ theory is not in agreement with f_{gMEAS} except for small values of Δf , the difference between the two calculated

gyrofrequencies. For small values of Δf , it is expected that it would be difficult to distinguish between the two theories because of the experimental uncertainties in the measurement.

Figure 3

The lower panel shows the amplitude of an example of continuum radiation as a function of frequency. These data were collected over the time interval shown on the frequency-time spectrogram in the upper panel. The abrupt lower frequency cutoff is apparent at 7.1 kHz; however, no enhanced wave amplitudes are observed between f_p and f_{UHR} , strongly suggesting that no substantive wave components are generated by Cerenkov radiation in this frequency interval.

Figure 4

The amplitude of the continuum radiation shown in Figure 2 as a function of frequency. Again, no enhanced amplitudes are observed for waves between f_p and f_{UHR} , as is typical of upper hybrid resonance noise observed at lower amplitudes within the plasmasphere and ionosphere.

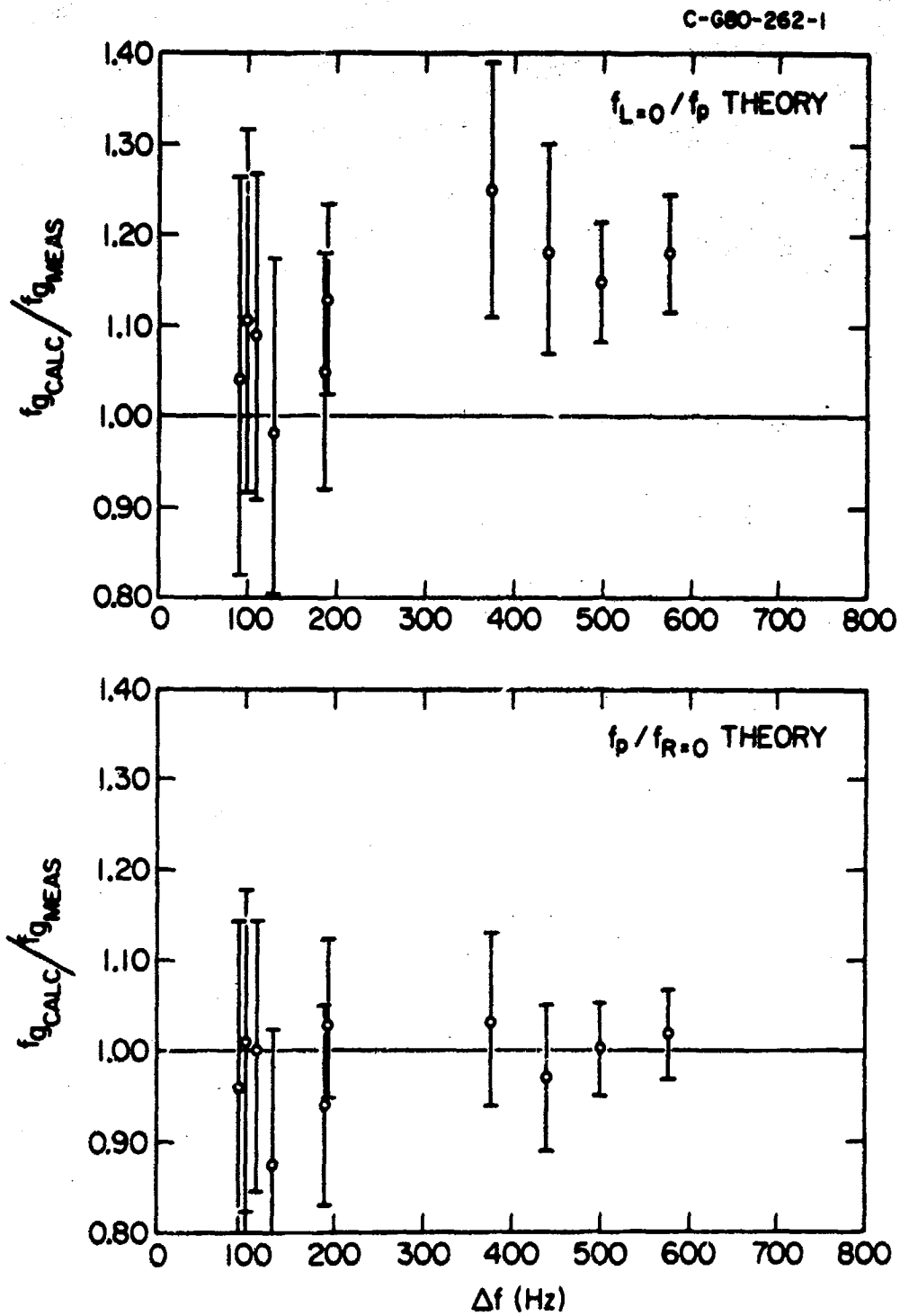


Figure 2

PRECEDING PAGE BLANK NOT FILMED

PLASMA OSCILLATIONS AND THE EMISSIVITY OF TYPE III RADIO BURSTS

D. A. Gurnett, R. R. Anderson and R. L. Tokar
Department of Physics and Astronomy
The University of Iowa
Iowa City, Iowa 52242

ABSTRACT

Plasma wave electric field measurements with the solar orbiting Helios spacecraft have shown that intense electron plasma oscillations occur in association with type III solar radio bursts, thereby confirming a well known mechanism for generating solar radio emissions first proposed by Ginzburg and Zheleznyakov in 1958. In this paper we review the principal characteristics of these plasma oscillations and compare the observed plasma oscillation intensities with recent measurements of the emissivity of type III radio bursts. The observed emissivities are shown to be in good agreement with two current models for the conversion of electrostatic plasma oscillations to electromagnetic radiation.

INTRODUCTION

As known from early studies of Wild [1950] type III radio bursts are produced by particles ejected from a solar flare and are characterized by an emission frequency which decreases with increasing time. The decreasing emission frequency with increasing time is attributed to the decreasing electron plasma frequency, f_p , encountered by the solar flare particles as they move outward through the solar corona. Emission can occur at either the fundamental, f_p , or harmonic, $2f_p$, of the local electron plasma frequency, although at low frequencies, ≤ 1 MHz, the harmonic emission appears to be the dominant component [Fainberg, 1974; Kaiser, 1975; Gurnett et al., 1978]. The particles responsible for the type III radio emissions are electrons with energies ranging from a few Kev to several tens of Kev. According to current ideas, the generation of the type III radiation is a two-step process in which (i) electron plasma oscillations are first produced at f_p by a two-stream instability excited by the solar flare electrons and (ii) the plasma oscillations are converted to electromagnetic radiation by nonlinear wave-particle interactions. This mechanism, first proposed by Ginzburg and Zheleznyakov [1958] and refined by numerous investigators [Tidman et al., 1966;

Kaplan and Tystovich, 1968; Papadopoulos et al., 1974; Smith, 1977], is illustrated in Figure 1, which shows the expected conversion of the electron stream energy to electron plasma oscillations, and the subsequent conversion to electromagnetic radiation at either the fundamental, f_p , or the harmonic, $2f_p$. The radiation at the fundamental is caused by interactions of the plasma oscillations with ion sound waves, and the radiation at the harmonic is caused by interactions between oppositely propagating electron plasma oscillations.

Since electron plasma oscillations are local plasma wave phenomena which cannot be detected remotely, in situ measurements must be used to confirm the presence of these oscillations. The first observations of electron plasma oscillations associated with a type III solar radio burst were obtained by Gurnett and Anderson [1976, 1977] using measurements from the Helios 1 and 2 spacecraft which are in orbit around the sun between about 0.3 to 1.0 A.U. The Helios observations are important not only because they confirm a basic radio emission mechanism proposed over twenty years ago, but also because they provide important new information on nonlinear plasma processes of considerable current interest. In this paper we review the principal results of the Helios plasma oscillation observations, including many new events which have been recently detected. The plasma oscillation intensities are also compared with the recent type III radio emissivity measurements given by Tokar and Gurnett [1979], to provide a quantitative evaluation of proposed emission mechanisms.

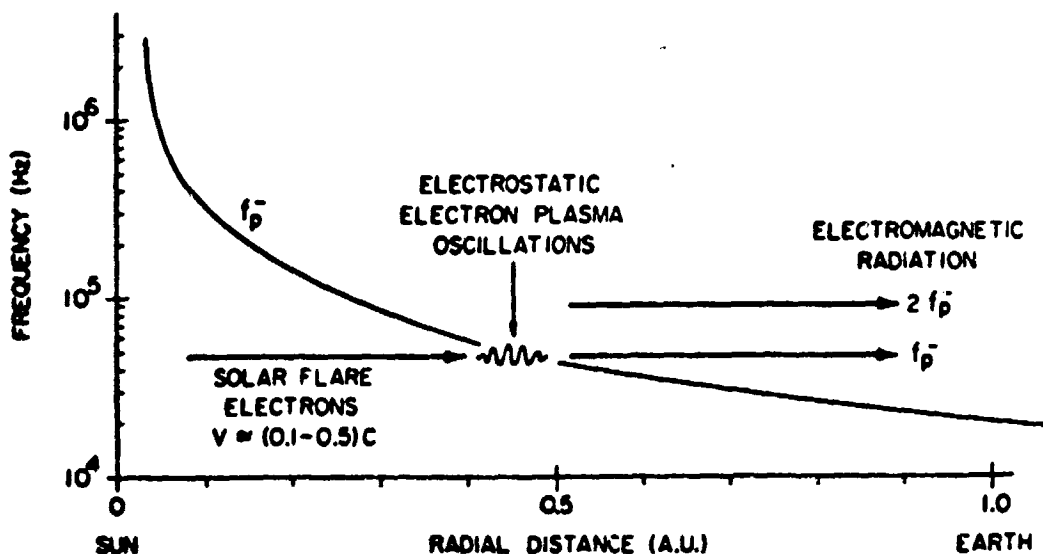


Figure 1. A representative radial profile of the electron plasma frequency in the solar wind illustrating the generation of electron plasma oscillations and the subsequent conversion to electromagnetic radiation at f_p and $2f_p$.

SURVEY OF PLASMA OSCILLATION CHARACTERISTICS

Only a small fraction, approximately 15%, of all the type III radio bursts detected by Helios can be associated with electron plasma oscillations. The relatively small occurrence of plasma oscillation events is almost certainly due to the fact that the radio emissions can be detected at large distances from the source, whereas the plasma oscillations can only be detected within the source region. Up to the present time a total of ninety electron plasma oscillation events have been identified in all the data available, which includes Helios 1 and 2, Voyager 1 and 2, and IMP 8. All but four of these events were detected by Helios 1 and 2.

A plasma oscillation event illustrating most of the features commonly observed is shown in Figure 2. The type III radio emission can be clearly identified in the 178 and 100 kHz channels by the rapid smooth rise to peak intensity followed by a somewhat longer smooth decay. The characteristic shift toward decreasing frequency with increasing time is also clearly evident. The intense narrow-band emissions in the 56.2 kHz channel, starting at about 1023 UT and ending about 1055 UT, are the associated electron plasma oscillations. The solid line is the peak

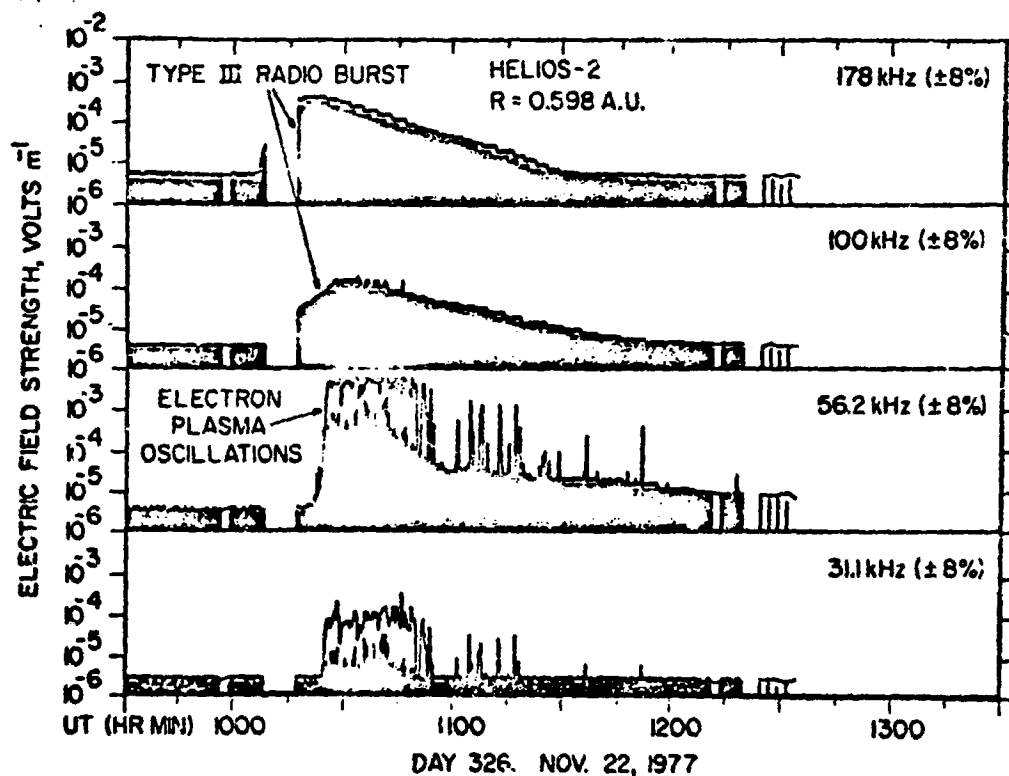


Figure 2. Intense electron plasma oscillations at $f_p^- = 56$ kHz detected by Helios 2 in association with a type III radio burst.

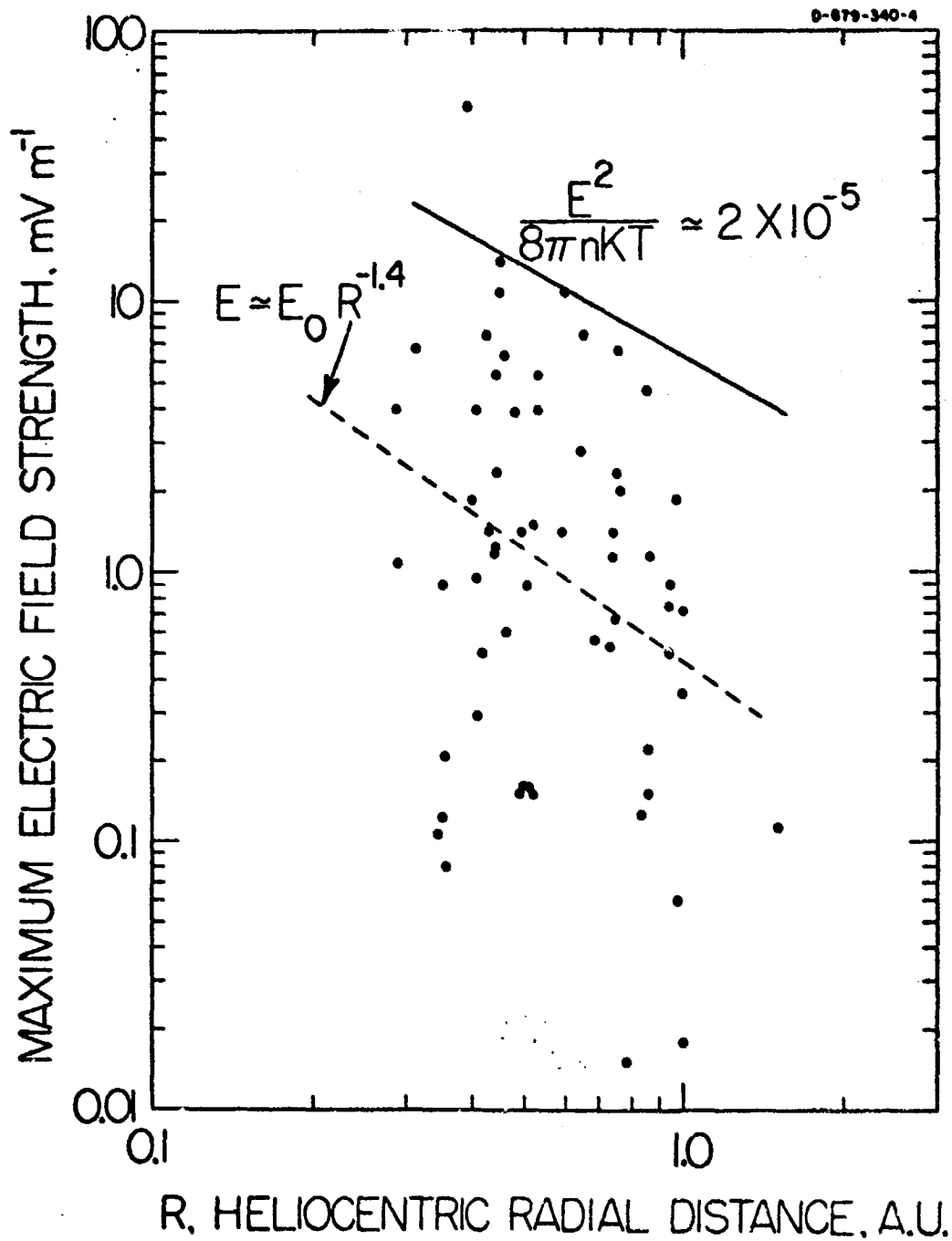


Figure 3. A plot of the peak electric field strength for all of the plasma oscillation events with type III bursts detected to date as a function of radial distance from the sun.

from about 0.3 to 1.0 A.U. where in situ measurements of plasma observations are available. In principle, a comparison of the radial variation of the plasma oscillation intensities and the type III emissivity provides a powerful test, since any given mechanism implies a specific relationship between these two parameters. Recently Tokar and Gurnett [1979] have completed an analysis of the radial variation of the emissivity of low frequency type III radio bursts. The technique used consists of computing the power ΔP emitted in volume ΔV with the emissivity defined as $J(2f_p) = \Delta P / 4\pi \Delta V$, where it is assumed, for simplicity, that the radiation is emitted isotropically over a solid angle of 4π . The power is computed from $\Delta P = 4\pi r^2 I \Delta f$, where r is the distance from the source to the spacecraft, Δf is the bandwidth and I is the power flux, in watts $m^{-2} Hz^{-1}$, at the spacecraft. The volume is computed from $\Delta V = R^2 \Delta \Omega$, where Ω is the solid angle of the emitting region as viewed from the sun. Since it is usually not possible to directly determine Ω , we have assumed that the source subtends a half-angle of 45.0° as viewed from the sun, which is consistent with the results of Baumbach et al. [1976]. The center of the source volume is assumed to follow the magnetic field line through the originating flare location using the magnetic field model of Parker [1958] with a solar wind velocity of $400 km s^{-1}$. The emission frequency is assumed to be at the harmonic of plasma frequency, following the radial variation given by Fainberg and Stone [1974]. The results of this analysis, as applied to thirty-six type III radio bursts, are shown in Figure 4. Because of the uncertainty in the solid angle Ω the absolute value of J probably has a substantial uncertainty, perhaps as much as a factor of 2 or 3. This uncertainty is, however, small compared to the variations from event to event. Except for certain special cases, for example when the source passes close to the spacecraft, the radial dependence tends to be rather independent of the assumptions used. In all cases the emissivity decreases monotonically with increasing radial distance from the sun and a power law provides a good fit to the radial variation. The average power law index for all of the events analyzed is -6.0 ± 0.3 . The best fit power law through all of the data points is shown by the dashed curve in Figure 4.

Having established the radial dependence and absolute intensity of both the plasma oscillations and the radio emissivity, comparisons can now be made with specific models for the generation of type III radio bursts. Two models will be evaluated, the coherent parametric (oscillating two-stream) mechanism of Papadopoulos et al. [1974], and the incoherent induced scattering mechanism of Smith [1977]. The emissivity given by Papadopoulos et al. [1974], converted to MKS units and evaluating constants (using $\alpha = 0.1$), is

$$J(2f_p) = 5.83 \times 10^{-15} \left(\frac{T}{T_0} \right)^{3/2} \frac{E^4}{\sqrt{n}}, \text{ watts } m^{-3} sr^{-1}, \quad (1)$$

where E is the electric field strength of the plasma oscillations in Volts m^{-1} , n is the electron density in cm^{-3} , T is the electron

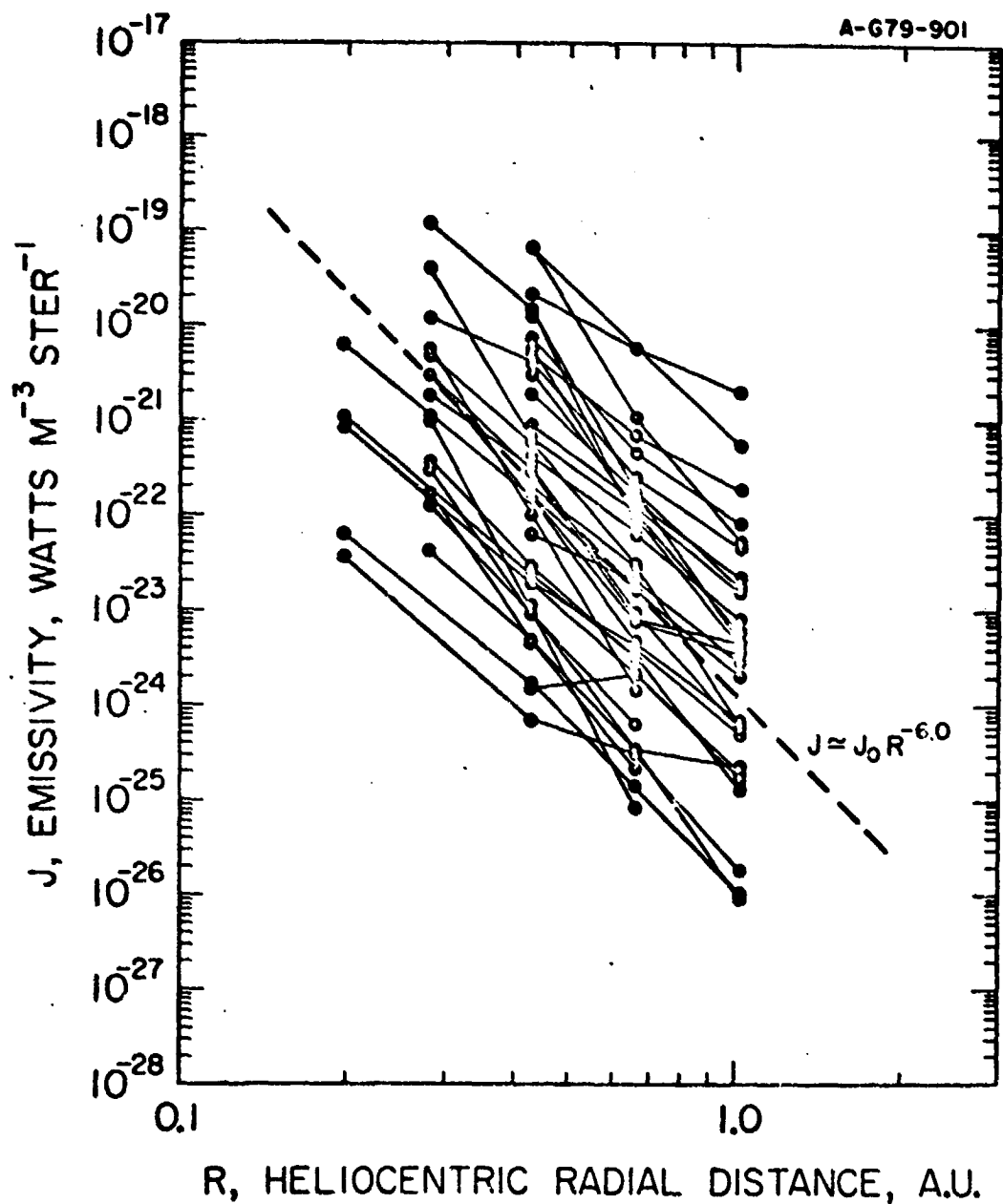


Figure 4. The emissivity as a function of radial distance from the sun determined from thirty-six type III radio bursts detected by IMP 8 and ISEE 1.

temperature in $^{\circ}\text{K}$, and T_0 is the electron temperature at 1 A.U., $\sim 1.2 \times 10^5$ K. The corresponding emissivity given by Smith [1977] is

$$J(2f_p^-) = 1.12 \times 10^{-13} \frac{E^4}{\sqrt{n}}, \text{ watts m}^{-3} \text{ sr}^{-1}, \quad (2)$$

where E is again in Volts m^{-1} , and n is in cm^{-3} . Both the coherent and incoherent mechanisms have essentially the same dependence on the electric field strength and electron density, and differ only slightly in the temperature dependence. As can be seen the dominant dependence, by far, is on the electric field strength of the plasma oscillations. Since the electron density and temperature in the solar wind vary as $n \sim (1/R)^2$ and $T \sim (1/R)^{2/7}$, and since J varies as $(1/R)^{6.0 \pm 0.3}$, the expected radial variation of E from Equation 1 for the model of Papadopoulos et al. [1974] should be $(1/R)^{1.64 \pm 0.1}$. For the model of Smith [1977] the corresponding radial variation of E from Equation 2 should be $(1/R)^{1.75 \pm 0.1}$. Both of these predictions compare very favorably with the observed radial variation for E of $(1/R)^{1.4 \pm 0.5}$.

In addition to comparing the radial variations with the theoretical predictions the absolute values of the emissivity can also be compared. From Figure 3 it is seen that the largest plasma oscillation field strength at 1 A.U. is about $E \approx 5 \text{ mVm}^{-1}$. Using this maximum field strength, the corresponding emissivities given by Papadopoulos et al. [1974], using Equation 1, and Smith [1977], using Equation 2, are 1.63×10^{-24} and $3.13 \times 10^{-23} \text{ watts m}^{-3} \text{sr}^{-1}$, respectively. Comparing these emissivities with Figure 4 it is seen that the emissivity computed from Smith's model would be able to account for about 85% of all the events observed at 1.0 A.U., whereas Papadopoulos' model would be able to account for only about 30% of the events observed. Thus, it appears that for the largest plasma oscillation intensities observed the incoherent model of Smith [1977] is able to account for the emissivity of all but the most intense radio bursts, whereas the model of Papadopoulos et al. [1974] is not able to account for a burst of average intensity. It should also be pointed out that Smith [1977] has already demonstrated in a specific case that the incoherent mechanism can account for the simultaneously observed radio emission intensities with a substantial margin. The case considered by Smith [1977] was, however, a particularly intense plasma oscillation event, with an intensity (14.8 mVm^{-1}) near the upper limits of the events shown in Fig 3. If instead of taking the most intense plasma oscillation event, one takes more typical intensities representative of, for example, the best fit power law (dashed line) in Figure 3, then the emissivity is drastically reduced because of the E^4 dependence in Equations 1 and 2. For these more typical plasma oscillation intensities, both the models of Papadopoulos et al. [1974] and Smith [1977] give emissivities well below the best fit curve (dashed line) shown in Figure 4. These difficulties are further complicated by the fact that the actual volume of the source is probably substantially smaller than has been assumed in Equations 1 and 2 because of the impulsive variations in the amplitude of the plasma oscillations. In summary it appears that the radial variation of the plasma oscillation intensities and type III emissivity are in good agreement with the current theoretical models but that in all except for the most intense plasma oscillation events the emissivity given by the theory is somewhat smaller than the observed emissivity. Several explanations can be advanced to account for this discrepancy in the absolute emissivity. Probably

the most likely possibility is that the plasma oscillations have substantial temporal fluctuations on a time scale short compared to the 50 msec. averaging time of the Helios instrument. If the fluctuations are very impulsive, as seems to be the case, then because of the E^4 dependence of the emissivity the radiation intensity may be substantially underestimated on the basis of the average electric field intensity. Another possibility is that the intense plasma oscillations are confined to very small spatial regions which are very unlikely to be encountered by the spacecraft, thereby tending to bias the electric field intensity measurements, as in Figure 3, more heavily toward lower intensities.

CONCLUSION

These comparisons of plasma oscillation intensities and the emissivity of type III radio bursts show good overall agreement with current theories for the conversion of electron plasma oscillations to electromagnetic radiation at $2f_p$. The primary questions remaining involve the fine time scale structure of the plasma oscillations and the relative importance of incoherent and coherent (soliton collapse) processes. Although the absolute emissivities computed in this study tend to favor the incoherent process, it is probably not possible to determine which mechanism is most important because of the uncertainty about the fine time scale variations in the plasma oscillation intensity. Further progress in understanding the possible role of soliton collapse processes in the generation of type III radio emissions will require much higher time resolution measurements than are currently available.

ACKNOWLEDGEMENTS

The authors wish to thank Drs. D. Smith and D. Papadopoulos for their assistance in the interpretation of these results, and A. Persoon for her help in analyzing the data. This research was supported by NASA through Grant NGL-16-001-043 and Contracts NAS5-11279, NAS5-11431, and NAS5-20093 with the University of Iowa. Part of this research was also conducted while one of us (D. Gurnett) was on leave at the Institute of Geophysics and Planetary Physics, University of California, Los Angeles.

REFERENCES

- Baumback, M.M., Kurth, W.S., and Gurnett, D.A.: 1976, Solar Phys. 48, p. 361.
- Fainberg, J., and Stone, R.G.: 1974, Space Sci. Rev. 16, p. 145.
- Ginzburg, V.L., and Zheleznyakov, V.V.: 1958, Sov. Astron. AJ2, p. 653.
- Gurnett, D.A., Baumback, M.M., and Rosenbauer, H.: 1978, J. Geophys. Res. 83, p. 616.
- Gurnett, D.A., and Anderson, R.R.: 1976, Science 194, p. 1159.

- 16
- Gurnett, D.A., and Anderson, R.R.: 1977, J. Geophys. Res. 82, p. 632.
Hundhausen, A.J.: 1972, Coronal Expansion and Solar Wind, Springer,
Berlin Heidelberg N. York, p. 58.
Kaiser, M.L.: 1975, Solar Phys. 45, p. 181.
Kaplan, S.A., and Tsyтовich, V.N.: 1968, Sov. Astron. AJ 11, p. 956.
Nicholson, D.R., Goldman, M.V., Hoyng, P., and Weatherall, J.C.: 1978,
Ap. J. 223, p. 605.
Papadopoulos, K., Goldstein, M.L., and Smith, R.A.: 1974, Astrophys. J.
190, p. 175.
Parker, E.N.: 1958, Ap. J. 128, p. 664.
Smith, D.F.: 1970, Adv. Astr. Ap. 7, p. 147
Smith, D.F.: 1977, Astrophys. J. 216, p. L53.
Tidman, D.A., Birmingham, T.J., and Stainer, H.M.: 1966, Astrophys. J.
146, p. 207.
Tokar, R.L., and Gurnett, D.A.: 1979, J. Geophys. Res., submitted for
publication.
Wild, J.P.: 1950, Aust. J. Sci. Ser. A3, p. 541.

**INTERPLANETARY PARTICLES AND FIELDS, NOVEMBER 22 - DECEMBER 6, 1977:
HELIOS, VOYAGER, AND IMP OBSERVATIONS BETWEEN 0.6 AU AND 1.6 AU**

by

L. Burlaga

R. Lepping

R. Weber

**NASA/Goddard Space Flight Center
Laboratory for Extraterrestrial Physics
Greenbelt, MD 20771**

T. Armstrong

University of Kansas

Dept. of Physics

Lawrence, KS 66044

C. Goodrich

J. Sullivan

**Massachusetts Institute of Technology
Cambridge, MA 02139**

D. Gurnett

University of Iowa

Dept. of Physics & Astronomy

Iowa City, IA 52242

P. Kellogg

University of Minnesota

Dept. of Physics

Minneapolis, MN 55455

E. Keppler

Max-Planck-Institut fur Aeronomie

Lindau/Harz

FEDERAL REPUBLIC OF GERMANY

F. Mariani

Istituto Fisica G. Marconi

Citta Universita

Rome, ITALY

F. Neubauer

Institut fur Geophysik der T. U.

3300 Braunschweig, Mendelssohnstr. 1A

FEDERAL REPUBLIC OF GERMANY

H. Rosenbauer

R. Schwenn

Max-Planck-Institut fur Aeronomie

Katlenburg-Lindau 3

FEDERAL REPUBLIC OF GERMANY

SUBMITTED TO: Journal of Geophysical Research

ABSTRACT

In the period November 22 - December 6, 1977, three types of interplanetary flows were observed--a corotating stream, a flare-associated shock wave, and a shock wave driven by ejecta. Helios-2, IMP-7, 8, and Voyager-1, 2 were nearly radially aligned at \approx 0.6 AU, 1 AU and 1.6 AU, respectively), while Helios-1 was at \approx 0.6 AU and 35° E of Helios-2. The instruments on these spacecraft provided an exceptionally complete description of the particles and fields associated with the three flows and corresponding solar events. Analysis of these data revealed the following results. 1) A coronal hole associated corotating stream, observed at 0.6 AU and 1 AU, which was not seen at 1.6 AU. The stream interface corotated and persisted with little change in structure even though the stream disappeared. A forward shock was observed ahead of the interface, and moved from Helios-2 at 0.6 AU to Voyager-1, 2, at 1.6 AU; although the shock was ahead of a corotating stream and interface, the shock was not corotating, because it was not seen at Helios-1, probably because the corotating stream was not stationary. 2) An exceptionally intense type III burst was observed in association with a 2B flare of November 22. The exciter of this burst--(a beam of energetic electrons)--and plasma oscillations (presumably caused by the electron beam) were observed by Helios-2. 3) A non-spherical shock was observed in association with the November 22, flare. This shock interacted with another shock between 0.6 AU and 1 AU, and they coalesced to form a single shock that was identified at 1 AU and at 1.6 AU. 4) A shock driven by ejecta was studied. In the ejecta the density and temperature were unusually low and the magnetic field intensity was relatively high. This region was preceded by a directional discontinuity at which the magnetic field intensity dropped appreciably. The shock appeared to move globally at a uniform speed, but locally there were fluctuations in speed and direction of up to 100 km/s and 40° , respectively. 5) Three types of electrostatic waves were observed at the shocks, in different combinations. The detailed wave profiles differed greatly among the shocks, even for spacecraft separations \lesssim 0.2 AU, indicating a strong dependence on local conditions. However, the same types of fluctuations were observed at 0.6 AU and at 1.6 AU. 6) Energetic (50-200 keV) protons were accelerated by the shocks. The intensities and

1

durations of the fluxes varied by a factor of 12 over longitudinal distances of ~ 0.2 AU. The intensities were higher and the durations were lower at 1.6 AU than at 0.6 AU, suggesting a cumulative effect. 7) Energetic (~ 50 keV) protons from the November 22, flare were observed by all the spacecraft. During the decay, Helios-1 observed no change in intensity when the interface moved past the spacecraft, indicating that particles were injected and moved uniformly on both sides of the interface. Helios-2 observed an increase in flux not seen by Helios-1, reaching maximum at the time that a shock arrived at Helios-2. The intensity dropped abruptly when the interface moved past Helios-2, indicating that the "extra" particles seen by Helios-2 did not penetrate the interface.

1. INTRODUCTION

It is customary to speak of three types of flows in the solar wind, which Chapman (1964) called streams, flare-shells, and solar wind. We shall refer to these, respectively, as 1) corotating streams (also known as corpuscular streams, stationary streams, and high-speed streams); 2) ejecta (also called nascent streams, flare ejecta, jets, active wind, drivers, and pistons); and 3) slow flows (also called quiet wind ambient wind and structureless wind). The term piston has been applied to both corotating streams (e.g., Dryer and Steinolfson, 1976) and to ejecta (e.g., Dryer et al., 1972). Corotating flows are separated from slow flows by a thin boundary called a stream interface (Belcher and Davis, 1971, Burlaga, 1974), which in some cases is a tangential discontinuity (Burlaga, 1974; Gosling et al., 1978). Ejecta are presumed to be separated from slow flows by a thin boundary called a contact surface (Lee and Chen, 1968, Dryer, 1979); this too is called a piston by some authors, (e.g., see Dryer, 1979). Both corotating streams and ejecta may be preceded by a shock.

There are numerous studies of the above phenomena based on observations from just one spacecraft, but these cannot separate spatial variations from temporal changes. Data from two or more widely separated spacecraft are needed to study non-stationary corotating streams, transient ejecta, and interacting flows. There have been relatively few such observational studies (e.g., Dryer et al., 1972; Gosling and Hundhausen, 1976; Intriligator, 1976; Lazarus et al., 1970; Schwenn et al., 1978, 1979; Smith and Wolfe, 1977, 1979; Vaisberg and Zastenker, 1976). Some attempts have been made to model multipoint observations (Gosling et al., 1976; Dryer et al., 1978a, 1978b).

In the period November 22 to December 6, 1977 Helios-1 and -2, IMP-7 and -8, and Voyager-1 and -2 were aligned very favorably for the investigation of solar outputs (Figure 1), and during this period, which was part of STIP Interval IV from October 15 to December 15, 1977, several significant solar events occurred. Recognizing that this interval (and a similar interval in September-October, 1977) offered a unique opportunity for a comprehensive study of interplanetary shocks, flows, magnetic fields, and energetic particle phenomena, a Workshop was organized to bring together experimenters from the Helios, Voyager and IMP programs. The meeting was organized by Dr. S. M. Krimigis, with the support of the

Voyager and Helios team leaders. This paper is based on some of the results of that Workshop. The purpose of this paper is to present a description and an analysis of the principal interplanetary events that were observed in the period November 22-December 6, 1977, by Helios-1, 2, Voyager-1, 2, and IMP-7, 8.

Three flow systems were observed in the period under consideration: 1) a corotating stream and a stream interface associated with a coronal hole, 2) a shock wave and an energetic particle event associated with a 2-B flare, and 3) an isolated shock wave whose origin is uncertain.

This paper is based on data from 28 experiments from 6 spacecraft. The experiments and the corresponding principal investigators are listed in Table 1. Nearly complete measurements of solar wind plasma, magnetic fields and plasma waves are available from all spacecraft. Radio waves, plasma waves and energetic electrons associated with the November 22, event are available from Helios-1,2 and Voyager-1, 2. Data describing low energy protons associated with the November 22, event are available from Helios-1, 2 and Voyager-1, 2.

We begin in Section 2 by discussing the corotating stream and its associated shock and interface; this flow system was relatively simple, and the other two events interacted with it. Section 3 discusses the particles, fields and flows associated with the flare of November 22. Section 4 analyses a relatively simple, isolated shock wave that passed all of the spacecraft in the early days of December, 1977. Plasma waves at the shocks in the three events are discussed qualitatively in Section 5. Energetic protons accelerated by the shocks and injected by the November 22 flare are described in Section 6. Section 7 summarizes the results.

2. COROTATING STREAM, INTERFACE AND SHOCK

A stream that was observed successively by Helios-1, Helios-2, IMP-7, 8, Voyager-1 and Voyager-2 is shown in Figure 2, which shows bulk speeds from the experiment of Rosenbauer on Helios-1, 2 and from the experiments of Bridge on IMP-7, 8 and Voyager-1, 2. Sixteen minute averages of V are plotted versus time, and the phase is chosen such that the arrival time of the stream interface at each spacecraft is coincident with the vertical line marked "interface". The stream interface is readily identified as an abrupt decrease in density and an abrupt increase in temperature at the

front of a stream (Belcher and Davis, 1971; Burlaga, 1974, 1975). In this case, the interface at each spacecraft can be seen in Figure 3, where the time profiles of 16-min averages of the density (n) and temperature (T) are plotted. Figure 2 shows that the interface and stream arrived at Helios-1 on November 23, at Helios-2 on November 25, at earth on November 27, and at Voyager-1 and -2 on November 29. The 2-day interval between successive encounters of the interface is approximately that which is expected for a "corotating spiral" corresponding to a streamline with a speed of 400 km/s, as illustrated at the bottom of Figure 2.

The precise corotation times of the interface from one spacecraft to the next are shown in Table 2, together with the "predicted" corotation times computed from the equation $t_2 - t_1 = (r_2 - r_1)/V + (\phi_2 - \phi_1)/\Omega_s$, with allowance for the spacecraft motions (here Ω_s is the sidereal rotation period of the sun; V is the solar wind speed; ϕ_1 and ϕ_2 are respectively the longitudes of the spacecraft at time t_1 (when the interface passed the first spacecraft) and a later time t_2 (when the interface passed the second spacecraft); and r_1 and r_2 are the radial distances from the sun of the two spacecraft at t_1 and t_2 .) Table 2 shows that the predicted corotation times are close to the observed corotation times, the difference being $\lesssim 15\%$ in the three largest time intervals. These small differences may be due to small irregularities in the shape of the surface of the interface. Thus, we conclude that the interface was a corotating feature, and we infer that the stream which followed it was likewise corotating.

The low densities in the stream (Figure 3) and the fact that it was corotating suggest that its source was a coronal hole (Hundhausen, 1977; Burlaga, 1979). A coronal hole, tentatively identified in the Kitt Peak He 10830Å maps, passed central meridian on November 24, 25. The observed peak speed of the stream in question was ~ 500 km/s; thus, if its source was the coronal hole, and if it propagated at nearly constant speed, the stream should have arrived at the earth on November 27, which in fact, it did.

The dynamical evolution of the corotating stream in Figure 2 is surprising and significant. Helios-1 and -2 observed similar profiles of $V(t)$, $n(t)$, and $T(t)$ following the interface, with a time delay of ~ 53 hrs consistent with corotation. At the earth, IMP-7 and IMP-8 also saw the stream with approximately the expected corotation delay. The surprising

result is that the stream appears to have been absent (or much slower) at Voyagers-1, and -2 (Figure 2), even though both spacecraft observed the stream interface (Figure 3). This is probably not a latitude effect like that reported by Schwenn *et al.*, (1978), since the latitudes of Voyager-1 and Earth differed by only 1.5° (the latitude of Voyager-2 was $\approx 5.2^\circ$ higher than that of Earth. The heliographic latitudes of Voyager-1 and Earth were 3° and 1° , respectively; these are well within the latitudinal range of the coronal hole (-2° to 10°) tentatively identified in Solar Geophysical Data, 1978.

A numerical model is needed to show quantitatively that a stream can evolve near 1 AU as just described, and this will be discussed in another paper. One can understand the result qualitatively as follows. Ahead of the stream, the density and hence the momentum flux were high (Figure 3). Inside the stream the density was low and the speed of the stream itself was relatively low; the momentum flux of the stream did not greatly exceed that of the flow ahead of it. As the stream evolved, stress was relieved somewhat by shear at the interface. Nevertheless, two compression waves formed, moving toward and away from the sun with respect to the interface, respectively. The wave moving toward the sun (i.e., into the stream) decelerated the stream. The wave moving away from the sun (i.e., ahead of the stream) evolved into a forward shock (see below). The importance of momentum flux in corotating stream dynamics has been discussed quantitatively by Pizzo (1979a,b) for some conventional stream profiles. A decrease of V with increasing distance has been discussed by Dryer and Steinolfson (1976).

The structure of the stream interface observed by Voyagers-1 and -2 is shown in Figure 4. In both cases, the density and temperature transitions occurred in ≈ 30 min, consistent with the durations of some of the interfaces observed at 1 AU by Burlaga (1974). The n , T profiles observed at Helios-1, 2 are very similar to those in Figure 4. The magnetic field intensity reached a maximum at the interface (see Figure 4), as is usually the case (Burlaga, 1974; Siscoe, 1972). In this case, there was a large change in magnetic field direction across the interface at both Voyager-1 and -2. It is significant that all of the parameters just described (n , T , V , and B) had nearly the same profile at Voyager-2 as at Voyager-1, despite the separation of ≈ 0.2 AU; this shows that the internal structure of a

stream interface can be coherent over a relatively large distance. Plasma wave observations at the interface at Voyager-2 (Figure 4) show no significant wave emission in the frequency range 10 Hz to 562 Hz, suggesting that the interface was relatively stable. Similar observations of a different interface described by Gurnett *et al.* (1979a) showed the same result.

A "corotating shock" (which we label shock B) was observed by Voyagers-1 and -2; this is shown at high resolution in Figure 5. The identification of the disturbance as a shock is based on the simultaneous, abrupt increases in V , N_p , T_p and $F \equiv |B|$, and on the simultaneous change in the characteristics of the plasma waves. The observation of a shock at Voyager-1 and -2 is not surprising, since models of corotating streams (e.g., Hundhausen, 1973; Hundhausen and Burlaga, 1975; Gosling *et al.*, 1976; Steinolfson *et al.*, 1975; and Dryer *et al.*, 1978) predict the development of corotating shocks as streams evolve with distance from the sun, and many such shocks have been observed beyond 1 AU (Smith and Wolfe, 1977). The shock normals computed from the Voyager plasma and magnetic field data using the method of Lepping and Argentiero (1971) were directed 9° and 14° west of radial, respectively (see Table 3 and Figure 2), consistent with corotation. At Voyager-2, the angle between the shock normal and the upstream magnetic field was 14.6° ; the corresponding angle at Voyager-1 was 15.8° . The local shock speed was $400, \pm 10$ km/s relative to a fixed frame shock at both Voyager-1 and Voyager-2 (Table 3). This speed and the computed shock normals imply a time delay between Voyager-1 and Voyager-2 of 4.5 ± 1.3 hr. This compares favorably with the observed time delay of 5 hr. 17 min.

Shock B probably passed Helios-2 and IMP-8 on November 25 and 26, respectively (see Table 3). This is significant, because shocks are rarely observed ahead of corotating streams at $\lesssim 1$ AU (Ogilvie, 1974). The identification of shock B at Helios-1 is based on the observations that 1) the magnetic field intensity measured by Neubauer's instrument increased from $\sim 7\gamma$ to $\sim 15\gamma$ within 2 minutes (it increased from 7.7γ to 11.5γ in 64s), and 2) the plasma speed density and temperature increased between 0122 and 0205 UT (see Figures 2 and 3). The shock normal computed from the magnetic field data using the coplanarity theorem, is $\lambda_n = 60^\circ$, $\theta_n = 14^\circ$, which is close to that expected for corotation in a 300 km/s wind, viz. λ_n

$\alpha = 50^\circ$, $\theta_n = 0$; here λ_n is the heliographic longitude which is taken to be zero for a vector pointing radially away from the sun, and θ_n is the latitude with respect to the ecliptic plane. The shock speed computed from the observed densities and bulk speeds using the coplanarity normal is 300 km/s, or 540 km/s in the radial direction. This implies that the shock should have arrived at earth 41 hrs after it passed Helios-2 (if it moved at constant speed), i.e., at hr 19 on November 26. A SSC was reported at 1704 UT on November 26, in good agreement with the prediction. IMP-8 was in the solar wind on November 26, but there are data gaps at the time of the SSC. Nevertheless, the magnetic field intensity nearly doubled at some time in a 2-hr interval centered about the SSC (Figure 3), and the plasma density, temperature and speed increased at some time in a 5-hr data gap which included the time of the SSC (Figures 2 and 3). Thus, the IMP-8 data are consistent with the presence of a shock at Earth at 1704 on November 26. Altogether, the data from Helios-2, IMP-8 and the SSC give fairly convincing evidence for a shock driven by a corotating stream, which moved nearly radially from 0.6 AU to 1 AU and on to Voyager-1, 2 at 1.6 AU. Figure 3 shows that the shock moved away from the interface during the time that it moved from 0.6 AU to 1.6 AU.

It is customary to refer to a shock ahead of a corotating stream as a corotating shock. This is not appropriate for shock B, however. If shock B were corotating, then it should have been detected at Helios-1 \sim 50-60 hr before it was observed at Helios-2 (i.e., late on November 23), because Helios-1 was at the same radial distance as Helios-2 and \sim 35° to the East. Although the Helios-1 observations are nearly complete and continuous, there is no evidence of a shock at Helios-1 (see Figures 2 and 3). A possible explanation is that the stream which produced the shock was corotating but not stationary. For example, the stream may have been produced by a coronal hole that rotated with the sun, but whose physical characteristics changed on a scale of 1 day, producing a time-varying stream profile. Indeed, Figure 2 shows that the speed profile measured by Helios-2 differs in some details from that measured by Helios-1, indicating some time variations in this case. Evidence for non-stationary, corotating streams was presented earlier by Burlaga *et al.* (1978). (A model of non-stationary flows was presented by Wu *et al.* (1979), but this does not include the dynamical effects of the sun's rotation.) Shock B was seen at

Helios-2, IMP-8, and Voyager-1, 2 because those spacecraft were near a radial line; once formed at ≤ 0.6 AU the shock persisted and was convected past the other spacecraft. But apparently conditions were different at the time the stream was at Helios-1, 35° E of Helios-2, and were not favorable for the production of a shock.

3. EVENTS ASSOCIATED WITH A FLARE

On November 22, 1977 at 2B flare at N23, W40 in McMath plage region 15031 was observed in H_α starting at 0946 UT and reaching maximum intensity at 1006 UT. Chambon *et al.* (1978) observed hard X-rays and γ rays from the flare starting at \approx 1000 UT. It produced a SID, a type IV burst (starting at 1002), a type III burst (beginning at 0959 UT), an interplanetary shock wave, and an energetic particle event. Thus, the event displayed a wide range of phenomena that one associates with a great flare (Dryer, 1974).

Type III Bursts. The type III solar radio burst produced by the flare is the most intense observed to date by Helios-1 and -2. Helios-2 radio observations of the November 22 burst are shown in Figure 6. They are from the University of Minnesota (52, 77 and 203 kHz) and Goddard Space Flight Center experiments. Electron observations from the Max-Planck-Institute fur Aeronomie experiment are also displayed in Figure 6, showing that electrons in and near the 20-65 keV energy range were present, consistent with the idea that low frequency type III solar radio emission is caused by electrons with energies 10 keV to 100 keV (Lin *et al.*, 1973). Despite the data gap around 1010 UT, it is clear that the radio burst was double-peaked at the higher frequencies, possibly due to two separate bursts; however there was only a single peak at lower frequencies. The first peak reached maximum intensity at 1001 UT for 3 MHz, and the merged peak is observed at 1032 UT for 77 kHz. Much of this delay corresponds to the transit time for the energetic electrons from a heliocentric distance of 0.05 AU (3 MHz level) out to 0.8 AU (77 kHz level), indicating an outward speed greater than $0.2c$ for the exciter. A few minutes of the delay arise from the difference in propagation time of the electromagnetic waves from the source levels to Helios-2, located at 0.6 AU.

Flux densities observed for this burst by Helios-2 reached maximum values exceeding $10^{-15} \text{ W m}^{-2} \text{ Hz}^{-1}$ for frequencies from 77 to 255 kHz; they decreased to approximately $10^{-16} \text{ W m}^{-2} \text{ Hz}^{-1}$ at 3 MHz, the highest Helios

observing frequency. The 52 kHz channel, which shows strong electrostatic noise from 1025 to 1050 UT, is at the peak of the electrostatic noise spectrum, and it is within 1-2 kHz of the local plasma frequency determined from the measured density. Similar bursts were reported by Gurnett *et al.* (1978) and Gurnett and Anderson (1977). The electrostatic bursts might be short compared to the sampling time of the tuned receiver. The bandwidth of the receiver is about 5 kHz and its rise time, therefore, is about 0.2 msec, which is instantaneous compared to the detector integration time to 50 msec. As a consequence, for signals whose duration is more than 0.2 msec, the measurement gives the input voltage averaged over 50 msec.

The 77 kHz channel is the lowest frequency which did not show electrostatic noise. Burst radio emission has been reported to be generated at twice the local plasma frequency (Alvarez *et al.*, 1972). Consequently the 77 kHz electromagnetic waves detected at 0.60 AU by Helios-2 were propagating backward toward the sun from a source level near 0.8 AU, where the plasma frequency is half of 77 kHz.

This burst and the associated electron beam were also observed by the Voyager-1 and -2 planetary radio astronomy experiment and low energy particle experiment, respectively. The burst arrival directions, found by the spinning Helios-1 and -2 antennas, together with the Helios and Voyager electron data, show that the exciter extends over a wide ($> 75^\circ$) range of solar longitudes. Analysis of the relative intensities and positions observed by Helios-1 and -2 also indicates that the centroid of the burst passed between these two spacecraft. Assuming a source longitude of 40° W and a spiral field configuration, a best fit to the intensity versus frequency data obtained by Helios-1 and -2 is obtained for a solar wind speed of 300 km/sec. This is consistent with the speeds measured by the Helios plasma instruments, which were near 300 km/sec for several days.

Interplanetary Shocks and Flows. The interplanetary shock wave produced by the flare was observed directly by Helios-1 and -2, IMP-8, and Voyager-1 and -2; it was also observed indirectly as a SSC at the earth (see Table 4 and Figure 7). The shock might have been driven by ejecta, as suggested by the sketch in Figure 8, but the ejecta were not actually observed, because no spacecraft was suitably positioned.

If one tries to determine the motion of the shock using a radial distance vs. time plot (Figure 9) and the customary assumption of spherical

symmetry, he encounters difficulties that would have been overlooked if there were fewer spacecraft. One difficulty is that the speed determined from the time delay between IMP-8 and Voyager-1 is 418 km/s, whereas the speed determined from the time delay between IMP-8 and Voyager-2 is 568 ± 20 km/s (the uncertainty is due to a data gap at Voyager-2 between 06:00 and 09:00 UT). This discrepancy is large, considering that Voyager-1 and Voyager-2 were separated by only 0.005 AU in the radial direction and by 0.2 AU in the transverse direction.

A second and more extreme example of the inadequacy of the assumption of spherical symmetry for computing shock speeds is the speed determined from the time delay between Voyager-1 and Voyager-2: 14 ± 2 km/s! This is obviously wrong, and it is far from the speed determined from the analysis of the shock data at Voyager-1 (Figure 10), viz. 302 km/s. The shock normal and speed computed from the Voyager-1 data using the method of Lepping and Argentiero (1971), were ($\lambda_n = -34^\circ$, $\theta_n = -10^\circ$) and $V_n = 302$ km/s, respectively (see Table 4). Using these numbers, assuming that the shock was plane between Voyager-1 and Voyager-2, and considering the inertial solar ecliptic positions of Voyager-1 ($r_1 = (2.280, -0.274, 0.115) \times 10^8$ km) and Voyager-2 ($r_2 = (2.285, -0.533, 0.267) \times 10^8$ km), one finds that the predicted time delay between Voyager-1 and Voyager-2 is 11 hrs, 13 min, which is reasonably close to the observed delay, (15 ± 1.5) hrs. (The ± 1.5 hr uncertainty is due to a data gap.) The small discrepancy may be attributed to uncertainties in the shock normal and to curvature of the shock surface. By contrast, the time delay predicted using the assumption of spherical symmetry is only 36 min. We conclude that the use of time delays and assumption of spherical symmetry does not always give accurate shock speeds, whereas the use of local jump conditions and observations did give reasonably accurate estimates of the shock speed and direction in this case. The observed orientation of the shock is consistent with that expected for a shock with a radius of curvature less than 1.6 AU, originating at the flare site.

Helios-2 observed two shocks (A_1 and A_2 , at 1610 UT on November 23 and at 0611 UT on November 24, respectively; see Figures 7 and 11). However IMP-8, which was at nearly the same latitude and longitude and which was only 0.36 AU away from Helios-2, observed only one shock (A_4 at 1213 UT on November 25; see Figures 7 and 10). We cannot unambiguously determine why

2 shocks passed Helios-2 (several origins can be imagined), but we can suggest why only one shock was subsequently observed at IMP-8 and at Voyagers-1 and -2. The radial speed of shock A_1 , determined from the local plasma and magnetic field observations of the shock by Method MD1 of Abraham-Shrauner and Yun (1976), was 353 km/s. The corresponding speed of A_2 was 467 km/s. Thus, although A_2 followed A_1 (i.e., it was closer to the sun, see Figure 7), it was moving faster than A_1 . Consequently, A_2 should have overtaken A_1 at some point; assuming constant speeds, this point was at 1.08 AU on the Helios-2-sun line. If the computed shock normals (Table 4 and Figure 7) are even approximately correct, the shocks should have interacted along the earth-sun line before they reached IMP-8 near the earth. The observation of only one shock at IMP-8 suggests that when the shocks interacted, they coalesced. This is in agreement with gas dynamic theory where the overtaking of one shock (A_1) by a following one (A_2) leads to a coalesced shock moving forward and a reverse rarefaction fan which, because of its spreading, is difficult to observe. (In MHD the interaction leads to seven distinct MHD-structures the most prominent ones of which are a forward fast shock and a reverse fast rarefaction wave.) The resultant shock propagated to Voyager-1, which was close to the earth-sun line. Its radial speed at V1, determined from the shock observations using the method of Lepping and Argentiero (1971), was 369 km/s, which is in reasonable agreement (considering typical normal errors) with the speed determined from the time delay between IMP-8 and Voyager-1, viz 427 km/s. Evidence for shock-coalescence in Pioneer data has been reported by Smith *et al.* (1977). A second alternative would be a sufficient weakening of one shock before it interacted with the other one. (Note that the very weak shock would still have to interact with the second shock.) This possibility is ruled out by the following two arguments: A_2 cannot be the weakened shock since it fits very nicely into the propagation diagram (Figure 9) in contrast to shock A_1 . We rule out a large weakening of shock A_1 since it is followed by a long-lasting region of increased momentum and energy flux as shown in Figure 7.

A remaining aspect which requires clarification is the observation of one shock only at Helios-1. A possible explanation for this observation may be the presence of the stream interface and an interaction region between Helios-1 and Helios-2 (Burlaga and Scudder, 1975). If we

approximate the interface as a tangential discontinuity, its interaction with A_1 may lead to the latter's disappearance (see e.g., Neubauer, 1976).

4. THE DECEMBER SHOCK

During the Helios-Voyager-IMP Workshop, it was noted that a shock was observed by Helios-1 and -2 on December 1 and by Voyagers-1 and -2 on December 2, and it was decided to include this event in the joint study. The interplanetary data are nearly complete for Helios-1, as shown in Figure 12. However, the solar data do not show any large flare which might have produced the shock. One candidate is an SN flare at S24, E85 which began in H_α at 0338 UT on November 30 and reached a maximum at 0350 UT. This small flare was associated with an X-ray burst (starting at 0330 UT, with a maximum at 0348 UT) and a SID (starting at 0334 UT, with a maximum at 0349 UT). This implies deceleration of the shock within 0.6 AU (see Gosling et al., 1968). In view of the uncertainty concerning the source of the shock, our discussion emphasizes the interplanetary observations.

Post-shock conditions. The density and temperature profiles in Figure 12 suggest that the shock observed by Helios-1 was followed by ejecta in which the density and temperature were low. There is also evidence for enhanced magnetic field intensities in the ejecta. Helios-2 may also have observed the ejecta (Figure 13), but this is less certain because of a data gap. The shock was also detected by Voyager-1 and -2 (See Figures 13 and 14), but they did not encounter ejecta like that seen by Helios-2. (Voyager-1 observed a small depression in density on December 4 and a small increase in B on December 4, 5; this was probably a local phenomenon, since it was not seen by Voyager-2 which was nearby. This signature is clearly different from that seen by Helios-1 so we do not identify it as ejecta.) Thus, the evidence is that the shock had a wide longitudinal extent ($> 40^\circ$; see Figure 15), and was driven ejecta less broad, originating east of the Voyager-Sun line.

Note that Voyager-2 observed a nearly monotonic decrease in speed, density, temperature, and magnetic field strength behind the shock (Figure 13). Many authors have interpreted such a signature as evidence for a blast wave, generally on the basis of observations from just one satellite (see Hundhausen, 1972). However, the observation of ejecta at Helios-1 indicates that this was probably not a blast wave; it was a driven

shock. Voyager-2 saw the shock, but it did not encounter the ejecta due to its more limited longitudinal extent. This shows that the signature of the post-shock flow is not sufficient to identify the type of a shock wave. This point was made previously by Ogilvie and Burlaga (1974) and by Rosenau and Frankenthal (1978); it has recently been demonstrated very clearly by Aouna *et al.* (1979). The concept of a broad shock driven by narrow ejecta is not new, although it is often forgotten or ignored. It dates back at least to Gold (1959).

Shock motion. Figure 16 gives a plot of radial distance versus time, showing the shock positions and times determined from the observations of Helios-1, -2, Voyager-1, -2 and from a sudden commencement at Earth. The points lie very close to a straight line with a slope corresponding to a speed of 555 km/s. Considering that Helios-1 was 19° east of the Voyager-2-sun line and that Earth was 17° west of that line, the straight line in Figure 16 suggests a nearly spherical shock front moving at a constant speed between 0.6 AU and 1.6 AU. Similar results for the August, 1972, events were reported by Smith *et al.* (1977) and Dryer *et al.* (1976). However, examination of the local shock speeds and normals reveals a more complicated picture. Since Voyager-2 and Helios-2 were nearly radially aligned, and since Figure 16 suggests a spherical shock, one expects that Voyager-2 and Helios-2 should have observed essentially the same shock speed and direction, the radial component of velocity being close to 555 km/s. The local jump conditions give rather different results (Table 5): 1) The local speeds were substantially less than the speed determined from the average speed determined from the time delay; and 2) the shock normal at Helios-2 ($\lambda_n = -3^\circ$, $\theta_n = 17^\circ$) was very different from that at Voyager-2 ($\lambda_n = 38^\circ$, $\theta_n = -6^\circ$). These differences are too large to be attributed to uncertainties in the computation of the local shock speed and direction. The field and plasma parameters were relatively steady before and after the shock, the field direction change was relatively large (18° at Helios-2), and we used both magnetic field and plasma observations, so we expect the uncertainty in speed to be $\lesssim 20$ km/s and the uncertainty in direction to be $\lesssim 10^\circ$ (Abraham-Shrauner and Yun, 1976; Lepping and Argentiero, 1971). Thus the observations suggest that locally the shock surface may have been distorted such that the normal was not radial, although the normal may have been radial on average. Likewise, locally the shock may have been

accelerated or decelerated giving local speeds higher than average in one place, lower than average in a second place, and near-average in a third place (Heineman and Siscoe, 1974; Burlaga and Souder, 1975). For example, the radial component of the local velocity at Voyager-2 (530 km/s) is consistent with the average speed determined from time delay (555 km/s) within the experimental uncertainties, but the radial component of the local velocity at Helios-2 (460 km/s) is substantially less than the average value. Since Helios-2 and Voyager-2 were nearly radially aligned, this suggests that the radial component of the shock velocity may have fluctuated as much as ± 100 km/s, and its direction may have fluctuated as much as $\pm 40^\circ$ as it moved between 0.6 AU and 1.6 AU. The alternative is to postulate very large azimuthal variations.

5. PLASMA WAVES AT SHOCKS

Helios-1, -2 and Voyager-1, -2 carried plasma wave instruments (see Gurnett and Anderson, 1977; and Scarf and Gurnett, 1977, respectively for a discussion of the instruments), which provided an extensive set of observations of waves near the interplanetary shocks discussed above. These observations were used as a means of searching for and confirming the identity of the shocks. More important, however, they provide an exceptionally large and complete record which form a basis for a comparative study of waves at interplanetary shocks. Only a few papers discussing plasma wave electric fields at interplanetary shocks have been published (Scarf, 1978; Scarf *et al.*, 1979, and Gurnett *et al.*, 1979a,b). Here we shall present only a qualitative discussion stressing the remarkable variety of signatures. A more comprehensive physical discussion is deferred to another paper.

The wave data are given together with the plasma and magnetic field observations of the shocks in Figures 5, 10, 11, 12, and 14. The electric field intensity is plotted versus time for each of several frequency channels on a logarithmic scale with a range of 100 db for each channel. The electric field strength ranges from about $1 \mu\text{V m}^{-1}$ at the bottom of the scale to 100 mV m^{-1} at the top of the scale. The solid lines represent peak electric field amplitudes and solid black areas (or vertical solid lines in some cases) represent the average electric field amplitude.

Let us consider the individual shock observations in the order in which shocks were introduced above, beginning with shock B. This shock had not developed at the position of Helios-1, but it was observed at both Voyager-1 and Voyager-2 (Figure 5), which were at essentially the same radial distance (1.6 AU) and separated by ≈ 0.2 AU. The Voyager-1 plasma wave observations show at least three different types of emissions:

1. turbulence extending downstream of the shock at frequencies $< f_p^+$, identified as whistler mode turbulence
2. waves extending upstream at frequencies from about 1.0 to 5.62 kHz, tentatively identified as ion acoustic waves, and
3. a short, well-defined broadband burst at the shock at frequencies from 10 Hz to 5.62 kHz.

These types of emissions have been discussed by Scarf *et al.* (1970), Gurnett and Frank (1978), and Gurnett *et al.* (1979b). Voyager-2 also observed the whistler mode turbulence extending downstream from the shock, and it observed a peak corresponding to the broadband emissions at the shock. There are no Voyager-2 data above 1 kHz, probably due to a failure in the spacecraft data system which reduced the sensitivity of these channels.

Plasma waves at shock A were observed by Helios-2 (Figure 11), and by IMP-8 and Voyager-1 (Figure 10). Whistler waves were not observed downstream of the shock at Helios-2 and IMP-8, but they were observed downstream of the shock at Voyager-1. The shock at Helios-2 is almost totally obscured by a broad region of ion acoustic wave turbulence from about 562 Hz to 10 kHz; these waves are not necessarily all associated with the shock (Gurnett and Frank, 1978). IMP-8 and Voyager-1 (Figure 10) observed ion acoustic waves upstream of the shock between f_p^+ and f_p^- . Helios-2 (Figure 11) observed a sharp burst of noise in the 311 and 562 Hz channels coincident with the passage of shock; IMP-8 found some evidence of a corresponding noise burst below f_p^+ , and Voyager-1 observed a noise burst at the shock in the range 31 Hz to ≈ 1.78 kHz.

Shock C was observed by Helios-1 and -2 and by Voyager-2 (Figures 12, 13, and 14). None of the spacecraft observed intense whistler mode turbulence behind the shock. Helios-1 and Helios-2 observed an enhancement in electric field intensity in the range 562 Hz to 10 kHz with a large peak to average ratio, probably due to Doppler-shifted ion-acoustic waves

(Gurnett and Frank, 1978). The waves extended both upstream and downstream at Helios-1, but only downstream at Helios-2. Voyager saw only weak emission of such waves, downstream of the shock. A sharp, intense (1 to 5 mV m⁻¹) broadband burst of electric field turbulence was observed at Helios-2, but it was absent at Voyager-2 and missing or obscured by the ion acoustic waves at Helios-1.

We conclude that at least three types of emissions (in various combinations) may be observed at an interplanetary shock, viz., downstream "whistler-mode turbulence", upstream "ion-acoustic" waves, and a brief broadband noise burst coincident with the shock. In some cases, only one or two of these is observed. In addition, the shock may be embedded in a broad region of "ion-acoustic" waves not necessarily caused by the shock. The combination of wave-types and the characteristics of each wave mode seen at one spacecraft may be very different from those observed by another spacecraft nearby. Apparently, the plasma waves at a shock depend strongly on the local characteristics of the medium. This is not surprising, since it has been observed in the case of the earth's bow shock (Greenstadt, et al., 1973). However, the basic types of emissions are the same at 0.6 AU as they are at 1.6 AU.

6. ENERGETIC PROTONS

In the interval November 22 to December 6, 1977, Helios and Voyager instruments observed energetic protons (\sim 50 to 200 keV) produced by at least two mechanisms: local shock acceleration and acceleration in a flare. It is convenient to begin by discussing the former, since shock accelerated particles are less complicated by propagation effects.

Shock Acceleration. Protons accelerated by a shock are seen most clearly in the case of shock C which was relatively isolated and uncomplicated, as discussed in Section 4. Recall that Voyager-1 and -2 observed a shock behind which the flow parameters and magnetic field intensity dropped gradually to the preshock values; there was no evidence of ejecta like those observed by Helios-1. Figure 17 shows enhancements in the counting rate of protons at Voyager-1 and -2 in the energy range \sim 50 keV to \sim 138 keV; the maximum intensity occurred at or just behind the shock. At Voyager-2 the peak counting rate was \sim 100 times the ambient value, and at Voyager-1 the enhancement was somewhat smaller. The

enhancement began \approx 15 hr ahead of the shock at both Voyager-1 and -2. It persisted for \approx 32 hr behind the shock at Voyager-1 and \approx 28 hr behind the shock at Voyager-2. There were small differences in the shapes of the profiles which might be due to differences in the local magnetic field configurations. Basically, however, the proton enhancement at Voyager-1 was similar to that at Voyager-2. This may be due to the simple geometry of the shock near Voyagers-1 and -2 and to their relatively small separation (0.2 AU).

The situation at Helios-1 and -2 was quite different. Both spacecraft observed an enhancement in counting rate of protons (Figure 17). The maximum enhancement at Helios-2 was only \approx 20 times the background counting rate and it occurred at the shock. Two maxima were observed by Helios-1, and the shock occurred between them. A compression wave was observed at the time of the second maximum (Figure 12), but the time resolution was not adequate to determine whether or not it was a shock. The counting rate dropped abruptly approximately 6 hr after the shock at both Helios-1 and -2, in contrast to the more gradual, longer lasting decline at Voyagers-1 and -2. This might be due, at least in part, to the presence of ejecta at Helios-1 and at Helios-2, which were not observed by Voyagers-1 and -2. (There is no accepted signature for the boundary of ejecta, and we cannot be certain that we have identified one. The vertical line labeled boundary in Figure 17 corresponds to an abrupt decrease in density observed behind the shocks in Figure 12 and 13). The enhancement began \approx 6 hr ahead of the shock at Helios-2 and a few hours ahead of the shock at Helios-1; the slight difference could be due to different acceleration efficiencies of the two shocks and/or to different upstream magnetic field conditions which gave connection to the shocks at slightly different times. There is a curious enhancement at Helios-1, occurring several hours ahead of the shock-associated enhancement but closely resembling it. One can imagine that this was due to a magnetic field geometry which provided a good connection between the observer and the shock for several hours before the shock arrived.

The differences between the enhancements at Helios-1 and Helios-2 and the differences between the enhancements at Voyager-1 and Voyager-2 indicate that local conditions do influence the intensity profile somewhat. Note, however, that the Voyager-1, -2 profiles have a greater maximum

enhancement and a greater upstream extent than the Helios-1, -2 profiles. One possible reason for this (but not the only one) is that Voyager-1, -2 were farther from the sun than Helios-1, -2, so that the shock at Voyager-1, -2 had been accelerating particles for a longer time and perhaps accelerated and accumulated more particles than it had when it was at the positions of Helios-1 and -2.

Flare-accelerated Particles. Now let us discuss the low energy (γ 25 - 200 keV) protons ejected by the flare of November 22, 1977 (see Section 3 for a discussion of the flare characteristics and the corresponding interplanetary flows). Helios-1 and -2 observed very different intensity-time profiles during the decay in intensity (Figure 18), even though they were at nearly the same radial distance and were separated in longitude by only 32° (see Figures 1 and 8). At Helios-1, the intensity decreased smoothly and monotonically for at least 3 days (Figure 18). The corotating, stream discussed in Section 2 was east of Helios-1 at the beginning of the event and the interface passed the spacecraft γ 16 hr later with only a small perturbation on the intensity-time profile. Apparently the flare injected particles over a broad range of longitudes near the sun, so that the intensity versus longitude was nearly uniform across the corotating interface. The particles in the slow flow ahead of the interface decayed freely (e.g., by diffusing to infinity, Kurt et al., 1978) for at least 16 hrs after the flare, and the particles in the corotating stream decayed similarly for at least three days after the flare. In particular, particles in the corotating stream were unaffected by the flare associated shock wave (shock A) and the post shock flow (see Section 3 and Figure 8).

The intensity-time profile at Helios-2 was quite different from that at Helios-1, probably because it was influenced by the flare-associated shock and post-shock flow. The early part of the decay seen by Helios-2 was very similar to that observed by Helios-1 (Figure 18), the flux decreasing monotonically for at least 12 hrs. As shock A_1 (produced by the flare) approached Helios-2, the counting rate of energetic protons began to increase, reaching a maximum at the time shock A_2 reached Helios-2. The maximum flux was 4×10^6 ions/cm² sec ster MeV. The maximum counting rate was γ 25 times that measured by Helios-1 at the same time, i.e., comparable to the increase which Helios-2 observed at shock C, as described above.

This increase may be due to: 1) particles accelerated by the shock, 2) flare particles trapped behind the shock, and/or 3) energetic storm particles. Following the shock, the counting rate again decreased until the interaction region of the corotating stream arrived at Helios-2, at which time there was slight increase in the counting rate, perhaps due to compression in the interaction region. When the interface arrived, the counting rate at Helios-2 dropped rapidly (exponentially with a time scale of 3 hr) to approximately the same level that Helios-1 recorded. Apparently particles accelerated by shock A could not penetrate the stream interface and many were trapped in a region bounded by the interface on one side and the shock on another side. The ejecta from the flare might have provided the third boundary. The scenario that has been described is represented schematically in Figure 8.

Voyager-1, and -2 observed intensity-time profiles of protons in the energy range ~ 50 keV - 138 keV (Figure 19) which resemble the profile recorded by Helios-2. During the early stage of the decay, both spacecraft observed a monotonic decrease in counting rate lasting ~ 16 hrs. (The initial increase in counting rate and the first hour or two of the decay includes an uncertain contribution to energetic, omni-directional particles.) The counting rate then increased gradually during the next 8 days, reaching a maximum counting rate at the time that shock A arrived. (Recall that there was a data gap at Voyager-2 between 06:00 and 09:00 UT, so the shock was not observed directly.) This gradual increase lasted too long to be due to particles accelerated by the shock alone. Probably, energetic storm particles were present. The rapid increase several hours ahead of the shock at Voyager-1 and -2, however, is probably a contribution due to shock acceleration. The enhancement is relatively small, no more than about 16 times the ambient value. It did not extend above 0.5 MeV for protons. No modulation of electrons in the range 0.03 - 1.5 MeV was observed. At the time of the shock, Voyager-1 observed a strong anisotropy (3.5:1), the particles flowing away from the sun. Shortly after the shock passed, the anisotropy direction reversed and particles were observed to be streaming toward the sun, consistent with the hypothesis that most of the particles observed near the shock were accelerated by the shock. Following the shock, the counting rate decreased, rapidly at first and then more slowly. Shock B (see Section 2) arrived at Voyagers-1 and -2 during the

decline in intensity, on November 29, and the corotating stream interface arrived several hours later. A very small increase in the counting rate of low energy protons was observed by Voyager-2 and an even smaller increase by Voyager-1, but those were insignificant compared to the other shock-associated enhancements described above. A small increase in counting rate was observed in the interaction region ahead of the interface (Figure 19), analagous to that observed on November 25 by Helios-2 when it encountered the interaction region (Figure 18).

7. SUMMARY

We have presented a wealth of data obtained at \sim 0.6 AU, 1 AU, and 1.6 AU, describing the evolution and interactions of particles, flows, and fields in the period November 22, to December 6, 1977. Some of the principal results of our analysis of these data are the following:

1. A small, corotating stream, originating in a coronal hole, was observed to disappear as it moved from 0.7 AU to 1.6 AU. A forward shock, (shock B), was produced by the stream and observed by Helios-2 (0.6 AU), IMP-8 and Earth (1 AU) and Voyager-1, 2, which were nearly radially aligned; however, the shock was not corotating because it was not seen at Helios-1, 35° E of Helios 2. Apparently, the flow was corotating, but non-stationary. The stream interface corotated from 0.7 AU to 1.6 AU and persisted even though the stream had dissipated; it was stable and its structure remained essentially the same at all positions.

2. An exceptionally intense type III burst, produced by the November 22, 1977 flare, was observed by Helios-1 and -2. The electron beam which caused it, and plasma oscillations excited by the beam were observed at 0.6 AU.

3. The shock produced by the flare of November 22 (shock A) was non-spherical, pointing 34° to the E and 10° S of the radial direction at 1.6 AU. It interacted with another shock beyond 0.6 AU, and they coalesced forming a single shock that was observed at 1 AU and at 1.6 AU.

4. A shock of uncertain origin (shock C) was observed by 5 spacecraft at radial distances from the sun ranging from 0.6 to 1.6 AU and with longitudinal separations up to 36° . The radial distances versus time diagram suggested a spherical shock moving at a constant speed, but analysis of data at the shocks showed local fluctuations of up to 100 km/s in speed and 40° in direction.

decline in intensity, on November 29, and the corotating stream interface arrived several hours later. A very small increase in the counting rate of low energy protons was observed by Voyager-2 and an even smaller increase by Voyager-1, but those were insignificant compared to the other shock-associated enhancements described above. A small increase in counting rate was observed in the interaction region ahead of the interface (Figure 19), analogous to that observed on November 25 by Helios-2 when it encountered the interaction region (Figure 18).

7. SUMMARY

We have presented a wealth of data obtained at ≈ 0.6 AU, 1 AU, and 1.6 AU, describing the evolution and interactions of particles, flows, and fields in the period November 22, to December 6, 1977. Some of the principal results of our analysis of these data are the following:

1. A small, corotating stream, originating in a coronal hole, was observed to disappear as it moved from 0.7 AU to 1.6 AU. A forward shock, (shock B), was produced by the stream and observed by Helios-2 (0.6 AU), IMP-8 and Earth (1 AU) and Voyager-1, 2, which were nearly radially aligned; however, the shock was not corotating because it was not seen at Helios-1, 35° E of Helios 2. Apparently, the flow was corotating, but non-stationary. The stream interface corotated from 0.7 AU to 1.6 AU and persisted even though the stream had dissipated; it was stable and its structure remained essentially the same at all positions.

2. An exceptionally intense type III burst, produced by the November 22, 1977 flare, was observed by Helios-1 and -2. The electron beam which caused it, and plasma oscillations excited by the beam were observed at 0.6 AU.

3. The shock produced by the flare of November 22 (shock A) was non-spherical, pointing 34° to the E and 10° S of the radial direction at 1.6 AU. It interacted with another shock beyond 0.6 AU, and they coalesced forming a single shock that was observed at 1 AU and 1.6 AU.

4. A shock of uncertain origin (shock C) was observed by 5 spacecraft at radial distances from the sun ranging from 0.6 to 1.6 AU and with longitudinal separations up to 36° . The radial distances versus time diagram suggested a spherical shock moving at a constant speed, but analysis of data of the shocks showed local fluctuations of up to 100 km/s in speed and 40° in direction.

5. One or more of three types of electrostatic waves were observed at interplanetary shocks: upstream waves with $f_p^- \lesssim f < f_p^+$, downstream waves with $f < f_p^-$, and broadband noise at the shock. These three types of emissions were observed at 1.6 AU as well as 0.6 AU. The specific pattern varied greatly among the shocks observed, even for the same shock observed at closely separated ($\lesssim 0.2$ AU) spacecraft, indicating a strong dependence on local shock and solar wind parameters.

6. Energetic protons ($\gtrsim 50$ to 200 keV) were observed to be accelerated at shocks. The maximum and half widths of the flux profiles at a shock differed by approximately a factor of 2 over distances of a few tenths of an AU, indicating a dependence on local conditions. The data suggest a tendency for the fluxes to become broader and more intense with increasing distance from the sun.

7. Energetic protons ($\gtrsim 50$ keV) from the November 22, 1977 flare were observed. Helios-1 observed that their intensity decayed monotonically in the corotating stream, with little change across the stream interface. Helios-2, 30° to the west of the interface, observed a very different profile, with a second increase to a maximum at the time the shock produced by the flare arrived. These "extra" particles apparently did not penetrate the interface, for the intensity at Helios-2 dropped abruptly to the intensity observed at Helios-1 when the interface corotated past Helios-2.

ACKNOWLEDGMENTS

This paper was made possible by the efforts of many people. The Project Leaders--Dr. H. Porsche, J. Trainor, A. Kutzer (DFVLR/ERNO) and Koehendorfer (NASA/HQ), representing Helios; Drs. E. Stone and M. Mitz (NASA/HQ), representing Voyager--made special efforts to coordinate the acquisition of Helios and Voyager data and to provide nearly complete data sets for the unique interval that we studied. The Workshop was proposed and organized by Dr. T. Krimigis. Four Principal Investigators, not listed as authors, generously provided us their data, which were essential for this study--Drs. H. Bridge, T. Krimigis, N. Ness, and R. Stone. The shocks were identified by the Workshop participants in presentations and round-table discussions. M. Denskat and Mr. Volkmer provided the data on the shock seen at Helios-2 on November 25.

REFERENCES

- Abraham-Shrauner, B., and S. H. Yun, Interplanetary shocks seen by Ames plasma probe on Pioneer 6 and 7, J. Geophys. Res., **81**, 2097, 1976.
- Aouna, M. H., L. F. Burlaga, R. P. Lepping, and N. F. Ness, Initial results from the Voyagers 1, 2 magnetic field experiments, Contributions to the Fourth Solar Wind Conference, NASA/TM 79711, to appear in Proceedings of the Fourth Solar Wind Conference, 1979.
- Alvarez, H., F. Haddock, and R. P. Lin, Evidence for electron excitation of type III radio burst emission, Solar Phys., **26**, 468, 1972.
- Belcher, J., and L. Davis, Jr., Large-amplitude Alfvén waves in the interplanetary medium, 2, J. Geophys. Res., **76**, 3534, 1971.
- Burlaga, L. F., Interplanetary stream interfaces, J. Geophys. Res., **79**, 3717, 1974.
- Burlaga, L. F., Interplanetary streams and their interaction with the earth, Space Sci. Rev., **17**, 327, 1975.
- Burlaga, L. F., Magnetic fields, plasmas, and coronal holes: the inner solar system, NASA/TM 79598, 1978, to appear in Space Sci. Rev., 1979.
- Burlaga, L. F., N. Ness, F. Mariani, B. Bavassano, U. Villante, H. Rosenbauer, R. Schwenn, and J. Harvey, Magnetic fields and flows between 1 AU and 0.3 AU during the primary mission of Helios 1, J. Geophys. Res., **83**, 5167, 1978.
- Burlaga, L. F., and J. D. Scudder, Motion of shocks through interplanetary streams, J. Geophys. Res., **80**, 4004, 1975.
- Chambon, G. Hurley, K., M. Niel, R. Talon, G. Vendrenne, O. B. Likine, A. V. Kovznetsov, and I. V. Estovline, A hard X-ray and gamma ray observation of the 22 November, 1977 solar flare, Colloques internationaux du C.N.R.S. N° 282-Contexte coronal des eruptions solaires.
- Chapman, S. Solar Plasma, Geomagnetism, and Aurora, p. 48, Gordon and Breach, New York, 1964.
- Dryer, M., Interplanetary shock waves generated by solar flares, Space Sci. Rev., **15**, 403, 1974.
- Dryer, M., Solar-generated disturbances and their propagation through the interplanetary medium Lecture Notes in Physics, Springer-Verlag, Berlin, W. Germany, to appear 1979.

- Dryer, M., and R. S. Steinolfson, MHD solution of interplanetary disturbances generated by simulated velocity perturbations, J. Geophys. Res., 81, 5413, 1976.
- Dryer, M., C. Candelaria, Z. Smith, R. Steinolfson, E. J. Smith, J. H. Wolfe, J. D. Mihalov, and P. Rosenau, Dynamic MHD modeling of the solar wind disturbances during the August 1972 events, J. Geophys. Res., 83, 532, 1978a.
- Dryer, M., Z. K. Smith, G. H. Endrud, and J. H. Wolfe, Pioneer 7 observations of the August 29, 1966, interplanetary shock-wave ensemble, Cosmic Electrodyn., 3, 184, 1972.
- Dryer, M., Z. K. Smith, E. J. Smith, J. D. Mihalov, J. H. Wolfe, R. S. Steinolfson, and S. T. Wu, Dynamic MHD modeling of solar wind corotating stream interaction regions observed by Pioneer 10 and 11, J. Geophys. Res., 83, 4347, 1978b.
- Dryer, M., Z. K. Smith, R. S. Steinolfson, J. D. Mihalov, J. H. Wolfe, and J. K. Chao, Interplanetary disturbances caused by the August 1972 solar flares as observed by Pioneer 9, J. Geophys. Res., 81, 4651, 1976.
- Gold, T., Plasma and magnetic fields in the solar system, J. Geophys. Res., 64, 1665, 1959.
- Gosling, J. T., J. R. Asbridge, S. J. Bame, A. J. Hundhausen, and I. B. Strong, Satellite observations of interplanetary shock waves, J. Geophys. Res., 73, 43, 1968.
- Gosling, J. T., A. J. Hundhausen, and S. J. Bame, Solar wind evolution at large heliocentric distances: Experimental demonstration and the test of a model, J. Geophys. Res., 81, 2111, 1976.
- Gosling, J. T., J. R. Asbridge, S. J. Bame, and W. C. Feldman, Solar wind stream interfaces, J. Geophys. Res., 83, 1401, 1978.
- Greenstadt, E. W., M. Dryer, and Z. K. Smith, Field-determined structure of interplanetary shocks, in Flare Produced Shock Waves in the Corona and in Interplanetary Space, p. 245, published by the High Altitude Observatory, National Center for Atmospheric Research, Boulder, Colorado, 1973.
- Gurnett, D. A., and R. R. Anderson, Plasma wave electric fields in the solar wind: Initial results from Helios 1, J. Geophys. Res., 82, 632, 1977.
- Gurnett, D. A., and L. A. Frank, Ion acoustic waves in the solar wind, J. Geophys. Res., 83, 58, 1978.

- Gurnett, D. A., M. M. Baumbach, and H. Rosenbauer, Stereoscopic direction finding analysis of a type III solar radio burst; evidence for emission at $2f_p$, J. Geophys. Res., 83, 616, 1978.
- Gurnett, D. A., E. Marsch, W. Pilipp, R. Schwenn, and H. Rosenbauer, Ion acoustic waves and related plasma observations in the solar wind, J. Geophys. Res., 84, 2029, 1979a.
- Gurnett, D. A., F. M. Neubauer, and R. Schwenn, Plasma wave turbulence associated with an interplanetary shock, J. Geophys. Res., 84, 541, 1979b.
- Heineman, M. A., and G. L. Siscoe, Two-dimensional simulation of flare-associated disturbances in the solar wind, J. Geophys. Res., 79, 1349, 1974.
- Hundhausen, A. J., Coronal Expansion and Solar Wind, Springer-Verlag, New York, 1972.
- Hundhausen, A. J., Non-linear model of high-speed solar wind streams, J. Geophys. Res., 78, 1528, 1973.
- Hundhausen, A. J., An interplanetary view of coronal holes, in Coronal Holes and High Speed Solar Wind Streams, edited by J. B. Zirker, p. 298, Colorado Associated Universities Press, Boulder, 1977.
- Hundhausen, A. J., and L. F. Burlaga, A model for the origin of solar wind stream interfaces, J. Geophys. Res., 80, 1845, 1975.
- Intriligator, D. S., The August 1972 solar-terrestrial events: Solar wind plasma observations, Space Sci. Rev. 19, 629, 1976.
- Kurt, V. G., Yu I. Logacher, V. G. Stolpovskii, N. F. Pissarenko, M. Gros, A. Ranart, L. Trieger, and T. Gombosi, Analysis of energetic particle events following solar flares of September 24 and November 22, 1977, Tech. Report KFKI-1978-37, 1978.
- Lazarus, A. J., K. W. Ogilvie, and L. F. Burlaga, Interplanetary shock observations by Mariner 5 and Explorer 34, Solar Phys., 13, 232, 1970.
- Lee, T. S., and T. Chen, Hydromagnetic interplanetary shock waves, Planetary Space Sci., 16, 1483, 1968.
- Lepping, R. P., and P. D. Argentiero, Single spacecraft method of estimating shock normals, J. Geophys. Res., 76, 4349, 1971.
- Lin, R. P., L. G. Evans, and J. Fainberg, Simultaneous observations of fast electrons and type III radio burst emissions near 1 AU, Astrophys. Letters, 14, 191, 1973.

- Neubauer, F. M., Solar wind discontinuities, J. Geophys. Res., **13**, 2248, 1976.
- Ogilvie, K. W., Corotating shock structures, in Solar Wind, edited by C. P. Sonett, P. J. Coleman, Jr., and J. M. Wilcox, NASA SP-308, Washington, D. C., 1972.
- Ogilvie, K. W., and L. F. Burlaga, A discussion of interplanetary post shock flows with two examples, J. Geophys. Res., **79**, 2324, 1974.
- Pizzo, V., An evaluation of corotating solar wind stream models, in Contributions to the Fourth Solar Wind Conference, NASA/TM 79711, p. 55, 1979, to appear in Proceedings of the Fourth Solar Wind Conference, 1979a.
- Pizzo, V., A three-dimensional model of corotating streams in the solar wind II. hydrodynamic streams, submitted to J. Geophys. Res., 1979b.
- Rosenau, P., and S. Frankenthal, Propagation of magnetohydrodynamic shocks in a thermally conducting medium, Phys. Fluids, **21**, 559, 1978.
- Scarf, F. L., Wave-particle interaction phenomena associated with shocks in the solar wind, Proceedings of the De Feiter Memorial Symposium on the Study of Traveling Interplanetary Phenomena, D. Reidel, Hingham, Mass., 1978.
- Scarf, F. L., R. W. Fredricks, L. A. Frank, C. T. Russell, P. J. Coleman, Jr., and M. Neugebauer, Direct correlations of large-amplitude waves with suprathermal protons in the upstream solar wind, J. Geophys. Res., **75**, 7316, 1970.
- Scarf, F. L., and D. A. Gurnett, A plasma wave investigation for the Voyager mission, Space Sci. Rev., **21**, 289, 1977.
- Scarf, F. L., D. A. Gurnett, W. S. Kurth, and R. R. Shaw, Voyager 1, 2, plasma wave observations for the September 1977 storm period, UAG Report on the September 1977 and November 1977 Solar-Geophysical Activity, 1979.
- Schwenn, R., M. D. Montgomery, H. Rosenbauer, H. Miggenrieder, K. H. Mulhauser, S. J. Bame, W. C. Feldman, and R. T. Hansen, Direct observations of the latitudinal extent of a high-speed stream in the solar wind, J. Geophys. Res., **83**, 1011, 1978.
- Schwenn, R., K. H. Mulhauser, and H. Rosenbauer, Two states of the solar wind at the time of solar activity minimum I. Boundary layers between fast and slow streams, Lecture Notes in Physics, Springer-Verlag, Berlin, W. Germany, to appear, 1979.

- Siscoe, G. L. Structure and orientation of solar wind interaction fronts: Pioneer 6, J. Geophys. Res., 77, 27, 1972.
- Smith, E. J., L. Davis, Jr., P. J. Coleman, Jr., D. S. Colburn, P. Dyal, and D. E. Jones, August 1972 solar-terrestrial events: observations of interplanetary shocks at 2.2 AU, J. Geophys. Res., 7, 1077, 1977.
- Smith, E. J. and J. H. Wolfe, Pioneer 10, 11 observations of evolving solar wind streams and shocks beyond 1 AU, in Study of Traveling Interplanetary Phenomena 1977, M. A. Shea et al. (eds.), p. 227-257, D. Reidel Publishing Co., Dordrecht-Holland, 1977.
- Smith, E. J., and J. H. Wolfe, Fields and plasmas in the outer solar system, Space Sci. Rev., 23, 217, 1979.
- Solar-Geophysical Data 401, Part 1, p. 27, January 1978, U. S. Department of Commerce (Boulder, Colorado, U. S. A. 80301, 1978.
- Steinolfson, R. S., M. Dryer, and Y. Nakagawa, Numerical MHD simulation of interplanetary shock pairs, J. Geophys. Res., 80, 1223, 1975.
- Vaisberg, O. L., and G. N. Zastenker, Solar wind and magnetosheath observations at earth during August 1972, Space Sci. Rev. 19, 687, 1976.
- Wu, S. T., S. M. Han, and M. Dryer, Two-dimensional, time dependent MHD description of interplanetary disturbances. 1. Simulation of high-speed solar wind interactions, Planetary Space Sci., 27, 255, 1979.

TABLE 1

PRINCIPAL INVESTIGATORS

	<u>Plasma Analyzer</u>	<u>Magnetometer</u>	<u>Magnetometer</u>	<u>Radio Waves</u>	<u>Plasma Waves</u>	<u>Plasma and Radio Waves</u>	<u>Energetic Particles</u>
Helios-1	Rosenbauer	Neubauer	Mariani/Ness	Stone	Gurnett	Kellogg	Keppeler
Helios-2	Rosenbauer	Neubauer	Mariani/Ness	Stone	Gurnett	Kellogg	Keppeler
Voyager-1	Bridge	Ness			Gurnett		Krimigis
Voyager-2	Bridge	Ness			Gurnett		Krimigis
IMP-7	Bridge	Ness			Gurnett		
IMP-8	Bridge	Ness			Gurnett		

TABLE 2

STREAM INTERFACECOROTATION

From	To	$\phi_2 - \phi_1$	$(\tau_2 - \tau_1)$ (AU)	$(\tau_2 - \tau_1)$ (hr) Predicted	$(\tau_2 - \tau_1)$ (hr) Observed
Helios-1 (11/23, 0245)	Helios-2 (11/25, 0721)	35.2°	-0.029	57	53
Helios-2	IMP (11/27, 02:00) $\pm 01:00$	$8.2^\circ \pm 0.1^\circ$	0.353	51	43 ± 1
IMP	Voy. 1 (11/29, 16:00) $\pm 00:15$	$-1.7^\circ \pm 0.8^\circ$	0.605	60 ± 3	62 ± 1
Voyager 1	Voy. 2 (11/29, 21:25)	0.9°	0.012	3	5

TABLE 3

SHOCK B

	Helios 2	SSC	Voy. 1	Voy. 2
Shock ID	B ₁	B ₂	B ₃	B ₄
Date	Nov. 25	Nov. 26	Nov. 29	Nov. 29
Hr: min.	01:47	17:04	02:04	07:21
$r(10^8 \text{ km})$	0.944	1.476	2.373	2.390
Normal λ_n	60°	--	9.1°	14.9°
Normal δ_n	14°	--	-0.7°	21.2°
V(km/s)	300	--	409	395
V_r (km/s)	540	--	409	423

TABLE 4

SHOCK A

	Helios 2	Helios 2	Helios 1	IMP-8	Voy. 2	Voy. 1
Shock I.D.	A ₁	A ₂	A ₃	A ₄	A ₅	A ₆
Date	Nov. 23	Nov. 24	Nov. 25	Nov. 25	Nov. 27	Nov. 27
Hr: min	16:10	06:11	22:28	12:13	07:30 + 01:30	22:26
r(10 ⁸ km)	0.916	0.927	1.018	1.476	2.361	2.533
Normal λ_n	16°	- 15°	4°			- 34°
Normal θ_n or δ_n	$\theta_n = -14^\circ$	$\theta_n = -48^\circ$	$\theta_n = 25^\circ$			$\delta_n = -10^\circ$
V(km/s)	330	304	352			302
V _r (km/s)	353	467	390	~ 418		369

TABLE 5

SHOCK C

SHOCK I.D.	Helios 2		Helios 1		IDP 7		Voy. 2		Voy. 1	
	C_1		C_2		C_3		C_4		C_5	
Date	Dec. 1		Dec. 1		Dec. 2		Dec. 3		Dec. 3	
Hr: min	01:29		05:14		02:15		21:41		23:18	
$r (10^8 \text{ km})$	1.042		1.111		---		2.455		2.445	
Normal λ_n	- 3°		3°		---		38.3°		---	
Normal θ_n	17°		-34°		---		-6°		---	
$V (\text{km/s})$	441		417		---		415		---	
$V_r (\text{km/s})$	460		501		---		530		---	

FIGURE CAPTIONS

- FIGURE 1 Ecliptic plane projection of the trajectories of Helios-1, -2 and Voyager-1, -2 shown in the inertial solar ecliptic coordinate system for the interval November 22 - December 6, 1977.
- FIGURE 2 Corotating interface. The top panel shows the associated stream relative to the interface at each spacecraft. The bottom panel shows the intersection of the interface with the ecliptic plane at the time that it passed each of the spacecraft. The dashed circular arc passing through Earth represents Earth's orbit. The position of shock B is also shown, and its orientation is illustrated in the bottom panel.
- FIGURE 3 The corotating stream interface (top) seen by each of the spacecraft. The interface is defined by the abrupt decrease in density and the corresponding increase in temperature. Times have been shifted so that the interfaces are aligned vertically, allowing a comparison of the density, temperature, and magnetic field intensity profiles (bottom).
- FIGURE 4 Structure of the interface, shown by a plot of high resolution magnetic field and plasma data (top), and corresponding plasma wave observations. The interface is relatively broad (30 min), its structure does not change appreciably over the 0.2 AU separation between Voyager-1 and Voyager-2, and there is no evidence of an instability that might produce waves ζf_p^+ at Voyager-2.
- FIGURE 5 Shock B, showing the high-resolution magnetic field and plasma data (top panel) and plasma wave observations (bottom panel) near the shock. The flow and field parameters are steady before and after the shock front, allowing accurate determination of its normal and speed. Whistler wave

turbulence is observed at $f < f_p^+$ behind the shock; a short burst of broadband turbulence is observed at the shock; and "ion-acoustic" waves are observed at $f_p^+ < f < f_p^-$ ahead of the shock.

FIGURE 6

A type III burst (77 kHz to 3000 kHz), the beam of electrons (20-65 keV) which produced the burst, and plasma waves (at the local plasma frequency, 52 kHz) produced locally by the electron beam. The profiles at 52, 77 and 20° kHz are from the University of Minnesota experiment; the others are from the Goddard Space Flight Center experiment on Helios-2.

FIGURE 7

Shocks A_1 , A_2 , A_3 and the stream interface. At 0600 UT, November 24, 1977, the interface had passed Helios-1, but had not reached Helios-2. One shock (A_3) was approaching Helios-1 and arrived at Helios-1 late on November 24. Two shocks were observed by Helios-2. One (A_2) arrived at Helios-2 at 0611 UT on November 24, and another was a short distance ahead of it. A_1 and A_2 coalesced into 1 shock (A_4) as they moved from Helios-1 to earth, where A_4 was detected by IMP-8.

FIGURE 8

A sketch, approximately to scale, showing the position of shock B, the stream interface, and shock A_2 at 0600 UT, when A_2 was approaching Helios-2. The positions of the spacecraft and the flare site at that time are also shown. The hypothetical ejecta were not observed. The flare produced energetic protons which escaped freely through the stream. Shock A_2 accelerated particles locally and perhaps trapped some of the flare particles, producing a local maximum in counting rates at the shock observed by Helios-2. These shock-accelerated particles did not penetrate the stream interface and were not observed by Helios-1.

FIGURE 9

Propagation of shock A. The radial position of the shock is shown at the times that the shocks arrived at Helios-1 (H1), Helios-2 (H2), IMP-8, Voyager-1 (V1) and Voyager-2 (V2). The two shocks observed by H2 coalesced into the one shock observed by IMP-8. Departures from spherical symmetry of shock A are indicated by the scatter of the points about a straight line.

FIGURE 10

High resolution magnetic field and plasma data show that A_4 (at IMP-8) and A_6 (at Voyager-1) are shocks. A narrow, broadband burst of electrostatic noise was observed at the time of the shock by both spacecraft. "Ion-acoustic" waves between f_p^- and f_p^+ were observed upstream by both spacecraft. Voyager-1 also observed whistler mode turbulence at $f < f_p^+$ behind the shock.

FIGURE 11

High resolution magnetic field and plasma data showing that A_1 and A_2 are shocks (or steep compressive waves). Electrostatic plasma wave data from Helios-2 show that the shock was imbedded in a broad region of doppler-shifted "ion-acoustic" waves. A narrow spike was observed at 562 and 311 Hz at the time of the shock.

FIGURE 12

High resolution plasma and magnetic field data showing shock C and a boundary behind it, which might be the boundary of the ejecta (contact surface). Note the depression in magnetic field intensity at the boundary. Electrostatic plasma waves are observed between f_p^- and f_p^+ at the shock, but no significant waves are observed at the contact surface.

FIGURE 13

Sixteen-min. averages of the speed, density, temperature, and magnetic field intensity, showing shock C, the pre- and post-shock conditions, and the post-shock conditions at Helios-1, -2 and at Voyager-1, -2. Note the drop in density and temperature and the high magnetic field intensities behind the shock at Helios-1 and -2, suggesting entry into the

ejecta. The parameters slowly decrease behind the shock at Voyager-2, to the pre-shock levels, indicating that this spacecraft did not penetrate the ejecta.

FIGURE 14 High resolution magnetic field data showing shock C. The plasma wave data show a short broadband burst at Helios-2, but not at Voyager-2. Electrostatic waves were observed behind shock C at frequencies between 311 Hz - 17.8 kHz by Helios-2, and over a more limited frequency range (178 Hz - 5.62 kHz) by Voyager-2.

FIGURE 15 A sketch, drawn approximately 'J' scale, illustrating the position of shock B, corresponding stream interface, the position of shock C and the corresponding ejecta at hour 0 on November 30, 1977. The positions of Helios-1, -2, Voyager-1, -2, and Earth at this time are also shown.

FIGURE 16 Propagation of shock C. The radial distance at the times that the shock passed each of the spacecraft are shown. The straight line fit suggests a uniform speed of 555 km/s and spherical symmetry, but local observations indicate appreciable scatter about those values.

FIGURE 17 Counting rates of energetic protons near shock C, observed by Helios-1, -2 and Voyager-1, -2. The broad, intense fluxes of particles at Voyagers-1 and -2 closely resemble one another, but they differ appreciably from the narrower, less intense fluxes observed by Helios-1 and -2. The Helios-2 profile differs appreciably from that of Helios-1. The abrupt decrease in counting rates behind the shock observed by Helios-1 and Helios-2 may be due to a flow boundary (e.g., a piston) behind the shock.

FIGURE 18

Counting rates of energetic protons produced by the November 22 flare and by shock A, as observed by Helios-1 and -2. The speed profiles are shown as an aid in describing the corresponding flows. Helios-1 and Helios-2 observed similar intensity-time profiles during the initial stage of the decay. Helios-1, which was in the corotating stream continued to observe an uninterrupted, monotonic decay to the background level three days later. Helios-2 observed a second increase of flux. The intensity dropped abruptly when the interface arrived, because the accelerated particles did not penetrate the interface.

FIGURE 19

Counting rates of energetic protons observed by Voyager-1 and -2. Speed profiles are shown to indicate the flow conditions. Both Voyager-1 and -2 observed flare particles on November 22. The broad increase between November 27 - November 29 may be due to energetic storm particles. Locally accelerated particles are observed at the transient shock A, but there is no significant increase at the stationary shock B.

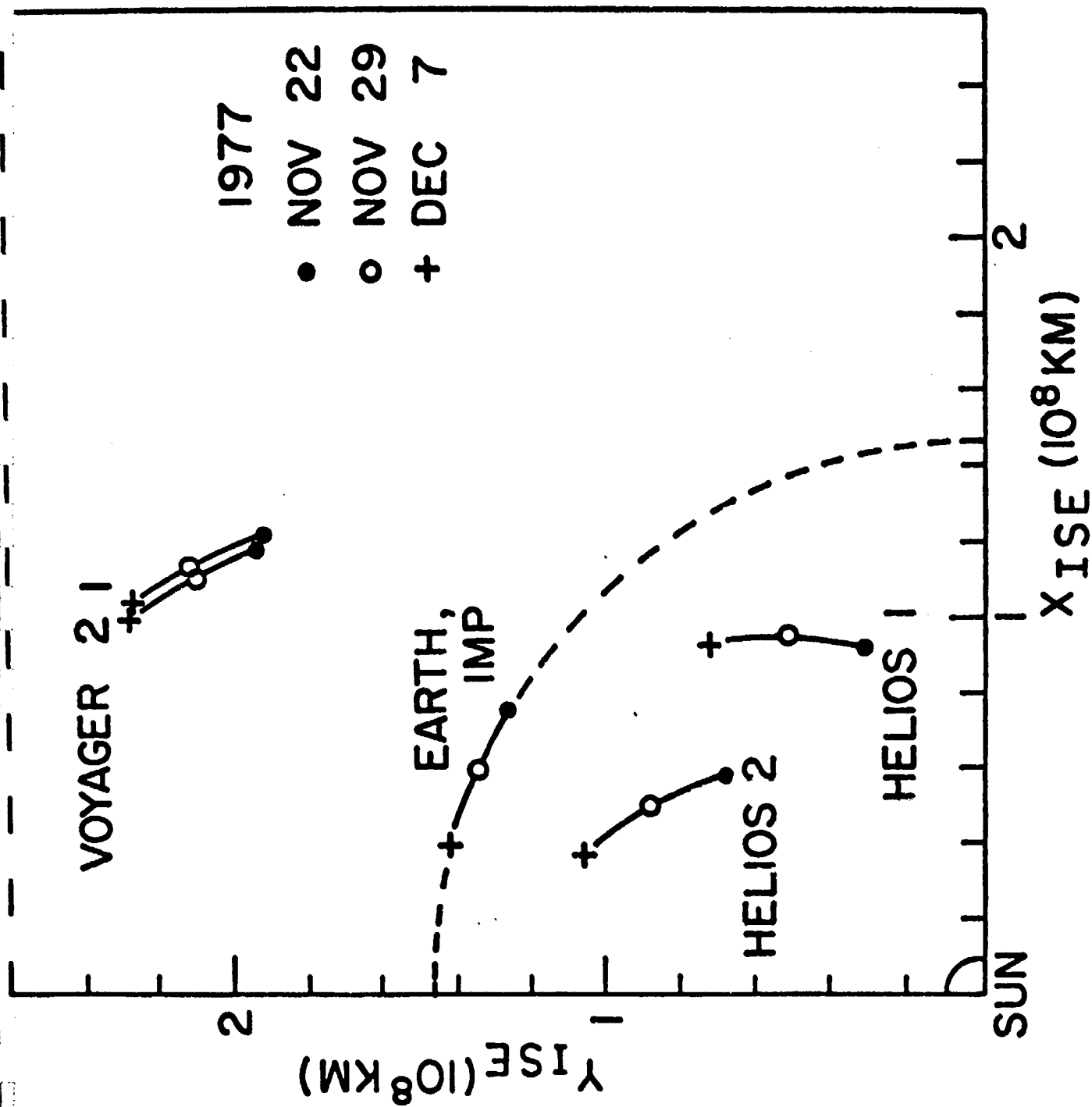


Figure 1

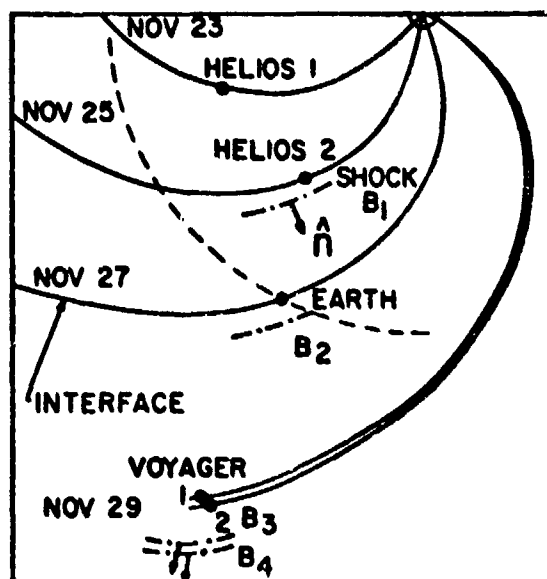
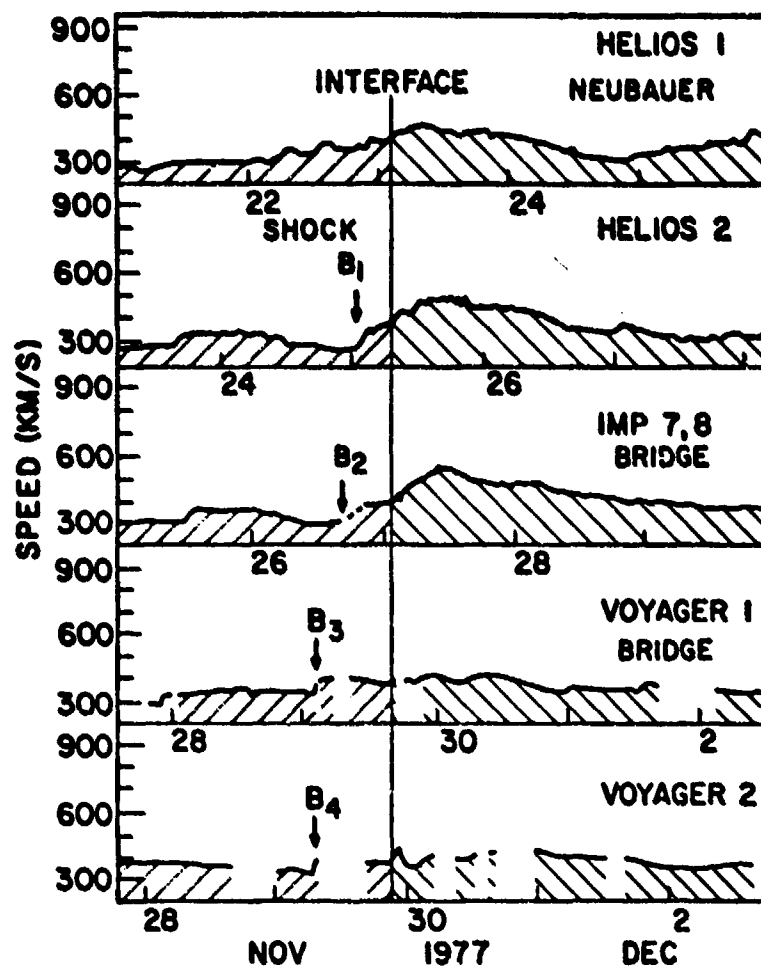


Figure 2

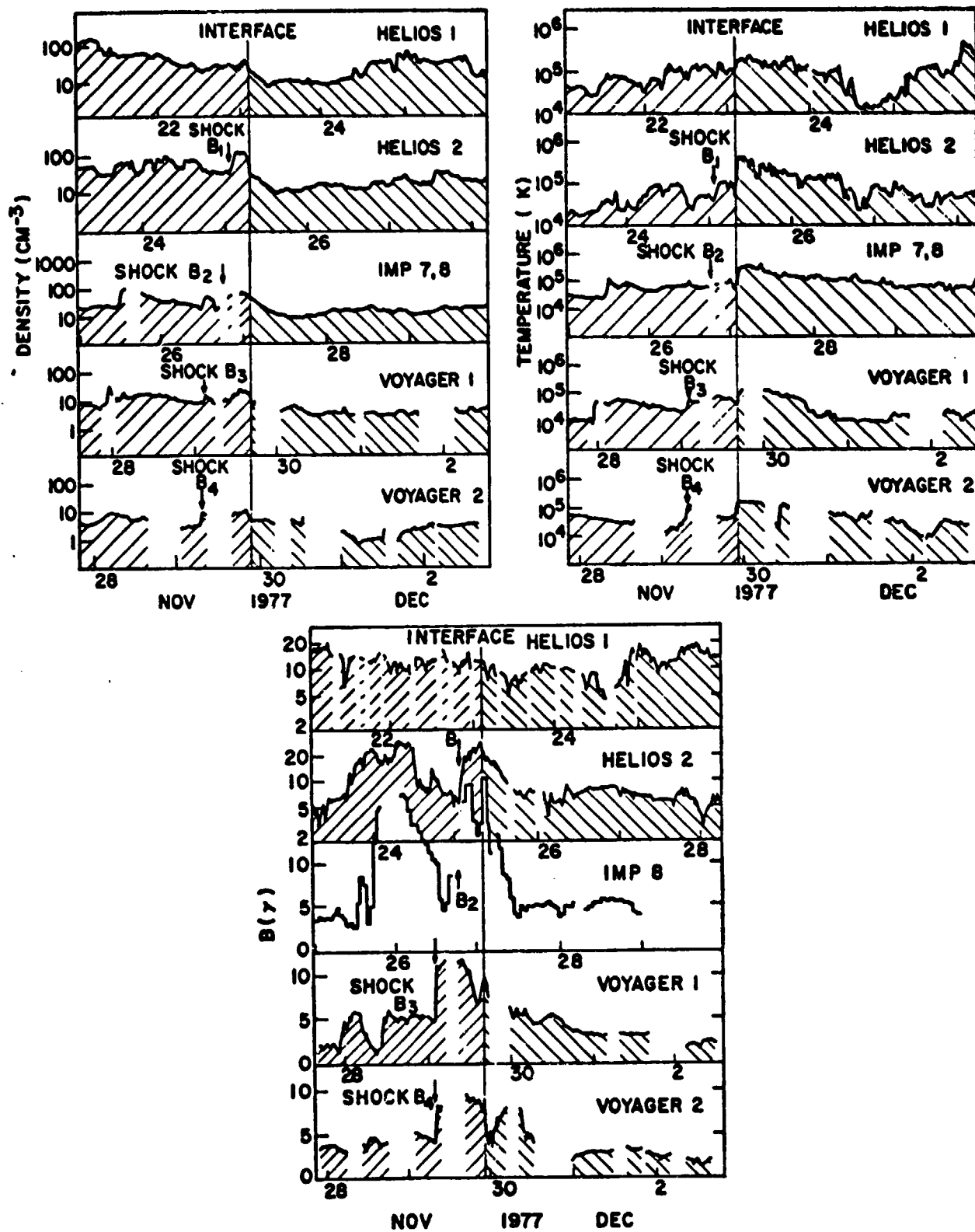


Figure 3

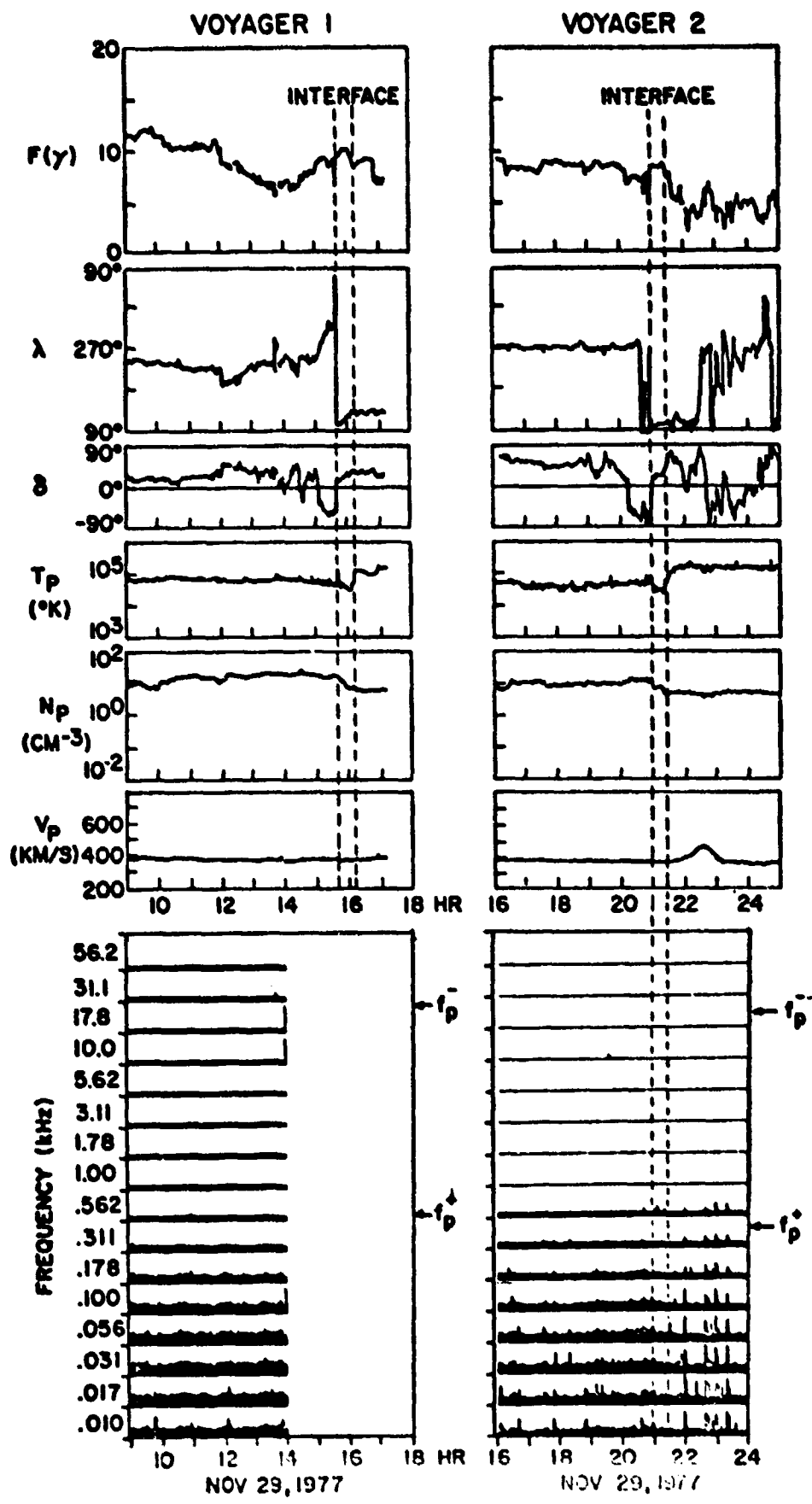
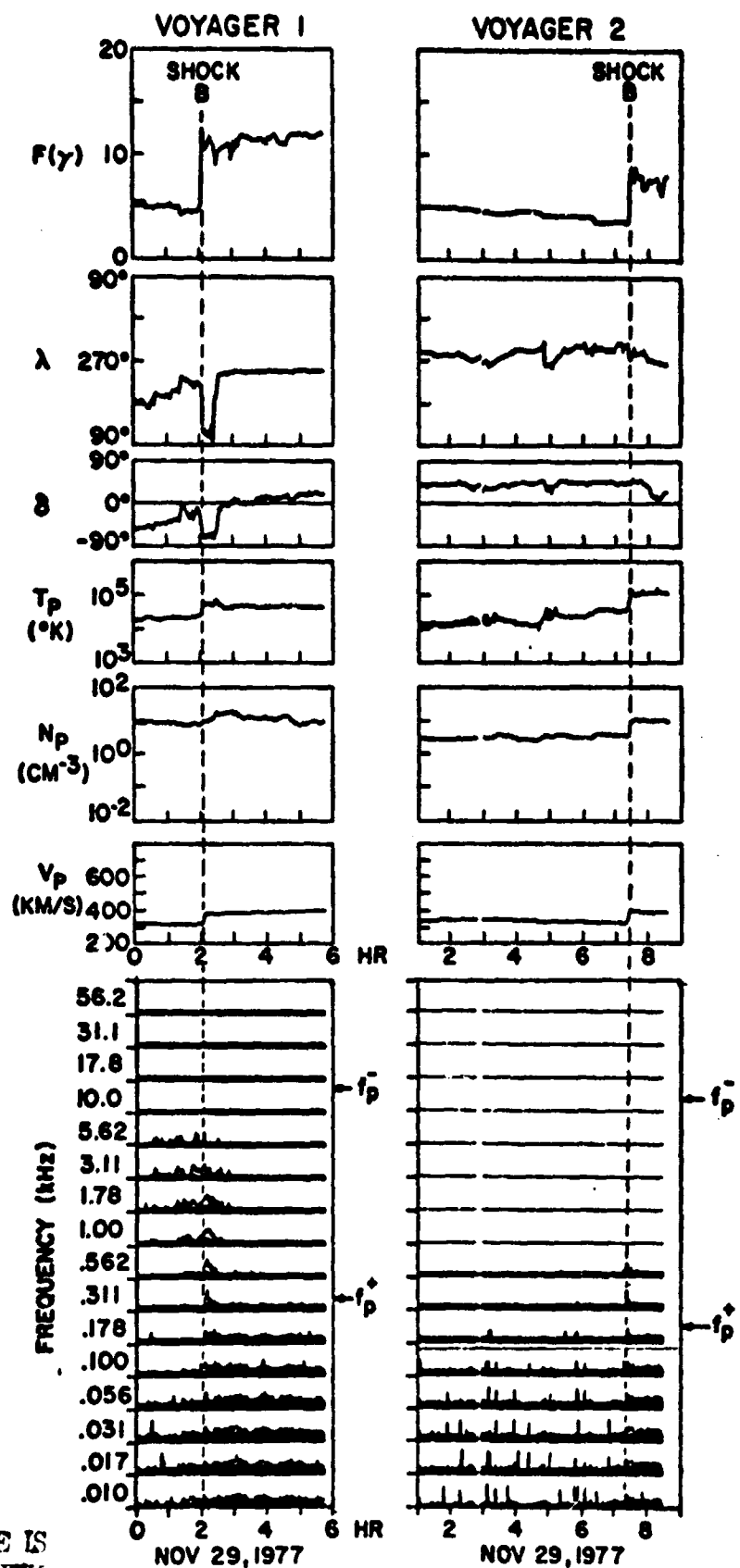


Figure 4



ORIGINAL PAGE IS
OF POOR QUALITY

Figure 5

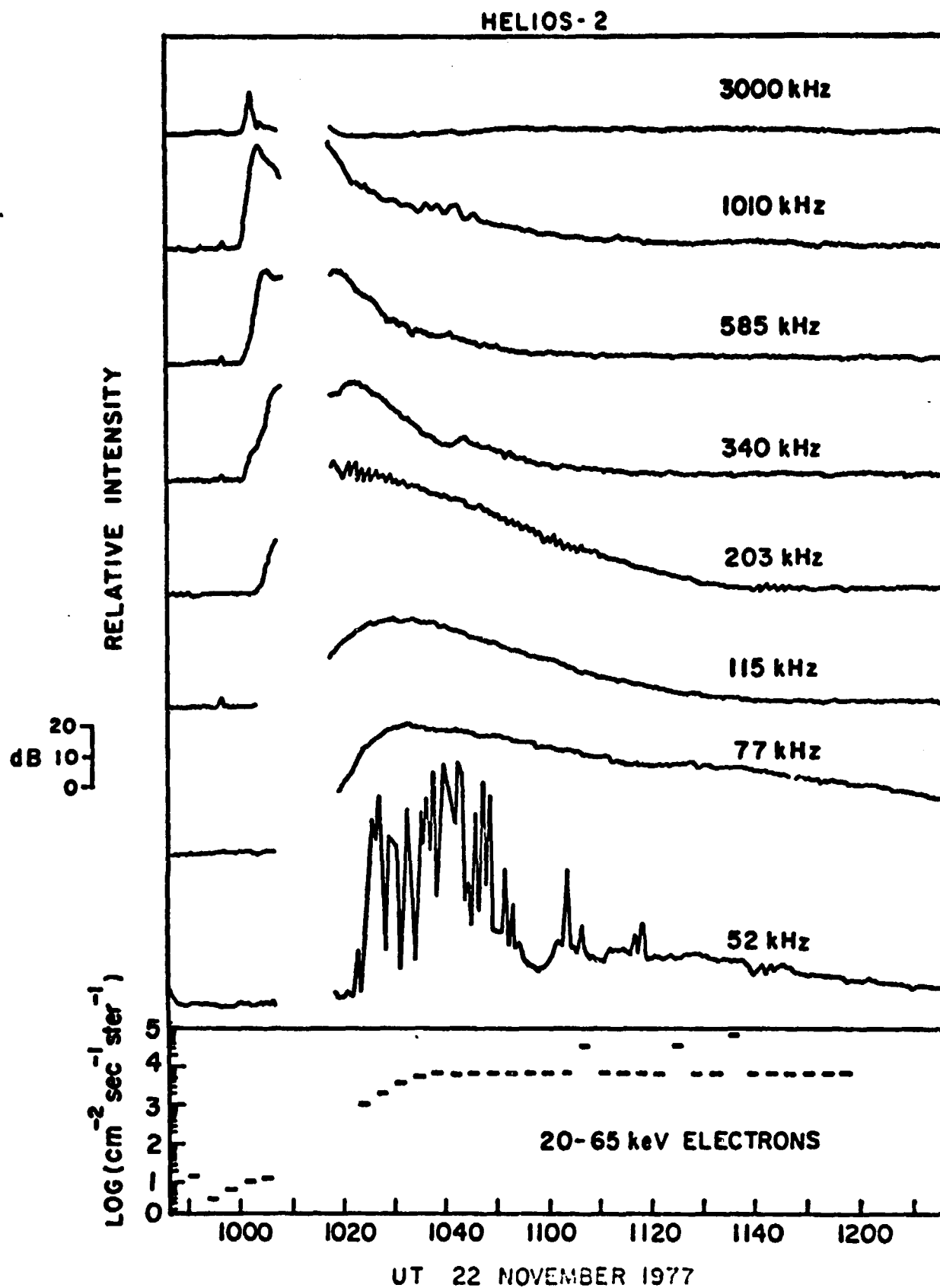


Figure 6

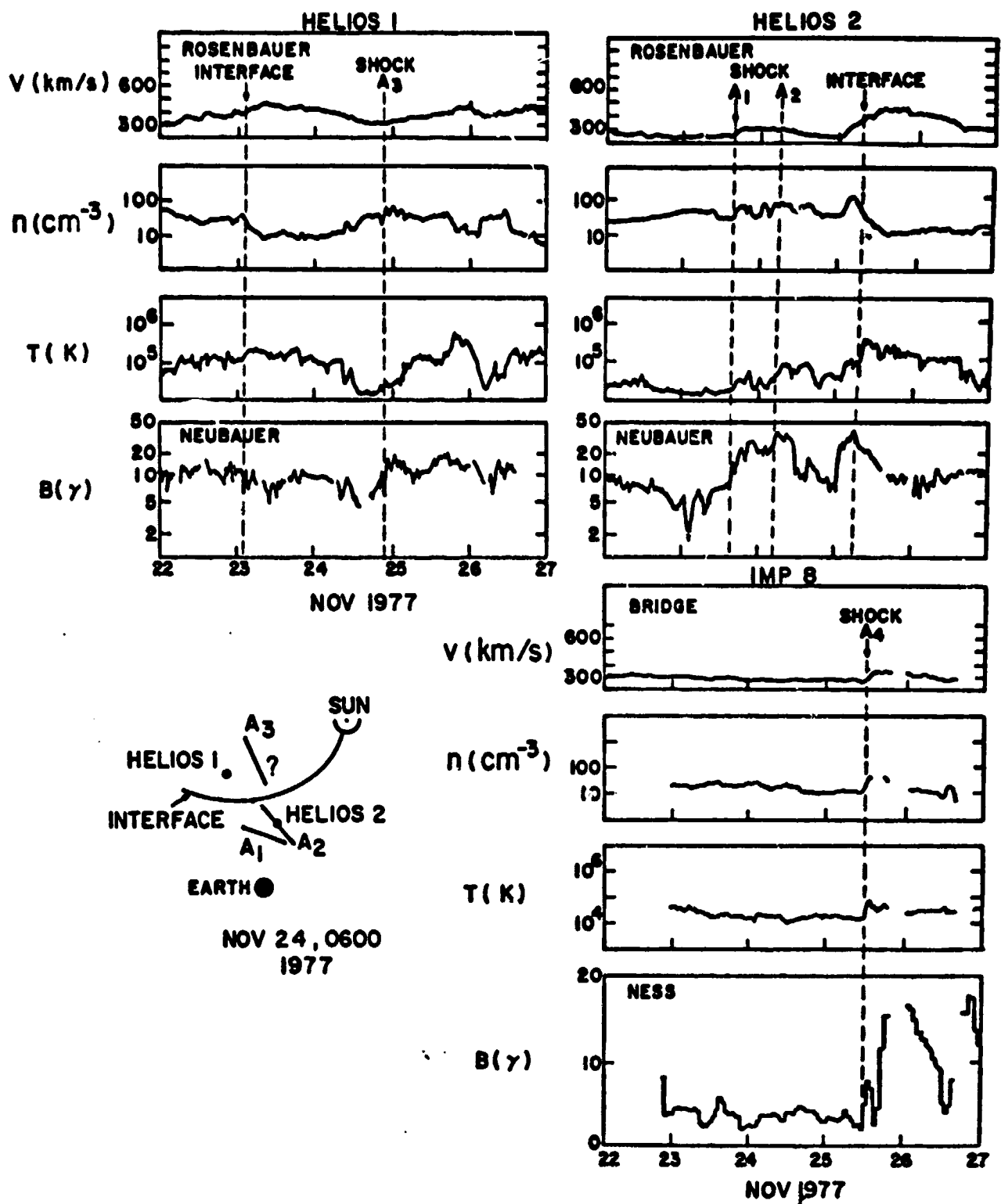


Figure 7

NOV 24, 1977
0600 UT

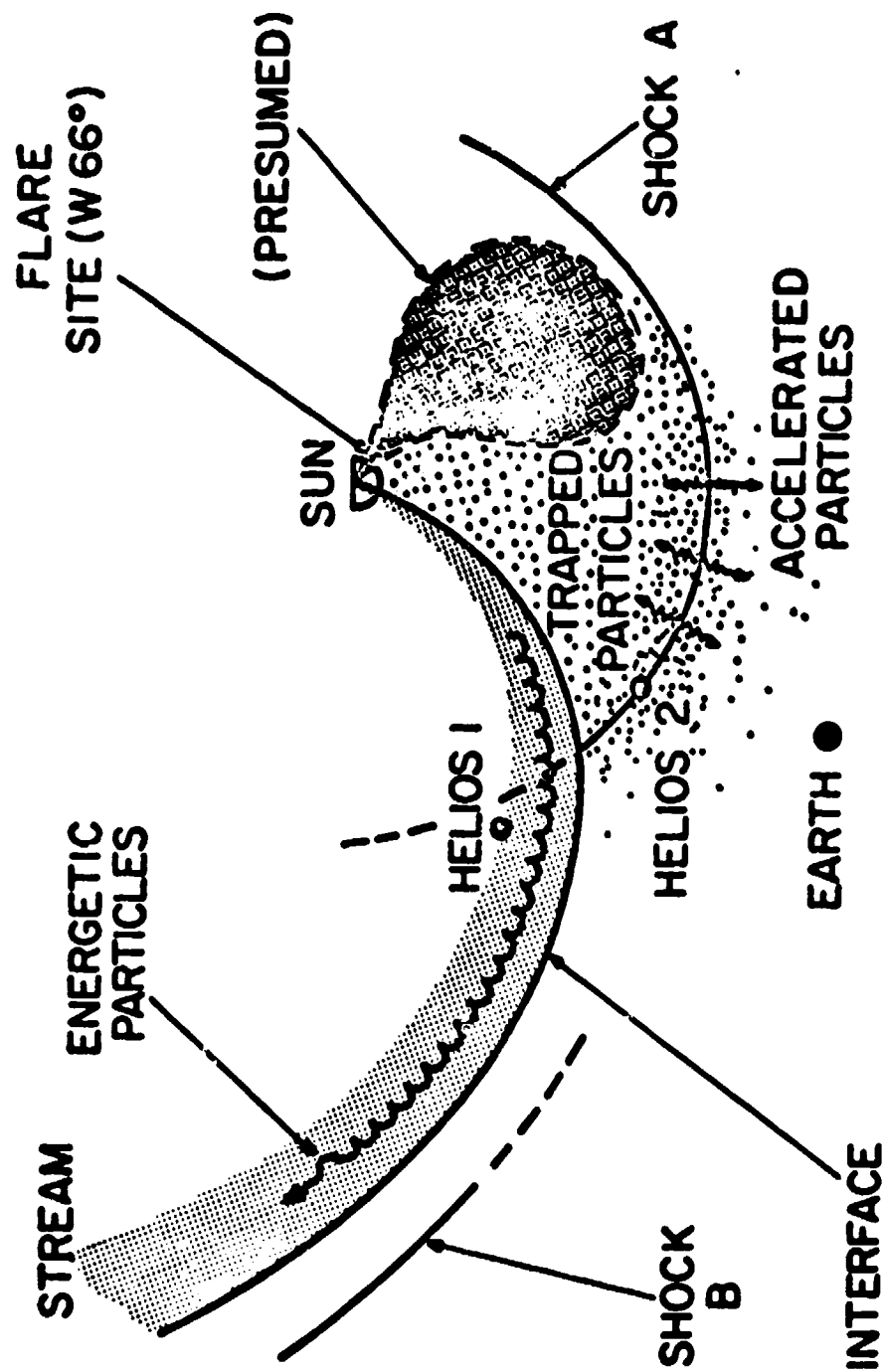


Figure 8

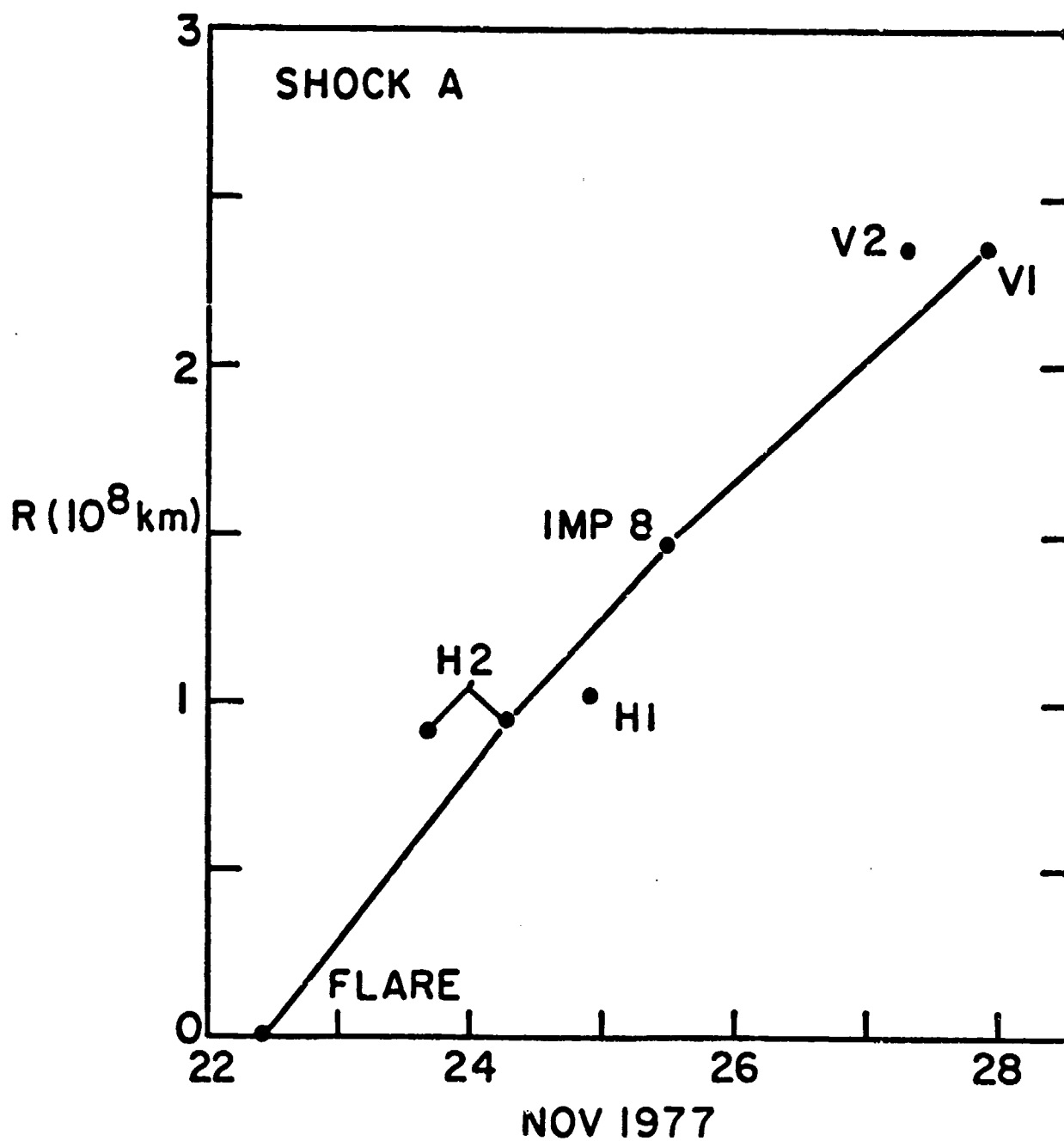
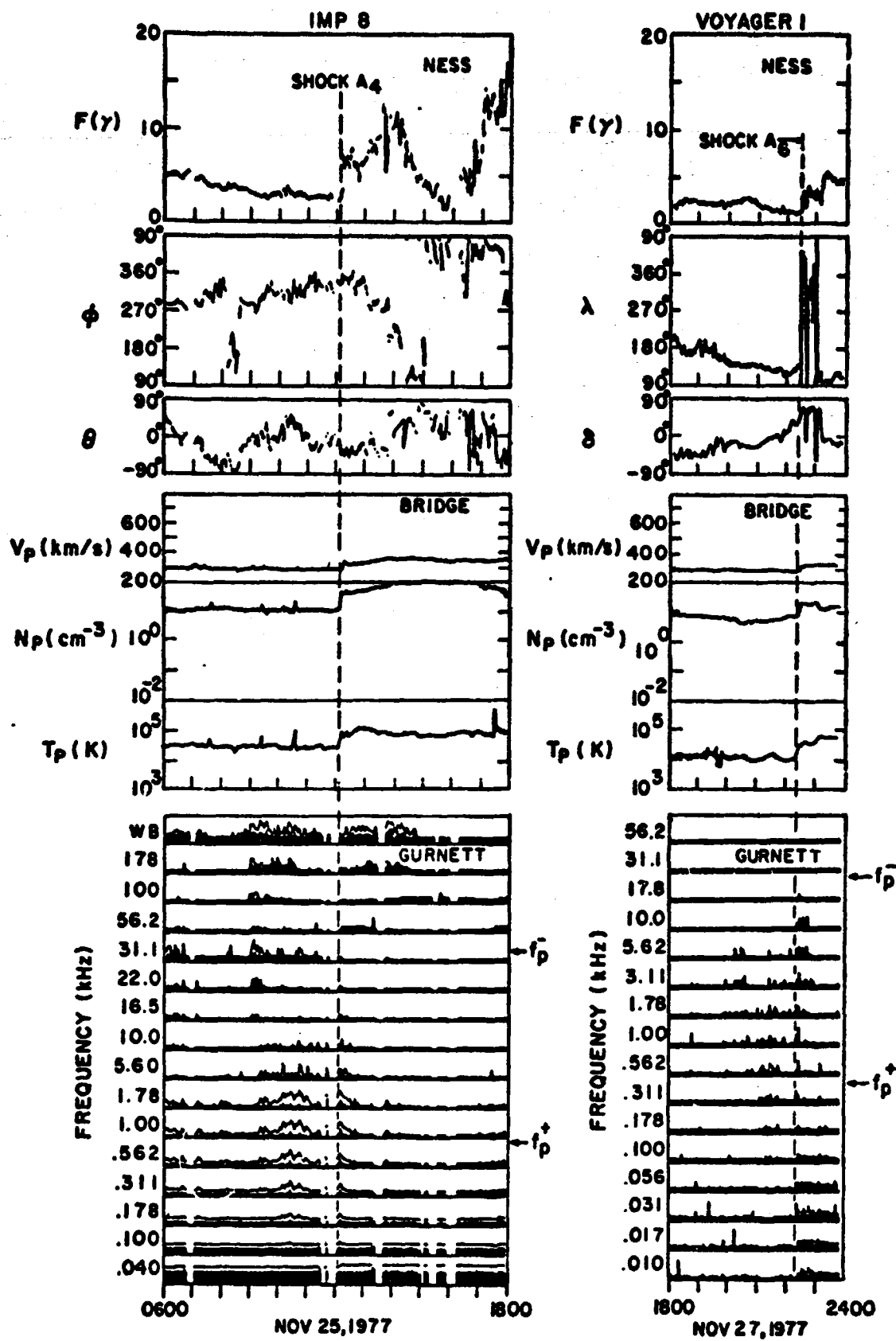


Figure 9



ORIGINAL PAGE IS
OF POOR QUALITY

Figure 10

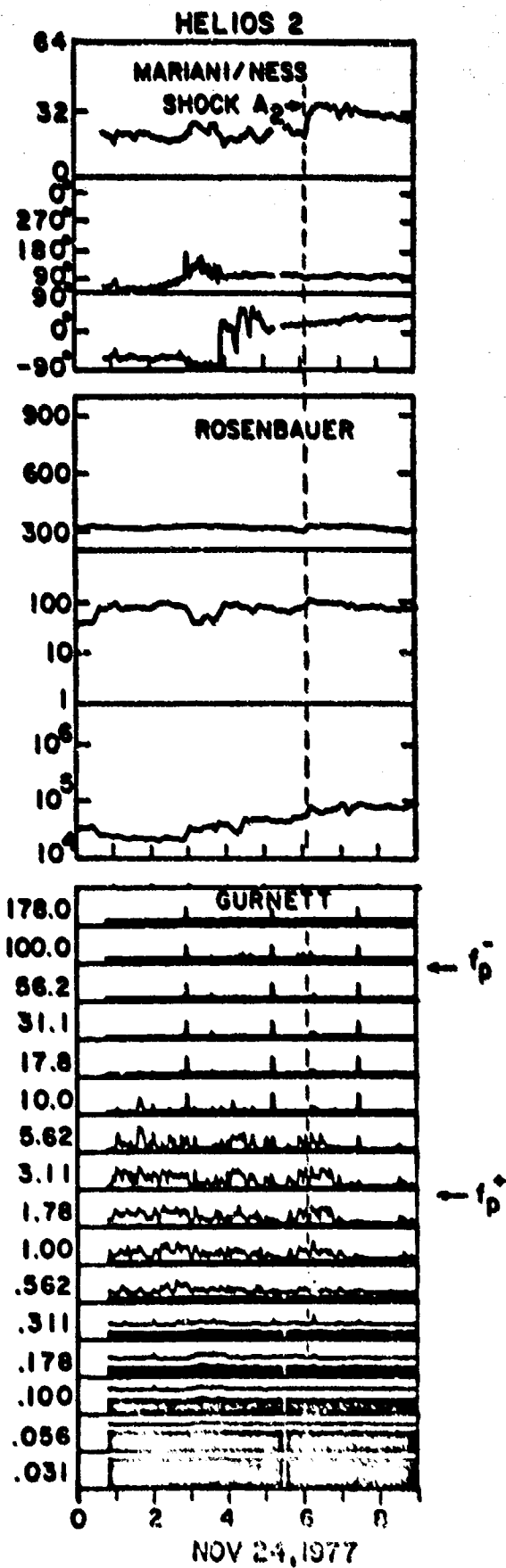
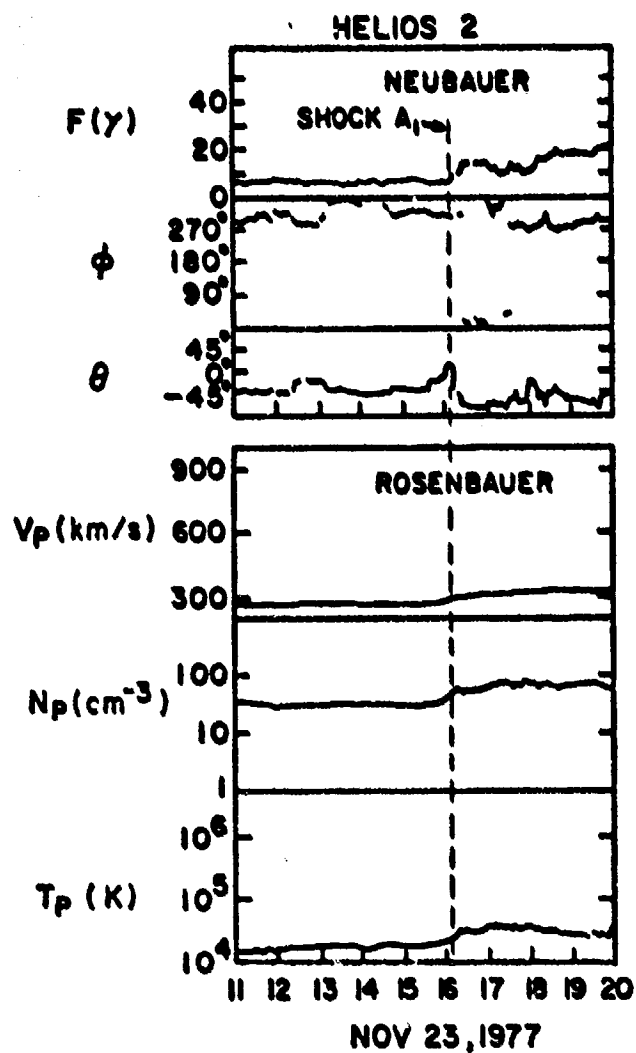


Figure 11

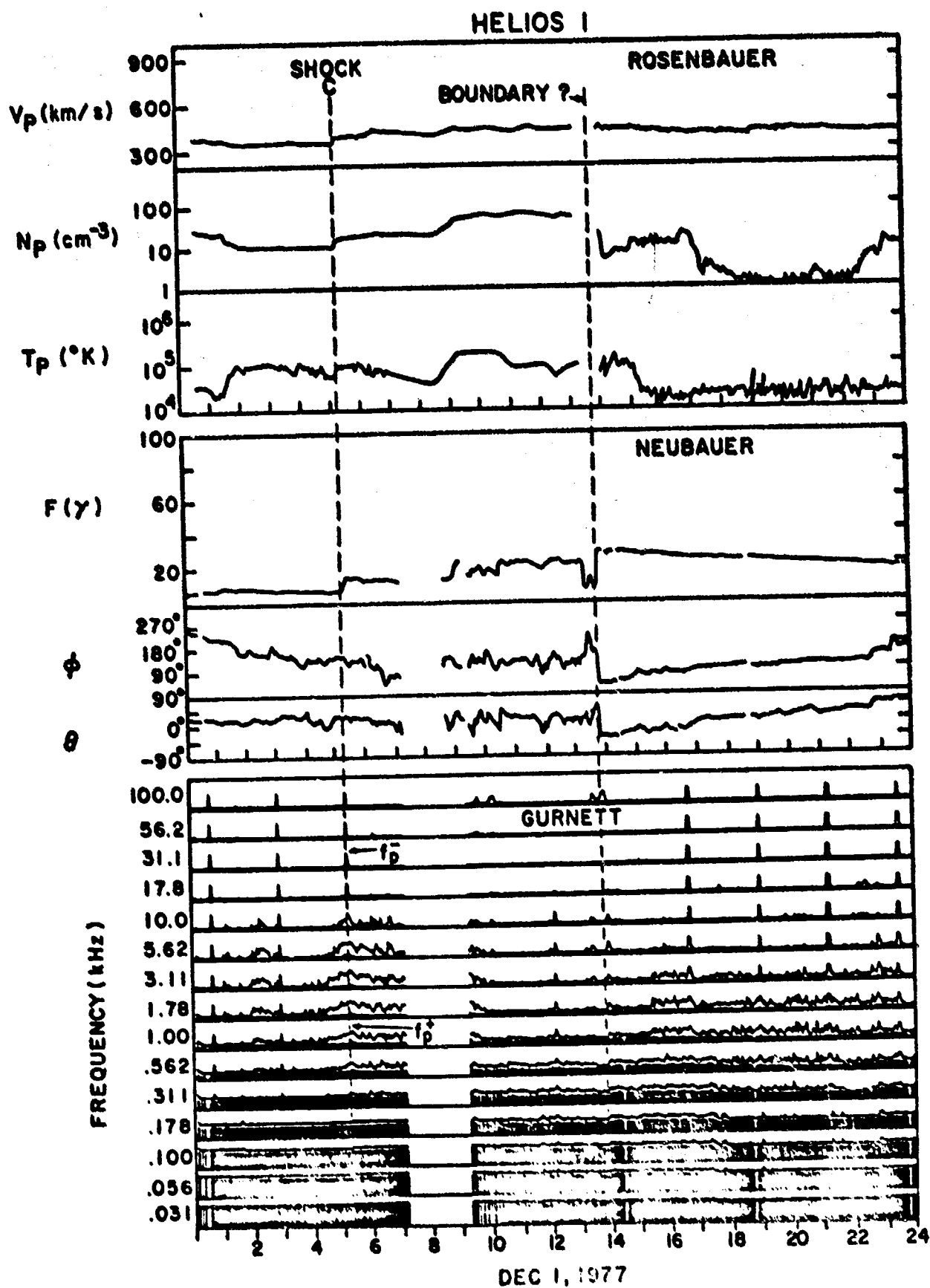


Figure 12

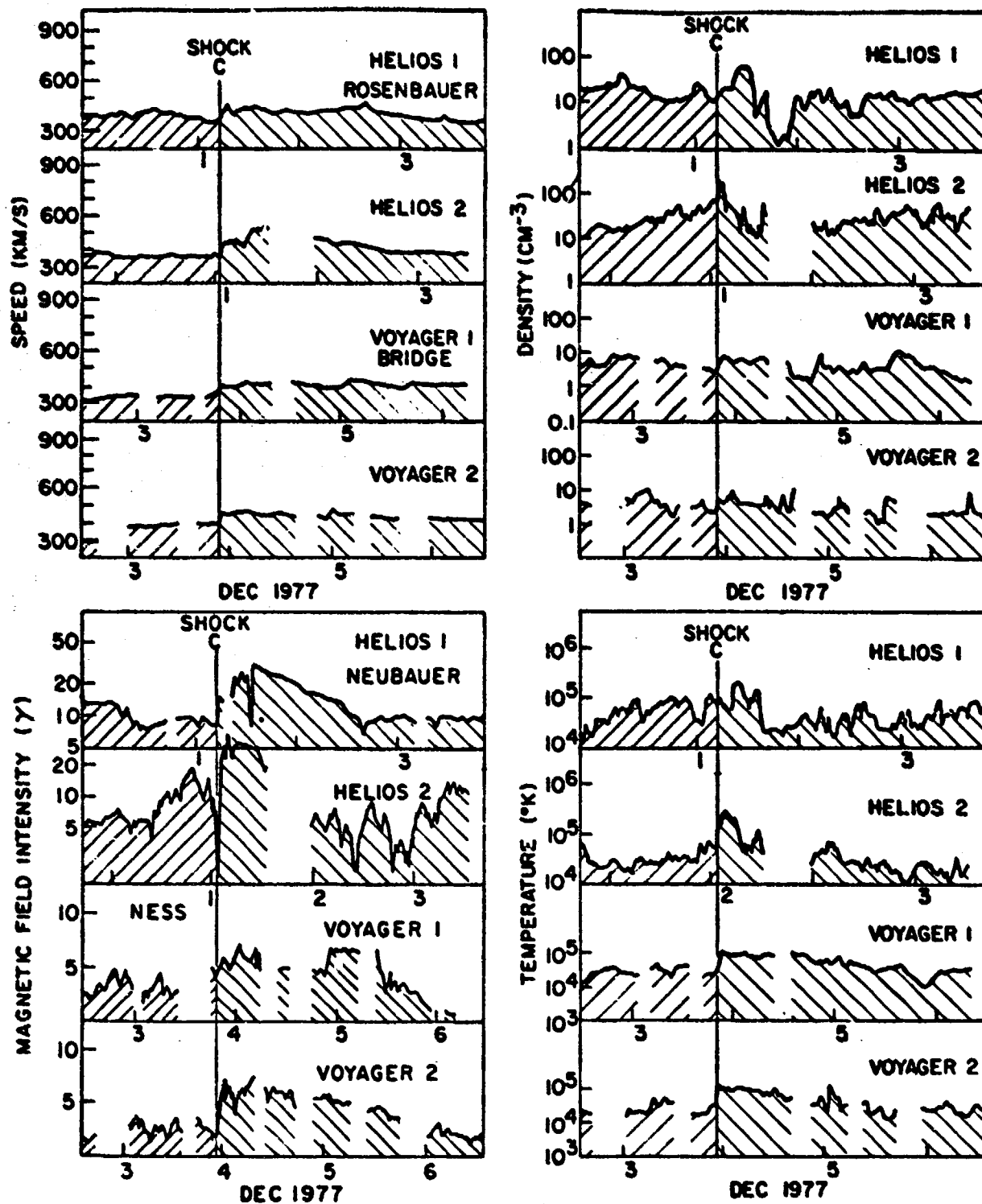


Figure 13

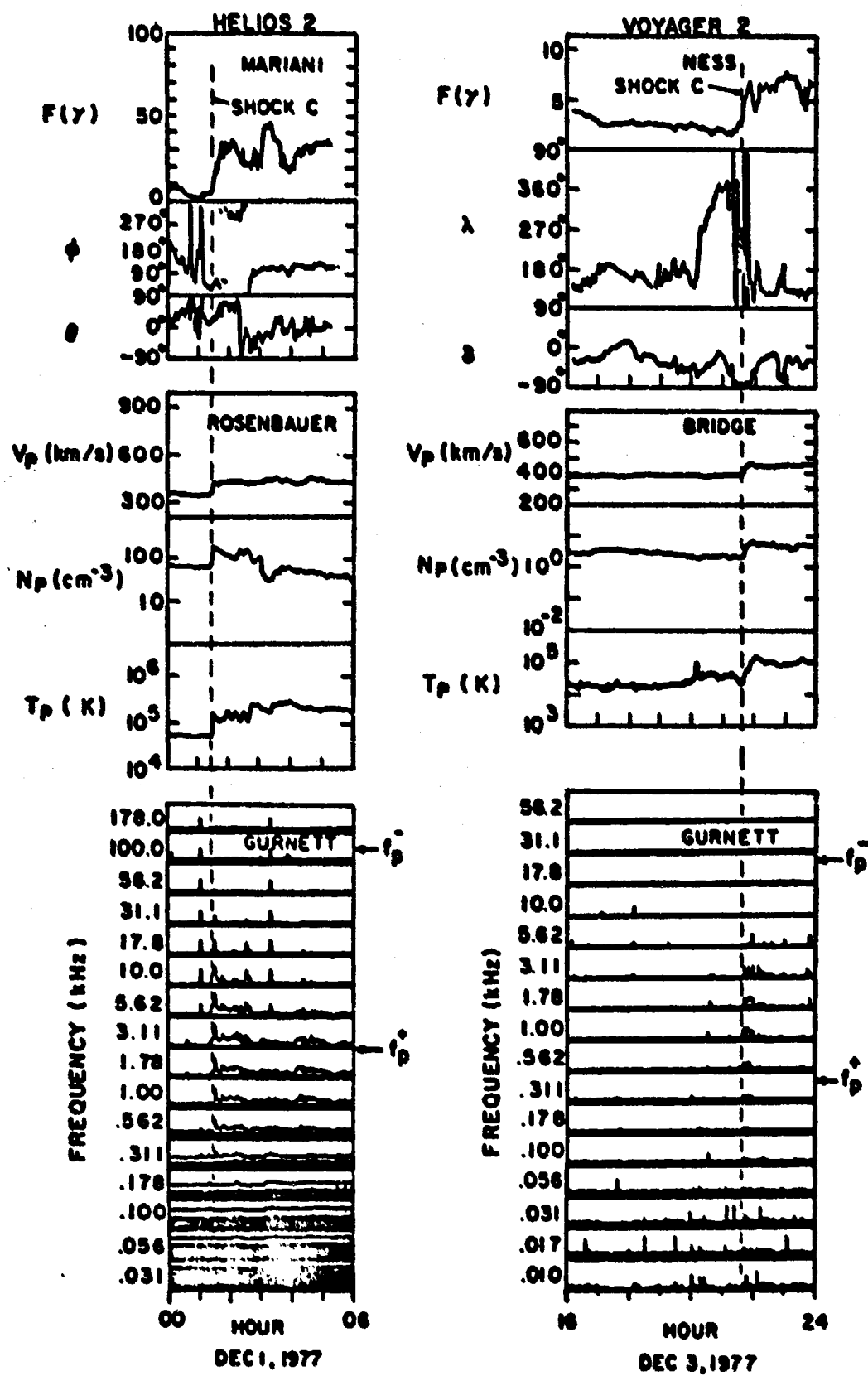


Figure 14

NOV 30, 1977

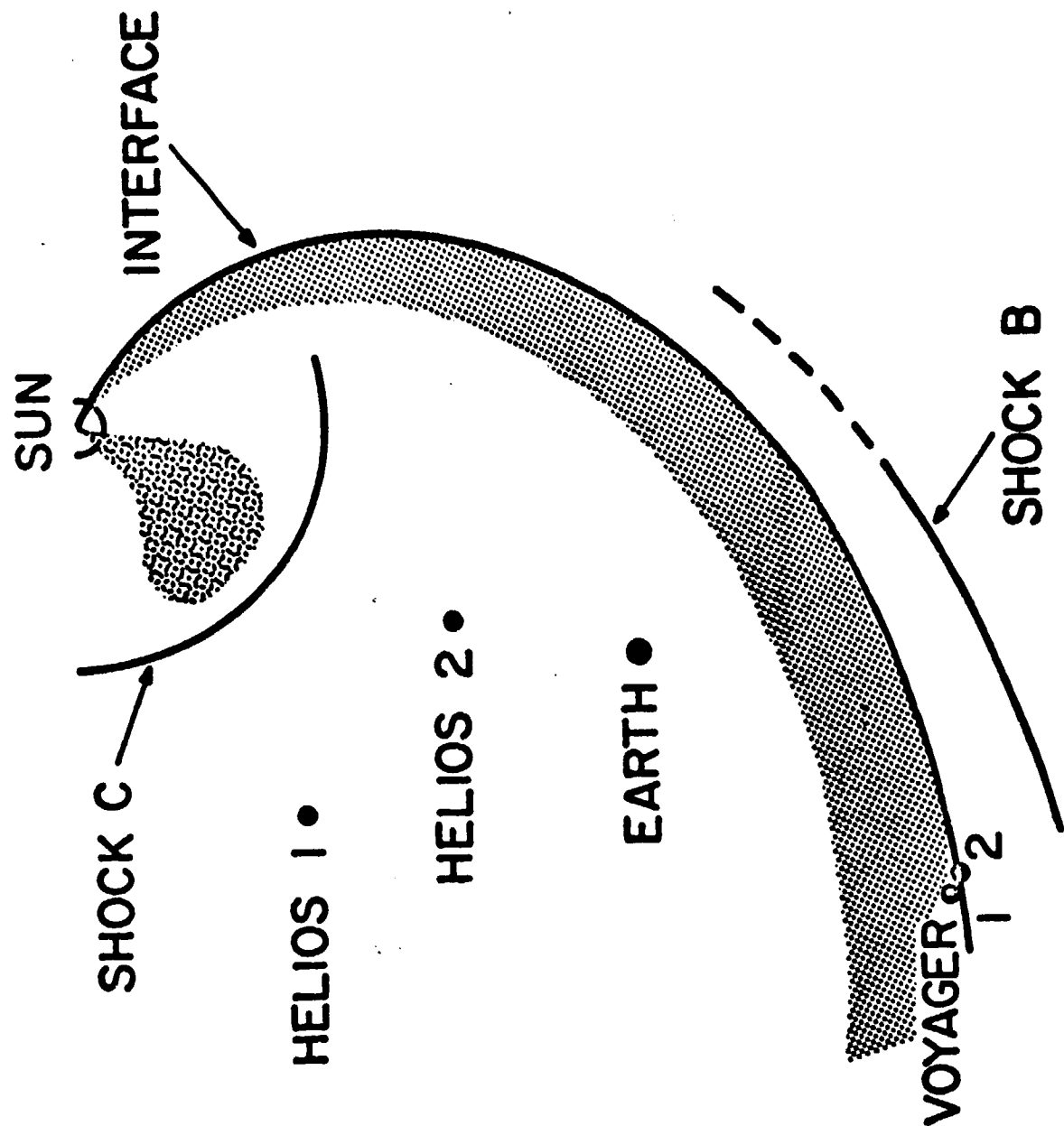


Figure 15

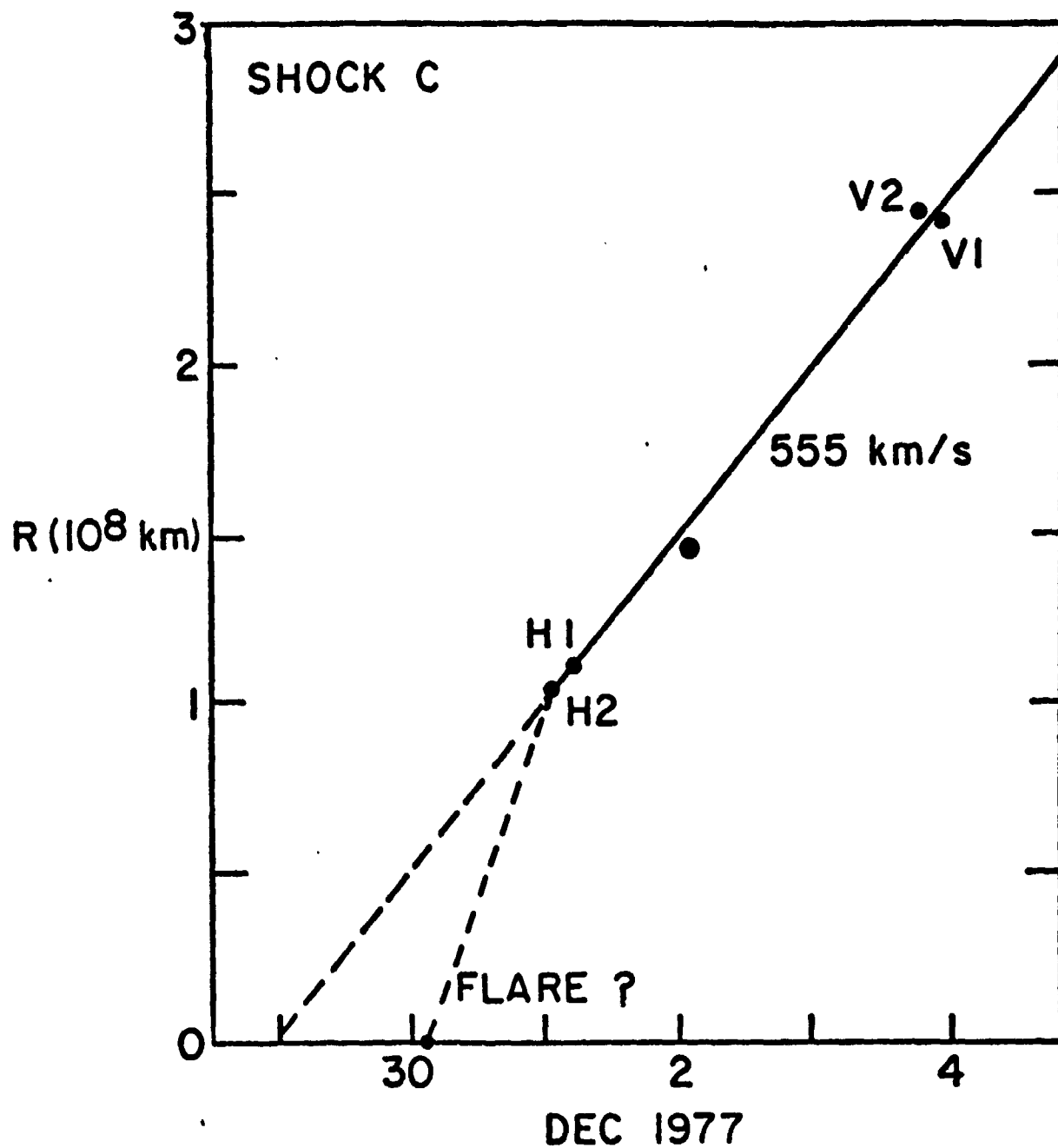


Figure 16

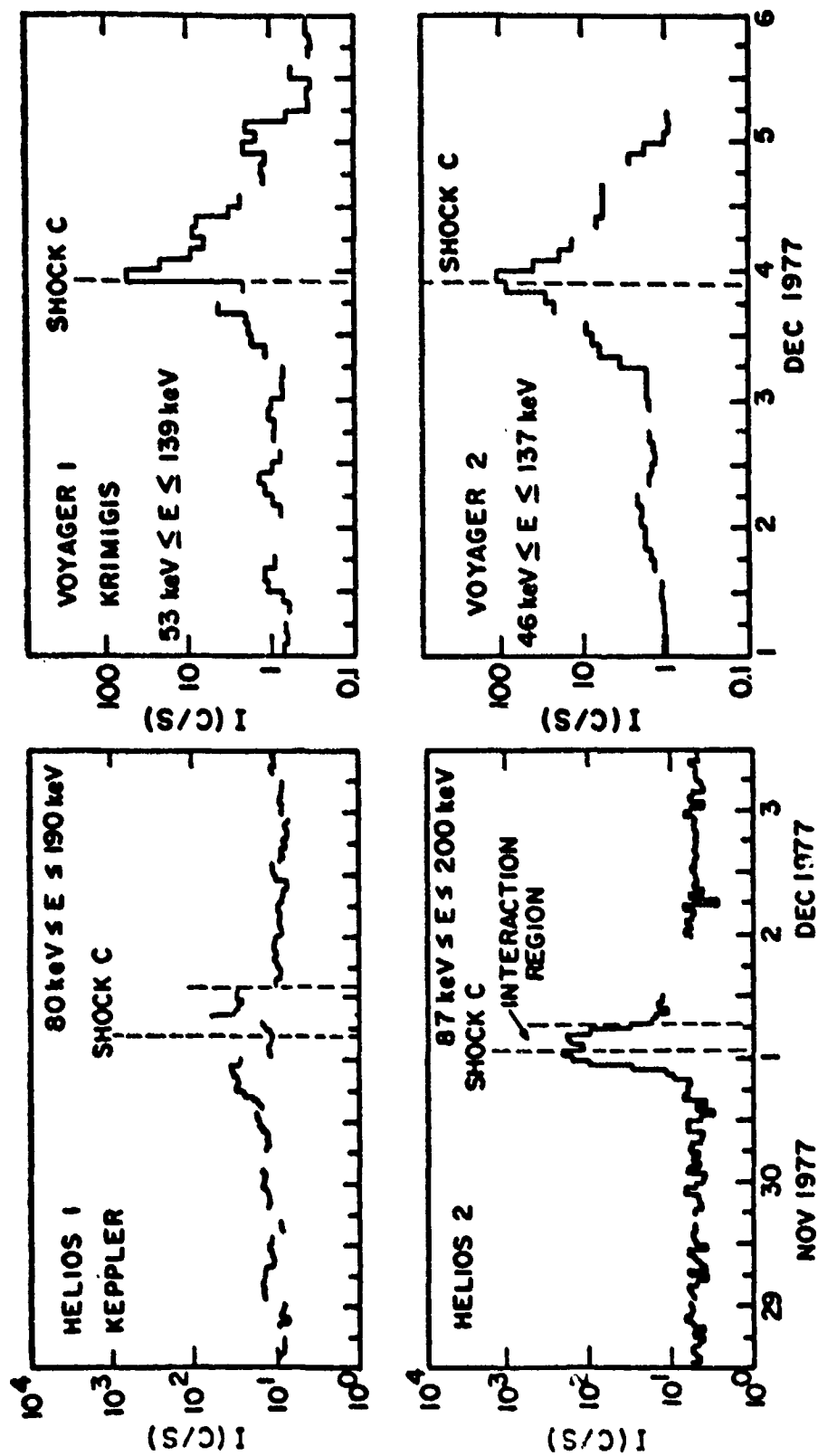


Figure 17

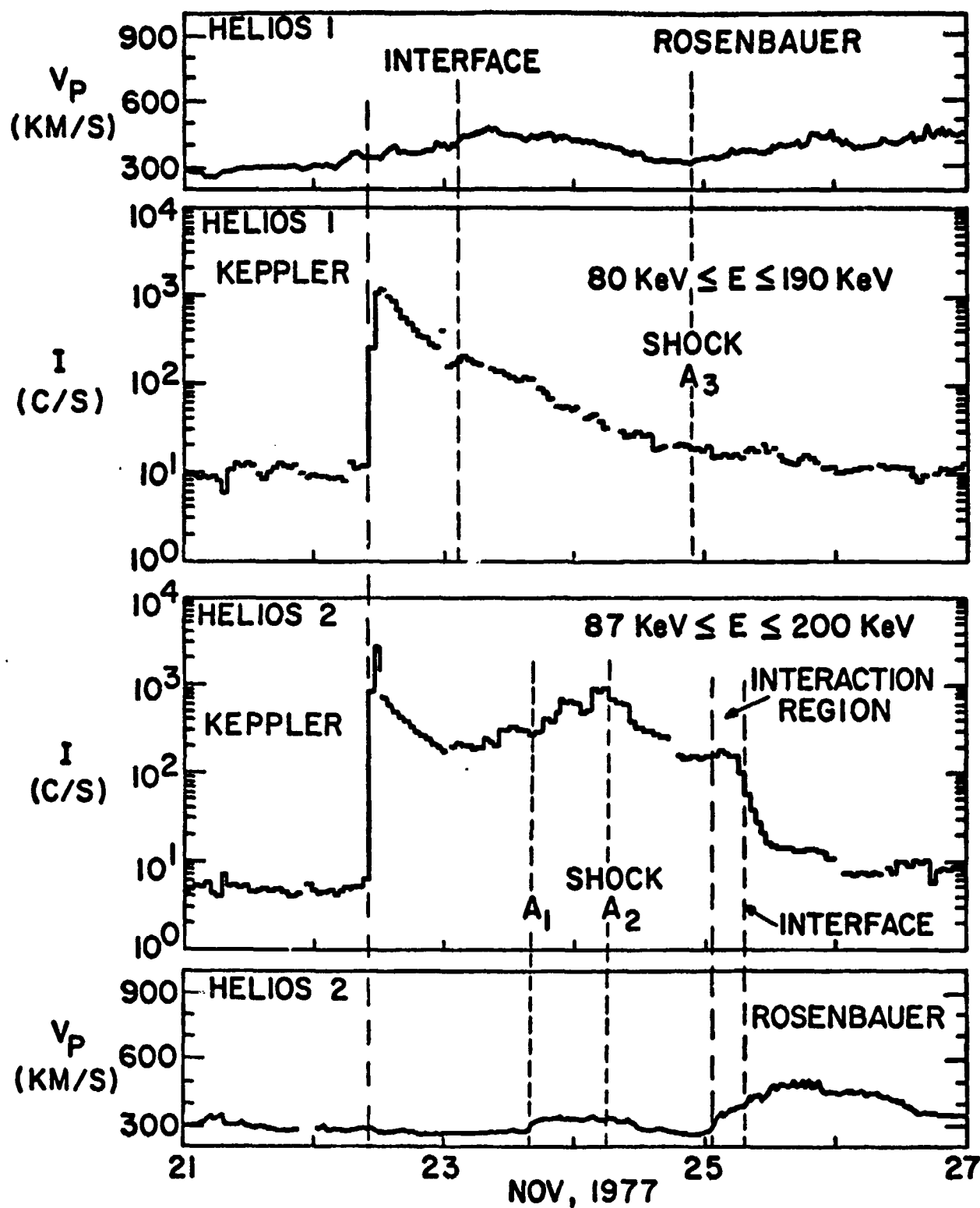
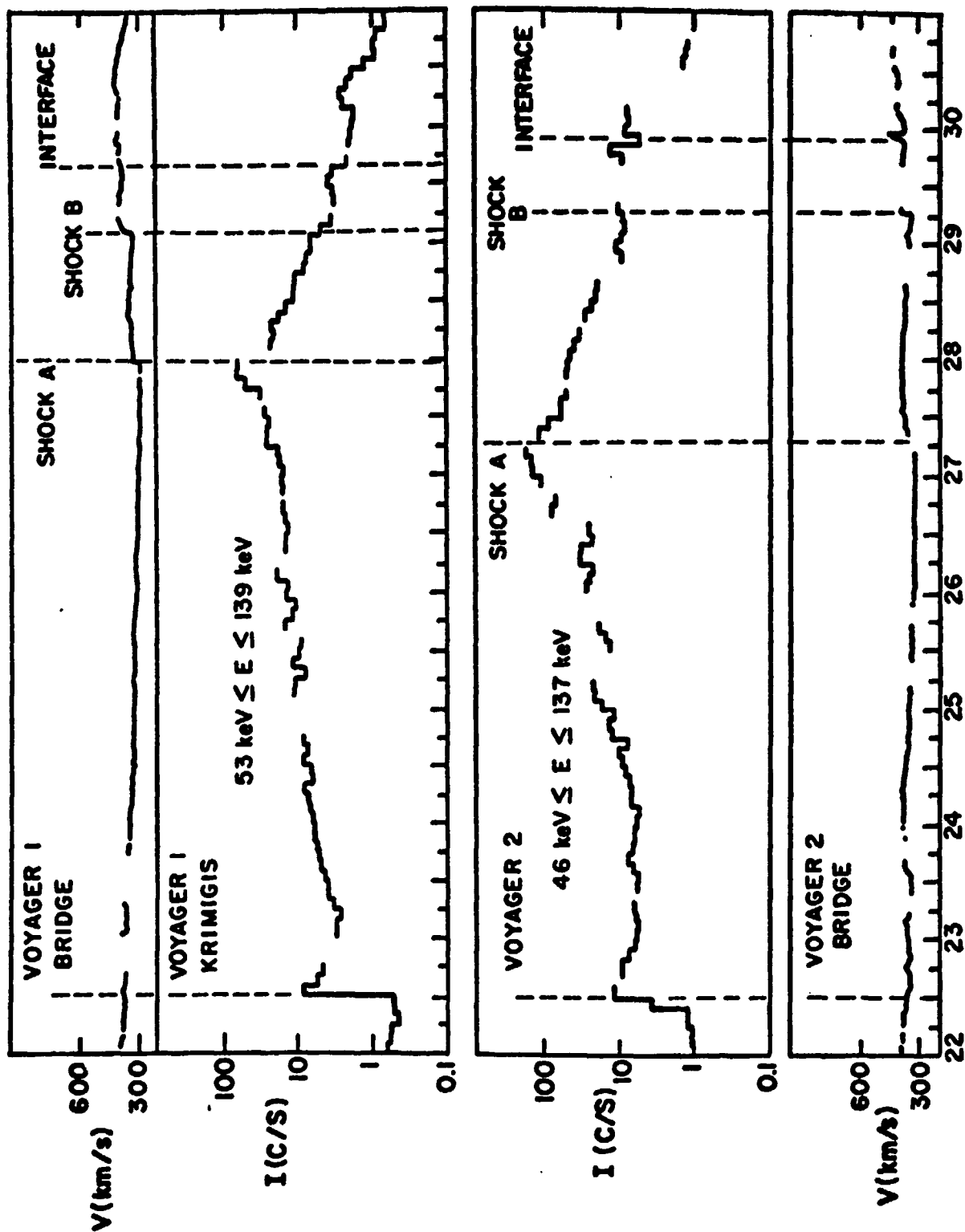


Figure 18



NOV 1977

Figure 19

U. of Iowa 79-41

The Volume Emissivity of
Type III Radio Bursts⁺

by

Robert L. Tokar and Donald A. Gurnett

October, 1979

Department of Physics and Astronomy
The University of Iowa
Iowa City, IA 52242

Submitted as a brief report to J. Geophys. Res.

⁺This research was supported by the National Aeronautics and Space Administration through Contracts NAS5-11431, NAS5-20093, Grant NGL-16-001-043, and by the U. S. Office of Naval Research through Contract N00014-76-C-0016.

UNCLASSIFIED

SECURITY CLASSIFICATION OF THIS PAGE (When Data Entered)

REPORT DOCUMENTATION PAGE		READ INSTRUCTIONS BEFORE COMPLETING FORM
1. REPORT NUMBER U. of Iowa 79-41	2. GOVT ACCESSION NO.	3. RECIPIENT'S CATALOG NUMBER
4. TITLE (and Subtitle) THE VOLUME EMISSIVITY OF TYPE III RADIO BURSTS		5. TYPE OF REPORT & PERIOD COVERED Progress, September, 1979
7. AUTHOR(s) R. L. Tokar and D. A. Gurnett		6. PERFORMING ORG. REPORT NUMBER
9. PERFORMING ORGANIZATION NAME AND ADDRESS Department of Physics and Astronomy The University of Iowa Iowa City, IA 52242		8. CONTRAST OR BRANT NUMBER(s) N00014-76-C-0016.
11. CONTROLLING OFFICE NAME AND ADDRESS Office of Naval Research Arlington, VA 22217		10. PROGRAM ELEMENT, PROJECT, TASK AREA & WORK UNIT NUMBERS
14. MONITORING AGENCY NAME & ADDRESS (if different from Controlling Office)		12. REPORT DATE September, 1979
		13. NUMBER OF PAGES 18
		15. SECURITY CLASS. (of this report) UNCLASSIFIED
		15a. DECLASSIFICATION/DOWNGRADING SCHEDULE
16. DISTRIBUTION STATEMENT (of this Report) Approved for public release; distribution is unlimited.		
17. DISTRIBUTION STATEMENT (of the abstract entered in Block 20, if different from Report)		
18. SUPPLEMENTARY NOTES To be published in <u>J. Geophys. Res.</u> , 1980		
19. KEY WORDS (Continue on reverse side if necessary and identify by block number) Type III Radio Bursts Emissivity		
20. ABSTRACT (Continue on reverse side if necessary and identify by block number) [See following page].		

DD FORM 1473
JAN 73EDITION OF 1 NOV 68 IS OBSOLETE
S/N 0103-014-60011

UNCLASSIFIED

SECURITY CLASSIFICATION OF THIS PAGE (When Data Entered)

ABSTRACT

The volume emissivity has been calculated for thirty-six type III solar radio bursts obtained from approximately 6.5 years of IMP 8 and ISEE 1 satellite data. Although the emissivities for these events vary over a large range, all the emissivities decrease rapidly with increasing heliocentric radial distance. The best fit power law for the emissivity, using the average power law index for all events analyzed, is $J = J_0 R^{-6.0}$, with $J_0 = 1.5 \times 10^{-24}$ watts m^{-3} ster $^{-1}$. This best fit emissivity is used to estimate the expected radial variation of the plasma oscillations responsible for the type III radio emission.

I. INTRODUCTION

Type III solar radio bursts are characterized by an emission frequency which decreases with increasing time. These bursts are produced by solar flare electrons traveling away from the sun along the interplanetary magnetic field lines. The decreasing emission frequency with increasing time is attributed to the decreasing electron plasma frequency encountered by the exciter electrons as they move outward away from the sun [Wild, 1950; Lin, 1970; Alvarez et al., 1972]. The generation of type III radio bursts is thought to be a two-step process in which electrostatic electron plasma oscillations are first produced by the energetic electron stream and are then converted to electromagnetic radiation by nonlinear interactions [Ginzburg and Zheleznyakov, 1958; Sturrock, 1961; Tidman et al., 1966; Papadopoulos et al., 1974; Smith, 1974]. For a review of low frequency type III bursts see, for example, Fainberg and Stone [1974]. Plasma oscillations associated with type III bursts are described by Gurnett and Anderson [1976, 1977] and Gurnett et al. [1978a].

The volume emissivity, which is the power emitted per unit volume per unit solid angle, is a fundamental quantity which characterizes all radio emission processes, including type III radio bursts. Because of the recent observations of electron plasma oscillations in association with type III bursts it is now possible to conduct quantitative evaluations of various mechanisms for generating the radio emission. Since

little is known concerning the emissivity of type III bursts, particularly in the low frequency range where direct comparisons with plasma oscillations are possible, it is the purpose of this paper to investigate the emissivity of some representative type III radio bursts. Particular attention will be given to the variation of the emissivity with heliocentric radial distance, since this variation can be directly compared with various generation mechanisms.

The type III events analyzed in this study were obtained from the Earth-orbiting IMP 8 and ISEE 1 satellites. The plasma wave instrumentation onboard IMP 8 and ISEE 1 are described by Gurnett [1974] and Gurnett et al. [1978b], respectively.

II. METHOD OF CALCULATING THE EMISSIVITY

The emissivity is calculated using the sun-centered coordinate system shown in Figure 1. The emissivity is defined as

$$J = \frac{\Delta P}{\Delta V \Delta \omega} \quad \text{watts m}^{-3} \text{ster}^{-1}, \quad (1)$$

where ΔP is the power radiated in volume ΔV into a solid angle $\Delta \omega$.

Since the angular distribution of the emitted radiation is not known, we will assume that the radiation is emitted isotropically (i.e., $\Delta \omega = 4\pi$).

To determine J we measure the spectral power flux at the Earth and compute ΔP using a $1/r^2$ law for the radial variation of the emitted radiation. The isotropy assumption and the simple propagation model used of course introduce an error, since any radiation propagating toward the sun will be reflected, thereby producing an anisotropy in the emitted radiation pattern. The error introduced is, however, at most a factor of two, which is small compared to the wide range of intensities observed from event to event. Also, the isotropy assumption does not affect the radial variation of the emissivity, since sources at all radial distances are treated equivalently.

To compute the power ΔP the distance from the source to the Earth must be determined. Since the source position cannot, in most cases, be determined by direct measurement a simple model is used for the trajectory of the type III source. The source is assumed to follow the magnetic

field in the solar wind starting from the flare location at the sun. The magnetic field model used is that of Parker [1958]: in the solar equatorial plane the magnetic field lines are Archimedian spirals, whereas in the meridian plane the field lines stay on a cone of constant heliographic latitude. The heliographic longitude of the associated flare, ϕ_0 , gives the heliographic longitude of the source region, ϕ , through the Archimedian spiral equation

$$\phi = \phi_0 - \left(\frac{\omega}{V_{sw}} \right) R \quad (2)$$

Here ω is the rotational velocity of the sun, V_{sw} is the solar wind velocity, taken as 400 km/sec, and R is the heliocentric radial distance to the source. R is related to the observed emission frequency using the emission level scale given by Fainberg and Stone [1974],

$$f = 66.8 R^{-1.315} \text{ MHz} \quad (3)$$

where f is the observed frequency of the type III burst and R is the heliocentric radial distance in solar radii. The position of the Earth above the solar equatorial plane is determined from a simple model for the Earth's orbit around the sun.

From the measured radiation intensity, I , at the time of maximum intensity the power radiated from the source, ΔP , in frequency interval Δf is calculated from

$$\Delta P = (4\pi r^2) I \Delta f \quad (4)$$

where r is the radial distance from the source to the Earth (see Figure 1). The volume of the source is determined by two factors, the angular size of the source as viewed from the sun, Ω , and the radial thickness ΔR . Since the electrons which produce the radio emission closely follow the interplanetary magnetic field lines, the angular size of the source as viewed from the sun is essentially constant, independent of radial distance from the sun. Since it is often not possible to determine the source size because of geometric considerations, we have assumed a half-angle for the source of 45° as viewed from the sun. The corresponding solid angle is $\Omega = 1.84$ ster. This source size is comparable to the source sizes measured by Baumbach et al. [1976] and Gurnett et al. [1978c], and is considered a reasonable estimate since both radio and charged particle measurements indicate that the source must be quite large. The relation of the radial thickness, ΔR , to the frequency interval, Δf , can be determined from Equation 3, which gives $\Delta R/R = 1.315 (\Delta f/f)$. Combining all of these factors, the volume of the source becomes

$$\Delta V = \Omega R^2 \Delta R = 1.315 \Omega R^3 \left(\frac{\Delta f}{f} \right) \quad (5)$$

and the emissivity is given by

$$J = \left(\frac{r^2 f}{1.315 \Omega R^3} \right) I \quad (6)$$

Since the emissivity is determined using average values for the solar wind parameters and since significant deviations from the average parameters may occur in specific cases, the approach taken is to analyze a large number of events and compute an average best fit emissivity, thereby hopefully averaging out the variations which may be present in individual cases. Although the absolute emissivity is probably uncertain by about a factor of two, mainly due to the difficulty in estimating the angular size of the source, the radial dependence of the emissivity is much more accurately determined since most of the parameters assumed are nearly independent of radial distance.

III. RESULTS AND DISCUSSION

Approximately 5 years of IMP 8 data and 1.5 years of ISEE 1 data were surveyed for type III bursts suitable for analyzing the emissivity. While type III bursts were frequently observed, two main factors limited the number of events used in this study: 1) clear burst maximums needed to be observed in at least three channels in order to give a reasonably accurate indication of the radial variation of the emissivity; and 2) for each event an associated solar flare had to be found in order to determine the trajectory of the source. Of a total of 117 events which showed clear burst maxima 54 had associated solar flares. Of these, 13 events were common to both satellites. Restricting the study to heliocentric distances less than 1.0 AU eliminated 3 events while 2 events were eliminated as being inconsistent. Consequently, 36 events were suitable for analysis. Table 1 contains the date, onset time, and flare coordinates for each event.

For each event the emissivity J was calculated as a function of the heliocentric radial distance R and fit to a power law of the form $J = J_0 R^{\alpha}$. In most cases a power law provided a good least square fit to the radial dependence, although in a few cases a substantial deviation from a power law was observed. In all cases the power law index α was negative, indicating a decreasing emissivity with increasing radial distance from the sun. Consult Table 1 for the derived J_0 and α values. The distribution of the power law indices obtained is shown by the

histogram of Figure 2. The highest frequency of occurrence of α falls in the interval from -4.0 to -6.0, and the average value of all the indices measured is $\bar{\alpha} = -6.0 \pm 1.9$. The standard deviation of the mean is 0.3. Figure 3 shows a composite summary of the emissivity for all the events analyzed. Points common to the same event are connected by a line. As can be seen, the emissivity varies over a large range from event to event. The dashed line shows the best fit of $\log J$ to $\log J_0 R^{-6.0}$. The best fit value for J_0 is 1.5×10^{-24} watts $m^{-3} \text{ster}^{-1}$.

It is clear from these results that the emissivity of low frequency type III radio bursts decreases very rapidly with increasing radial distance from the sun, with an average power law index of about -6.0. This decrease in the emissivity must be related to a corresponding decrease in the plasma oscillation intensity with increasing radial distance from the sun. From the currently available evidence on type III radio bursts the dominant emission at low frequencies is thought to be at the harmonic, $2f_p^-$, of the local electron plasma frequency [Fainberg et al., 1972; Haddock and Alvarez, 1973; Kaiser, 1975; Gurnett et al., 1978c]. In all current theories for harmonic emission the essential dependence of the emissivity on the electric field strength, E , of the plasma oscillations is $J \propto E^4$. Neglecting for the moment other weaker radial dependences, the $R^{-6.0}$ dependence of J would imply a $R^{-1.5}$ variation of E with radial distance from the sun. This radial variation of the plasma oscillation intensities is not nearly as steep as the $R^{-3.5}$ dependence reported recently by Gurnett et al. [1978a]. However, the plasma oscillation intensities given by Gurnett et al. [1978a] are based on so few points it is probably not possible to make a meaningful quantitative comparison until more plasma oscillation events are analyzed. Such a study is

currently under way. Nevertheless, it is interesting to note that the $R^{-1.5}$ variation implied by the above considerations agrees reasonably well with what would be expected for the saturation amplitude of plasma oscillations in the solar wind. Saturation effects are usually characterized by a dimensionless ratio of the electric field to plasma energy density, $E^2/8\pi nkT$, which reaches an approximately constant asymptotic value after the instability has grown into the nonlinear regime. Since the electron density varies approximately as $n \propto 1/R^2$, and the electron temperature varies approximately as $T \propto R^{-0.28}$ [Hundhausen, 1972], the saturation electric field strength should vary approximately as $E \propto R^{-1.14}$ if $E^2/8\pi nkT$ is constant, which is very close to the radial dependence estimated from the emissivity.

ACKNOWLEDGEMENTS

This research was supported by the National Aeronautics and Space Administration through Contracts NAS5-11431, NAS5-20093 and Grant NGL-16-001-043, and by the U. S. Office of Naval Research through Contract N00014-76-C-0016.

REFERENCES

- Alvarez, H., F. T. Haddock and R. P. Lin, Evidence for electron excitation of type III radio burst emission, Solar Phys., 26, 468, 1972.
- Baumback, M. M., W. S. Kurth and D. A. Gurnett, Direction-finding measurements of type III radio bursts out of the ecliptic plane, Solar Phys., 48, 361, 1976.
- Fainberg, J., L. G. Evans and R. G. Stone, Radio tracking of solar energetic particles through interplanetary space, Science, 178, 743, 1972.
- Fainberg, J. and R. G. Stone, Satellite observations of type III solar radio bursts at low frequencies, Space Sci. Rev., 16, 145, 1974.
- Ginzburg, V. L. and V. V. Zheleznyakov, On the possible mechanism of sporadic solar radio emission (radiation in an isotropic plasma), Sov. Astron., AJ2, 653, 1958.
- Gurnett, D. A., The Earth as a radio source: Terrestrial kilometric radiation, J. Geophys. Res., 79, 4227, 1974.
- Gurnett, D. A. and R. R. Anderson, Electron plasma oscillations associated with type III radio bursts, Science, 194, 1159, 1976.

- Gurnett, D. A. and R. R. Anderson, Plasma wave electric fields in the solar wind: Initial results from Helios 1, J. Geophys. Res., 82, 632, 1977.
- Gurnett, D. A., R. R. Anderson, F. L. Scarf and W. S. Kurth, The helio-centric radial variation of plasma oscillations associated with type III radio bursts, J. Geophys. Res., 83, 4147, 1978a.
- Gurnett, D. A., M. M. Baumbach and H. Rosenbauer, Stereoscopic direction finding analysis of a type III solar radio burst: Evidence for emission at $2f_p^-$, J. Geophys. Res., 83, 616, 1978c.
- Gurnett, D. A., F. L. Scarf, R. W. Fredricks and E. J. Smith, The ISEE-1 and ISEE-2 plasma wave investigation, Geoscience Electronics, GE-16, 225, 1978b.
- Haddock, F. T., and H. Alvarez, The prevalence of second harmonic radiation in type III bursts observed at kilometric wavelengths, Solar Phys., 29, 183, 1973.
- Hundhausen, A. J., Coronal Expansion and Solar Wind, Springer, Berlin Heidelberg N. York, 57, 1972.
- Kaiser, M. L., The solar elongation distribution of low frequency radio bursts, Solar Phys., 45, 181, 1975.

Lin, R. P., The emission and propagation of 40 keV solar flare electrons, Solar Phys., 12, 266, 1970.

Papodopoulos, K., M. L. Goldstein and R. A. Smith, Stabilization of electron streams in type III solar radio bursts, Astrophys. J., 190, 175, 1974.

Parker, E. N., Dynamics of the interplanetary gas and magnetic fields, Astrophys. J., 128, 664, 1958.

Smith, D. F., Type III radio bursts and their interpretation, Space Sci. Rev., 16, 91, 1974.

Sturrock, P. A., Spectral characteristics of type III solar radio bursts, Nature, 192, 58, 1961.

Tidman, D. A., T. J. Birmingham and H. M. Stainer, Line splitting of plasma radiation and solar radio outbursts, Astrophys. J., 146, 207, 1966.

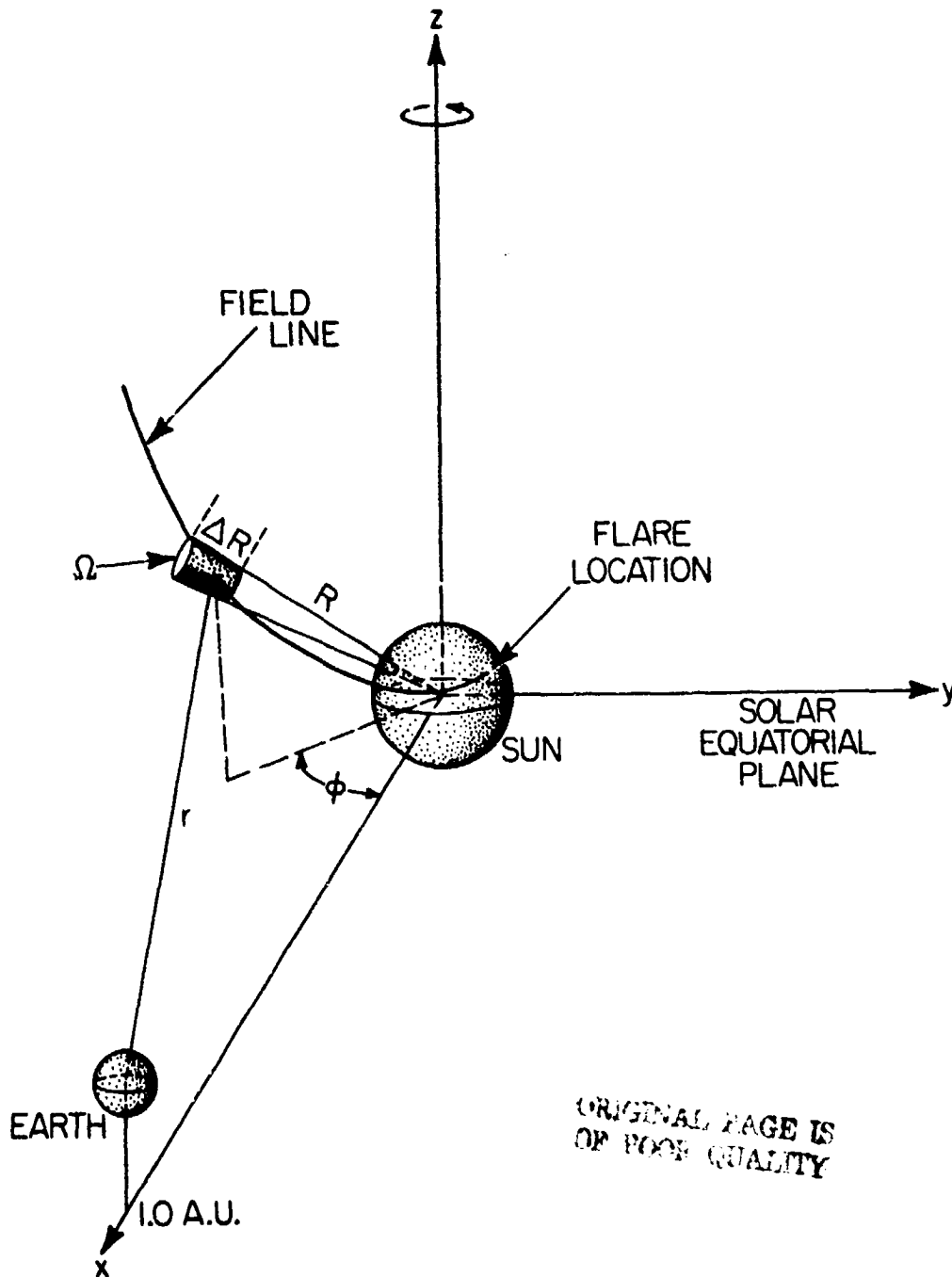
Wild, J. P., Observations of the spectrum of high-intensity solar radiation at metre wavelengths (III. Isolated bursts), Aust. J. Sci. Res., A3, 541, 1950.

TABLE 1

DATE	ONSET TIME (UT)	FLARE COORDINATES (Heliographic)	J_0	α
			$\frac{W}{m^2 - ster}$	
Dec. 23, 73	0800	S16 W35	6.84×10^{-25}	-5.8
Jan. 18, 74	0230	N4 W65	3.22×10^{-25}	-2.5
Apr. 5, 74	1800	S11 W35	5.73×10^{-25}	-4.4
May 8, 74	0100	S16 E3	2.57×10^{-26}	-4.5
May 9, 74	2300	S5 W45	1.41×10^{-26}	-5.3
Sept. 18, 74	0530	N9 W37	2.17×10^{-25}	-5.4
Sept. 18, 74	1130	N10 W42	2.16×10^{-25}	-5.2
Jan. 4, 77	1720	S22 W72	1.47×10^{-23}	-6.2
Oct. 10, 77	2035	N6 E10	9.51×10^{-25}	-6.8
Nov. 22, 77	1000	N23 W41	3.25×10^{-24}	-8.7
Dec. 7, 77	0330	S22 W16	7.42×10^{-23}	-5.3
Dec. 9, 77	0650	S24 W41	2.48×10^{-26}	-9.8
Dec. 23, 77	0630	N23 E6	8.93×10^{-28}	-11.0
Dec. 24, 77	1840	N22 W12	2.10×10^{-25}	-7.6
Jan. 6, 78	0730	N35 W4	3.52×10^{-24}	-3.7
Jan. 8, 78	0710	S12 W85	2.92×10^{-25}	-5.6
Feb. 11, 78	1430	N14 E6	5.12×10^{-23}	-8.5
Mar. 4, 78	1200	N18 E39	4.88×10^{-24}	-9.3
Mar. 12, 78	0210	N20 W69	9.15×10^{-24}	-4.7
Apr. 11, 78	1410	N22 W56	5.06×10^{-23}	-4.4
Apr. 18, 78	0100	N14 W45	6.10×10^{-22}	-5.6
May 6, 78	1635	N19 W53	2.20×10^{-24}	-5.1
May 13, 78	0750	S28 W70	1.90×10^{-23}	-5.6
May 22, 78	0200	S27 W44	1.96×10^{-21}	-2.8
May 31, 78	1620	N21 W56	4.21×10^{-24}	-8.4
Jun. 1, 78	1330	N21 W17	1.81×10^{-22}	-3.8
Jul. 1, 78	1145	N21 E65	1.35×10^{-25}	-4.3
Jul. 11, 78	1050	S20 W28	2.95×10^{-24}	-5.9
Sept. 8, 78	1815	N15 W64	2.39×10^{-24}	-4.7
Sept. 23, 78	1010	N34 W50	5.01×10^{-23}	-4.6
Oct. 5, 78	1405	S18 E4	1.31×10^{-26}	-7.5
Oct. 13, 78	1235	S18 W1	7.29×10^{-25}	-6.5
Oct. 31, 78	0915	N20 W36	2.70×10^{-26}	-7.3
Dec. 18, 78	1630	N11 E17	2.62×10^{-24}	-5.4
Feb. 18, 79	0650	N19 E16	7.57×10^{-27}	-7.8
Feb. 18, 79	1640	N18 W16	5.77×10^{-24}	-6.6

FIGURE CAPTIONS

- Figure 1 A perspective drawing showing the geometry used to calculate the emissivity of a type III burst source region. The spectral power flux at the Earth gives the power radiated out of the source region and this together with the volume of the source region gives the emissivity.
- Figure 2 A histogram of the power law indexes obtained from the 36 events analyzed. The highest frequency of occurrence is in the interval -4.0 to -6.0 , and the average index is -6.0 ± 1.9 . The standard deviation of the mean is 0.3 .
- Figure 3 A composite plot of the emissivity for the 36 events used in this study. Points common to one event are connected by a line and the best fit power law is shown by a dashed line. This plot shows that the emissivity decreases rapidly with increasing radial distance from the sun.



ORIGINAL PAGE IS
OF POOR QUALITY

Figure 1

A-679-902

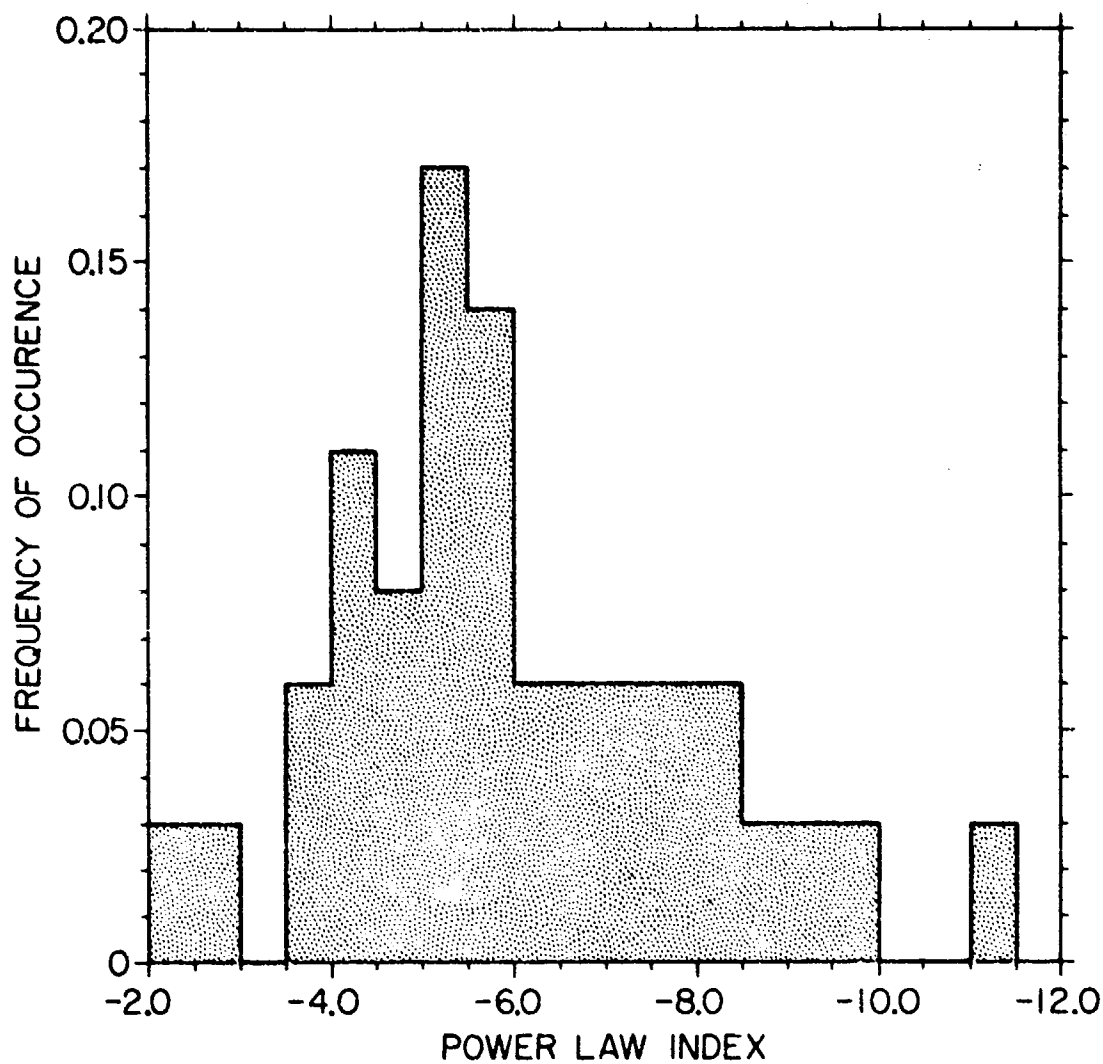


Figure 2

ORIGINAL PAGE 17
OF 1000 CYCLES

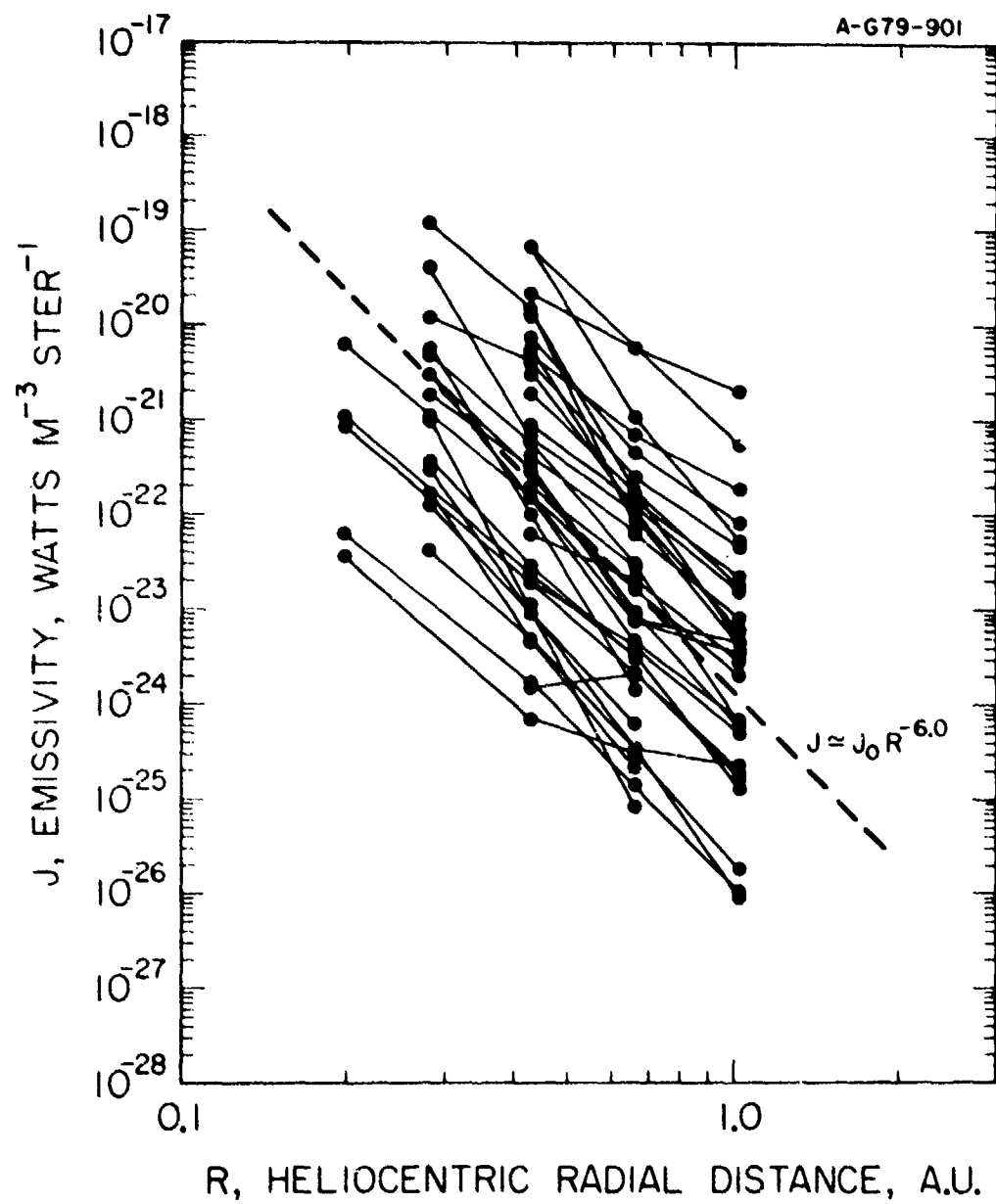


Figure 3